The Relation Between Temperature Shift and Helium Injection Rate in Dual-Ion Irradiation that Replicates Neutron-Irradiated Cavity Microstructures in Ferritic-Martensitic Steel T91

by

Valentin Pauly

A dissertation submitted in partial fulfillment
of the requirements for the degree of
Doctor of Philosophy
(Nuclear Engineering and Radiological Sciences)
in the University of Michigan
2025

Doctoral Committee:

Professor Emeritus Gary S. Was, Chair
Professor Kevin G. Field
Professor Emmanuelle Marquis
Dr. Stephen A. Taller, Oak Ridge National Laboratory

Valentin Mathieu Simon Pauly

vpauly@umich.edu

ORCID iD: 0000-0003-1034-6139

© Valentin Pauly 2025

All rights reserved.

Dedication

To my mother,

whose love and support are the foundation of all my achievements.

Acknowledgements

I start these acknowledgements by thanking my advisor, Prof. Gary S. Was, for the opportunity to conduct cutting-edge research in the field of radiation materials science. Through his guidance and insight, I have grown as both a researcher and a person. Although our discussions were mostly technical, I also learned a great deal from him about sharing my passion for research with others and believing in myself when things became difficult.

I would also like to thank my committee members, Prof. Kevin Field, Prof. Emmanuelle Marquis, and Dr. Stephen Taller, for their input and advice over the years, which improved this thesis.

I am grateful to the past members of the Was research group for sharing their experience with me: Dr. David Woodley, Dr. Rigel Hanbury, Dr. Katey Thomas, Dr. Drew Johnson, Dr. Gerrit VanCoevering, Dr. Peng Wang, Dr. Charlie Hirst, Dr. Aaron Penders, Dr. Zhexian Zhang, Dr. Gokul Subramanian, Dr. Abdullah Sinjlawi, and Connor Shamberger. I am particularly thankful to Dr. Stephen Taller, whose mentorship has been instrumental to my success over the years and who has been an inspiration throughout my graduate school career. I look forward to working with all of you in the future.

A very special acknowledgement goes to Logan Clowers for the brotherhood we have shared since starting our journeys together in 2019. Through the pandemic, classes, quals, thesis writing, and long hours in MIBL, I knew I could always count on his help and support. I am happy to call you my friend, and I look forward to what lies ahead of us.

My experience during graduate school would not have been as enjoyable were it not for the many friends I have made during my time at the University of Michigan: Mackenzie Warwick, Wyatt Peterson, John Waugh, Diego Macias, Diego Muzquiz, Brian Carpman, Colleen Campbell, Max Robbins, Jack Kuchta, Anwesha Saha, Elise Shauf, Yuhao Wang, Angel Chavira, Justin Hamil, Hangyu Li, Ethan Polselli, Crewse Peterson, Zhenyu Fei, Daniele Fatto Offidani, Robby Renfrow, Hannah Hutton, and Lauryn Kortman. I want to give a special mention to Matt Lynch for his efforts over the years to build a community among the NERS materials people. You have created a home away from home for many of us, and I feel lucky to call you my friend.

Thank you to the past and present staff members at the Michigan Ion Beam Laboratory: Dr. Zhijie Jiao, Dr. Fabian Naab, Dr. Prashanta Niraula, Alexander Flick, Dr. Ovidiu Toader, Thomas Kubley, Robert Hensley, and Catherine Nicoloff, who have constantly worked to improve the laboratory and make the user experience better. Without their hard work, the experiments presented in this thesis would not have been possible.

I also want to thank the staff at the Michigan Center for Materials Characterization for helping and training me on the various instruments of this world-class facility: Dr. Kai Sun, Bobby Kerns, Dr. Allen Hunter, Dr. Tao Ma, and Deanna Hecht.

Thank you to the DOE-NE IRP programs DE-NE0000639 and DE-NE0009419 for providing funding for this work, along with the University of Michigan College of Engineering for financial support of the Michigan Center for Materials Characterization. Thank you to the Low Activation Materials Development and Analysis (LAMDA) laboratory at ORNL for their assistance in providing access to BOR-60 neutron-irradiated materials and hot FIBs. Thank you to A. Schemer-Kohrn and R. Prabhakaran at PNNL for their assistance in providing access to the FFTF neutron-irradiated materials and hot FIBs.

To my dog, Sammy “The Samster” Doobidoo, who has no idea why I leave early in the morning and yet always greets me with the same excitement when I get home. Treats and pets cannot repay the joy she has brought me over the past two years.

I would not be where I am now without the support of my family. My parents, Marie-Odile and Dominique Pauly, have always kindled my curiosity and encouraged me to pursue new adventures, even when it meant letting me move across the ocean and miss a few Christmases. I now recognize the sacrifices that meant for my mom, and I am grateful for your courage. My brothers, Mathieu and Simon, whom I have always looked up to, have been there to support me and have shaped me into the man I am today.

And lastly, I want to thank my girlfriend, Gabriella Bruno, for the support and love you have given me. Words cannot describe how grateful I am to have you in my life. When times were hard and hours in MIBL felt endless, your company always lifted my spirits, and you made me feel heard and supported. You are an example of kindness to others, and I strive to be a better person because of you. I cannot wait for the next chapter of our life together.

Table of Contents

Dedication ii

Acknowledgements iii

List of Tables x

List of Figures xiv

List of Appendices xxvii

Abstract xxviii

Chapter 1 Introduction 1

Chapter 2 Background 6

2.1 Ferritic-Martensitic Steels 6

2.1.1 Microstructure: Common Phases and Heat Treatments 7

2.1.2 Mechanical Properties 13

2.2 Radiation Effects in Ferritic Martensitic Steels 14

2.2.1 Cavities and swelling 15

2.2.2 Dislocation loops 42

2.2.3 Radiation-induced segregation and phase changes 54

2.3 Ion irradiation as a surrogate for neutron irradiation 65

2.3.1 Difference in damage rate 65

2.3.2 Difference in particle type 69

2.3.3 Other aspects 71

2.3.4 Direct comparison between ion and neutron irradiations 75

Chapter 3 Objective 77

Chapter 4 Experimental Procedures and Modeling 79
4.1 Alloy and Sample Preparation 79
4.2 Dual-Ion Irradiations 82
4.2.1 Ion Irradiation Experiments 82
4.2.2 SRIM Damage and Helium Implantation Calculations 84
4.2.3 Irradiation Stage 86
4.2.4 The Multi-Beam Chamber 88
4.2.5 Irradiation Procedure 90
4.3 Neutron Irradiations 95
4.3.1 BOR-60 Reactor 95
4.3.2 Fast Flux Test Facility (FFTF) 96
4.4 Post-Irradiation Characterization 97
4.4.1 TEM Specimen Preparation 97
4.4.2 TEM Imaging and Characterization 99
4.4.3 Determination of Valid Region of Analysis 116
4.5 Model for cavity microstructure evolution 119
4.5.1 Mean-field rate theory 119
4.5.2 Description of the model 121
Chapter 5 Experimental Results 135
5.1 Pre-irradiated microstructure 135
5.2 Irradiation conditions 136
5.3 BOR-60 139
5.3.1 Cavity microstructures 139
5.3.2 Dislocation loop microstructures 146
5.3.3 Radiation-induced segregation 150

5.3.4 Radiation-induced precipitation 158
5.4 Dual-ion irradiation companion to BOR-60 162
5.4.1 Cavity microstructures 162
5.4.2 Dislocation loop microstructures 169
5.4.3 Radiation-induced segregation 174
5.4.4 Radiation-induced precipitation 180
5.5 FFTF 186
5.5.1 Cavity microstructures 186
5.5.2 Dislocation loop microstructures 190
5.5.3 Radiation-induced segregation 192
5.5.4 Radiation-induced precipitation 197
5.6 Dual-ion irradiation companion to FFTF 201
5.6.1 Cavity microstructures 201
5.6.2 Dislocation loop microstructures 207
5.6.3 Radiation-induced segregation 209
5.6.4 Radiation-induced precipitation 214
Chapter 6 Discussion 218
6.1 Comparison of BOR-60 and dual-ion-irradiated microstructures 218
6.1.1 Comparison of BOR-60-irradiated microstructure at 369-376°C, 450-453°C and 515-517°C and companion dual-ion irradiations 219
6.1.2 The special case of BOR-60-irradiated microstructure at 402-404°C and companion dual-ion irradiation 234
6.2 Rate theory model fitting 240
6.2.1 Initial fit using dual ion irradiation at 445°C 241
6.2.2 Fit using BOR-60 irradiation at 369-376°C 248
6.2.3 Optimizing the fit for BOR-60 and dual-ion collectively 251

6.3 Validation of the model on additional dual-ion irradiations 255
6.4 Dual-ion and FFTF irradiations 264
6.4.1 Comparison of FFTF and dual-ion-irradiated microstructures 264
6.4.2 Modeling of temperature excursion effect on size distribution 285
6.5 Justification for temperature shift and increase in helium production rate 295
Chapter 7 Conclusions 309
Chapter 8 Future Work 312
Appendices 316
Bibliography 333

List of Tables

Table 2.1: Precipitation in normalized-and-tempered, aged and creep-rupture tested high-chromium martensitic steels [5]. 12

Table 2.2: Expressions for the dose rate dependence of temperature shift under various limiting conditions of point defect removal [107]. 66

Table 4.1: Composition (wt%) of T91 heat 30176 provided by PNNL and Luvak [13]. 80

Table 4.2: Irradiation conditions for BOR-60 reactor specimens. 96

Table 4.3: Irradiation history for FFTF reactor specimens. 97

Table 4.4: Molar mass (g/mol) of elements in T91 heat 30176. 114

Table 4.5: Diffusion coefficients in the cavity growth rate equation. 124

Table 4.6: Parameters used in the cavity growth rate equation. 124

Table 4.7: Radius, helium content and helium pressure for cavities at equilibrium [215]. 126

Table 4.8: Parameters used to calculate vacancy concentration at cavity surfaces. 127

Table 4.9: Fitting coefficients for the capture efficiency equations. 129

Table 4.10: Sink strengths in the microstructure. 131

Table 4.11: Coefficients used to calculate point defect concentrations and helium partitioning. 132

Table 4.12: Parameters used to calculate point defect concentrations and helium partitioning. 132

Table 5.1: Segregation behavior at grain boundaries in unirradiated T91. 136

Table 5.2: BOR-60 conditions and sample designations. 137

Table 5.3: FFTF conditions and sample designations. 137

Table 5.4: Dual-ion conditions and sample designations. 138

Table 5.5: Cavity microstructures of BOR-60-irradiated T91 30176. 144

Table 5.6: Dislocation loop microstructures of BOR-60-irradiated T91 30176. 148

Table 5.7: Radiation-induced segregation of BOR-60-irradiated T91 30176. 152

Table 5.8: Ni/Si-cluster microstructures of BOR-60-irradiated T91 30176. 160

Table 5.9: Cavity microstructures of dual-ion-irradiated T91 30176. 167

Table 5.10: Dislocation loop microstructures of dual-ion-irradiated T91. 172

Table 5.11: Radiation-induced segregation of dual-ion-irradiated T91 30176. 176

Table 5.12: Ni/Si-cluster microstructures of dual-ion-irradiated T91 30176. 183

Table 5.13: Cavity microstructures of FFTF-irradiated T91 30176. 189

Table 5.14: Dislocation loop microstructures of FFTF-irradiated T91 30176. 192

Table 5.15: Radiation-induced segregation of FFTF-irradiated T91 30176. 194

Table 5.16: Ni/Si-cluster microstructures of FFTF-irradiated T91 30176. 199

Table 5.17: Cavity microstructures of dual-ion-irradiated T91 30176. 205

Table 5.18: Dislocation loop microstructures of dual-ion-irradiated T91 30176. 209

Table 5.19: Radiation-induced segregation of dual-ion-irradiated T91 30176. 211

Table 5.20: Ni/Si-cluster microstructures of dual-ion-irradiated T91 30176. 216

Table 6.1: Cavity microstructures of irradiated T91 30176 for BOR-60 conditions and companion dual-ion irradiations. 224

Table 6.2: Dislocation loop microstructures for BOR-60 samples and companion dual-ion irradiations. 227

Table 6.3: Radiation-induced segregation of irradiated T91 30176 for BOR-60 conditions and companion dual-ion irradiations. 229

Table 6.4: Ni/Si-cluster microstructures of irradiated T91 30176 for BOR-60 conditions and companion dual-ion irradiations. 232

Table 6.5: Cavity microstructures of irradiated T91 30176 for BOR-60 conditions and dual-ion irradiations. 239

Table 6.6: Dislocation loop microstructures for BOR-60 samples and companion dual-ion irradiations. 240

Table 6.7: Cavity densities, swelling and nucleation rates of regularized BOR-60 and dual-ion conditions. 244

Table 6.8: Comparison of predicted vs. measured (regularized) dual-ion- and BOR-60-irradiated cavity microstructures. 247

Table 6.9: Comparison of predicted vs. measured (regularized) dual-ion- and BOR-60-irradiated cavity microstructures. 250

Table 6.10: Comparison of predicted vs. measured (regularized) dual-ion- and BOR-60-irradiated cavity microstructures. 254

Table 6.11: Cavity densities, swelling and nucleation rates of regularized dual-ion conditions. 258

Table 6.12: Comparison of predicted vs. measured (regularized) dual-ion- and BOR-60-irradiated cavity microstructures. 263

Table 6.13: Irradiation history for FFTF reactor specimens considering annealing during MOTA-1C (crossed out values are not considered in the effective temperature, damage level and damage rate). 268

Table 6.14: Cavity microstructures of irradiated T91 30176 for FFTF conditions and companion dual-ion irradiations. 277

Table 6.15: Dislocation loop microstructures of irradiated T91 30176 for FFTF samples and companion dual-ion irradiations. 278

Table 6.16: Radiation-induced segregation of irradiated T91 30176 for all FFTF conditions and companion dual-ion irradiations. 281

Table 6.17: Ni/Si-cluster microstructures of irradiated T91 30176 for all FFTF conditions and companion dual-ion irradiations. 284

Table 6.18: Cavity densities, swelling and nucleation rates of regularized FFTF conditions. ... 286

Table 6.19: Comparison of predicted vs. measured FFTF-irradiated cavity microstructures. ... 294

Table 6.20: Simulated BOR-60-equivalent cavity microstructures in various irradiation conditions. 301

Table 6.21: Simulated FFTF-equivalent cavity microstructures in various irradiation conditions. 308

Appendix Table 1: Complete list of cavity microstructures of irradiated T91 30176. 321

Appendix Table 2: Significance of temperature (+/- 1°C) in the prediction of the BOR-60-irradiated cavity microstructure at 369°C:32-72dpa, 0.77appmHe/dpa. 326

Appendix Table 3: Significance of helium rate (+/- 10^{-4}) in the prediction of the BOR-60-irradaited cavity microstructure at 369°C:32-72dpa, 0.77appmHe/dpa. 327

Appendix Table 4: Comparison of predicted vs. measured (regularized) BOR-60-irradiated cavity microstructures to 72 dpa at multiple temperature-helium-rate combinations. 329

Appendix Table 5: Significance of key parameters in the prediction of the irradiated cavity microstructure. 331

List of Figures

Figure 1.1: Overview of operating temperatures, displacement damage regimes and corrosion susceptibilities for structural materials in current and future reactors [4]. 2

Figure 2.1: Effect of chromium on the constitution of Fe-Cr-C alloys containing 0.1% C; note that $(CrFe)_4C$ is $M_{23}C_6$ carbide [32]..... 9

Figure 2.2: Typical microstructure of ferritic-martensitic steels after tempering..... 13

Figure 2.3: (a) Void swelling as a function of local damage level averaged over selected depth intervals of 200 nm thickness with swelling rates of 0.1 and 0.2%/dpa included on the figure for comparison. (b) Plot of the average void radius and concentration as a function of local dpa for the depth region of 400 nm-600 nm. [56]. 19

Figure 2.4: Effect of damage level on void diameter in 5 MeV Fe^{2+}-irradiated HT9 at 440, 460 and 480°C with 10 appm He pre-implanted [57]..... 20

Figure 2.5: Cavity size distribution for dual-ion-irradiated T91 at 445°C with 4 appm He/dpa as a function of damage level [17]. 21

Figure 2.6: Void (a) diameter and (b) number density as function of damage in 5 MeV Fe^{2+}-irradiated HT9, T91 and T92 at 460°C with 10 appm He pre-implanted [60]. 22

Figure 2.7: Swelling in HT9 heat 84425 irradiated with 5 MeV Fe^{2+} with pre-implanted He versus damage curve calculated with no corrections to the damage or region of interest analyzed [61]..... 22

Figure 2.8: Swelling in nickel as a function of irradiation temperature for a fluence of 5×10^{19} n/cm^2 [6]..... 24

Figure 2.9: Size distribution of cavities for T91 irradiated in BOR-60 [13]. 25

Figure 2.10: Cavity size distribution for dual-ion-irradiated T91 to ~ 16 dpa with 4 appm He/dpa as a function of temperature [17]. 27

Figure 2.11: Average cavity diameter (a), density (b) and swelling (c) for cavities greater than 2 nm in diameter for dual ion-irradiated T91 with 4 appm He/dpa and BOR-60-irradiated T91 [16]. 27

Figure 2.12: Comparison of the (a) cavity size (diameters) and (b) density in ion-irradiated Fe and Fe-Cr alloys at 400°C-550°C [63]. 28

Figure 2.13: Dependence of cavity swelling on irradiation temperature in dual-ion-irradiated Fe and Fe-Cr alloys [63]. 29

Figure 2.14: Compilation of literature data to show the effect of the helium/dpa ratio on (a) average cavity size, (b) average cavity density, and (c) swelling [17]. 31

Figure 2.15: Cavity size distribution for multiple helium injection rate for dual-ion-irradiated T91 [17]. 32

Figure 2.16: Average void diameter (a), void density (b) and swelling (c) as a function of helium co-injection rate (appm He/dpa) for dual-ion-irradiated T91 at 445°C at various damage levels [67]. 33

Figure 2.17: a) Average cavity diameter, b) number density, and c) swelling as a function of damage in T91 for pre-implanted He levels of 0, 1, 10, 100, and 1000 appm [68]. 34

Figure 2.18: Variation of swelling as a function of Cr concentration in high-purity Fe and Fe-Cr dual-ion-irradiated samples [63]. 36

Figure 2.19: Cavity size distribution for multiple damage rate in dual-ion-irradiated T91 [17]. . 38

Figure 2.20: Cavity size distribution for Fe-10Cr implanted with 300 appm He, annealed, and irradiated to 30 dpa [77]. 41

Figure 2.21: (a) Dislocation loop diameter (blue) and loop number density (red) for HT9, and (b) Loop (green) and network (black) line length for HT9. Results from T91 and T92 are plotted at 350 dpa only [60]. 44

Figure 2.22: Dislocation loop densities and diameters for a⟨100⟩ and a/2⟨111⟩ loops are plotted as a function of damage for the 10 appm He condition [68]. 45

Figure 2.23: Dislocation size distribution after irradiation of T91 in BOR-60 [13]. 46

Figure 2.24: (a) Average dislocation loop diameter and (b) dislocation loop density as a function of irradiation temperature for BOR60-irradiated and dual-ion-irradiated T91 [16,17]. 47

Figure 2.25: Average dislocation loop size and dislocation loop density as a function of helium concentration for proton-irradiated T91 at different damage levels [81]. 49

Figure 2.26: (a) Average dislocation loop diameter and (b) loop density as a function of helium injection rate for dual-ion-irradiated T91 [17]. 49

Figure 2.27: Average dislocation loop diameter (a) and dislocation loop density (b) for dual-ion-irradiated T91 at 445°C at 17 (blue) and 0, 0.02, 0.2 and 4 appm He/dpa and at 0.2 appm He/dpa at 17 (blue), 50 (red) and 150 (black) dpa [67]. 50

Figure 2.28: Densities and diameters for a⟨100⟩ dislocation loops in ion-irradiated T91 heat C2269 as a function of helium content at 150 dpa [68]. 51

Figure 2.29: Comparison of (a) dislocation density, (b) dislocation loop number density, and (c) average diameter of the dislocation loops in Fe-10Cr irradiated at ~500°C with helium production rate of 0.1–50 appm He/dpa [69]. 52

Figure 2.30: (a) Average dislocation loop diameter and (b) loop density as a function of damage rate for dual-ion-irradiated T91 [17]. 53

Figure 2.31: Irradiation damage level and temperature effect on enrichment of Cr, Ni and Si at the grain boundary in BOR-60-irradiated T91 [13]. 55

Figure 2.32: RIS of several elements in T91 irradiated with 2 MeV protons at 3 dpa [96]. 56

Figure 2.33: Irradiation damage level and temperature effect on the segregation of (a) Cr, (b) Ni, and (c) Si at the grain boundary for dual-ion-irradiated and BOR-60 irradiated T91 [16]. 57

Figure 2.34: Length (closed markers) and volume fraction (open markers) of M_2X formed at 460°C from 250 to 650 dpa in HT9, T91 and T92 [60]. 61

Figure 2.35: Number density, diameter, and volume fraction of G-phase plotted as a function of damage with 10 appm He pre-implanted in ion-irradiated T91 [68]. 62

Figure 2.36: Calculated average vacancy diffusion distance plotted against the Ni/Si cluster density for dual-ion-irradiated T91 at 445°C with BOR-60-irradiated T91 at 376°C [102]. 64

Figure 2.37: Description of damage morphologies for irradiation with various particles of the same energy. T is the average energy transfer per PKA and ε is the efficiency of producing freely migrating defects available to affect radiation-induced segregation [105]. 69

Figure 2.38: Calculated surviving defect fraction (normalized to the NRT dpa) versus PKA energy for displacement events in Fe at 100 K [103]. 71

Figure 4.1: Iron and helium depth profiles for dual ion irradiations using (a) 5 MeV Fe^{2+} ions and degraded 2.85 MeV He^{2+} ions to 16.6 dpa at 600 nm for 4 appm He/dpa or (b) 9 MeV Fe^{3+} ions and degraded 3.42 MeV He^{2+} to 16.6 dpa at 1200 nm in alloy T91. 83

Figure 4.2: Displacement rates as a function of depth for (blue) 5 MeV Fe^{2+} and (red) 9 MeV Fe^{3+} in T91. 85

Figure 4.3: Schematic of the stage used for dual-ion irradiations (reproduced from [149]). 87

Figure 4.4: Picture of a stage (four half-bars and two guide bars) ready to be irradiated. 87

Figure 4.5: Schematic of the Multi-Beam Chamber with beamlines (adapted from [17]). 88

Figure 4.6: Laser-illuminated samples revealing the irradiation marks. Reflections of the laser are also visible on the copper sheet on the right but do not represent the path of the beam. 91

Figure 4.7: (a) Laser on the alumina after alignment on the stage. (b) Beam on the alumina after moving the slits to match the position of the laser. 92

Figure 4.8: Example of the current intensity profile of the defocused heavy-ion beam. Red dashed lines delimit +/-10% from the average of the signal. 92

Figure 4.9: Example of the change in helium current with the rotation of the foil. 93

Figure 4.10: Example (a) HAADF and (b) BF images for T91 irradiated in FFTF. 101

Figure 4.11: Example (a) underfocused (-1 μm) and (b) overfocused (+1 μm) images of T91 after dual-ion irradiation to 72 dpa at 460°C. 102

Figure 4.12: Schematic of dislocation loop orientations when observing down the [001] zone axis adapted from [172]. 108

Figure 4.13: Example on-zone [001] STEM-BF image for the characterization of dislocation loops. 109

Figure 4.14: Calculated temperature- and depth-dependent regions affected by the free surface and injected ions for Fe-10%Cr steel irradiated with 5 MeV Fe^{+} ions at 10^{-3} dpa/s to dose levels of 50–500 dpa [103]. 117

Figure 4.15: Diagram of the cavity size distribution prediction model. 123

Figure 4.16: Capture efficiencies of cavities of diameter (a) 1 nm and (b) 1.5 nm as a function of helium-to-vacancy ratio for different temperatures [215]. 128

Figure 5.1: Swelling of BOR-60-irradiated T91 30176 as a function of damage level. 140

Figure 5.2: (a) Void density and (b) average void diameter of BOR-60-irradiated T91 30176 as a function of damage level. 140

Figure 5.3: (a) Bubble density and (b) average bubble diameter of BOR-60-irradiated T91 30176 as a function of damage level. 141

Figure 5.4: Cavity size distributions of BOR-60-irradiated T91 30176 at 369-375°C to (a) 16 dpa, (b) 32 dpa, (c) 47 dpa and (d) 72 dpa. 141

Figure 5.5: Cavity size distributions of BOR-60-irradiated T91 30176 at 402-404°C to (a) 17 dpa, (b) 29 dpa and (c) 86 dpa. 142

Figure 5.6: Cavity size distributions of BOR-60-irradiated T91 30176 at 450-453°C to (a) 19 dpa and (b) 32 dpa. 142

Figure 5.7: Cavity size distributions of BOR-60-irradiated T91 30176 at 515-517°C to (a) 15 dpa and (b) 25 dpa. 143

Figure 5.8: STEM-HAADF micrographs of BOR-60-irradiated T91 30176 at 369-375°C and 402-404°C. 145

Figure 5.9: (a) Loop density and (b) average loop diameter of BOR-60-irradiated T91 30176 as a function of damage level. 146

Figure 5.10: Dislocation loop size distributions of BOR-60-irradiated T91 30176 at 369-376°C to (a) 16 dpa, (b) 32 dpa, (c) 47 dpa and (d) 72 dpa. 147

Figure 5.11: Dislocation loop size distributions of BOR-60-irradiated T91 30176 at 404°C to 17 dpa. 147

Figure 5.12: STEM BF micrographs of BOR-60-irradiated T91 30176 at 369-376°C and 402-404°C. Yellow arrows indicate some a⟨100⟩ loops and red arrows indicate some a/2⟨111⟩ loops. 149

Figure 5.13: (a) Fe, (b) Cr, (c) Ni and (d) Si enrichments at grain boundaries of BOR-60-irradiated T91 30176. 151

Figure 5.14: EDS (wt%) maps of Fe, Cr, Ni and Si of BOR-60-irradiated T91 30176 at (a) 369°C:16dpa and (b) 372°C:32dpa. 153

Figure 5.15: EDS (wt%) maps of Fe, Cr, Ni and Si of BOR-60-irradiated T91 30176 at (a) 376°C:47dpa and (b) 375°C:72dpa. 154

Figure 5.16: EDS (wt%) maps of Fe, Cr, Ni and Si of BOR-60-irradiated T91 30176 at (a) 404°C:17dpa, (b) 402°C:29dpa and (c) 404°C:86dpa. 155

Figure 5.17: EDS (wt%) maps of Fe, Cr, Ni and Si of BOR-60-irradiated T91 30176 at (a) 453°C:19dpa and (b) 450°C:32dpa. 156

Figure 5.18: EDS (wt%) maps of Fe, Cr, Ni and Si of BOR-60-irradiated T91 30176 at (a) 517°C:15dpa and (b) 515°C:25dpa. 157

Figure 5.19: (a) Cluster density, (b) average cluster diameter and (c) volume fraction of BOR-60-irradiated T91 30176. 158

Figure 5.20: Cluster size distributions of BOR-60-irradiated T91 30176 at 369-376°C to (a) 16 dpa, (b) 32 dpa, (c) 47 dpa and (d) 72 dpa. 159

Figure 5.21: Cluster size distributions of BOR-60-irradiated T91 30176 at 404°C to 17dpa. ... 159

Figure 5.22: EDS Ni map (wt%) of BOR-60-irradiated T91 30176 at (a) 369°C:16dpa, (b) 372°C:32dpa, (c) 376°C:47dpa and (d) 375°C:72dpa. 160

Figure 5.23: EDS Ni map (wt%) of BOR-60-irradiated T91 30176 at (a) 404°C:17dpa, (b) 402°C:29dpa and (c) 402°C:86dpa. 161

Figure 5.24: Swelling of dual-ion-irradiated T91 30176 as a function of damage level. 163

Figure 5.25: (a) Void density and (b) average void diameter of dual-ion-irradiated T91 30176 as a function of damage level. 163

Figure 5.26: (a) Bubble density and (b) average bubble diameter of dual-ion-irradiated T91 30176 as a function of damage level. 164

Figure 5.27: Cavity size distributions of dual-ion-irradiated T91 30176 at 445°C to (a) 16.6 dpa, (b) 35 dpa, (c) 54 dpa and (d) 72 dpa. 164

Figure 5.28: Cavity size distributions of dual-ion-irradiated T91 30176 at 460°C to (a) 16.6 dpa, (b) 33 dpa and (c) 72 dpa. 165

Figure 5.29: Cavity size distributions of dual-ion-irradiated T91 30176 at 520°C to (a) 16.6 dpa and (b) 28 dpa. 165

Figure 5.30: Cavity size distributions of dual-ion-irradiated T91 30176 at 570°C to (a) 15.4 dpa and (b) 28 dpa. 166

Figure 5.31: STEM HAADF micrographs of dual-ion-irradiated T91 30176 at 445°C and 460°C. The dashed lines indicate the depth of interest for the dual-ion-irradiated samples. 168

Figure 5.32: (a) Loop density and (b) average loop diameter of dual-ion-irradiated T91 30176 as a function of damage level. 169

Figure 5.33: (a) Loop density and (b) average loop diameter of dual-ion-irradiated T91 30176 as a function of temperature. 170

Figure 5.34: Dislocation loop size distributions of dual-ion-irradiated T91 30176 at 445°C to (a) 16.6 dpa, (b) 35 dpa, (c) 54 dpa and (d) 72 dpa. 170

Figure 5.35: Dislocation loop size distributions of dual-ion-irradiated T91 30176 at 460°C to (a) 16.6 dpa, (b) 33 dpa and (c) 72 dpa. 171

Figure 5.36: STEM BF micrographs of dual-ion-irradiated T91 30176 at 445°C and 460°C. Yellow arrows indicate some a⟨100⟩ loops and red arrows indicate some a/2⟨111⟩ loops. 173

Figure 5.37: (a) Fe, (b) Cr, (c) Ni and (d) Si enrichments at grain boundaries of dual-ion-irradiated T91 30176. 175

Figure 5.38: EDS (wt%) maps of Fe, Cr, Ni and Si of dual-ion-irradiated T91 30176 at 445°C:3.1-4.3appmHe/dpa to (a) 16.6 dpa, (b) 54 dpa and (c) 70 dpa. 177

Figure 5.39: EDS (wt%) maps of Fe, Cr, Ni and Si of dual-ion-irradiated T91 30176 at 460°C:3.1-4.3appmHe/dpa to (a) 33 dpa and (b) 72 dpa. 178

Figure 5.40: EDS (wt%) maps of Fe, Cr, Ni and Si of dual-ion-irradiated T91 30176 at 520°C:3.2-4.3appmHe/dpa to (a) 16.6 dpa and (b) 28 dpa and (c) at 570°C:4.3appmHe/dpa to 28 dpa. 179

Figure 5.41: (a) Cluster density, (b) average cluster diameter and (c) volume fraction of dual-ion-irradiated T91 30176. 180

Figure 5.42: Cluster size distributions of dual-ion-irradiated T91 30176 at 445°C to (a) 16.6 dpa, (b) 35 dpa, (c) 54 dpa and (d) 70 dpa. 181

Figure 5.43: Cluster size distributions of dual-ion-irradiated T91 at 460°C to (a) 16.6 dpa, (b) 33 dpa, and (c) 72 dpa. 182

Figure 5.44: EDS Ni map (wt%) of dual-ion-irradiated T91 30176 at 445°C:3.1-4.3appmHe/dpa to (a) 16.6 dpa, (b) 35 dpa, (c) 54 dpa and (d) 70 dpa. 184

Figure 5.45: EDS Ni map (wt%) of dual-ion-irradiated T91 30176 at 460°C:3.1-4.3appmHe/dpa to (a) 16.6 dpa, (b) 33 dpa and (c) 72 dpa. 185

Figure 5.46: Swelling of FFTF-irradiated T91 30176 as a function of damage level. 186

Figure 5.47: (a) Void density and (b) average void diameter of FFTF-irradiated T91 30176 as a function of damage level. 187

Figure 5.48: (a) Bubble density, (b) average bubble diameter of FFTF-irradiated T91 30176 as a function of damage level. 187

Figure 5.49: Cavity size distributions of FFTF-irradiated T91 30176 to (a) 73 dpa, (b) 151 dpa, (c) 170 dpa and (d) 184 dpa. 188

Figure 5.50: STEM HAADF micrographs of FFTF-irradiated T91 30176. 189

Figure 5.51: (a) Loop density and (b) average loop diameter of FFTF-irradiated T91 30176 as a function of damage level. 190

Figure 5.52: STEM BF micrographs of FFTF-irradiated T91 30176. 191

Figure 5.53: (a) Fe, (b) Cr, (c) Ni and (d) Si enrichments at grain boundaries of FFTF-irradiated T91 30176. 193

Figure 5.54: EDS (wt%) maps of Fe, Cr, Ni and Si of FFTF-irradiated T91 30176 at (a) 407°C:73dpa and (b) 415°C:151dpa. 195

Figure 5.55: EDS (wt%) maps of Fe, Cr, Ni and Si of FFTF-irradiated T91 30176 at (a) 415°C:170dpa and (b) 415°C:184dpa. 196

Figure 5.56: (a) Cluster density, (b) average cluster diameter and (c) volume fraction of FFTF-irradiated T91 30176. 198

Figure 5.57: Cluster size distributions of FFTF-irradiated T91 30176 to (a) 73 dpa, (b) 151 dpa, (c) 170 dpa and (d) 184 dpa. 199

Figure 5.58: EDS Ni map (wt%) of FFTF-irradiated T91 30176 at (a) 407°C:73dpa, (b) 415°C:151dpa, (c) 415°C:170dpa and (d) 415°C:184dpa. 200

Figure 5.59: Swelling of dual-ion-irradiated T91 30176 as a function of damage level. 202

Figure 5.60: (a) Void density and (b) average void diameter of dual-ion-irradiated T91 30176 as a function of damage level. 202

Figure 5.61: (a) Bubble density and (b) average bubble diameter of dual-ion-irradiated T91 30176 as a function of damage level. 203

Figure 5.62: Cavity size distributions of dual-ion-irradiated T91 30176 at 460°C:0.2appmHe/dpa to (a) 72 dpa, (b) 110 dpa, (c) 184 dpa, at 460-490-460°C:0.2appmHe/dpa to (d) 170 dpa and at 490°C:0.8appmHe/dpa to (e) 72 dpa and (f) 170 dpa. 204

Figure 5.63: STEM HAADF micrographs of dual-ion-irradiated T91 30176. The dashed lines indicate the depth of interest for the dual-ion-irradiated samples. 206

Figure 5.64: (a) Loop density and (b) average loop diameter of dual-ion-irradiated T91 30176 as a function of damage level. 207

Figure 5.65: STEM BF micrographs of dual-ion-irradiated T91 30176. 208

Figure 5.66: (a) Fe, (b) Cr, (c) Ni and (d) Si enrichments at grain boundaries of dual-ion-irradiated T91 30176. 210

Figure 5.67: EDS (wt%) maps of Fe, Cr, Ni and Si of dual-ion-irradiated T91 30176 at 460°C:0.2appmHe/dpa to (a) 72 dpa and (b) 110 dpa. 212

Figure 5.68: EDS (wt%) maps of Fe, Cr, Ni and Si of dual-ion-irradiated T91 30176 at (a) 460-490-460°C:0.2appmHe/dpa to 170 dpa and at 490°C:0.8appmHe/dpa to (b) 72 dpa and (c) 170 dpa. 213

Figure 5.69: (a) Cluster density, (b) average cluster diameter and (c) volume fraction of dual-ion-irradiated T91 30176. 214

Figure 5.70: Cluster size distributions of dual-ion-irradiated T91 30176 at 460°C:0.2appmHe/dpa to (a) 72 dpa, (b) 110 dpa, at 460-490-460°C:0.2appmHe/dpa (c) to 170 dpa, at 490°C:0.8appmHe/dpa to (d) 72 dpa and (e) 170 dpa. 215

Figure 5.71: EDS Ni map (wt%) of dual-ion-irradiated T91 30176 at 460°C:0.2appmHe/dpa to (a) 72 dpa and (b) 110 dpa, at 460-490-460°C:0.2appmHe/dpa to (c) 170 dpa, at 490°C:0.8appmHe/dpa to (d) 72 dpa and (e) 170 dpa. 217

Figure 6.1: Ratios of swelling, void density and average void diameter between dual-ion irradiation at 445°C:3.1-4.3appmHe/dpa and BOR-60 at 369-376°C. 221

Figure 6.2: Cavity size distributions of irradiated T91 30176 for BOR-60 at 369-375°C and dual-ion conditions at 445°C to (a) 16 dpa, (b) 32-35 dpa, (c) 47-54 dpa and (d) 72 dpa. 222

Figure 6.3: Cavity size distributions of irradiated T91 30176 for BOR-60 at 450-453°C and dual-ion conditions at 520°C to (a) 16.6-19 dpa and (b) 28-32 dpa. 222

Figure 6.4: Cavity size distributions of irradiated T91 30176 for BOR-60 at 515-517°C and dual-ion conditions at 570°C to (a) 15 dpa and (b) 25-28 dpa. 223

Figure 6.5: Ratios of loop density, average loop diameter and loop sink strength between dual-ion irradiation at 445°C:3.1-4.3appmHe/dpa and BOR-60 at 369-376°C. 225

Figure 6.6: Dislocation loop size distributions of irradiated T91 30176 for BOR-60 at 369-376°C and dual-ion at 445°C to (a) 16 dpa, (b) 32-35 dpa, (c) 47-54 dpa and (d) 72 dpa. 226

Figure 6.7: Ratios of segregation at grain boundaries of Fe, Cr, Ni and Si (a) between dual-ion irradiation at 445°C:3.1-4.3appmHe/dpa and BOR-60 at 369-376°C, (b) between dual-ion irradiation at 520°C:3.2-4.3appmHe/dpa and BOR-60 at 450-453°C, and (c) between dual-ion irradiation at 570°C:4.3appmHe/dpa and BOR-60 at 515-517°C. 228

Figure 6.8: Ratios of cluster density, average cluster diameter and volume fraction between dual-ion irradiation at 445°C:3.1-4.3appmHe/dpa and BOR-60 at 369-376°C. 230

Figure 6.9: Cluster size distributions of irradiated T91 30176 for BOR-60 at 369-376°C and dual-ion irradiations at 445°C to (a) 16 dpa, (b) 32-35 dpa, (c) 47-57 dpa and (d) 70-72 dpa... 231

Figure 6.10: Swelling (inset in (b)) as a function of temperature in ferritic-martensitic steels irradiated in various reactors and equivalent dual-ion irradiation to 16-208 dpa. The legend is the same for both plots. 235

Figure 6.11: Void density as a function of temperature in ferritic-martensitic steels irradiated in various reactors and equivalent dual-ion irradiation to 16-184 dpa. 236

Figure 6.12: Dislocation loop density as a function of temperature in ferritic-martensitic steels irradiated in various reactors and equivalent dual-ion irradiation to 16-184 dpa. 237

Figure 6.13: Ni/Si cluster density as a function of temperature in ferritic-martensitic steels irradiated in various reactors and equivalent dual-ion irradiation to 16-184 dpa. 238

Figure 6.14: Linear regressions of (a) BOR-60 void densities (369-376°C), (b) dual-ion void densities at 445°C:3.1-4.3appmHe/dpa, (c) dual-ion void densities at 460°C:3.1-4.3appmHe/dpa, and (d) bubble densities (BOR-60 at 369-376°C, dual-ion at 445°C and 460°C). 243

Figure 6.15: Prediction of the BOR-60-irradiated cavity microstructures at (a) 32 dpa, (c) 47 dpa and (e) 72 dpa, and of the dual-ion-irradiated cavity microstructures at (b) 35dpa:4.3appmHe/dpa, (d) 54dpa:3.1appmHe/dpa and (f) 72dpa:3.6appmHe/dpa. 246

Figure 6.16: Adjusted prediction of the BOR-60-irradiated cavity microstructures at (a) 32 dpa, (c) 47 dpa and (e) 72 dpa, and of the dual-ion-irradiated cavity microstructures at (b) 35dpa:4.3appmHe/dpa, (d) 54dpa:3.1appmHe/dpa and (f) 72dpa:3.6appmHe/dpa. 249

Figure 6.17: Adjusted prediction of the BOR-60-irradiated cavity microstructures at (a) 32 dpa, (c) 47 dpa and (e) 72 dpa, and of the dual-ion-irradiated cavity microstructures at (b) 35dpa:4.3appmHe/dpa, (d) 54dpa:3.1appmHe/dpa and (f) 72dpa:3.6appmHe/dpa. 253

Figure 6.18: Linear regressions of (a) dual-ion void densities at 460°C:0.2appmHe/dpa (b) dual-ion void densities at 475°C:0.2appmHe/dpa, (c) dual-ion void densities at 475°C:0.8appmHe/dpa, and (d) dual-ion void densities at 490°C:0.8appmHe/dpa. 256

Figure 6.19: Linear regressions of (a) dual-ion bubble densities at 460°C:0.2appmHe/dpa (b) dual-ion bubble densities at 475°C:0.2appmHe/dpa, (c) dual-ion bubble densities at 475°C:0.8appmHe/dpa, and (d) dual-ion bubble densities at 490°C:0.8appmHe/dpa. 257

Figure 6.20: (a) Starting cavity microstructure from dual-ion irradiation at 460°C:4.3appmHe/dpa at 16.6 dpa used to predict the dual-ion-irradiated cavity microstructures at (b) 33dpa:3.1appmHe/dpa, (c) 35dpa:4.3appmHe/dpa, (d) 72dpa:3.7appmHe/dpa and (e) 100dpa:4.3appmHe/dpa. 260

Figure 6.21: (a) Starting cavity microstructure from dual-ion irradiation at 460°C:0.2appmHe/dpa at 72 dpa used to predict the dual-ion-irradiated cavity microstructures to (b) 110 dpa and (c) 184 dpa. 261

Figure 6.22: (a) Starting cavity microstructure from dual-ion irradiation at 475°C:0.2appmHe/dpa at 72 dpa used to predict the dual-ion-irradiated cavity microstructures to (b) 150 dpa. 261

Figure 6.23: (a) Starting cavity microstructure from dual-ion irradiation at 475°C:0.8appmHe/dpa at 72 dpa used to predict the dual-ion-irradiated cavity microstructures to (b) 184 dpa. 262

Figure 6.24: (a) Starting cavity microstructure from dual-ion irradiation at 490°C:0.8appmHe/dpa at 72 dpa used to predict the dual-ion-irradiated cavity microstructures to (b) 170 dpa. 262

Figure 6.25: Cavity size distributions of irradiated T91 30176 for all FFTF conditions. 265

Figure 6.26: Swelling values of T91 samples irradiated in FFTF at 400-420°C [50,62,287]. ... 266

Figure 6.27: Cavity size distributions of irradiated T91 30176 for (a) FFTF:73dpa and 460°C:72dpa, 0.2appmHe/dpa, (b) FFTF:170dpa and 460°C:184dpa, 0.2appmHe/dpa, and (c) FFTF:170dpa and 460°C:110dpa, 0.2appmHe/dpa. 267

Figure 6.28: Cavity size distributions of irradiated T91 30176 to FFTF:170dpa and 460-490-460°C:170dpa, 0.2appmHe/dpa. 269

Figure 6.29: Ratios of loop density, average loop diameter and loop sink strength (a) between dual-ion irradiation at 460°C:0.2appmHe/dpa and FFTF, (b) between dual-ion irradiation at 460-490-460°C:0.2appmHe/dpa and FFTF, and (c) between dual-ion irradiation at 490°C:0.8appmHe/dpa and FFTF. 271

Figure 6.30: Cavity size distributions of irradiated T91 30176 for (a) FFTF:73dpa and 460°C:72dpa, 0.2appmHe/dpa, (b) FFTF:170dpa and 460°C:184dpa, 0.2appmHe/dpa, and (c) FFTF:170dpa and 460°C:110dpa, 0.2appmHe/dpa. 272

Figure 6.31: Ratios of swelling, void density and average void diameter (a) between dual-ion irradiation at 460°C:0.2appmHe/dpa and FFTF, (b) between dual-ion irradiation at 460-490-460°C:0.2appmHe/dpa and FFTF, and (c) between dual-ion irradiation at 490°C:0.8appmHe/dpa and FFTF. 273

Figure 6.32: (a) Bubble density and (b) average bubble diameter for samples irradiated in FFTF and companion dual-ion irradiations. 274

Figure 6.33: (a) Fe, (b) Cr, (c) Ni and (d) Si enrichments at grain boundaries of irradiated T91 30176 for FFTF conditions and companion dual-ion irradiations. 279

Figure 6.34: Ratios of segregation of Fe, Cr, Ni and Si (a) between dual-ion irradiation at 460°C:0.2appmHe/dpa and FFTF, (b) between dual-ion irradiation at 460-490-460°C:0.2appmHe/dpa and FFTF, and (c) between dual-ion irradiation at 490°C:0.8appmHe/dpa and FFTF. 280

Figure 6.35: (a) Cluster density, (b) average cluster diameter and (c) volume fraction of irradiated T91 30176 for all FFTF conditions and companion dual-ion irradiations. 282

Figure 6.36: Ratios of cluster density, average cluster diameter and volume fraction (a) between dual-ion irradiation at 460°C:0.2appmHe/dpa and FFTF, (b) between dual-ion irradiation at 460-490-460°C:0.2appmHe/dpa and FFTF, and (c) between dual-ion irradiation at 490°C:0.8appmHe/dpa and FFTF. 283

Figure 6.37: Linear regressions of (a) FFTF bubble densities (407-417°C), (b) FFTF void densities, (c) FFTF bubble densities with adjusted damage levels, and (d) FFTF void densities with adjusted damage levels. 285

Figure 6.38: (a) Starting cavity microstructure from dual-ion irradiation at 460°C:0.2appmHe/dpa at 72 dpa used to predict the dual-ion-irradiated cavity microstructures (b) after temperature excursion of 490°C for 38 dpa and, (c) with an added 60 dpa at 460°C after temperature excursion. (d) Swelling of measured and predicted size distributions with temperature excursion. 287

Figure 6.39: Predicted FFTF-irradiated cavity microstructures (a) to 170 dpa and (b) to 104 dpa. (c) Swelling of the measured and predicted FFTF size distributions. 289

Figure 6.40: Predicted FFTF-irradiated cavity microstructures at 407°C (a) to 28 dpa and (b) to 73 dpa. (c) Swelling of the measured and predicted FFTF size distributions to 73 dpa. 290

Figure 6.41: Predicted FFTF-irradiated cavity microstructures of (a) 407°C:28dpa, (b) 407°C:28dpa + 439°C:38dpa and (c) 407°C:28dpa + 439°C:38dpa + 407°C:104dpa. (d) Swelling of the measured and predicted size distributions. 291

Figure 6.42: Predicted FFTF-irradiated cavity microstructures (a) at 407°C:52.2dpa, (b) at 407°C:52.2dpa + 495°C:13.8dpa, and (c) at 407°C:52.2dpa + 495°C:13.8dpa + 407°C:104dpa. (d) Swelling of measured and predicted size distributions. 292

Figure 6.43: Predicted net vacancy fluxes in the BOR-60 microstructure irradiated at (a) 369°C:0.77appmHe/dpa, 8×10^{-7} dpa/s, (b) 369°C:0.77appmHe/dpa, 7.5×10^{-4} dpa/s, (c) 445°C:0.77appmHe/dpa, 7.5×10^{-4} dpa/s and (d) 445°C:3appmHe/dpa, 7.5×10^{-4} dpa/s..... 297

Figure 6.44: Predicted helium content in the BOR-60 microstructure irradiated at (a) 369°C:0.77appmHe/dpa, 8×10^{-7} dpa/s, (b) 369°C:0.77appmHe/dpa, 7.5×10^{-4} dpa/s, (c) 445°C:0.77appmHe/dpa, 7.5×10^{-4} dpa/s and (d) 445°C:3appmHe/dpa, 7.5×10^{-4} dpa/s..... 298

Figure 6.45: Predicted cavity microstructure in BOR-60 irradiated at (a) 369°C:0.77appmHe/dpa, 8×10^{-7} dpa/s, (b) 369°C:0.77appmHe/dpa, 7.5×10^{-4} dpa/s, (c) 445°C:0.77appmHe/dpa, 7.5×10^{-4} dpa/s and (d) 445°C:3appmHe/dpa, 7.5×10^{-4} dpa/s..... 299

Figure 6.46: Predicted cavity interstitial bias at 72 dpa in the BOR-60 microstructure irradiated at (a) 369°C:0.77appmHe/dpa, 8×10^{-7} dpa/s, (b) 369°C:0.77appmHe/dpa, 7.5×10^{-4} dpa/s, (c) 445°C:0.77appmHe/dpa, 7.5×10^{-4} dpa/s and (d) 445°C:3appmHe/dpa, 7.5×10^{-4} dpa/s..... 300

Figure 6.47: Predicted net vacancy fluxes in the FFTF microstructure irradiated at (a) 407°C:0.21appmHe/dpa, 1.25×10^{-6} dpa/s, (b) 407°C:0.21appmHe/dpa, 7.5×10^{-4} dpa/s, (c) 460°C:0.21appmHe/dpa, 7.5×10^{-4} dpa/s and (d) 460°C:0.82appmHe/dpa, 7.5×10^{-4} dpa/s.... 303

Figure 6.48: Predicted helium content in the FFTF microstructure irradiated at (a) 407°C:0.21appmHe/dpa, 1.25×10^{-6} dpa/s, (b) 407°C:0.21appmHe/dpa, 7.5×10^{-4} dpa/s, (c) 460°C:0.21appmHe/dpa, 7.5×10^{-4} dpa/s and (d) 460°C:0.82appmHe/dpa, 7.5×10^{-4} dpa/s.... 304

Figure 6.49: Predicted cavity microstructure in FFTF irradiated at (a) 407°C:0.21appmHe/dpa, 1.25×10^{-6} dpa/s, (b) 407°C:0.21appmHe/dpa, 7.5×10^{-4} dpa/s, (c) 460°C:0.21appmHe/dpa, 7.5×10^{-4} dpa/s and (d) 460°C:0.82appmHe/dpa, 7.5×10^{-4} dpa/s. 305

Figure 6.50: Predicted cavity interstitial bias in the FFTF microstructure irradiated at (a) 407°C:0.21appmHe/dpa, 1.25×10^{-6} dpa/s, (b) 407°C:0.21appmHe/dpa, 7.5×10^{-4} dpa/s, (c) 460°C:0.21appmHe/dpa, 7.5×10^{-4} dpa/s and (d) 460°C:0.82appmHe/dpa, 7.5×10^{-4} dpa/s.... 306

Appendix Figure 1: Size distributions of dual-ion-irradiated T91 with and without helium reduction at (a) 445°C with comparison with BOR-60, and at (b) 460°C. 317

Appendix Figure 2: Size distributions of T91 irradiated in FFTF to 73 dpa and after dual-ion irradiation to 72 dpa at (a) 460°C:3.2appmHe/dpa, (b) 475°C:0.2appmHe/dpa and 475°C:0.4appmHe/dpa, (c) 475°C:0.8appmHe/dpa and 475°C:3.2appmHe/dpa, and (d) 475°C:1.6appmHe/dpa with and without using shutters. 318

Appendix Figure 3: Size distributions of T91 irradiated in FFTF to 170 dpa and after dual-ion irradiation to 150-184 dpa at (a) 460°C:0.8appmHe/dpa and 460°C:3.2appmHe/dpa, (b)

475°C:0.2appmHe/dpa and 475°C:0.8appmHe/dpa, and (c) 490°C:0.2appmHe/dpa and 490°C:0.4appmHe/dpa. 319

Appendix Figure 4: Significance of temperature (+/- 1°C) on the predicted BOR-60-irradiated (a-b) cavity size distribution and (c) helium content in cavities at 369°C:72dpa, 0.77appmHe/dpa. 325

Appendix Figure 5: Significance of helium production rate (+/- 10^{-4}) on the predicted BOR-60-irradiated (a-b) cavity size distribution and (c) helium content in cavities at 369°C:72dpa, 0.77appmHe/dpa. 326

Appendix Figure 6: Predictions of BOR-60-irradiated cavity microstructures to 72 dpa at 420°C:0.77appmHe/dpa. 327

Appendix Figure 7: Predictions of BOR-60-irradiated cavity microstructures to 72 dpa at (a) 405°C:0.55appmHe/dpa and (b) 420°C:0.3appmHe/dpa. 328

Appendix Figure 8: Significance of *eff* on size distribution for (a) DDI, 445C-3.6Hedpa-72dpa and (b) BOR-60, 369C-0.77Hedpa-72dpa. 331

Appendix Figure 9: Significance of *bias* on size distribution for (a) DDI, 445C-3.6Hedpa-72dpa and (b) BOR-60, 369C-0.77Hedpa-72dpa. 332

Appendix Figure 10: Significance of z_v on size distribution for (a) DDI, 445C-3.6Hedpa-72dpa and (b) BOR-60, 369C-0.77Hedpa-72dpa. 332

Appendix Figure 11: Significance of $E_b^{He,cav1}$ on size distribution for (a) DDI, 445C-3.6Hedpa-72dpa and (b) BOR-60, 369C-0.77Hedpa-72dpa. 332

List of Appendices

Appendix A Neutron and Dual-Ion Irradiations 317

Appendix B Effect of Temperature and Helium on Predicted Cavity Microstructures 323

Appendix C Significance Analysis of Rate Theory Model 330

Abstract

For advanced economies, nuclear power has been the biggest low-carbon source of electricity for more than 30 years, and it has played an important role in the security of energy supplies in several countries. With an aging nuclear reactor fleet and an increased demand for greener, low-carbon production of energy, many countries are considering Generation IV reactors as a solution with the added benefits of advances in sustainability, economics, safety, reliability and proliferation-resistance.

Ferritic-martensitic steels are candidate materials for fuel cladding and structural components in next-generation nuclear reactors due to their swelling resistance. Yet, dimensional instability and hardening caused by the nucleation and growth of defect clusters remain a life-limiting factor in future reactor designs expected to reach 200 dpa. Predictive tools can quicken the qualification of nuclear materials at these damage levels across irradiation conditions and will accelerate the deployment of new reactors. Ion irradiation offers the opportunity to reach high damage levels in short periods of time with precise control of the irradiation parameters, making it ideal for replicating neutron damage and validating computational models. To match the microstructure evolution of neutron-irradiated samples via ion irradiation, a temperature shift and increased helium injection rate are often necessary.

The objective of this work is to determine how temperature shift and helium injection rate interact in ion irradiation so as to replicate the neutron-irradiated cavity microstructure in ferritic-martensitic alloy T91. The cavity and loop microstructures of FM T91 heat 30176 irradiated in two reactors (BOR-60 and FFTF) up to 184 dpa were characterized and matched using dual-ion

irradiation. In both cases, a temperature shift was required, but only BOR-60 required an increased helium injection rate. The radiation-induced segregation and precipitation behaviors were partially matched via dual-ion irradiation. Characterization also revealed errors in temperature histories reported for BOR-60 and FFTF.

In parallel, a rate theory model including helium partitioning and cavity interstitial bias was developed to predict the evolution of cavity microstructures from irradiation parameters. The results of the BOR-60 and dual-ion irradiations were used to fit this model. A single set of parameters, consistent with literature values, was able to predict the cavity microstructure evolution of dual-ion and BOR-60-irradiated T91 up to 72 dpa. The predictive capability of the model was validated against results from other dual-ion irradiations with different temperatures, helium injection rates and starting microstructures. Simulated FFTF cavity microstructures confirmed the temperature excursion that was identified from experiments and provided more details about the magnitude and duration of the temperature perturbation.

The rate theory model reveals two cases when matching the cavity microstructure evolution at higher damage rate based on helium production. At high helium production rate, temperature shift and increased helium injection rate maintain the helium content in bubbles to a high level at higher damage rates. This results in a net flux of vacancies to voids comparable to reactor level due to a high consumption rate by bubbles. At low helium production rate, the bubble density is lower, and their interstitial bias is higher. There is no need for an increased helium injection rate under dual-ion irradiation since the vacancy absorption rate by bubbles is low in reactor, and the vacancy flux to voids remains high.

This work provided significant insights into the capabilities of dual-ion irradiation and rate theory models to predict neutron-irradiated cavity microstructures.

Chapter 1 Introduction

For advanced economies, nuclear power has been the biggest low-carbon source of electricity for more than 30 years, and it has played an important role in the security of energy supplies in several countries [1]. With an aging nuclear reactor fleet and an increased demand for greener, low-carbon production of energy, many countries are considering Generation IV reactors as a solution with the added benefits of advances in sustainability, economics, safety, reliability and proliferation-resistance [2].

The core of a nuclear reactor is characterized by high temperature, stress, corrosive coolant, and high radiation levels. Structural materials in the core must reliably perform in this environment for long periods of time. Core materials in the next generation of nuclear reactors (such as sodium fast reactor, lead fast reactor, molten salt reactor, and traveling wave reactor (TWR)) must be able to withstand damage levels of 200-600 dpa and temperatures in excess of 400°C (Figure 1.1), effectively making materials a limiting factor of the lifetime of reactors [3].

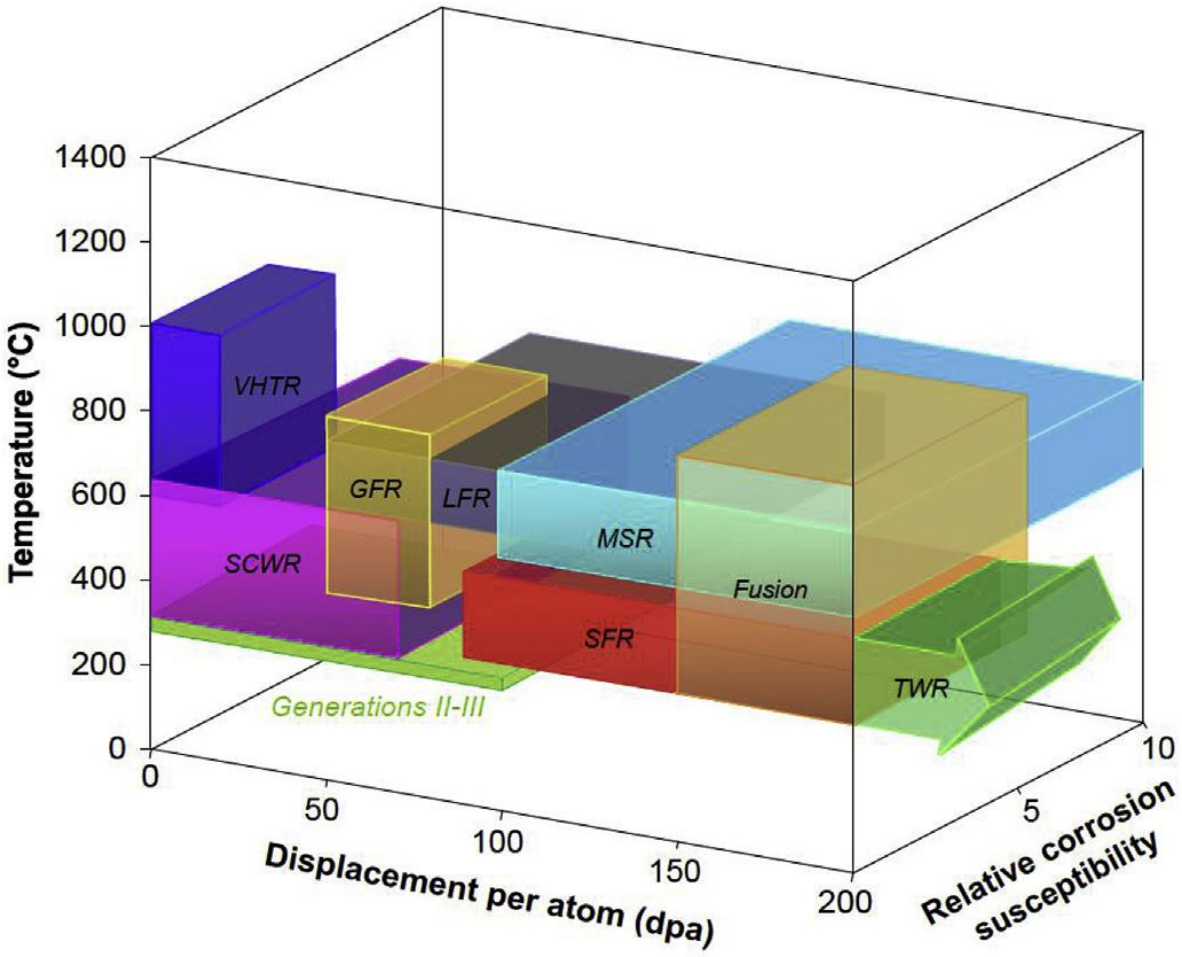


Figure 1.1: Overview of operating temperatures, displacement damage regimes and corrosion susceptibilities for structural materials in current and future reactors [4].

Energetic neutrons produced by the chain reaction in the reactor interact with components either via displacement cascades in the lattice or via the creation of impurity atoms by transmutation reactions. Displacement cascades create numerous point defects (vacancies and interstitials) that diffuse in the matrix and lead to the formation of cavities or dislocation loops but also impact the elemental distribution of the alloy: radiation-induced segregation and radiation-induced precipitation are major phenomena in irradiated metals [5,6]. Consequently, the development of materials able to withstand the harsh environments of nuclear reactors requires an understanding of the mechanisms of microstructure evolution under irradiation.

Ferritic-martensitic steels are candidate materials for next-generation fast reactor applications. High-chromium ferritic/martensitic steels typically contain 9-12 %Cr along with various alloying elements that affect the microstructure, the tempering resistance and may improve the high-temperature mechanical (hardenability, toughness, etc.) and corrosion properties [5,7,8]. Ferritic-martensitic steels must be resistant to radiation damage from neutron bombardment and the subsequent radiation effects that affect microstructure and properties; they became of interest for nuclear applications because of their swelling resistance compared to austenitic stainless steels with steady-state rates of ~0.2%/dpa and ~1%/dpa for ferritic and austenitic steels, respectively, but also for their higher thermal conductivity and lower thermal expansion [5,9–11]. 9Cr ferritic–martensitic steels are much more resistant to high temperature helium embrittlement than austenitic steels [12]. In fast reactors, ferritic-martensitic steels are considered primarily in the fuel subassembly as fuel pin cladding and wrapper material [5]. The major degradation modes in alloy T91 are likely to be dimensional instability caused by void swelling, hardening and/or embrittlement due to phase stability at high damage levels [13].

The microstructure obtained by neutron irradiation in a test reactor is likely to be the most representative of the microstructure evolution in commercial reactors. Yet, discrepancies in irradiated microstructure from one reactor to another for similar materials exposed to the same damage level and temperature have been reported. Differences in damage rate, neutron spectrum and irradiation history make interpretation of neutron irradiations difficult. The paucity of worldwide test reactors combined with the impossibility to create radiation damage significantly faster than that in commercial reactors has pushed for the development of other techniques to induce radiation damage [3,14]. Heavy-ion irradiations have the benefit of high damage rates, dense cascades, like those produced by neutrons, and low cost. Limitations include the need for a

large temperature shift, a short penetration depth and varying damage rate over the penetration depth, as well as injected interstitials [3].

The emulation of neutron-irradiated microstructure with heavy-ion irradiation could be a game-changer in the accelerated qualification of structural materials for advanced reactors [15]. While some aspects of the microstructure such as cavities and dislocation loops have been mimicked at low damage levels in ferritic-martensitic steels, other aspects such as radiation-induced segregation and radiation-induced precipitates are more challenging to replicate [16]. Besides, very few studies have compared the microstructure of FM steels in reactor and heavy-ion irradiation at high damage level (>100 dpa) [14]. Beyond the experimental emulation of neutron-irradiated microstructure, predictive tools including computational materials modeling such as rate theory models [17,18] or cluster dynamics models [19–23] represent a step forward toward the qualification of materials for future nuclear reactor. In particular, with known reactor parameters (temperature, helium production rate, damage rate, etc.), being able to compute the temperature shift and helium injection rate in ion irradiation that will replicate the cavity microstructure of neutron-irradiated samples would establish dual-ion irradiations as a predictive tool that is validated by experimental benchmarking.

This thesis will determine the degree to which dual-ion irradiation replicates neutron-irradiated cavity microstructures in ferritic-martensitic steel. Specimens irradiated with heavy ions at the Michigan Ion Beam Laboratory and with neutrons in two different reactors had their irradiated microstructure characterized. A rate theory model including helium partitioning to sinks was used to calculate and predict the cavity microstructure of samples under irradiation. Chapter 2 provides the current state of the art of neutron and ion irradiation of ferritic-martensitic steels and their impact on the microstructure. Chapter 3 articulates the objective of the thesis and lays

out the approach to achieve the objective. Chapter 4 describes the neutron and ion irradiation experiments and the techniques used for post irradiation characterization. It also explains the choice of rate theory modeling and how it is implemented. Chapter 5 presents the results gathered from the characterization of irradiated samples. Chapter 6 compares the microstructures of neutron-irradiated and dual-ion-irradiated specimens. It also offers an interpretation and discussion of the experimental results in relation to the modeling results and addresses the objective. Chapter 7 draws the conclusions from this thesis. Chapter 8 lists potential future work.

Chapter 2 Background

2.1 Ferritic-Martensitic Steels

The focus of this work is the modified 9Cr-1MoVNb (T91) type of steel, in which the V and Nb contents have been optimized. This material has been increasingly used for superheater tubing, headers, and piping with conventional steam conditions and for advanced plants with steam inlet temperatures up to 593°C [5]. Martensitic steels with 7-9% Cr have been favored over 12% Cr steels, because of the difficulty of eliminating δ-ferrite in a 12% Cr steel without increasing carbon or manganese for austenite stabilization. δ-ferrite can lower toughness, and manganese promotes chi-phase precipitation during irradiation, which can cause embrittlement [24].

Different alloying elements in ferritic-martensitic steels play different roles in modifying the microstructure, mechanical and corrosion properties. Chromium is a ferrite stabilizing element that is generally added to steels for oxidation and corrosion resistance. It provides little solid solution strengthening when added to iron and reacts with carbon to form carbides [25]. Nitrogen can also be utilized as an austenite stabilizer and was added to compensate for the loss of strength caused by the reduction of carbon [11]. Carbon and nitrogen both have a very small solubility in ferrite, which gives rise to the formation of carbides, nitrides and carbonitrides [25]. Nickel is usually used in steels for non-nuclear applications but is not as effective as carbon and nitrogen as an austenite stabilizer [5]. Manganese is inferior to nickel as an austenite stabilizer, and high addition of it in 12Cr-0.1C steels was not sufficient to prevent the formation of δ-ferrite [5]. In the tempered condition, molybdenum is distributed between the solid solution and that incorporated

in the $M_{23}C_6$ and MX and provides relatively high solid solution strengthening of iron [26]. However, molybdenum is a ferrite stabilizer, and its amount must be limited to avoid formation of δ-ferrite. Vanadium and niobium are strong carbide-, nitride- and carbonitride-forming elements and are expected to form MX, where V and Nb are enriched in the M, and X is either carbon, nitrogen, or a combination of the two [25,27]. Thus, micro-alloying additions of V, Nb and N promotes the formation of fine scale Nb and V carbonitrides/nitrides that can interact with dislocations and provide strengthening, while removing the austenite formers carbon and/or nitrogen from solution as insoluble carbides and nitrides [5]. Niobium carbides or carbonitrides are extremely stable, and it is necessary to heat to temperatures beyond normal austenitizing temperatures for them to dissolve completely. However, undissolved niobium carbides restrict grain growth during austenitization, thus producing a refined prior austenite grain size relative to a steel without niobium [25]. Silicon is soluble in the matrix, and causes the lattice parameter to decrease, thereby increasing tempering resistance [5]. Silicon can provide additional oxidation resistance, improves weldability in 9Cr-1Mo and provides solid solution hardening effect. Since ferritic-martensitic steels are candidate materials for nuclear applications, the consequences of alloying elements on activation and radiation effects must be considered. Calculations indicated that common alloying elements used in steels (Mo, Nb, Ni, Cu, and N) should be eliminated or minimized [9,28]. Some of them (Mo, Nb, and Ni) could be replaced by elements such as W, V, Mn, Ta, and Ti, which have equivalent or similar effects on the constitution and structures [5,9].

2.1.1 Microstructure: Common Phases and Heat Treatments

The heat treatment of ferritic-martensitic steels is typically a multistep process aimed at creating a specific crystal structure with desired mechanical properties. A solutionizing treatment (austenitizing) produces austenite (face-centered cubic crystal structure) and dissolves the

carbides: complete carbides dissolution in 9Cr-1MoVNb happens during austenitization between 1000°C and 1100°C after only 5 minutes [27]. The 9Cr-1Mo steel is air hardened since it transforms to martensite (body-centered cubic crystal structure) after austenitizing, for a wide range of cooling rates [5]. The austenitization plus air cool is referred to as the normalization treatment. Typical normalized microstructures consist of a martensite lath network: completely martensitic microstructure occurs for 9Cr-1MoVNb when air cooled from the austenitizing temperature [27]. The steel would be almost impossible to use in this condition so the heat treatments employed commercially aim to reduce the hardness by tempering the martensite, or by slowing the cooling rate down through annealing, so that a microstructure of carbides may be produced [29]. The alloying additions made to balance the constitution or improve the tempering resistance of the steels also lower the martensite start (M_s) and finish (M_f) temperatures, resulting in a tendency for retained austenite to be present if the M_s is close to or below room temperature [5]. T91 has a M_s of 350°C and a M_f of 134°C [30] which are consistent with the M_s and M_f for high-chromium steels that usually range from 250 to 350°C and 80 to 190°C respectively [5]. It is essential that the tempering of the martensite is performed at temperatures below the Ac_1 (the temperature at which the α to γ transformation starts on heating) to avoid reaustenitization and thereby achieve the optimum combination of strength and toughness [5]. In commercial practice, normalized steels are tempered by heating between 650 to 780°C [27].

As shown in Figure 2.1, the γ-Fe loop in the Fe-Cr equilibrium diagram [5] is closed if the chromium content exceeds about 12%. Steels with 9 and 10% Cr are usually free of δ-ferrite and in 11% Cr residues (<1%) of δ-ferrite are found; the steels with 12, 13, 14% Cr can exhibit mean δ-ferrite fractions of 5 to 20% and of 25%, respectively [7]. However, the austenite-stabilizing

elements (C, N, Ni, Mn) extend the γ-phase field, while the ferrite-forming elements (Cr, Mo, Nb, V, W, Si, Ti, Al) reduce it [5,31].

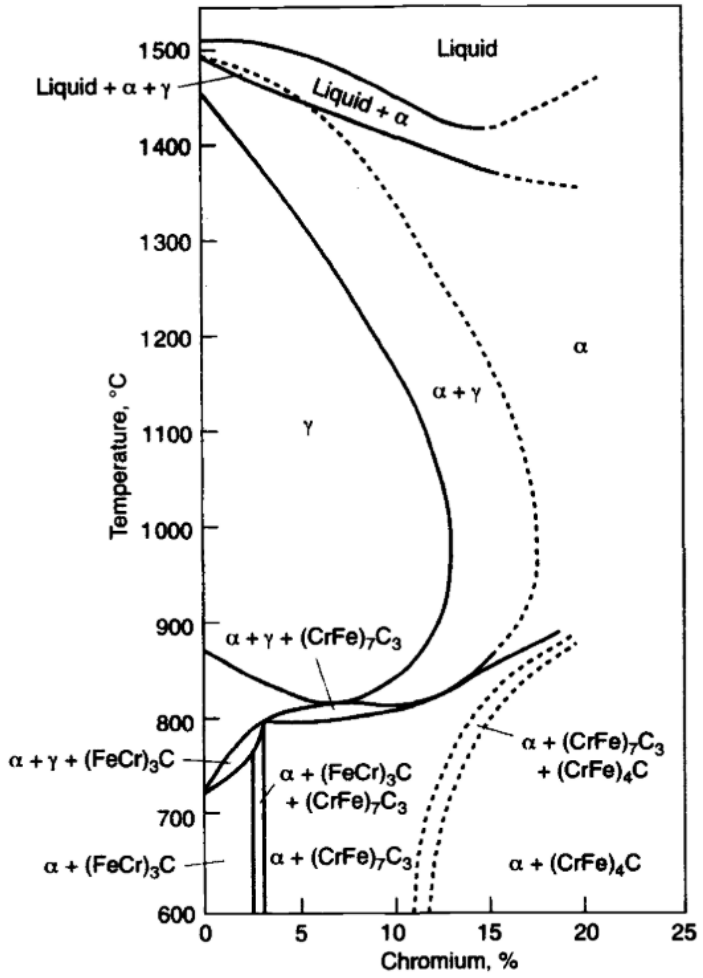


Figure 2.1: Effect of chromium on the constitution of Fe-Cr-C alloys containing 0.1% C; note that $(CrFe)_4C$ is $M_{23}C_6$ carbide [32].

The grain size of Cr-Mo steels is a direct function of the austenitizing temperature since the carbides of chromium and molybdenum are completely dissolved in austenite at temperatures not exceeding 1000°C [29]. The austenitizing temperatures for Cr-Mo steels do not significantly exceed the Ac_3 temperatures (temperature at which transformation of ferrite to austenite is completed), thus resulting in a fine grain size with complete solution of the alloying elements [29]. Austenite grain boundaries act as inhomogeneous nucleation sites for precipitates. As the

austenitization time or temperature is increased, the available nucleation sites for precipitation during cooling decrease, and the degree of precipitation also decreases [27].

It has been demonstrated that interfacial segregation of alloying and impurity elements in the fully martensitic high-chromium steels can occur during cooling from the austenitization temperature and because of tempering and aging [5]. Phosphorus, chromium, and silicon segregate at the prior austenite grain boundaries of 9Cr and 9Cr-1Mo steels during tempering [33,34]. Silicon and phosphorus segregate at critical cooling rates of 20-50 and 50°C/s, respectively, while some of the other alloying elements segregate at lower rates of 2.5 (Mo), 3.0 (V), and 1.5°C/s (Nb) [5,35,36]. Desegregation may also occur during subsequent high-temperature tempering treatments, with the exact rates being dependent on the diffusivities of the elements in the steel matrices [5].

Carbide precipitation plays an important role in the microstructure of ferritic-martensitic steels and subsequently on their mechanical properties. Vitek and Klueh (as cited in [11]) showed that essentially all carbon in solution precipitates when normalized 9Cr-1MoVNb and 12Cr-1MoVW steels are tempered 1 h or more at 700-780°C [27]. The amount of precipitate in the fully tempered condition is 1.5 wt% for 9Cr-1MoVNb: the amount of precipitate is directly related to the carbon level. The conditions for producing fine and numerous carbides usually occur when the steels are heat treated or see service at 0.4 - 0.5 T_m and have a carbon content of 0.1 – 0.2% [29].

The primary precipitate in modified 9Cr-1Mo (0.1 %C) is $M_{23}C_6$, 60–150 nm in size (normal distribution in logarithmic scale with average at 100 nm [37]), and of irregular shape [13,25,29]. The carbides consist of 50 at% Cr, 20 at% C, 25 at% Fe and others (W, V, Si) which can be identified as $M_{23}C_6$ with mainly Cr as the metal [30]. They precipitate primarily on prior

austenite, lath and sub-grain boundaries and less frequently also with dislocations within a matrix in all the steels [5,30,38]; they provide pinning, thus stabilizing the microstructure [25,38].

Other types of carbides are also present: some Cr_7C_3 carbides have been measured [25,29], Cr-rich M_2X (Cr_2N) can also form in steels containing nitrogen for some conditions [25,27,39] and low amounts of small, globular or disc-shaped particles, 20–80 nm in size, niobium- and vanadium-rich MC are present [27,38].

Some MX carbonitride exist even at temperature higher than 1000°C and remain on prior austenite grain boundaries after normalizing heat treatment [37]. The variations of Cr–Nb–V balance of Nb-rich MX and V-rich MX are limited within a range of 84–95 wt% Nb, 3–11 wt% V and 0–5 wt% Cr for Nb-rich MX and that of 6–30 wt% Nb, 60–78 wt% V and 7–28 wt% Cr for V-rich MX [37].

Orr and Woollard [40] investigated the VN precipitate phase in a 9Cr-1MoNbVN steel with a normalized and tempered (1050°C + 750°C) condition and indicated that the composition of the metal fraction in the VN phase can be roughly expressed as $(V_{0.6}Cr_{0.3}Fe_{0.1})N$. They also observed some precipitate particles with compositions approximately halfway between VN and NbC, so that the precipitate phase can be roughly expressed as $(V_{0.5}Nb_{0.25}Cr_{0.15}Fe_{0.1})N$. Two-phase separation of primary MX into Nb-rich MX and V-rich MX occurs during tempering heat treatment [37].

Along with the reduction in dislocation density, the $M_{23}C_6$ particles coarsen allowing the martensite laths to transform to more equiaxed subgrains. Along with the coarsening of the $M_{23}C_6$, there is also a coarsening in the MX precipitate distribution, although these particles coarsen much more slowly than $M_{23}C_6$. During coarsening, changes occur in the composition of the M in the precipitates as equilibrium is approached [25].

Laves phase $(FeCr)_2(Mo,W)$ forms during thermal aging and creep, and at 600°C and above, it quickly coarsens, with the coarsening proceeding more quickly under stress. Laves phase formation is important because it removes the solid solution strengthening elements tungsten and molybdenum from solution [25].

Table 2.1 lists the precipitates that can be present in high-chromium martensitic steels after normalization, tempering, aging and creep-rupture testing.

Table 2.1: Precipitation in normalized-and-tempered, aged and creep-rupture tested high-chromium martensitic steels [5].

Precipitate phase	Crystal structure and lattice parameter	Typical composition	Distribution of precipitates
$M_{23}C_6$	FCC a = 1.066 nm	$(Cr_{16}Fe_6Mo)C_6$ $(Cr_4Fe_{12}Mo_4Si_2WV)C_6$	Coarse particles at prior austenite grain and martensite lath boundaries and fine intra-lath particles
MX	FCC a = 0.444 - 0.447 nm	NbC, NbN, VN, (CrV)N, Nb(CN) and (NbV)C	Undissolved particles and fine precipitates at martensite lath boundaries
M_2X	Hexagonal a = 0.478 nm c = 0.444 nm	Cr_2N, Mo_2C and W_2C	Martensite lath boundaries (Cr_2N and Mo_2C); prior austenite grain boundaries (Mo_2C); intra-lath (Mo_2C and W_2C); δ-ferrite in duplex steels [$(Cr_2(CN)$ and $(CrMo)_2(CN)$]
Z-phase	Tetragonal a = 0.286 nm c = 0.739 nm	(CrVNb)N	Large plate-like particles in the matrix after creep straining at 600°C
η-carbide	Diamond cubic a = 1.07 – 1.22 nm	M_6C $(Fe_{39}Cr_6Mo_4Si_{10})C$	Prior austenite grain and martensite lath boundaries and intra-lath
Vanadium carbide	FCC a = 0.420 nm	V_4C_3	Low number density in matrix

Laves	Hexagonal a = 0.4744 nm c = 0.7725 nm	Fe_2Mo Fe_2W and $Fe_2(MoW)$	Prior austenite grain and martensite lath boundaries and intra-lath; δ-ferrite in duplex steels
Chi (χ)	BCC a = 0.892 nm	$M_{18}C$ or $Fe_{35}Cr_{12}Mo_{10}C$	Intra-martensite lath; δ-ferrite in duplex steels

Figure 2.2 presents the microstructure typically obtained for martensitic steels following tempering [41].

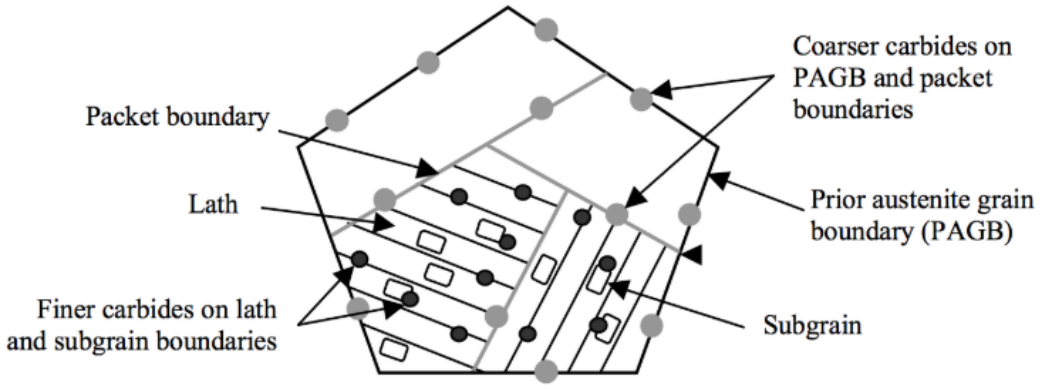


Figure 2.2: Typical microstructure of ferritic-martensitic steels after tempering.

2.1.2 Mechanical Properties

Martensitic steels containing 9-12% Cr with about 1% Mo, 0.1-0.2% C and combinations of small amounts of V, W, Nb, etc., have the elevated-temperature strength and thermal properties (conductivity and expansion coefficient) that result in excellent resistance to thermal stresses [5]. Yet, intermetallic compounds (Laves, chi and sigma) formed at moderate service temperatures can lead to a loss of creep strength, ductility and toughness, and higher susceptibility to cracking after prolonged high temperature service [5]. Additionally, elevated temperature exposure causes a reduction in the dislocation density, with the reduction generally greater during a creep test than for thermal aging without a stress [25]. Additionally, susceptibility to the ductile/brittle transition at lower temperatures is common to BCC materials and is a known disadvantage [42].

The creep-rupture strengths of highly alloyed 9%Cr martensitic steels are determined primarily by (i) solid-solution strengthening by Cr, Mo, and W and (ii) precipitation hardening by VN and Nb(CN) particles produced during tempering [5,40]. Creep strength of 9Cr-1MoVNb is adequate from 550 to 600°C and they have been used at these temperatures in the power-generation, chemical and petrochemical industries [5]. It is controlled by carbide distribution which varies according to the chemical composition and heat treatment [29]. Steels have been designed with higher strength gained by the addition of niobium and vanadium that form fine and stable carbonitrides [29,37]. Indeed, complex carbonitrides of spherical Nb(C,H) and plate-like V-nitrides were shown to be effective obstacles against dislocation glide. Sizes of the carbonitrides (length of the major axis of plate-like V-nitrides) were one of the controlling factors of creep resistance [43]. The ferrite phase inhibits austenite grain growth, but it adversely influences the strength and, directly or indirectly, the toughness [5,42], particularly if present as films between the grains of the austenite, which is subsequently transformed to martensite and tempered. Overall, improvements in creep resistance have been achieved by close control of the major and minor alloying element concentrations so as to: (a) optimize the constitution and δ-ferrite content by additions of the austenite-stabilizing elements, (b) maximize the solid solution strengthening by W, Mo, and N, (c) stabilize the martensite dislocation structure and the $M_{23}C_6$ type precipitates, and (d) enhance the precipitation strengthening by the formation of fine particles of VN and Nb(CN), which are highly resistant to coarsening [5].

2.2 Radiation Effects in Ferritic Martensitic Steels

Components located near the reactor core are irradiated with neutrons having an energy above 10 keV in fast reactors and from approximately 2 MeV down to 0.025 eV in thermal reactors. Energetic neutrons interact with these components either via the displacement of atoms

in the lattice because of nuclear collisions or via the creation of solid and gaseous impurity atoms by (n,γ), (n,α), and (n,p) transmutation reactions. The displacement cascade resulting from the neutron-atom nuclear collisions create numerous point defects (vacancies and interstitials) that can affect the microstructure of the material. Diffusion of the point defects may trigger clustering leading to the formation of cavities (vacancies) or dislocation loops (vacancies or interstitials), but also impact the elemental distribution of the alloy: radiation-induced segregation and radiation-induced precipitation are major phenomena in irradiated metals. These microstructure changes will affect the mechanical properties of the alloy and cause hardening, embrittlement, irradiation creep and reductions in fracture toughness and fatigue endurance [5]. Ion irradiation can yield high damage rates with negligible (proton irradiation) or no (heavy-ion irradiation) residual radioactivity and at very low cost. The advantages of ion irradiation are many: damage rates 10^4 times that of reactor irradiation can be attained. Because there is little or no activation, samples are easily handled, reducing the cost associated with post-irradiation characterization. Control of ion irradiation experiments (temperature, damage rate, damage level) is much better than irradiations in reactor and damage can even be observed in situ [14].

This section covers the effect of neutron and ion irradiation in ferritic-martensitic steels in terms of microstructure and mechanical changes. Models for the estimation of radiation damage and effects are reviewed.

2.2.1 Cavities and swelling

Under irradiation, two types of cavities can form: bubbles and voids. Bubbles contain gas atoms at a pressure in equilibrium or higher than the surface tension. Voids can contain gas atoms, but the pressure is less than the equilibrium pressure. Therefore, under irradiation, it is possible for large numbers of inert gas bubbles and larger cavities to form, which significantly alter the physical

and mechanical properties of metals [5,6]. The formation of void nuclei by the random coalescence of diffusing vacancies is very unlikely in the absence of gas, because small vacancy clusters can readily collapse into dislocation loops [44,45]. Therefore, bubbles and larger cavities are likely to form in the presence of dissolved gases and cause an increase in volume (swelling) via bias-driven void growth. This absorption of vacancies is possible because certain sinks such as network dislocations are biased toward interstitials which they are more likely to absorb [5,46]. If the density of these biased sinks is too low, the net absorption of vacancies is not enough to trigger bias-driven growth. On the opposite, if the biased sinks density is too high, most of the vacancies will not be absorbed by voids and no growth occur either [6]. The void nucleation and growth can be impaired by trapping sites where the dissolved gas accumulate but void nuclei are not forming [5], although heterogeneous nucleation of cavities can occur on dislocations, precipitates and impurity particles [47]. In addition to bias-driven growth, Singh et al. [45,47] developed a theory in which bubbles are mobile following Brownian movements and can coalesce into bigger cavities to reach critical size prior to experiencing bias-driven growth. High swelling levels can cause dimensional instabilities: (1) initial shapes and dimensions can become unstable; (2) non-uniform swelling consequential to different temperature and damage rate can lead to bowing of components and to buildup of stresses; and (3) the lifetimes of components may be severely limited if operational problems are to be avoided [48].

2.2.1.1 Damage level effect

The void swelling-fluence relation has been represented in terms of an incubation dose (D_0), below which the swelling is negligible (~0.1%). After this initial phase, a transient period occurs before the steady-state swelling (S) regime during which BCC steels show a swelling rate (A) of ~0.1-0.2%/dpa compared to the typically 1%/dpa for austenitic stainless [5,10,49]:

$$S = A * (D - D_0) \ \ for\ D > D_0 \qquad \text{Eq. 2.1}$$

Extensive data are also available on pure iron and iron alloys, low, intermediate, and high chromium ferritic, bainitic, and martensitic steels that have demonstrated that these body-centered-cubic (BCC) materials have considerably greater resistance to irradiation-induced void swelling than the face-centered-cubic (FCC) austenitic steels [5].

For T91 heat 30176 irradiated in BOR-60, the reported average void size was 6.9 nm at 376°C:17.1dpa and was virtually unchanged when the irradiation dose increased to 35.1 dpa (6.5 nm). However, the void density nearly doubled (7.3×10^{20} m^{-3} at 17.1 dpa vs. 1.5×10^{21} m^{-3} at 35.1 dpa) when the irradiation dose increased while the bubble density decreased from 1.2×10^{23} m^{-3} to 2.2×10^{22} m^{-3}. Void swelling was 0.016% at 376°C:17.1 dpa and it increased to 0.033% at 378°C:35.1dpa (does not take into account bubble swelling) [13]. This seems to indicate that at this temperature 35 dpa is still in the incubation zone. If the damage is raised to 184 dpa at 413°C, bias-driven growth starts and swelling increases: the reported average size is 29 nm with density of 8.3×10^{20} m^{-3} corresponding to 1.6% swelling [50].

Kai and Klueh [51] reported the void morphology of 9Cr-1MoVNb and 12-Cr-1MoVW after irradiation to 35 dpa in FFTF at 420°C. For 9Cr-1MoVNb, a mean void diameter of 30 nm combined with a void density of 6×10^{20} m^{-3} gives a swelling of 0.85%.

Maziasz and Klueh in [52] reported the mean void diameter and number density in 9Cr-1MoVNb and 12Cr-1MoVW irradiated to 47 dpa at ~400°C in HFIR and FFTF. Samples irradiated in FFTF to 47 dpa only presented a few detectable voids (7 to 23-nm diameter). Because of a neutron spectrum yielding more He production, samples irradiated in HFIR exhibited multiples cavities. For 9Cr-1MoVNb, a mean cavity diameter of 9.2 nm and mean bubble diameter of 3.8 nm with corresponding number densities of 2.71×10^{21} m^{-3} and 1.6×10^{22} m^{-3}, respectively, were

measured. For 12Cr-1MoVW, a mean cavity diameter of 12.5 nm and mean bubble diameter of 3.5 nm with corresponding number densities of 2.2×10^{21} m^{-3} and 3.5×10^{22} m^{-3}, respectively, were measured.

Vitek and Klueh [53] reported an average cavity diameter of 15 nm and number density of 1.1×10^{21} m^{-3} for 9Cr-1MoVNb irradiated to 36 dpa at 400°C in HFIR.

Sencer et al. [54] reported the cavity microstructure of HT-9 irradiated to 155 dpa at 443°C in FFTF. The mean cavity size is ~28 nm with a number density of $\sim 2.5 \times 10^{20}$ m^{-3} with a mean void swelling of ~0.3%.

Gelles [55] reported cavity microstructure observations for T91 and HT-9 after irradiation to ~200 dpa at 420°C in FFTF. For T91, a mean void size of 21.4 nm with a void density of 4.8×10^{21} m^{-3} yielded a swelling of 1.76%. For HT-9, the mean void diameter varied between 21.2 and 32.2 nm with a corresponding number density of 3.1×10^{20} m^{-3} and 5.6×10^{20} m^{-3}, respectively.

Several studies have been conducted to characterize the cavity microstructure of ferritic-martensitic steels under ion irradiation. Gigax et al. [56] irradiated T91 30176 at 475°C using 3.5 MeV Fe^{2+} ions to achieve peak damage levels of 250, 750, and 1000 dpa. Voids were clearly observed in all specimens, but their sizes and distributions varied significantly. The highest measured ion-induced swelling rate between the last two high-dose data points is ~0.11%/dpa as shown in Figure 2.3. The earliest onset of bias-driven growth was at 300 dpa which indicates a very long incubation regime.

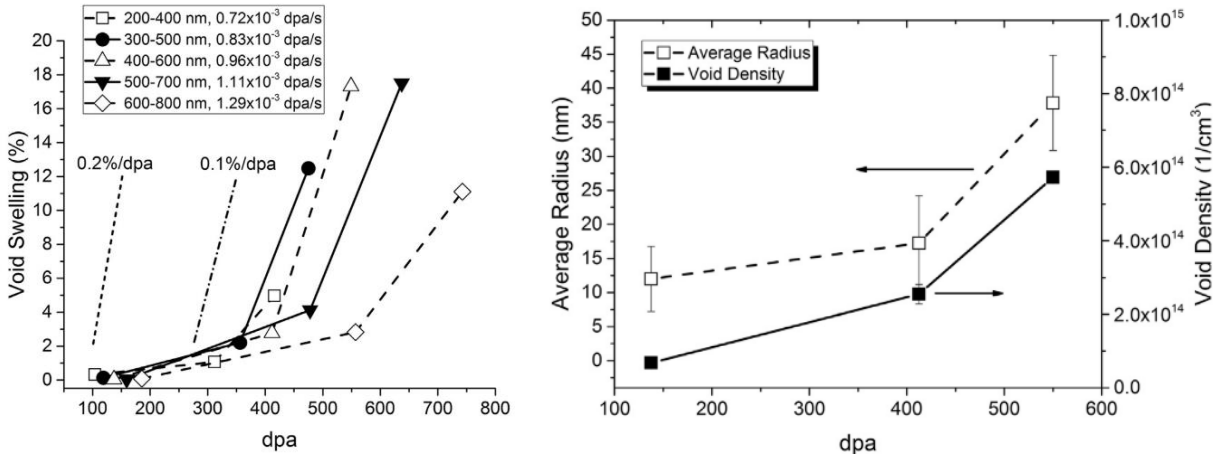


Figure 2.3: (a) Void swelling as a function of local damage level averaged over selected depth intervals of 200 nm thickness with swelling rates of 0.1 and 0.2%/dpa included on the figure for comparison. (b) Plot of the average void radius and concentration as a function of local dpa for the depth region of 400 nm-600 nm. [56].

Getto et al. [57] irradiated HT9 heat 84478 with 5 MeV Fe^{2+}. Some samples were pre-implanted with helium ions at 1, 10 and 100 appmHe. The irradiations were conducted up to 375 dpa at 440, 460 and 480°C. The microstructure analysis revealed consistent increase in void size (as shown in Figure 2.4) and number density with increasing damage levels with and without helium implantation.

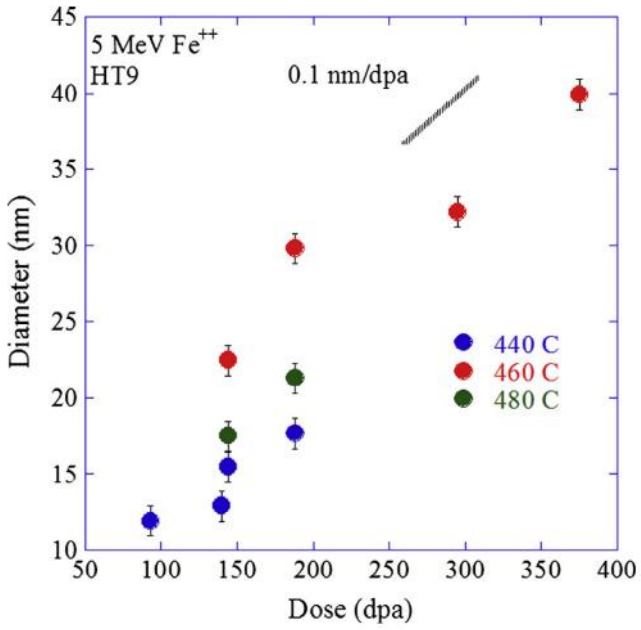


Figure 2.4: Effect of damage level on void diameter in 5 MeV Fe^{2+}-irradiated HT9 at 440, 460 and 480°C with 10 appm He pre-implanted [57].

Asano et al. [58] reported the microstructural evolution of HT9 under dual-ion irradiation. Samples were irradiated to 100 dpa at 450°C with 4 MeV Ni^{3+} and 1 MeV He^{+} at 3×10^{-3} dpa/s. At 15 appmHe/dpa, a bimodal cavity population was formed, and it produced a swelling of 0.14%. The number density and average radius were 1.5×10^{21} m^{-3} and 1.7 nm for small cavities and 1.2×10^{21} m^{-3} and 5.5 nm for large cavities, respectively. Irradiations to 98 dpa with no helium injection formed no visible cavities but only dislocation loops at 430°C.

Ayrault [59] reported the damage level dependence of cavity formation in 9Cr-1Mo for two irradiation configurations. Some samples were dual-ion-irradiated with 3 MeV Ni^{+} and degraded 0.83 MeV He^{+} at 15 appmHe/dpa, while others were pre-implanted with 15 appm He and subsequently single-ion-irradiated. Samples were irradiated up to 25 dpa at 500°C. The average cavity size increased with the damage level and preferential formation of cavities at dislocations within grains, and also at subgrain boundaries and the surfaces of $M_{23}C_6$ precipitates, was observed at all damage levels.

Taller [17] reported the evolution of the cavity size distribution as a function of damage level for dual-ion-irradiated T91 as shown in Figure 2.5. The density of bubbles decreased while bias-driven growth continued which led to an increase in the number of large cavities.

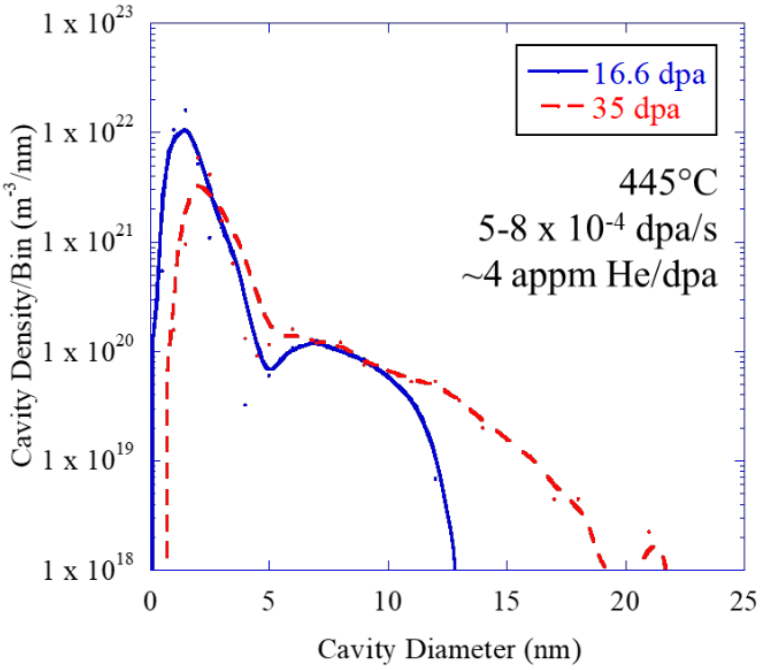


Figure 2.5: Cavity size distribution for dual-ion-irradiated T91 at 445°C with 4 appm He/dpa as a function of damage level [17].

Getto et al. [60] pre-implanted HT9, T91 and T92 with 10 appm He and subsequently irradiated the samples with 5 MeV Fe^{2+} in raster-scanning mode between 75 and 650 dpa at 460°C to study the high-damage-level effect of irradiation on the microstructure. Figure 2.6 shows the evolution of void diameter and number density as a function of damage level.

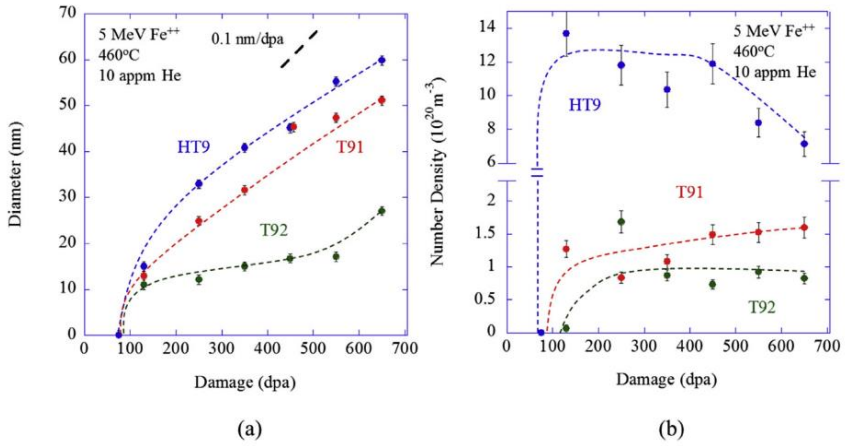


Figure 2.6: Void (a) diameter and (b) number density as function of damage in 5 MeV Fe^{2+}-irradiated HT9, T91 and T92 at 460°C with 10 appm He pre-implanted [60].

Once voids started to appear at 130 dpa, their number density quickly saturated while their average diameter increased with damage level, indicating enhanced void growth.

Getto et al. [61] presented a typical swelling evolution for HT9 heat 84425 pre-implanted with 10 appmHe and irradiated to 650 dpa with Fe^{2+} as shown in Figure 2.7.

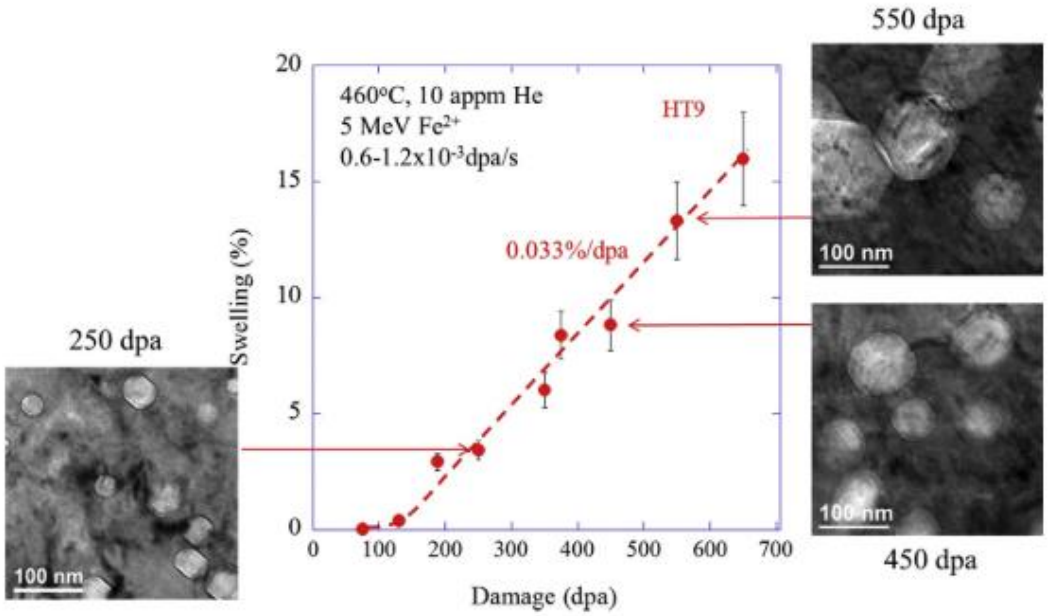


Figure 2.7: Swelling in HT9 heat 84425 irradiated with 5 MeV Fe^{2+} with pre-implanted He versus damage curve calculated with no corrections to the damage or region of interest analyzed [61].

Comparing these studies with one another is challenging because of the differences in temperature, alloy composition and reactor environment. Yet, it appears that the cavity number density saturates at a certain damage level in reactor while bias-driven growth continues, leading to higher average cavity diameters at higher damage levels. Therefore, an incubation period is observed followed by a growth regime of existing cavities where swelling increases by about ~0.2%/dpa for ferritic-martensitic steels [5]. Similar to reactor irradiation, during ion irradiation, it appears that the cavity number density plateaus at a high damage level in the presence of helium while voids keep growing. Yet not all ion irradiations follow the same helium implantation procedure (raster-scanned vs. defocused, pre-implanted vs. co-injected) which make these evaluations more difficult.

2.2.1.2 Temperature effect

For void swelling to occur, the temperature must be high enough (>$0.3T_m$) for the vacancies to be mobile and low enough for vacancy supersaturation (above the thermal equilibrium value) to occur [5,6,46]. Therefore, swelling in metals presents a bell-shape curve with temperature as shown in Figure 2.8 for nickel.

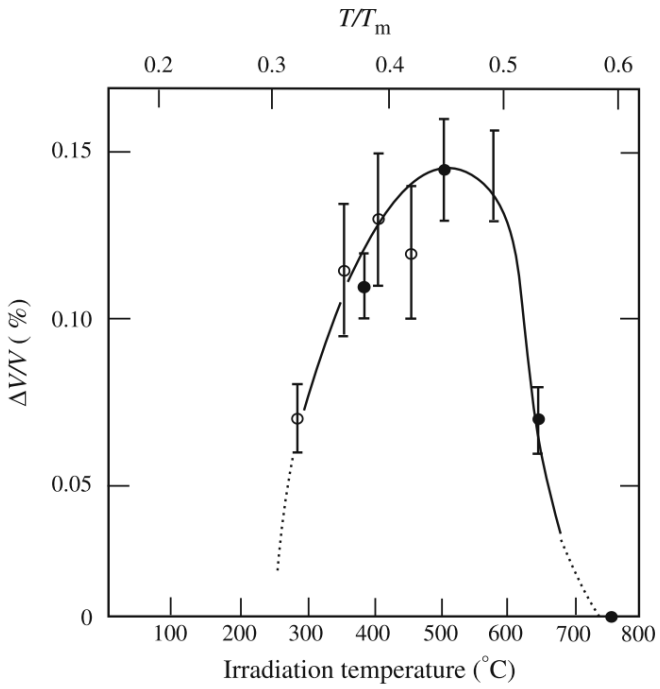


Figure 2.8: Swelling in nickel as a function of irradiation temperature for a fluence of 5×10^{19} n/cm^2 [6].

This evolution has been confirmed for T91 by Jiao et al. [13] as shown in Figure 2.9 in which the number density of cavities after irradiation in BOR-60 at ~16 dpa drops between 376°C, 415°C and 460°C. The presence of a high density of small bubbles resulted in a bimodal cavity distribution. No voids were observed at the 460°C:14.6dpa condition but small bubbles are observed with a number density of 3.2×10^{21} m^{-3}. Small bubbles with an estimated number density of 3.3×10^{21} m^{-3} were also observed in the 524°C:15.4dpa condition.

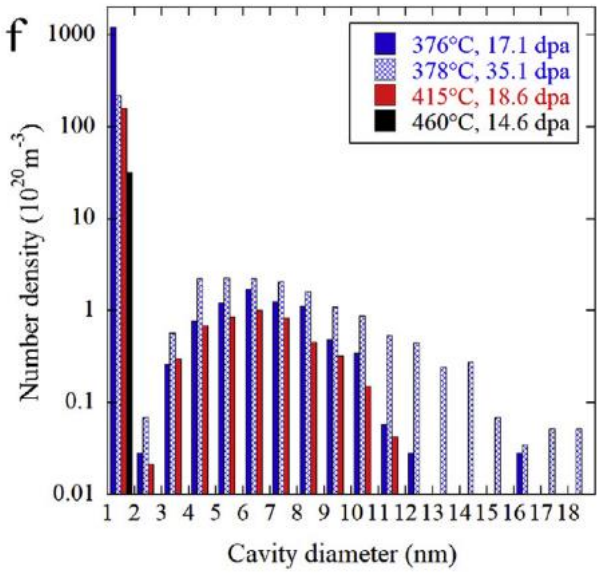


Figure 2.9: Size distribution of cavities for T91 irradiated in BOR-60 [13].

A similar behavior is observed for 9Cr-1MoVNb irradiated in HFIR at 36 dpa. At 300°C, only a few bubbles are visible. At 400°C, the number density rose to 1.1×10^{21} m^{-3} with an average diameter of 15 nm corresponding to 0.19% swelling. At 500 and 600°C, only a few cavities were observed, 4 to 6 nm in diameter but unlike lower temperature where the cavities were evenly distributed, they were located at lath boundaries and dislocations preferentially [53,62]. Finally, helium (up to 440 appm) enhances bubble formation at 300 to 600°C in nickel-doped 9- and 12-Cr steels irradiated in HFIR to ~38 dpa, but voids (bias-driven cavities) formed only at 400 and 500°C [52].

Getto et al. [57] irradiated HT9 heat 84478 with 5 MeV Fe^{2+}. The peak swelling temperature was measured at 460°C with void diameter and number density both peaking at this temperature compared to irradiations conducted at 440 and 480°C. The void growth rate was found to be independent of temperature at doses between 93 and 375 dpa, suggesting that there is a temperature-independent steady state swelling rate. The primary effect of temperature appears to

be on the time to void nucleation. At 440°C and 480°C, swelling was still within the nucleation and transient regime and had not yet reached steady state swelling by 188 dpa.

Ayrault [59] reported the damage level and temperature dependence of cavity formation in 9Cr-1Mo for two irradiation configurations. Some samples were dual-ion-irradiated with 3 MeV Ni^{+} and degraded 0.83 MeV He^{+} at 15 appmHe/dpa, while others were pre-implanted with 15 appm He and subsequently single-ion-irradiated. For both configurations, the damage rate was ~ 4×10^{-3} dpa/s for the damage-dependence experiments and ~ 3×10^{-3} dpa/s for the temperature-dependence experiment. Samples were irradiated at 25 dpa between 450 and 600°C to study the effect of temperature. The size of cavities at subgrain boundaries consistently increased with temperature between 450 and 600°C while the size of intragranular cavities decreased. Yet, the swelling peak was reached at 450°C with cavities as large as 15 nm in diameter.

Taller [17] reported the evolution of the cavity size distribution as a function of temperature for dual-ion-irradiated T91 with 4 appm He/dpa at ~16 dpa as shown in Figure 2.10. At low temperatures, the diffusion of vacancies is too low to trigger bias-driven growth and cavities remain small and do not evolve into voids. The maximum diameter peaks around 460°C with voids up to 24 nm in diameter. As the temperature keeps increasing, the thermal emission of vacancies becomes dominant and bias-driven growth is limited: the growth of voids is possible, but their nucleation is very weak as shown in Figure 2.11.

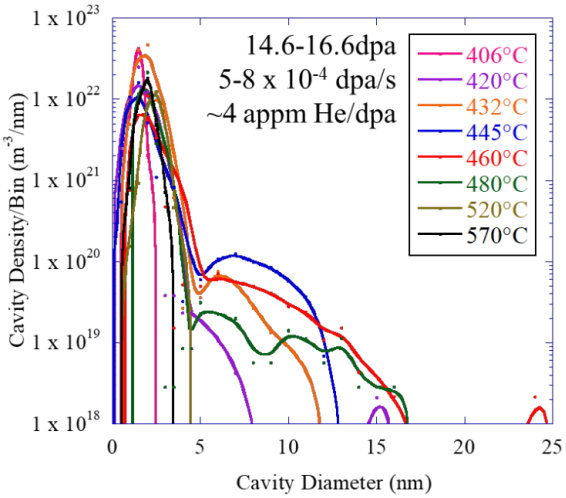


Figure 2.10: Cavity size distribution for dual-ion-irradiated T91 to ~ 16 dpa with 4 appm He/dpa as a function of temperature [17].

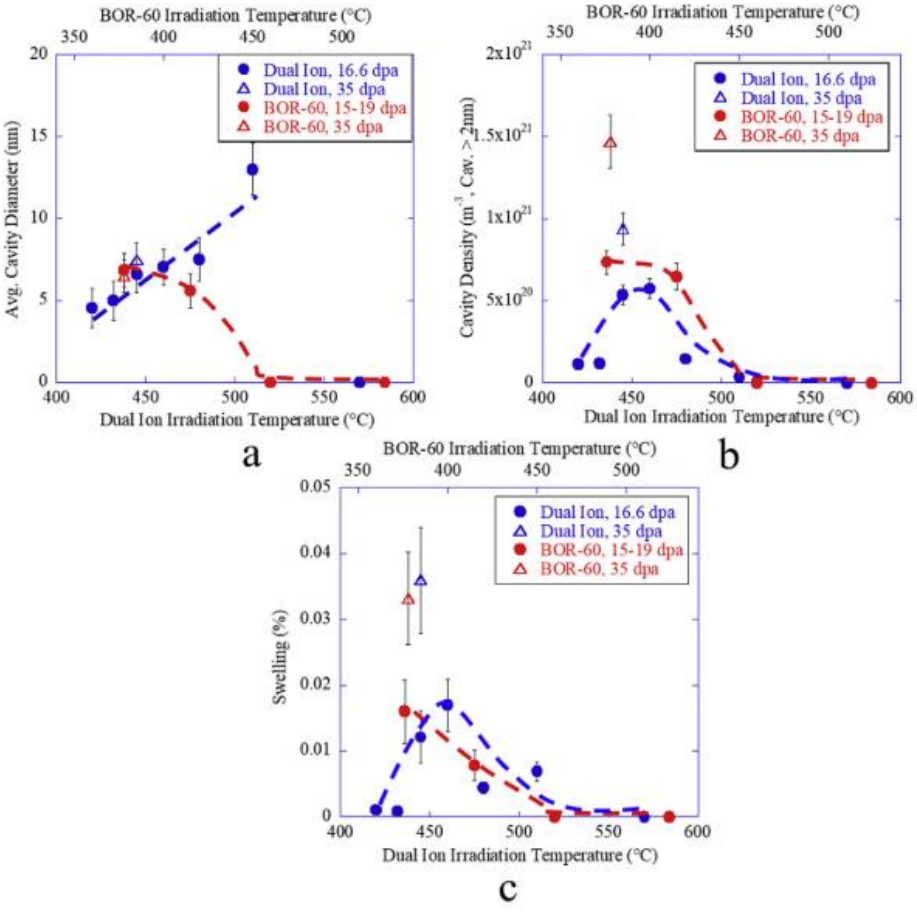


Figure 2.11: Average cavity diameter (a), density (b) and swelling (c) for cavities greater than 2 nm in diameter for dual ion-irradiated T91 with 4 appm He/dpa and BOR-60-irradiated T91 [16].

Lin et al. [63] performed multi-temperature (400, 435, 470, 500, and 550°C) simultaneous dual-ion irradiations using 8 MeV Ni^{3+} ions and energy-degraded 3.5 MeV He^{2+} ions with 0.1 appmHe/dpa on a series of ultra-high purity BCC Fe and Fe-Cr alloys with 3-14%Cr content. Fe-10Cr with 780 wt. ppm C and Eurofer97 reduced activation FM steel were also included. Figure 2.12 shows the evolution of average diameter and number density of cavities as a function of temperature while Figure 2.13 shows the evolution of swelling as a function of temperature. Below 470°C, cavities in Fe had the largest size and the highest number density. When the temperature increased above 435°C, the cavity sizes in Fe-3Cr, Fe-10Cr, and Fe-14Cr started to rapidly increase. All Fe-Cr alloys exhibited the typical bell-curve of void density as a function of temperature centered around 475-500°C. The peak swelling temperature for all the Fe-Cr alloys was around 500°C.

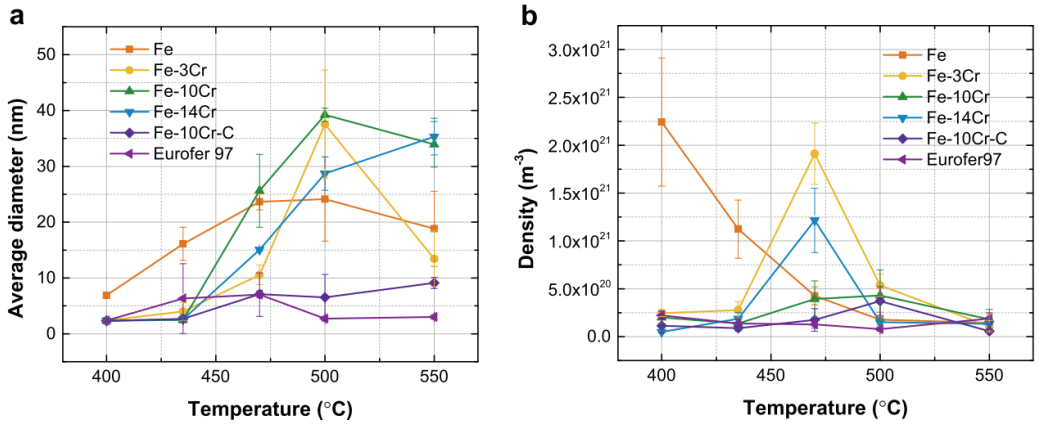


Figure 2.12: Comparison of the (a) cavity size (diameters) and (b) density in ion-irradiated Fe and Fe-Cr alloys at 400°C-550°C [63].

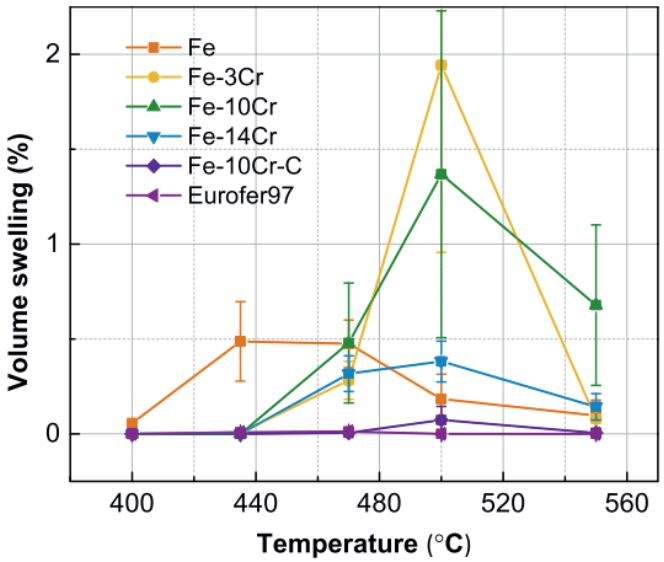


Figure 2.13: Dependence of cavity swelling on irradiation temperature in dual-ion-irradiated Fe and Fe-Cr alloys [63].

In both reactor and ion irradiations, the void density exhibits a bell-shaped behavior with temperature while the void diameter increases with temperature. As a result, swelling also exhibits a bell-shaped behavior at slightly higher temperatures than the void density. In the presence of helium, it seems that the bubble microstructure is not significantly affected by temperature compared to the void microstructure.

Well-controlled materials irradiation tests (such as ion irradiation or temperature-controlled tests in reactor) will probably yield lower swelling values compared to that where the temperature history is more typical of normal reactor operation because of thermal cycles happening during operation [49].

2.2.1.3 Helium and helium-to-dpa effect

This section shows that helium has a significant effect on cavity microstructure in irradiated FM steels. In dual-ion irradiation, helium is either pre-implanted or co-injected while it is always co-produced with damage in reactor. The overall effect of helium is the same whether it is pre-

implanted or co-injected/produced, but the magnitude of the effect might be different. When it is not pre-implanted, helium is usually added to the microstructure at a constant rate. Thus, the total amount of helium and the helium-to-dpa ratio in an irradiation are equivalent and conclusions are similar for both.

Baskes (as cited in [44]) calculated the stability of three-dimensional vacancy clusters and concluded that vacancy loops are more favorable to form in gas-free materials whereas in the presence of helium, bubbles would form. Helium needs to agglomerate to form bubbles, typically at various microstructural trapping sites. The bubbles can serve as nucleation sites of growing voids through displacement damage [12]. The helium generation rate is found to be the most important parameter for bubble formation at all temperatures, especially during the incubation period [5,64,65]. It is postulated that a high helium concentration yields a high cavity sink strength which increases recombination of point defects at the cavities. This reduces the point defect supersaturations and inhibits bubble-to-void conversion [65].

This phenomenon was reported by Getto et al. [57] who irradiated HT9 heat 84478 with 5 MeV Fe^{2+}. At every temperature and damage level, the cavity number density increased with increasing helium concentration. Yet, the average diameter increased with concentration at 460°C but decreased at 440 and 480°C. Helium affected void nucleation by decreasing the time to appearance of visible voids. However, at higher doses, but still in the transition regime, helium was found to decrease swelling by enhancement of nucleation of small voids, which inhibited void growth.

Asano et al. [58] reported the microstructural evolution of HT9 under dual-ion irradiation. Samples were irradiated to 100 dpa at 450°C with 4 MeV Ni^{3+} and 1 MeV He^{+} with 5-15 appmHe/dpa at 3×10^{-3} dpa/s. At 15 appmHe/dpa, a bimodal cavity population was formed, and

it produced a swelling of 0.14%. The number density and average radius were 1.5×10^{21} m^{-3} and 1.7 nm for small cavities and 1.2×10^{21} m^{-3} and 5.5 nm for large cavities, respectively. When the injection rate was reduced to 5 appmHe/dpa, only small cavities were visible indicating that bubbles still had not reached the critical radius as the accumulation of helium atoms was insufficient.

Taller compiled data on the evolution of average cavity size, cavity density and swelling as a function of helium production/injection rate as shown in Figure 2.14. More details are given in Figure 2.15 with the evolution of the cavity size distribution as a function of the helium injection rate for dual-ion-irradiated T91.

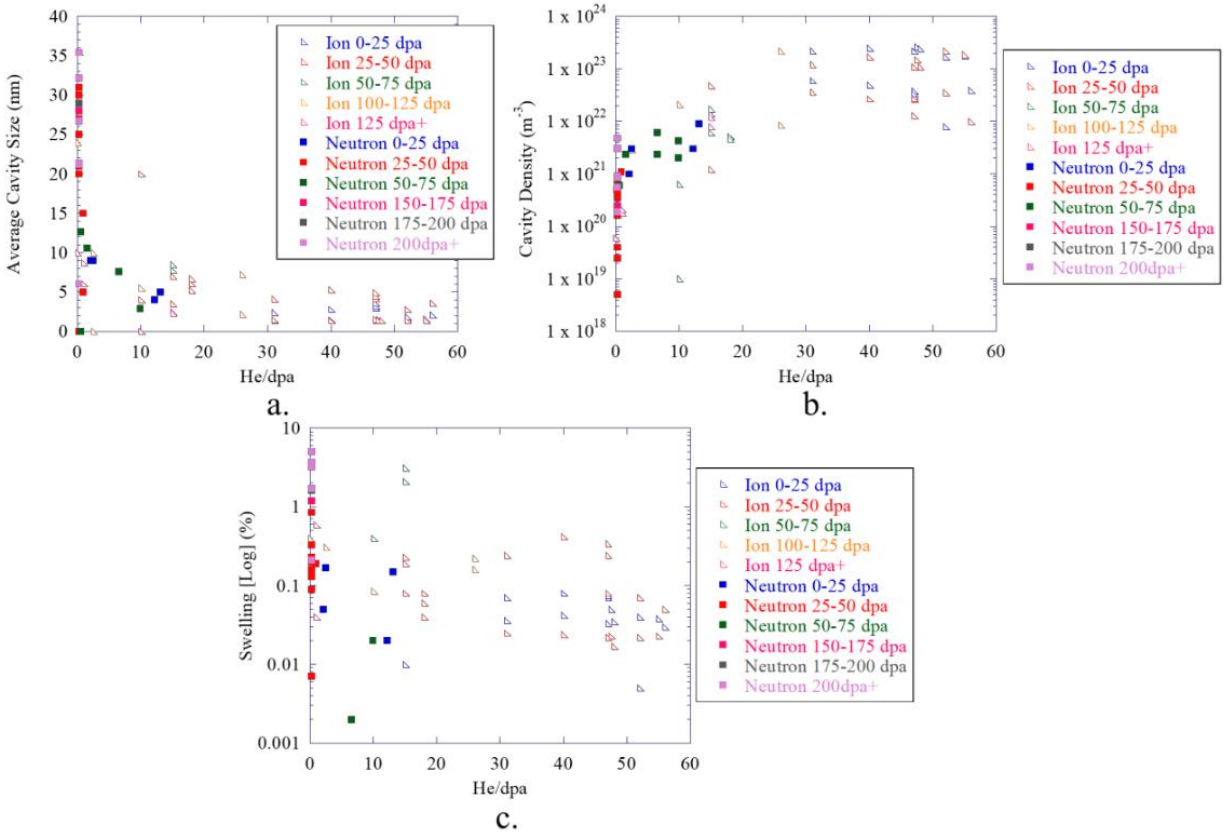


Figure 2.14: Compilation of literature data to show the effect of the helium/dpa ratio on (a) average cavity size, (b) average cavity density, and (c) swelling [17].

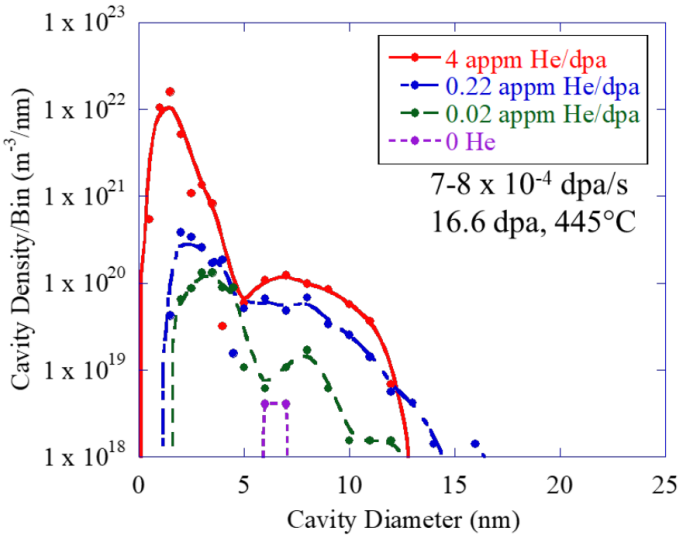


Figure 2.15: Cavity size distribution for multiple helium injection rate for dual-ion-irradiated T91 [17].

The results confirm that increasing He/dpa ratio increases the void density and decreases the average cavity size which corresponds to bubbles being dominant over voids.

These observations are reinforced by Wang et al. [66] who reported an increase in void density (3.6×10^{20} m^{-3} to 20.5×10^{20} m^{-3}) and a decrease in void diameter (40.6 nm to 29.1 nm) for CNS I irradiated with 5 MeV Fe^{2+} to 188 dpa et 460°C when the pre-implanted helium increased from 10 appm to 100 appm He.

Woodley et al. [67] performed irradiations with 5.0 MeV Fe^{2+} ions and degraded He^{2+} ions at 445°C up to damage levels of 150 dpa and helium co-injection rates of 0, 0.02, 0.2 and 4 appm He/dpa in T91, and at 460°C to a damage level of 188 dpa and helium co-injection rates of 0, 0.06 and 4 appm He/dpa in HT9. Results of the void microstructure characterization are presented in Figure 2.16. The average void diameter was relatively constant as a function of helium co-injection rates at 17 and 50 dpa, while the void density increased. At the highest damage level of 150 dpa, the average void diameter dropped significantly between 0 and 4 appm He/dpa and the void density peaked at 0.2 appm He/dpa. The resulting swelling maximum occurs at the highest helium co-

injection rates at 17 dpa, shifting to an intermediate helium co-injection rate at 50 dpa, and finally peaks at zero helium at 150 dpa. The helium-to-dpa ratio at which the maximum swelling occurs shifts to lower helium-to-dpa levels as the damage level increases in ferritic-martensitic steels.

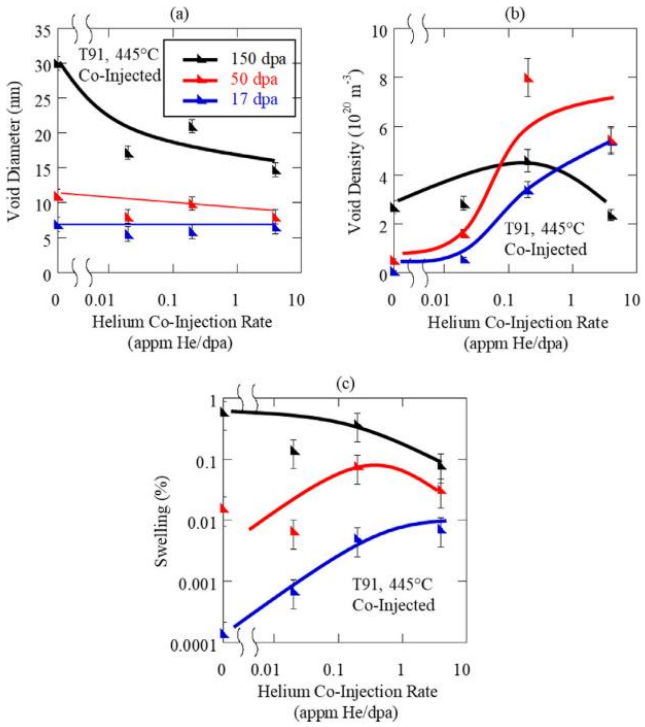


Figure 2.16: Average void diameter (a), void density (b) and swelling (c) as a function of helium co-injection rate (appm He/dpa) for dual-ion-irradiated T91 at 445°C at various damage levels [67].

The bubble diameter varies little with appm He/dpa, but varies with damage level, from ~3 nm at 17 dpa to ~2 nm at 50 dpa and ~1 nm at 150 dpa. The bubble density shows a monotonic increase in density with increasing damage level. Similar trends were reported for HT9.

Monterrosa et al. [68] implanted T91 heat C2269 with He^{+} to levels of 0, 1, 10, 100 and 1000 appm. Samples were then irradiated with raster-scanned 4.4 or 5.0 MeV Fe^{2+} at 460°C to 50, 150 and 300 dpa at 1.4×10^{-3} dpa/s. Results of the cavity microstructure characterization are shown in Figure 2.17. Bubbles were only visible at the higher implantation levels (100 and 1000 appm) hence the much higher cavity density compared to lower implantation levels. This caused cavity

distributions to evolve from unimodal to bimodal as the damage increased to 300 dpa at high implantation levels. Except for 0 appm He where it increases between 50 and 150 dpa, the cavity number density was rather constant with increasing damage level. For 0, 1 and 10 appm He levels, the average cavity diameter kept increasing significantly with increasing damage level. Yet, for 100 and 1000 appm He levels, the average cavity diameter was kept rather small because of the high density of bubbles. This significant bubble density with sizes <4nm yielded a clear suppression of growth resulting in low swelling at all damage levels. Bubbles do not behave as neutral sinks and are thought to be biased toward interstitials. For bubbles up to a size of 4 nm, this bias toward interstitials can range from 10 to 20% [68].

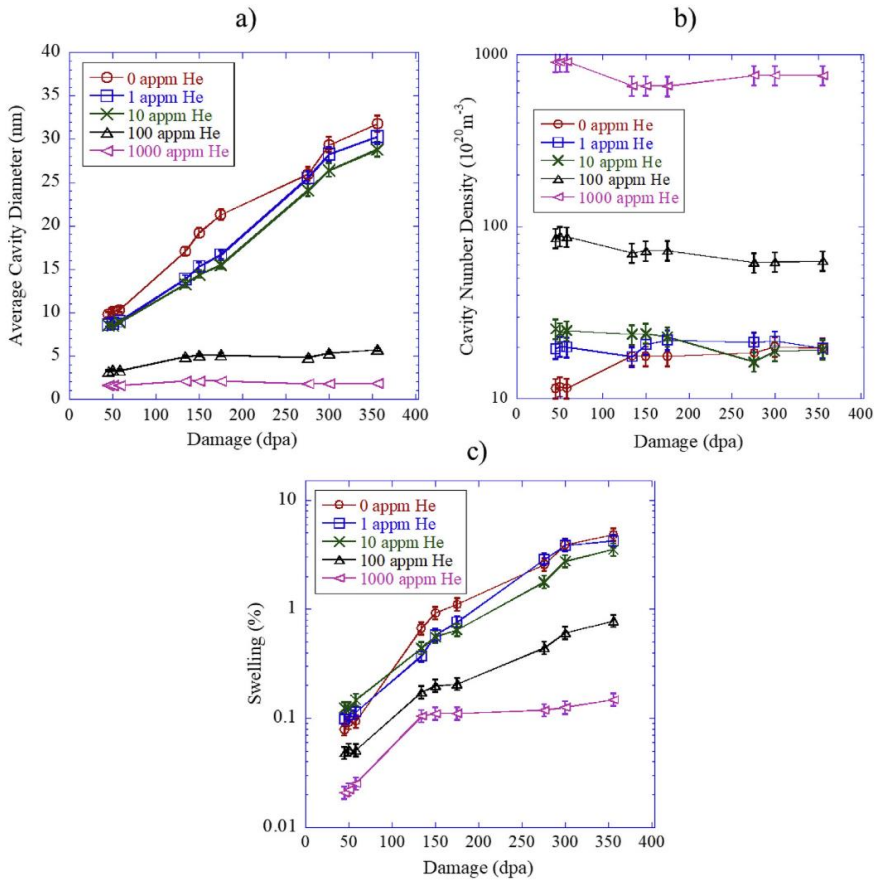


Figure 2.17: a) Average cavity diameter, b) number density, and c) swelling as a function of damage in T91 for pre-implanted He levels of 0, 1, 10, 100, and 1000 appm [68].

Lin et al. [69] irradiated Fe and Fe-10Cr with 8 MeV Ni ions and co-implanted He ions at 500°C up to 30 displacements per atom (dpa) with He implantation rates of 0.1, 10 and 50 appm He/dpa. In both materials, the average void diameter decreased with increasing helium concentration (by ~60% and ~82% for Fe and Fe-10Cr, respectively), whereas the average bubble diameter was nearly constant or slightly decreased. At lower helium levels (0.1-10 appm He/dpa), the void density increased by two orders of magnitude, whereas it decreased by almost a factor of 10 at higher helium levels (10-50 appm He/dpa). From 10-50 appm He/dpa, the bubble density increased by a factor of 1.5 and 2.4 for Fe and Fe-10Cr, respectively.

Li et al. [70] irradiated F82H, ODS, SIMP and T91 steels with 6.4 MeV Fe^{3+} and 1.0 MeV He^{+} ions at 300°C and 450°C with 60, 200 and 600 appmHe/dpa. At 300°C, the average size of bubbles decreases with increasing helium injection ratio. At 400°C, the average size of observed bubbles increases with increasing helium injection ratio.

The effect of increasing helium content on the cavity microstructure evolution is to increase the density of bubbles and voids while decreasing the average void diameter at low to intermediate damage levels. The effect on average bubble diameter is not very conclusive. As the damage level increases, overnucleation of bubbles in the microstructure can lead to lower void density and lower swelling at high helium concentrations compared to intermediate concentrations, because of the dominating bubble sink strength and their bias towards interstitials.

2.2.1.4 Microstructure & composition effect

Little and Stow [71] studied the swelling of Fe-Cr binary alloys and observed a decrease in swelling for chromium up to 5%. Similarly, Lin et al. [63] reported that increasing chromium solute levels dramatically suppress cavity swelling in the ion-irradiated Fe-Cr alloys below ~450°C as shown in Figure 2.18. At the two highest investigated irradiation temperatures, maximum

swelling values were found for 3%Cr and 10%Cr at 500°C and 550°C, respectively. However, the overall swelling variation was non-monotonic with respect to Cr content and exhibited different general behavior at different temperatures.

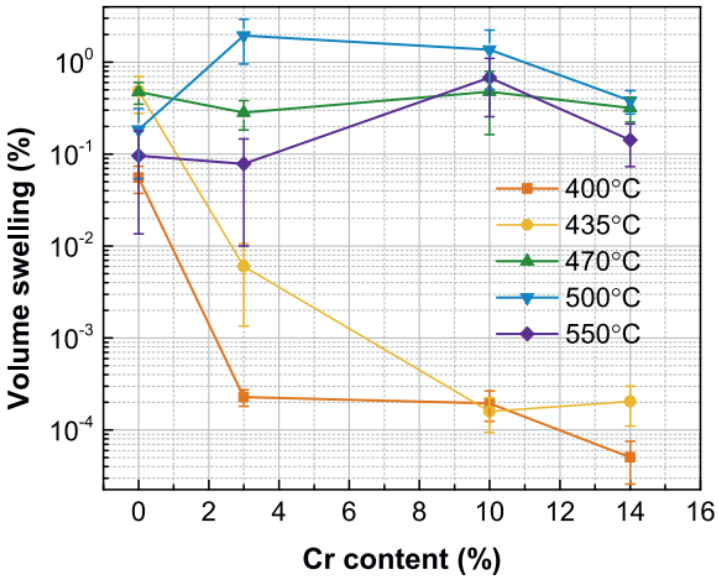


Figure 2.18: Variation of swelling as a function of Cr concentration in high-purity Fe and Fe-Cr dual-ion-irradiated samples [63].

Several theories have been developed to explain this observation. Little et al. [71] explained their results by solute trapping; the suppression of the void nucleation rate by the enhanced recombination of vacancies and interstitials due to the trapping effects caused by the weak interactions between chromium atoms and vacancies. Solute-atom trapping involves both interstitial and substitutional elements that bind preferentially to irradiation-produced point defects; it retards the migration of the defects to sinks, thus enhancing vacancy-interstitial recombination [71]. However, high vacancy mobility and high sink densities in commercial alloys at low temperatures, and detrapping at higher temperatures, suggest that recombination effects in the matrix might be small compared to recombination at sinks via absorption [10,72]. This result is supported by Ayrault [59] who reported that bigger size grains contain bigger cavities, and

largest cavities tend to be located at the center of the grains for dual-ion-irradiated 9Cr-1Mo since grain boundaries are strong sinks at small grain sizes. Results from Little [73] for binary Fe-Cr alloys demonstrated that chromium in solid solution is not primarily responsible for the high swelling resistance of the 9-13% Cr martensitic grades.

On the other hand, Huang et al. [74] suggested that the presence of chromium in FM steels strongly contributes to their swelling resistance. The removal of interstitials from the bulk via fast one-dimensional (1-D) motion of interstitial clusters to sinks was identified as the predominant mechanism leading to the accumulation of excess vacancies in the matrix of low-alloyed iron. Both ab initio studies and some based on advanced interatomic potentials have shown that Cr interacts strongly with interstitials acting as a trap for migrating interstitial clusters. Additionally, the release of vacancies from the complicated $M_{23}C_6$/matrix interface were detected, indicating that metal carbides have a strong effect on void swelling resistance.

Looking at the swelling behavior of other alloys can provide some explanations. For ODS, void growth was delayed with increasing microstructural complexity, namely by increasing the dislocation density and immobilizing dislocations via nanoscale oxide particles and clusters as well as nucleation of a high density of cavities by trapping helium atoms at particle-matrix interfaces [75].

Kim et al. [76] irradiated HT9 with reduced and increased nitrogen content with 3.5 MeV Fe^{2+} at 450°C to 200, 400 and 600 peak dpa. The low-nitrogen HT9 exhibited a much higher swelling (3.7%) compared to the high-nitrogen HT9 (0.5%), both at 392.6 local dpa. The main difference was in the presence of VN precipitates before irradiation in the high-nitrogen HT9. Under ion irradiation, those VN precipitates were not stable and dissolved into the matrix. Nitrogen

atoms are known to trap vacancies and interstitials and form defect-solute atom complexes that can act as a recombination site and reduce swelling.

It appears that the cavity microstructure evolution in FM steels is affected by the matrix composition due to solute atoms impacting the diffusion of point defects and defect clusters. Cr solute atoms are reported to trap vacancies which increases their recombination with interstitials and limits the nucleation of cavities. The presence of a high density of sinks such as carbides and oxide particles also affects nucleation and growth by providing additional recombination and nucleation sites as well as pinning of dislocations.

2.2.1.5 Damage rate effect

The effect of damage rate in neutron-irradiated metals is difficult to identify in literature as the damage rate is rarely reported and is coupled with temperature, which makes it difficult to control independently. However, ion irradiation has precise control of damage rate: Taller [17] reported the evolution of the cavity size distribution as a function of damage rate for dual-ion-irradiated T91 as shown in Figure 2.19.

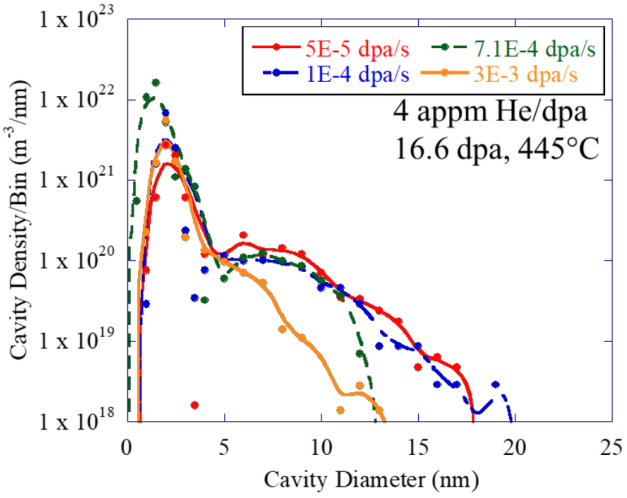


Figure 2.19: Cavity size distribution for multiple damage rate in dual-ion-irradiated T91 [17].

When the damage rate increases, supersaturation of point defects increases, leading to higher recombination and fewer vacancies available for void growth [6]. The irradiation temperature can be increased to an extent to enhance migration and counterbalance this effect. For damage rates above 10^{-4} dpa/s, voids are getting smaller on average and their density decreases.

Taller [17] provided an in-depth explanation of these results based on the availability of helium with increasing damage rate. With increasing damage rate, void nucleation is more likely because of the increased vacancy supersaturation. Without spontaneous nucleation or stochastic fluctuations, the only path to void nucleation is the accumulation of helium in bubbles to reach the critical radius. They estimated that all irradiations below a damage rate of 1×10^{-4} dpa/s should not nucleate voids spontaneously. Yet, the density of voids decreases with increasing damage rate. So, the amount of helium arriving at cavities must decrease with damage rate to account for the decreased void nucleation rate. With increasing damage level, the helium concentration in the matrix and at dislocation loops begins to level off between 1 to 10 dpa. However, the cavities continue to accumulate helium, leading to the continual nucleation of bubbles. Evidence for this comes from the increase in void density with dpa while maintaining a constant average diameter.

With increasing damage rate, helium concentration in the matrix and helium trapped at dislocation loops increase significantly, therefore reducing helium available for cavities at a given damage level. This is likely from the lack of time for helium to de-trap from the weaker traps and flow to the bubbles and voids. The decreased helium per cavity favors a population of bubbles over voids because bubbles are stabilized with less helium than voids.

2.2.1.6 Unimodal/bimodal size distribution

Bimodal cavity distributions typically contain a distribution of small cavities with an average diameter of a few nanometers (referred to as bubbles) as well as a second population of

larger cavities (referred to as voids) [57,58,63,67,72,77,78] . The critical radius concept is often referenced as an explanation for this phenomenon where bubbles did not achieve bias-driven growth because their radii are less than the critical value. Thus, the upper cut-off radius for the bubbles approximately equals the theoretical minimum critical radius [77]. Theory explains that as the number of gas atoms in a bubble increases the critical cavity radius decreases since helium stabilizes cavities. Taller et al. [72] confirmed this after observing a reduction in the peak bubble radius and critical radius with increasing He co-injection rate in T91 at 445°C irradiated to 16 dpa at 7-8 $\times 10^{-4}$ dpa/s. If the number of gas atoms within a bubble exceeds a critical value, the critical radius effectively disappears, and bias-driven cavity growth occurs regardless of the cavity radius [77].

Horton and Mansur [77] studied the critical cavity radius in Fe-10Cr. Specimens were implanted with 300 appm He at room temperature and subsequently annealed for 2 hours at 1000K to generate a population of bubbles. After annealing, the population was unimodal and had an average diameter of 2.7 nm with density of 6×10^{21} m^{-3}. The specimens were then bombarded with 4 MeV Fe^{2+} ions to 30 dpa at 850K and 8×10^{-3} dpa/s. After irradiation a bimodal size distribution appeared with a critical diameter of ~5 nm as shown Figure 2.20.

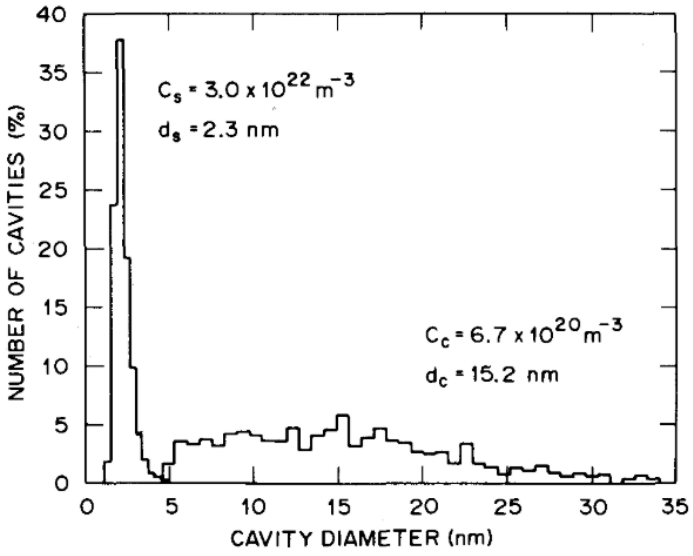


Figure 2.20: Cavity size distribution for Fe-10Cr implanted with 300 appm He, annealed, and irradiated to 30 dpa [77].

As the damage level increases, two competing effects for the evolution of the uni/bimodality of the cavity microstructure have been identified. With an increasing helium content with relatively stable bubble and void densities, the number of helium atoms in cavities might increase until it exceeds the critical value and erases the bimodality at higher damage levels [72]. Yet, Stoller [65] explained that the effective vacancy supersaturation decreases at the onset of cavity growth regime since the capture efficiencies of cavities increase. Thus, transition from bubbles to voids is more difficult and the critical number of gas atoms increases. This causes bubbles formed later in the irradiation to be trapped below the critical size and contributes to the formation of bimodal cavity distributions.

Lin et al. [69] irradiated Fe and Fe-10Cr with 8 MeV Ni ions and co-implanted He ions at 500°C up to 30 displacements per atom (dpa) with He implantation rates of 0.1, 10 and 50 appm He/dpa. At 50 appmHe/dpa, the average diameter of the cavities for Fe and Fe-10Cr was 7.9 and 3.6 nm, respectively. The maximum cavity diameter in Fe (37.8 nm) was about double compared

to Fe-10Cr (19.3 nm). The critical radius estimated from the local minimum in the size distribution was ~1.9 nm for both of these materials, which is comparable to the value at 10 appmHe/dpa.

Bimodal cavity size distribution results from the presence of helium which stabilizes small cavity nuclei. However, a minimum helium injection rate around 0.1 appm He/dpa appears necessary to create a bimodal distribution.

2.2.2 Dislocation loops

Below ~0.3 T_m, interstitials are mobile relative to vacancies, and the interstitials combine to form dislocation loops that increase the strength and decrease the ductility of the material. Dislocation loops with two Burgers vector orientations are possible in ferritic/martensitic steels: a cube-edge loop with a⟨100⟩ Burgers vectors on {100} planes and glissile edge loops with a/2⟨111⟩ Burgers vectors on {111} planes [5,13]. It has been suggested that a⟨100⟩-type loops have a strong interstitial bias that results in a/2⟨111⟩-type loops becoming sinks for the vacancies (E. A. Little et al. as cited in [5]). Electron irradiation studies verified that a⟨100⟩-type loops have a strong bias for interstitials, while a/2⟨111⟩-type loops are essentially neutral sinks (R. Bullough et al. as cited in [5]). These latter loops therefore become sinks for the vacancies [55], thereby reducing the vacancies available to cause cavity growth.

2.2.2.1 Damage level effect

For neutron and proton irradiation, Renterghem et al. [79] reported that T91 irradiated between 1 and 4.35 dpa between 254 and 290°C exhibited an increase in loop density and average loop diameter from 3.9×10^{21} m^{-3} to 2.4×10^{22} m^{-3} and from ~5 nm to 12.2 nm, respectively.

Gupta et al. [80] studied the microstructure of proton-irradiated T91 at 2×10^{-5} dpa/s up to 10 dpa. Average size and number density of dislocation loops increased with increasing damage

level at 400 and 500°C to 10 and 7 dpa, respectively. Jiao et al. [81] found similar results for T91 irradiated with protons up to 9.2 dpa at 450°C, while Wharry et al. [82] reported that the dislocation loop microstructure at 400°C saturated by 7 dpa both in terms of density and diameter.

Liu et al. [83] examined the loop microstructure of T91 irradiated with 1 MeV Kr ions at 300, 400 and 500°C up to a fluence of 4.2×10^{15} ions/cm^2 (1.04×10^{-3} dpa/s and 7.0 dpa). Loops begin to appear around 1 dpa and both the average diameter and density increased at 3 dpa until the number density plateaued at 3×10^{21} m^{-3} when interactions with line dislocations and grain boundaries become apparent. Past 3 dpa, only the average loop diameter kept increasing to 7 dpa.

Getto et al. [60] pre-implanted HT9, T91 and T92 with 10 appm He and subsequently irradiated the samples with 5 MeV Fe^{2+} between 75 and 650 dpa at 460°C. Figure 2.21 shows the evolution of the loop diameter and number density as well as loop line length and network line length as a function of damage level in HT9. At 130 dpa, an important number (9×10^{20} m^{-3}) of small (~21 nm) loops were measured. As the damage level increases, the density sharply drops and saturates at ~2×10^{20} m^{-3} while the average loop size remains constant initially before sharply increasing around 400 dpa to ~78 nm. It also appears that the network dislocations behavior dominates that of loops based on the order-of-magnitude difference in line length at any damage level.

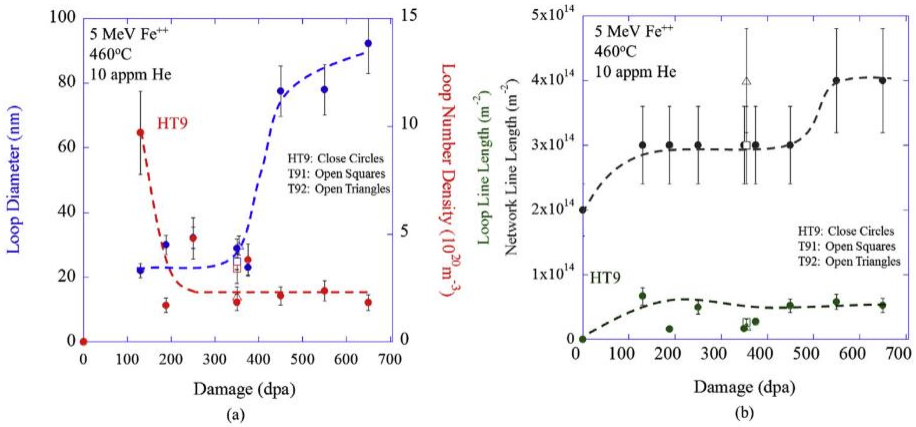


Figure 2.21: (a) Dislocation loop diameter (blue) and loop number density (red) for HT9, and (b) Loop (green) and network (black) line length for HT9. Results from T91 and T92 are plotted at 350 dpa only [60].

Monterrosa et al. [68] implanted T91 heat C2269 with He^+ to levels of 0, 1, 10, 100 and 1000 appm. Samples were then irradiated with 4.4 or 5.0 MeV Fe^{2+} at 460°C to 50, 150 and 300 dpa at 1.4×10^{-3} dpa/s. Results are presented in Figure 2.22. For both a⟨100⟩ and a/2⟨111⟩ loops, a higher density was observed at 50 dpa, which dropped by 150 dpa and stabilized by 300 dpa. Both types of loops also experienced a small amount of growth from 50 to 300 dpa. Overall, a⟨100⟩ loops were observed in a higher density by 3-4 times, and about twice the size of a/2⟨111⟩ loops at any given damage level.

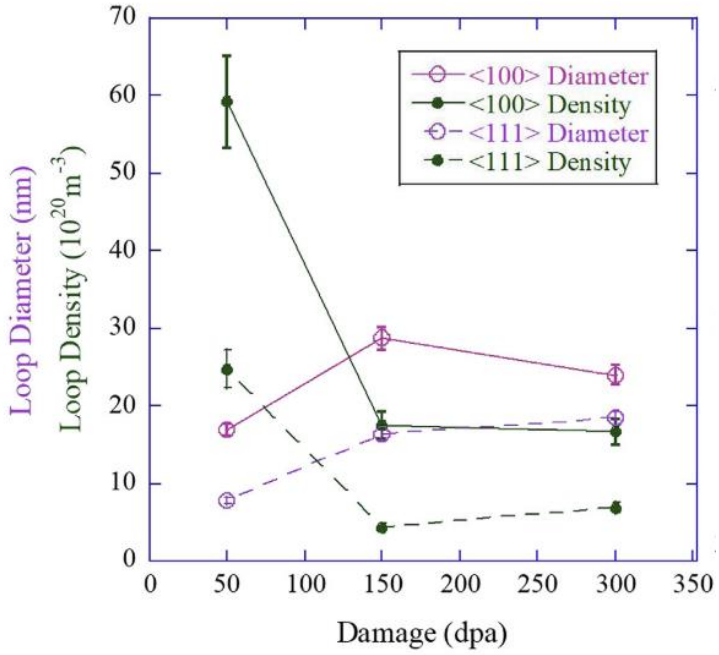


Figure 2.22: Dislocation loop densities and diameters for a⟨100⟩ and a/2⟨111⟩ loops are plotted as a function of damage for the 10 appm He condition [68].

Taller et al. [16] reported that the dislocation loop density slightly decreased from 3.5 × 10^{21} m^{-3} to 2.8 × 10^{21} m^{-3} and the average loop diameter decreased from 25.3 ± 3.0 nm to 19.0 ± 2.3 nm with the size distribution shifting to lower diameters with increasing damage level from 16.6 to 35 dpa at 445°C.

Zheng et al. [84] irradiated HT9 in the BOR-60 reactor to ~17.1 and ~35.1 dpa at 377 ± 23°C. The average dislocation loop diameters are 18.6 ± 1.8 nm and 16.7 ± 1.5 nm, and the total number densities are 3.9 ± 0.4 × 10^{21} m^{-3} and 8.0 ± 0.8 × 10^{21} m^{-3} for 17.1 dpa and 35.1 dpa, respectively. The proportions of a ⟨100⟩ loops/total are 77.2 ± 7.7% and 79.3 ± 7.9%.

Xiu [85] irradiated HT9 and additively manufactured HT9 with dual-ion irradiation up to 250 dpa and between 400°C and 500°C. High sink strength strongly suppresses the growth of dislocation loops of both a⟨100⟩ and a/2⟨111⟩ types with increasing damage levels, and a⟨100⟩

loops show significant growth and stability with higher irradiation temperatures. This response is identical in both additive manufactured and traditionally processed high-Cr steels.

Thus, it appears that dislocation loops in FM steels nucleate very early during irradiation with both density and average diameter stabilizing at intermediate damage levels. At high damage levels (>150 dpa), loop diameter is susceptible to drastically increase and loop density to drastically decrease based on overall sink strength.

2.2.2.2 Temperature effect

After irradiation in BOR-60 at 376°C:17.1 dpa and 378°C:35.1 dpa, the dislocation loops are ~90% a⟨100⟩ with ~10% a/2⟨111⟩. The average dislocation loop diameters are 21.8 nm and 22.9 nm and the number densities are 2.9×10^{21} m^{-3} and 1.9×10^{21} m^{-3} for 17.1 dpa and 35.1 dpa, respectively [13]. When the temperature increased, at 415°C:18.6 dpa, the average dislocation loop diameter and number density increased to 25.8 nm and decreased to 2.0×10^{21} m^{-3}, respectively. No dislocation loops were identifiable for 460°C:14.6 dpa and 524°C:15.4 dpa in BOR-60. Figure 2.23 shows the size distribution of dislocation loops in T91 after irradiation in BOR-60.

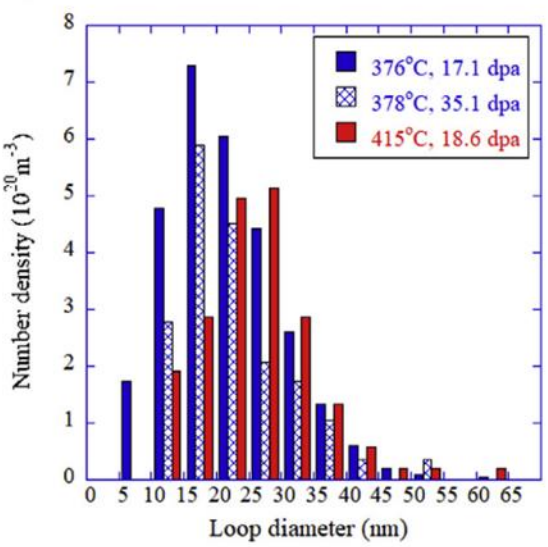


Figure 2.23: Dislocation size distribution after irradiation of T91 in BOR-60 [13].

These results indicate that the average loop size typically increases while the loop density decreases with irradiation temperature, which is consistent with other publications [80,86].

Dislocation loop microstructure is very sensitive to small variations in reactor irradiation parameters. Additional studies, supposedly conducted at comparable conditions as those presented previously (469°C:4.3 dpa in ATR [87] and at 420°C:35 dpa in FFTF [51]) reported very different results (density of 6.0×10^{22} m^{-3} but smaller size of 5.3 ± 2.0 nm, and density of 5×10^{19} m^{-3} but larger average diameter of 100 nm, respectively).

For heavy ion irradiation, Getto et al. [57] reported a peak in loop size and number density at 460°C for HT9 irradiated with 5 MeV Fe^{2+} with and without helium pre-implantation. No loops were observed at 480°C.

For dual-ion-irradiated T91 (4 appmHe/dpa), Figure 2.24 shows that the loop size increases with temperature while the loop density decreases until it reaches 500°C where essentially no loops are present.

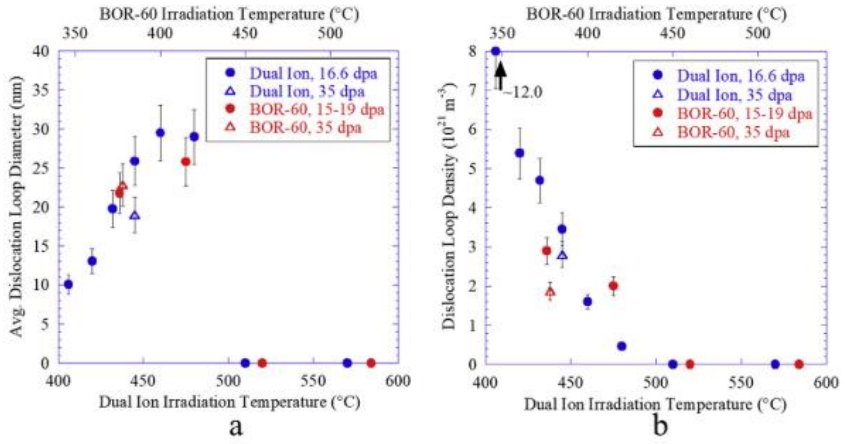


Figure 2.24: (a) Average dislocation loop diameter and (b) dislocation loop density as a function of irradiation temperature for BOR60-irradiated and dual-ion-irradiated T91 [16,17].

Liu et al. [83] examined the loop microstructure of T91 irradiated with 1 MeV Kr ions at 300, 400 and 500°C up to a fluence of 4.2×10^{15} ions/cm^2 (1.04×10^{-3} dpa/s and 7.0 dpa). As the

temperature increases, the proportion of $a_0\langle 100\rangle$ augments with an estimated $\langle 111\rangle/\langle 100\rangle$ ratio around 1.02 ± 0.38 for the 400°C case. At 500°C, the loops were found to be predominantly $a_0\langle 100\rangle$ type.

The evolution of the dislocation loop microstructure in FM steels under irradiation indicates that as the temperature increases, the average loop diameter increases, and the loop density decreases until no loops are present. $a\langle 100\rangle$-type loops seem to dominate at high temperatures while $a/2\langle 111\rangle$ are prevalent at lower temperatures.

2.2.2.3 Helium effect

Historically, the influence of helium on dislocations has received considerably less attention than that on cavities [46]. The effects of helium on dislocation densities should be explored during nucleation before the onset of significant swelling. When in vacancy, helium slightly reduces migration and recombination with interstitials, which could indirectly create more interstitial loops. Bias-driven cavity growth starts earlier, and the dislocation structure expands accordingly. However, the first loops formed in this process are more likely to accumulate helium and other impurities and their growth is restricted compared to subsequently generated loops [46].

Jiao et al. [81] studied the evolution of dislocation loop average diameter and number density as a function of helium concentration in proton-irradiated T91 up to 9.2 dpa at 450°C. On average, increasing the helium concentration at a fixed damage level caused an increase in number density and a decrease in average diameter of loops as shown in Figure 2.25.

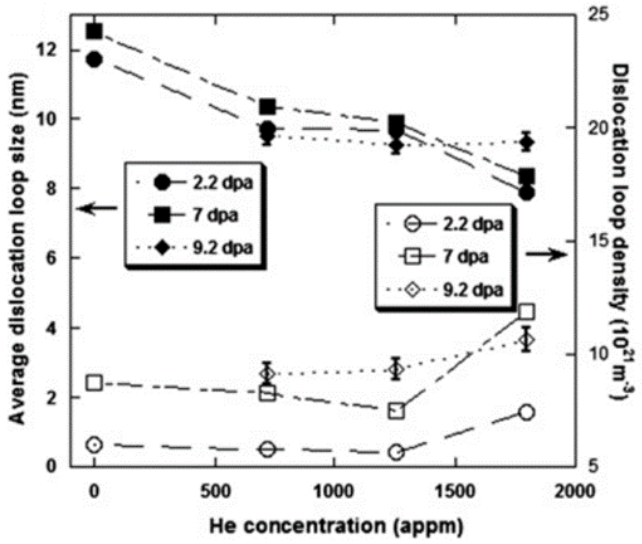


Figure 2.25: Average dislocation loop size and dislocation loop density as a function of helium concentration for proton-irradiated T91 at different damage levels [81].

In heavy-ion irradiation, Taller [17] reported almost no impact of helium injection rate on the loop diameter or loop density except for a slight increase in loop size at 4 appmHe/dpa compared to lower injection rates as shown in Figure 2.26.

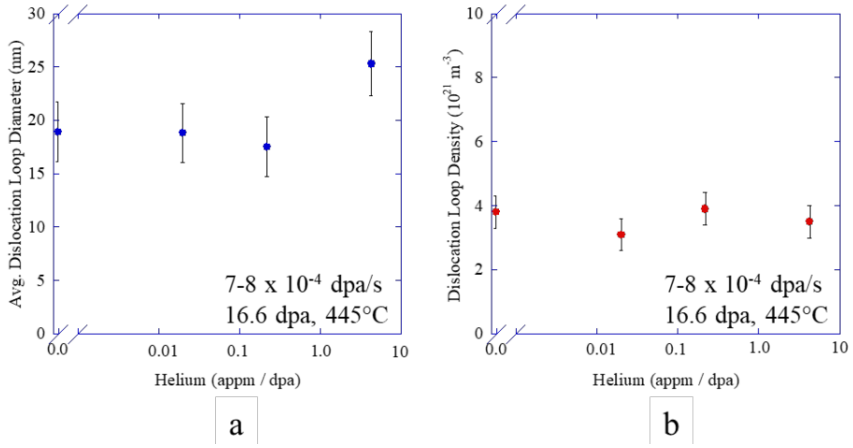


Figure 2.26: (a) Average dislocation loop diameter and (b) loop density as a function of helium injection rate for dual-ion-irradiated T91 [17].

Woodley et al. [67] conducted irradiations with 5.0 MeV Fe^{2+} ions and degraded He^{2+} ions at 445°C up to damage levels of 150 dpa and helium co-injection rates of 0, 0.02, 0.2 and 4 appm He/dpa in T91, and at 460°C to a damage level of 188 dpa and helium co-injection rates of 0, 0.06

and 4 appm He/dpa in HT9. The average dislocation loop diameter did not change significantly with helium co-injection rate at 17 dpa from 18 nm to 25 nm. The dislocation loop density did not significantly change with helium co-injection rate at 17 dpa in the range of 3.1×10^{21} m^{-3} to 3.9×10^{21} m^{-3} as shown in Figure 2.27. Dislocation lines were observed at all helium co-injection rates, and no significant alteration of the existing network dislocation density was noted compared to the as-tempered condition.

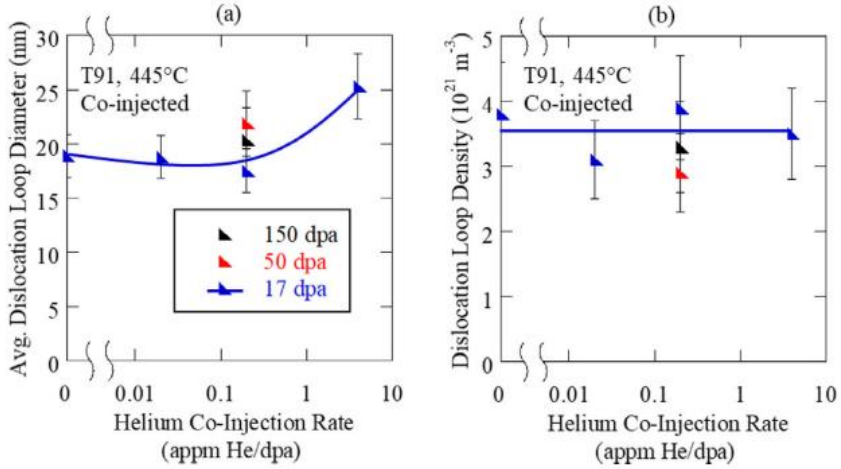


Figure 2.27: Average dislocation loop diameter (a) and dislocation loop density (b) for dual-ion-irradiated T91 at 445°C at 17 (blue) and 0, 0.02, 0.2 and 4 appm He/dpa and at 0.2 appm He/dpa at 17 (blue), 50 (red) and 150 (black) dpa [67].

Monterrosa et al. [68] implanted T91 heat C2269 with He^+ to levels of 0, 1, 10, 100 and 1000 appm. Samples were then irradiated with 4.4 or 5.0 MeV Fe^{2+} at 460°C to 150 dpa at 1.4×10^{-3} dpa/s. For the pre-implanted cases, the loop diameter and density did not significantly change with helium content apart from the 0 appm He condition exhibiting a slightly larger loop diameter as shown in Figure 2.28. The dislocation network showed an even higher insensitivity to helium. The total line length remained insensitive to helium content, which varied between $6\text{-}7 \times 10^{14}$ m^{-2} for the pre-implanted cases and was slightly higher for the 0 appm He condition.

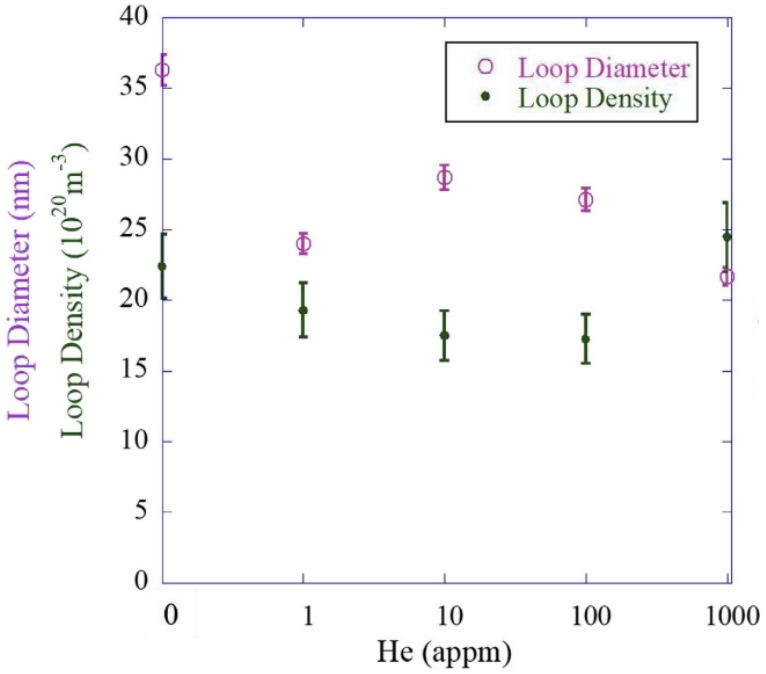


Figure 2.28: Densities and diameters for a⟨100⟩ dislocation loops in ion-irradiated T91 heat C2269 as a function of helium content at 150 dpa [68].

Lin et al. [69] irradiated Fe-10Cr with 8 MeV Ni ions and co-implanted He ions at 500°C up to 30 dpa with helium implantation rates of 0.1, 10 and 50 appm He/dpa. The dislocation loop diameter decreased with increasing helium production rate, while the density increased as shown in Figure 2.29. This observation was attributed to the reduction in loop mobility due to helium [88–91] and seem to be heavily dependent on temperature and sink density: helium induces higher concentration of a⟨100⟩ loops at higher irradiation temperatures, while a/2⟨111⟩ loops form in high proportions at low irradiation temperatures.

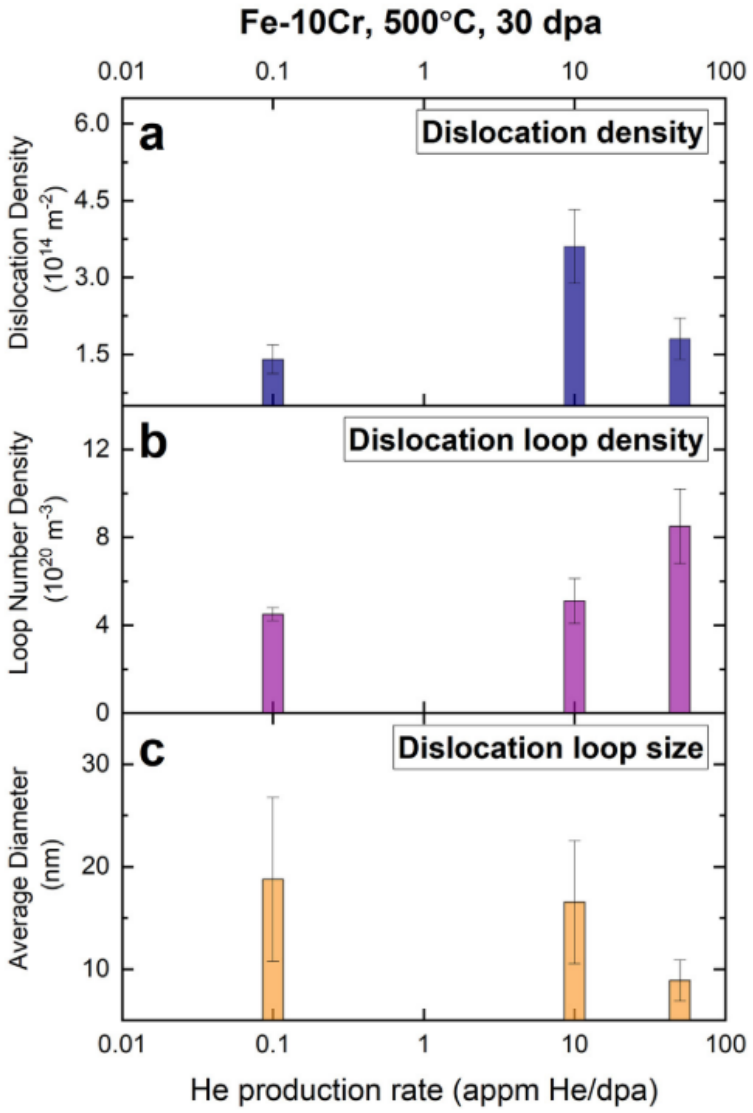


Figure 2.29: Comparison of (a) dislocation density, (b) dislocation loop number density, and (c) average diameter of the dislocation loops in Fe-10Cr irradiated at ~500°C with helium production rate of 0.1–50 appm He/dpa [69].

In summary, the effect of helium on dislocation loop microstructure is not very clear. While several papers reported almost no effect of helium, others indicated significant effects on density and Burger's vector dependent on temperature due to the reduction in loop mobility caused by helium atoms.

2.2.2.4 Damage rate effect

Taller studied the effect of damage rate on the dislocation loop microstructure in dual-ion-irradiated T91 as shown in Figure 2.30. The loop diameter appears constant up to 10^{-3} dpa/s and decreases by a factor of two at 2×10^{-3} dpa/s. At the same time, the number density is consistently increasing with increasing damage rate.

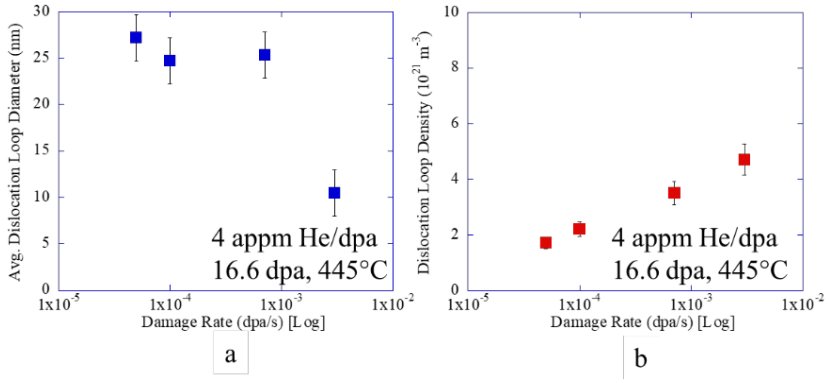


Figure 2.30: (a) Average dislocation loop diameter and (b) loop density as a function of damage rate for dual-ion-irradiated T91 [17].

Adisa et al. [92] reported the microstructure evolution of T91 irradiated to 3 dpa at 500°C using neutron and Fe^{2+} ions, with damage rates of ~10^{-7} dpa/s and ~2×10^{-4} dpa/s, respectively. The average size of dislocation loops is comparable between neutron (11.2 ± 4.0 nm) and ion (10.4 ± 3.6 nm) irradiations.

When comparing different irradiation methods, Swenson and Wharry [93] reported the dislocation loop microstructure of HCM12A and HT9 after neutron (10^{-7} dpa/s), proton (10^{-5} dpa/s) and Fe^{2+}-ion (10^{-4} dpa/s) irradiation to ~3 dpa at 500°C. For HCM12A, similar dislocation sizes (7.7 ± 2.4, 7.6 ± 2.4 and 7.5 ± 2.2 nm, respectively) and number densities ($2.2 \pm 0.3 \times 10^{21}$ m^{-3}, $4.4 \pm 1.1 \times 10^{21}$ m^{-3} and $4.0 \pm 0.9 \times 10^{21}$ m^{-3}) were reported for all three irradiation methods. The same observations were made for HT9 regarding the dislocation mean sizes (7.6 ± 2.3, 7.5 ± 2.1

and 7.6 ± 2.2 nm, respectively) and number densities ($2.0 \pm 0.3 \times 10^{21}$ m^{-3}, $2.4 \pm 0.5 \times 10^{21}$ m^{-3} and $2.4 \pm 0.5 \times 10^{21}$ m^{-3}).

The effect of damage rate on dislocation loop microstructure has not been studied extensively but does not seem to be extensive. Density appears relatively stable at all damage rates while the average loop diameter was only reported to decrease at damage rates above 10^{-3} dpa/s.

2.2.3 Radiation-induced segregation and phase changes

The strong interaction between solutes atoms and point defects results in coupled transport of the solute atoms by the point-defect fluxes to and away from sinks, such as grain boundaries, free surfaces, dislocations loops, void surfaces, etc. The solute-point defect binding energy determines whether the solute flow is towards or away from the sinks [5]. Although some of the observations of radiation-induced segregation (RIS) in the ferritic and high-chromium martensitic steels are ambiguous, it has been concluded [73] that the segregation is markedly dependent on the displacement damage and the irradiation temperature in the approximate range 300 to 625°C [5]. Additionally, enrichment of elements may result from the partial dissolution of precipitates during irradiation, leading to an increase in the local composition and possible nucleation of new particles (Little et al. as cited in [5]).

As such, the evolution of the precipitates in FM steels under irradiation is determined by the stability under irradiation of the phases produced during heat treatment and during aging, as well as the formation of new, non-equilibrium precipitate phases under irradiation [5]

While the typical changes to pre-existing phases ($M_{23}C_6$, M_2X, Laves phase, etc.) by irradiation has been reported in the literature [5,52,73,94], it is important to keep in mind that these behaviors depend on temperature, damage rate, damage level and initial microstructure. As such, because of the significant impact of composition on the formation of precipitates and segregation

behavior, only results for T91 (or 9Cr-1MoVNb) are reported: Ni/Si/Mn clusters, Cu-rich precipitates, intermetallic chi-phase and sigma (σ) phase were all reported to form under ion irradiation and irradiation in various reactors [5,51,94].

2.2.3.1 Temperature effect

Jiao et al. [13] studied the RIS in T91 irradiated in BOR-60 between 376°C and 524°C up to 35.1 dpa. Iron depleted at all irradiation conditions with the maximum depletion occurring at 460°C. Enrichment of Cr was observed for all profiles with minimal enrichment of <3 wt% at 376-378°C and maximal enrichment of ~6 wt% at 460°C. Both Ni and Si enriched at the grain boundary, and the enrichment was minimal at 524°C (~0.2 wt%). Figure 2.31 shows the irradiation damage/temperature effect on RIS for T91 irradiated in BOR-60.

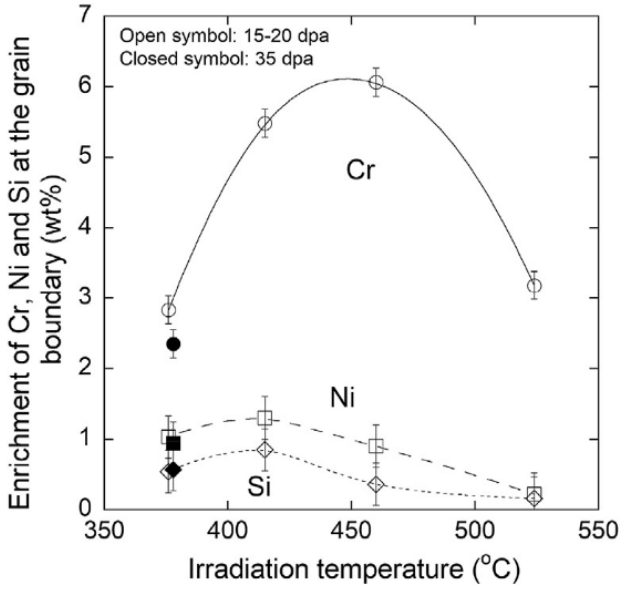


Figure 2.31: Irradiation damage level and temperature effect on enrichment of Cr, Ni and Si at the grain boundary in BOR-60-irradiated T91 [13].

T91 irradiated at 469°C:4.3 dpa in ATR exhibited ~2.5 wt% Cr enrichment, ~2.6 wt% Fe depletion, slight enrichment of Mn (~0.18 wt%) and Si (~0.14 wt%) without noticeable RIS for Mo, V, and Cu [87].

Wharry et al. [95] applied a model for RIS and found the Cr:Fe vacancy diffusion coefficient ratio crosses that for interstitials at 530°C at 1×10^{-5} dpa/s. Yet, experimental results indicated a value between 600 and 700°C for T91 irradiated with 2 MeV protons as shown in Figure 2.32. This discrepancy between prediction and experimental observations is attributed to the complex microstructure evolution of T91 under irradiation [95]. Additionally, it has been reported that concentration peaks get broader with increasing irradiation temperature [96].

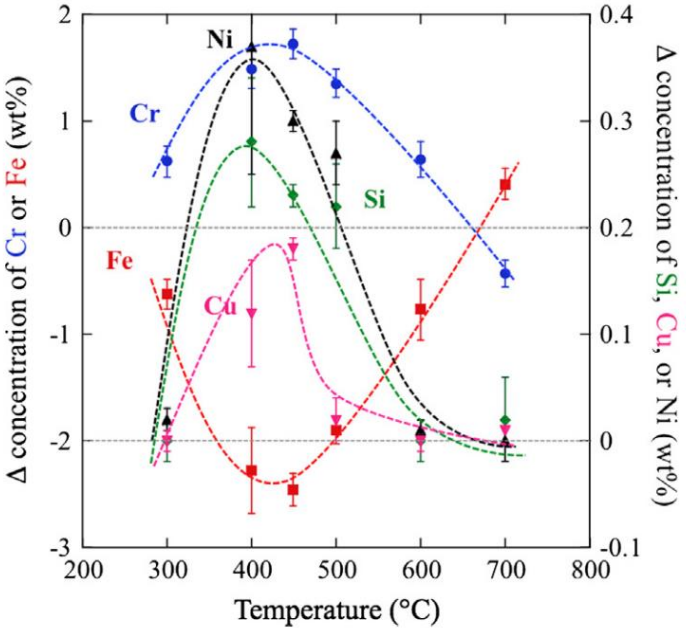


Figure 2.32: RIS of several elements in T91 irradiated with 2 MeV protons at 3 dpa [96].

Gupta et al. [80] measured an enrichment of 4.7 wt% Cr, 0.6 wt% V and a depletion of 5.3 wt% Fe after proton-irradiation of T91 up to 10 dpa at 450°C, consistent with the observations from Wharry. No significant changes were measured for Mn and Mo.

Taller et al. [16] reported the microstructural changes of T91 irradiated to ~17 and 35 dpa at temperatures between 406 and 570°C using 5 MeV Fe^{2+} ions. Fe depleted at the grain boundary for all examined conditions. Both Ni and Si enriched for all observed temperature conditions with Ni enrichment peaking at 445°C:16.6dpa and the largest amount of enrichment of Si at

520°C:14.6dpa. Figure 2.33 shows the evolution of the radiation-induced segregation of Cr, Ni and Si in T91 as a function of temperature, damage level and method of irradiation.

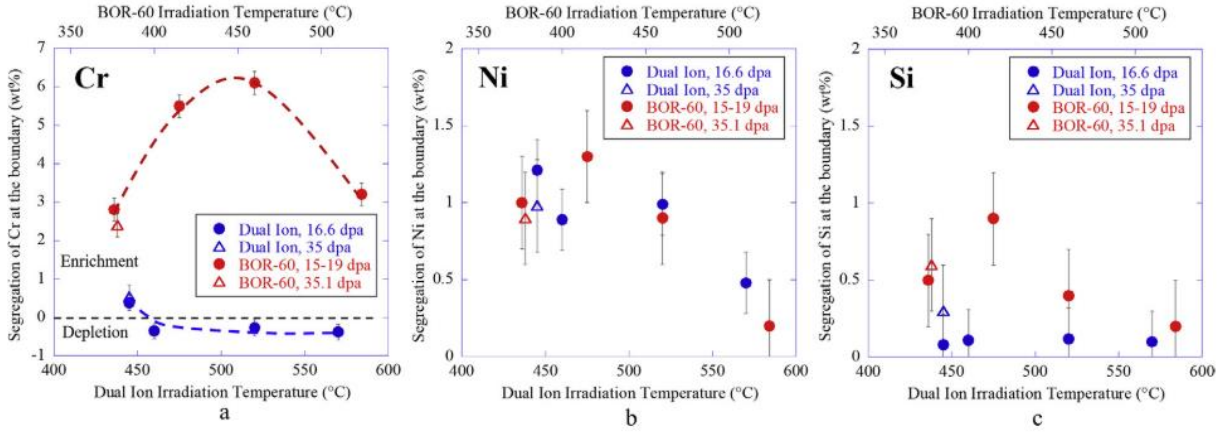


Figure 2.33: Irradiation damage level and temperature effect on the segregation of (a) Cr, (b) Ni, and (c) Si at the grain boundary for dual-ion-irradiated and BOR-60 irradiated T91 [16].

At 300/400/600°C in HFIR at 36 dpa, the precipitate morphology and distribution of 9Cr-1MoVNb were unchanged by the irradiation, implying no new precipitation occurred. At 500°C, occasional areas with large, elongated precipitates were present [53]. However, Maziasz et al. [52] also reported the precipitates evolution of 9Cr-1MoVNb after irradiation to 36-39dpa in HFIR at 300, 400, 500 and 600°C and did not observe any additional precipitation but measured some dissolution of the existing precipitates up to 500°C (especially small MC particles). This discrepancy between these two studies conducted in seemingly the exact same conditions demonstrates the difficulty of drawing clear conclusions on precipitate formation.

Gupta et al. [80] did not measure any change in precipitate size or density in T91 after proton irradiation at 2×10^{-5} dpa/s up to 10 dpa between 400 and 500°C. Similar results were found by Jiao et al. [13], both pre-existing Cr-carbides and V, Cr-nitrides remained in T91 after irradiation in BOR-60. Irradiation at 415°C:18.6 dpa resulted in slightly larger precipitates (6.7 nm) with lower density (3.0×10^{21} m^{-3}) compared to the 376°C:17.1dpa irradiation (5.8 nm and 3.6×10^{21} m^{-3}). No clusters were observed at 460°C and 524°C. Both Ni/Si/Mn-rich and Cu-rich

precipitates exhibited core regions containing around 40 at% Ni, 20 at% Si and 10 at% Mn, which is close to the composition of G-phase ($Mn_6Ni_{16}Si_7$). Other clusters show much lower Ni/Si/Mn concentration than that of G-phase and are thought to be G-phase precursors. Yet, G-phase particles were only found infrequently or not at all in Auger Electron Microscopy studies on T91 irradiated in the range 300 to 600°C to <39 dpa in HFIR and at ~400°C to 47 dpa in FFTF (Maziasz et al. as cited in [5]) which demonstrated the variability in the formation of precipitates under neutron irradiation.

Ni/Si/Mn-rich clusters and Cu-precipitates were observed by Jiao et al. [94] in T91 after proton irradiation to 7 dpa at 400°C and 500°C. For Ni/Si/Mn-rich clusters, the average radius increased almost by a factor of 2 with increasing temperature but the number density dropped by an order of magnitude. Similar trends were observed for Cu-rich precipitates although to a lesser degree. There were no independent Cu-rich precipitates unattached to Ni–Si–Mn precipitates, indicating the Ni–Si–Mn-rich precipitates are favorable nucleation sites for Cu-rich precipitates. Precipitates were found to preferentially nucleate at dislocations which were enriched in Si due to RIS [82].

After proton irradiation at 400°C, $M_{23}C_6$ precipitates in T91 were greatly enriched in Mo and slightly in Cr compared to the unirradiated composition. Yet, after irradiation at 500°C, $M_{23}C_6$ precipitates were even more enriched in Mo but depleted in Cr [94].

Taller et al. [16] reported the microstructural changes of T91 irradiated to ~17 dpa at temperatures between 406 and 570°C using 5 MeV Fe^{2+} ions. Ni/Si clusters were observed in all examined conditions except for the 520°C:14.6 dpa and 570°C:15.4 dpa conditions. Because of their low density, it was not possible to determine the trends of Ni/Si-rich cluster evolution with temperature.

The behavior of radiation-induced segregation and precipitation as a function of temperature in FM steels has been reported for neutron and ion irradiation. RIS exhibits a bell-shaped behavior with temperature where solute atoms tend to enrich at grain boundaries while Fe depletes, except at high temperatures. Precipitation exhibits a lot of variability from one environment to another, but new phases tend to form at intermediate temperatures (~350-500°C) only.

2.2.3.2 Damage level effect

Jiao et al. [13] reported that an increase in the irradiation damage from 17.1 dpa to 35.1 dpa for T91 irradiated in BOR-60 at ~375°C did not appear to affect the magnitude of enrichment for Cr, Ni and Si. It is thought that saturation of RIS occurs when the concentration gradient at the grain boundary balances with the backward diffusion.

Wharry et al. [95] also predicted that the segregation would saturate after a certain damage level. Yet, experimental results for T91 irradiated with protons to 10 dpa at 400°C exhibited a decrease in enrichment above 3 dpa (from ~1.7 to ~1.1 wt%) [82,96]. A hypothesis for this phenomenon is that the increased concentration of Ni, Si, and Cu at the grain boundary could decrease the lattice parameter near the grain boundary. Cr atoms would become less undersized, and the migration energy of Cr would increase locally, causing a reduction in the amount of Cr enrichment [96].

Adisa et al. [92] reported enrichment of Si, Ni, and Cu and depletion of Mn and Fe in T91 at grain boundaries after Fe^{2+}-irradiation to 3 dpa at 500°C. Interestingly, the solutes are mostly redistributed after irradiation to 100 dpa.

Taller et al. [16] reported the microstructural changes of T91 irradiated to ~17 and 35 dpa at 445°C using 5 MeV Fe^{2+} ions. With increasing damage level from 445°C:16.6dpa to

445°C:35dpa, the Cr enrichment increased slightly from 0.38 wt% to 0.54 wt%, the Ni enrichment decreased slightly from 1.21 wt% to 0.98 wt%, and the Si enrichment increased from 0.08 wt % to 0.30 wt%. These results reveal that Cr and Ni segregation has likely saturated by 17 dpa while Si segregation might still be evolving after 35 dpa.

Wharry et al. and Jiao et al. [82,94] reported the formation of Cu and Ni-Si-Mn-rich clusters in T91 irradiated to 7 dpa with protons at 10^{-5} dpa/s at 400°C. No radiation-induced precipitates were observed at 1 dpa. At 7 dpa, the average Cu-rich-precipitate diameter was 3.1 ± 1.0 nm and the average Ni–Si–Mn-rich-precipitate diameter was 4.1 ± 1.2 nm. The number density of Cu-rich precipitates was 5.6×10^{22} m^{-3}, and the number of Ni–Si–Mn-rich precipitates was slightly larger at 7.4×10^{22} m^{-3}, indicating that the minimum dose for RIPs was between 1 and 7 dpa.

For T91 irradiated in BOR-60, Jiao et al. [13] reported that the average Ni/Si-rich precipitate size increased slightly from 5.8 nm at 376°C:17.1 dpa to 7.0 nm at 378°C:35.1 dpa while the number density slightly decreased from 3.6×10^{21} m^{-3} to 2.4×10^{21} m^{-3}.

Getto et al. [60] pre-implanted HT9, T91 and T92 with 10 appm He and subsequently irradiated the samples with 5 MeV Fe^{2+} between 75 and 650 dpa at 460°C. Figure 2.34 shows the evolution of M_2X (M = Cr and X = C in general) in terms of length and volume fraction for HT9, T91 and T92 as a function of damage level.

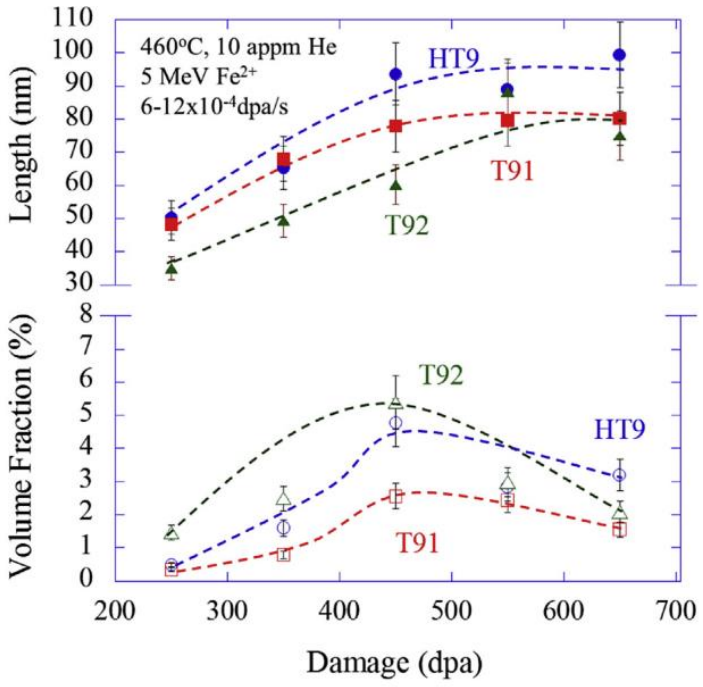


Figure 2.34: Length (closed markers) and volume fraction (open markers) of M_2X formed at 460°C from 250 to 650 dpa in HT9, T91 and T92 [60].

Regardless of alloy, the M_2X precipitate size saturated in length at approximately 450 dpa, 200 dpa after they are first observed. In general, more M_2X formed in HT9, likely due to higher levels of carbon in HT9 relative to that in T91 and T92. The decrease in volume fraction after the initial increase is a consequence of the decrease in number density beyond 450 dpa attributed to a loss in coherency of the M_2X as it increases to a very large length of approximately 100 nm.

Taller et al. [16] reported phase changes in T91 irradiated to 16.6 and 35 dpa at 445°C using 5 MeV Fe^{2+} ions. Ni/Si clusters were observed in all examined conditions with an average size of ~5.6 ± 1.3 nm and number densities of 0.25 and 0.52 × 10^{21} m^{-3} for 16.6 and 35 dpa, respectively.

Monterrosa et al. [68] implanted T91 heat C2269 with He^{+} to levels of 0, 1, 10, 100 and 1000 appm. Samples were then irradiated with 4.4 or 5.0 MeV Fe^{2+} at 460°C to 50, 150 and 300 dpa at 1.4 × 10^{-3} dpa/s. As shown in Figure 2.35, as the damage level increased, the precipitates

exhibited slight coarsening as the size increased and the density decreased, resulting in an increase in the total volume fraction up to about 0.04% by 300 dpa. The sink strength for these clusters remained low, ranging from 0.36 to 0.58 × 10^{14} m^{-2}.

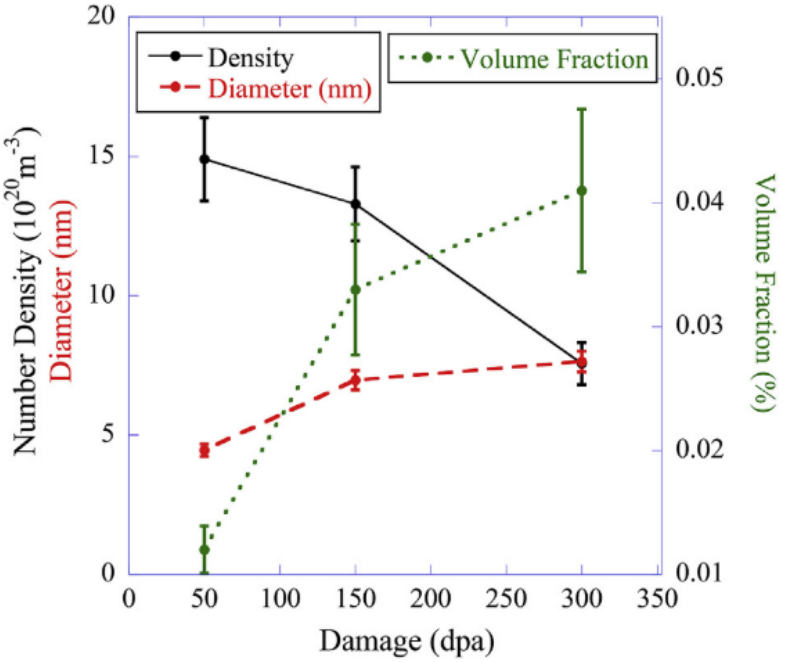


Figure 2.35: Number density, diameter, and volume fraction of G-phase plotted as a function of damage with 10 appm He pre-implanted in ion-irradiated T91 [68].

These results indicate that after an initial nucleation phase (increase in both diameter and density), precipitates created under irradiation in T91 coarsen and their density decrease with increasing damage level (also observed in other materials [60,97,98]). At very high damage level, this coarsening can sometimes cause the precipitates to effectively not be measured anymore due to their extremely low density [97,99]. For some precipitates, their nucleation phase started only after 250 dpa under ion irradiation [60].

2.2.3.3 Damage rate effect

The inverse Kirkendall model modified by Wharry [41] predicted a decreasing amount of Cr RIS in T91 with increasing damage rate, since it does not allow sufficient time between damage

events for point defects to diffuse to grain boundaries. Was and Allen [100] studied the evolution of Cr depletion in 304 SS for different damage rates and concluded that a decreasing displacement rate shifts the segregation to lower temperature and a higher maximum: a lower damage rate yields lower point defect concentrations, reducing the number of defects lost to recombination. Faulkner et al. [101] modeled a similar behavior for silicon in a ferritic steel matrix.

Taller et al. [102] reported the evolution of Ni/Si clusters and of the radiation-induced segregation of Fe, Cr, Ni and Si at grain boundaries in T91 after irradiation in BOR-60 at ~375°C:17dpa and dual-ion irradiation at 445°C:16.6dpa with damage rates of 5×10^{-5}, 1×10^{-4}, 7.5×10^{-4} and 3×10^{-3} dpa/s. In the as-received condition, Fe was depleted, Cr was slightly enriched, and there was no significant segregation of Ni and Si. After dual-ion irradiation, Cr enrichment decreased below the as-received condition whereas Ni and Si enriched. Ni and Si enrichment (resp. Fe depletion) decreased with increasing damage rate. The authors explained this behavior by a combination of the growing fraction of point defects lost to recombination and the inverse Kirkendall effect. As the damage rate increased, the volume fraction of Ni/Si clusters decreased due to the decrease in density and diameter. The correlation between the vacancy diffusion distance and cluster density across dual-ion irradiations and BOR-60 irradiation shown in Figure 2.36 suggests that the lack of time for thermal diffusion is a significant limiting factor for Ni/Si cluster formation.

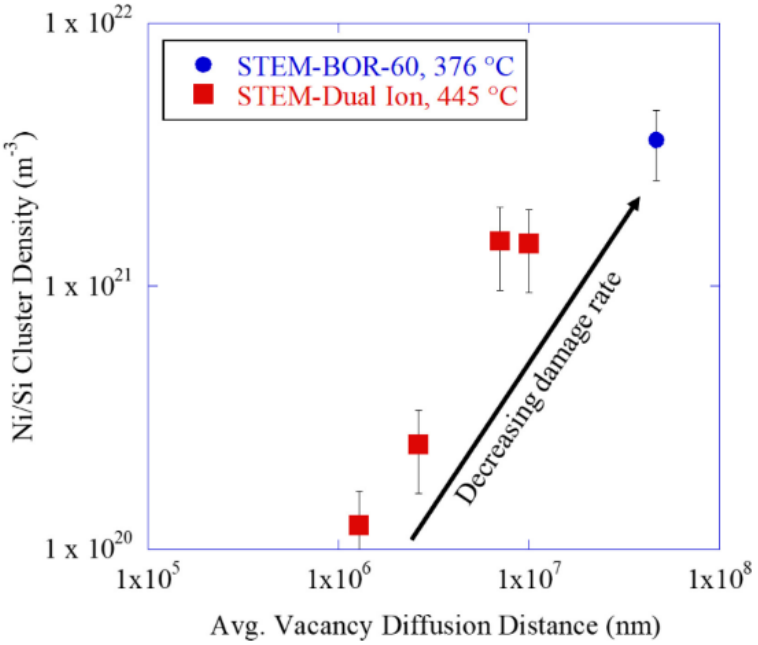


Figure 2.36: Calculated average vacancy diffusion distance plotted against the Ni/Si cluster density for dual-ion-irradiated T91 at 445°C with BOR-60-irradiated T91 at 376°C [102].

For T91, Adisa et al. [92] reported enrichment of Si, Ni, and Cu and depletion of Fe and Mn at grain boundaries after neutron irradiation to 3 dpa at 500°C. For Fe^{2+}-irradiated samples, similar segregation is observed with higher magnitude, especially for Ni, Mn and Fe. The segregation behavior around dislocation between neutron and heavy-ion irradiation is also reported to be similar (although with Mn enrichment this time). Self-ion irradiation induced the largest average size of Mn-Si-Ni-rich nanoclusters at 7.59 ± 1.50 nm, while clusters after neutron irradiation are 4.78 ± 1.63 nm. Meanwhile, the number density of these clusters was lower after Fe^{2+} irradiation to 3 dpa (12×10^{21} m^{-3}) compared to neutrons irradiation (145×10^{21} m^{-3}). In a similar trend, Cu-rich clusters were larger following Fe^{2+} irradiation (7.54 ± 2.32 nm) than neutron irradiation (4.18 ± 1.07 nm), while number density after neutron irradiation was higher (100×10^{21} m^{-3}) than after Fe^{2+} irradiation (14×10^{21} m^{-3}).

Although only a few studies on the effect of damage rate on radiation-induced segregation and precipitation are available, results are relatively consistent between them. Increased damage

rate leads to lower density of precipitates and lower segregation. These observations are consistent with the Inverse Kirkendall Effect and the reduced time for solute atoms to cluster together at high damage rates.

2.3 Ion irradiation as a surrogate for neutron irradiation

It is well established that ion irradiations can create essentially all the standard microstructural features observed in neutron-irradiated materials (dislocation loops, cavities, radiation-induced solute segregation, radiation-induced precipitation, etc.) [14,16]. Charged particle irradiations are a valuable complementary tool to bulk neutron irradiation studies, and in many cases provide unique capabilities to explore radiation effects phenomena. They allow the possibility to carefully and systematically control irradiation conditions over a wide range of damage levels to explore important test conditions such as temperature, damage rate and primary knock-on atom (PKA) energy [103]. Additionally, the relative unavailability and low damage rate of test reactors make ion irradiation a valuable tool to the development of nuclear materials [14]. Yet, key differences need to be considered when comparing ion irradiation to neutron irradiation: strong spatial gradients, higher damage rates, shorter irradiation times, mode of irradiation (raster-scanned or defocused), particle type and injected interstitials [3,6,14,15,104,105]. Another consideration is the definition of equivalent exposures, and of the use of displacement per atom (dpa) across different irradiation methods [106].

2.3.1 Difference in damage rate

Difference in damage rate between ion and neutron irradiations will cause a discrepancy in the defect arrival rates at sinks which necessitate a temperature shift to be equal [103]. Mansur [107–109] determined a temperature-damage rate relationship to maintain the net flux of vacancies

to sinks across damage rates. As the damage rate increases, the vacancy supersaturation and the fraction of point defect lost to recombination increase [110]. Higher temperature increases the migration to sinks, thus lowering point defect concentrations in the matrix, while also reducing recombination. Simultaneously, increasing the temperature increases the thermal vacancy emission rate. The ratio of thermally emitted vacancies to the absorption of vacancies by voids under a limiting regime (recombination-dominated regime or sink-dominated regime) describes the growth rate of voids. Equating two ratios at different damage rates and solving for the temperature gives the temperature shift needed to yield the same growth rate as given by Eq. 2.2 and Table 2.2.

$$T^{(2)} - T^{(1)} = \frac{\dfrac{kT^{(1)2}}{E_v^m + n(E_v^f + E_v^*)}\left[\ln\dfrac{G^{(2)}S_i^{(1)}S_v^{(1)}}{G^{(1)}S_i^{(2)}S_v^{(1)}} + \ln R\right]}{1 - \dfrac{kT^{(1)}}{E_v^m + n(E_v^f + E_v^*)}\left[\ln\dfrac{G^{(2)}S_i^{(1)}S_v^{(1)}}{G^{(1)}S_i^{(2)}S_v^{(2)}} + \ln R\right]} \qquad \text{Eq. 2.2}$$

Table 2.2: Expressions for the dose rate dependence of temperature shift under various limiting conditions of point defect removal [107].

Mode of absorption at voids	Values of R and n in eq. (14) when dominant process of point defect removal is:	
	recombination (n = 2)	sinks (n = 1)
Interstitial and vacancy reaction controlled	$\dfrac{r_c^{(1)}}{r_c^{(2)}}\left[\dfrac{S_i^{(2)}\exp(-E_v^*/kT^{(2)}) - S_v^{(2)}\exp(-E_i^*/kT^{(2)})}{S_i^{(1)}\exp(-E_v^*/kT^{(1)}) - S_v^{(1)}\exp(-E_i^*/kT^{(1)})}\right]^2$	$\dfrac{L^{(2)}}{L^{(1)}}\left[\dfrac{Z_i^d\exp(-E_v^*/kT^{(2)}) - Z_v^d\exp(-E_i^*/kT^{(2)})}{Z_i^d\exp(-E_v^*/kT^{(1)}) - Z_v^d\exp(-E_i^*/kT^{(1)})}\right]$
Interstitial and vacancy diffusion controlled	$\dfrac{r_c^{(1)}}{r_c^{(2)}}\left[\dfrac{L^{(2)}}{L^{(1)}}\right]^2$	$\dfrac{L^{(2)}}{L^{(1)}}$
Interstitial reaction, vacancy diffusion controlled	$\dfrac{r_c^{(1)}}{r_c^{(2)}}\left[\dfrac{bS_i^{(2)} - S_v^{(2)}r_v\exp(-E_i^*/kT^{(2)})}{bS_i^{(1)} - S_v^{(1)}r_v\exp(-E_i^*/kT^{(1)})}\right]^2$	$\dfrac{L^{(2)}}{L^{(1)}}\left[\dfrac{bZ_i^d - r_vZ_v^d\exp(-E_i^*/kT^{(2)})}{bZ_i^d - r_vZ_v^d\exp(-E_i^*/kT^{(1)})}\right]$

This expression is highly dependent on the values selected for the parameters (diffusion coefficients, migration energies, dislocation bias, etc.) and the result can vary widely from one set of values to another.

Besides their growth, nucleation of voids is equally important when trying to replicate the cavity microstructure of neutron-irradiated samples with ion irradiation. Taller et al. [21] compared the net vacancy absorption and the thermal vacancy emission in T91 irradiated in BOR-60 and under dual-ion irradiation and concluded that homogeneous nucleation was impossible in neutron-irradiated samples. They postulated that the strain field around a nucleation site could contribute to nucleation. The stress from this strain field reduces the emission of vacancies, and the absorption exceeds emission at a radius of 2-4 mm making nucleation possible in BOR-60. In dual-ion irradiation, high damage rate increases the vacancy concentration orders of magnitude above that in reactor such that homogenous nucleation is possible. Taller et al. [21] also developed a cluster dynamics (CD) model that treats each vacancy-helium cluster as a sink that evolves in the microstructure. This approach allows some assumptions made by Mansur (whose formula predicted a +120°C temperature shift) to be relaxed and has the advantage of considering helium in the nucleation process [21]. The model considers a constant density of static trapping sites in the microstructure to immobilize helium, which is then released in proportion to a binding energy. A trap binding energy of 1.0 eV with a density of 10^{20} m^{-3} (consistent with the experimentally observed void density) produces a predicted temperature shift of about + 70°C which is consistent with experimental values [16,17]. Based on the trapping/de-trapping effect of helium to sinks, the helium content per trap can be computed. As the damage rate increases, the amount of helium trapped at sinks other than cavities will increase as helium rapidly partitions to microstructural features with insufficient time to de-trap during the shorter irradiation period. The longer

irradiation time in reactor allows the helium to migrate to the strongest traps, leading to quick saturation of weak-binding traps. This observation is different from that explained in another paper where the helium accumulation in traps was linked to the injection rate [72]. Because of the lack of time to de-trap from dislocation loops at the higher damage rate of ion irradiation, the flow of helium from dislocation loops to cavities occurs much later in damage level compared with reactor irradiation. To obtain the same concentration of helium in cavities, the helium injection rate must be increased with an increase in damage rate to compensate for the insufficient time for helium release from weaker traps and flow to cavities. It is important to note that the CD model underpredicted cavity density and overpredicted cavity size.

2.3.2 Difference in particle type

Comparing the damage induced by different particles requires the use of a common damage level unit. Radiation damage, in the form of the number of displacements per atom, is generally determined using the Kinchin-Pease (KP) displacement model [105]. Yet, this value does not represent the number of defects that migrate and cause long-range radiation effects. It can be adjusted by the displacement efficiency defined as the fraction of point defects created, which survive the cascade quench, referred to as "freely migrating" [111] or "available migrating" [110] defects. Figure 2.37 shows the relationship between damage morphology and the displacement efficiency for various particle types impinging on a sample of pure nickel at 1 MeV.

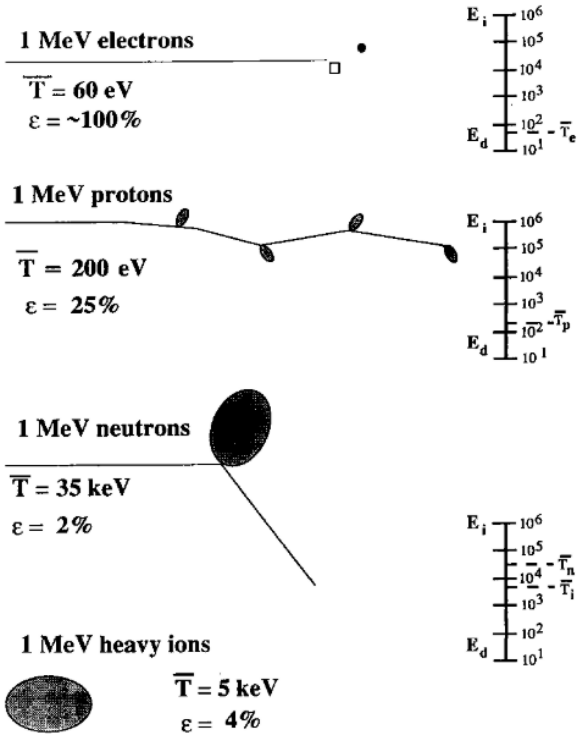


Figure 2.37: Description of damage morphologies for irradiation with various particles of the same energy. T is the average energy transfer per PKA and ε is the efficiency of producing freely migrating defects available to affect radiation-induced segregation [105].

Neutrons and heavy ions produce dense cascades that result in substantial recombination. Electrons typically produce a few widely spaced Frenkel pairs that have a low probability of

recombination. Protons produce small widely spaced cascades due to the Coulomb interaction [105]. This phenomenon indicates that a correction of the damage level and damage rate must be conducted to obtain representative values between the different particle types. The same conclusion was drawn by Rehn [111] who studied the formation of freely migrating defects and showed that higher recoil energy leads to higher localized defect densities enhancing defect recombination and lowering damage efficiency.

The difference in irradiating particles also leads to different primary knock-on atom (PKA) energies. For ion irradiations, over 80% of the PKAs have energies <1 keV for 1 MeV self-ion irradiation of medium mass targets such as Cu or Fe whereas the maximum PKA energy extends up to 1 MeV; in contrast, about 80% of the PKAs from 1 MeV neutron irradiation have energies within a factor of two of the maximum PKA energy of ~60 keV [112].

Zinkle et al. [103] indicated that the large fraction of low energy PKAs for ion irradiation produces smaller-sized defect clusters in cascade and a higher surviving defect fraction per dpa compared to neutron irradiations. Additionally, energetic ion beams (>1 MeV) produce high amounts of ionization and low energy transfers (below the displacement energy) which may lead to increased defect diffusion and point defect recombination. Figure 2.38 shows the calculated surviving defect fraction as a function of PKA energy in Fe and the calculated weighted defect recoil spectra W(T) versus PKA energy for 1 MeV neutrons and several ions in Cu. Low- and high-energy recoils contribute significantly to damage in ion irradiations.

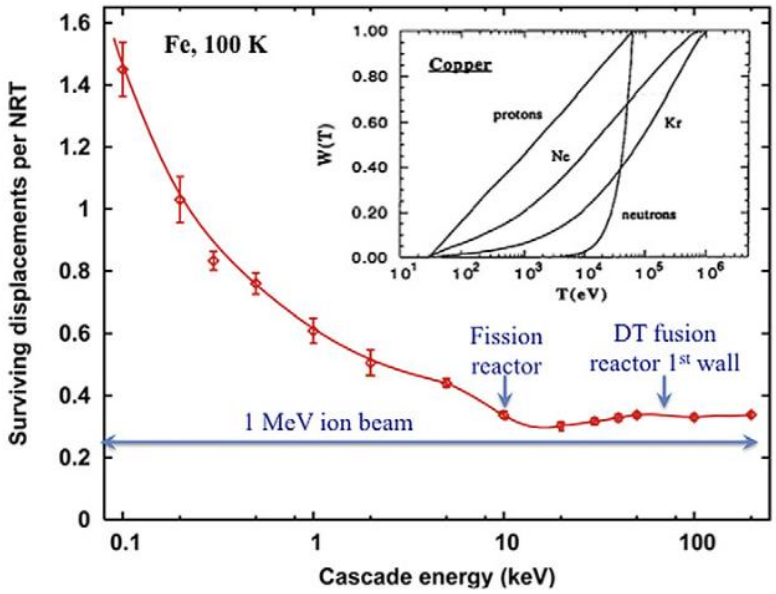


Figure 2.38: Calculated surviving defect fraction (normalized to the NRT dpa) versus PKA energy for displacement events in Fe at 100 K [103].

Garner [106] proved the importance of irradiating particle in experiments when they irradiated Fe-15Cr-25Ni with different particles: nickel ions (2.8, 3.5, 5.0 MeV), protons (0.75 MeV) and electrons (1.0 MeV). At all three incident energies, nickel ions were found to create swelling in the steady-state regime at essentially the same rate per dpa, although the duration of the transient regime of swelling varied. Electrons were found to be approximately six times more effective per calculated displacement than nickel ions in creating swelling and 0.75 MeV protons appeared to be roughly twenty times more effective than 1.0 MeV electrons.

2.3.3 Other aspects

Operational variability in reactors is common and must be considered when using ion irradiation as a surrogate for commercial reactor irradiation. Several studies have shown that the irradiation conditions of experiments conducted in nuclear reactors are reported partially and often do not include the complete irradiation history [113]. It is not unusual for irradiation experiments to experience numerous temperature reductions, sometimes as many as 237 in a single year

between 50 and 550°C [6,114,115]. Variation in irradiation temperature can be caused by uncertainty in gamma heating, changes in experiments or fuel loading, fuel burn-up and changes in thermal resistance which varies with swelling, creep, densification, and dilation [114]. Irradiation history has been shown to have a massive impact on the microstructure and on mechanical properties of the materials including fracture toughness and IASCC susceptibility [114,116,117].

For materials irradiations to truthfully replicate the microstructural evolution of materials during their life in reactors, the irradiation history must be considered and its impact on the microstructure along with its mechanisms must be understood. When the temperature increases during operation, dislocation loop and void number densities decrease almost immediately during irradiation, whereas the final average size of voids increases. This behavior has been observed for loops in F82H [117], Fe-10Cr and JLF-5 (modified Fe-12Cr-2W) [118], austenitic steel [119,120], vanadium alloys [121,122], Ni alloys [113,123] and for voids in Ni alloys [123] and austenitic steel [124]. Complete annihilation at high temperature has also been reported for loops in austenitic steel [119,120,125,126], vanadium alloys [121,122,127], nickel [126] and for voids in austenitic steel [125] and vanadium alloys [127]. These evolutions are also dependent on damage level before and after perturbation [118,119,124,128]. After a temperature decrease, void and loop microstructures typically consist in the union of the microstructures created at higher and lower temperatures since the mobility of point defects is reduced which tend to freeze the pre-existing microstructure. This behavior has been reported for voids in nickel [128] and for loops in vanadium alloys [121,122] and nickel [129]. Additionally, reactor operation is often cyclical which presents its own effect on microstructure evolution [117,123,126,127,130,131]. While some reactor experiments can be conducted with an active temperature control [116,132–134], they are rarely

representative of the behavior in commercial reactors. Finally, it is crucial to keep in mind that the microstructure evolution of loops and voids is intertwined, and their behaviors might be opposite [125]. The relative sink strength between the two irradiation features must be put in perspective of the bias effect to understand the microstructure evolution under temperature variation [123,125]. Ion irradiation must take into account the operational variability of reactors to be effective as a predicting tool [14].

Gigax et al. [104] studied the effect of irradiation mode (raster-scan vs. defocus) on the swelling of pure iron using 3.5 MeV iron ions to at 450°C to 32 and 96 dpa with a time-averaged dpa rate of 1.74×10^{-3} dpa/s. The beam was scanned at 15.6, 1.94, and 0.244 Hz and the resulting microstructure was compared with that produced by a defocused beam. With decreasing rastering frequencies, void sizes tend to be smaller and densities higher. In comparison, defocusing results in larger voids. Rastering tends to suppress void swelling. Getto et al. [135] reported similar observation for irradiations of pre-implanted HT9 and T91with 5 MeV Fe^{2+} ions using both raster-scanned and defocused beam modes. Raster-scanning was performed with a raster frequency of 2016 Hz in the "y" direction and a frequency of 255 Hz in the "x" direction for full coverage of the irradiated area every 3.92 ms. Enhancement of void diameter, number density and swelling as well as G-phase diameter and number density and loop diameter with defocusing was consistent across all alloys and helium levels examined. These results are consistent with the Fully Dynamic Rate Theory model proposed by Ghoniem et al., which predicts that in-cascade annealing of point defects between pulses decreases the vacancy supersaturation leading to decreased growth of microstructural features [135–139].

Gigax et al. [104] also reported that, under ion irradiation, the interstitial distribution was slightly deeper than that of vacancies because of the collimated beam (knock-on interactions favor

momentum transfer in the forward direction). This resulted in a vacancy-rich near-surface region and an interstitial-rich region near the end of range. These differences in spatial distribution led to a dramatic suppression of void swelling near the end of ion range.

In terms of spatial differences, a defect-depleted zone is typically observed in irradiated materials in the vicinity of planar sinks such as grain boundaries or free surfaces [103,140]. This region can sometimes be followed by a region of unusually large swelling [103,141]. On the other hand, the effect of injected interstitials has been observed in different materials and needs to be accounted for [103,104,106,142]. More details are provided in Section 4.4.3.

In ion irradiation, the damage rate is a function of depth but also of swelling as presented by Getto et al. [61]. With cavities forming, the effective density of the material decreases and so does the damage rate. This time/dpa-evolution in damage rate as a function of depth needs to be accounted for when statistically significant (swelling >10%).

While not inherent to ion irradiation, the issue of carbon contamination must be addressed [143,144]. Monterrosa et al. [145] studied the effect of carbon uptake on cavity microstructure in T91 after heavy-ion irradiation. The uptake of carbon was due to vacuum carburization catalyzed by the ion beam. Residual CO and CO_2 molecules in the vacuum system, with the aid of the ion beam, adsorbed onto the surface and then diffused inward (Singer et al. as cited in [145]). The suppression of swelling can be attributed to the presence of carbides (Gigax et al. as cited in [145]), as the dislocation sink strengths did not change significantly and the carbide sink strength ranged between a factor of 2-4x that of the dislocation sink strength. Additionally, carbides provided a site for helium atoms and vacancies which annihilated the bubble microstructure at high damage level.

2.3.4 Direct comparison between ion and neutron irradiations

Taller et al. [16,21] reported the microstructure of T91 after dual-ion irradiation (445 to 570°C) and after neutron irradiation in BOR-60 (375 to 520°C) up to 35 dpa to compare the two methods of irradiation. A temperature shift of +60°C was used. The helium injection rate was set to 4 appmHe/dpa, much greater than the computed 0.22 appmHe/dpa of BOR-60 due to (n,α) reactions. With these adjustments, the authors measured cavity and dislocation loops microstructure of dual-ion-irradiated samples in good agreement with those of neutron-irradiated samples. However, some discrepancies between the two methods were noted for Ni/Si clusters and radiation-induced segregation.

Was et al. reported similar microstructure features for HT9 84425 irradiated to 155 dpa in FFTF at 443°C and ion-irradiated to 188 dpa at 460°C with 1 appmHe pre-injected, with similar loop size (~20 nm) and number density (5-9 × 10^{20} m^{-3}), as well as precipitate microstructure. Despite heterogeneous void formation, their size and number density were similar, as were the void size distribution [14].

Lin et al. [63] calculated a temperature shift of about 64°C, when comparing ion irradiation cavity swelling result on Fe (1.4 × 10^{-3} dpa/s) to previous neutron irradiation studies on Fe performed at ~ 8 × 10^{-7} dpa/s. Assuming Fe-Cr alloys with the same value of formation and migration energy as pure Fe, the predicted temperature shift of Fe-Cr alloys was approximately 74°C. Experimentally, the peak swelling temperature shifts for ion and neutron irradiation of Fe, Fe-10Cr, and Fe-14Cr were 54°C (449°C vs 395°C), 78°C (503°C vs 425°C), and 73°C (498°C vs 425°C), respectively, close to the calculated value.

In summary, very few studies have used dual-ion irradiation to match the cavity and loop microstructures of neutron-irradiated FM steels, and only a single condition goes beyond low

damage levels (<35 dpa). Since the benefit of using dual-ion irradiation for materials qualification is to create high damage levels in a short amount of time, it would be interesting to evaluate if the temperature shift and helium injection rate used at low damage level is still valid to match the cavity and loop microstructure when materials are irradiated to end-of-life dose. In particular, cluster dynamics simulations suggest that the increase in helium injection rate must be reduced with increasing damage level [21]. Mansur's invariance theory overestimates the temperature shift necessary to match the cavity microstructure because it does not account for the presence of helium trapping sites that partially decorrelates the nucleation process from temperature. The required increase in helium injection rate is justified by the time compression at high damage rate that limits the migration of helium from weak-binding sinks to cavities. It would be of value to the scientific community to evaluate if the temperature shift and increase in helium injection rate remain constant with different reactor temperature and helium injection rate by matching the cavity and loop microstructures from similar materials irradiated in different reactors.

No physics-based model has quantitatively predicted the cavity microstructure evolution in reactor and under dual-ion irradiation. Developing such a model in parallel to dual-ion irradiation would provide additional predictive capabilities that could support the materials qualification process.

Finally, no studies have considered the impact of reactor irradiation history on the match between dual-ion and neutron-irradiated microstructure. Temperature and flux excursions as well as start-ups and shut-downs are inherent to commercial reactor operation and need to be considered when using dual-ion irradiation and models to predict the neutron-irradiated cavity microstructure evolution.

Chapter 3 Objective

The objective of this work is to **determine how temperature shift and helium injection rate interact in ion irradiation so as to replicate the neutron-irradiated cavity microstructure in ferritic-martensitic alloy T91**.

To achieve the objective, several aspects of microstructure evolution must be ascertained:

A. Cavity embryo nucleation rates in dual-ion and neutron irradiations.
B. Cavity growth rates in dual-ion and neutron irradiations.
C. Helium (de)trapping rates during dual-ion and neutron irradiations.
D. Point defects concentrations and net absorptions at sinks during dual-ion and neutron irradiations.
E. Relation between helium (de)trapping rates and point defect concentrations and net absorptions at sinks that governs cavity growth rates.

The approach to reaching the objective was divided into four tasks. Task 1 directly measured bubble nucleation and cavity growth rates from the irradiation microstructure of specimens irradiated with heavy ions at the Michigan Ion Beam Laboratory and with neutrons in BOR-60 and FFTF (aspects A and B). In Task 2, helium (de)trapping rates, point defect concentrations and net absorption at sinks (aspects C and D) were calculated by a rate theory model including helium partitioning to sinks. Task 3 determined the relation between helium (de)trapping rates and point defect concentrations and net absorption at sinks that governs cavity growth rate (aspect E). Task

4 determined the relation between temperature shift and helium injection rate that replicates neutron-irradiated cavity microstructures by combining the results of Tasks 1, 2 and 3.

Chapter 4 Experimental Procedures and Modeling

This chapter describes the experimental procedures used to irradiate, characterize and analyze the T91 samples used in this dissertation. It includes details about the Michigan Ion Beam Laboratory, the BOR-60 reactor and Fast Flux Test Facility (FFTF) as well as the methods used to characterize the irradiated microstructures.

4.1 Alloy and Sample Preparation

Alloy T91 heat 30176 is the only alloy studied in this dissertation although other alloys such as HT9 heat 84425, 800H heat 35175 and 21Cr32Ni heat 2192 have also been irradiated at the Michigan Ion Beam Laboratory and in the BOR-60 reactor. Alloy T91 is a ferritic-martensitic steel with composition given in Table 4.1. The PNNL composition is extracted from previous publications using the same material [50,55]. To confirm the composition provided, an independent chemical analysis was performed by Luvak Inc., as reported by Taller [17], using combustion infrared detection to measure carbon and sulfur content (ASTM E1019 [146]), inert gas fusion to measure oxygen and nitrogen content (ASTM E1019 [146]) and direct current plasma emission spectroscopy to measure all other elements (ASTM E1097[147]).

Table 4.1: Composition (wt%) of T91 heat 30176 provided by PNNL and Luvak [13].

Element	Fe	Cr	Ni	Si	Mo	V	Mn	C
Luvak	89.05	8.76	0.1	0.25	0.86	0.23	0.44	0.091
PNNL	89.52	8.6	0.09	0.11	0.89	0.21	0.37	0.08
Element (continued)	N	Al	P	S	Ti	Cu	Nb	W
Luvak	0.052	0.004	0.007	0.002	0.003	0.062	0.086	0.004
PNNL	0.054	-	-	-	-	-	0.072	-

T91 is a candidate for fast reactor applications because of its high-temperature strength and good swelling resistance compared to austenitic steels [5]. The alloy was heat-treated to improve its toughness as described by Taller [17]: as-received T91 samples were encapsulated in a quartz tube that was evacuated twice and then backfilled with 0.25 atmosphere of argon. The samples were normalized at 1038°C for 30 minutes and subsequently air-cooled. Tempering was performed at 760°C for 30 minutes and air-cooled. The timer for each step of the heat treatment process began when the temperature of a thermocouple touching the quartz tube read within 5°C of the target temperature. The resulting unirradiated microstructure of T91 after tempering included prior austenite grain boundaries (PAGB), laths, coarse chromium carbides (mostly $M_{23}C_6$ at PAGB and lath boundaries), fine V,Cr-carbonitrides in the matrix or adjacent to Cr carbides, and network dislocations.

The sample preparation procedure from Taller [17] was replicated for consistency with previous studies. Due to the limited irradiation area of ion irradiations, samples of T91 were cut in the form of 1.5 × 1.5 × 10-20 mm bars using electrical discharge machining (EDM) with a geometric precision on the order of 1μm. Samples and guide bars (spare ferritic-martensitic steel to bookend the irradiation samples) were then mounted on a heated metal puck using Crystalbond™ adhesive resin and placed like they would be on the irradiation stage. The puck was

then allowed to cool to harden the adhesive, sometimes using de-ionized water to expedite the process. The samples were then hand-polished on wetted silicon carbide grinding paper mounted on a variable speed grinding wheel. If samples exhibited uneven heights, they were polished using a 400 grit first to even the surface. Then, grits of 600, 800 and 1200 with only the weight of the puck as downward pressure were used to polish the sample. The polishing direction was rotated 90 degrees between each grit step to identify when the scratches induced by the previous polishing step had been removed. The samples were also rinsed with deionized water between grinding steps to remove stray particles. After the 1200 grit grinding step, the puck was re-heated, and the samples were flipped to the opposite side which will be the irradiated side. The grinding process starting at the 600 grit was repeated for the opposite face. The surface was further polished with cloth pads and high-viscosity polycrystalline diamond slurries of 3 μm, 1 μm and 0.25 μm for 5 minutes each (rotated 90° in-between) with only the weight of the puck as applied pressure. The samples were then removed from the puck by heating once again. Any residual adhesive was removed by leaving the samples in acetone until the adhesive completely dissolved. Samples were then successively cleaned with methanol then ethanol and allowed to dry in air.

The damage layer induced by mechanical polishing (estimated to be 2-5× the size of the last particle used), was removed by electropolishing. Electropolishing uses electrical current to transform a thin layer of the samples into an oxide that is then dissolved by the acid solution the samples are immerged in. A 500 mL solution of 10% perchloric acid (~70% concentration) and 90% methanol in a 1000 mL beaker was cooled to between -40 and -50°C (measured by an analog thermometer in solution) using a methanol bath with dry ice. A magnetic stirrer rotating at 250-300 rpm created a ~0.75”-diameter vortex in the electropolishing solution to improve the removal of the oxide formed during electropolishing. The to-be-irradiated surface of the sample was

oriented to face the cathode, a 25 × 25 mm square platinum wire mesh, which was also submerged in the solution. The sample itself served as the anode. The samples were kept electrically biased at all times so that they would never be in solution without the applied voltage of 40V. Samples were submerged for approximately 20 seconds, one at a time. During the electropolishing, the sample was agitated within the vortex to refresh the flow of solution at the surface. This procedure was estimated to remove about 2 μm of material based on the polishing curve presented in [148]. If the surface lost too much of its shine because of the insufficient removal of oxide, the sample was submerged once again but this time with the to-be-irradiated surface facing away from the cathode to limit the formation of oxide.

Prior to irradiation in the BOR-60 nuclear reactor, slices of thickness of 0.4 mm were cut from the heat-treated T91 samples using wire EDM and were thinned down to 0.25 mm by double sided diamond lapping to a 0.25 μm finish. 3-mm diameter disks were then punched out from the thinned slices using a Gatan TEM disc punch system. Each of the disks was then laser engraved for identification before they were loaded into capsules for BOR-60 irradiation [13].

4.2 Dual-Ion Irradiations

4.2.1 Ion Irradiation Experiments

The T91 samples were irradiated using the dual-beam configuration at the Michigan Ion Beam Laboratory at the University of Michigan [149] in which the sample is facing a defocused 5 or 9 MeV $Fe^{2+/3+}$ beam used to produce a damage rate of ~7.5×10^{-4} dpa/s at 600 or 1200 nm from the surface, respectively. Helium was injected simultaneously (at a 60° angle from the normal to the stage) using a raster-scanned beam. In order to inject the helium at the correct depth range, a 2.85 MeV He^{2+} beam was degraded through a 2.6-μm-thick aluminum foil when the heavy-ion beam was at 5 MeV as shown in Figure 4.1(a). When the Fe beam was at 9 MeV, a 3.42 MeV He^{2+}

beam was degraded with a 6.2-µm-thick aluminum foil to create a constant appmHe/dpa profile between 600 and 1500 nm from the surface as shown in Figure 4.1(b).

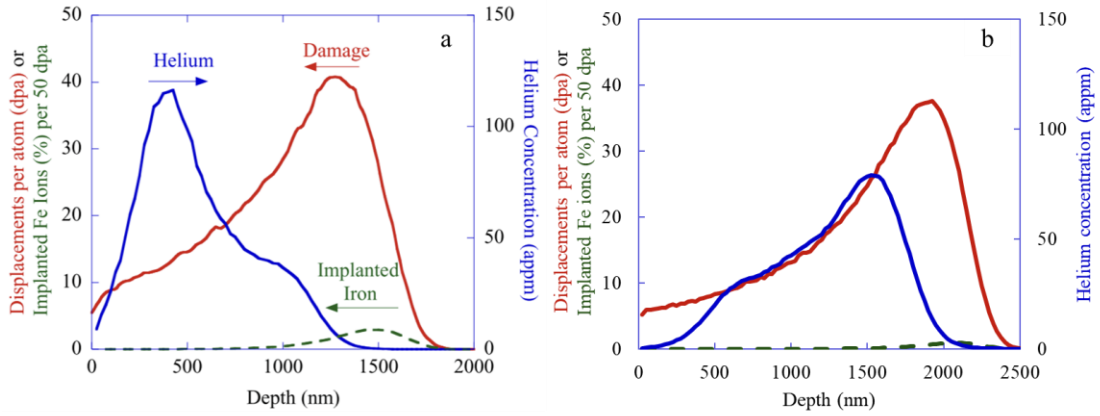


Figure 4.1: Iron and helium depth profiles for dual ion irradiations using (a) 5 MeV Fe^{2+} ions and degraded 2.85 MeV He^{2+} ions to 16.6 dpa at 600 nm for 4 appm He/dpa or (b) 9 MeV Fe^{3+} ions and degraded 3.42 MeV He^{2+} to 16.6 dpa at 1200 nm in alloy T91.

The heavy-ion Fe beam was produced from a NEC SNICS-II or Peabody Scientific PS 120 sputter source and a FeO target and accelerated through the 3 MV NEC Pelletron accelerator. An electron cyclotron resonance (ECR) source created the He^{2+} beam which was accelerated through the 1.7 MV General Ionex Tandem Accelerator. A description of the stage and multi-beam chamber used for these irradiations is provided in Sections 4.2.3 and 4.2.4.

A slit aperture system consisting of four independently controlled and electrically isolated slits was used for each beamline to define the irradiated area by moving into and out of the beam path via digital control. The slit apertures also measured the unsuppressed current incident on each individual slit to ensure that the whole irradiation area received beam. The area of irradiation from each ion beam was determined using the geometry of the stage relative to the beamline. For example, with the iron ion beam, if a 4mm × 4mm irradiation area was desired, both X slits were set to a distance of 2 mm and the Y slits were set to a distance of 2 mm, resulting in a total area between the slits of 4mm × 4mm. However, for the helium ion beam which impacted the stage at

a 60° angle relative to the heavy-ion beam, the X slits were adjusted by the cosine of the angle. For example, the X slits were set to a distance of 2.5-3 mm and the Y slits were set to a distance of 5 mm, the total area hit on the stage was 10-12mm × 10mm [17].

To achieve a uniform damage profile, the heavy-ion beam was defocused using a quadrupole such that it completely covered the area defined by the slit aperture system. The shape of the beam was assessed using a beam profile monitor (BPM) and a 2D profiler mounted in Beamline 4 after the slits.

4.2.2 SRIM Damage and Helium Implantation Calculations

Stopping and Range of Ions in Matter (SRIM-2013) [150] was used to calculate a depth-dependent damage profile, given the ion energy and the target material atomic composition. The SRIM damage calculations were performed using the quick Kinchin-Pease mode using the displacement energies taken from Table 1-1 of Ref. [151]: 25 eV was used for Al, 30 eV for Ti and Cu, 40 eV for Fe, Cr, Ni, V, and Mn, and 60 eV for Nb and Mo and 90 eV for W. For all other elements, a displacement energy of 25 eV was assumed. The composition for the SRIM calculation was the Luvak composition of the target material detailed in Table 4.1. Simulation were run for 100,000 ions to obtain accurate damage and implantation curves with adequate counting statistics. Figure 4.2 shows the SRIM calculated displacement rate and injected interstitials with depth for 5 and 9 MeV $Fe^{2+/3+}$ ions in T91. The damage level at 600/1200 ± 100 nm from the surface was used as the nominal damage level for 5/9 MeV experiments, respectively, as this region is far from the surface and avoids the profile of the injected ions [103]. The damage rate from the energy degraded helium ions was determined to be several orders of magnitude lower than the damage rate from the heavy ion beam and considered negligible.

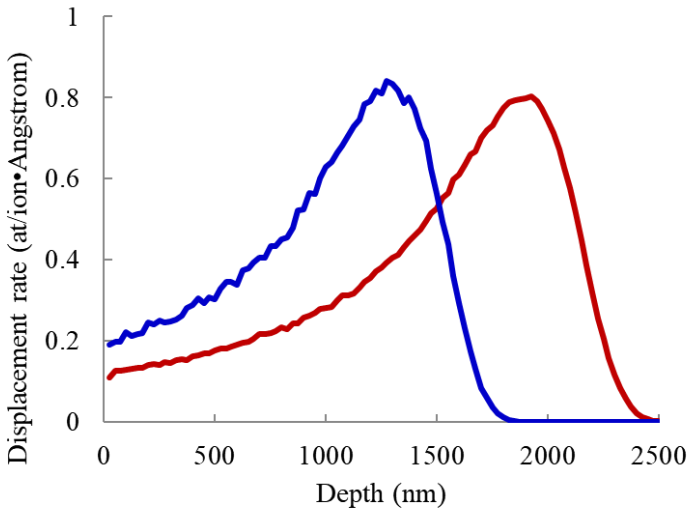


Figure 4.2: Displacement rates as a function of depth for (blue) 5 MeV Fe^{2+} and (red) 9 MeV Fe^{3+} in T91.

The SRIM displacement rate was used to estimate the total irradiation time and ion current required to reach any given damage level. Eq. 4.1 and Eq. 4.2 estimated the total dpa for a given condition (the units for each input and appropriate conversions are also given):

$$dpa = \frac{(SRIM\ Displacement\ Rate)\sum(ion\ beam\ current * time)}{(Atomic\ Number\ Density)(Ion\ Charge)(Irradiation\ Area)} \quad \text{Eq. 4.1}$$

$$\frac{displacement}{atom} = \frac{\frac{disp}{\text{Å} * ion} * \sum\left(\frac{\mu C}{s} * s\right) * 10^8 \frac{\text{Å}}{cm}}{\frac{atom}{cm^3} * \frac{C}{ion} * \frac{10^6\ \mu C}{C} * cm^2} \quad \text{Eq. 4.2}$$

Using the measured thickness of the aluminum foil from Section 4.2.4, SRIM was used to calculate the energy, position, and direction, for each ion exiting the foil and for each angle of foil rotation, in one degree increments as described in [17,152]. Individual ions were then propagated from the foil to the sample surface following the direction vectors calculated. To ensure an even distribution of ions across the sample surface, the beam was raster scanned across a 6 mm wide and 10 mm high area on the aluminum foil. Due to an error in the original helium foil degrader

calculation methodology, the He/dpa ratio for samples irradiated at 16.6 dpa and at 445°C:35dpa is non-uniform and not expected to significantly impact the results in the area of interest 500-700 nm from the surface [17].

4.2.3 Irradiation Stage

The stage configuration is similar to what was used in previous work [17]. An irradiation stage was used to hold the samples in place and provide heating and cooling. A schematic of the stage is shown in Figure 4.3. The samples and guide bars are fastened to a thermally conductive copper or nickel alloy head via hold-down bars, pressure plate and screws. Hold down bars and pressure plate have notches 1 mm in width and 1 mm apart to aid in the alignment of the samples. A 0.25-mm-thick piece of copper foil was placed between the stage and the samples to enhance heat conduction. The head of the stage is attached to a stainless-steel tube welded onto a 6" ConFlat® flange that can be mounted on the Multi-Beam Chamber. The stage was designed to place the samples at the intersection (eucentric) point of ion beams from the beamlines. Two channels were machined in the stage for cooling via pressurized air and a hole machined into the non-vacuum side for a resistive cartridge heater approximately 4cm long and 1cm in diameter, with a temperature rating of up to 760°C. Additionally, a Type-J contact thermocouple was inserted into the back of the stage 5mm to the side of the heater into an approximately 1mm diameter hole to monitor the temperature of the back of the stage. Type J thermocouples using 0.005-0.01" diameter iron and constantan wires were spot-welded to samples inside the irradiation area when possible. These thermocouples are used to calibrate a 2D infrared thermal pyrometer viewing the irradiation stage through a Ge window. Prior to irradiation, irradiation marks were placed on the samples using a razor blade to define the irradiation area and facilitate beam alignment and area identification as shown on the photograph of a completely built stage in Figure

4.4. Before loading the stage in the Multi-Beam Chamber, the stage was heated in air to 70°C to ensure all thermocouples were reading within 2°C of each other.

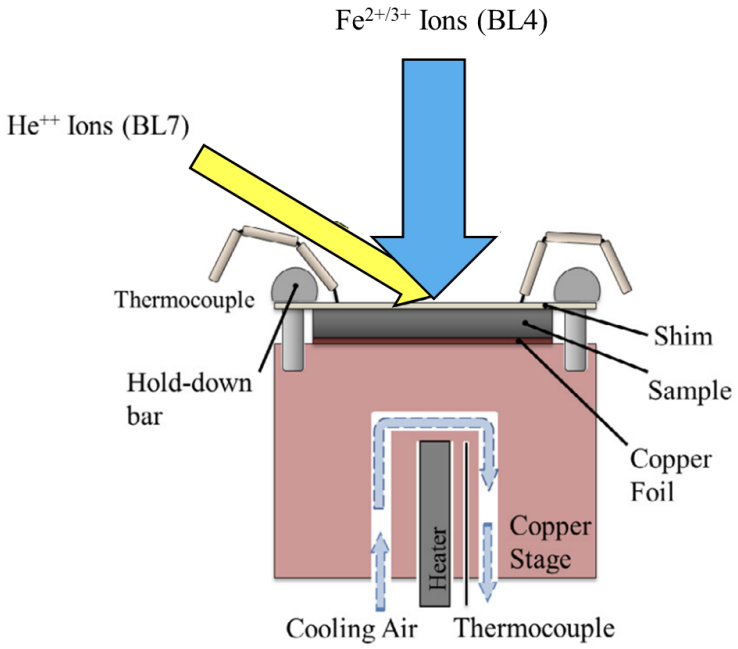


Figure 4.3: Schematic of the stage used for dual-ion irradiations (reproduced from [149]).

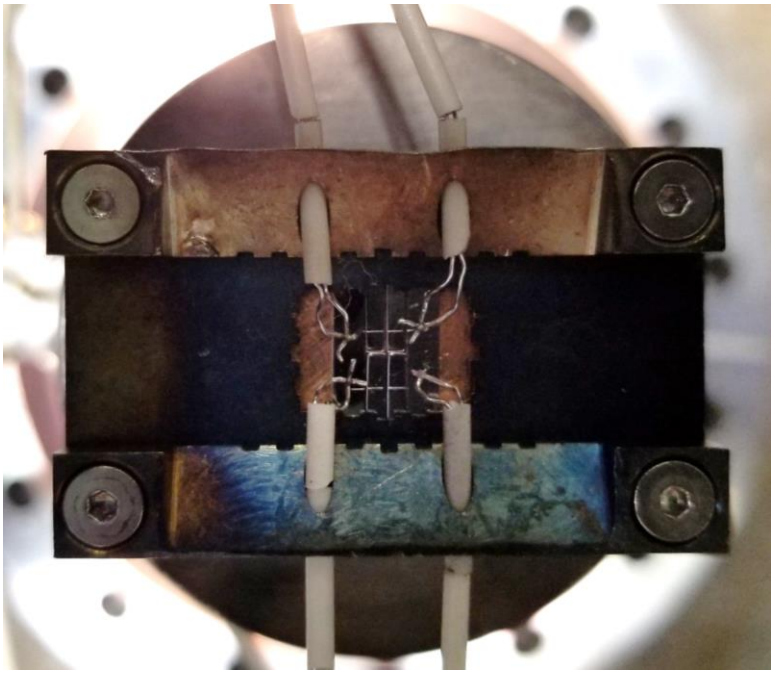


Figure 4.4: Picture of a stage (four half-bars and two guide bars) ready to be irradiated.

4.2.4 The Multi-Beam Chamber

The Multi-Beam Chamber (MBC) was designed to provide a fixed intersection point for each of the three accelerators at the Michigan Ion Beam Laboratory [17,153]. A schematic of the MBC is provided in Figure 4.5.

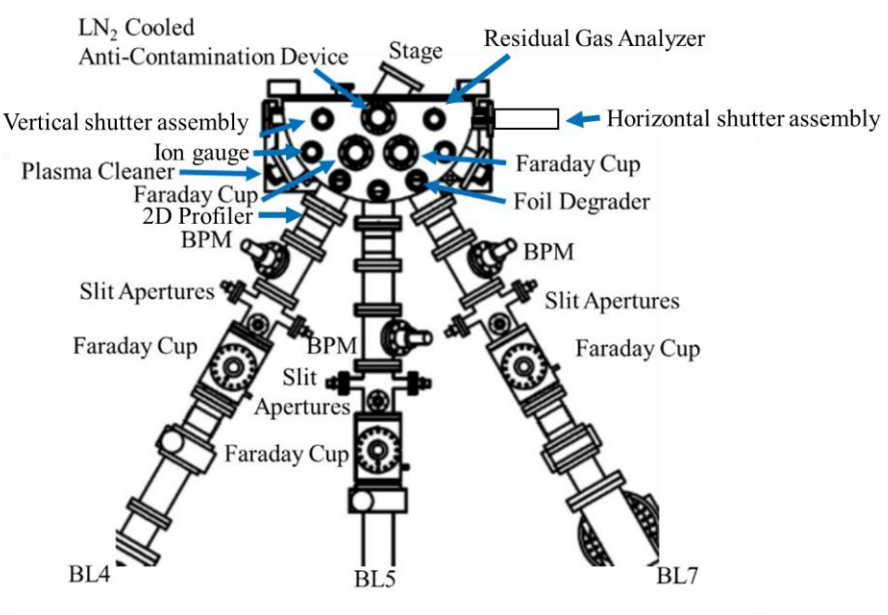


Figure 4.5: Schematic of the Multi-Beam Chamber with beamlines (adapted from [17]).

All dual ion beam irradiations included in this thesis were conducted with the stage facing beamline 4 (BL4), perpendicular to the heavy-ion beam. The stage was mounted to the back panel of the chamber using a copper gasket and tightened down with 16 pairs of nuts and bolts.

Each beamline is equipped with two Faraday cups to record the ion beam current: one before the slit system to measure the total current in the beamline and one in the MBC to measure the current hitting the stage. In beamlines 5 and 7 (BL5 and BL7), inside the chamber but right before the MBC Faraday cups, two aluminum foils are mounted on a rotating feedthrough connected to a stepper motor allowing energy reduction of the beam. The pressure in the vacuum chamber is monitored using an InstruTech Inc. model IGM402 hot cathode ionization vacuum

gauge. The chamber can be evacuated by a scroll pump and a cryopump. The partial pressure of each gas species in the vacuum is monitored using an Inficon Transpector® MPS Residual Gas Analyzer. The chamber is equipped with an Evactron EP Series Plasma De-Contaminator directly aimed at the stage to plasma-clean the chamber and remove hydrocarbons from the surface of the stage. A large copper shield can be cooled via conduction with liquid nitrogen and acts as an anti-contamination device to trap moisture and hydrocarbons [144] since carbon has been shown to affect swelling significantly [145]. A series of automated valves pulled the liquid nitrogen from a large tank into a dewar on top of the MBC with a large copper surface.

Several quartz windows allow live viewing of the irradiation stage using a Nikon digital camera interfaced through the internal laboratory network for beam alignment. A 2D FLIR® infrared thermal pyrometer allows live monitoring of the stage temperature through a germanium window: it records surface temperatures of user-defined regions of interest on the specimens at a rate of 3.125 Hz. These diagnostics are connected to computer systems, which record and display the information using custom-built LabView™ programs.

The latest additions to the MBC were the two shutter systems (one vertical for BL5 and one horizontal for BL7) that allowed for the insertion of two small stainless-steel plates to block the BL5 and/or BL7 beams from hitting a portion of the stage. The BL7 shutter plate was connected via a feedthrough to a motor and was used either to create a gradient of helium injection rates across the sample by the repeated insertion/retraction of the shutter throughout the experiment or to achieve two damage levels in a single irradiation by initially masking half of the stage for a desired amount of time before retracting the shutter.

4.2.5 Irradiation Procedure

With the stage mounted in the MBC, the oil-free scroll pump was used to evacuate the chamber to 0.15 torr. The plasma cleaner was then run at 15W forward power for 2hrs with the pressure maintained at ~0.13 torr. After plasma cleaning, the scroll pump evacuated the chamber to $<10^{-2}$ torr, a high enough vacuum to switch the evacuation from the scroll pump to the cryopump by opening/closing two gate valves. The chamber was left to be evacuated overnight and typically reached a pressure of $\sim10^{-7}$ torr the next morning. Cooling of the anti-contamination device started around 8am to ensure that it would effectively trap contaminants before beams were put on the samples. The heating of the stage started around 10am by applying a voltage to the cartridge heater and maintained 10°C under the target irradiation temperature starting at 12:00pm (for 5/9 MeV $Fe^{2+/3+}$, beam heating ranged from 1-10°C depending on the ion flux, while 2.85/3.42 MeV He^{2+} beam heating was usually <1°C). The heating rate was low enough to prevent warming up the cold trap too much or outgassing the stage too abruptly. When the desired irradiation temperature was reached, the thermal imager was calibrated against the thermocouple measurements for user-defined areas of interest (AOI) by adjusting the emissivity of each AOI until agreement is reached. A 2x2-pixel AOI roughly equated to a 1x1-mm irradiation on the sample: at least two AOIs were placed on each sample in addition to two 2 × 5-pixel AOIs on each guide bar.

MIBL staff were responsible for starting the ion sources and accelerators for the day: the defocused heavy-ion beam and the raster-scanned helium beam were typically ready for alignment around 12:00pm and 10:00am respectively. The alignment of the beams was then checked with lasers which had been previously aligned with the beam path for BL4 and BL7. The lasers are mounted on a viewport located at the end of the beamline on the accelerator side opposite the

MBC. The alignment of the laser illuminated area was checked via the camera on the samples to-be-irradiated as shown in Figure 4.6.

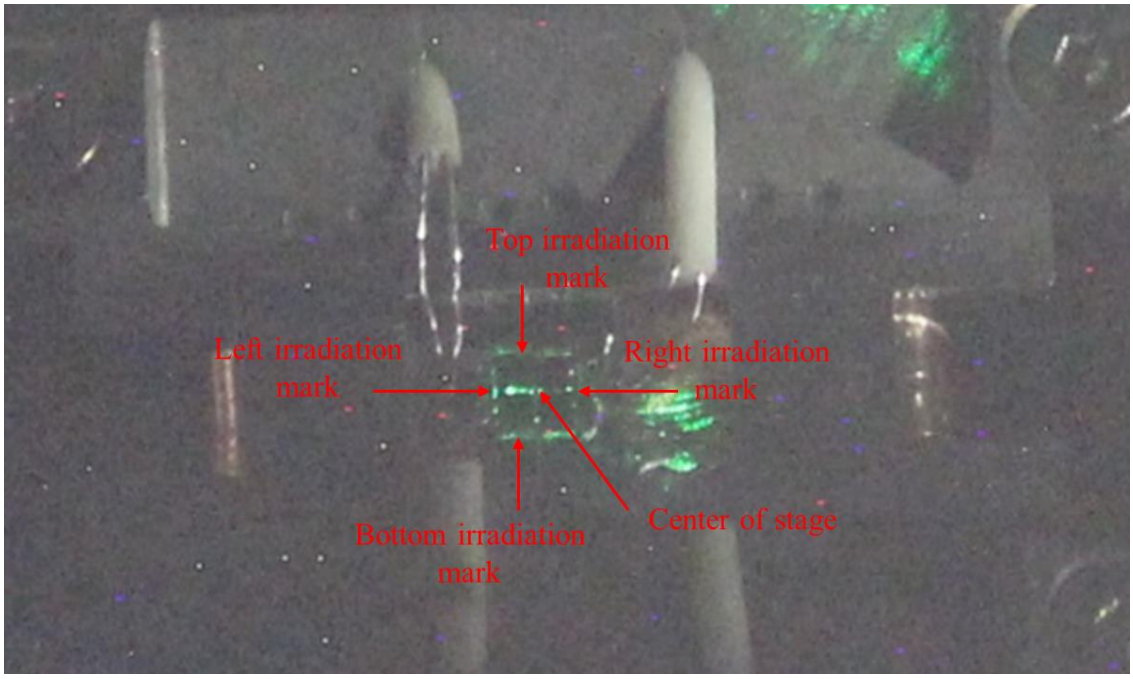


Figure 4.6: Laser-illuminated samples revealing the irradiation marks. Reflections of the laser are also visible on the copper sheet on the right but do not represent the path of the beam.

Following laser alignment on the samples, a sheet of alumina (with a 2 mm grid) was slid in front of the irradiation stage ~1/2" away using a linear motion feedthrough. Since alumina fluoresces when struck with ion beams, the slits were adjusted to place the ion beam where the laser was as shown in Figure 4.7. The alumina piece is retracted prior to irradiation.

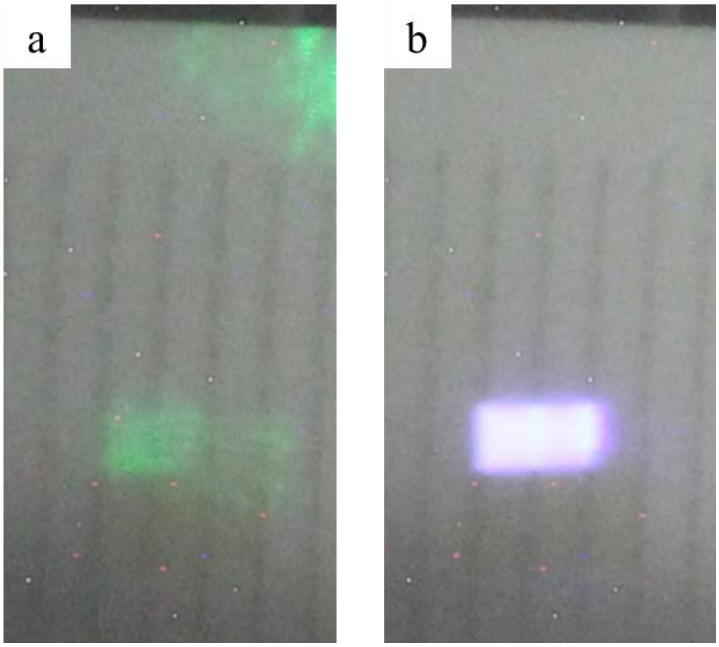


Figure 4.7: (a) Laser on the alumina after alignment on the stage. (b) Beam on the alumina after moving the slits to match the position of the laser.

Following beam alignment on the stage, the BPM and 2D profiler in beamline 4 were used together to measure the profile of the defocused beam and ensure that the current density remains within 10% of the average value as shown in Figure 4.8.

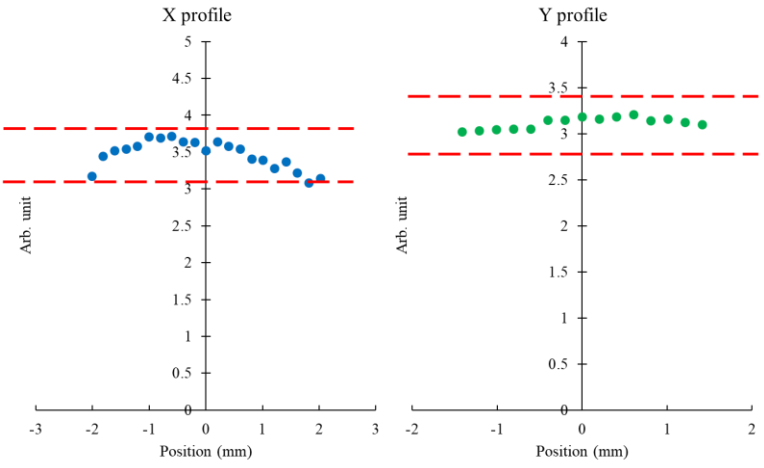


Figure 4.8: Example of the current intensity profile of the defocused heavy-ion beam. Red dashed lines delimit +/-10% from the average of the signal.

For beamline 7, the aluminum foil was inserted into the path of the beam following beam alignment with the aluminum foil. The helium beam current was measured at a series of foil angles to calibrate its position and ensure that the foil is as perpendicular to the beam as possible in the 0° position as shown in Figure 4.9. With the angle calibration completed, the coefficients for the foil degrader were input in a LabView program to control the rotation of the foil degrader and produce the correct implantation profile as explained in Section 4.2.2.

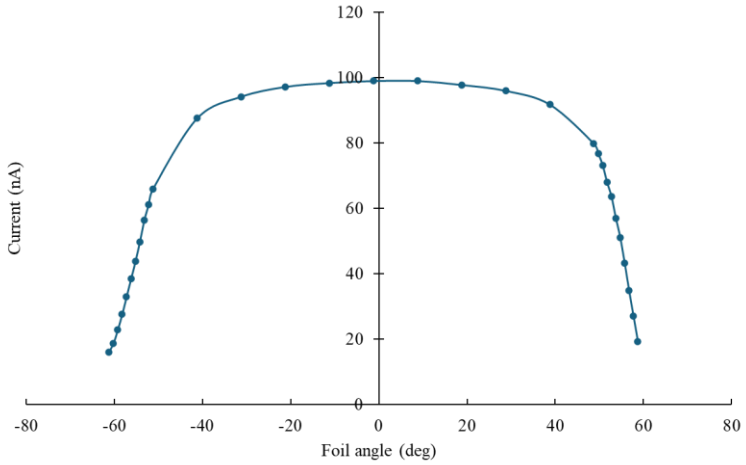


Figure 4.9: Example of the change in helium current with the rotation of the foil.

The irradiation was subsequently started by removing the Faraday cups in the way of the beams and activating the rotation of the foil degrader. The vacuum chamber pressure was monitored to ensure that it stayed below 10^{-7} torr ($< 1.3 \times 10^{-5}$ Pa). For all irradiations, the average of the AOI temperatures was maintained within ±10°C of the desired target temperature and in many cases with a 2σ standard deviation less than ±5°C. Since the thermocouples are not always in the irradiated region, they were only used for recalibration of the AOIs during long irradiations for which the oxidation of the samples might change the emissivity of the samples. A series of alarms were used to monitor the irradiation parameters throughout the duration:

- Temperature alarm if any of the AOIs deviate more than ±10°C from the target temperature. Appropriate adjustments were made to the voltage on the cartridge heater as a response.
- Alarm for the slits current which is usually an indicator of changes in current on the stage. Adjustments to the stage current were made by adjusting the alignment of the beam from the source through the accelerator and to the stage, adjusting the current produced by the source or changing the defocusing of the beam (for heavy-ion beam).
- Alarm for the anti-contamination device to alert that the liquid nitrogen tank is empty. The tank was promptly swapped with a full one to ensure that the cold trap stayed just above the boiling temperature of nitrogen.

Suppressed Faraday cups were used for simultaneous current measurements for both beamlines every 30min with the BL7 foil degrader perpendicular to the helium beam. Both Faraday cups had to be inserted at the same time as electrons emitted from the stage due to either ion beam would hit the back of the inserted Faraday cup, causing a spurious signal. If at any point during the irradiation the pressure, current, or temperature were compromised for more than 20 minutes (due to a power outage, accelerator or source malfunction, etc.), the samples were cooled down to room temperature rapidly and the Faraday cups inserted to prevent any potential oxidation, annealing or undesired irradiation. The irradiation could be resumed after the issue had been resolved, by heating the samples like start-up, and recalibrating the AOIs.

Once the target damage level was reached, the shutdown procedure started. Faraday cups were inserted, cartridge heater voltage dropped to 0V, refill of the cold trap stopped, and high-pressure air applied to the air-cooling lines. Samples on the stage would typically reach below 100°C within 10 minutes. The samples were kept under high vacuum for at least 12 hours to allow for the liquid

nitrogen cooled cold trap to warm up enough to reduce water condensation on the cold trap when the MBC was vented.

4.3 Neutron Irradiations

4.3.1 BOR-60 Reactor

TEM disks were enclosed in capsules and inserted into the BOR-60 reactor in 2013 at different positions in the core of the reactor to achieve various irradiation temperatures and damage levels. The targeted irradiation temperatures were 360, 400, 450 and 525°C and the targeted doses were 20, 40, 60, 100 and 120 dpa. All the TEM capsules went through multiple irradiation cycles. Actual sample temperatures were calculated based on the coolant temperature reported during each irradiation cycle (coolant is in direct contact with the capsule) and the calculated temperature rise through the capsule to the TEM samples due to gamma heating. Irradiation doses were calculated based on the integral of the displacement cross section and the BOR60 neutron energy spectrum. There were slight cycle-to-cycle variations in sample temperature (<10°C) and the durations at each cycle also varied from 9 to 83 days [13,17]. The individual cycle histories were provided by Terrapower, LLC from the Research Institute of Atomic Reactors (RIAR) and are not publicly available [17].

The irradiation conditions for the BOR-60-irradiated T91 are provided in Table 4.2. All specimens were irradiated with a damage rate between 6-9 × 10^{-7} dpa/s and helium production rate of 0.77 appmHe/dpa. Over the course of this work, multiple estimates of the helium generation rate of T91 irradiated in BOR-60 were produced using SPECTER (0.20 appm He/dpa) [154] and FISPACT-II (0.22 – 0.77 appm He/dpa) [155] using ENDF libraries [156] in both codes. The most recent revision of these calculations established 0.77 appmHe/dpa as the most accurate estimate.

Table 4.2: Irradiation conditions for BOR-60 reactor specimens.

Capsule identification	Damage level (dpa)	Temperature (°C)	Reference
P027	16 ± 1	369 ± 9	[13,17]
P028	32 ± 2	372 ± 7	[13,17]
P031	47 ± 3	376 ± 4	This work
P029	72 ± 5	375 ± 5	This work
P033	17 ± 1	404 ± 18	[13,17]
P036	29 ± 1	402 ± 6	This work
P034	86 ± 4	402 ± 8	This work
P037	19 ± 1	453 ± 9	[13,17]
P038	32 ± 2	450 ± 7	This work (with S. A. Taller)
P042	15 ± 1	517 ± 10	[13,17]
P043	25 ± 1	515 ± 10	This work (with S. A. Taller)

4.3.2 Fast Flux Test Facility (FFTF)

The Fast Flux Test Facility (FFTF) is a 400 MW_{th}, sodium cooled, nuclear test reactor situated in the Hanford Site, which is located in the state of Washington. Between 1983 and 1992, nine Materials Open Test Assemblies (MOTA) were irradiated: MOTAs 1A through 1G, and MOTAs 2A and 2B. Each MOTA was irradiated for approximately one year, except MOTA 1B which was only irradiated for four months [157]. Each MOTA contained multiple canisters placed either below-core, in-core or above-core. Table 4.3 shows the irradiation history for the four specimens presented in this work. Samples VH03, VH20 and NP04 were originally 0.63" compact-tension (CT) specimen whereas FA33 was a Charpy V-notch (CV) sample. All specimens in this work were placed in weeper canisters directly in contact with the sodium coolant: the temperature reported corresponds to the average temperature measured by the thermocouple placed in the canister throughout the MOTA experiment. Radial gradients within a canister were reported to be as high as 20°C (usually 5-15°C) whereas axial gradients for weeper canisters were estimated between 5 and 10°C since the sodium coolant heats up as it travels through the MOTA. The damage

levels and damage rates were estimated for Fe-18Cr-8Ni stainless steel using the SPECTER code [154,158–162] and the ENDF/B-V library [163], and changed significantly based on the position of the canister and the MOTA. The helium production rate was calculated via FISPACT-II to be 0.21 appmHe/dpa, relatively close to the value computed by Garner et al. [164] for Fe-12Cr in MOTA 1A, 1B and 2B (0.08 appmHe/dpa).

Table 4.3: Irradiation history for FFTF reactor specimens.

Sample	MOTA	1A	1B	1C	1D	1E	1F	Total
VH03	Temperature (°C)					410	404	407 ± 3
	Damage level (dpa)					35.7	37.4	73
	Damage rate (× 10^{-6} dpa/s)					1.21	1.30	1.25 ± 0.04
VH20	Temperature (°C)		409	439	408	410	404	415 ± 14
	Damage level (dpa)		9.2	38	27.5	38.6	37.4	151
	Damage rate (× 10^{-6} dpa/s)		0.97	1.71	1.71	1.31	1.30	1.46 ± 0.23
NP04	Temperature (°C)	410	409	439	408	410	404	415 ± 13
	Damage level (dpa)	18.2	9.9	38	27.5	38.6	38	170
	Damage rate (× 10^{-6} dpa/s)	1.05	1.05	1.71	1.71	1.31	1.31	1.42 ± 0.25
FA33	Temperature (°C)	410	409	439	408	410	404	415 ± 13
	Damage level (dpa)	22	11.9	40.4	29.2	41.4	39	184
	Damage rate (× 10^{-6} dpa/s)	1.26	1.26	1.82	1.82	1.40	1.35	1.52 ± 0.24

4.4 Post-Irradiation Characterization

4.4.1 TEM Specimen Preparation

The shallow penetration depth of 5-9 MeV Fe ions in dual-ion-irradiated specimens and the residual radioactivity of the neutron-irradiated samples make the FIB (focused ion beam) lift-out method very advantageous to prepare TEM samples. It allows for the preparation of cross-sectional electron-transparent lamellas typically 20 µm wide and 4-7 µm deep. Using small samples also prevents any magnetic distortion during TEM imaging caused by large magnetic T91 samples.

The TEM foils were prepared using a dual-beam FIB system. This instrument utilizes a vertical electron beam for imaging, and a gallium ion gun (52° from the electron beam) for imaging

and milling. The currents and energies of these beams could be varied up to 65 nA and 30 kV, respectively. The specific instruments used in this work were Thermo Fisher Helios NanoLab™ 650 Dual Beam™ and Nova 200 NanoLab™ DualBeam™ focused ion beam workstations for the dual-ion-irradiated T91 and FEI Versa NanoLab™ Dual Beam™ and Quanta NanoLab™ DualBeam™ for the neutron-irradiated T91 at the Low Activation Materials Development Analysis (LAMDA) laboratory [165] at Oak Ridge National Laboratory and at the Materials Science and Technology Building at Pacific Northwest National Laboratory.

Given the shallow irradiated region of dual-ion-irradiated samples, Electron Backscatter Diffraction (EBSD) was occasionally used in the Helios 650 with the electron beam at 30 kV and 6.4 nA to find a grain with an orientation anywhere between crystal directions [100] and [110] pointing at the surface. If such a grain was found, the FIB procedure could be conducted to make the lamella perpendicular to the [100] zone axis, making the imaging of dislocation loops easier as explained in Section 4.4.2.2. However, because of the shallow probing of EBSD and the small grain/lath size of T91, the signal obtained on the surface did not always correspond to the grain orientation deeper into the sample.

The FIB lift-out method consisted of different steps. With the irradiated specimen mounted irradiated side up at eucentric height in the FIB chamber, the stage was tilted 52° to be perpendicular to the ion beam. After injecting the gas injector needle, a 16 keV gallium beam was used to deposit a 20 × 2 µm 3-µm-thick layer of platinum on the target surface, using a current of ~1 nA. Using a higher current between 21 and 65 nA and an energy of 30 keV, 28 × 10µm trenches were created using a regular cross section pattern about 10 µm deep on the long sides of platinum deposition. The deposition sides of the trenches were cleaned up using lower current (3-9 nA) with the cleaning cross section pattern. A J-cut was then performed on both sides with the stage tilted

to 7° to start the lifting process. With the stage tilted to 0°, the top of the lamella was attached to a micromanipulator (Omniprobe™ needle) with a 1µm cube platinum weld. After cutting it free, the lamella was lifted out of the sample and placed in the center of a chevron on a Cu or Au TEM grid. The two lower corners of the lift-out were platinum welded on both sides of the lamella. At this point, the specimen was still ~2 µm in thickness. To achieve the target thickness of 100 nm, multiple thinning steps are required. The sample was tilted to 52° and two 6 µm-wide windows were created side-to-side using 0.79 nA cleaning cross-section patterns. The resulting frame provided support for the lift-out to minimize bending or twisting. Successive thinning with cleaning cross-section patterns on both sides at 0.79, 0.43 and 0.23 nA was conducted ±2° about 52° until the lamella appeared bright in the 5 kV, 0.4 nA electron beam, indicating a thickness close to 100 nm. To mitigate FIB damage in the TEM lamella, two cleaning steps of 5 min at ±5° about 52° on each side was conducted with a rectangular pattern at 5 kV and 2 kV and ~40 pA.

4.4.2 TEM Imaging and Characterization

TEM lamellas were imaged using a ThermoFisher Scientific™ (formerly FEI) Talos™ F200X G2 TEM (referenced as Talos), a ThermoFisher Scientific™ Tecnai G2 F30 TWIN TEM (referenced as TF30) and a JEOL 2100F Cs Corrected Analytic Electron Microscope (referenced at 2100F) at the Michigan Center for Materials Characterization $(MC)^2$.

The Talos [166] was operated at 200 keV and used for imaging cavities, dislocation loops, radiation-induced segregation and precipitation. Its point resolution was 0.25 nm in CTEM mode and 0.16 nm in STEM mode, respectively, and was equipped with a Gatan One View bottom mount camera for high-speed 4k × 4k imaging. Energy Dispersive X-Ray Spectroscopy (EDS) was conducted using a Super-X window-less detector consisting of four equal crystals with an active area of 4 × 30 mm^2 and a solid angle of 0.9 srad, detecting all elements down to and including

boron. Lastly, a Gatan Continuum S spectrometer with ultra-fast electrostatic shutter and high-speed DualEELS (energy resolution: 0.8 eV) was used for lamella thickness measurement. The TF30 [167] operated at 300 kV and was used for imaging small bubbles in CTEM mode with a resolution of 0.24 nm point-to-point on a 2k × 2k Gatan camera. The JEOL 2100F was operated at 200 keV in STEM mode for cavity and dislocation loop imaging. Software suites (DigitalMicrograph® or Velox®) were used to acquire the images. Specimens were mounted on a JEOL Double-tilt holder or a FEI High-visibility low-background double-tilt holder.

For thickness measurement, a condenser aperture (C2) of 70 μm is used (convergence semi-angle of 10 mrad) along with a camera length set to 47 mm (for a corresponding collection semi-angle of about 31.52 mrad). A zero-loss spectrum was taken in an area without going through the sample to calibrate the zero-loss peak. Then an EELS spectrum map with a 100 nm grid size was taken across every window to a depth of 2.5 μm for dual-ion-irradiated samples and over the whole area available for neutron-irradiated samples. The DigitalMicrograph® software included an algorithm to calculate the thickness by calculating the error in a logarithmic fit of the inelastic mean free path of the electrons through the sample. The error in this calculation (μ_{EELS}) is estimated to be around 10% [168].

4.4.2.1 Cavity Imaging and Characterization

To determine the size and density of cavities, imaging of the entire lift-out was performed using STEM mode on the Talos or 2100F, and CTEM mode on the Talos or TF30. In STEM mode, high-angle annular dark field (HAADF) and bright field (BF) images were taken simultaneously. The contrast in STEM HAADF images is mainly due to thickness and "Z-contrast," which is dependent on the atomic number of the material. Cavities lack thickness and have an effective atomic number of 0 making them appear black in these conditions. The HAADF images can be

taken to minimize parasitic contrast caused by dislocation networks. BF images are impacted by more phenomena such as diffraction contrast and grain orientation but will be used to confirm the nature of cavities since they appear bright with a clear edge in these pictures. Examples of a typical HAADF image and the corresponding BF image for T91 irradiated in FFTF are shown in Figure 4.10.

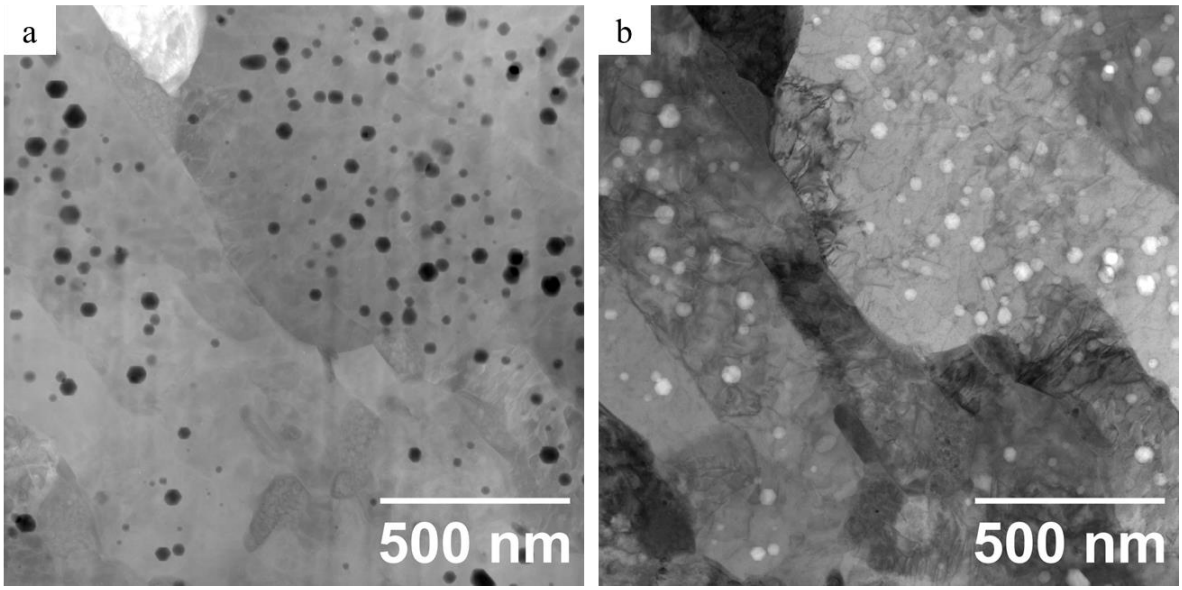


Figure 4.10: Example (a) HAADF and (b) BF images for T91 irradiated in FFTF.

Images were taken with a field of view of about 1.5 × 1.5 microns with a 4k × 4k resolution, leading to a pixel size of about 0.37 nm. Images were taken over the whole sample with a slight overlap. The pixel size and the low signal-to-noise ratio were limiting factors for imaging small (<5nm diameter) cavities in STEM mode. Thus, a through-focus series of CTEM BF images were collected to determine the size and density of cavities smaller than 5 nm in diameter using the Talos or TF30. An objective aperture of 10 μm centered around the transmitted beam in the diffraction pattern was used to produce a bright field image to minimize the influence of diffracted beams and improve contrast. A series of underfocused and overfocused images was collected from a focus value of -2 μm to +2 μm in 0.5 μm steps. When the image was out of focus, the interface

between the matrix and the cavity created Fresnel fringes rendering cavities as small as 0.5 nm in diameter visible in a 100-nm-thick lamella. In underfocused images, cavities appear as lighter features with a darker fringe around them, and in overfocused images, the cavities appear as darker features with a lighter rim around them [17]. However, the diameter of such small cavities is not reliable for focus values less than -1 μm or greater than +1 μm [169]. Therefore, the overfocused images collected at +1 μm were used to estimate the size of a cavity and the underfocused images at -1 μm was used to confirm the feature being measured is indeed a cavity. Example images of underfocused and overfocused cavities for T91 after dual-ion irradiation to 72 dpa at 460°C are shown in Figure 4.11.

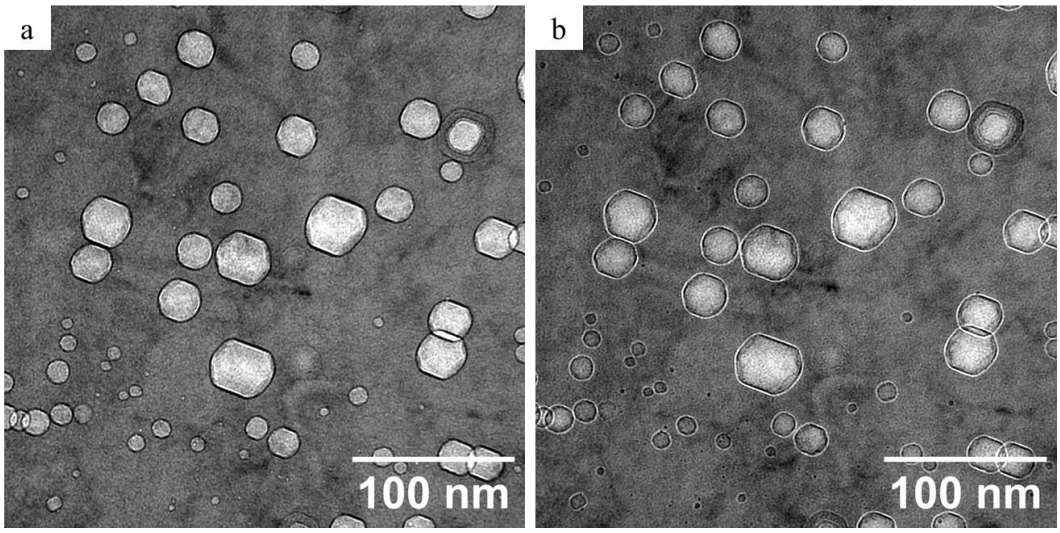


Figure 4.11: Example (a) underfocused (-1 μm) and (b) overfocused (+1 μm) images of T91 after dual-ion irradiation to 72 dpa at 460°C.

Images were taken at a field of view of about 320 × 320 nm on a 4k × 4k camera with a pixel size of about 0.08 nm. At least ten series of images were collected per irradiation condition.

Counting and measuring of the cavities was performed using the image-processing suite FIJI [170]. All HAADF images had their contrast and brightness adjusted and were stitched together manually to produce a complete picture of the window and avoid double-counting. During

counting, the BF images were used to confirm the cavities being counted were actual cavities and not precipitates, contrast from dislocations, or other microstructural features. On each overfocused BF CTEM image at the +1 μm focal point, cavities smaller than 5 nm in diameter were counted and their diameter measured. The positions and diameters of all cavities in STEM HAADF and CTEM BF were saved in CSV files. Following counting, the results were fed into a custom script written in MATLAB® able to compute the size distribution of cavities based on the number of cavities counted, their sizes, the area of the stitched image and the thickness map provided. The script also sorts cavities into 100 nm depth bins, starting at the surface of the sample, so that the evolution of the cavity microstructure with depth can be evaluated. Finally, the difficulty of obtaining clear contrast over the whole window given their area made it necessary to design a feature in the script allowing the user to remove 100 × 100 nm squares on the images from the analysis. The volume of each cavity was calculated assuming the cavity was a sphere. The sum of the volume of each cavity was tallied for each region of interest in the sample. This sum is the total change in volume, ΔV, in the area. Swelling was then calculated as the change in volume divided by the original volume. Therefore, the swelling of any area could be expressed as a percentage:

$$Swelling = \frac{\Delta V}{V - \Delta V} = \frac{\sum_i \frac{4}{3} * \pi * \left(\frac{d_i}{2}\right)^3}{w * t * h - \sum_i \frac{4}{3} * \pi * \left(\frac{d_i}{2}\right)^3} \quad \text{Eq. 4.3}$$

where h is the height of the area, w is the width, and t is the thickness, i indexes all cavities in the area, and d_i is the diameter of the individual i^{th} cavity. Additionally, a cavity size distribution with number density plotted as a function of cavity diameter can be calculated. Bin densities in the size distribution were computed with a resolution of 0.5 nm per bin from 0 to 5 nm and 1 nm per bin

for cavities equal or greater than 5 nm in diameter. These bin densities were normalized by the width of the bin to normalize the size distributions.

For all conditions in this thesis, an error analysis (established from [148,171]) was conducted to quantify the uncertainty in swelling, densities and diameters of cavities. Sources of uncertainties included: user measurement uncertainty in diameter (μ_d) and density (μ_ρ), inherent thickness uncertainty from EELS (μ_{EELS}), TEM resolution (σ_{TEM}) and counting uncertainty. One aspect that was not considered in the uncertainty propagation is the high degree of spatial inhomogeneity inherent to ferritic-martensitic steels. Grain-to-grain variation in the microstructure adds to the uncertainty of swelling measurements, as cavity nucleation and growth can vary extensively in adjacent grains. To neglect the spatial inhomogeneity and to minimize the error due to counting statistics, at least two TEM lamellas for each condition were extracted so that multiple prior-austenite grains and laths were analyzed. For dual-ion irradiations, this was equivalent to ~5 μm^2 of region of analysis area about 100nm thick. For neutron-irradiated conditions, the surface analyzed was anywhere from 50 to 120 μm^2 depending on the depth of the lamellas.

Since dual-ion-irradiated size distributions are only from a 200-nm band in the lift-out, they exhibit much lower counting statistics compared to neutron-irradiated samples leading to more noise and variation from one bin to another. In addition, this smaller sampling volume limits the measurable density of voids in the bins of size distributions. This shortcoming creates a threshold density below which cavities cannot be correctly measured in dual-ion size distributions. These 'undetectable' regions are shown in corresponding size distributions in Chapter 5 and Chapter 6.

The uncertainties for each bin must be separated from the uncertainty for global values. In the cavity size distributions, the diameter of the bins is fixed and only the uncertainty on the

densities is assessed. With the density $\rho_i = \frac{N_i}{V_i}$, where N_i is the number of cavities counted for the i^{th} bin and V_i is the volume of material under consideration, the uncertainty on the density is defined by Eq. 4.4, Eq. 4.5 and Eq. 4.6:

$$\sigma(\rho_i) = \sqrt{\frac{\sigma^2(N_i)}{V_i^2} + \sigma^2(V_i) * \left(\frac{N_i}{V_i^2}\right)^2} \quad \text{Eq. 4.4}$$

$$\sigma(N_i) = \sqrt{N_i + \left(N_i * \mu_\rho\right)^2} \quad \text{Eq. 4.5}$$

$$\sigma(V_i) = \mu_{EELS} * V_i \quad \text{Eq. 4.6}$$

The uncertainty on the number of cavities $\sigma(N_i)$ is computed as a combination of counting uncertainty $\sqrt{N_i}$ and the user measurement error in density for each bin $N_i * \mu_\rho$.

The uncertainty on the diameter of a bubble or a void (including average values for a distribution) depends on the user measurement uncertainty and TEM resolution:

$$\sigma(d_i) = \sqrt{(\mu_d * d_i)^2 + \sigma_{TEM}^2} \quad \text{Eq. 4.7}$$

Finally, the total swelling is the sum of the bubble swelling and void swelling as described in Eq. 4.3:

$$swelling_{tot} = swelling_{bub} + swelling_{void} \quad \text{Eq. 4.8}$$

The uncertainty in swelling for a particular set of bins (bubbles or voids for instance) is:

$$\sigma(swelling_i) = \sqrt{\sigma(\Delta V_i)^2 * \left(\frac{V_i^2}{(V_i - \Delta V_i)^4}\right) + \sigma(V_i)^2 * \left(\frac{\Delta V_i^2}{(V_i - \Delta V_i)^4}\right)} \quad \text{Eq. 4.9}$$

The change in volume ΔV_i is the sum of the volume of each individual cavity:

$$\Delta V_i = \sum_j \frac{4}{3}\pi\left(\frac{d_j}{2}\right)^3 \qquad \text{Eq. 4.10}$$

Thus, the corresponding uncertainty depends on the uncertainty on the diameter of each single cavity and the user measurement error in density as described in Eq. 4.11:

$$\sigma(\Delta V_i) = \sqrt{\sum_j \left(\frac{4}{3}\pi * \frac{3 * d_j^2}{8} * \sigma(d_j)\right)^2 + \mu_\rho^2 * \Delta V_i^2} \qquad \text{Eq. 4.11}$$

$$= \sqrt{\sum_j \left(\frac{\pi}{2} * d_j^2 * \sigma(d_j)\right)^2 + \mu_\rho^2 * \Delta V_i^2}$$

To determine the uncertainty on the total swelling (combining both bubbles and voids), Eq. 4.9 is used with:

$$\Delta V_{total} = \Delta V_{bubbles} * \frac{V_{void}}{V_{bubbles}} + \Delta V_{void} \qquad \text{Eq. 4.12}$$

$$V_{total} = V_{void}$$

And the corresponding uncertainties:

$$\sigma(\Delta V_{total}) \qquad \text{Eq. 4.13}$$

$$= \sqrt{\begin{array}{c}\sigma(\Delta V_{bubbles})^2 * \left(\frac{V_{void}}{V_{bubbles}}\right)^2 + \sigma(V_{void})^2 * \left(\frac{\Delta V_{bubbles}}{V_{bubbles}}\right)^2 + \\ \sigma(V_{bubbles})^2 * \left(\frac{\Delta V_{bubbles} * V_{void}}{V_{bubbles}^2}\right)^2 + \sigma(\Delta V_{void})^2\end{array}}$$

$$\sigma(V_{total}) = \sigma(V_{void})$$

The resolution for the HAADF images taken was 0.37 nm/pixel. Because the diameters are measured by drawing a line connecting opposite sides of the voids, σ_{STEM} will be twice the STEM pixel resolution. The resolution for CTEM BF underfocused and overfocused images was 0.08nm/pixel for the magnification used for imaging. However, the imaging resolution of the instrument for CTEM was 0.25 nm for point-to-point resolution which was used for σ_{CTEM}.

4.4.2.2 Dislocation Loop Imaging and Characterization

Two types of loops exist in ferritic-martensitic alloys: sessile a⟨100⟩ loops on the [100] habit planes and glissile a/2⟨111⟩ loops on the [111] habit planes [172]. Historically, CTEM has been used to investigate the presence of these loops using the weak two-beam condition. However, this method possesses several shortcomings. It requires a sequence of images in the same area with varying diffraction vectors g to satisfy the dislocation loop g·b invisibility criterion. This is particularly difficult in ferritic-martensitic steels which typically exhibit small grains with limited orientations. Additionally, this technique is more susceptible to thickness-dependent contrast which can obscure large areas of the image. As a result, newer methods to image dislocation loops using STEM mode have been used to more easily characterize these loops [173]. STEM mode smears out thickness-dependent contrast, resulting in a cleaner image, it can be performed on thicker samples, and the traditional g·b invisibility criterion can remain applicable. STEM on-zone imaging in particular has proven advantageous since imaging down the [001] zone axis results in a⟨100⟩ loops to appear edge-on aligned with the [100] directions on the CCD while a/2⟨111⟩ loops appear as elongated ellipses aligned with the [110] directions as shown in Figure 4.12. It also images all possible diffraction vectors for the [001] zone axis simultaneously, allowing for viewing of a⟨100⟩, a/2⟨111⟩ loops and dislocation lines all in the same image.

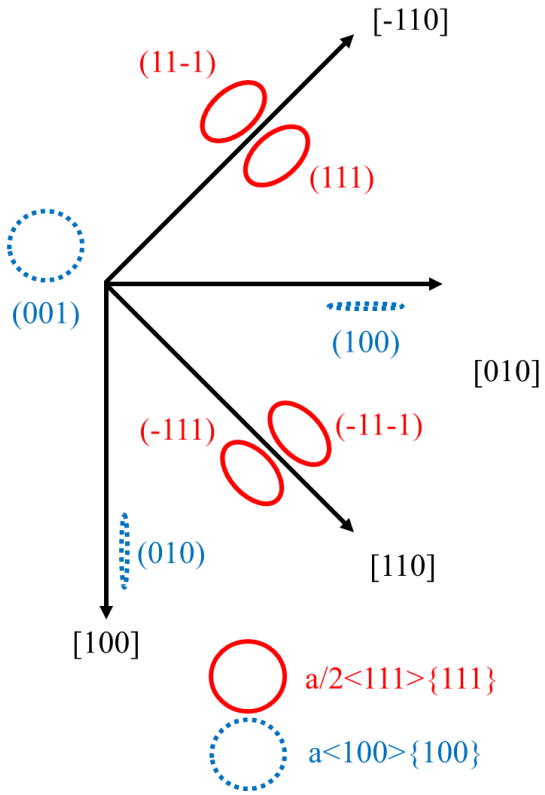


Figure 4.12: Schematic of dislocation loop orientations when observing down the [001] zone axis adapted from [172].

In practice, the loops were imaged in STEM mode a few degrees off of the [001] zone axis to prevent diffraction contrast. An example micrograph showing a⟨100⟩ loops, and dislocation lines of BOR-60-irradiated T91 is shown in Figure 4.13.

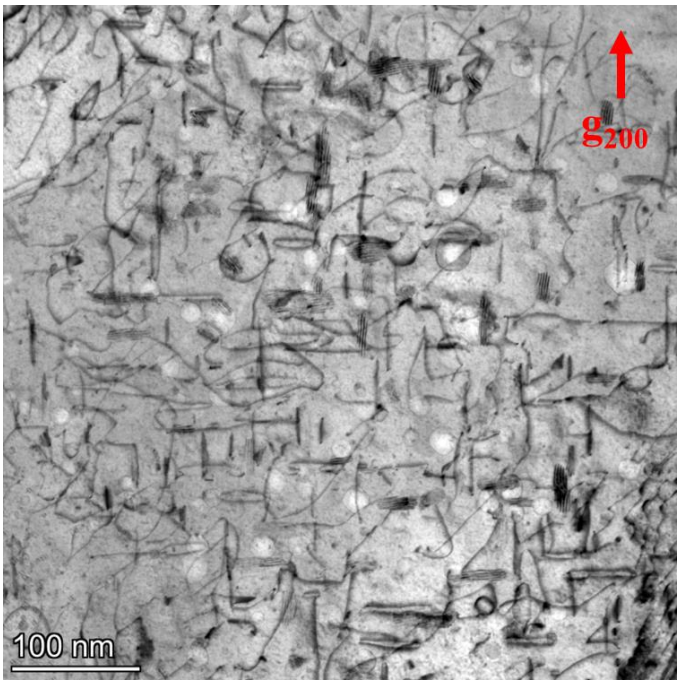


Figure 4.13: Example on-zone [001] STEM-BF image for the characterization of dislocation loops.

Images of loops were taken from at least two different areas in the region of interest for every condition. Using FIJI, loops were counted and their diameter measured in all available directions. However, because of the difficulty of the technique, the lift-out was not always perfectly oriented to reveal all loops at the same time. In that case, only loops in the visible directions were counted and the corresponding directions were recorded. A custom MATLAB® script was used to compute the average diameter, density and size distributions of loops in a similar fashion for cavities. The script accounted for the number of directions visible in each image and adjusted the loop density accordingly: if only one (respectively two) direction(s) of a⟨100⟩ loops were visible, their density was multiplied by 3 (resp. 1.5) to account for the other two (resp. single other) invisible direction(s). Except for dual-ion-irradiation temperatures lower than 445°C, only a⟨100⟩ loops were present and no a/2⟨111⟩ loops were visible. The dislocation loop size distribution allocated loops in 5 nm bins from 0 to 100 nm and densities were not normalized by

bin width since all bins were of the same width unlike cavity size distribution. The dislocation network density was calculated for this heat of T91, heat 30176, in previous work done by Jiao et. al [13] and estimated to be 10^{14}-10^{15} m^{-2}. A nominal value of 5×10^{14} m^{-2} was assumed for the dislocation network density.

Images were taken with a field of view of about 500 × 500 nm with a 4k × 4k resolution, leading to a pixel size of about 0.12 nm. The uncertainty propagation for the average diameter is like that of cavities described in Section 4.4.2.1. The uncertainty propagation for densities is

$$\sigma\left(\rho_{loops}\right) = \sqrt{\frac{\sigma^2\left(N_{loops}\right)}{V^2} + \sigma^2(V) * \left(\frac{N_{loops}}{V^2}\right)^2} \quad \text{Eq. 4.14}$$

$$\sigma\left(N_{loops}\right) = \frac{N_{loops}}{N_{counted}} * \sqrt{N_{counted} + \left(N_{counted} * \mu_\rho\right)^2} \quad \text{Eq. 4.15}$$

Where $N_{counted}$ is the number of loops actually counted manually on the images and N_{loops} is the number of loops in the image corrected for the number of visible loop directions.

4.4.2.3 Radiation-Induced Segregation and Precipitation Imaging and Characterization

Atom probe tomography (APT) is superior to STEM-EDS for characterizing the density and size of sub nanometer scale clusters and radiation-induced segregation [174–176], but it requires careful tip preparation via FIB and long data collection and analysis procedures. For precipitates larger than 2 nm in diameter, STEM-EDS has the advantage of a much larger sampling volume which provides better counting statistics. Due to time constraints, only STEM-EDS is used to characterize the radiation-induced segregation at grain boundaries and in-grain radiation-induced precipitation. Since these results are not validated against APT for very small precipitates, only clusters 2 nm and larger are considered as described later in this section.

The Talos microscope was used to acquire all EDS maps. For segregation at grain boundaries, the sample was tilted to place the boundary edge-on by minimizing its projected width in the STEM images. Lath boundaries with precipitate formation were avoided when possible. The character of grain boundaries (lath vs. prior-austenite grain, misorientation angle and axis) was not determined, and at least two different grain boundaries were mapped per condition. These images were taken with a field of view of about 269 × 269 nm with a 1024 × 1024-pixel resolution, leading to a pixel size of about 262.7 pm. For radiation-induced precipitation, maps were taken in the center of grains away from grain boundaries and large $M_{23}C_6$ precipitates when possible, and at least two different maps were collected per condition. These images were taken with a field of view of about 752 × 752 nm with a 1024 × 1024 resolution, leading to a pixel size of about 367 pm. All maps were collected for one hour of real time each, with camera length of 98 mm, a C2 aperture of 70 μm, and a spot size of 2 or 3 so that the count rate is in the range of 5×10^4 to 1.5×10^5 counts/s and <30% dead time, depending on the effective thickness of the lamella. The influence of foil thickness on the quantification was not evaluated. The peak of the Fe K-α signal is at least 2 million counts. Typical dwell time was ~20 μs such that about 150 frames were collected for each map. The weight percent and atomic percent compositional maps extracted from Velox™ proved to be inaccurate (Mn wt% reported at 2% instead of ~0.5% and Si wt% reported at 0.4% instead of ~0.1% in the matrix). Thus, "net" count maps were extracted instead. These maps were created in Velox™ by selecting all elements referenced in Table 4.1 plus gold (TEM grid material for certain lamellas) and letting the software conduct the spectrum fit. Then, still through Velox™, the background was subtracted from the spectrum using a parabolic fit and the number of counts was adjusted for self-absorption of characteristics X-ray using a nominal thickness of 100 nm, a density of 7.672 g/cm^3 and the Schreiber-Wims ionization cross-section

model (reported to be the most accurate for transition metals). Finally, to account for any miscalibration of energy collection in the detectors, the optimized spectrum fit function of Velox™ was used to improve the fit of the energy spectrum. Using these "net" count maps, compositional maps were computed using the Cliff-Lorimer method [177]. To calibrate the K-factors (also called sensitivity factors), a low-magnification EDS of the as-tempered T91 heat 30176 was collected. Collecting an EDS map inside the grain away from grain boundaries and precipitates for calibration was rejected since some elements present in T91 (e.g. C, Cr, V, Nb) have a different concentration in precipitates than in the matrix. Collecting a low-magnification EDS map that included both matrix and precipitates was more representative of the concentration provided in Table 4.1. The total net count of each element *i* (N_i) was obtained by summing the counts of each pixel for each element separately. The corresponding uncertainty in counting is $\sigma(N_i) = \sqrt{N_i}$. The ratio of counts for element *i* versus iron was computed as $r_i = \frac{N_i}{N_{Fe}}$. The uncertainty in this ratio is given by Eq. 4.16:

$$\sigma(r_i) = \sqrt{\frac{\sigma(N_i)^2}{N_{Fe}^2} + \sigma(N_{Fe})^2 * \left(\frac{N_i}{N_{Fe}^2}\right)^2} \qquad \text{Eq. 4.16}$$

The sensitivity factor for element *i* is based on the ratio of counts and ratio of atomic percent in the material:

$$k_i = \frac{a_{Fe}}{a_i} * r_i \qquad \text{Eq. 4.17}$$

The corresponding uncertainty is:

$$\sigma(k_i) = \frac{a_{Fe}}{a_i} * \sigma(r_i) \qquad \text{Eq. 4.18}$$

Once these k-factors were calibrated, they were used to compute the weight percent of elements at each pixel of the map of interest. Carbon, copper and gold were the three elements that were not included in the computation of the weight percentage because of inherent carbon contamination during hour-long EDS scans and spurious signals from the TEM grid made of copper or gold. From $\sum_i a_i = 1$, the atomic concentration of iron and the corresponding uncertainty are:

$$a_{Fe} = \frac{1}{1 + \sum_{i \neq Fe} \frac{r_i}{k_i}} \quad \text{Eq. 4.19}$$

$$\sigma(a_{Fe}) \quad \text{Eq. 4.20}$$

$$= \sqrt{\sum_{i \neq Fe} \sigma(r_i)^2 * \left(\frac{k_i}{\left(r_i + k_i * \sum_{j \neq i} \frac{r_j}{k_j} \right)^2} \right)^2 + \sum_{i \neq Fe} \sigma(k_i)^2 * \left(\frac{r_i}{\left(r_i + k_i * \sum_{j \neq i} \frac{r_j}{k_j} \right)^2} \right)^2}$$

Finally, from Eq. 4.17, the atomic percent of any element can be computed with its associated uncertainty:

$$a_i = \frac{a_{Fe}}{k_i} * r_i \quad \text{Eq. 4.21}$$

$$\sigma(a_i) = \sqrt{\left(\sigma(k_i) * \frac{r_i * a_{Fe}}{k_i^2} \right)^2 + \left(\sigma(r_i) * \frac{a_{Fe}}{k_i} \right)^2 + \left(\sigma(a_{Fe}) * \frac{r_i}{k_i} \right)^2} \quad \text{Eq. 4.22}$$

To change these maps in weight percent map, a simple conversion was employed with the corresponding uncertainty propagation:

$$w_i = \frac{a_i * \rho_i}{\sum_j (a_j * \rho_j)} \quad \text{Eq. 4.23}$$

$$\sigma(w_i) = \sqrt{\sum_{j \neq i} \left(\sigma(a_j) * \frac{a_j * \rho_j}{(\sum_k a_k * \rho_k)^2} \right)^2 + \left(\sigma(a_i) * \frac{\sum_{k \neq i} a_k * \rho_k}{(\sum_k a_k * \rho_k)^2} \right)^2} \quad \text{Eq. 4.24}$$

With molar masses ρ_i given in Table 4.4:

Table 4.4: Molar mass (g/mol) of elements in T91 heat 30176.

Element	Fe	Cr	Ni	Si	Mo	V	Mn	C	N	Al	P	S	Ti	Cu	Nb	W
g/mol	56	52	59	28	96	51	55	12	14	27	31	32	48	64	93	184

For radiation-induced segregation, weight maps were resized to 512 × 512 pixels using bilinear interpolation to have a smoother profile. Line scans (extending at least 40 nm on each side of the grain boundary) were produced using MATLAB® by averaging the weight percentage across 50 nm parallel to the boundary. The uncertainty of each slice *i* along the line is:

$$\sigma(w_i) = \frac{1}{n_i} \sqrt{\sum_j w_{i,j}^2} \quad \text{Eq. 4.25}$$

Where n_i is the number of pixels in each 50-nm slice and *j* indexes the pixels in this slice.

The composition of the background is computed by averaging the weight percentages of all the datapoints more than 20 nm from the grain boundary. The associated uncertainty is:

$$\sigma(w_{bkg}) = \sqrt{\frac{1}{n_{bkg}^2} \left(\sum_{i \text{ in } bkg} \sigma(w_i)^2 \right) + std(w_{i=bkg})^2} \quad \text{Eq. 4.26}$$

The radiation-induced segregation for each map is estimated as:

$$w_{RIS,map} = w_{peak,map} - w_{bkg,map} \quad \text{Eq. 4.27}$$

$$\sigma(w_{RIS,map}) = \sqrt{\sigma(w_{peak,map})^2 + \sigma(w_{bkg,map})^2} \quad \text{Eq. 4.28}$$

The values of peak, background and RIS are then averaged across multiple maps (indexed *j*) are the final uncertainty is:

$$\sigma\left(w_{RIS,peak\ or\ bkg}\right) \qquad \text{Eq. 4.29}$$

$$= \sqrt{\frac{1}{n_{maps}^2}\left(\sum_{map\ j}\sigma\left(w_{RIS,peak\ or\ bkg}\right)^2\right) + std\left(w_{j=map}\right)^2}$$

For radiation-induced precipitation, the Ni weight percent maps are used to measure the size and density of Ni-Si-Mn clusters. These maps are smoothed using the Smooth function in FIJI before using the MaxEntropy filter to automatically identify the clusters. This filter was selected because it gives the closest match with hand counting. In cases where the density of clusters is high, the 2D projection of this density in Ni maps can cause them to be superimposed/touching. Thus, a Watershed process is used to separate clusters that are in contact. Finally, only clusters larger than 6 pixels in area were considered since it corresponds to a threshold of 2 nm in diameter. The areas of the Ni clusters can be extracted from FIJI and the diameter and volume can be derived from it:

$$d_j = \sqrt{\frac{4 * area_j}{\pi}} \qquad \text{Eq. 4.30}$$

$$\sigma(d_i) = \sqrt{(\mu_d * d_i)^2 + \sigma_{TEM}^2} \qquad \text{Eq. 4.31}$$

$$V_{PPT} = \sum_i \frac{4}{3}\pi\left(\frac{d_i}{2}\right)^3 \qquad \text{Eq. 4.32}$$

$$\sigma(V_{PPT}) = \sqrt{\sum_j \left(\frac{\pi}{2} * d_j^2 * \sigma(d_j)\right)^2 + \mu_\rho^2 * V_{PPT}^2} \qquad \text{Eq. 4.33}$$

With the density $\rho_i = \frac{N_i}{V}$, where N_i is the number of clusters counted for the ith bin (bin size = 0.5 nm) and V is the volume of material under consideration, the uncertainty on the density is defined by:

$$\sigma(\rho_i) = \sqrt{\frac{\sigma^2(N_i)}{V^2} + \sigma^2(V) * \left(\frac{N_i}{V^2}\right)^2} \quad \text{Eq. 4.34}$$

$$\sigma(N_i) = \sqrt{N_i + \left(N_i * \mu_\rho\right)^2} \quad \text{Eq. 4.35}$$

$$\sigma(V) = \mu_{EELS} * V \quad \text{Eq. 4.36}$$

The volume fraction of the clusters is:

$$VF_{PPT} = \frac{V_{PPT}}{V} \quad \text{Eq. 4.37}$$

$$\sigma(VF_{PPT}) = \sqrt{\frac{\sigma^2(V_{PPT})}{V^2} + \sigma^2(V) * \left(\frac{V_{PPT}}{V^2}\right)^2} \quad \text{Eq. 4.38}$$

4.4.3 Determination of Valid Region of Analysis

As seen in Figure 4.1, the damage level changes as a function of depth and it is important to carefully select the depth at which to place the target damage. Two phenomena limit the depth of the valid region of analysis: free surface effect and injected interstitials. Near the surface of the sample, a defect-depleted zone is typically observed in irradiated materials due to the reduction of

point defect supersaturation [103]. This region can sometimes be followed by a region of unusually large swelling [103,178]. The injected ions come to rest in a region slightly deeper than the displacement damage peak. Even in the case of self-ion irradiation where the chemical effect can be neglected, they may exert excess-interstitial defect imbalance effects [103] such as modifying dislocation loop evolution or suppress void swelling in metals [179]. Plumton et al. [180] simulated the effect of various amounts of injected interstitials on void nucleation in pure Ni and showed that when the injected interstitials exceed 0.01% of those produced by displacements, void nucleation was severely suppressed at low temperatures. At high temperatures, the distribution of injected interstitials broadens due to thermal and radiation-enhanced diffusion and cannot be overlooked [103]. Zinkle et al. [103] determined the valid depths of analysis for a Fe-10Cr system irradiated with 5 MeV iron ions as shown in Figure 4.14.

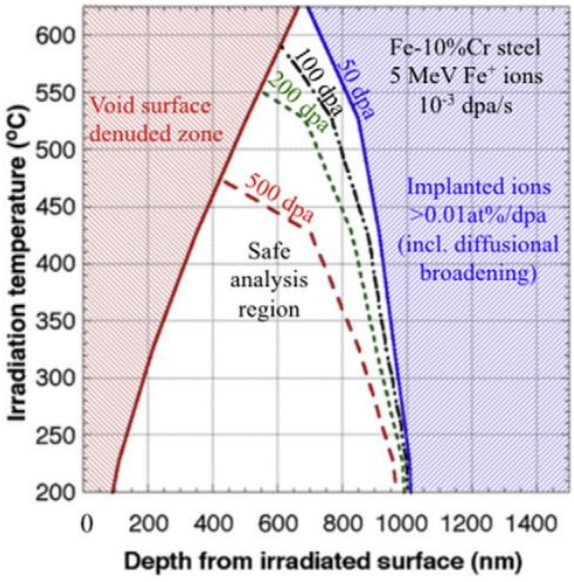


Figure 4.14: Calculated temperature- and depth-dependent regions affected by the free surface and injected ions for Fe-10%Cr steel irradiated with 5 MeV Fe^{+} ions at 10^{-3} dpa/s to dose levels of 50–500 dpa [103].

In Section 4.2.1, it was specified that a depth of 600 nm or 1200 nm was used as the nominal damage level when the heavy-ion beam energy was 5 MeV or 9 MeV, respectively. These depths

were chosen as they adequately avoid the effects of injected interstitials and are outside the void surface denuded zone. Increasing the heavy ion energy helps broaden the safe analysis region but at very high ion energies new radiation effects phenomena appear. Intense localized ion track ionization can lead to higher defect production (point defects and defect clusters), enhanced annealing of defects, and phase transformations. Yet, for medium mass materials the self-ion energy for the onset of these additional ion effects is typically in the range of 50 MeV (radiation-sensitive materials) to several hundred MeV (moderate ion track sensitivity) [103].

4.5 Model for cavity microstructure evolution

4.5.1 Mean-field rate theory

While the experimental comparison of the microstructures from BOR-60 and FFTF to those produced after dual-ion can provide concrete values for temperature shift and helium injection rates, their value can be increased by providing a framework for multiple combinations of reactor parameters. One way to achieve this is by developing a model capable of predicting the microstructure evolution of irradiated FM steels based on reactor parameters.

Many options are available when considering solutions for this task. Empirical models (e.g. fits) make direct use of the measured microstructures (sometimes aided by machine learning) to establish an equation for materials properties at high dose [181,182]. These models excel at quantifying the impact of input parameters on the results, but they require relatively large data sets to provide accurate models, but are not predictive, and do not provide any understanding of the physical phenomena taking place.

Computational descriptions of radiation damage theory (RDT) can prove complex and must span the relevant time and length scales: point defect generation and migration on the order of 10^{-15} s on the atomic scale, and physical property evolution taking place across decades on the engineering scale [19,183].

Atomistic models (density functional theory, molecular dynamics and kinetic Monte Carlo simulations) are relevant solutions to atomic scale events. While the results of such simulations are useful and included in the model used in this work, these approaches are inadequate for large scale microstructure evolution such as swelling.

Phase-field models [184–187] have been used extensively to simulate microstructural evolution at the mesoscale. They provide a spatial and time-dependent description of materials and

interfaces via a set of conserved and non-conserved phase-field variables. The diffuse-interface description often used dictates that interfaces have a finite width and variations in properties are continuous [186]. However, because these are spatial models, they rely on a large number of parameters related to thermodynamic properties of phases, interfacial energy, width and mobility, etc., which significantly increases the complexity of the simulations.

Rate theory (RT) models are well-suited to predict long-term microstructural behavior under high-damage conditions because of its calculation speed and applicability to long time scales. They rely on the mean-field approximation where the location and relative position of microstructure features is replaced by a homogeneous description of the material based on sink strength. Point defect balance equations are solved to calculate the concentrations of point defects which can then be used to compute their rate of recombination or absorption at sinks. In reality, the evolution of microstructure features is not homogeneous because of localized effects such as void-denuded zones near grain boundaries, or gradients in damage and helium injection during dual-ion irradiation. Additionally, molecular dynamics (MD) simulations have revealed that damage cascades produce a significant fraction of defect clusters and not only point defects [19]. Finally, mean-field rate theory (MFRT) is very limited in its description of the nucleation processes [188]. An attempt at solving these limitations of early RT models is the cluster dynamics (CD) method to include clusters of point defects in addition to the SIA and vacancy monomers, as well as adding spatial considerations. However, this method is computationally expensive and time-consuming due to the complex description of the point defect clusters and inclusion of alloying elements, gaseous transmutation, radiation-induced segregation, etc. [181].

Hybrid models have been designed to alleviate some of the limitations present when using a single approach, but these are out of the scope of this work [188]. Consequently, the simplicity

of the mean field rate theory and its relevance to our study make it the best candidate to achieve the objective.

4.5.2 Description of the model

The purpose of the model is to quantitively predict the cavity size distribution (and swelling) resulting from an initial microstructure that is irradiated to a higher damage level. To achieve this, the model takes materials properties, a starting microstructure (cavities, loops, precipitates, etc.) and irradiation conditions (temperature, damage rate, helium rate and damage levels) as inputs and will return the predicted cavity size distribution after additional irradiation to a given damage level. Chapter 6 will show how the model is fitted to dual-ion and BOR-60-irradiated cavity size distributions and validated against size distribution evolution in different irradiation conditions. Beyond predictive capabilities, the model will be used in this work to gain information on reactor irradiation history and the influence of reactor parameters on temperature shift and helium injection rate.

Before diving into more detail, here are the assumptions of the model:

- Mean-field approximation (as described in Section 4.5.1) assumes a homogeneous medium without grain-to-grain variation, denuded zones etc.
- Reactions of point defects with sinks are diffusion-controlled as opposed to reaction-rate-controlled.
- All sinks are unsaturable for helium and point defects.
- Radiation damage (neutrons or heavy ions) only produces point defects and no clusters.
- Thermal emission of interstitials from sinks is neglected.

The model is limited in the microstructure evolution phenomena it can capture:

- The evolution of secondary phases is not modeled. The sink strength of Ni/Si clusters and pre-existing precipitates are included after being measured experimentally.
- The radiation-induced segregation at grain boundaries, cavities and dislocations is not modeled. As such, the effect of segregation on surface energy for cavities is not captured.
- Nucleation of cavities is calculated from experimental measurements and is not predicted.
- The effect of small (< 5 vacancies) mobile helium-vacancy clusters is not included.
- Ballistic dissolution and mixing of solute atoms and clusters are not considered.
- Coalescence of sinks, noticeably bubbles, is not captured.

The iterative approach of the model is divided into two steps. First, cavity growth rates at each radius are calculated and applied to the current cavity size distribution over a small increase in damage level to simulate the evolution of the cavity microstructure. Then, the injected helium corresponding to this increase in damage level is added to the microstructure, and the total helium content is partitioned to the sinks with the new cavity size distribution. This two-step process is repeated until the total increase in damage level reaches the desired value as shown in Figure 4.15. The first version of the model was developed by Taller et al. [21]: the new version presented here has been significantly modified to better simulate the evolution of the cavity microstructure.

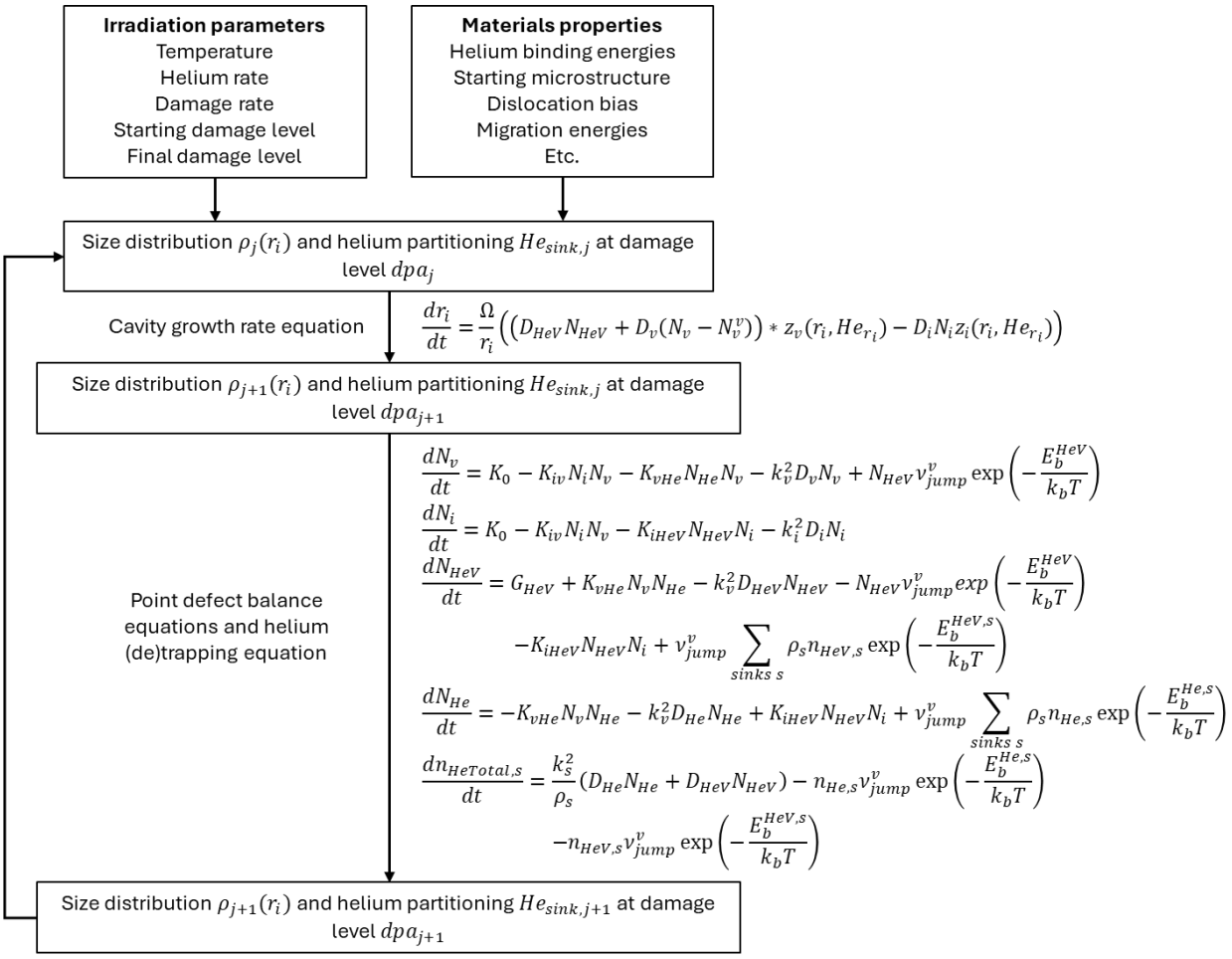


Figure 4.15: Diagram of the cavity size distribution prediction model.

First, the cavity growth rate equation defined at each cavity radius r_i is used to predict the cavity microstructure to a higher damage level [6]:

$$\frac{dr_i}{dt} = \frac{\Omega}{r_i}\left(\left(D_{HeV}N_{HeV} + D_v\left(N_v - N_v^v(r_i)\right)\right) z_v(r_i, He_{r_i}) - D_i N_i z_i(r_i, He_{r_i})\right) \quad \text{Eq. 4.39}$$

Where $\Omega = \frac{1}{\mathrm{N_{at}}}$ is the atomic volume, N_{HeV} is the helium-vacancy pair concentration, N_v is the vacancy concentration, N_v^v is the vacancy concentration at the cavity surface, N_i is the interstitial concentration, $z_v(r_i, He_{r_i})$ (respectively $z_i(r_i, He_{r_i})$) is the vacancy (respectively interstitial)

cavity capture efficiency at radius r_i and helium-to-vacancy ratio He_{r_i}. The diffusion coefficients used in Eq. 4.39 are given in Table 4.5 and the corresponding parameters are listed in Table 4.6.

Table 4.5: Diffusion coefficients in the cavity growth rate equation.

Name and unit of coefficient	Equation	
Interstitial diffusion (m^2/s)	$D_i = \frac{a^2}{6} * \nu_{jump}^i * \exp\left(-\frac{E_m^i}{k_b * T}\right)$	Eq. 4.40
Vacancy diffusion (m^2/s)	$D_v = a^2 * \nu_{jump}^v * \exp\left(-\frac{E_m^v}{k_b * T}\right)$	Eq. 4.41
He-vacancy pair diffusion (m^2/s)	$D_{Hev} = D_0^{Hev} * \exp\left(-\frac{E_m^{Hev}}{k_b * T}\right) + C_v D_0^{Hev,sub} * \exp\left(-\frac{E_m^{Hev,sub}}{k_b * T}\right)$	Eq. 4.42

Table 4.6: Parameters used in the cavity growth rate equation.

Parameter	Values in literature	Value used	Reference
Atomic density, N_{at}	8.34×10^{28} at/m^3		[189]
Lattice parameter, a	0.288 nm		[190,191]
Vacancy migration energy, E_m^v	0.49-0.85 eV in Fe 0.55-1.25 eV in Cr 0.51-0.69 eV in Fe10Cr	0.62 eV	[189,192–206]
Interstitial migration energy, E_m^i	0.23-0.35 eV in Fe 0.28 eV in Cr 0.25-0.39 eV in FeCr	0.34 eV	[189,195,196,200,202,204–208]
He-vacancy pair substitutional migration energy, $E_m^{HeV,sub}$	0.3-0.32 eV	0.31 eV	[12,21,200,209]
He-vacancy pair direct migration energy, E_m^{HeV}	2.35 eV		
Pre-exponent factor for substitutional diffusion of He-v pairs, $D_0^{HeV,sub}$	6.4×10^{-7} m^2/s		[12,21,200]

Pre-exponent factor for direct diffusion of He-v pairs, D_0^{HeV}	2.8×10^{-4} m^2/s		
Vacancy jump attempt frequency, ν_{jump}^{v}	1.34-1.6 × 10^{13} s^{-1}	1.5 × 10^{13} s^{-1}	[189,206]
Interstitial jump attempt frequency, ν_{jump}^{i}	2.9-23 × 10^{12} s^{-1}	6.36 × 10^{12} s^{-1}	[189,206,208,210]

The vacancy concentration at the cavity surface is given by:

$$N_v^v(r_i) = N_v^0 \exp\left(\frac{\Omega}{k_b T}\left(\frac{2\gamma}{r_i} - p_{He} - \sigma\right)\right) \quad \text{Eq. 4.43}$$

It depends on the thermal vacancy concentration N_v^0, the surface energy γ, the helium pressure p_{He} and the stress term σ created by network dislocations:

$$N_v^0 = N_{at} * exp\left(\frac{S_f^v}{k_b}\right) * exp\left(-\frac{E_f^v}{k_b * T}\right) \quad \text{Eq. 4.44}$$

$$\sigma = \frac{bE}{2\pi(1-\nu)} * \frac{\sin(\theta)}{r_{c-N}} \quad \text{Eq. 4.45}$$

Where b is the Burgers vector (equal to lattice parameter). θ, the angle between the Burgers vector and the cavity-dislocation direction, and r_{c-N}, the distance between the cavity and the network dislocation are both input parameters selected by the user. The default values for these parameters are $\theta = 90°$ and $r_{c-N} = 2.85\ nm$.

The surface energy parameter γ is often considered constant across cavity radii and helium pressures. Recent works [211–213] reported a significant decrease in the surface energy at small radius and high pressure coupled with the evolution of surface stress that can lead to loop punching or interstitial emission [214]. The approach selected in this work is based on Tolman's equation [213]:

$$\gamma = \frac{\gamma_0}{1 + \frac{\delta}{r_c}} \quad \text{Eq. 4.46}$$

The δ parameter (1.632nm) was determined using KMC simulation results presented in Table 4.7.

Table 4.7: Radius, helium content and helium pressure for cavities at equilibrium [215].

Radius (nm)	Helium-to-vacancy ratio (-)	Helium pressure (GPa)
0.5	0.609	2.754
0.75	0.669	1.702
1	0.753	1.720

Many equations of state (EOS) are available to compute the helium pressure in cavities. Popular ones include the ideal gas law and the hard-sphere equation of state [216], but they can produce unrealistic results for very small bubbles (< 1 nm in diameter). Several attempts were made to improve the applicability of EOS at these diameters [217,218], sometimes in combination with MD results [213,219,220]. The compressibility computed via MD is larger than that of the hard-sphere equation of state for high helium content, because the strong, short-range Fe–He repulsion confines helium atoms to a smaller volume. This difference in effective radius between the position of the outermost helium atoms and the bubble surface is nearly independent of the bubble radius [219].

The modified hard-sphere equation of state proposed by Stoller et al. [219] offers the best available compromise between a physics-based model and MD simulations valid at radii as small as ~0.5 nm and reasonable helium-to-vacancy ratios (0-1).

$$d_g(nm) = 0.319332 * \left(0.865456 - 0.041802 * \ln\left(\frac{T}{9.228038}\right)\right) \quad \text{Eq. 4.47}$$

$$y = \left(\frac{\pi d_g^3}{6}\right)\left(\frac{n_{He,r_i}}{V_{eff}}\right) \quad \text{Eq. 4.48}$$

$$V_{eff}(nm^3) = \frac{4}{3}\pi(r_i - 0.057389)^3 \quad \text{Eq. 4.49}$$

$$Z = \frac{1 + y + y^2 - y^3}{(1-y)^3} \quad \text{Eq. 4.50}$$

$$p_{He} = \frac{n_{He} k_b T Z}{V_i} \quad \text{Eq. 4.51}$$

$$V_i(nm^3) = \frac{4}{3}\pi r_i^3 \quad \text{Eq. 4.52}$$

The parameters used to calculate N_v^v are defined in Table 4.8.

Table 4.8: Parameters used to calculate vacancy concentration at cavity surfaces.

Parameter	Values in literature	Value used	Reference
Surface energy, γ_0	2.2-2.6 J/m^2 for Fe 2.72 J/m^2 for Fe10Cr	2.5 J/m^2	[221–225]
Vacancy formation energy, E_f^v	1.41-2.23 eV in Fe 2.25-2.64 eV in Cr 1.72 eV in Fe10Cr	1.72 eV	[189,190,193–196,198–200,226,227]
Vacancy formation entropy, S_f^v	-1 - 2.3 × k_b eV/K	0 eV/K	[6,228–231]
Young modulus, E	175-194 GPa @ 400°C 165-184 GPa @ 500°C	185 GPa	[232–236]
Poisson ratio, ν	0.3		[235]

The capture efficiencies at cavities are different between interstitials and vacancies. Some equations can be found in the literature based on MD simulations of cavities with various helium contents [237,238], but they require to know the helium pressure in cavities. Due to the limitation of equations of state [216–219,239,240] to accurately calculate high helium pressure in nanocavities, and their lack of applicability across various temperatures, the model calculates capture efficiencies directly from computational simulation results. Wang [215] used both MD and kinetic Monte Carlo (KMC) to obtain the ratio between the sink strength including the cavity-

induced strain with or without helium, and the sink strength that arises from a strain-free matrix preserving only the cavity's surface lattice effect. These ratios are equal to interstitial and vacancy capture efficiencies at cavities. A ratio above 1 indicates the strain field promotes defect absorption, and a ratio below 1 means the strain field suppresses defect absorption. Values are shown as a function of temperature, radius and helium-to-vacancy ratio in Figure 4.16.

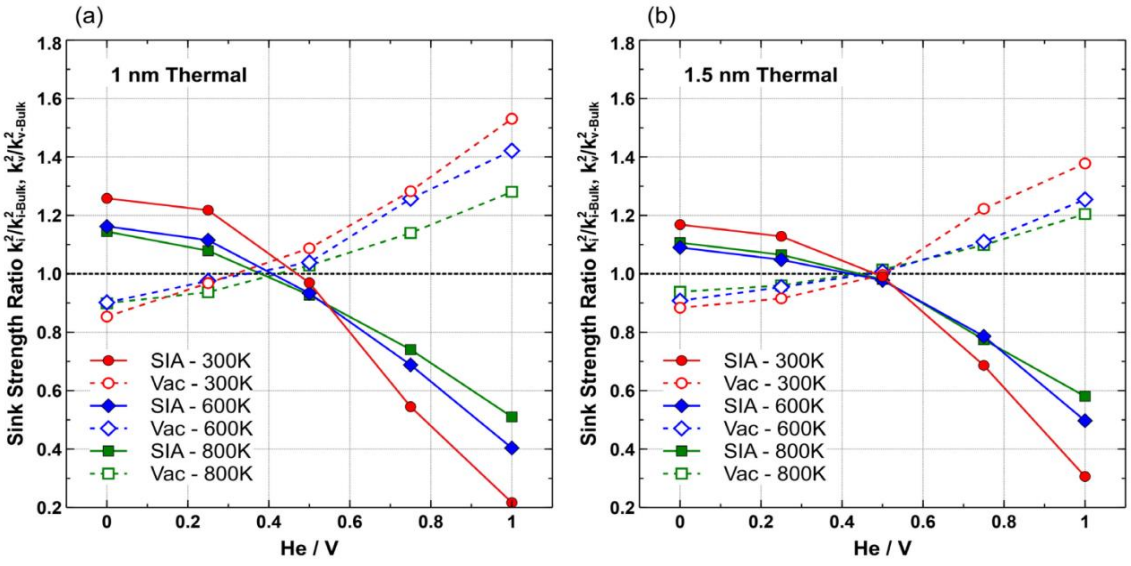


Figure 4.16: Capture efficiencies of cavities of diameter (a) 1 nm and (b) 1.5 nm as a function of helium-to-vacancy ratio for different temperatures [215].

Since this data set only covers two radii, it was fitted with an equation to extrapolate the capture efficiency to radius up to 50 nm. The fitting equations used at 600K and 800K are shown in Eq. 4.53 and are inspired from fits reported in the literature with the constraint that the capture efficiency converges to 1 at 50 nm radius with 0 He/vac [215,237]. The final capture efficiencies, $z_{i,v}(r, He_{ratio})$, of a cavity of radius r and with a helium-to-vacancy ratio He_{ratio}, at the desired temperature are computed via linear interpolation of the values at 600 K and 800 K.

$$z_{i,v}(r, He_{ratio}) = \frac{r_2}{r} * He_{ratio}^2 + \frac{r_1}{r} * He_{ratio} + \frac{r + r_0}{r} \qquad \text{Eq. 4.53}$$

Table 4.9 lists the fitting coefficients for vacancy and interstitial capture efficiencies.

Table 4.9: Fitting coefficients for the capture efficiency equations.

Coefficient	Vacancy, 600K	Vacancy, 800K	Interstitial, 600K	Interstitial, 800K
r_0	-0.05377	-0.04925	0.07846	0.07645
r_1	0.06507	0.04786	-0.02721	-0.09743
r_2	0.1939	0.1451	-0.3785	-0.2506

As shown by Wang [215], helium plays a crucial role in the sink strength of cavities. To accurately compute the cavity size distribution evolution, the partitioning of helium to the sinks in the microstructure must be computed by considering the additional amount of injected gas following the increase in damage level. To achieve this, a set of differential equations is used to describe the migration and trapping behavior of helium, based on an approach developed by Taller [21].

The point defect balance equations (PDBE) are defined first:

$$\frac{dN_v}{dt} = K_0 - K_{iv}N_iN_v - K_{vHe}N_{He}N_v - k_v^2D_vN_v + N_{HeV}\nu_{jump}^v \exp\left(-\frac{E_b^{HeV}}{k_bT}\right) \quad \text{Eq. 4.54}$$

$$\frac{dN_i}{dt} = K_0 - K_{iv}N_iN_v - K_{iHeV}N_{HeV}N_i - k_i^2D_iN_i \quad \text{Eq. 4.55}$$

$$\frac{dN_{HeV}}{dt} = G_{HeV} + K_{vHe}N_vN_{He} - k_v^2D_{HeV}N_{HeV} \quad \text{Eq. 4.56}$$

$$- N_{HeV}\nu_{jump}^v exp\left(-\frac{E_b^{HeV}}{k_bT}\right) - K_{iHeV}N_{HeV}N_i$$

$$+ \nu_{jump}^v \sum_{sinks\ s} \rho_s n_{HeV,s} \exp\left(-\frac{E_b^{HeV,s}}{k_bT}\right)$$

$$\frac{dN_{He}}{dt} = -K_{vHe}N_vN_{He} - k_v^2D_{He}N_{He} + K_{iHeV}N_{HeV}N_i \quad \text{Eq. 4.57}$$

$$+ \nu_{jump}^v \sum_{sinks\ s} \rho_s n_{He,s} \exp\left(-\frac{E_b^{He,s}}{k_bT}\right)$$

Where G_{HeV} is the injection/production rate of helium in m^{-3}/s (assuming helium atoms create a helium-vacancy pair when coming to rest), D_{He} is the helium interstitial diffusion coefficient in the matrix, N_{He} is the helium interstitial concentration in the matrix, $n_{HeV,s}$ (resp. $n_{He,s}$) is the number of helium-vacancy pairs (resp. helium interstitials) contained per sink *s*, $E_b^{HeV,s}$ (resp. $E_b^{He,s}$) is the binding energy of helium-vacancy pairs (resp. helium interstitials) to sink *s*, and k_v^2 (resp. k_i^2) is the total sink strength applied to vacancies (resp. interstitials). It is assumed that both helium interstitials and helium-vacancy pairs behave like vacancies in terms of absorption to sinks, hence k_v^2 is used in their PDBE. At any point, if the point defect concentrations are below the thermal concentrations (resp. negative for He-v pairs), they are set to the thermal concentration value (resp. 0 m^{-3} for He-v pairs).

To determine the total helium content per each type of sink, the following differential equation is used for each sink type:

$$\frac{dn_{HeTotal,s}}{dt} = \frac{k_s^2}{\rho_s}(D_{He}N_{He} + D_{HeV}N_{HeV}) - n_{He,s}\nu_{jump}^{v}\exp\left(-\frac{E_b^{He,s}}{k_bT}\right) - n_{HeV,s}\nu_{jump}^{v}\exp\left(-\frac{E_b^{HeV,s}}{k_bT}\right) \quad \text{Eq. 4.58}$$

Where k_s^2 is the corresponding sink strength.

To differentiate helium interstitials from helium-vacancy pairs contained in each sink *s*, the total helium content is compared to the number of vacancies in the sink $n_{vac,s}$ (equal to number of vacancies absorbed minus the number of interstitials absorbed, can be negative):

$$n_{He,s} = \min\left(n_{HeTotal,s} - n_{vac,s}, n_{HeTotal,s}\right) \text{ with minimum value of 0} \quad \text{Eq. 4.59}$$

$$n_{HeV,s} = n_{HeTotal,s} - n_{He,s} \quad \text{Eq. 4.60}$$

The number of vacancies in the sink is tracked using the following equation:

$$\frac{dn_{vac,s}}{dt} = \frac{k_s^2}{\rho_s}\left(D_v N_v + D_{HeV} N_{HeV} - D_i N_i\right) - n_{HeV,s}\nu_{jump}^{v} \exp\left(-\frac{E_b^{HeV,s}}{k_b T}\right) \quad \text{Eq. 4.61}$$

The sink strengths are presented in Table 4.10. The equations and parameters used to calculate point defect concentrations and helium partitioning are shown in Table 4.11 and Table 4.12. In particular, the helium binding energy to cavities is calculated and measured in many ways in literature [198–200,241,242] with wide ranges of values. Most studies agree that the binding energy decreases with increasing helium-to-vacancy ratio. The equation used in this work to compute the helium binding energy is shown in Table 4.11 and is selected during the fitting of the model as described in Section 6.2.

Table 4.10: Sink strengths in the microstructure.

Sink	Sink strength (m^{-2})	
Network dislocations	$k_{N,v}^2 = z_{d,v}\rho_N$ for vacancies $k_{N,i}^2 = (1 + bias) z_{d,v}\rho_N$ for interstitials	Eq. 4.62 Eq. 4.63
Precipitate ($M_{23}C_6$, V,Nb-C,N and Ni-Si-Mn clusters)	$k_{PPT}^2 = \sum_i 4\pi * r_i * \rho_i$	Eq. 4.64
Dislocation loops	$k_{l,v}^2 = z_{d,v}\sum_i 4\pi * r_i * \rho_i$ for vacancies $k_{l,i}^2 = (1 + bias) z_{d,v}\sum_i 4\pi * r_i * \rho_i$ for interstitials	Eq.4.65 Eq.4.66
Cavities	$k_{cav}^2 = \sum_i 4\pi * r_i * \rho_{cav}(r_i) * z_{i,v}(r_i, He_{r_i})$	Eq. 4.67
Grain boundaries	$k_{ins}^2 = k_l^2 + k_N^2 + k_{M23C6}^2 + k_{VNb}^2 + k_{NiSiMn}^2 + k_{bub}^2 + k_{void}^2$	Eq. 4.68

	$k_{gb}^2 = \rho_{gb} * 4\pi * r_{gb} * \frac{\left(\sqrt{k_{ins}^2} * r_{gb} * cosh\left(\sqrt{k_{ins}^2} * r_{gb}\right) - sinh\left(\sqrt{k_{ins}^2} * r_{gb}\right)\right)}{sinh\left(\sqrt{k_{ins}^2} * r_{gb}\right) - \sqrt{k_{ins}^2} * r_{gb}}$	Eq. 4.69

Table 4.11: Coefficients used to calculate point defect concentrations and helium partitioning.

Name and unit of coefficient	Equation	
Point defect production rate ($m^{-3}s^{-1}$)	$K_0 = eff * \frac{damagerate}{\Omega}$	Eq. 4.70
He interstitial diffusion (m^2/s)	$D_{He} = D_0^{He} * \exp\left(-\frac{E_m^{He}}{k_b * T}\right)$	Eq. 4.71
Point defect recombination rates (m^3/s)	$K_{iv} = 4\pi * r_{iv} * (D_i + D_v)$ $K_{iHev} = 4\pi * r_{iv} * (D_i + D_{Hev})$ $K_{vHe} = 4\pi * r_{iv} * (D_v + D_{He})$	Eq. 4.72 Eq. 4.73 Eq. 4.74

Table 4.12: Parameters used to calculate point defect concentrations and helium partitioning.

Parameter	Values in literature	Value used	Reference
He interstitial migration energy, E_m^{He}	0.06-0.1 eV	0.064 eV	[197–200,202,209,227,243–245]
Pre-exponent factor for diffusion of He interstitials, D_0^{He}	2.8×10^{-8} - 5×10^{-7} m^2/s	2.8×10^{-8} m^2/s to stay consistent with E_m^{He}	[200,246]
Dislocation bias, $bias$	-5% for network disl. 6% for a/2⟨111⟩ loops 3% for a⟨100⟩ loops 1-50% total from analytical studies 5-15% total in rate theory models	10 %	[10,247–251]

Dislocation capture efficiency of vacancies, $z_{d,v}$	1-3	0.8	[252–256]
Fraction of network dislocations with edge character, *edge_frac*	20-41%	40%	[257–260]
Recombination radius, r_{iv}	2.21-3.3a_0	2.24a_0	[205,206,261]
Damage efficiency, eff	0.2-0.4 for ARC-DPA 0.05-0.1 for CRC-DPA in Fe at T>230°C	0.025	[252,262–265]
Helium binding energy to dislocations, E_b^N and E_b^l	Substitutional: 0.25-0.28 eV (screw), 0.5-1.4 eV (edge) Interstitial: 0.50-1.05 eV (screw), 1.3-2.58 eV (edge)	Substitutional: 0.26 eV (screw), 1.0 eV (edge) Interstitial: 1.05 eV (screw), 2.58 eV (edge)	[226,227,241,266–269]
Helium binding energy to vacancies, E_b^{HeV}	1.4-4 eV	2.3 eV	[198–201,203,209,242,270]
Helium binding energy to cavities, E_b^{cav}	Decreases with increasing He/V ratio: 1-6 eV	3.5 - 2 × (He/v)	[198–200,241,242]
Helium binding energy to grain boundaries, E_b^{gb}	Substitutional: 0.13-0.83 eV Interstitial: 0.14-2.66 eV	Substitutional: 0.5 eV Interstitial: 1.4 eV	[243,244,266,270]
Helium binding energy to $M_{23}C_6$ precipitates, E_b^{M23C6}	Substitutional: 0.31-1.22 eV Interstitial: 0-1.12 eV	Substitutional: 0.9 eV Interstitial: 0.6 eV	[271]
Helium binding energy to V,Nb carbonitrides, E_b^{VNb}	Same as $M_{23}C_6$		

Helium binding energy to G-phase precursors, E_b^{Gphase}	Substitutional: 1.03-2.49 eV Interstitial: 2.01-2.46 eV	Substitutional: 1.7 eV Interstitial: 2.2 eV	[272]

The timestep used to solve the differential equations controlling the point defect concentrations and helium content at sinks is determined by the MATLAB® *ode15s* function with a relative tolerance of 5×10^{-4}. This tolerance corresponds to the maximum allowed estimated error in the solution. It is selected as the largest value that keeps the solution consistent with tighter tolerances.

The timestep used to grow and nucleate cavities in the size distribution depends on the computed cavity growth rates. The timestep is selected so that cavities in the fastest growing bin *i* (with growth rate $\dot{r}_i$ in nm/dpa) grow by 0.05 nm in radius (10% of the 0.5 nm radius bin width) which gives:

$$timestep = \frac{0.05nm}{\dot{r}_i * damage\ rate} \quad \text{Eq. 4.75}$$

This two-step process is repeated until the desired damage level is reached, and the resulting cavity size distribution is then compared to the measured microstructure if applicable. Although the final size distributions calculated after a fixed total amount of additional damage were comparable using steps of 0.01, 0.05 and 0.25 nm, the helium repartition changed slightly and 0.05 nm was selected as a compromise between accuracy and computation time.

Chapter 5 Experimental Results

This chapter presents the results of the characterization of the unirradiated microstructure as well as of the BOR-60, FFTF and dual-ion irradiation experiments introduced in Sections 4.2 and 4.3. After presenting the pre-irradiated microstructure and irradiation conditions, the results are divided into four sections: BOR-60 and companion dual-ion irradiations, and FFTF and companion dual-ion irradiations. For each section, results for cavities, dislocation loops, radiation-induced segregation and radiation-induced precipitation microstructures are presented.

5.1 Pre-irradiated microstructure

The microstructure of T91 heat 30176 after tempering includes prior austenite grain boundaries (PAGB), laths, coarse chromium carbides (mostly $M_{23}C_6$ at PAGB and lath boundaries), fine V,Cr-carbonitrides in the matrix or adjacent to Cr carbides, and network dislocations. Jiao and Taller [13,17] measured the average diameter of $M_{23}C_6$ to be ~100 nm with a density of 10^{18}-10^{19} m^{-3} while the average diameter for (V,Cr)-C,N was approximately 40 nm with an estimated number density between 10^{18} m^{-3} and 10^{19} m^{-3} [13]. The lath length and width are estimated at ~5 μm and ~0.5 μm, respectively [41,189]. The dislocation density varied from grain-to-grain and area-to-area and was estimated to be ~5×10^{14} m^{-2} [11,13,17,25]. It has been reported to change with temperature and damage level in FM steels [273], but since it is not measured for irradiated specimens in this work, it is assumed to be constant in all conditions. No significant segregation at grain boundaries was measured as shown in Table 5.1.

Table 5.1: Segregation behavior at grain boundaries in unirradiated T91.

Fe (wt%)		Cr (wt%)		Ni (wt%)		Si (wt%)	
Peak	ΔFe	Peak	ΔCr	Peak	ΔNi	Peak	ΔSi
89.3±1.5	-1.0±1.2	8.3±1.1	0.7±0.8	0.11±0.01	0.00±0.00	0.24±0.04	0.00±0.02

5.2 Irradiation conditions

Table 5.2, Table 5.3 and Table 5.4 contain the details of all the BOR-60, FFTF and dual-ion irradiation conditions that are reported in this work (dual-ion irradiations are abbreviated 'DDI' for 'defocused dual-ion'). Dual-ion conditions are split between the ones compared to BOR-60 and the ones compared to FFTF. Some BOR-60 and dual-ion conditions have already been studied and characterized by Drs. Stephen A. Taller and Zhijie (George) Jiao in previous works [13,16,17,72,102], but will be referenced here again for comparison.

Table 5.2: BOR-60 conditions and sample designations.

Irradiation mode	Sample	Condition	Damage level (dpa)	Temperature (°C)	Damage rate (dpa/s)	Reference
BOR-60	P027-T03	369C-0.77Hedpa-16dpa	16 ± 1	369 ± 9	8.03×10^{-7}	[13,17]
BOR-60	P028-T05	372C-0.77Hedpa-32dpa	32 ± 2	372 ± 7	7.76×10^{-7}	[13,17]
BOR-60	P031-T98	376C-0.77Hedpa-47dpa	47 ± 3	376 ± 4	7.37×10^{-7}	This work
BOR-60	P029-T11	375C-0.77Hedpa-72dpa	72 ± 5	375 ± 5	7.72×10^{-7}	This work
BOR-60	P033-T24	404C-0.77Hedpa-17dpa	17 ± 1	404 ± 18	8.54×10^{-7}	[13,17]
BOR-60	P036-T100	402C-0.77Hedpa-29dpa	29 ± 1	402 ± 6	8.10×10^{-7}	This work
BOR-60	P034-T32	402C-0.77Hedpa-86dpa	86 ± 4	402 ± 8	8.19×10^{-7}	This work
BOR-60	P037-T55	453C-0.77Hedpa-19dpa	19 ± 1	453 ± 9	1.00×10^{-6}	This work and [13,17]
BOR-60	P038-T61	450C-0.77Hedpa-32dpa	32 ± 2	450 ± 7	9.23×10^{-7}	This work (with S. A. Taller)
BOR-60	P042-T67	517C-0.77Hedpa-15dpa	15 ± 1	517 ± 10	7.89×10^{-7}	[13,17]
BOR-60	P043-T108	515C-0.77Hedpa-25dpa	25 ± 1	515 ± 10	8.10×10^{-7}	This work (with S. A. Taller)

Table 5.3: FFTF conditions and sample designations.

Irradiation mode	Sample	Condition	Damage level (dpa)	Temperature (°C)	Damage rate (dpa/s)
FFTF	VH03	407C-0.21Hedpa-73dpa	73	407 ± 3	1.26×10^{-6}
FFTF	VH20	415C-0.21Hedpa-151dpa	151	415 ± 14	1.46×10^{-6}
FFTF	NP04	415C-0.21Hedpa-170dpa	170	415 ± 13	1.42×10^{-6}
FFTF	FA33	415C-0.21Hedpa-184dpa	184	415 ± 13	1.52×10^{-6}

Table 5.4: Dual-ion conditions and sample designations.

Irradiation mode	Sample	Condition	Damage level (dpa)	Temperature (°C)	Helium injection rate (appmHe/dpa)	Damage rate (dpa/s)	Reference
DDI	092717	445C-4.3Hedpa-16.6dpa	16.6	445	4.3	7.1×10^{-4}	[13,17]
DDI	053018-1	445C-4.3Hedpa-35dpa	35	445	4.3	7.6×10^{-4}	[13,17]
DDI	070120-1	445C-3.1Hedpa-54dpa	54	445	3.1	7.5×10^{-4}	This work
DDI	102120-1 (cavities and loops) 020720 (RIS and RIP)	445C-3.6Hedpa-72dpa 445C-3.2Hedpa-70dpa	72 70	445	3.6 3.2	7.5×10^{-4}	This work
DDI	092917	460C-4.3Hedpa-16.6dpa	16.6	460	4.3	7.5×10^{-4}	[13,17]
DDI	071320-1	460C-3.1Hedpa-33dpa	33	460	3.1	7.5×10^{-4}	This work
DDI	091420-1	460C-3.2-3.7Hedpa-72dpa	72	460	3.2-3.7*	7.5×10^{-4}	This work
DDI	020320	520C-3.2Hedpa-16.6dpa	16.6	520	3.2	7.5×10^{-4}	This work and [13,17]
DDI	091719	520C-4.3Hedpa-28dpa	28	520	4.3	7.5×10^{-4}	This work (with S. A. Taller)
DDI	110117	570C-4.3Hedpa-15.4dpa	15.4	570	4.3	6.7×10^{-4}	[13,17]
DDI	111219	570C-4.3Hedpa-28dpa	28	570	4.3	7.5×10^{-4}	This work (with S. A. Taller)
DDI	062424	460C-0.2Hedpa-72dpa	72	460	0.2	7.5×10^{-4}	This work
DDI	012025-2	460C-0.2Hedpa-110dpa	110	460	0.2	7.5×10^{-4}	This work
DDI	101424	460C-0.2Hedpa-184dpa	184	460	0.2	7.5×10^{-4}	This work
DDI	050825	460-490-460C-0.2Hedpa-170dpa	170	460-490-460[#]	0.2	7.5×10^{-4}	This work
DDI	040225	490C-0.8Hedpa-72dpa	72	490	0.8	7.5×10^{-4}	This work
DDI	040425	490C-0.8Hedpa-170dpa	170	490	0.8	7.5×10^{-4}	This work

*The first 7 dpa were injected with 3.2 appmHe/dpa and the remaining 68 dpa with 3.7 appmHe/dpa

[#]First 72 dpa at 460°C followed by 38 dpa at 490°C and 60 dpa at 460°C.

5.3 BOR-60

5.3.1 Cavity microstructures

The cavity microstructure evolution was characterized in all BOR-60 conditions via STEM-HAADF and CTEM-BF through-focus imaging. As shown in Figure 5.1, swelling increases with increasing damage level in BOR-60 samples irradiated at 369-376°C but does not significantly vary with damage level at 402-404°C, 450-453°C and 515-517°C.

These swelling increases are directly related to the evolution of the void (cavities larger than 5 nm in diameter) microstructure shown in Figure 5.2. Both void density and average void diameter increase with damage level in BOR-60 samples irradiated at 369-376°C. Unexpectedly, the BOR-60 samples irradiated at 402-404°C exhibit a decrease in void density from 2.8×10^{20} m^{-3} at 17 dpa to $<5 \times 10^{19}$ m^{-3} at 29 and 86 dpa. The reason for this evolution is discussed in Chapter 6. No voids are observed in BOR-60 samples irradiated at 450-453°C and 515-517°C. Bubbles are observed in BOR-60 conditions without any clear trend in terms of density or average diameter with increasing damage level as shown in Figure 5.3.

Looking at cavity size distributions, Figure 5.4 and Figure 5.5 show that BOR-60 created bi-modal size distributions at 369-376°C and 402-404°C, respectively. At 369-376°C, the density of smaller voids (~5 nm in diameter) stays around 10^{20} m^{-3} with increasing damage level, while the size distribution extends to larger maximum void diameter. Figure 5.6 (resp. Figure 5.7) show the cavity size distributions of BOR-60 samples irradiated at 450-453°C (resp. 515-517°C). Results are tabulated in Table 5.5. Representative STEM-HAADF micrographs are shown in Figure 5.8 for BOR-60 samples irradiated at 369-376°C and 402-404°C.

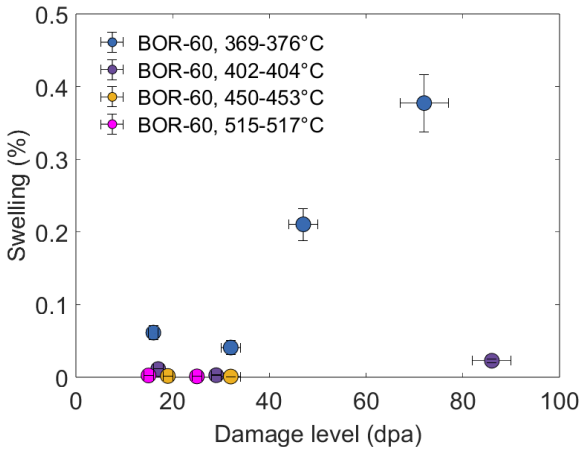


Figure 5.1: Swelling of BOR-60-irradiated T91 30176 as a function of damage level.

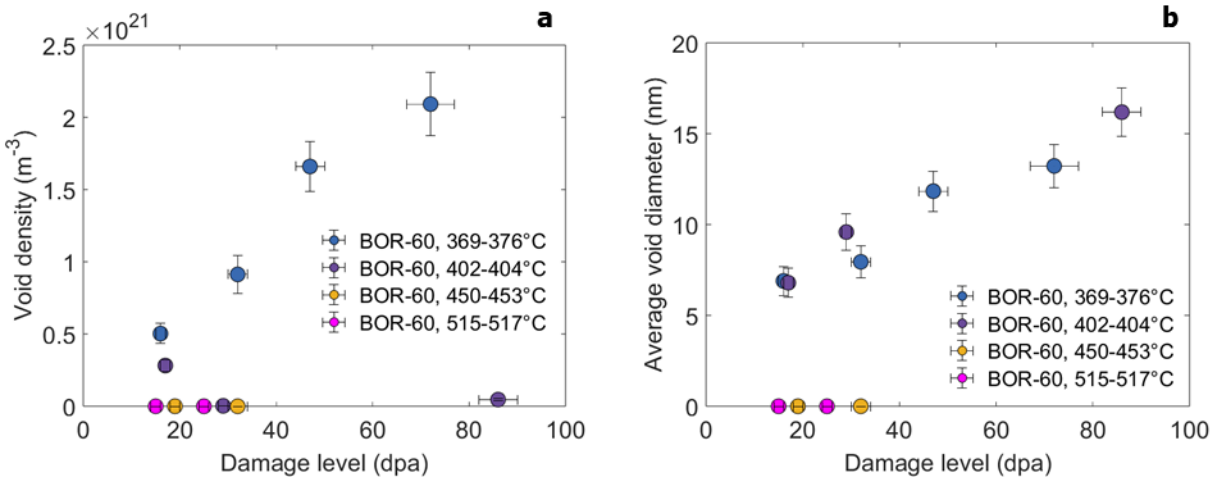


Figure 5.2: (a) Void density and (b) average void diameter of BOR-60-irradiated T91 30176 as a function of damage level.

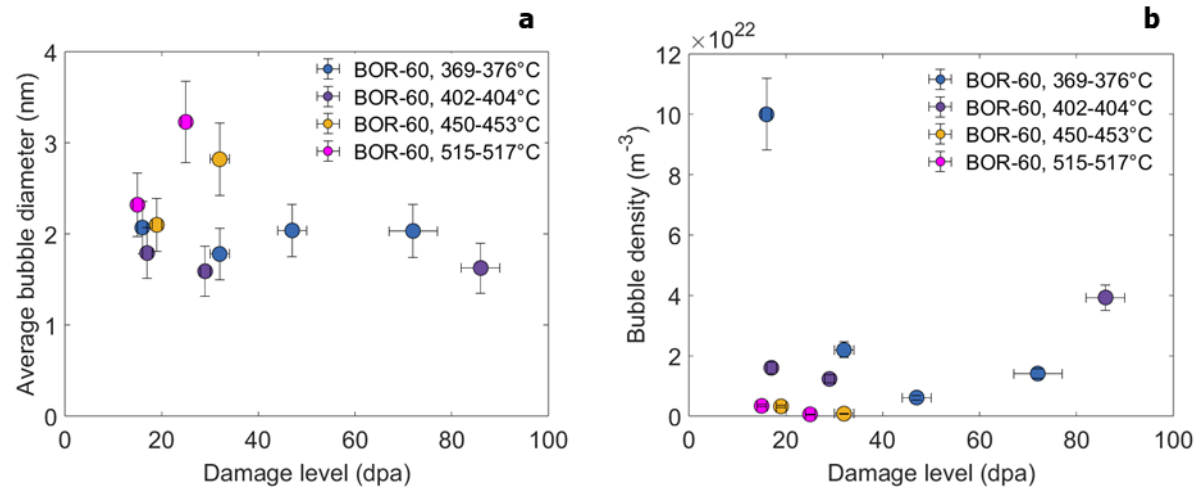


Figure 5.3: (a) Bubble density and (b) average bubble diameter of BOR-60-irradiated T91 30176 as a function of damage level.

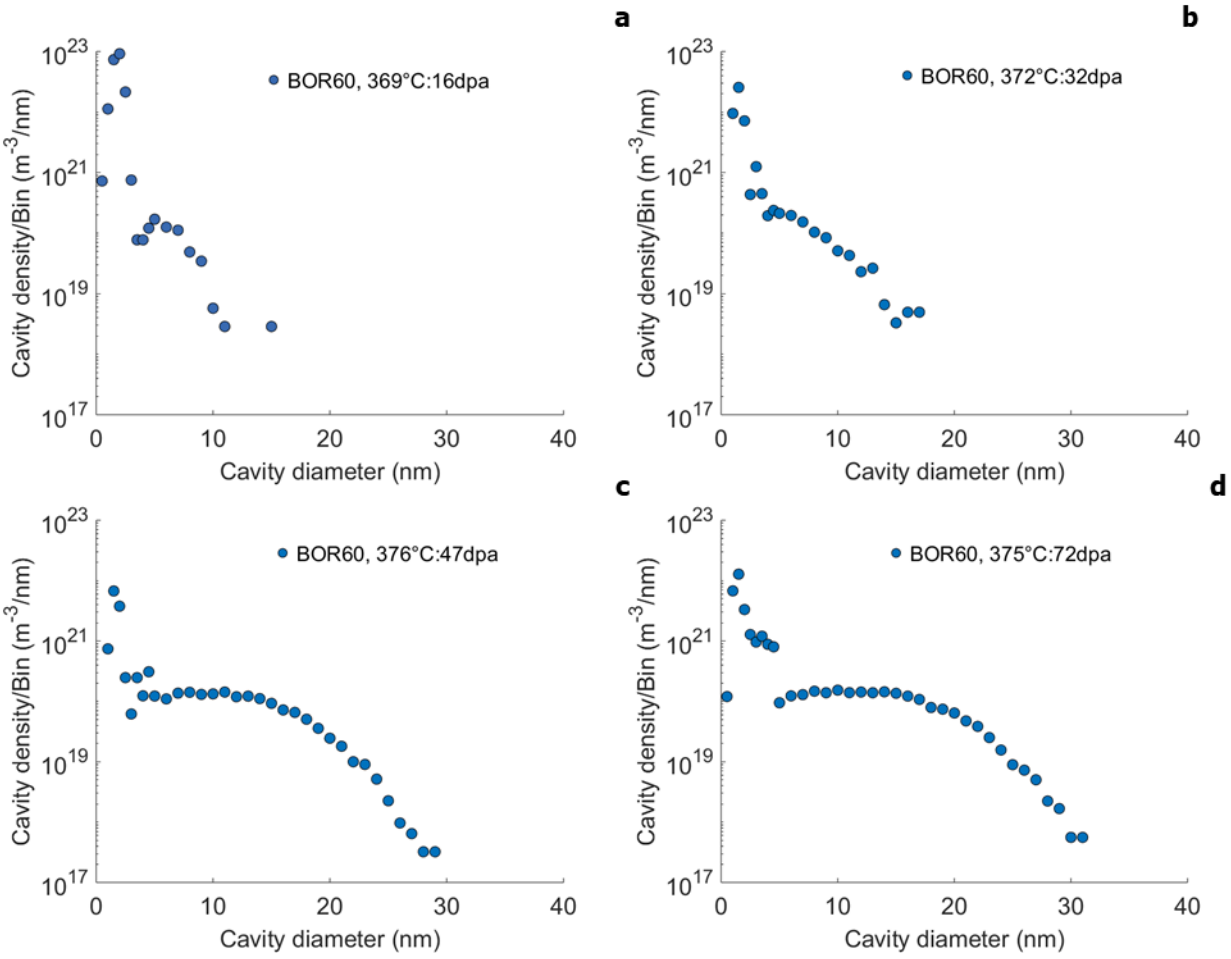


Figure 5.4: Cavity size distributions of BOR-60-irradiated T91 30176 at 369-375°C to (a) 16 dpa, (b) 32 dpa, (c) 47 dpa and (d) 72 dpa.

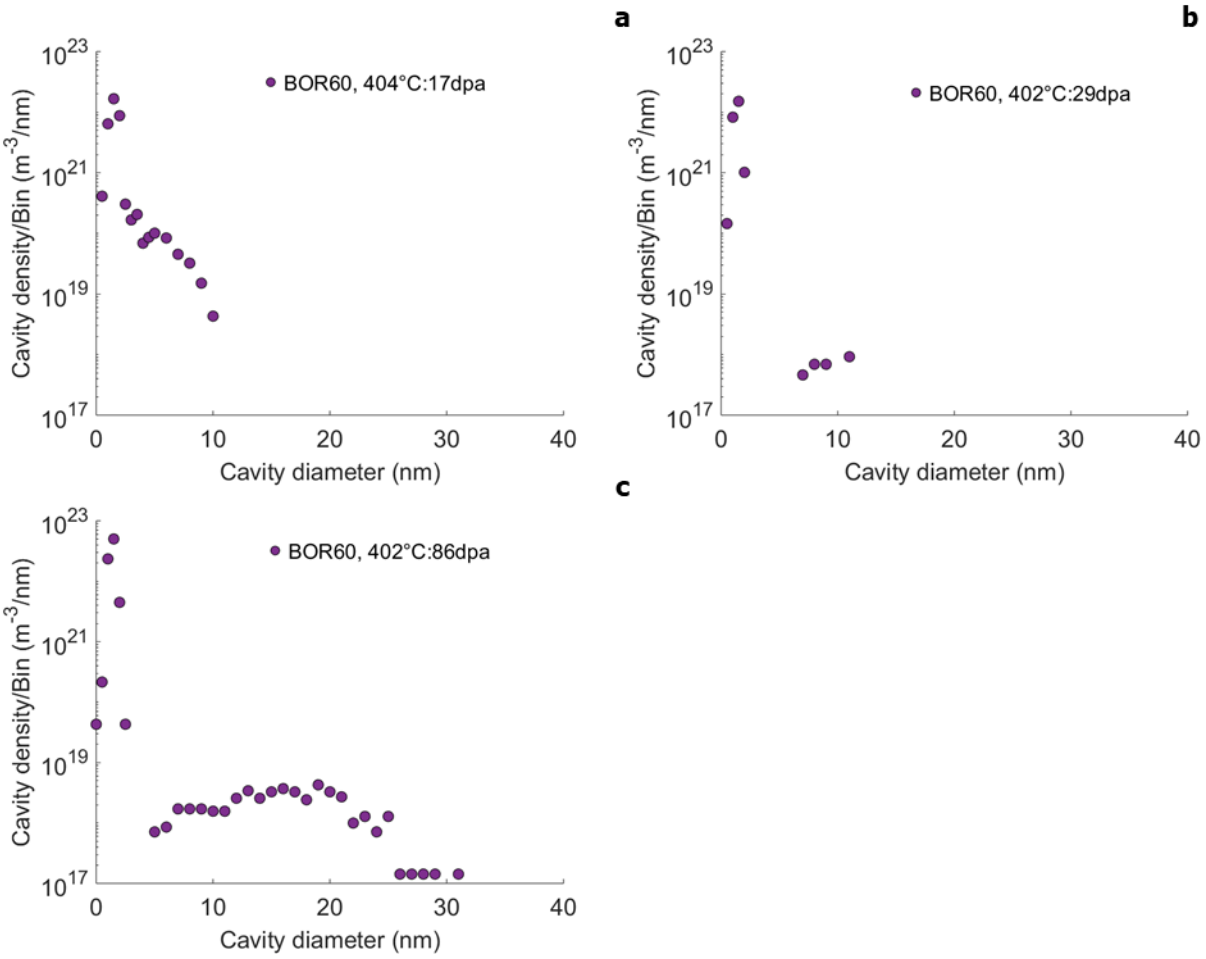


Figure 5.5: Cavity size distributions of BOR-60-irradiated T91 30176 at 402-404°C to (a) 17 dpa, (b) 29 dpa and (c) 86 dpa.

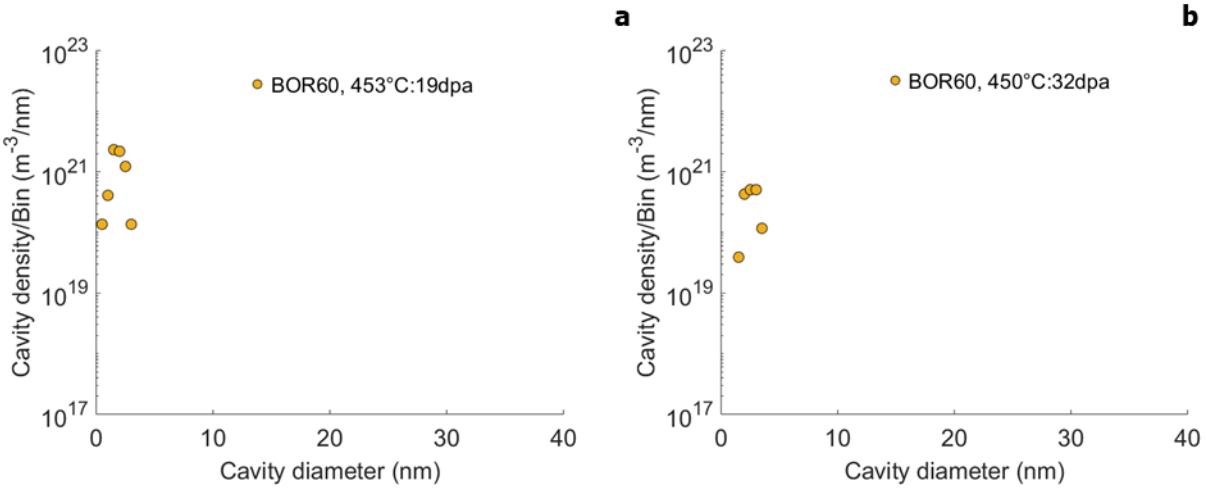


Figure 5.6: Cavity size distributions of BOR-60-irradiated T91 30176 at 450-453°C to (a) 19 dpa and (b) 32 dpa.

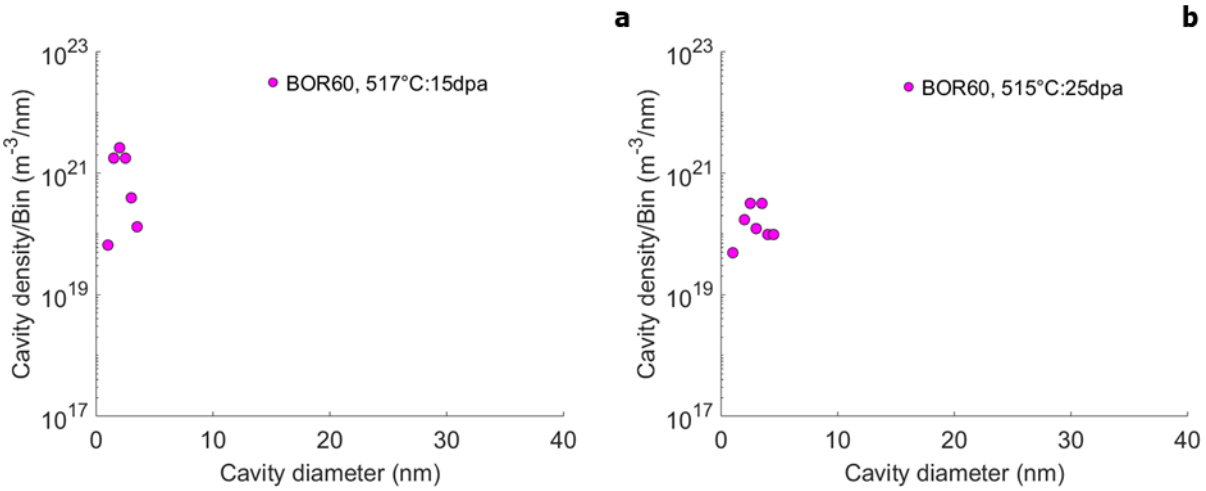


Figure 5.7: Cavity size distributions of BOR-60-irradiated T91 30176 at 515-517°C to (a) 15 dpa and (b) 25 dpa.

Table 5.5: Cavity microstructures of BOR-60-irradiated T91 30176.

Irradiation mode	Sample	Condition	Swelling (%)	Bubble density ($\times 10^{20}$ m^{-3})	Average bubble diameter (nm)	Void density ($\times 10^{20}$ m^{-3})	Average void diameter (nm)	Number of bubbles/voids counted (-)
BOR-60	P027-T03	369C-0.77Hedpa-16dpa	0.06 ± 0.01	1000 ± 119	2.07 ± 0.29	5.0 ± 0.7	6.9 ± 0.8	254/549
BOR-60	P028-T05	372C-0.77Hedpa-32dpa	0.04 ± 0.01	219 ± 26	1.78 ± 0.28	9.1 ± 1.3	8.0 ± 0.9	218/240
BOR-60	P031-T98	376C-0.77Hedpa-47dpa	0.21 ± 0.02	61 ± 8	2.04 ± 0.29	16.6 ± 1.8	11.8 ± 1.1	198/5145
BOR-60	P029-T11	375C-0.77Hedpa-72dpa	0.38 ± 0.04	141 ± 16	2.03 ± 0.29	20.9 ± 2.2	13.2 ± 1.2	703/3744
BOR-60	P033-T24	404C-0.77Hedpa-17dpa	0.01 ± 0.00	160 ± 19	1.79 ± 0.28	2.8 ± 0.4	6.8 ± 0.8	218/549
BOR-60	P036-T100	402C-0.77Hedpa-29dpa	0.003 ± 0.001	123 ± 14	1.59 ± 0.27	0.03 ± 0.01	9.6 ± 1.0	508/12
BOR-60	P034-T32	402C-0.77Hedpa-86dpa	0.023 ± 0.003	393 ± 42	1.63 ± 0.28	0.46 ± 0.05	16.2 ± 1.4	1824/325
BOR-60	P037-T55	453C-0.77Hedpa-19dpa	0.002 ± 0.000	32 ± 4	2.09 ± 0.29	N/O	N/O	47/0
BOR-60	P038-T61	450C-0.77Hedpa-32dpa	0.001 ± 0.000	8 ± 1	2.82 ± 0.40	N/O	N/O	N/R /0
BOR-60	P042-T67	517C-0.77Hedpa-15dpa	0.003 ± 0.000	34 ± 4	2.33 ± 0.35	N/O	N/O	103/0
BOR-60	P043-T108	515C-0.77Hedpa-25dpa	0.001 ± 0.000	6 ± 1	3.23 ± 0.45	N/O	N/O	N/R /0

N/O = Not observed
N/R = Not reported

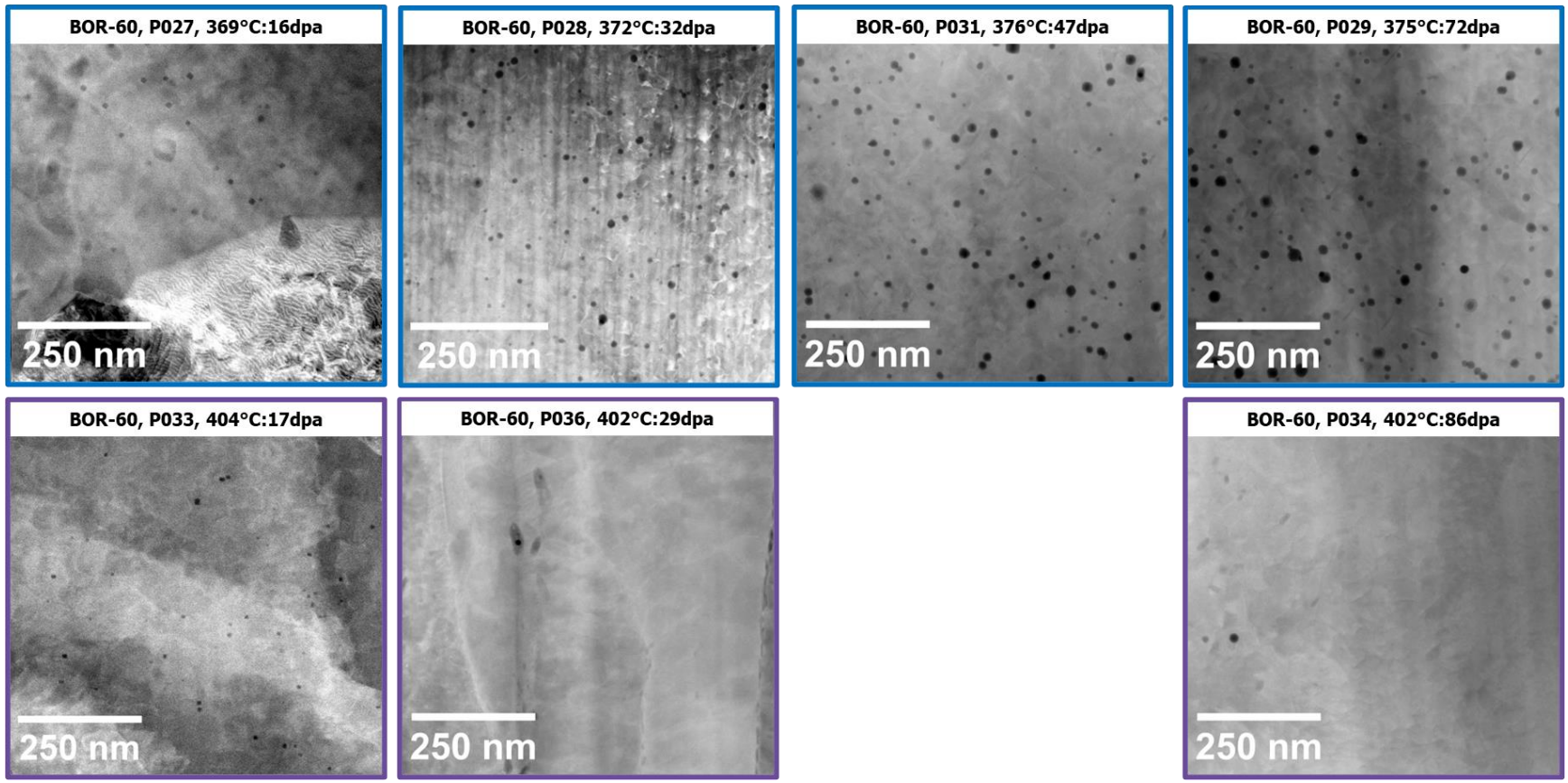


Figure 5.8: STEM-HAADF micrographs of BOR-60-irradiated T91 30176 at 369-375°C and 402-404°C.

5.3.2 Dislocation loop microstructures

The loop microstructure evolution was characterized in all BOR-60 conditions via on-zone STEM-BF imaging. The vacancy or interstitial nature of dislocation loops is not determined experimentally in this work, but all loops are believed to be interstitial type since vacancy loops have never been reported in FM steels irradiated in the presence of helium as it limits the collapse of vacancy clusters into vacancy loops [5,274]. Loops with a Burgers vector of a⟨100⟩ dominate the microstructure at all conditions where dislocation loops are present. Some a/2⟨111⟩ loops can be observed but typically represent less than 10% of the total density (none observed out of 46 loops total at 376°C:47dpa, 4 out of 164 loops total at 375°C:72dpa). No dislocation loops are observed in BOR-60 samples irradiated at 402°C:29dpa, 402°C:86dpa, 450-453°C and 515-517°C.

As shown in Figure 5.9, damage level does not have any significant impact on loop density or average loop diameter for BOR-60 samples at 369-376°C.

The loop size distributions are shown in Figure 5.10 and Figure 5.11. Results are tabulated in Table 5.6 and STEM micrographs are presented in Figure 5.12.

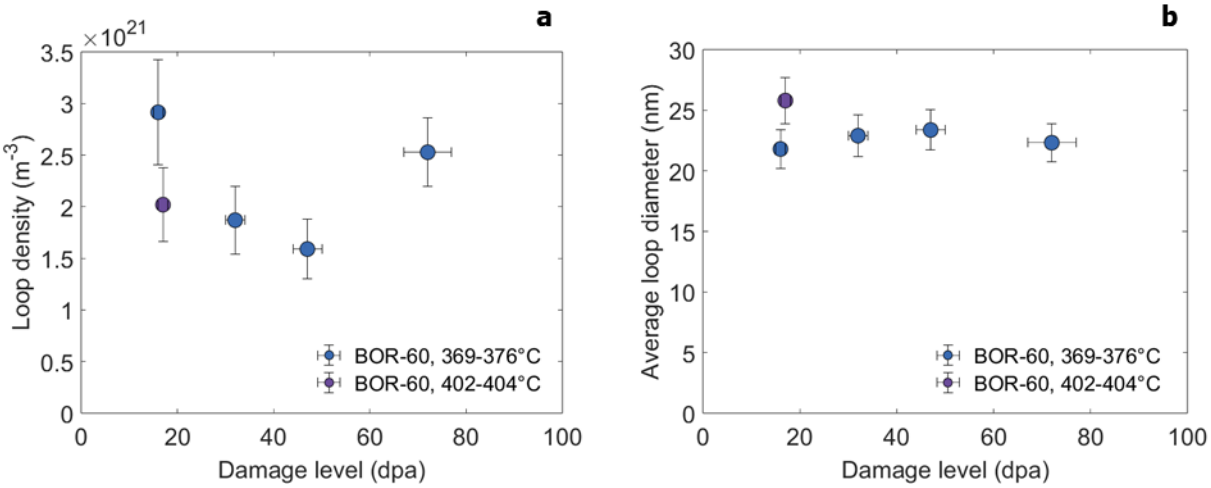


Figure 5.9: (a) Loop density and (b) average loop diameter of BOR-60-irradiated T91 30176 as a function of damage level.

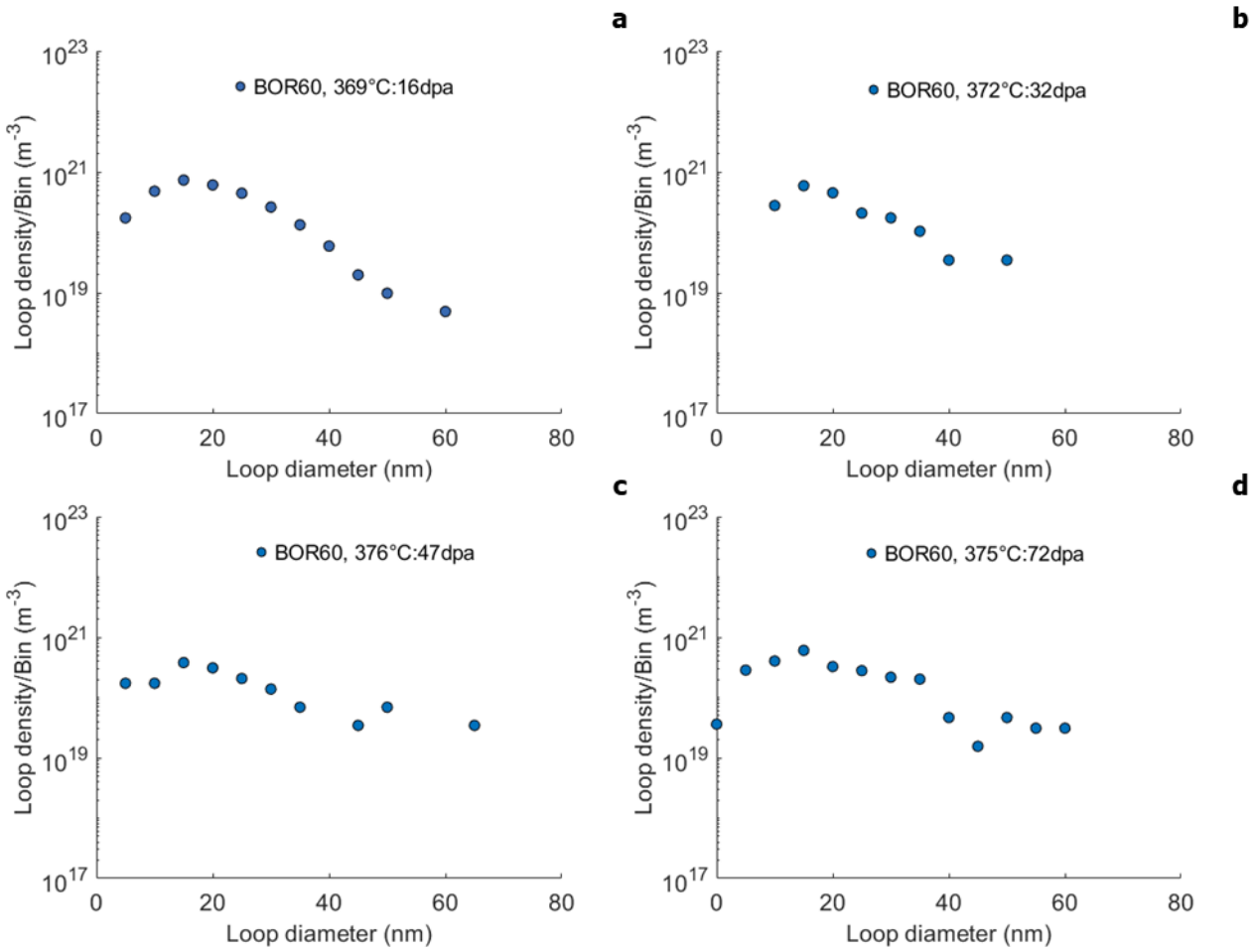


Figure 5.10: Dislocation loop size distributions of BOR-60-irradiated T91 30176 at 369-376°C to (a) 16 dpa, (b) 32 dpa, (c) 47 dpa and (d) 72 dpa.

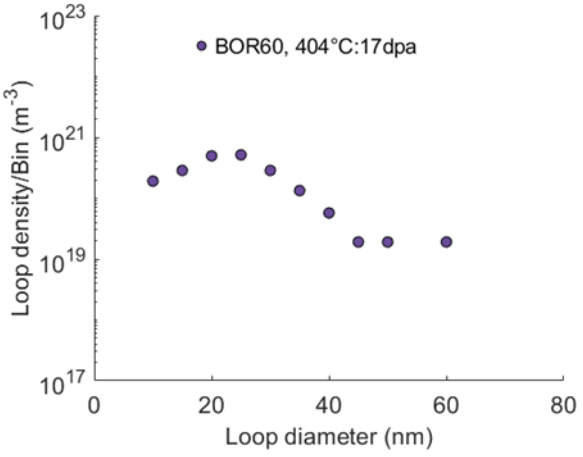


Figure 5.11: Dislocation loop size distributions of BOR-60-irradiated T91 30176 at 404°C to 17 dpa.

Table 5.6: Dislocation loop microstructures of BOR-60-irradiated T91 30176.

Irradiation mode	Sample	Condition	Loop density ($\times 10^{20}$ m^{-3})	Average loop diameter (nm)	Loop sink strength ($\times 10^{14}$ m^{-2})	Number of loops counted (-)
BOR-60	P027-T03	369C-0.77Hedpa-16dpa	29.1 ± 5.1	21.8 ± 1.6	2.0	N/R
BOR-60	P028-T05	372C-0.77Hedpa-32dpa	18.7 ± 3.3	22.9 ± 1.7	1.3	N/R
BOR-60	P031-T98	376C-0.77Hedpa-47dpa	15.9 ± 2.9	23.4 ± 1.7	1.2	46
BOR-60	P029-T11	375C-0.77Hedpa-72dpa	25.3 ± 3.3	22.3 ± 1.6	1.8	164
BOR-60	P033-T24	404C-0.77Hedpa-17dpa	20.2 ± 3.6	25.8 ± 1.9	1.7	N/R
BOR-60	P036-T100	402C-0.77Hedpa-29dpa	N/O	N/O	-	0
BOR-60	P034-T32	402C-0.77Hedpa-86dpa	N/O	N/O	-	0
BOR-60	P037-T55	453C-0.77Hedpa-19dpa	Negl.	Negl.	Negl.	N/R
BOR-60	P038-T61	450C-0.77Hedpa-32dpa	N/O	N/O	-	0
BOR-60	P042-T67	517C-0.77Hedpa-15dpa	N/O	N/O	-	0
BOR-60	P043-T108	515C-0.77Hedpa-25dpa	N/O	N/O	-	0

*N/O = Not observed
N/R = Not reported

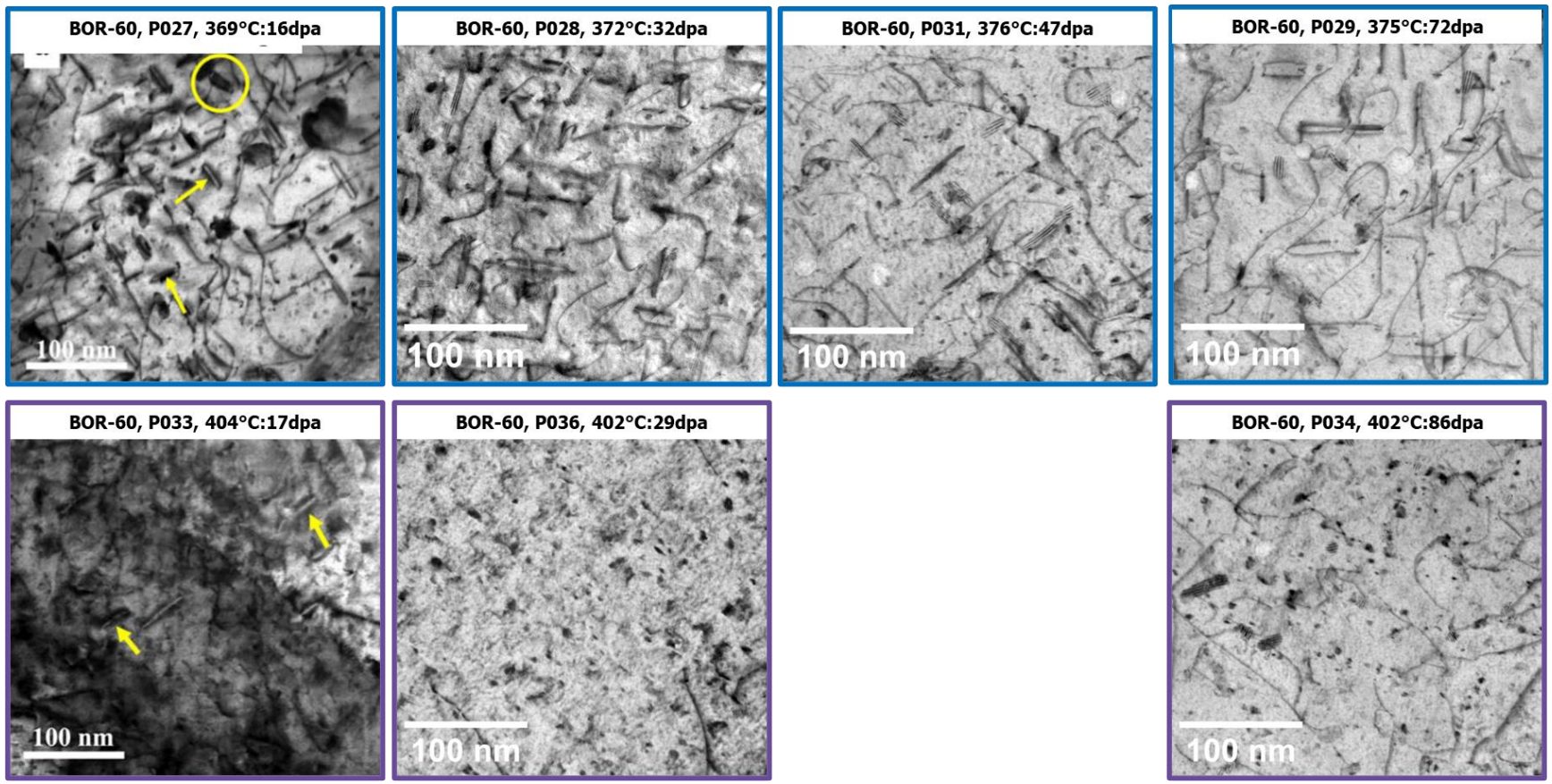


Figure 5.12: STEM BF micrographs of BOR-60-irradiated T91 30176 at 369-376°C and 402-404°C. Yellow arrows indicate some a⟨100⟩ loops and red arrows indicate some a/2⟨111⟩ loops.

5.3.3 Radiation-induced segregation

The radiation-induced segregation behavior of Fe, Cr, Ni and Si at grain boundaries was characterized in all BOR-60 conditions. Depletion of Fe and enrichment of Cr at grain boundaries is measured in all BOR-60 conditions as shown in Figure 5.13 (a-b). The enrichment in Ni is comparable between 369-376°C, 402-404°C and 450-453°C, but is lower at 515-517°C. For Fe, Cr and Ni, damage level does not appear to have an impact on enrichment/depletion at any temperature.

Enrichment of Si increases slightly with increasing damage level for BOR-60 at 369-376°C. At 402-404°C, the Si enrichment at 29 and 86 dpa is much lower than at 17 dpa, and closer to the enrichment measured at 450-453°C and 515-517°C in BOR-60 as shown in Figure 5.13 (d). Results are tabulated in Table 5.7. Representative EDS maps are presented in Figure 5.14, Figure 5.15, Figure 5.16, Figure 5.17 and Figure 5.18.

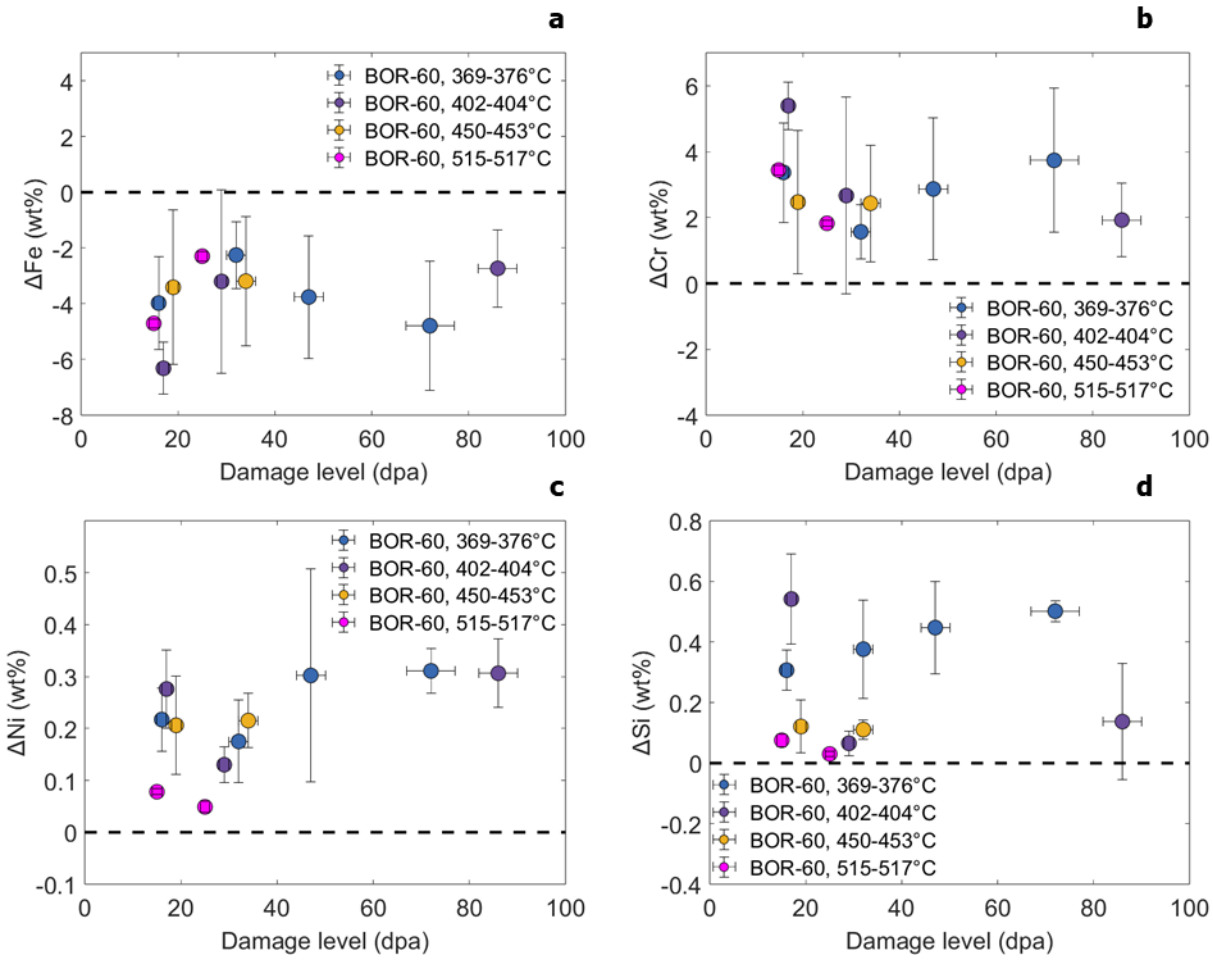


Figure 5.13: (a) Fe, (b) Cr, (c) Ni and (d) Si enrichments at grain boundaries of BOR-60-irradiated T91 30176.

Table 5.7: Radiation-induced segregation of BOR-60-irradiated T91 30176.

Irradiation mode	Sample	Condition	Fe (wt%)		Cr (wt%)		Ni (wt%)		Si (wt%)	
			Peak	ΔFe	Peak	ΔCr	Peak	ΔNi	Peak	ΔSi
BOR-60	P027-T03	369C-0.77Hedpa-16dpa	85.9±1.7	-4.0±1.7	10.9±1.5	3.4±1.5	0.32±0.06	0.22±0.06	0.60±0.07	0.31±0.07
BOR-60	P028-T05	372C-0.77Hedpa-32dpa	88.3±1.2	-2.3±1.2	9.5±0.8	1.6±0.8	0.31±0.07	0.18±0.08	0.72±0.19	0.38±0.16
BOR-60	P031-T98	376C-0.77Hedpa-47dpa	86.5±2.2	-3.8±2.2	10.5±2.0	2.9±2.2	0.43±0.17	0.30±0.21	0.70±0.21	0.45±0.15
BOR-60	P029-T11	375C-0.77Hedpa-72dpa	86.0±2.0	-4.8±2.3	11.0±2.2	3.7±2.2	0.45±0.02	0.31±0.04	0.75±0.02	0.50±0.03
BOR-60	P033-T24	404C-0.77Hedpa-17dpa	83.7±0.9	-6.3±0.9	12.9±0.5	5.4±0.7	0.36±0.08	0.28±0.08	0.85±0.20	0.54±0.15
BOR-60	P036-T100	402C-0.77Hedpa-29dpa	87.4±3.3	-3.2±3.3	10.2±3.2	2.7±3.0	0.26±0.07	0.13±0.03	0.27±0.10	0.07±0.04
BOR-60	P034-T32	402C-0.77Hedpa-86dpa	88.3±1.4	-2.7±1.4	8.9±1.1	1.9±1.1	0.43±0.07	0.31±0.07	0.31±0.20	0.14±0.19
BOR-60	P037-T55	453C-0.77Hedpa-19dpa	86.3±2.6	-3.4±2.8	9.7±2.1	2.5±2.2	0.31±0.09	0.21±0.10	0.39±0.09	0.12±0.09
BOR-60	P038-T61	450C-0.77Hedpa-32dpa	86.6±1.6	-3.2±2.3	10.3±1.3	2.4±1.8	0.30±0.04	0.22±0.05	0.33±0.03	0.11±0.03
BOR-60	P042-T67	517C-0.77Hedpa-15dpa	84.8±0.5	-4.7±0.2	10.7±0.1	3.4±0.2	0.19±0.01	0.08±0.01	0.40±0.01	0.08±0.02
BOR-60	P043-T108	515C-0.77Hedpa-25dpa	87.7±0.2	-2.3±0.2	9.8±0.2	1.8±0.1	0.14±0.02	0.05±0.01	0.25±0.06	0.03±0.01

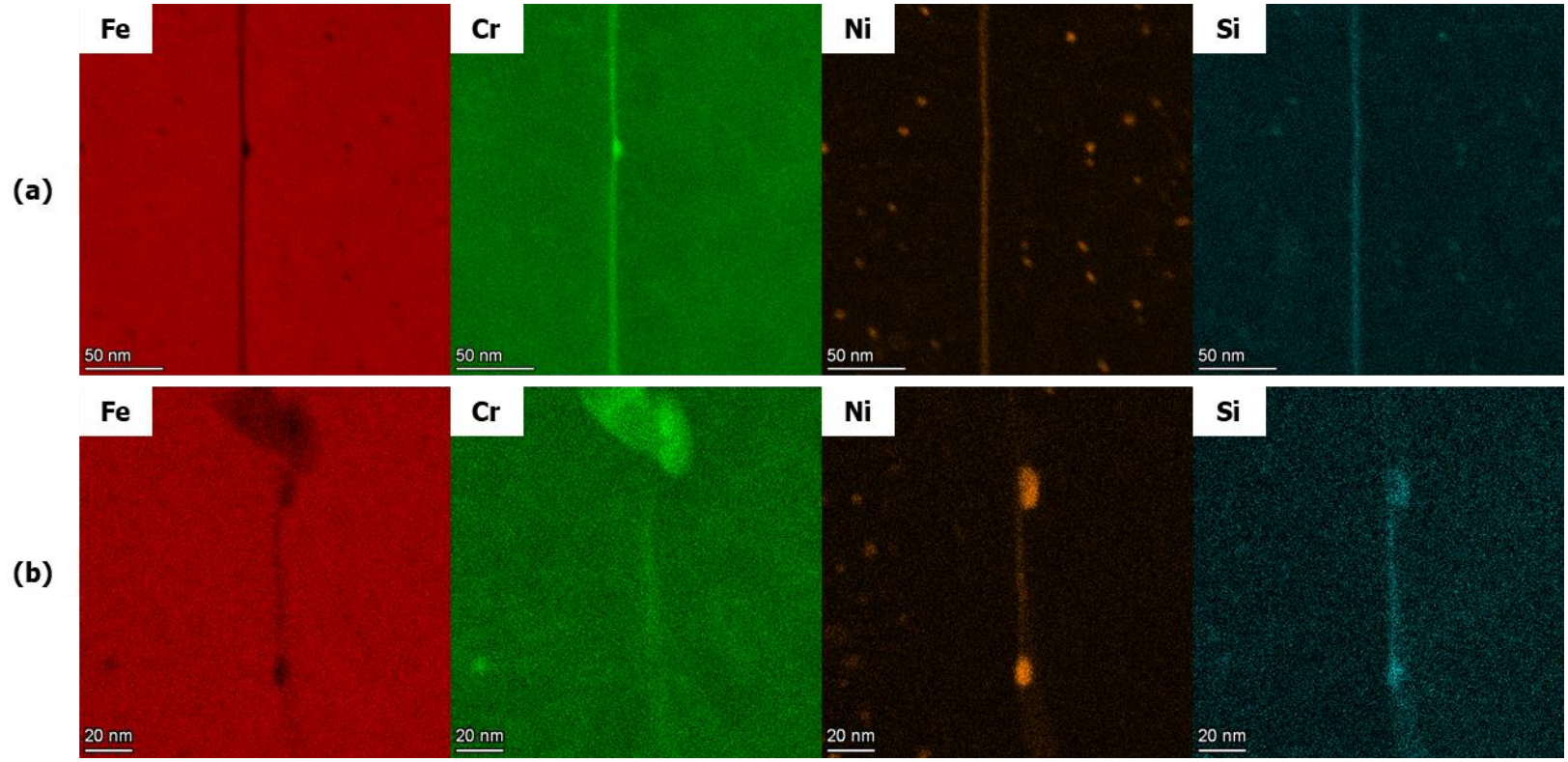


Figure 5.14: EDS (wt%) maps of Fe, Cr, Ni and Si of BOR-60-irradiated T91 30176 at (a) 369°C:16dpa and (b) 372°C:32dpa.

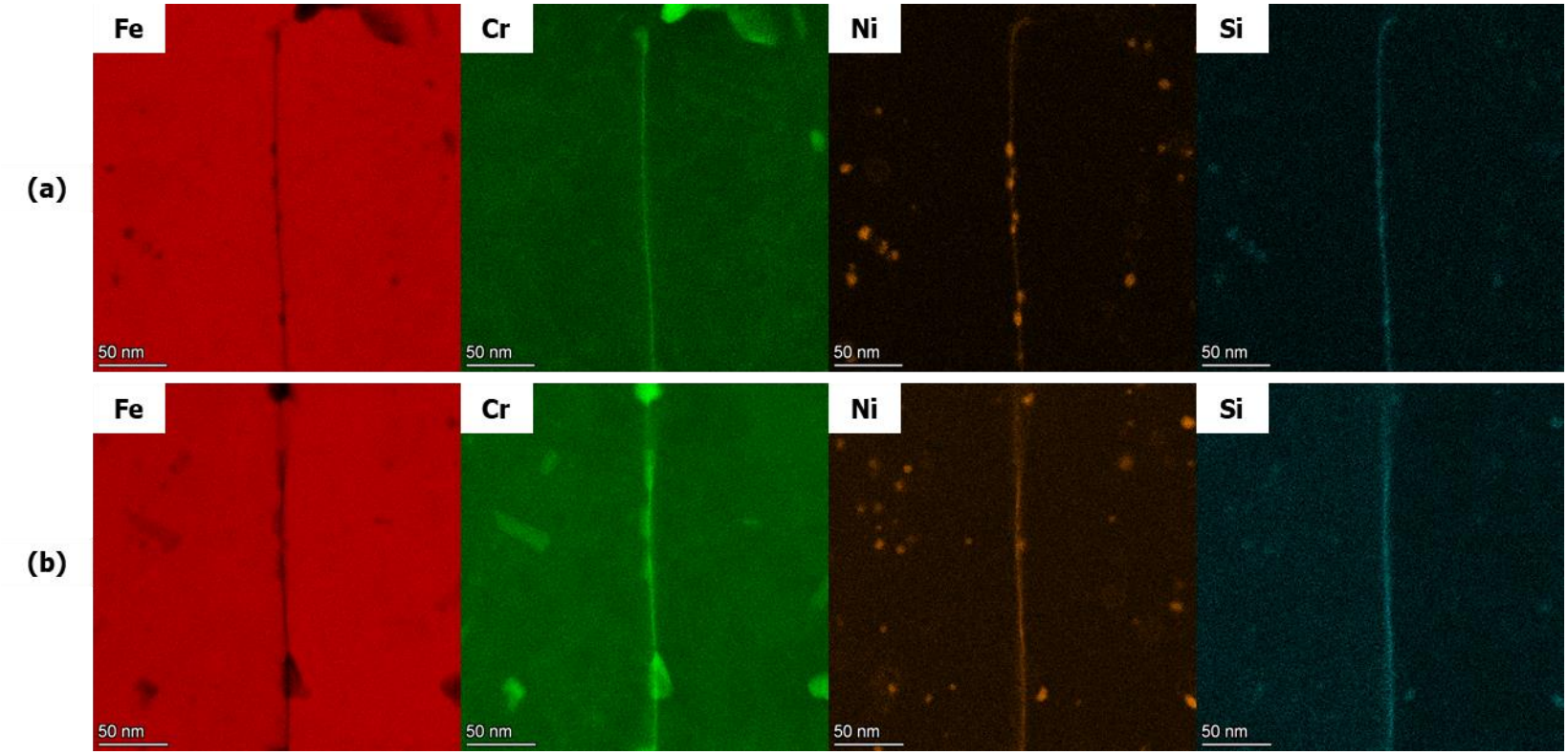


Figure 5.15: EDS (wt%) maps of Fe, Cr, Ni and Si of BOR-60-irradiated T91 30176 at (a) 376°C:47dpa and (b) 375°C:72dpa.

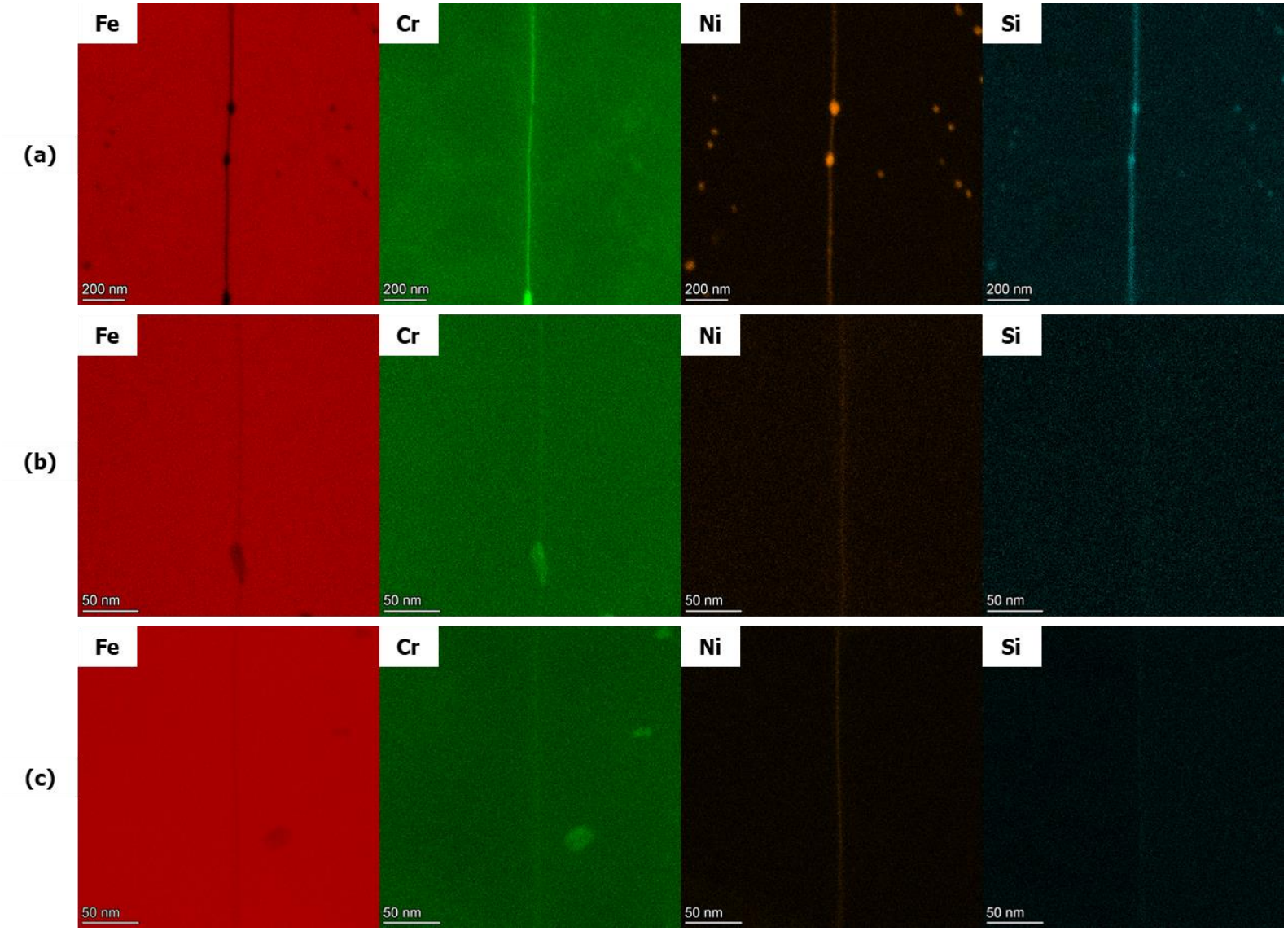


Figure 5.16: EDS (wt%) maps of Fe, Cr, Ni and Si of BOR-60-irradiated T91 30176 at (a) 404°C:17dpa, (b) 402°C:29dpa and (c) 404°C:86dpa.

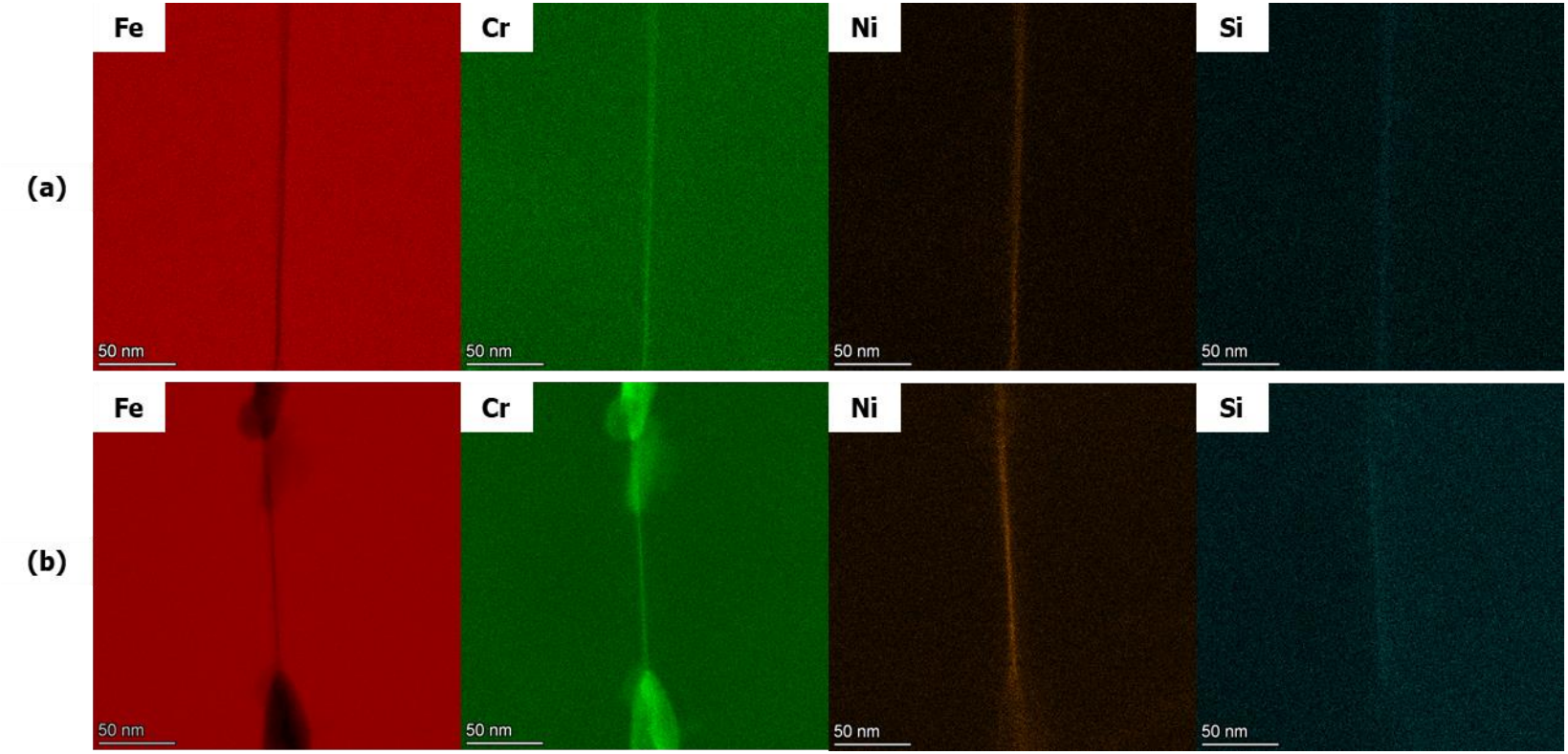


Figure 5.17: EDS (wt%) maps of Fe, Cr, Ni and Si of BOR-60-irradiated T91 30176 at (a) 453°C:19dpa and (b) 450°C:32dpa.

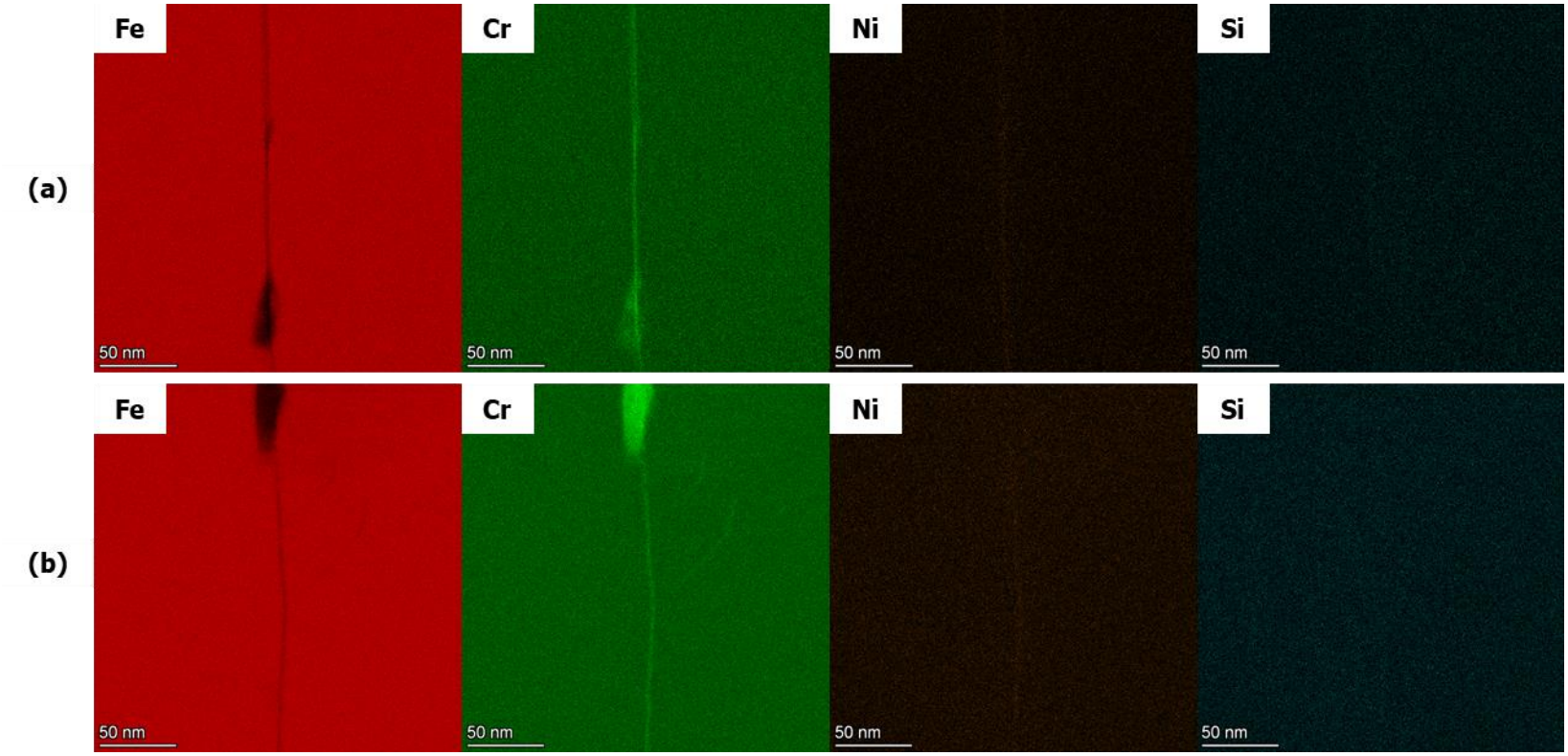


Figure 5.18: EDS (wt%) maps of Fe, Cr, Ni and Si of BOR-60-irradiated T91 30176 at (a) 517°C:15dpa and (b) 515°C:25dpa.

5.3.4 Radiation-induced precipitation

The formation of Ni-Si-Mn clusters was characterized in all BOR-60 conditions. In BOR-60, clusters are observed at 369-376° between 16 and 72 dpa and at 402-404°C at 17 dpa but not at 29 or 86 dpa. No clusters are observed at 450-453°C or 515-517°C. Figure 5.19 shows the evolution of Ni-Si-Mn cluster density, average void diameter and volume fraction as a function of damage level. The cluster density, average cluster diameter and volume fraction appear constant across damage levels. The size distributions are shown in Figure 5.20 and Figure 5.21. Results are tabulated in Table 5.8. EDS Ni maps are presented in Figure 5.22 and Figure 5.23.

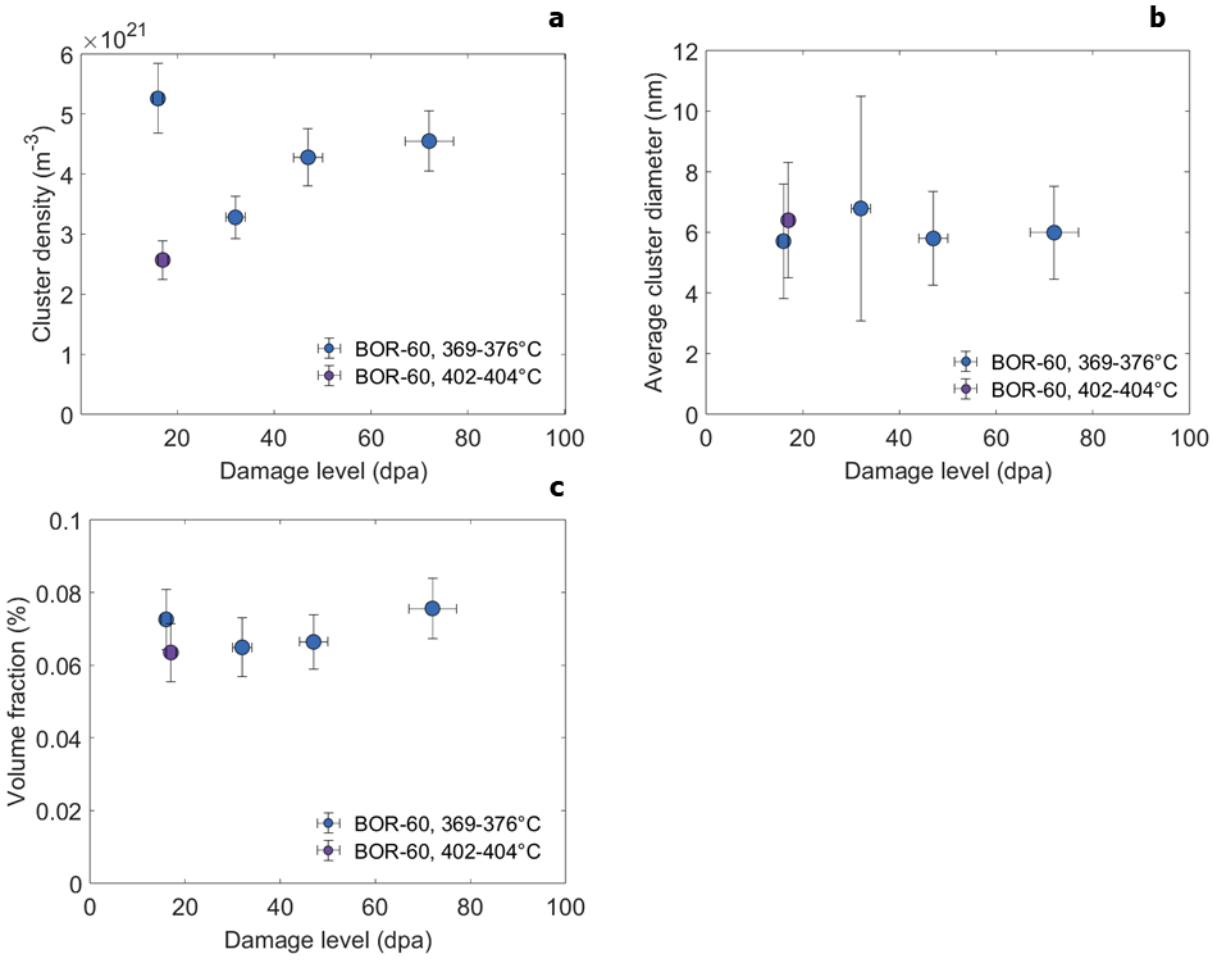


Figure 5.19: (a) Cluster density, (b) average cluster diameter and (c) volume fraction of BOR-60-irradiated T91 30176.

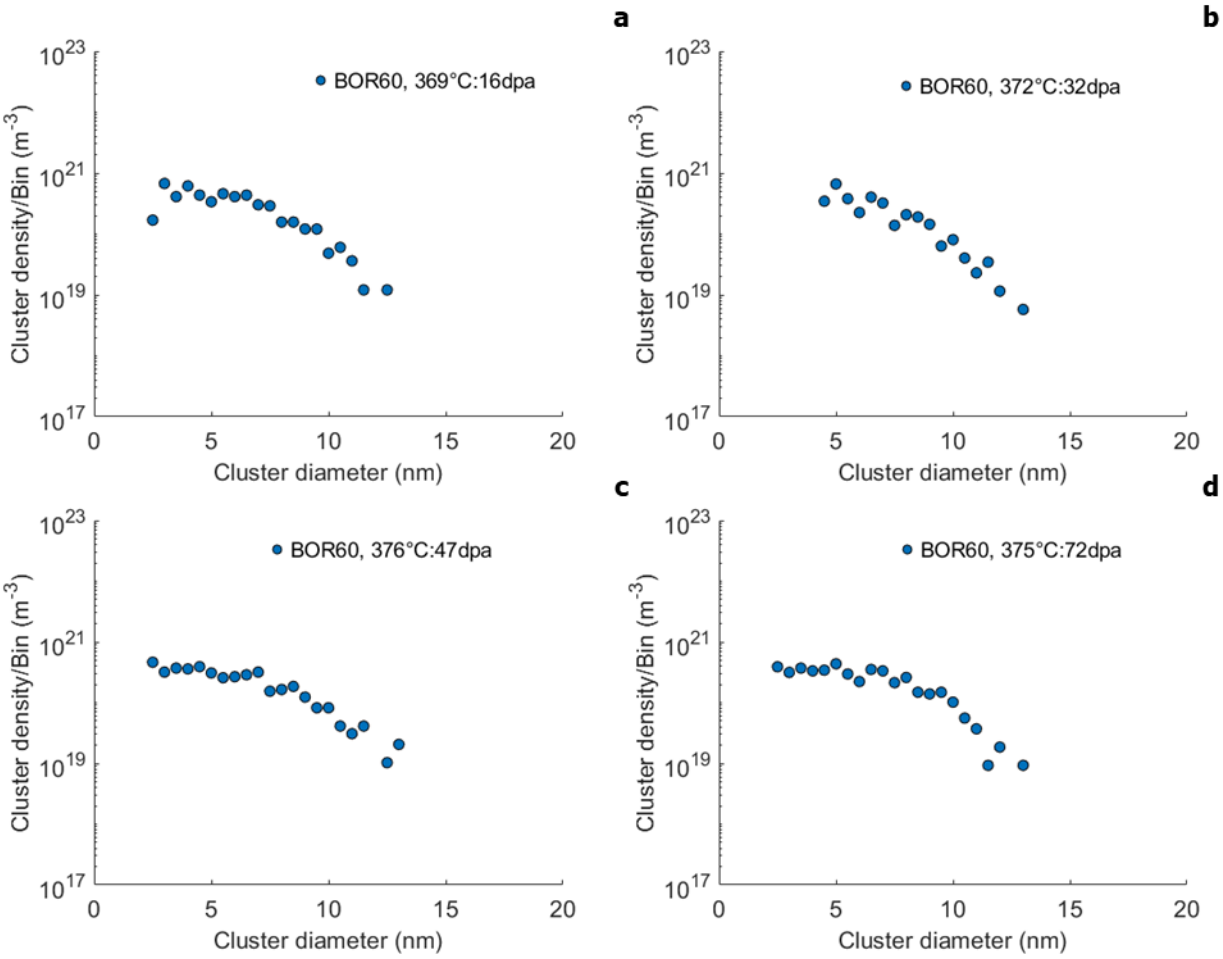


Figure 5.20: Cluster size distributions of BOR-60-irradiated T91 30176 at 369-376°C to (a) 16 dpa, (b) 32 dpa, (c) 47 dpa and (d) 72 dpa.

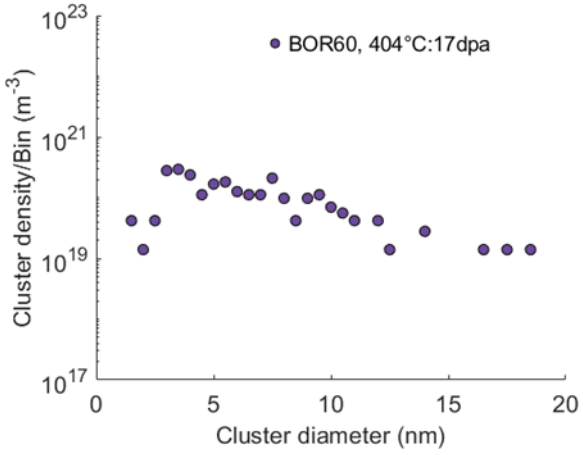


Figure 5.21: Cluster size distributions of BOR-60-irradiated T91 30176 at 404°C to 17dpa.

Table 5.8: Ni/Si-cluster microstructures of BOR-60-irradiated T91 30176.

Irradiation mode	Sample	Condition	Cluster density ($\times 10^{20}$ m^{-3})	Average cluster diameter (nm)	Volume fraction (%)	Number of clusters counted (-)
BOR-60	P027-T03	369C-0.77Hedpa-16dpa	52.6 ± 5.8	5.7 ± 1.9	0.07 ± 0.01	436
BOR-60	P028-T05	372C-0.77Hedpa-32dpa	32.8 ± 3.6	6.8 ± 3.7	0.07 ± 0.01	569
BOR-60	P031-T98	376C-0.77Hedpa-47dpa	42.8 ± 4.8	5.8 ± 1.5	0.07 ± 0.01	416
BOR-60	P029-T11	375C-0.77Hedpa-72dpa	45.5 ± 5.0	6.0 ± 1.5	0.08 ± 0.01	490
BOR-60	P033-T24	404C-0.77Hedpa-17dpa	25.7 ± 3.2	6.4 ± 1.9	0.06 ± 0.01	184
BOR-60	P036-T100	402C-0.77Hedpa-29dpa	N/O	N/O	-	0
BOR-60	P034-T32	402C-0.77Hedpa-86dpa	N/O	N/O	-	0
BOR-60	P037-T55	453C-0.77Hedpa-19dpa	N/O	N/O	-	0
BOR-60	P038-T61	450C-0.77Hedpa-32dpa	N/O	N/O	-	0
BOR-60	P042-T67	517C-0.77Hedpa-15dpa	N/O	N/O	-	0
BOR-60	P043-T108	515C-0.77Hedpa-25dpa	N/O	N/O	-	0

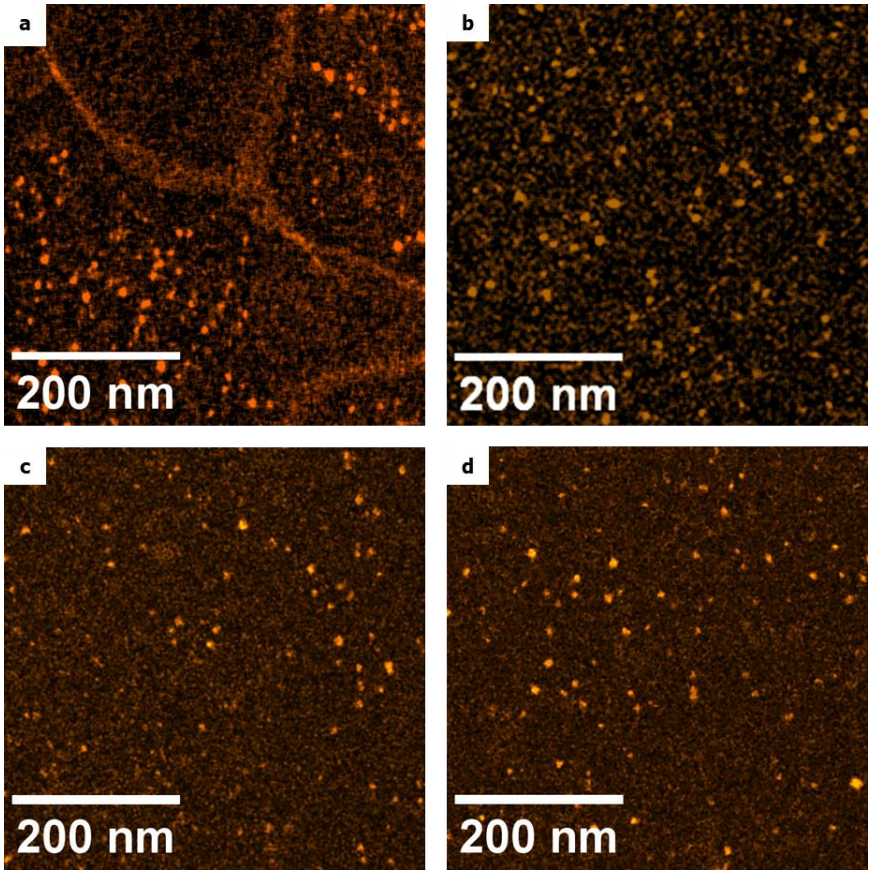


Figure 5.22: EDS Ni map (wt%) of BOR-60-irradiated T91 30176 at (a) 369°C:16dpa, (b) 372°C:32dpa, (c) 376°C:47dpa and (d) 375°C:72dpa.

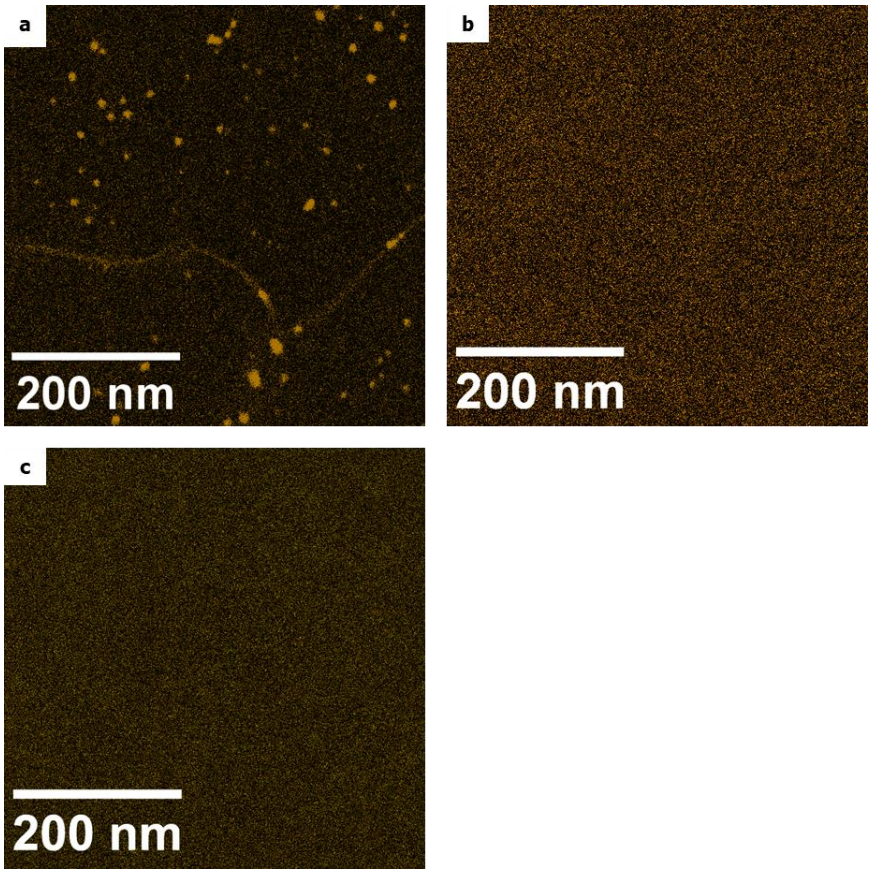


Figure 5.23: EDS Ni map (wt%) of BOR-60-irradiated T91 30176 at (a) 404°C:17dpa, (b) 402°C:29dpa and (c) 402°C:86dpa.

5.4 Dual-ion irradiation companion to BOR-60

5.4.1 Cavity microstructures

The cavity microstructure evolution was characterized in all dual-ion conditions via STEM-HAADF and CTEM-BF through-focus imaging. As shown in Figure 5.24, swelling increases with increasing damage level in dual-ion samples irradiated at 445°C and 460°C up to 72 dpa. In samples irradiated at 520°C and 570°C, the swelling does not significantly vary with damage level.

These swelling increases are directly related to the evolution of the void (cavities larger than 5 nm in diameter) microstructure shown in Figure 5.25. Both void density and average void diameter increase with damage level in dual-ion samples irradiated at 445°C and 460°C.

Bubbles are observed at all dual-ion conditions without any clear trend in terms of density or average diameter with increasing damage level as shown in Figure 5.26.

Looking at cavity size distributions, Figure 5.27 and Figure 5.28 show that dual-ion irradiation created bi-modal size distributions at 445°C and 460°C, respectively. In these cases, the density of smaller voids (~5 nm in diameter) stays around 10^{20} m^{-3} with increasing damage level, while the size distribution extends to larger maximum void diameter. In addition, the small sampling volume of dual-ion-irradiated specimens limits the measurable density of voids in the bins of a size distribution. This shortcoming creates a threshold density below which cavities cannot be correctly detected in dual-ion size distributions. These 'undetectable' regions are shown in the size distributions in Figure 5.27, Figure 5.28, Figure 5.29, and Figure 5.30.

Figure 5.29 (resp. Figure 5.30) shows the cavity size distributions of dual-ion samples irradiated at 520°C (resp. 570°C). Both conditions exhibit very few voids. Results are tabulated in

Table 5.9. Representative STEM HAADF micrographs are shown in Figure 5.31 after dual-ion irradiation at 445°C and 460°C.

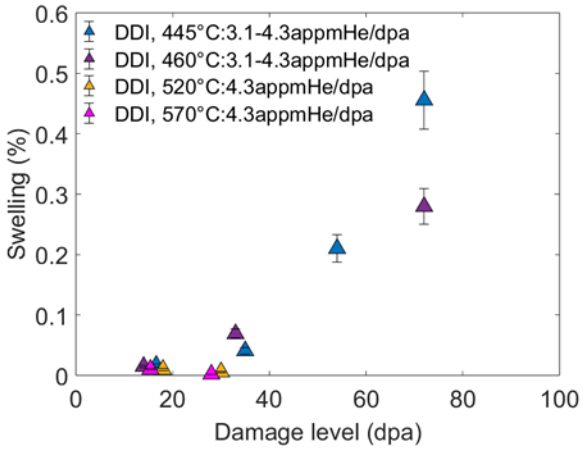


Figure 5.24: Swelling of dual-ion-irradiated T91 30176 as a function of damage level.

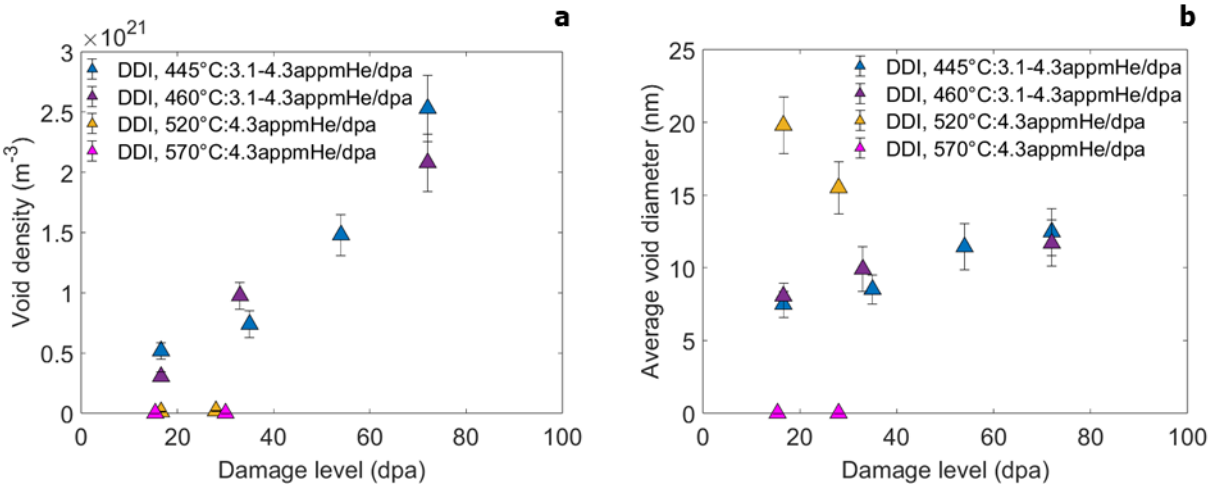


Figure 5.25: (a) Void density and (b) average void diameter of dual-ion-irradiated T91 30176 as a function of damage level.

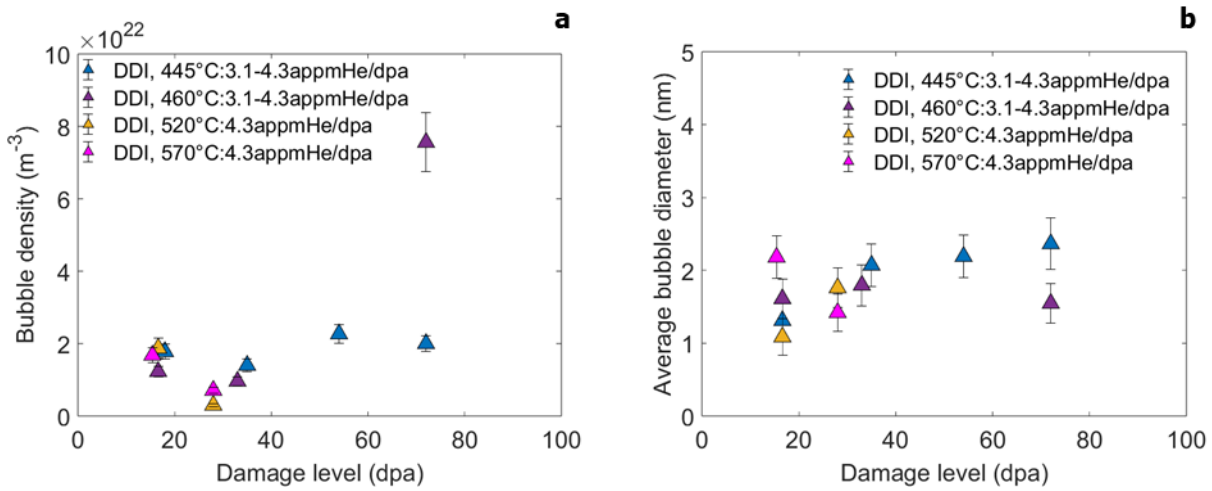


Figure 5.26: (a) Bubble density and (b) average bubble diameter of dual-ion-irradiated T91 30176 as a function of damage level.

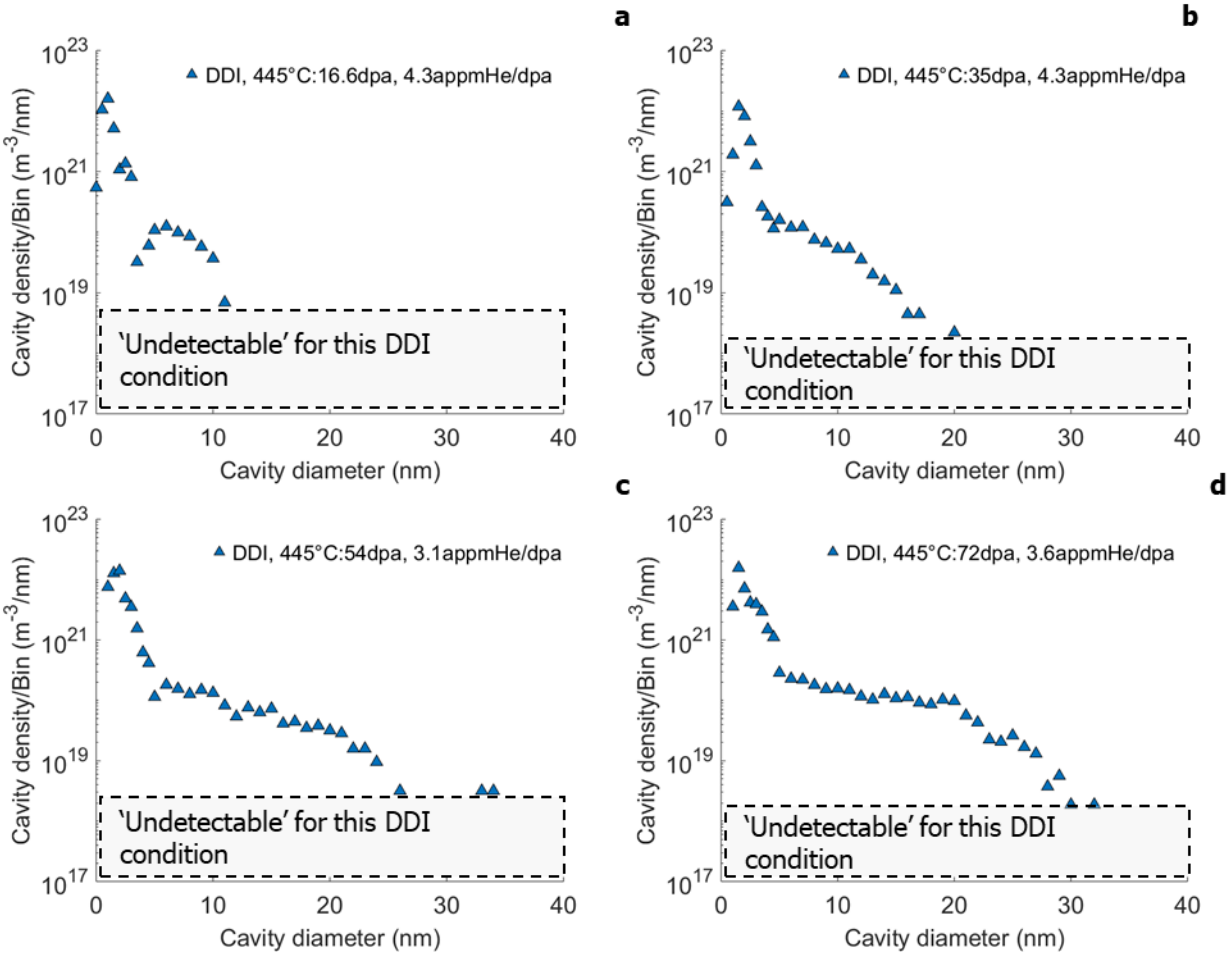


Figure 5.27: Cavity size distributions of dual-ion-irradiated T91 30176 at 445°C to (a) 16.6 dpa, (b) 35 dpa, (c) 54 dpa and (d) 72 dpa.

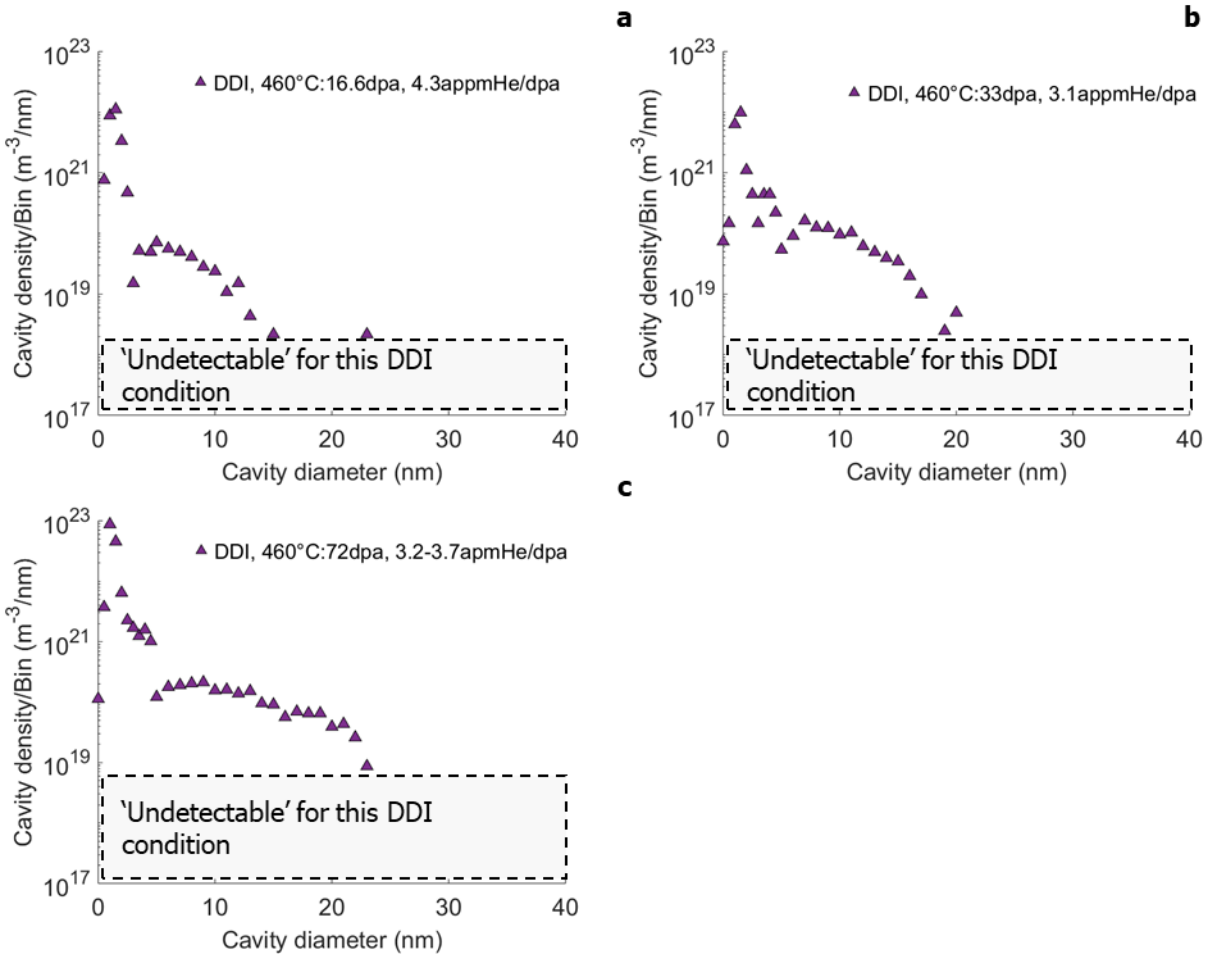


Figure 5.28: Cavity size distributions of dual-ion-irradiated T91 30176 at 460°C to (a) 16.6 dpa, (b) 33 dpa and (c) 72 dpa.

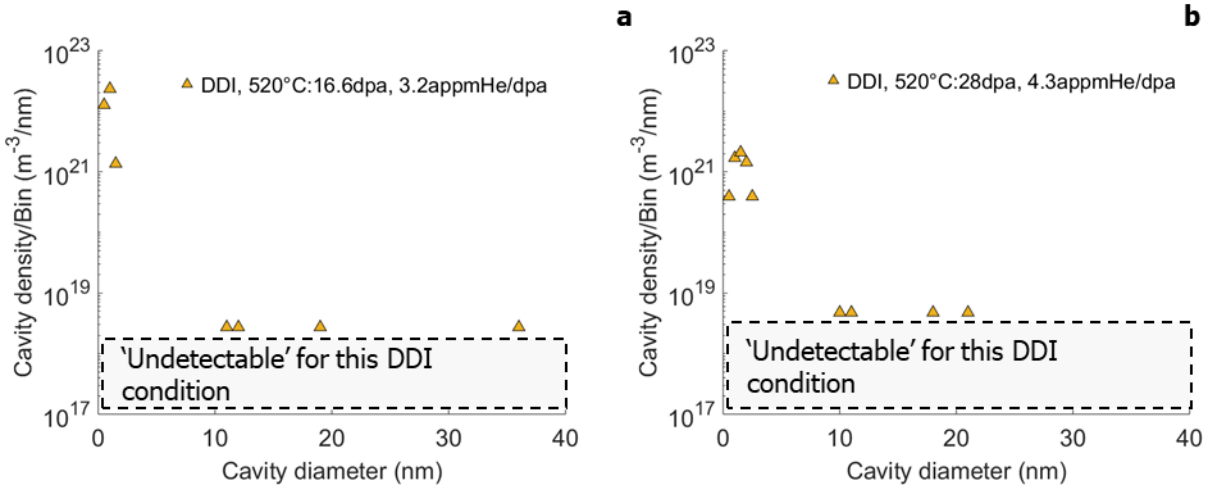


Figure 5.29: Cavity size distributions of dual-ion-irradiated T91 30176 at 520°C to (a) 16.6 dpa and (b) 28 dpa.

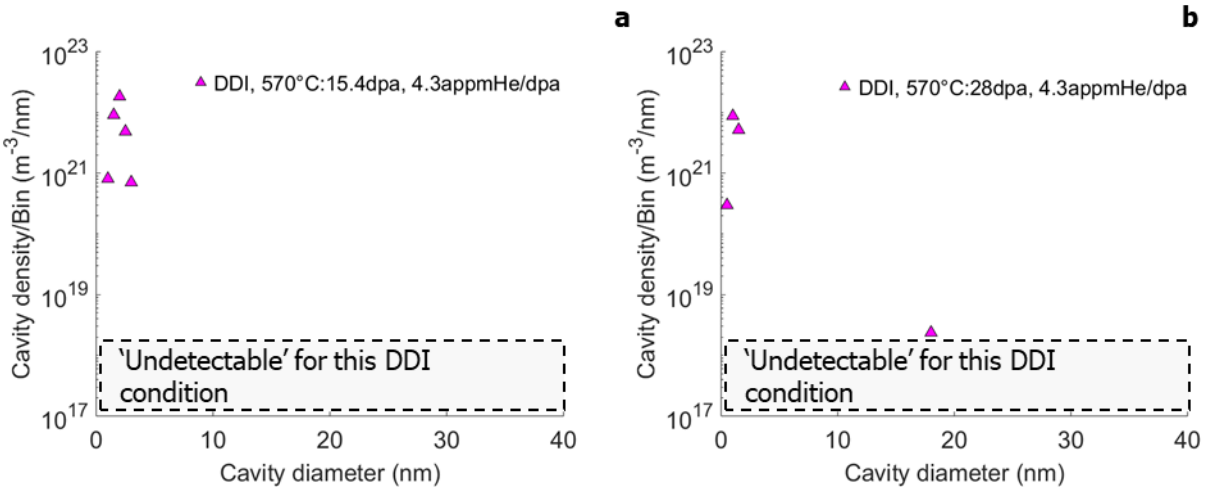


Figure 5.30: Cavity size distributions of dual-ion-irradiated T91 30176 at 570°C to (a) 15.4 dpa and (b) 28 dpa.

Table 5.9: Cavity microstructures of dual-ion-irradiated T91 30176.

Irradiation mode	Sample	Condition	Swelling (%)	Bubble density ($\times 10^{20}$ m^{-3})	Average bubble diameter (nm)	Void density ($\times 10^{20}$ m^{-3})	Average void diameter (nm)	Number of bubbles/ voids counted (-)
DDI	092717	445C-4.3Hedpa-16.6dpa	0.017 ± 0.002	178 ± 21	1.31 ± 0.26	5.2 ± 0.7	7.5 ± 0.9	131/423
DDI	053018-1	445C-4.3Hedpa-35dpa	0.041 ± 0.006	140 ± 17	2.09 ± 0.29	7.4 ± 1.1	8.5 ± 1.0	573/426
DDI	070120-1	445C-3.1Hedpa-54dpa	0.21 ± 0.02	227 ± 26	2.19 ± 0.29	14.8 ± 1.7	11.4 ± 1.6	437/466
DDI	102120-1	445C-3.6Hedpa-72dpa	0.46 ± 0.05	200 ± 22	2.37 ± 0.35	25.3 ± 2.7	12.5 ± 1.6	1043/1352
DDI	092917	460C-4.3Hedpa-16.6dpa	0.015 ± 0.002	123 ± 15	1.64 ± 0.27	3.0 ± 0.4	8.1 ± 0.9	657/161
DDI	071320-1	460C-3.1Hedpa-33dpa	0.07 ± 0.01	96 ± 12	1.80 ± 0.28	9.8 ± 1.1	9.9 ± 1.5	261/397
DDI	091420-1	460C-3.2-3.7Hedpa-72dpa	0.28 ± 0.03	756 ± 82	1.55 ± 0.27	20.8 ± 2.4	11.7 ± 1.6	1338/478
DDI	020320	520C-3.2Hedpa-16.6dpa	0.010 ± 0.002	188 ± 28	1.09 ± 0.25	0.11 ± 0.02	19.8 ± 1.9	440/4
DDI	091719	520C-4.3Hedpa-28dpa	0.006 ± 0.001	30 ± 4	1.73 ± 0.27	0.19 ± 0.03	15.5 ± 1.8	N/R
DDI	110117	570C-4.3Hedpa-15.4dpa	0.010 ± 0.001	168 ± 20	2.18 ± 0.29	N/O	N/O	334/0
DDI	111219	570C-4.3Hedpa-28dpa	0.002 ± 0.000	71 ± 8	1.42 ± 0.26	Negl.	Negl.	N/R

N/O = Not observed
N/R = Not reported

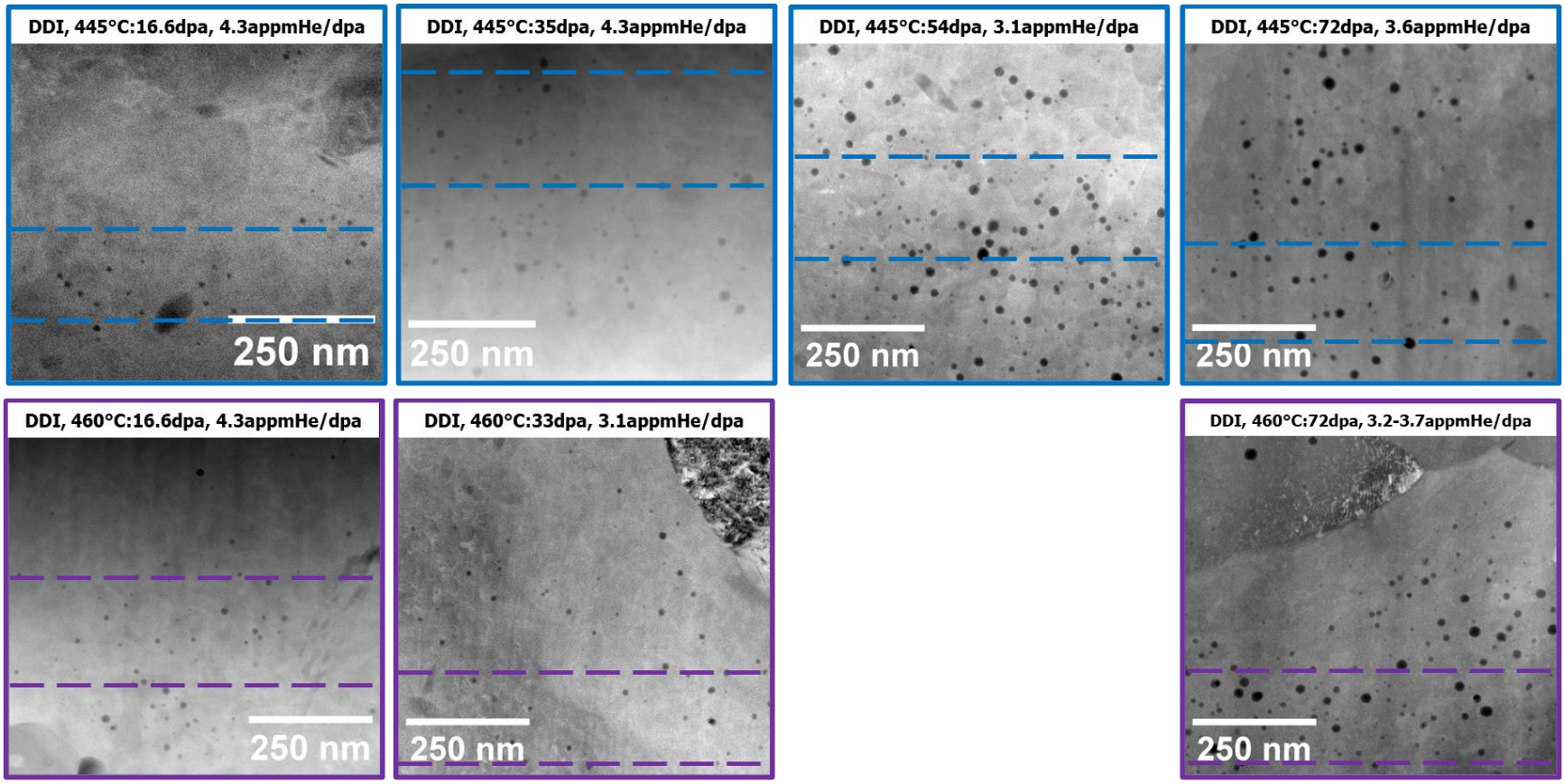


Figure 5.31: STEM HAADF micrographs of dual-ion-irradiated T91 30176 at 445°C and 460°C. The dashed lines indicate the depth of interest for the dual-ion-irradiated samples.

5.4.2 Dislocation loop microstructures

The loop microstructure evolution was characterized in all dual-ion irradiations via on-zone STEM-BF imaging. Loops with a Burgers vector of a⟨100⟩ dominate the microstructure at all conditions where dislocation loops are present. Some a/2⟨111⟩ loops can be observed but typically represent less than 10% of the total density (5 out of 66 loops total at 445°C:54dpa and 5 out of 79 loops total at 445°C:72dpa). No dislocation loops are observed in dual-ion samples irradiated at 520°C or 570°C.

As shown in Figure 5.32, damage level does not have any significant impact on loop density or average loop diameter at 445°C and 460°C. Average loop diameter appears to increase while loop density decreases with increasing temperature after dual-ion irradiation as shown in Figure 5.33.

The loop size distributions are shown in Figure 5.34 and Figure 5.35. Results are tabulated in Table 5.10 and STEM micrographs are presented in Figure 5.36.

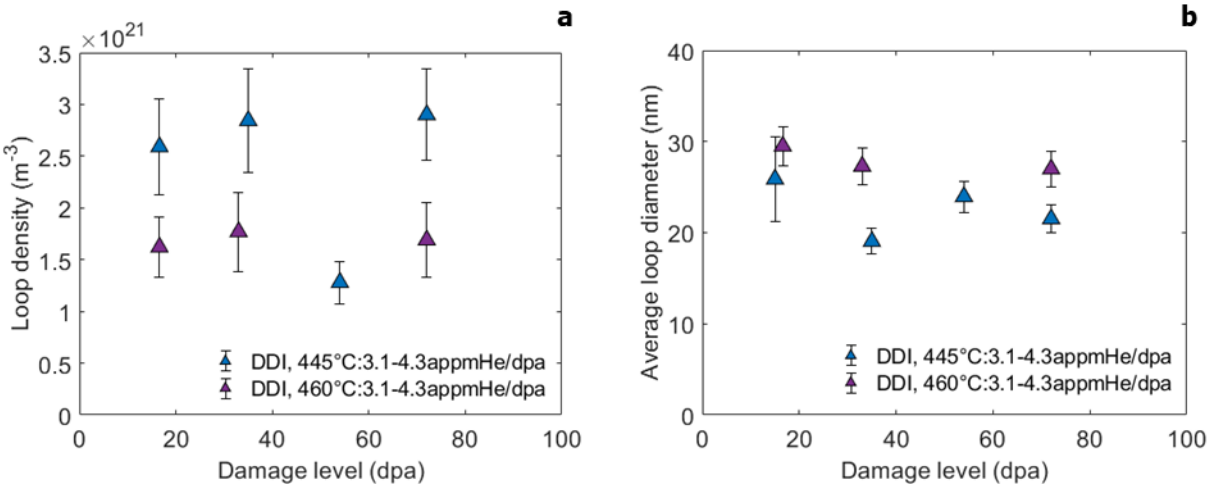


Figure 5.32: (a) Loop density and (b) average loop diameter of dual-ion-irradiated T91 30176 as a function of damage level.

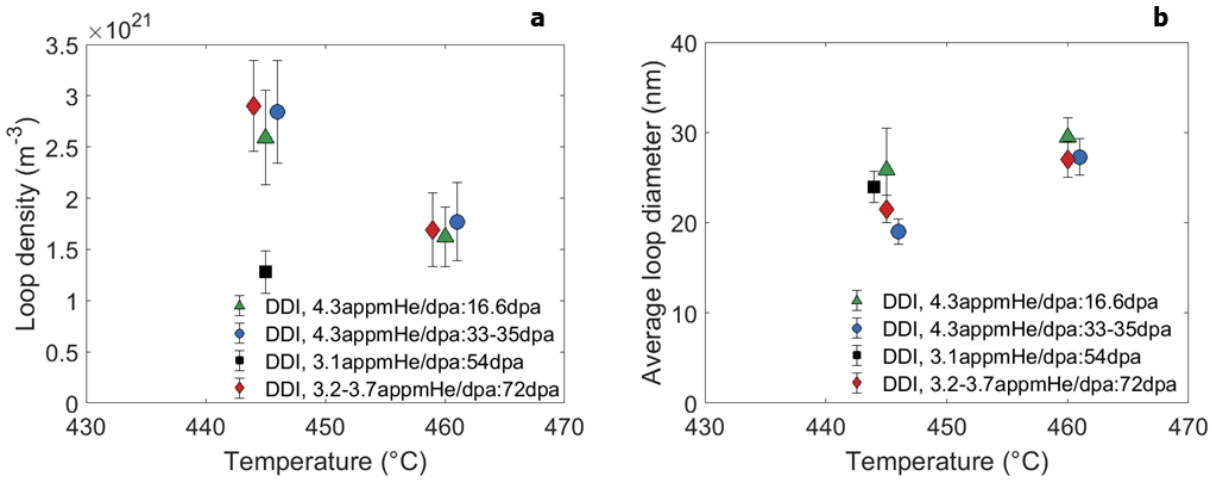


Figure 5.33: (a) Loop density and (b) average loop diameter of dual-ion-irradiated T91 30176 as a function of temperature.

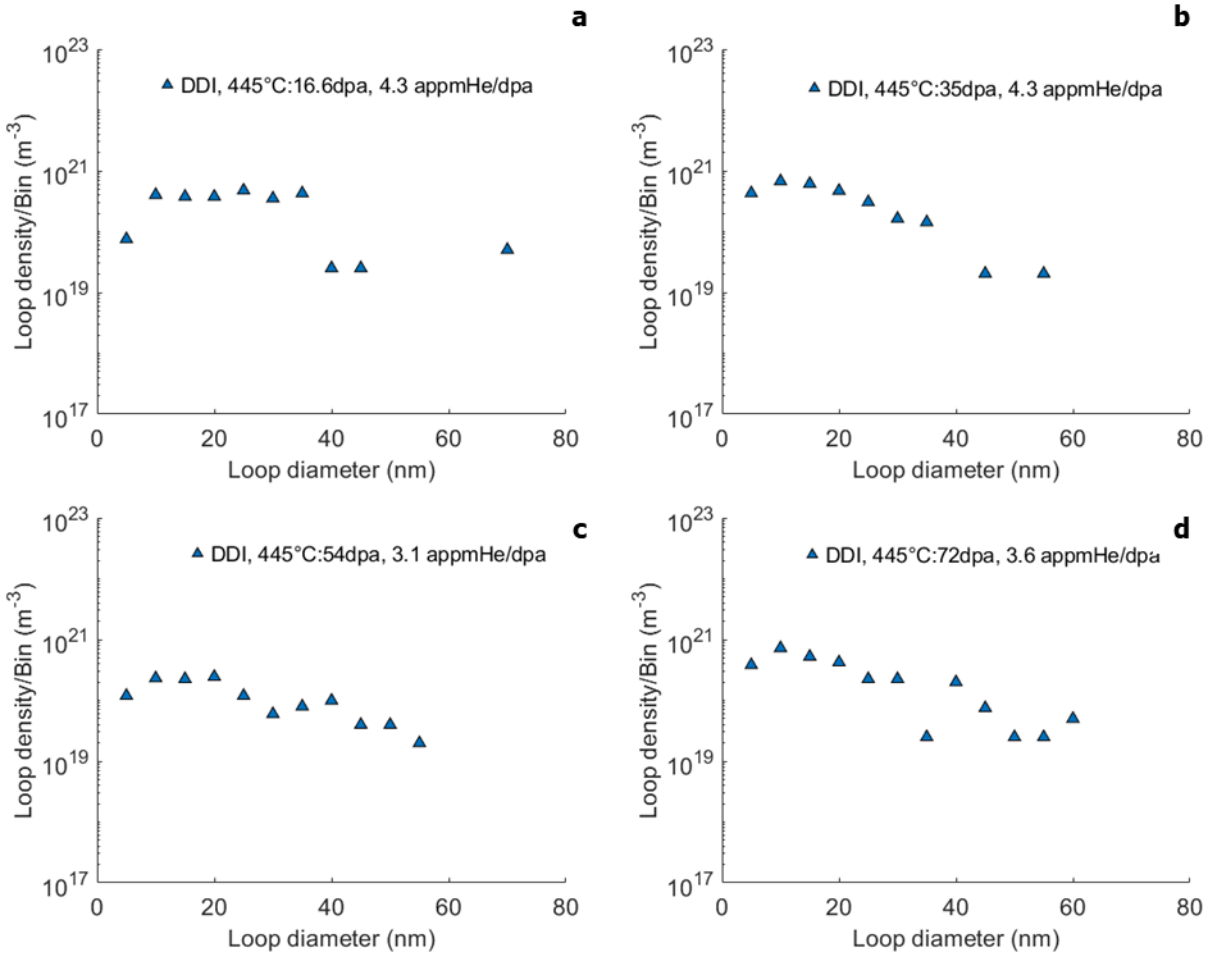


Figure 5.34: Dislocation loop size distributions of dual-ion-irradiated T91 30176 at 445°C to (a) 16.6 dpa, (b) 35 dpa, (c) 54 dpa and (d) 72 dpa.

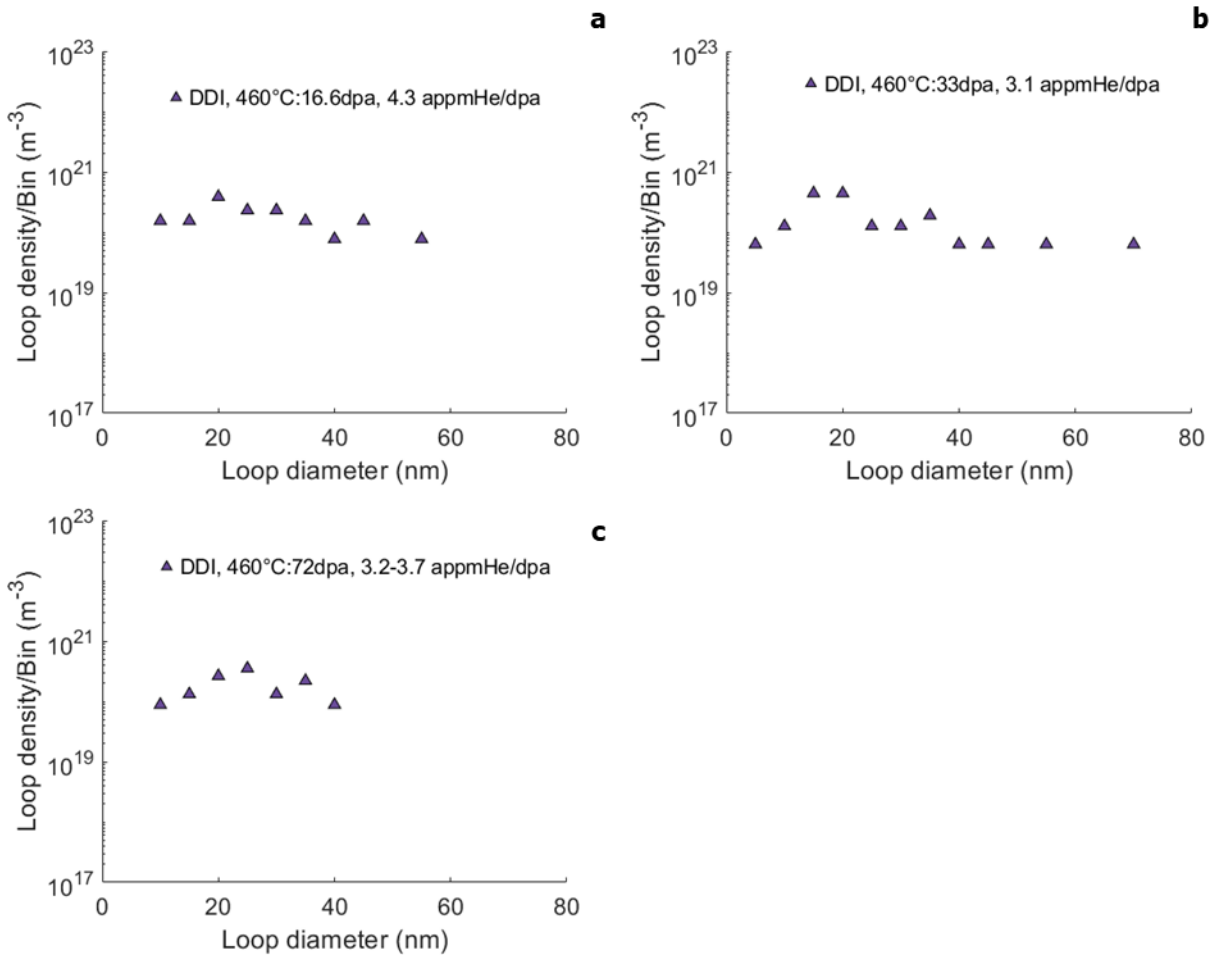


Figure 5.35: Dislocation loop size distributions of dual-ion-irradiated T91 30176 at 460°C to (a) 16.6 dpa, (b) 33 dpa and (c) 72 dpa.

Table 5.10: Dislocation loop microstructures of dual-ion-irradiated T91.

Irradiation mode	Sample	Condition	Loop density ($\times 10^{20}$ m^{-3})	Average loop diameter (nm)	Loop sink strength ($\times 10^{14}$ m^{-2})	Number of loops counted (-)
DDI	092717	445C-4.3Hedpa-16.6dpa	25.9 ± 4.6	25.9 ± 1.9	2.1	103
DDI	053018-1	445C-4.3Hedpa-35dpa	28.4 ± 5.0	19.0 ± 1.4	1.7	139
DDI	070120-1	445C-3.1Hedpa-54dpa	12.8 ± 2.1	24.0 ± 1.7	1.0	66
DDI	102120-1	445C-3.6Hedpa-72dpa	29.0 ± 4.5	21.5 ± 1.5	2.0	79
DDI	092917	460C-4.3Hedpa-16.6dpa	16.2 ± 2.9	29.5 ± 2.1	1.5	59
DDI	071320-1	460C-3.1Hedpa-33dpa	17.7 ± 3.8	27.3 ± 2.0	1.5	28
DDI	091420-1	460C-3.2-3.7Hedpa-72dpa	16.9 ± 3.6	27.0 ± 2.0	1.5	29
DDI	020320	520C-3.2Hedpa-16.6dpa	N/O	N/O	-	0
DDI	091719	520C-4.3Hedpa-28dpa	N/O	N/O	-	0
DDI	110117	570C-4.3Hedpa-15.4dpa	N/O	N/O	-	0
DDI	111219	570C-4.3Hedpa-28dpa	N/O	N/O	-	0

*N/O = Not observed

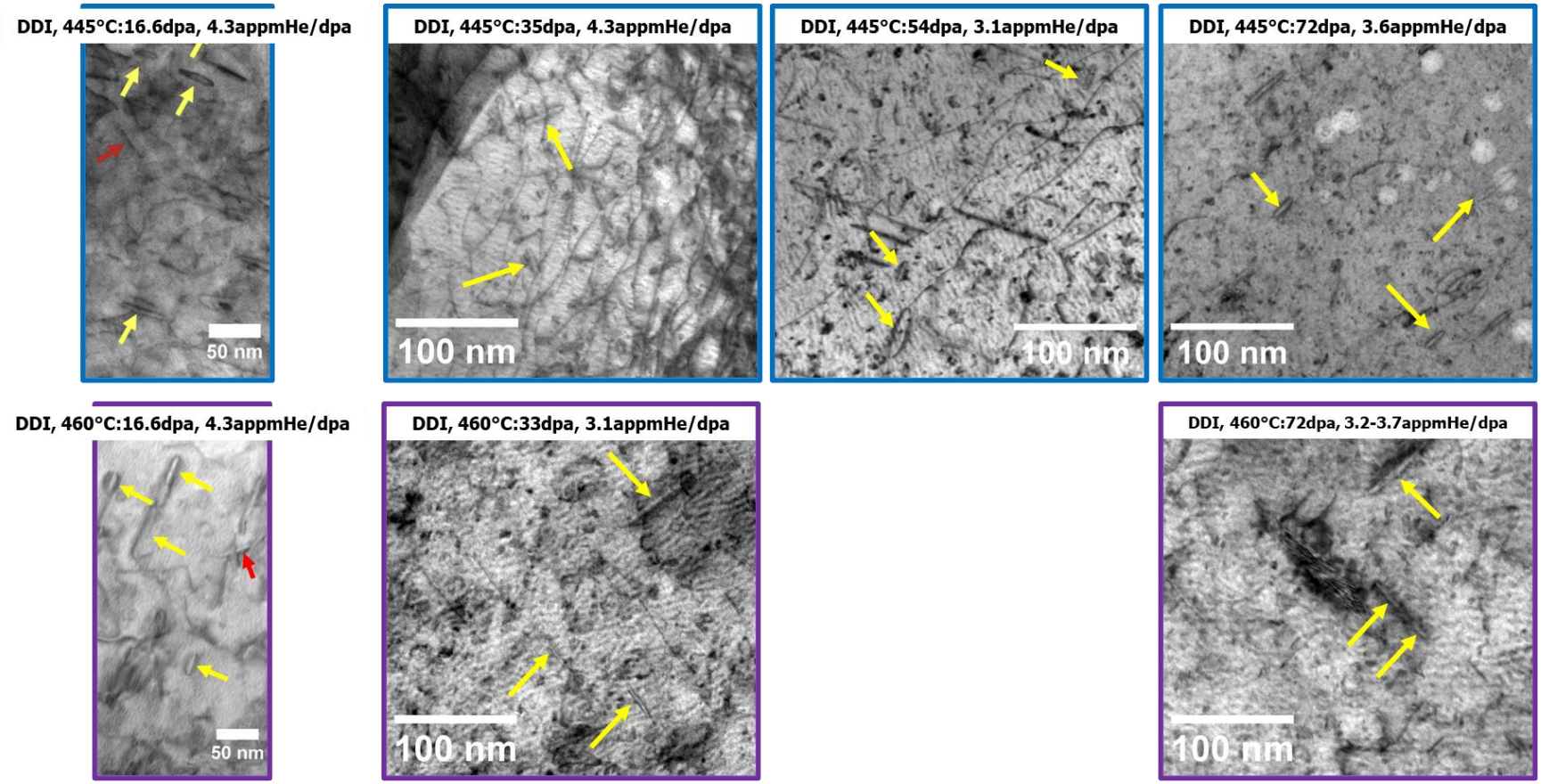


Figure 5.36: STEM BF micrographs of dual-ion-irradiated T91 30176 at 445°C and 460°C. Yellow arrows indicate some a⟨100⟩ loops and red arrows indicate some a/2⟨111⟩ loops.

5.4.3 Radiation-induced segregation

The radiation-induced segregation behavior of Fe, Cr, Ni and Si at grain boundaries was characterized in all dual-ion irradiations. There is a lot of variability in the segregation behavior of Fe and Cr with some samples exhibiting enrichment while others exhibit depletion as shown in Figure 5.37 (a-b). All conditions exhibit Ni and Si enrichment, although they are lower at 570°C compared to lower temperatures as shown in Figure 5.37 (c-d). For Fe, Cr and Ni, damage level does not appear to have an impact on enrichment/depletion at any condition. Enrichment of Si increases slightly with increasing damage level for dual-ion irradiations at 445°C. Results are tabulated in Table 5.11. Representative EDS maps are presented in Figure 5.38, Figure 5.39 and Figure 5.40.

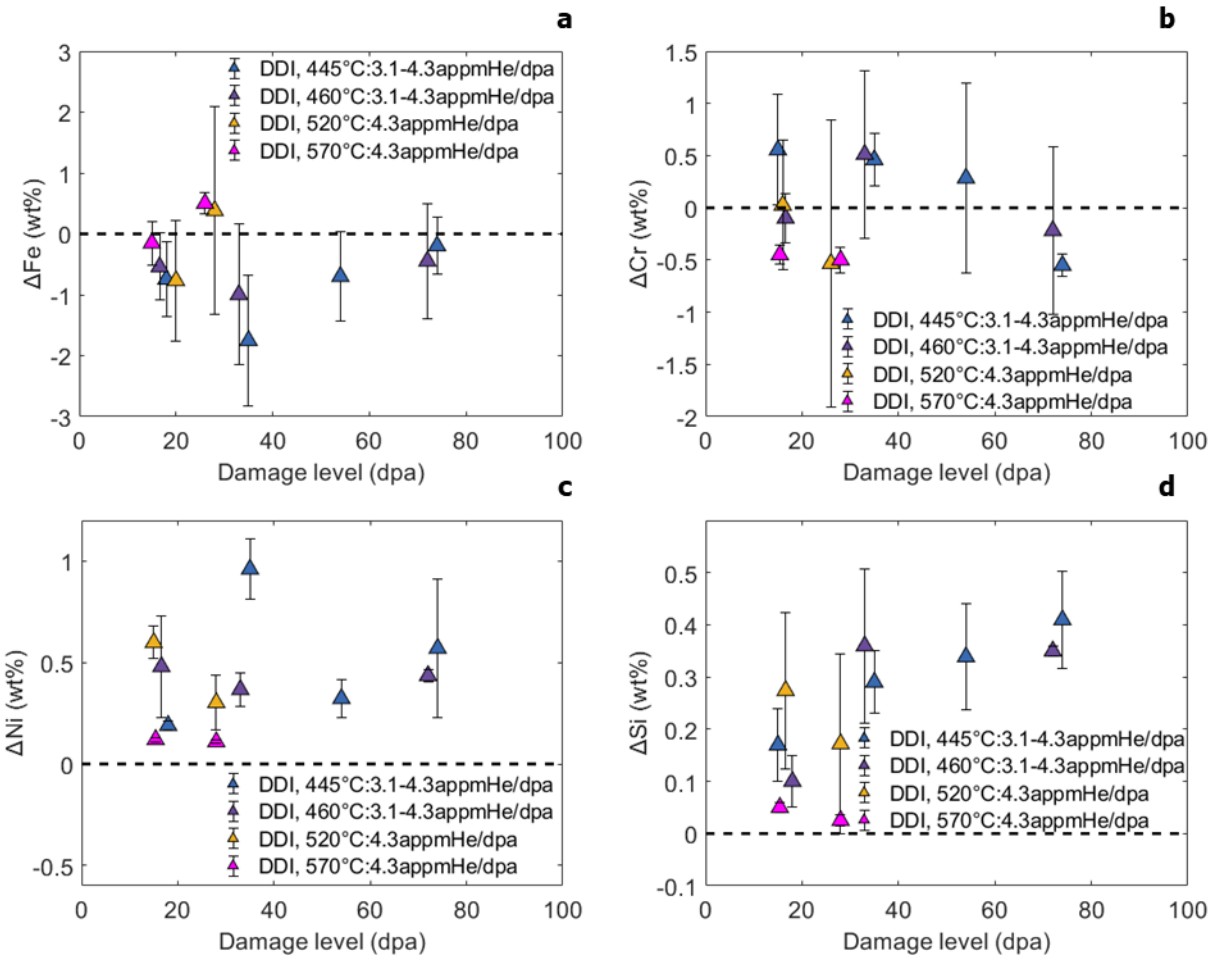


Figure 5.37: (a) Fe, (b) Cr, (c) Ni and (d) Si enrichments at grain boundaries of dual-ion-irradiated T91 30176.

Table 5.11: Radiation-induced segregation of dual-ion-irradiated T91 30176.

Irradiation mode	Sample	Condition	Fe (wt%)		Cr (wt%)		Ni (wt%)		Si (wt%)	
			Peak	ΔFe	Peak	ΔCr	Peak	ΔNi	Peak	ΔSi
DDI	092717	445C-4.3Hedpa-16.6dpa	89.5±0.7	-0.7±0.6	8.2±0.6	0.6±0.5	0.31±0.02	0.19±0.02	0.39±0.02	0.17±0.07
DDI	053018-1	445C-4.3Hedpa-35dpa	87.7±1.1	-1.8±1.1	6.9±0.2	0.5±0.3	1.42±0.15	0.96±0.15	0.75±0.06	0.29±0.06
DDI	070120-1	445C-3.1Hedpa-54dpa	89.1±1.2	-0.7±0.7	8.2±1.1	0.3±0.9	0.45±0.08	0.32±0.09	0.71±0.01	0.34±0.10
DDI	020720	445C-3.2Hedpa-70dpa	89.4±0.3	-0.2±0.5	7.5±0.2	-0.6±0.1	0.72±0.35	0.57±0.34	0.67±0.08	0.41±0.09
DDI	092917	460C-4.3Hedpa-16.6dpa	88.2±1.0	-0.5±0.6	6.3±0.3	-0.1±0.2	0.93±0.24	0.48±0.25	0.55±0.04	0.10±0.05
DDI	071320-1	460C-3.1Hedpa-33dpa	89.2±1.0	-1.0±1.2	8.4±0.7	0.5±0.8	0.49±0.08	0.37±0.08	0.59±0.13	0.36±0.15
DDI	091420-1	460C-3.2-3.7Hedpa-72dpa	89.8±0.2	-0.5±1.0	7.6±0.4	-0.2±0.8	0.57±0.03	0.44±0.03	0.57±0.08	0.35±0.01
DDI	020320	520C-3.2Hedpa-16.6dpa	89.5±1.2	-0.8±1.0	7.6±0.7	0.0±0.6	0.74±0.08	0.60±0.08	0.49±0.16	0.27±0.15
DDI	091719	520C-4.3Hedpa-28dpa	90.7±2.2	0.4±1.7	7.0±1.8	-0.5±1.4	0.41±0.14	0.30±0.14	0.44±0.17	0.17±0.17
DDI	110117	570C-4.3Hedpa-15.4dpa	88.4±0.4	-0.2±0.4	7.1±0.1	-0.5±0.1	0.23±0.01	0.12±0.01	0.30±0.01	0.05±0.01
DDI	111219	570C-4.3Hedpa-28dpa	90.7±0.1	0.5±0.2	7.5±0.1	-0.5±0.1	0.22±0.00	0.11±0.01	0.23±0.00	0.03±0.01

*Values estimated from [16]

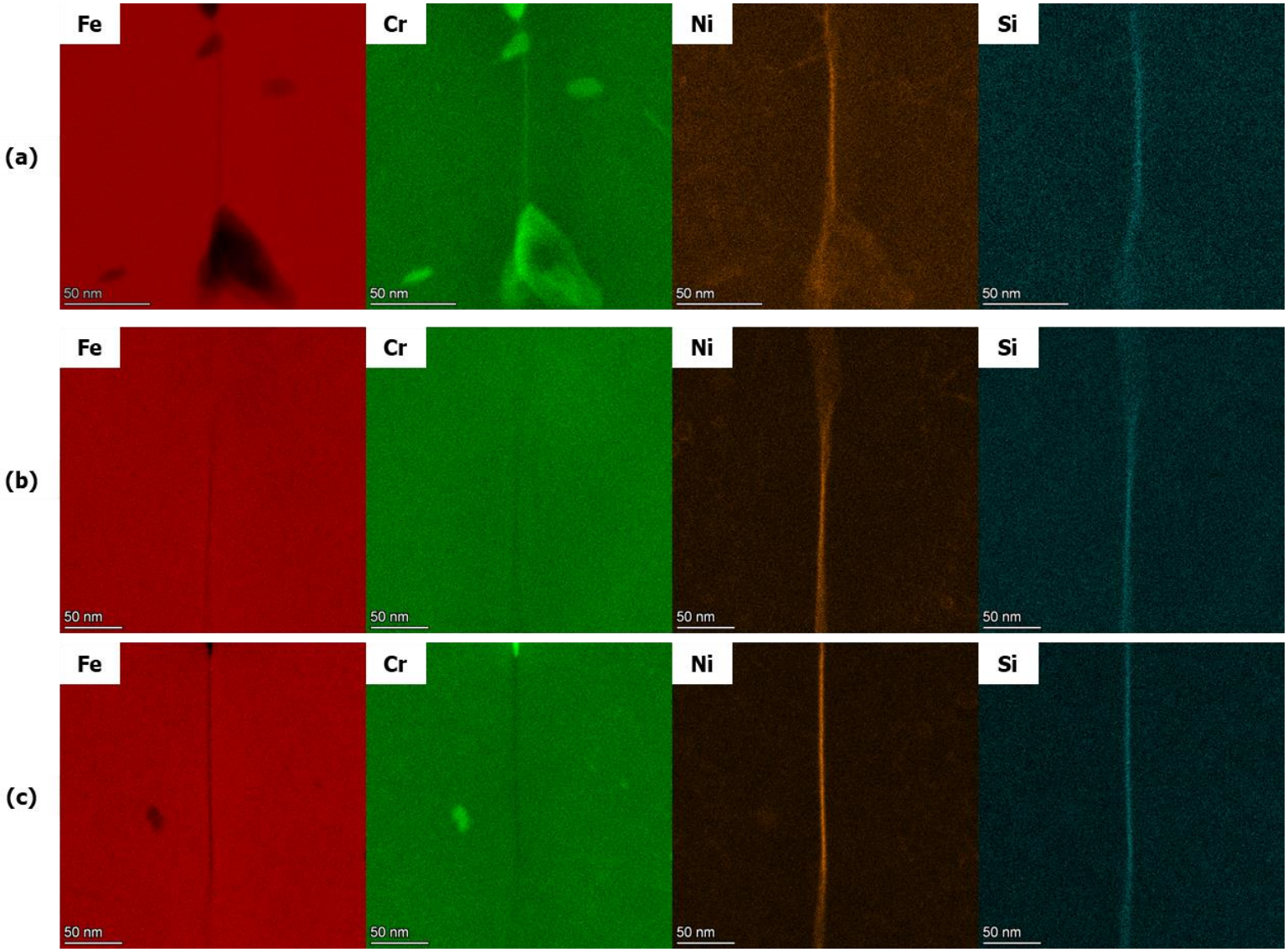


Figure 5.38: EDS (wt%) maps of Fe, Cr, Ni and Si of dual-ion-irradiated T91 30176 at 445°C:3.1-4.3appmHe/dpa to (a) 16.6 dpa, (b) 54 dpa and (c) 70 dpa.

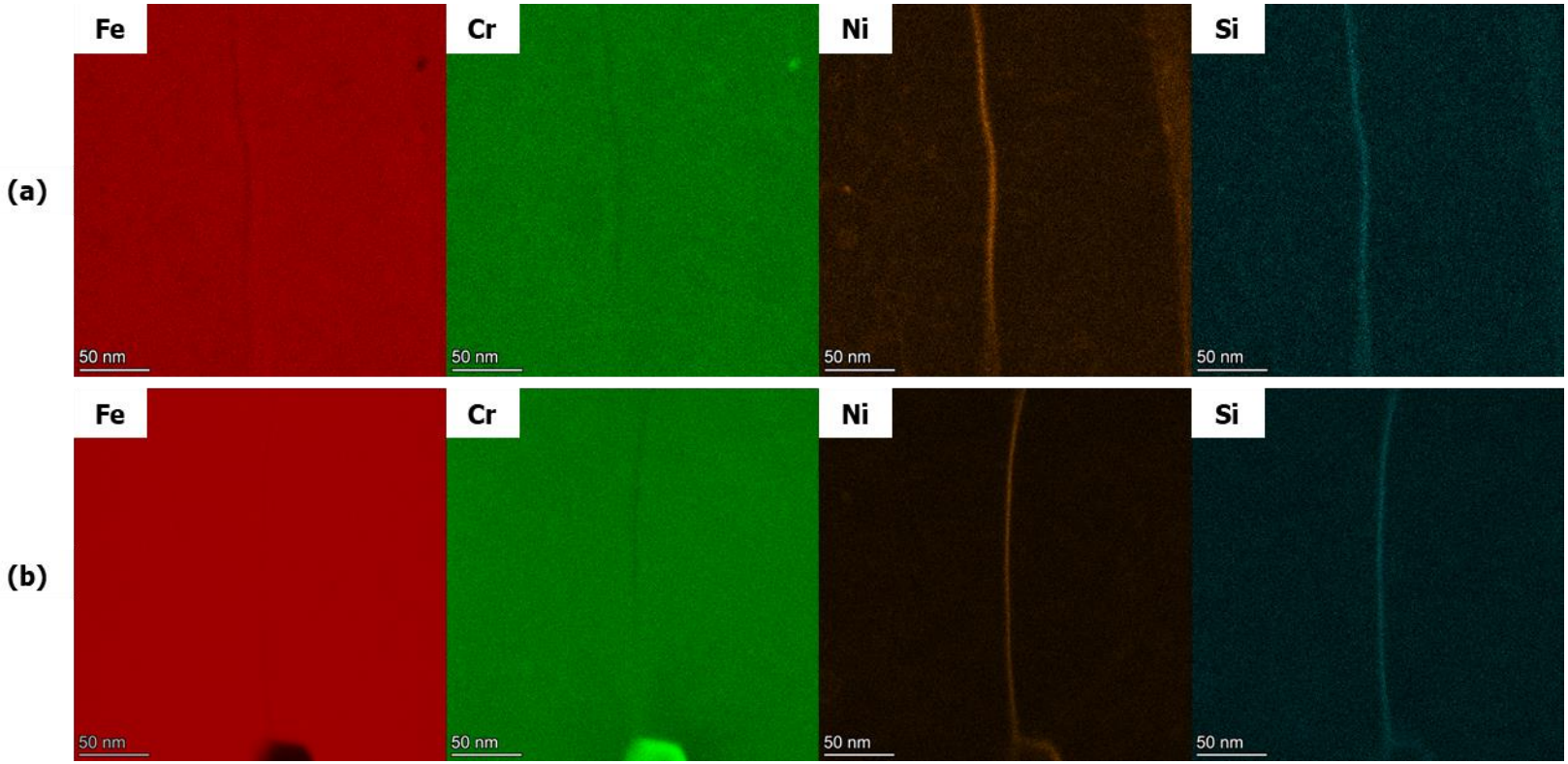


Figure 5.39: EDS (wt%) maps of Fe, Cr, Ni and Si of dual-ion-irradiated T91 30176 at 460°C:3.1-4.3appmHe/dpa to (a) 33 dpa and (b) 72 dpa.

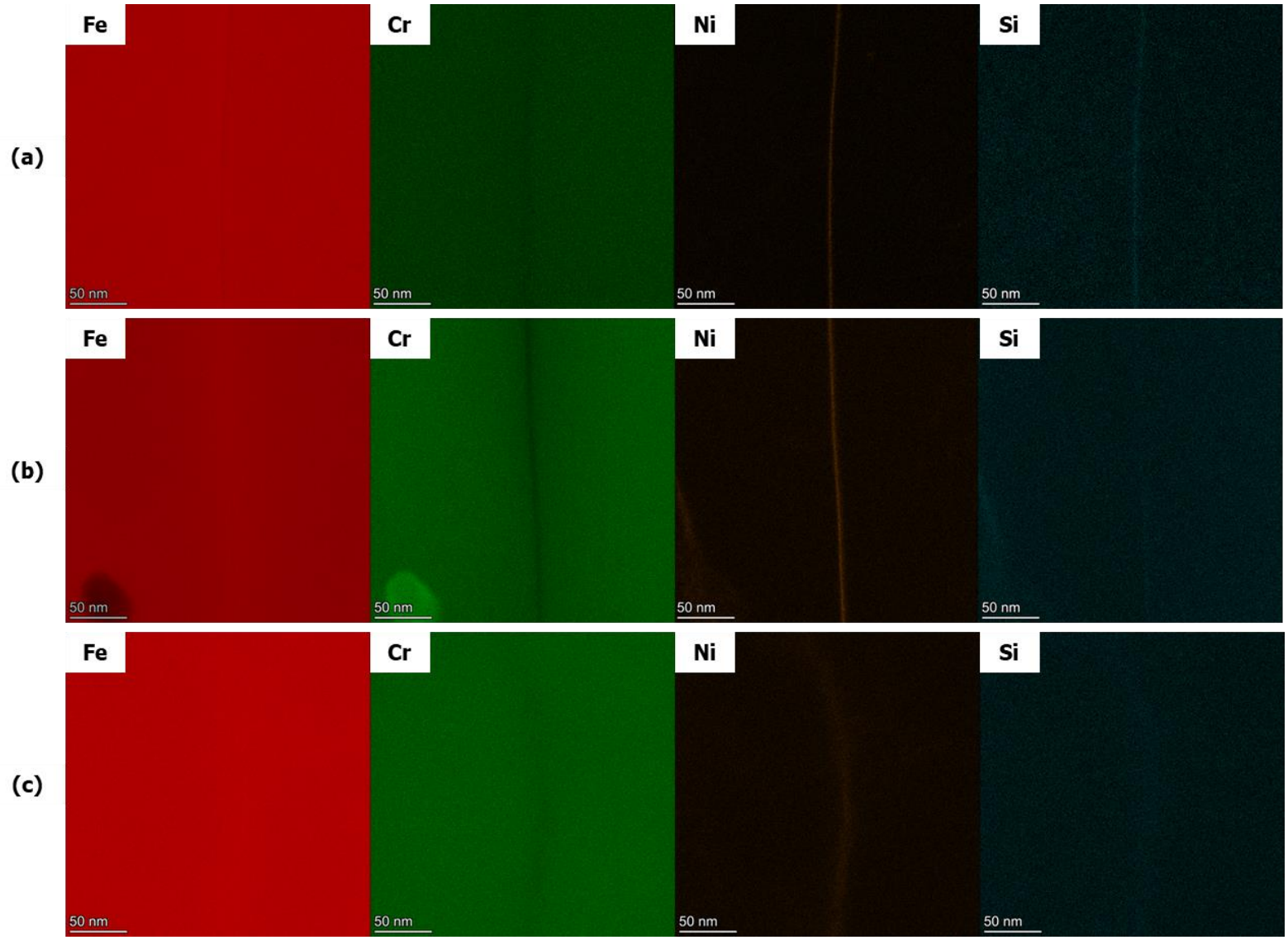


Figure 5.40: EDS (wt%) maps of Fe, Cr, Ni and Si of dual-ion-irradiated T91 30176 at 520°C:3.2-4.3appmHe/dpa to (a) 16.6 dpa and (b) 28 dpa and (c) at 570°C:4.3appmHe/dpa to 28 dpa.

5.4.4 Radiation-induced precipitation

The formation of Ni-Si-Mn clusters was characterized in all dual-ion irradiation conditions. Clusters are observed at 445 and 460°C at all damage levels but not at 520°C or 570°C. Figure 5.41 shows the evolution of Ni-Si-Mn cluster density, average void diameter and volume fraction as a function of damage level. The cluster density, average cluster diameter and volume fraction appear constant across damage levels. The size distributions are presented in Figure 5.42 and Figure 5.43. Results are tabulated in Table 5.12. EDS Ni maps are presented in Figure 5.44 and Figure 5.45.

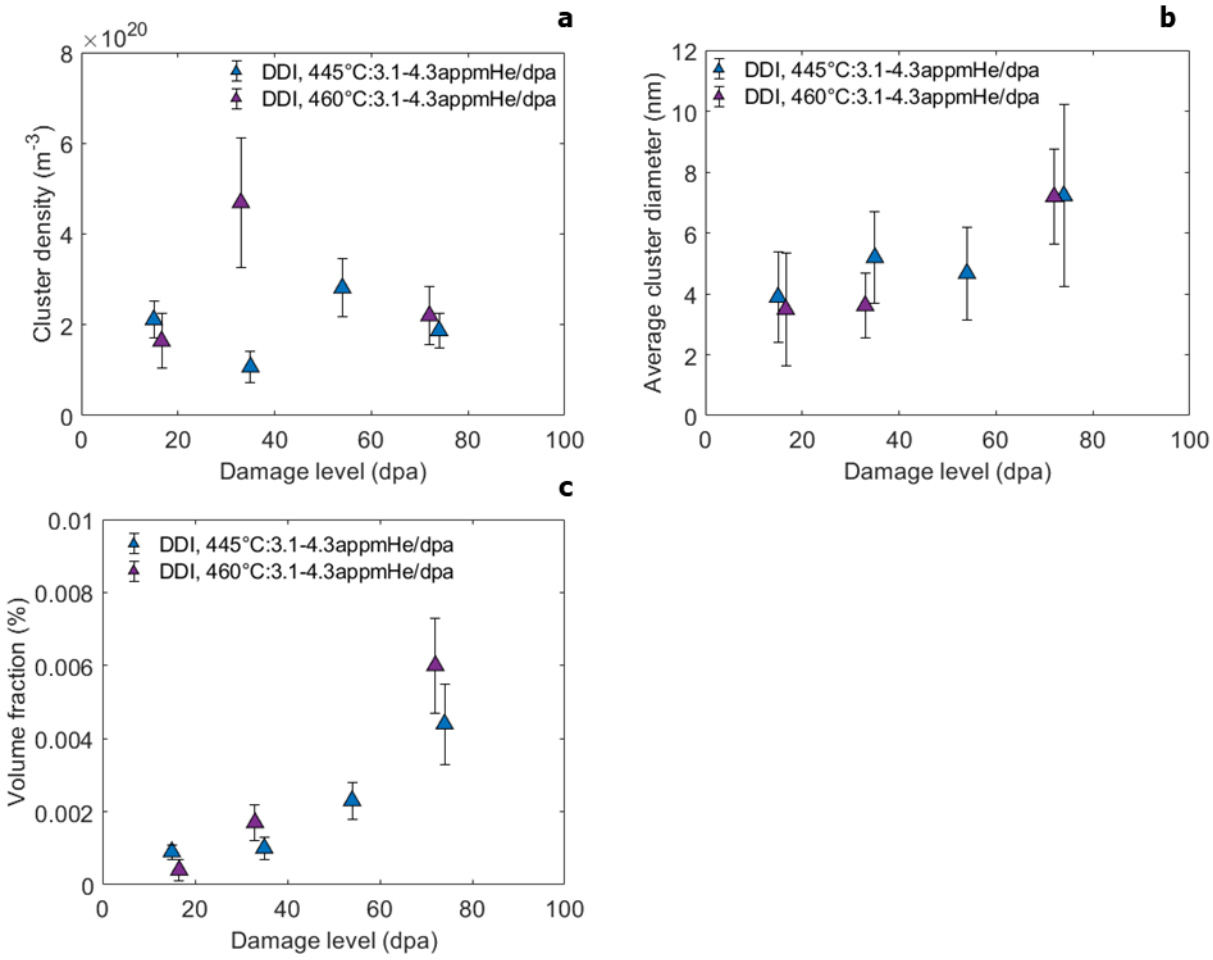


Figure 5.41: (a) Cluster density, (b) average cluster diameter and (c) volume fraction of dual-ion-irradiated T91 30176.

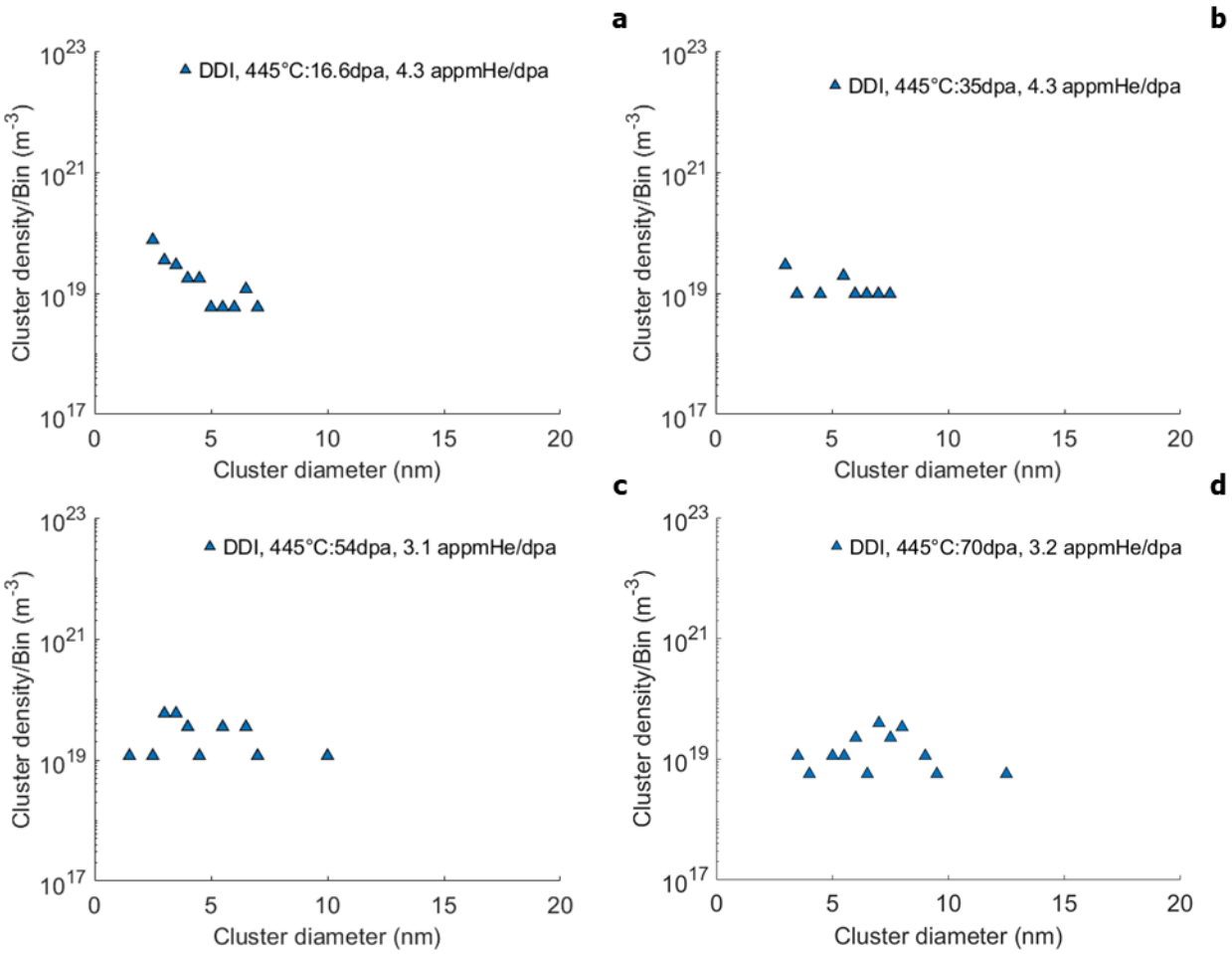


Figure 5.42: Cluster size distributions of dual-ion-irradiated T91 30176 at 445°C to (a) 16.6 dpa, (b) 35 dpa, (c) 54 dpa and (d) 70 dpa.

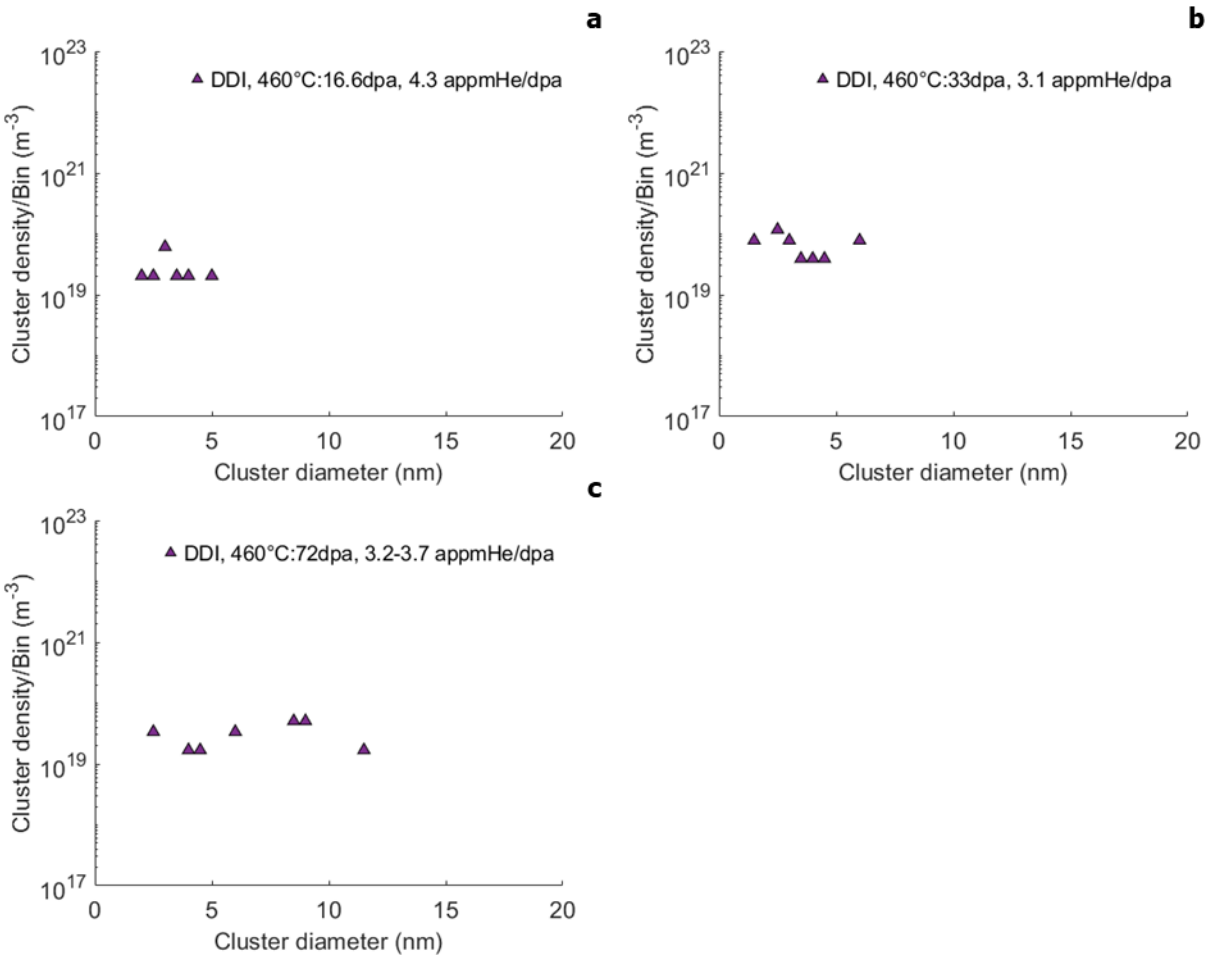


Figure 5.43: Cluster size distributions of dual-ion-irradiated T91 at 460°C to (a) 16.6 dpa, (b) 33 dpa, and (c) 72 dpa.

Table 5.12: Ni/Si-cluster microstructures of dual-ion-irradiated T91 30176.

Irradiation mode	Sample	Condition	Cluster density ($\times 10^{20}$ m^{-3})	Average cluster diameter (nm)	Volume fraction (%)	Number of clusters counted (-)
DDI	092717	445C-4.3Hedpa-16.6dpa	2.1 ± 0.4	3.9 ± 1.5	0.0009 ± 0.0002	36
DDI	053018-1	445C-4.3Hedpa-35dpa	1.1 ± 0.3	5.2 ± 1.5	0.001 ± 0.0003	11
DDI	070120-1	445C-3.1Hedpa-54dpa	2.8 ± 0.6	4.7 ± 1.5	0.0023 ± 0.0005	24
DDI	020720	445C-3.2Hedpa-70dpa	1.9 ± 0.4	7.2 ± 3.0	0.0044 ± 0.0011	33
DDI	092917	460C-4.3Hedpa-16.6dpa	1.6 ± 0.6	3.5 ± 1.9	0.0004 ± 0.0003	8
DDI	071320-1	460C-3.1Hedpa-33dpa	4.7 ± 1.4	3.6 ± 1.1	0.0017 ± 0.0005	12
DDI	091420-1	460C-3.2-3.7Hedpa-72dpa	2.2 ± 0.6	7.2 ± 1.6	0.006 ± 0.0013	13
DDI	020320	520C-3.2Hedpa-16.6dpa	N/O	N/O	-	0
DDI	091719	520C-4.3Hedpa-28dpa	N/O	N/O	-	0
DDI	110117	570C-4.3Hedpa-15.4dpa	N/O	N/O	-	0
DDI	111219	570C-4.3Hedpa-28dpa	N/O	N/O	-	0

*N/O = Not observed

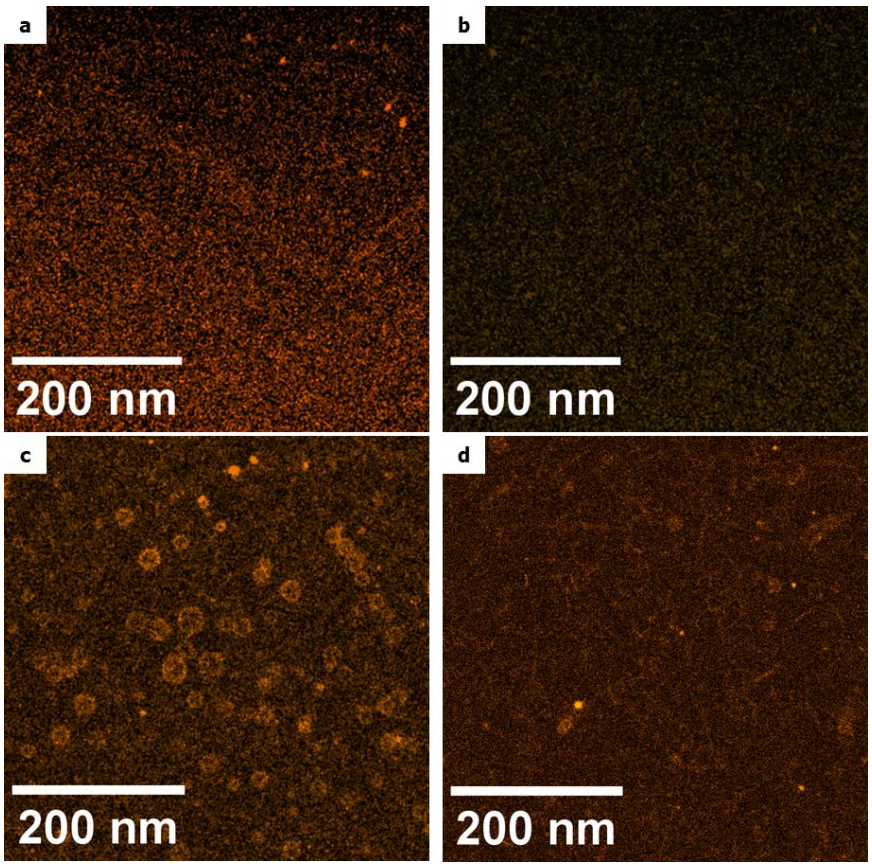


Figure 5.44: EDS Ni map (wt%) of dual-ion-irradiated T91 30176 at 445°C:3.1-4.3appmHe/dpa to (a) 16.6 dpa, (b) 35 dpa, (c) 54 dpa and (d) 70 dpa.

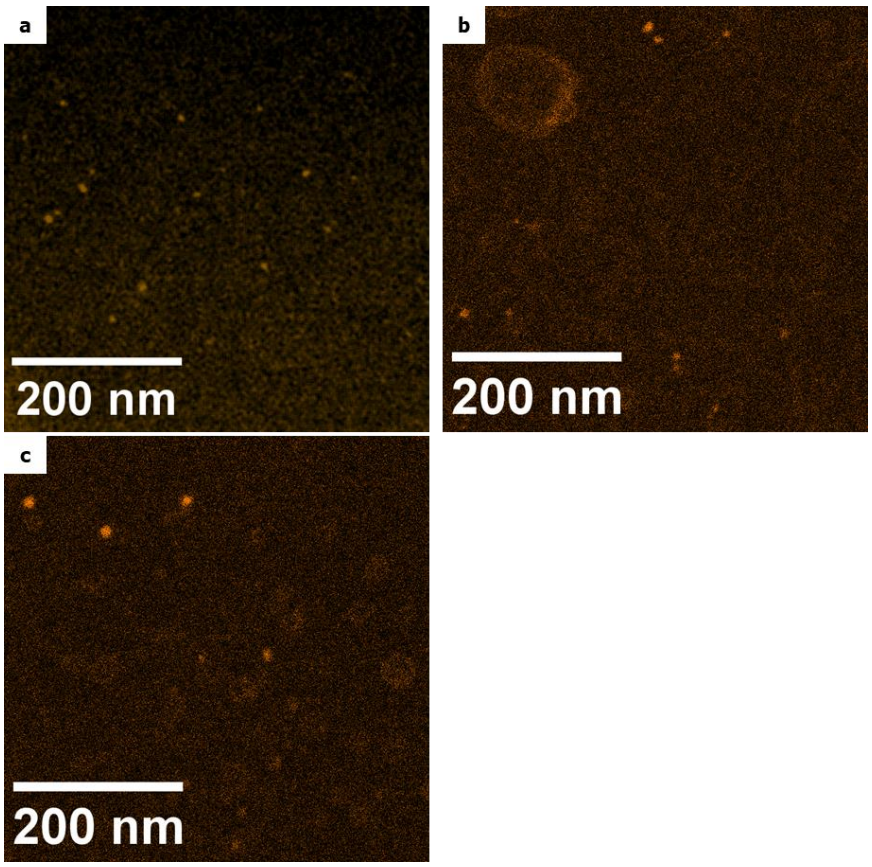


Figure 5.45: EDS Ni map (wt%) of dual-ion-irradiated T91 30176 at 460°C:3.1-4.3appmHe/dpa to (a) 16.6 dpa, (b) 33 dpa and (c) 72 dpa.

5.5 FFTF

5.5.1 Cavity microstructures

The cavity microstructure evolution was characterized in all FFTF conditions via STEM-HAADF and CTEM-BF through-focus imaging. As shown in Figure 5.46 and Figure 5.47, swelling, void density and average void diameter increase with increasing damage level in FFTF samples (except at 184 dpa). Average bubble diameter is comparable across all conditions as shown in Figure 5.48 despite an increase in bubble density at 184 dpa.

The cavity size distributions are presented in Figure 5.49. In all FFTF conditions, a valley is present between the bubble and void distributions around 5 nm in diameter. The densities of cavities between 5 and 20 nm in diameter remain constant with increasing damage level while the overall size distribution extends to larger void diameters.

Results are tabulated in Table 5.13 and representative STEM-HAADF micrographs are shown in Figure 5.50.

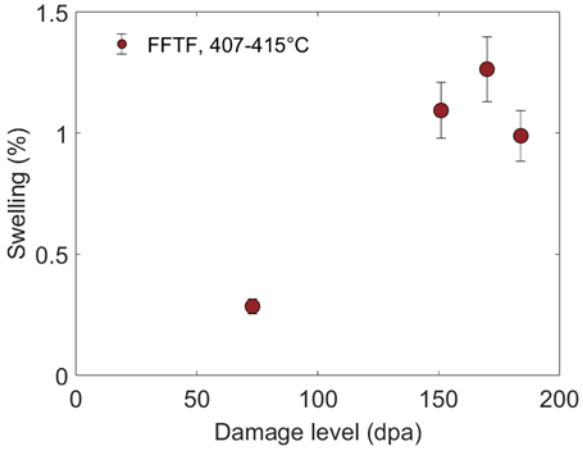


Figure 5.46: Swelling of FFTF-irradiated T91 30176 as a function of damage level.

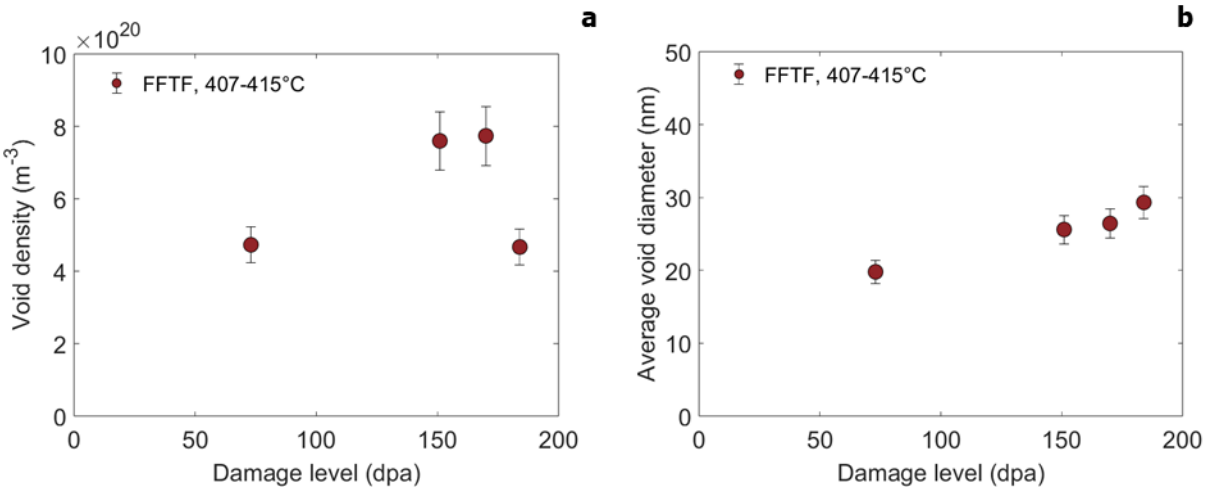


Figure 5.47: (a) Void density and (b) average void diameter of FFTF-irradiated T91 30176 as a function of damage level.

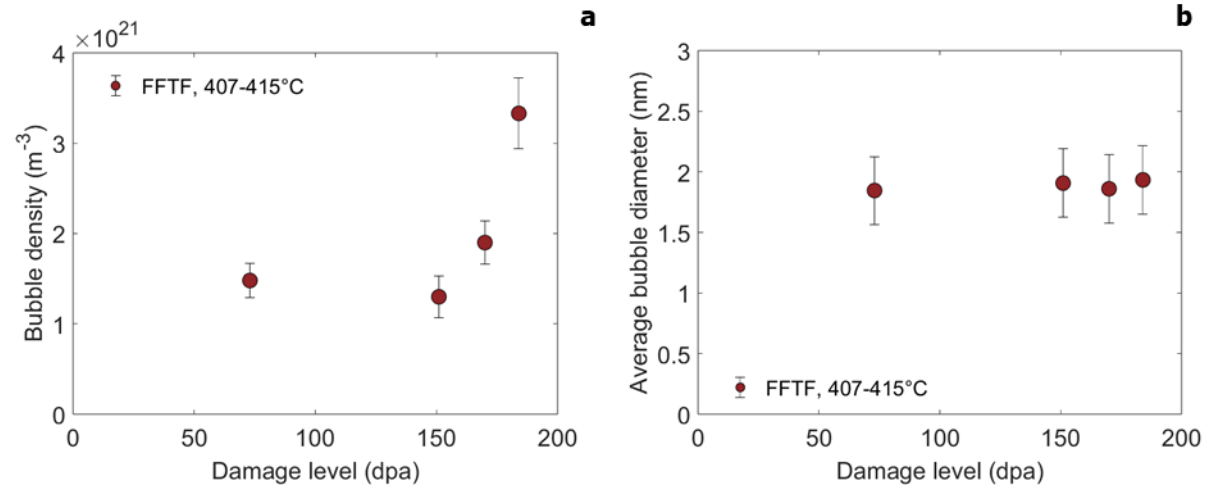


Figure 5.48: (a) Bubble density, (b) average bubble diameter of FFTF-irradiated T91 30176 as a function of damage level.

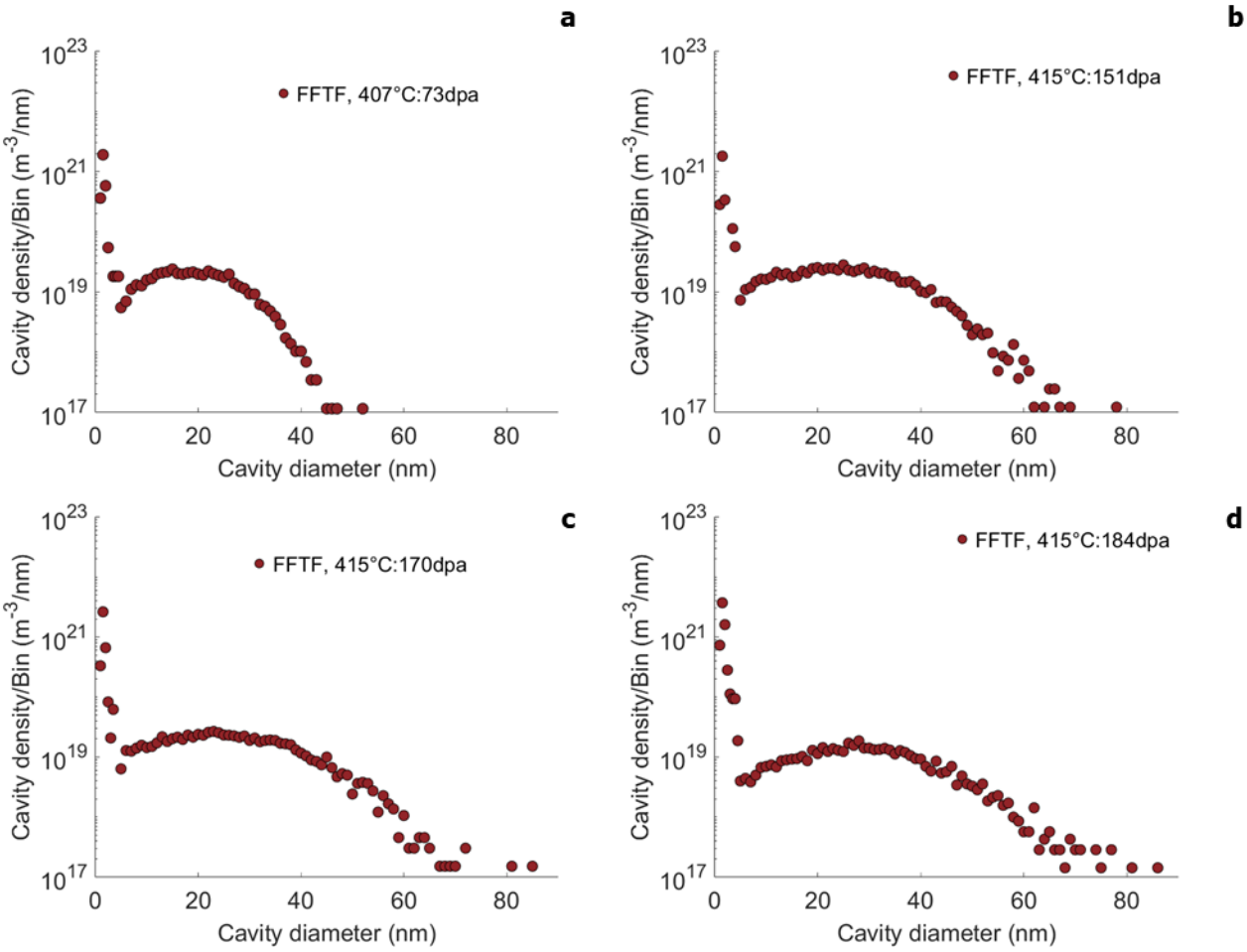


Figure 5.49: Cavity size distributions of FFTF-irradiated T91 30176 to (a) 73 dpa, (b) 151 dpa, (c) 170 dpa and (d) 184 dpa.

Table 5.13: Cavity microstructures of FFTF-irradiated T91 30176.

Irradiation mode	Sample	Condition	Swelling (%)	Bubble density ($\times 10^{20}$ m^{-3})	Average bubble diameter (nm)	Void density ($\times 10^{20}$ m^{-3})	Average void diameter (nm)	Number of bubbles/ voids counted (-)
FFTF	VH03	407C-0.21Hedpa-73dpa	0.28 ± 0.03	14.8 ± 1.9	1.85 ± 0.28	4.7 ± 0.5	19.8 ± 1.6	163/4135
FFTF	VH20	415C-0.21Hedpa-151dpa	1.09 ± 0.12	13.0 ± 2.3	1.91 ± 0.28	7.6 ± 0.8	25.6 ± 1.9	46/6266
FFTF	NP04	415C-0.21Hedpa-170dpa	1.26 ± 0.13	19.0 ± 2.4	1.86 ± 0.28	7.7 ± 0.8	26.4 ± 2.0	183/5125
FFTF	FA33	415C-0.21Hedpa-184dpa	0.99 ± 0.10	33.3 ± 3.9	1.93 ± 0.28	4.7 ± 0.5	29.3 ± 2.2	356/3287

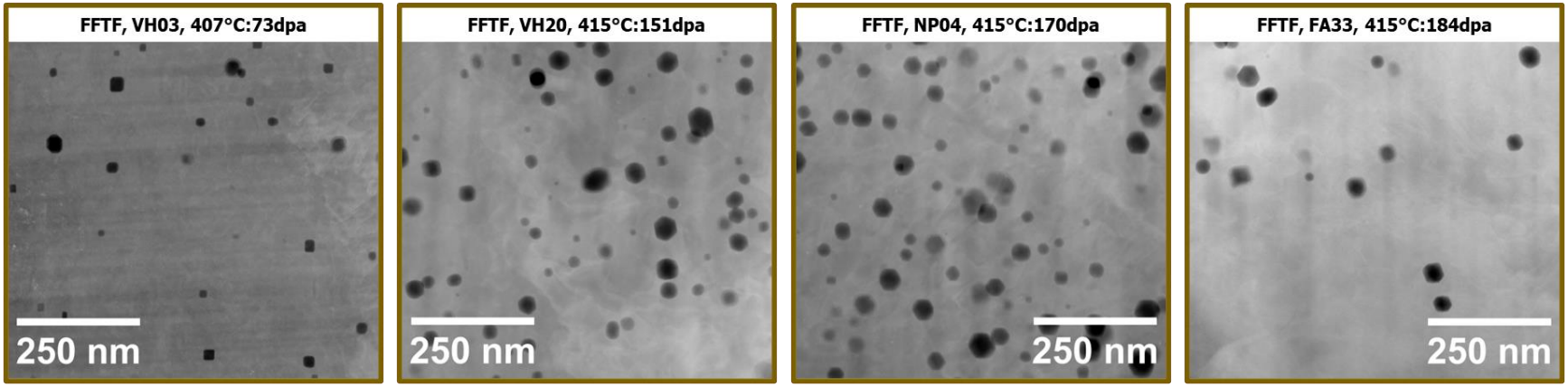


Figure 5.50: STEM HAADF micrographs of FFTF-irradiated T91 30176.

5.5.2 Dislocation loop microstructures

The loop microstructure evolution was characterized in all FFTF conditions via on-zone STEM-BF imaging. Out of 100 dislocation loops observed in total, only 3 were of a/2⟨111⟩ type across all conditions. The loop densities and average void diameters shown in Figure 5.51 indicate that damage level does not appear to have a significant impact on loop microstructure beyond 73 dpa. STEM BF micrographs are presented in Figure 5.52 and results are tabulated in Table 5.14.

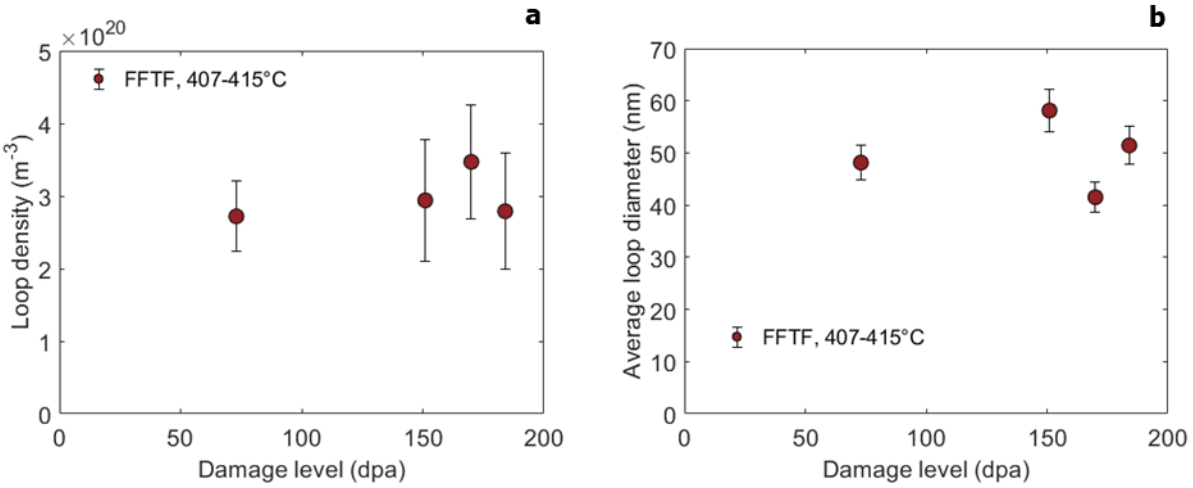


Figure 5.51: (a) Loop density and (b) average loop diameter of FFTF-irradiated T91 30176 as a function of damage level.

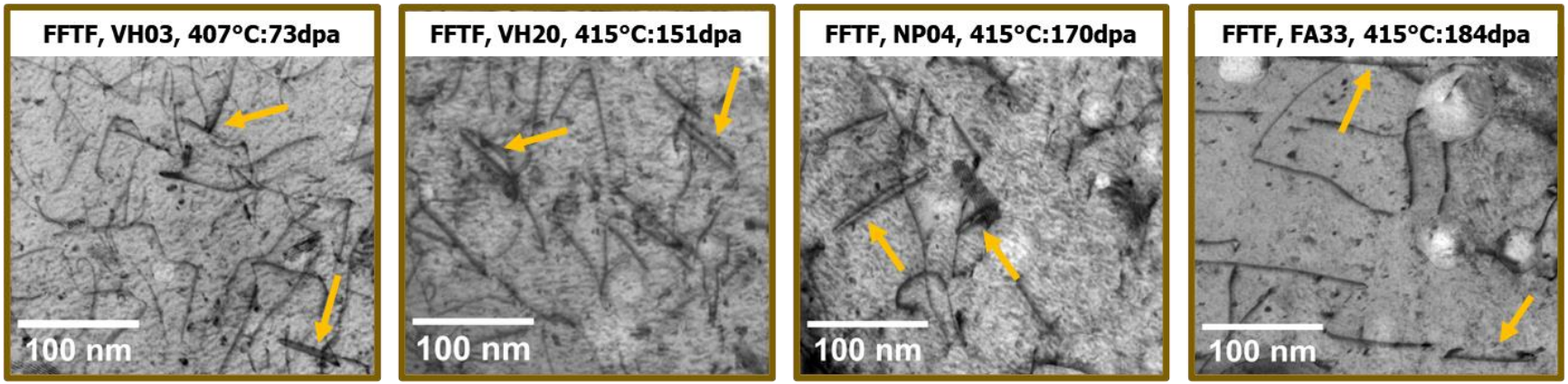


Figure 5.52: STEM BF micrographs of FFTF-irradiated T91 30176.

Table 5.14: Dislocation loop microstructures of FFTF-irradiated T91 30176.

Irradiation mode	Sample	Condition	Loop density ($\times 10^{20}$ m^{-3})	Average loop diameter (nm)	Loop sink strength ($\times 10^{14}$ m^{-2})	Number of loops counted (-)
FFTF	VH03	407C-0.21Hedpa-73dpa	2.7 ± 0.5	48.1 ± 3.4	0.4	47
FFTF	VH20	415C-0.21Hedpa-151dpa	2.9 ± 0.8	58.1 ± 4.0	0.5	14
FFTF	NP04	415C-0.21Hedpa-170dpa	3.5 ± 0.8	41.5 ± 2.9	0.5	25
FFTF	FA33	415C-0.21Hedpa-184dpa	2.8 ± 0.8	51.4 ± 3.6	0.4	14

5.5.3 Radiation-induced segregation

The radiation-induced segregation behavior of Fe, Cr, Ni and Si at grain boundaries was characterized in all FFTF conditions. Results are tabulated in Table 5.15.

Clear enrichment in Cr, Ni and Si and depletion in Fe is observed in FFTF without any clear trend with increasing damage level as shown in Figure 5.53. Representative EDS maps are presented in Figure 5.54 and Figure 5.55.

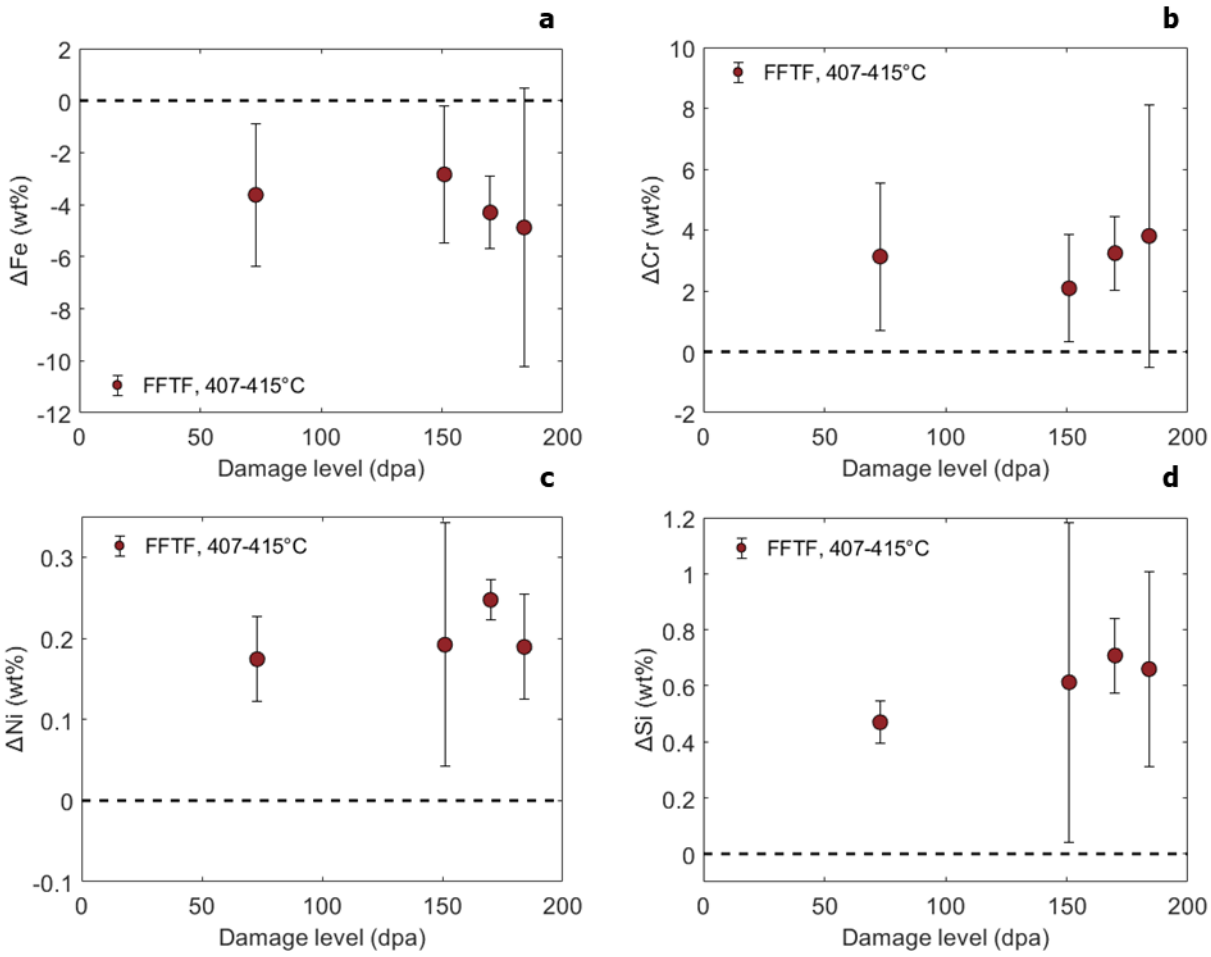


Figure 5.53: (a) Fe, (b) Cr, (c) Ni and (d) Si enrichments at grain boundaries of FFTF-irradiated T91 30176.

Table 5.15: Radiation-induced segregation of FFTF-irradiated T91 30176.

Irradiation mode	Sample	Condition	Fe (wt%)		Cr (wt%)		Ni (wt%)		Si (wt%)	
			Peak	ΔFe	Peak	ΔCr	Peak	ΔNi	Peak	ΔSi
FFTF	VH03	407C-0.21Hedpa-73dpa	87.1±2.5	-3.6±2.8	10.3±2.3	3.1±2.4	0.25±0.04	0.17±0.05	0.67±0.05	0.47±0.07
FFTF	VH20	415C-0.21Hedpa-151dpa	87.5±2.4	-2.8±2.7	9.7±1.4	2.1±1.8	0.27±0.15	0.19±0.15	0.84±0.61	0.61±0.57
FFTF	NP04	415C-0.21Hedpa-170dpa	85.4±2.3	-4.3±1.4	11.3±1.7	3.2±1.2	0.34±0.04	0.25±0.02	0.97±0.18	0.71±0.13
FFTF	FA33	415C-0.21Hedpa-184dpa	85.4±4.7	-4.9±5.4	11.4±3.8	3.8±4.3	0.29±0.07	0.19±0.06	0.94±0.31	0.66±0.35

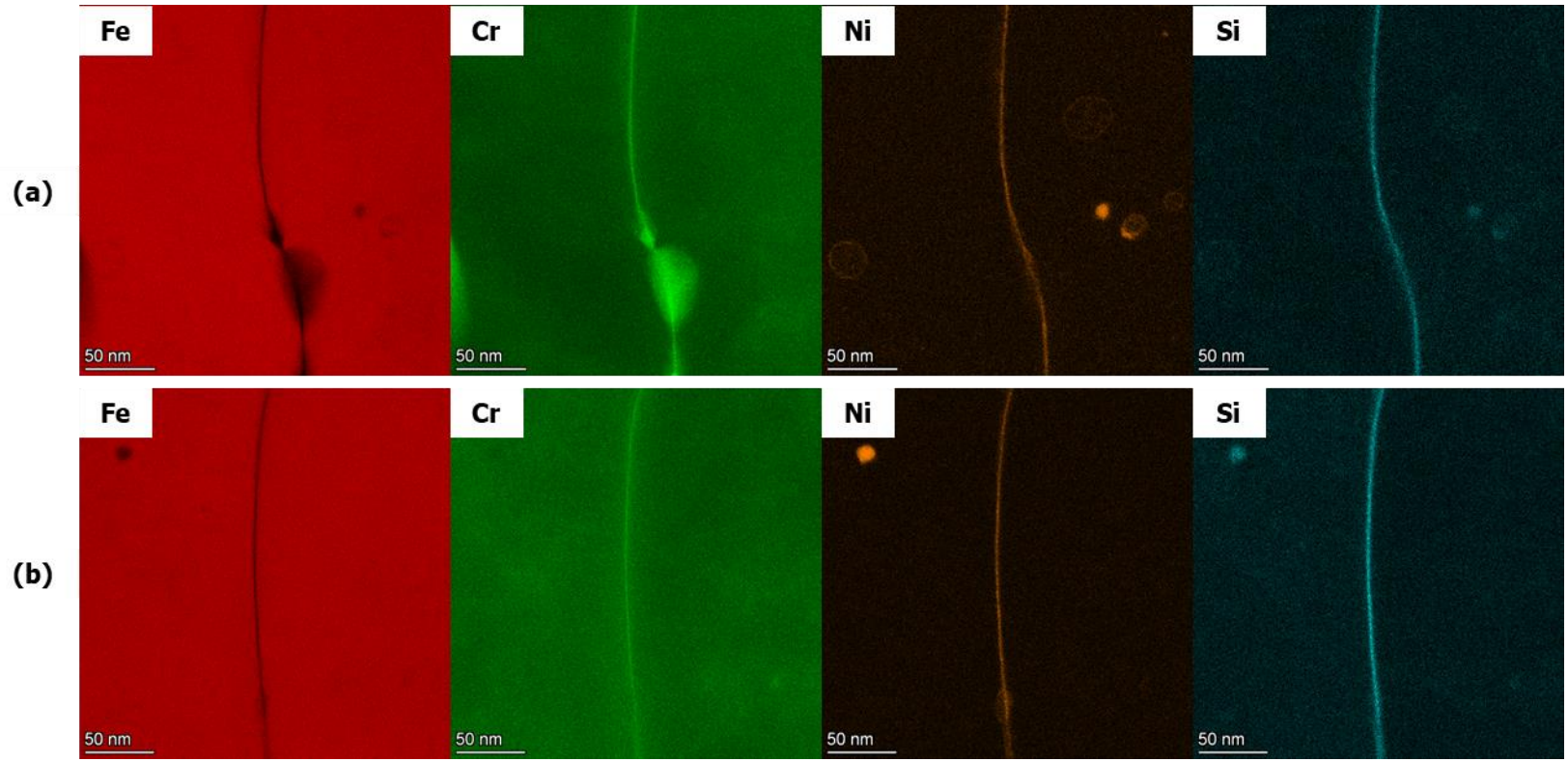


Figure 5.54: EDS (wt%) maps of Fe, Cr, Ni and Si of FFTF-irradiated T91 30176 at (a) 407°C:73dpa and (b) 415°C:151dpa.

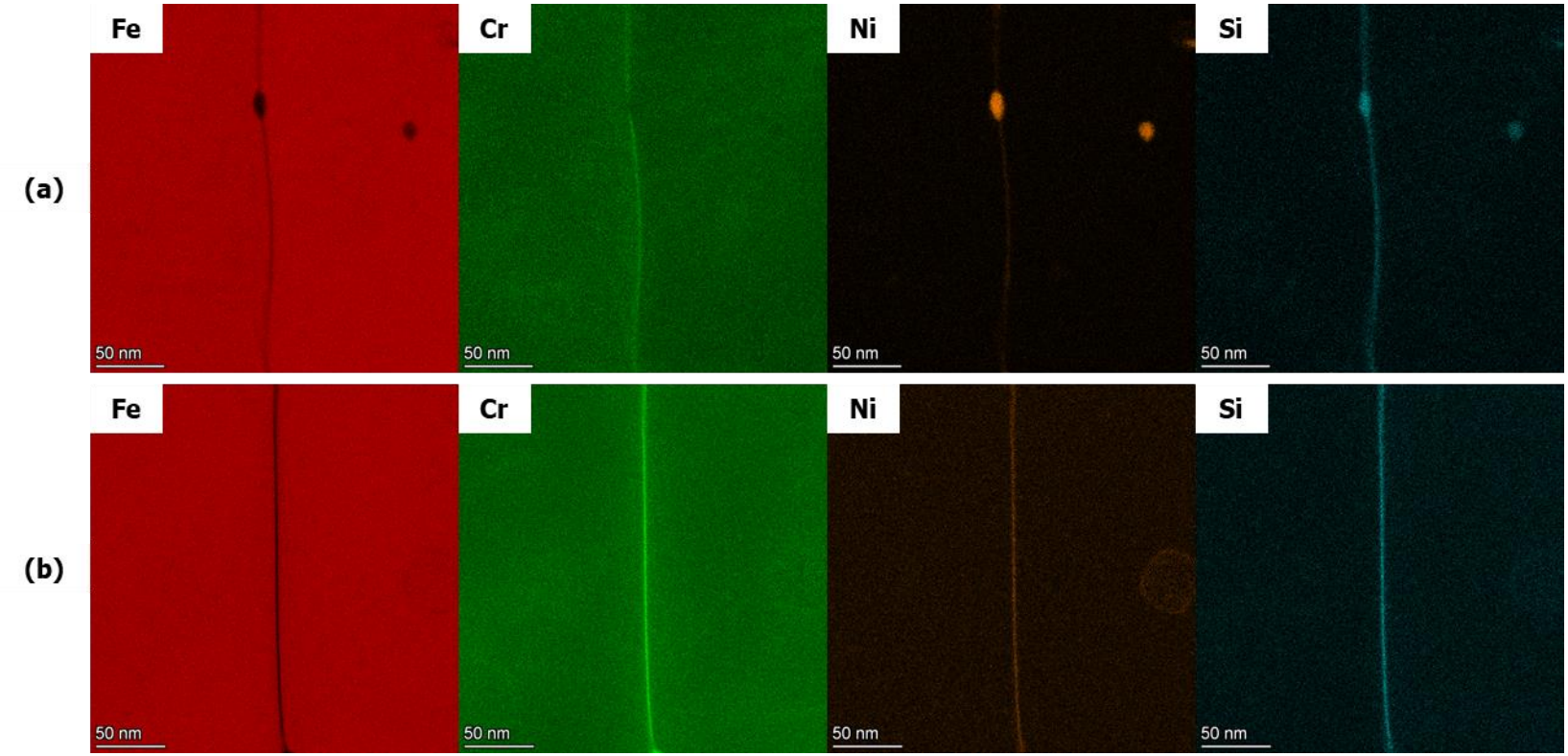


Figure 5.55: EDS (wt%) maps of Fe, Cr, Ni and Si of FFTF-irradiated T91 30176 at (a) 415°C:170dpa and (b) 415°C:184dpa.

5.5.4 Radiation-induced precipitation

Ni-Si-Mn clusters were characterized in all FFTF conditions. Figure 5.56 shows the evolution of cluster density, average cluster diameter and volume fraction as a function of damage level for all samples. The cluster density decreases between 72 and 184 dpa while the average diameter slightly increases. The volume fraction remains relatively constant at all damage levels.

FFTF cluster size distributions presented in Figure 5.57 indicate that the density of clusters smaller than 10nm in diameter decreases with increasing damage level while the density of clusters larger than 12nm increases. Results are tabulated in Table 5.16. EDS Ni maps are presented in Figure 5.58.

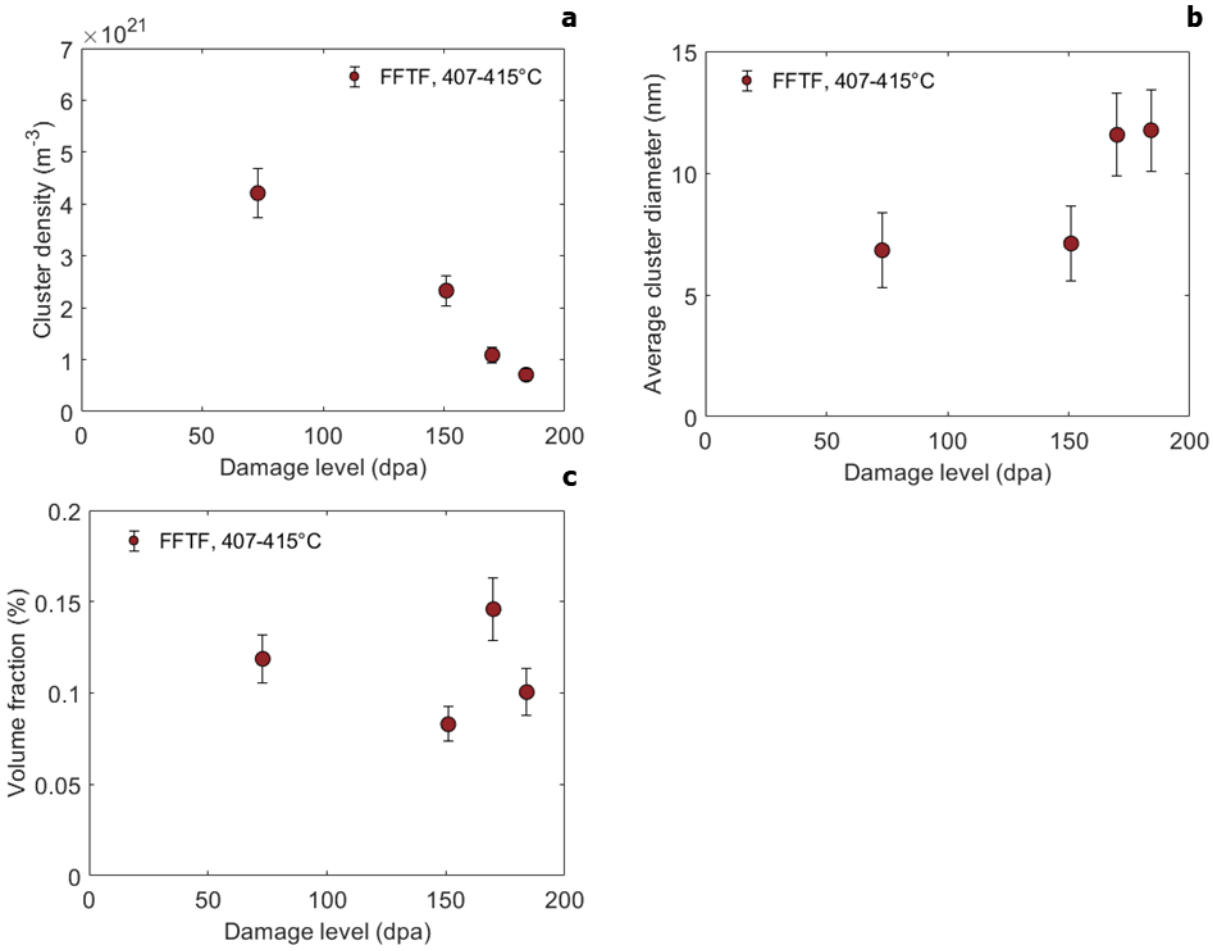


Figure 5.56: (a) Cluster density, (b) average cluster diameter and (c) volume fraction of FFTF-irradiated T91 30176.

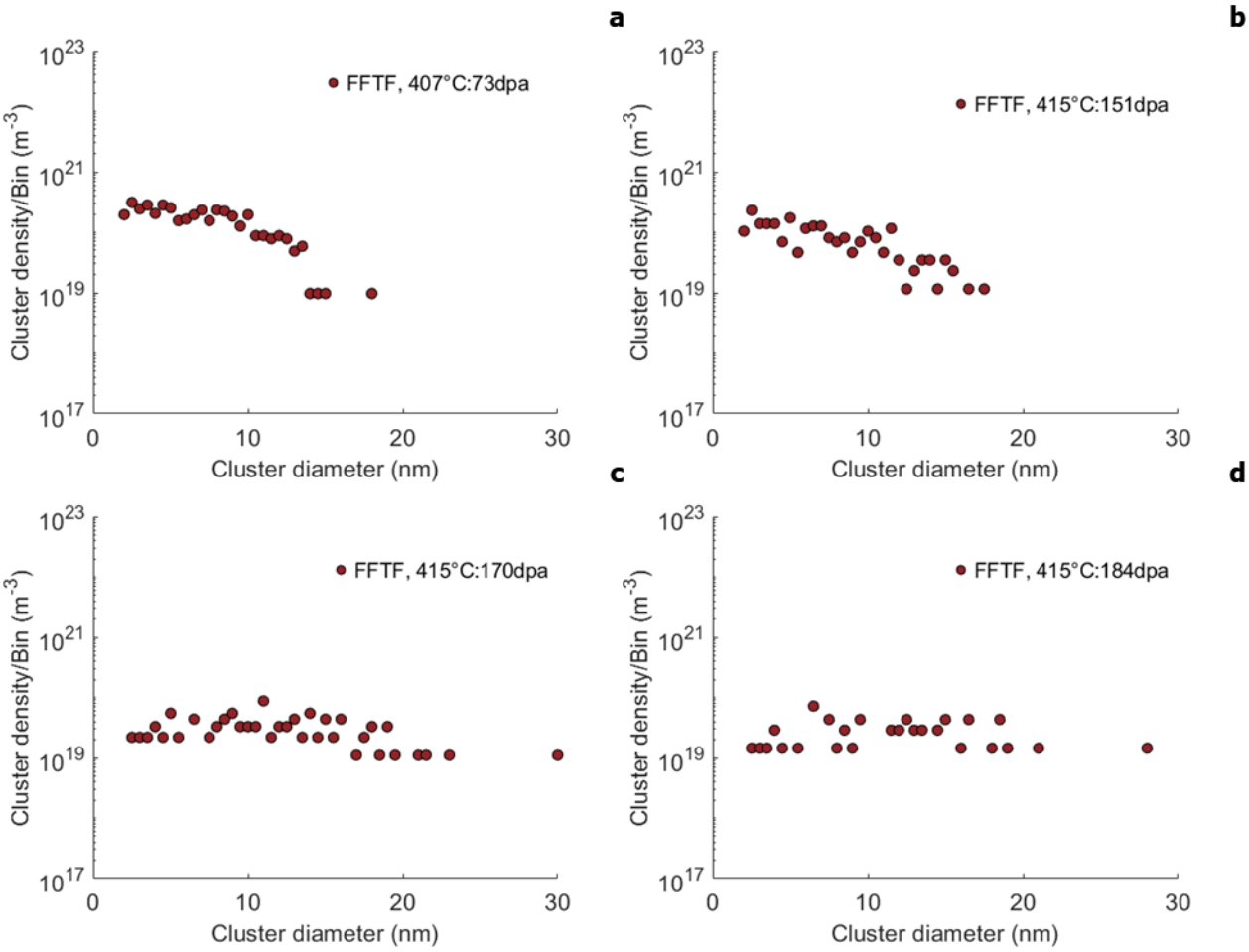


Figure 5.57: Cluster size distributions of FFTF-irradiated T91 30176 to (a) 73 dpa, (b) 151 dpa, (c) 170 dpa and (d) 184 dpa.

Table 5.16: Ni/Si-cluster microstructures of FFTF-irradiated T91 30176.

Irradiation mode	Sample	Condition	Cluster density ($\times 10^{20}$ m^{-3})	Average cluster diameter (nm)	Volume fraction (%)	Number of clusters counted (-)
FFTF	VH03	407C-0.21Hedpa-73dpa	42.1 ± 4.7	6.8 ± 1.5	0.119 ± 0.013	432
FFTF	VH20	415C-0.21Hedpa-151dpa	23.3 ± 2.9	7.1 ± 1.6	0.083 ± 0.010	202
FFTF	NP04	415C-0.21Hedpa-170dpa	10.9 ± 1.6	11.6 ± 1.7	0.146 ± 0.017	99
FFTF	FA33	415C-0.21Hedpa-184dpa	7.1 ± 1.2	11.8 ± 1.7	0.101 ± 0.013	49

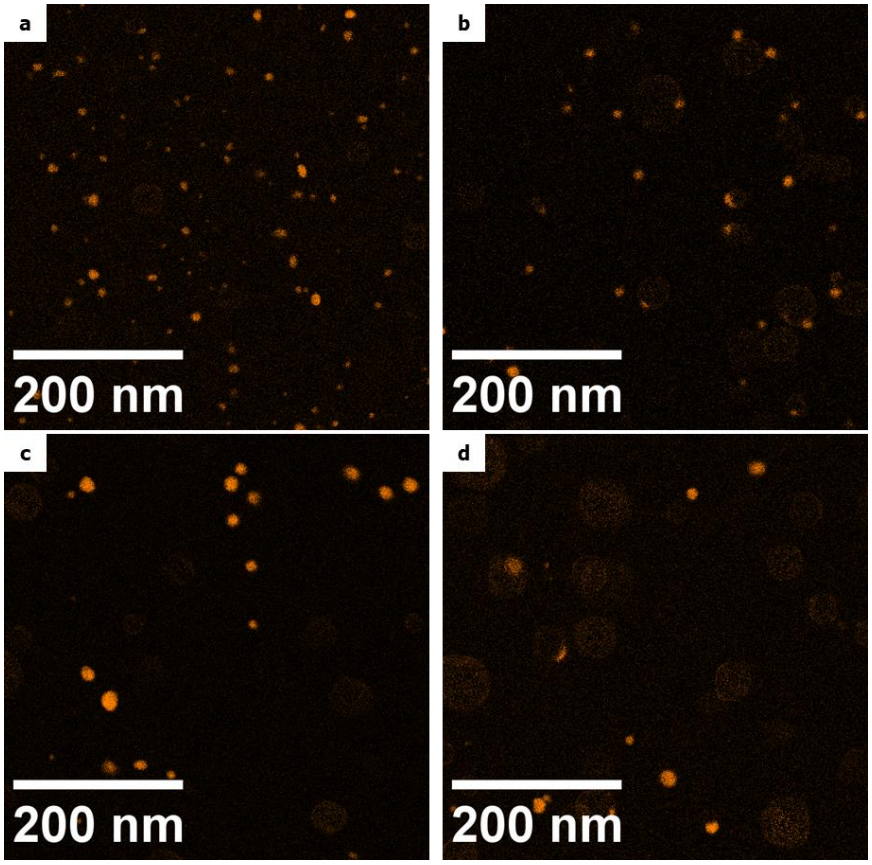


Figure 5.58: EDS Ni map (wt%) of FFTF-irradiated T91 30176 at (a) 407°C:73dpa, (b) 415°C:151dpa, (c) 415°C:170dpa and (d) 415°C:184dpa.

5.6 Dual-ion irradiation companion to FFTF

5.6.1 Cavity microstructures

The cavity microstructure evolution was characterized in all dual-ion irradiations via STEM-HAADF and CTEM-BF through-focus imaging. As shown in Figure 5.59 and Figure 5.60, swelling, void density and average void diameter increase with increasing damage level in dual-ion samples irradiated at 460°C:0.2appmHe/dpa up to 184 dpa and 490°C:0.8appmHe/dpa up to 170 dpa. The temperature excursion experiment at 460-490-460°C:0.2appmHe/dpa irradiated to 170 dpa increases in swelling, void density and average void diameter compared to the sample at 460°C:0.2appmHe/dpa irradiated to 72 dpa. Bubble density at 460-490-460°C:170dpa is higher than at other conditions. Average bubble diameter is comparable across all conditions as shown in Figure 5.61.

The cavity size distributions of all conditions are presented in Figure 5.62. A valley between bubbles and voids is present for 460°C:0.2appmHe/dpa but not very pronounced at 490°C:0.8appmHe/dpa and completely absent at 460-490-460°C:0.2appmHe/dpa.

Results are tabulated in Table 5.17 and representative STEM-HAADF micrographs are shown in Figure 5.63.

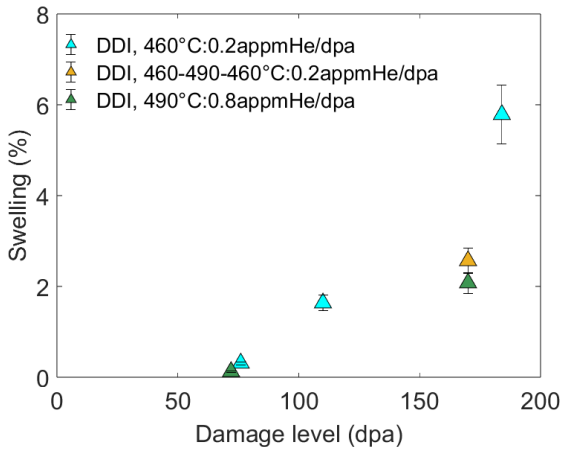


Figure 5.59: Swelling of dual-ion-irradiated T91 30176 as a function of damage level.

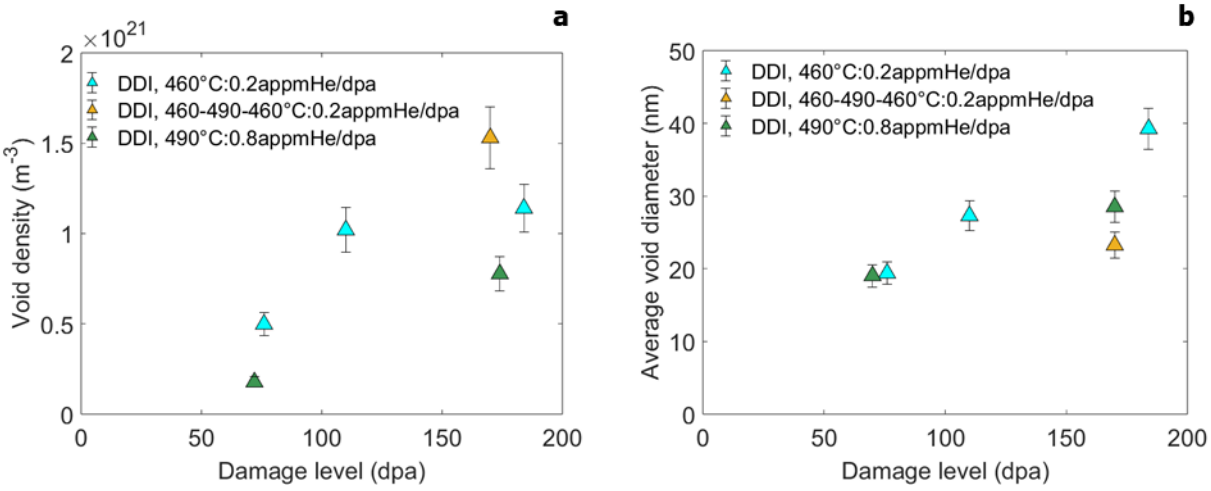


Figure 5.60: (a) Void density and (b) average void diameter of dual-ion-irradiated T91 30176 as a function of damage level.

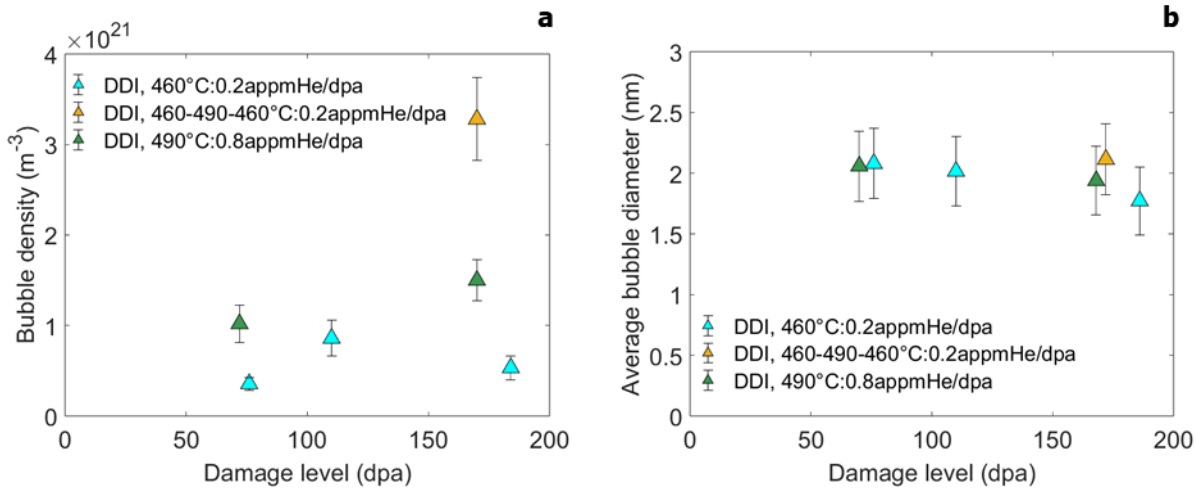


Figure 5.61: (a) Bubble density and (b) average bubble diameter of dual-ion-irradiated T91 30176 as a function of damage level.

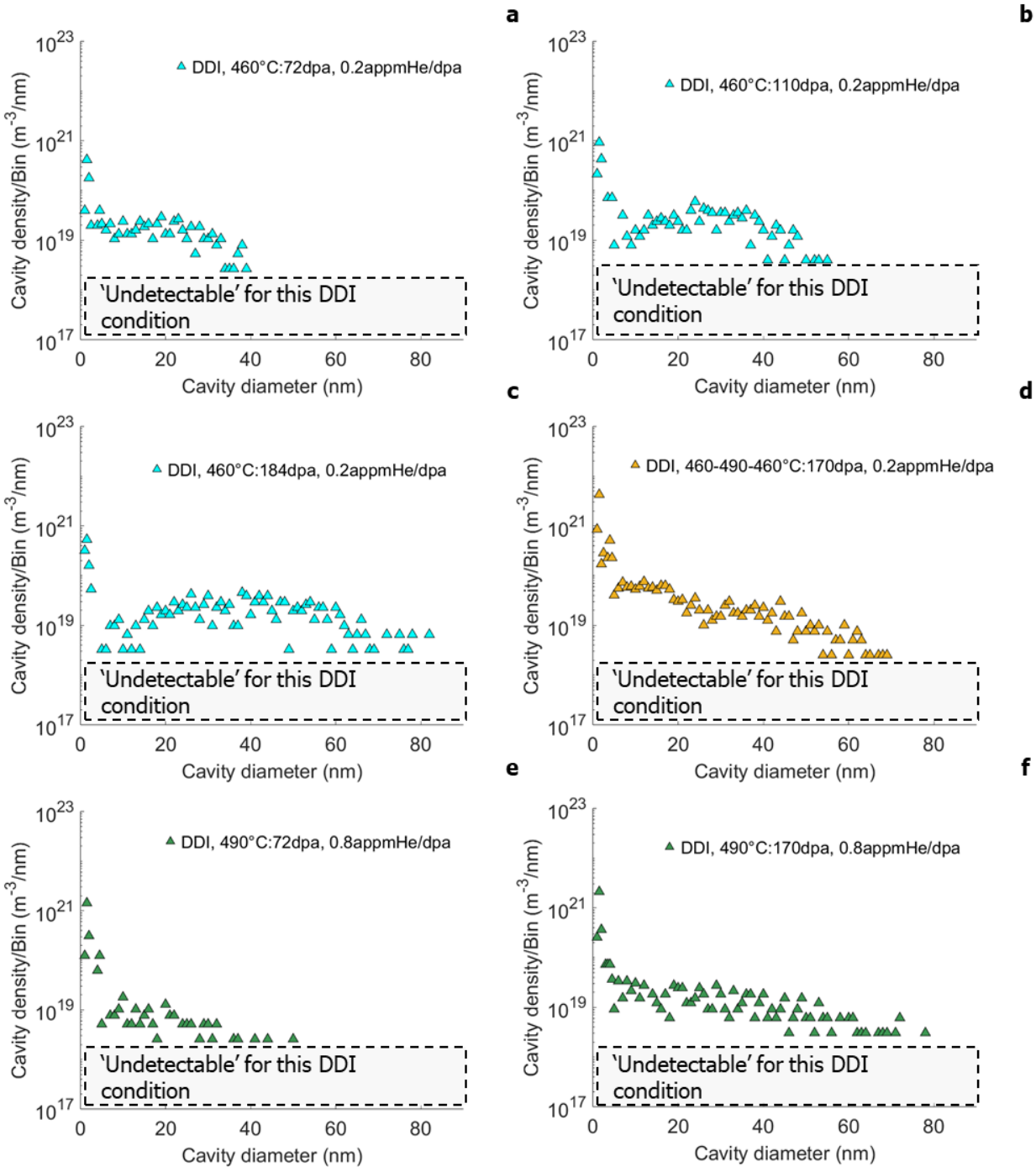


Figure 5.62: Cavity size distributions of dual-ion-irradiated T91 30176 at 460°C:0.2appmHe/dpa to (a) 72 dpa, (b) 110 dpa, (c) 184 dpa, at 460-490-460°C:0.2appmHe/dpa to (d) 170 dpa and at 490°C:0.8appmHe/dpa to (e) 72 dpa and (f) 170 dpa.

Table 5.17: Cavity microstructures of dual-ion-irradiated T91 30176.

Irradiation mode	Sample	Condition	Swelling (%)	Bubble density ($\times 10^{20}$ m^{-3})	Average bubble diameter (nm)	Void density ($\times 10^{20}$ m^{-3})	Average void diameter (nm)	Number of bubbles/ voids counted (-)
DDI	062424	460C-0.2Hedpa-72dpa	0.31 ± 0.03	3.6 ± 0.7	2.08 ± 0.29	5.0 ± 0.6	19.4 ± 1.5	36/187
DDI	012025-2	460C-0.2Hedpa-110dpa	1.64 ± 0.18	8.6 ± 2.0	2.02 ± 0.29	10.2 ± 1.2	27.3 ± 2.1	24/255
DDI	101424	460C-0.2Hedpa-184dpa	5.78 ± 0.64	5.3 ± 1.3	1.77 ± 0.28	11.4 ± 1.3	39.3 ± 2.9	20/394
DDI	050825	460-490-460C-0.2Hedpa-170dpa	2.57 ± 0.28	32.8 ± 4.6	2.11 ± 0.29	15.3 ± 1.7	23.3 ± 1.8	115/605
DDI	040225	490C-0.8Hedpa-72dpa	0.12 ± 0.01	10.2 ± 2.1	2.06 ± 0.29	1.8 ± 0.3	19.0 ± 1.5	33/69
DDI	040425	490C-0.8Hedpa-170dpa	2.08 ± 0.23	15.0 ± 2.3	1.94 ± 0.28	7.8 ± 0.9	28.5 ± 2.1	82/254

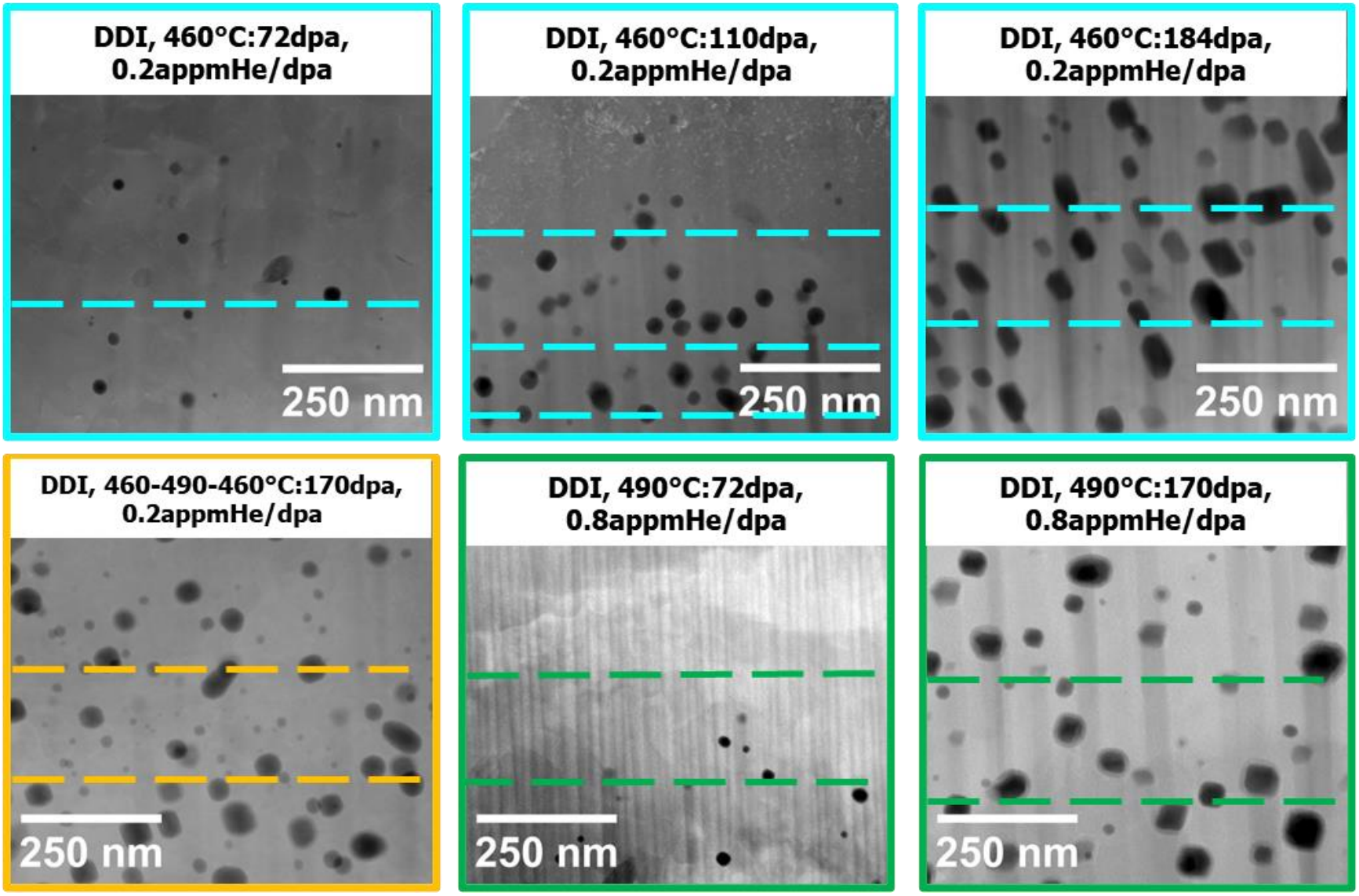


Figure 5.63: STEM HAADF micrographs of dual-ion-irradiated T91 30176. The dashed lines indicate the depth of interest for the dual-ion-irradiated samples.

5.6.2 Dislocation loop microstructures

The loop microstructure evolution was characterized in all dual-ion irradiations except 460°C:0.2appmHe/dpa at 184 dpa via on-zone STEM-BF imaging. The loop densities and average loop diameters shown in Figure 5.64 indicate that damage level does not appear to have a significant impact on loop microstructure beyond 73 dpa, except at 460°C:0.2appmHe/dpa for which the loop density decreases slightly and the average loop diameter increases from 72 to 110 dpa. Very few a/2⟨111⟩ loops are observed at all conditions (none out of 52 loops total at 460°C:72dpa, 2 out of 57 loops total at 460°C:110dpa, none out of 13 loops total at 490°C at both damage levels).

The temperature excursion dual-ion irradiation at 460-490-460°C:0.2appmHe/dpa exhibits a loop density and average diameter comparable to that of 460°C:0.2appmHe/dpa. On the other hand, the 490°C:0.8appmHe/dpa condition creates a lower density of loop but with slightly larger average diameter compared to the other two dual-ion conditions. This observation is consistent with the evolution seen between dual-ion samples at 445°C and 460°C in Section 5.4.2.

STEM BF micrographs are presented in Figure 5.65 and results are tabulated in Table 5.18.

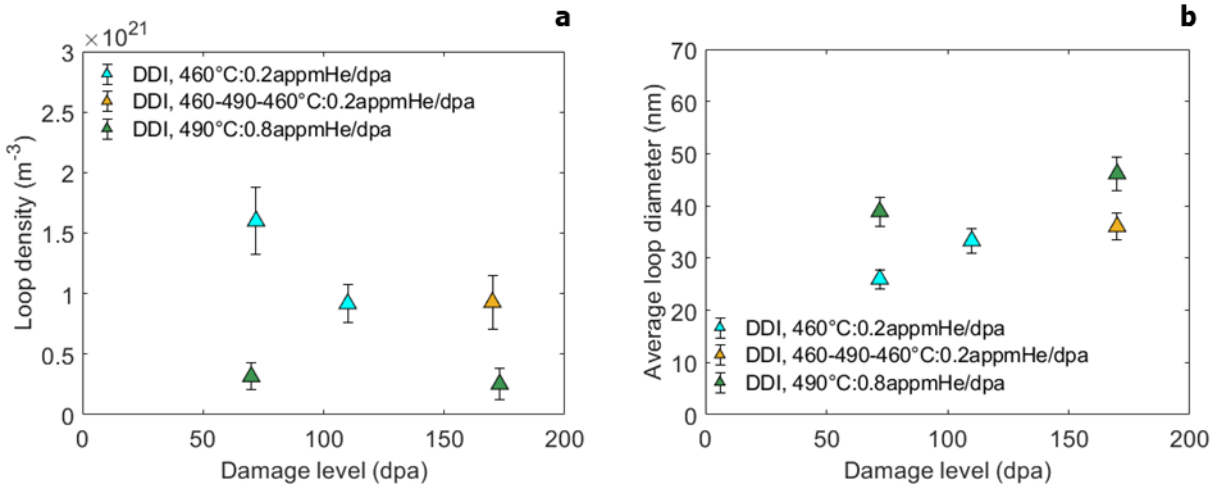


Figure 5.64: (a) Loop density and (b) average loop diameter of dual-ion-irradiated T91 30176 as a function of damage level.

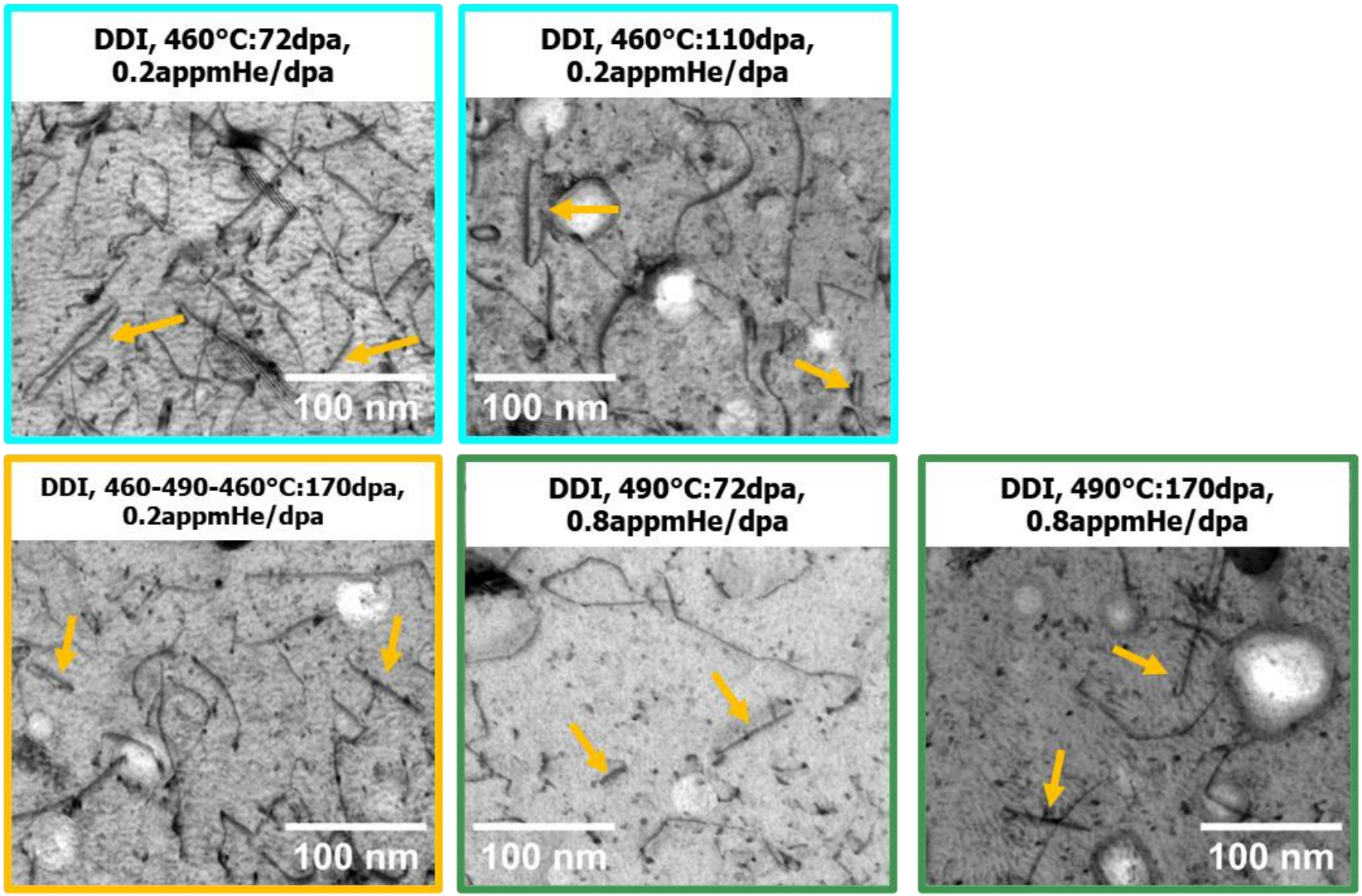


Figure 5.65: STEM BF micrographs of dual-ion-irradiated T91 30176.

Table 5.18: Dislocation loop microstructures of dual-ion-irradiated T91 30176.

Irradiation mode	Sample	Condition	Loop density ($\times 10^{20}$ m^{-3})	Average loop diameter (nm)	Loop sink strength ($\times 10^{14}$ m^{-2})	Number of loops counted (-)
DDI	062424	460C-0.2Hedpa-72dpa	16.0 ± 2.8	26.0 ± 1.8	1.3	52
DDI	012025-2	460C-0.2Hedpa-110dpa	9.2 ± 1.6	33.3 ± 2.3	1.0	57
DDI	050825	460-490-460C-0.2Hedpa-170dpa	9.3 ± 2.2	36.0 ± 2.5	1.1	22
DDI	040225	490C-0.8Hedpa-72dpa	3.2 ± 1.1	38.9 ± 2.7	0.4	9
DDI	040425	490C-0.8Hedpa-170dpa	2.5 ± 1.1	46.2 ± 3.2	0.4	4

5.6.3 Radiation-induced segregation

The radiation-induced segregation behavior of Fe, Cr, Ni and Si at grain boundaries was characterized in all dual-ion irradiations except 460°C:0.2appmHe/dpa at 184 dpa. Results are tabulated in Table 5.19.

Segregation values for Fe and Cr are close to zero in all conditions and no clear enrichment or depletion is observed. All conditions exhibit Ni and Si enrichment with approximately the same intensity as shown in Figure 5.66 (c-d). For all elements, damage level does not appear to have an impact on enrichment/depletion at any condition. Representative EDS maps are presented in Figure 5.67 and Figure 5.68.

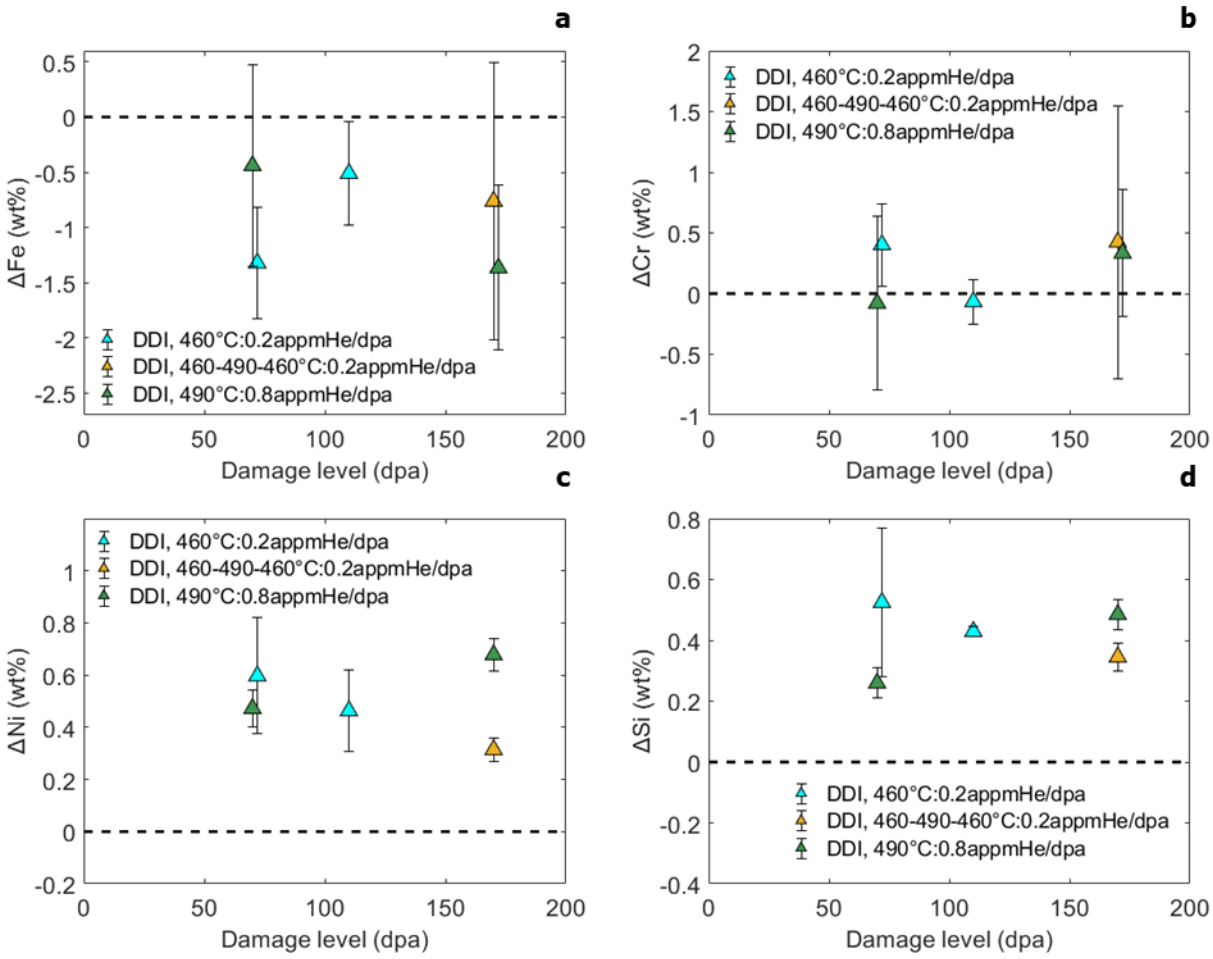


Figure 5.66: (a) Fe, (b) Cr, (c) Ni and (d) Si enrichments at grain boundaries of dual-ion-irradiated T91 30176.

Table 5.19: Radiation-induced segregation of dual-ion-irradiated T91 30176.

Irradiation mode	Sample	Condition	Fe (wt%)		Cr (wt%)		Ni (wt%)		Si (wt%)	
			Peak	ΔFe	Peak	ΔCr	Peak	ΔNi	Peak	ΔSi
DDI	062424	460C-0.2Hedpa-72dpa	88.3±0.6	-1.3±0.5	8.6±0.1	0.4±0.3	0.70±0.23	0.60±0.22	0.76±0.29	0.53±0.24
DDI	012025-2	460C-0.2Hedpa-110dpa	89.9±0.1	-0.5±0.5	7.6±0.2	-0.1±0.2	0.57±0.17	0.46±0.16	0.64±0.04	0.43±0.02
DDI	050825	460-490-460C-0.2Hedpa-170dpa	88.7±0.5	-0.8±1.3	8.8±0.4	0.4±1.1	0.41±0.05	0.31±0.05	0.56±0.03	0.35±0.05
DDI	040225	490C-0.8Hedpa-72dpa	89.6±0.9	-0.4±0.9	8.1±0.6	-0.1±0.7	0.57±0.06	0.47±0.07	0.46±0.07	0.26±0.05
DDI	040425	490C-0.8Hedpa-170dpa	88.5±0.8	-1.4±0.7	8.3±0.5	0.3±0.5	0.79±0.07	0.68±0.06	0.74±0.07	0.49±0.05

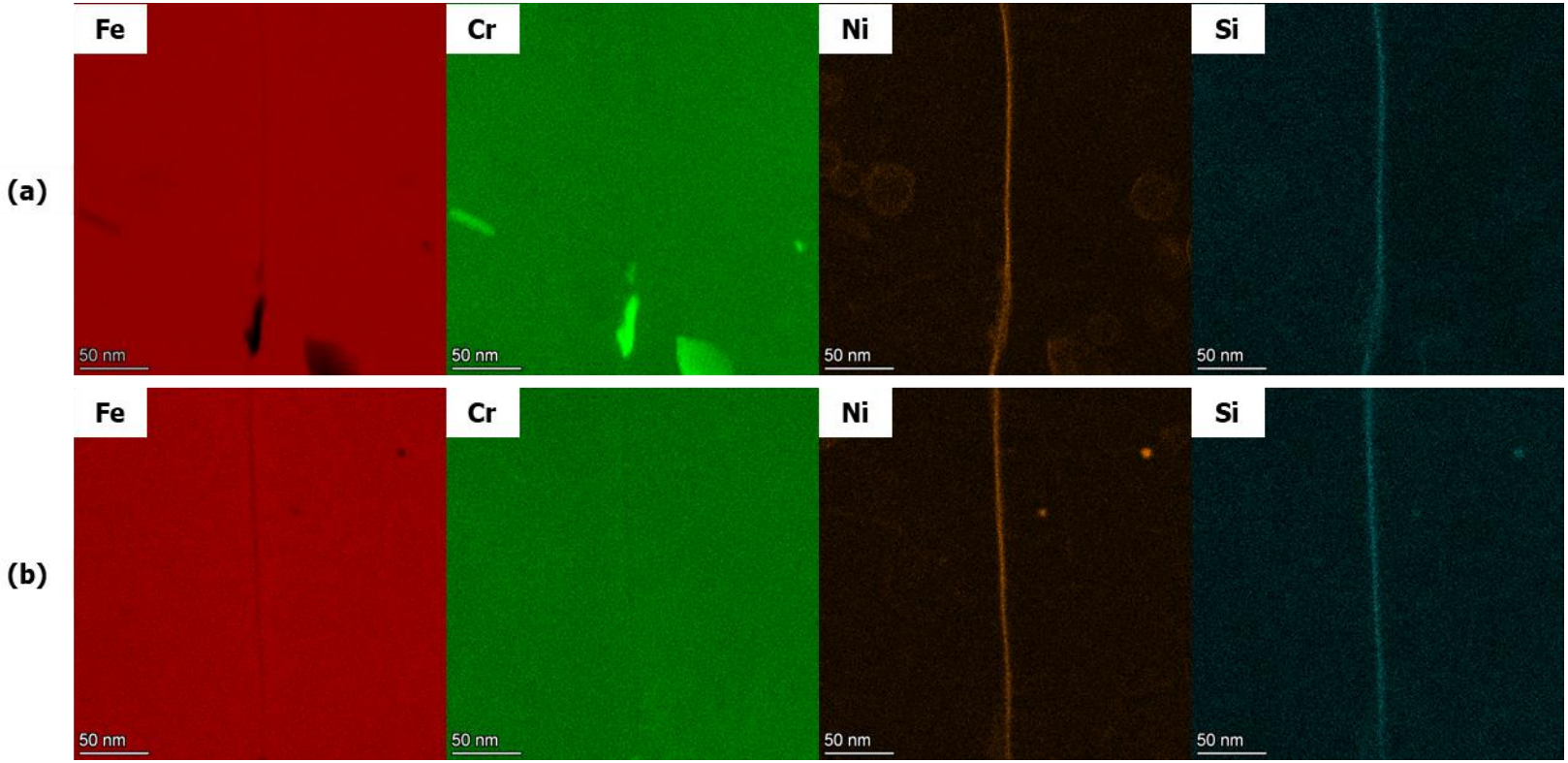


Figure 5.67: EDS (wt%) maps of Fe, Cr, Ni and Si of dual-ion-irradiated T91 30176 at 460°C:0.2appmHe/dpa to (a) 72 dpa and (b) 110 dpa.

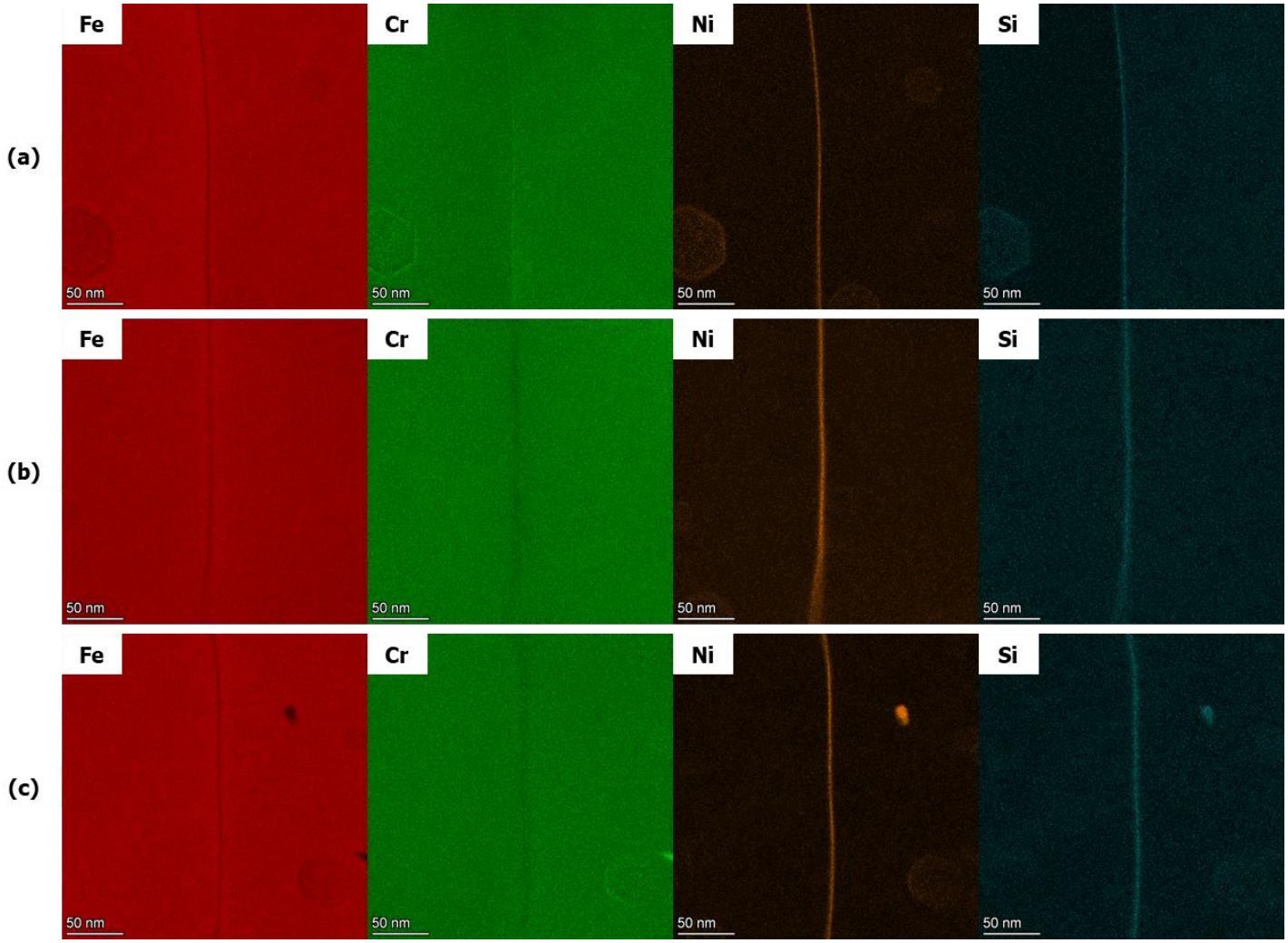


Figure 5.68: EDS (wt%) maps of Fe, Cr, Ni and Si of dual-ion-irradiated T91 30176 at (a) 460-490-460°C:0.2appmHe/dpa to 170 dpa and at 490°C:0.8appmHe/dpa to (b) 72 dpa and (c) 170 dpa.

5.6.4 Radiation-induced precipitation

Ni-Si-Mn clusters were characterized in all dual-ion irradiation conditions except 460°C:0.2appmHe/dpa at 184 dpa. Figure 5.69 shows the evolution of cluster density, average cluster diameter and volume fraction as a function of damage level for all samples.

The cluster density decreases between 72 and 184 dpa while the average diameter slightly increases. The volume fractions of all but one (490°C:72dpa) dual-ion irradiations are comparable. FFTF cluster size distributions are presented in Figure 5.70. Results are tabulated in Table 5.20. EDS Ni maps are presented in Figure 5.71.

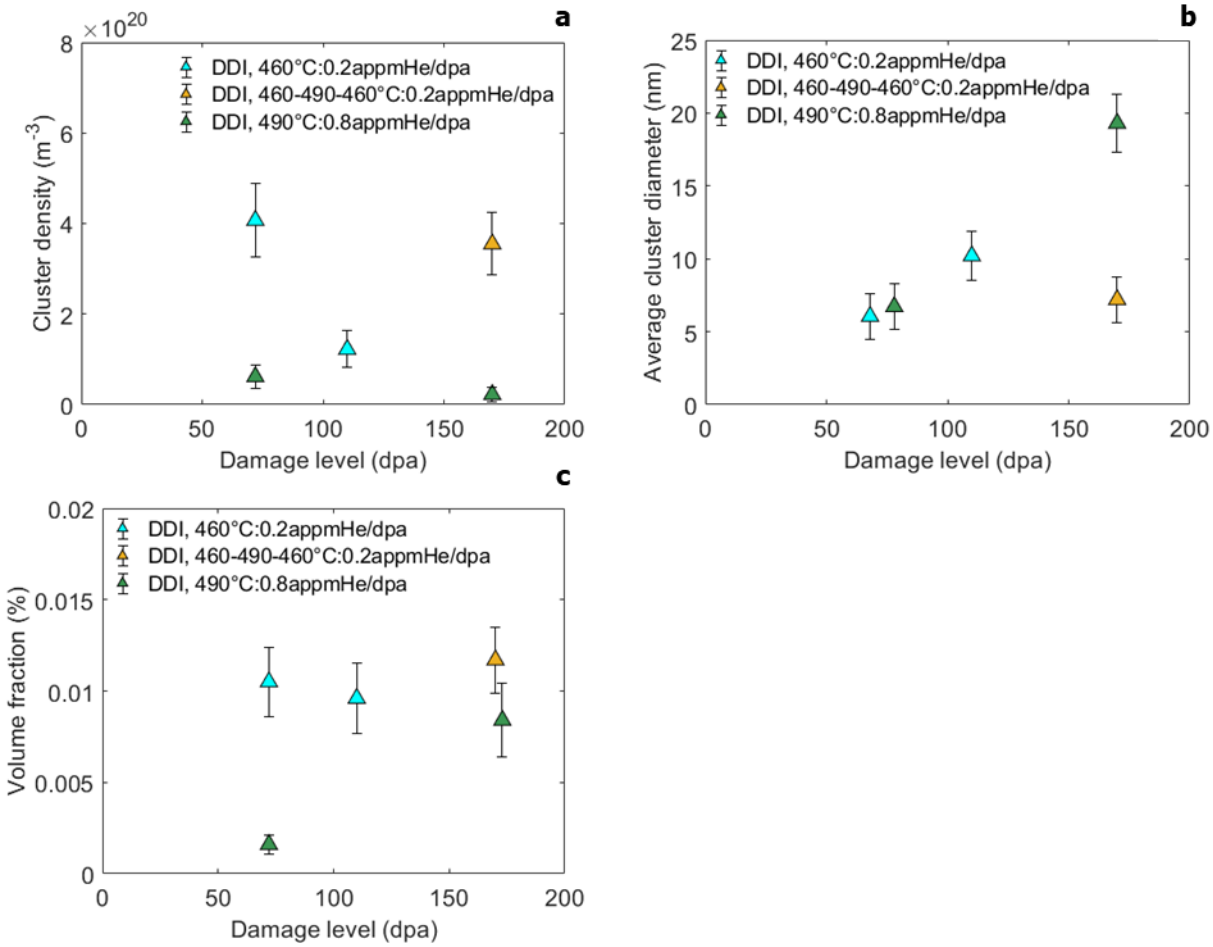


Figure 5.69: (a) Cluster density, (b) average cluster diameter and (c) volume fraction of dual-ion-irradiated T91 30176.

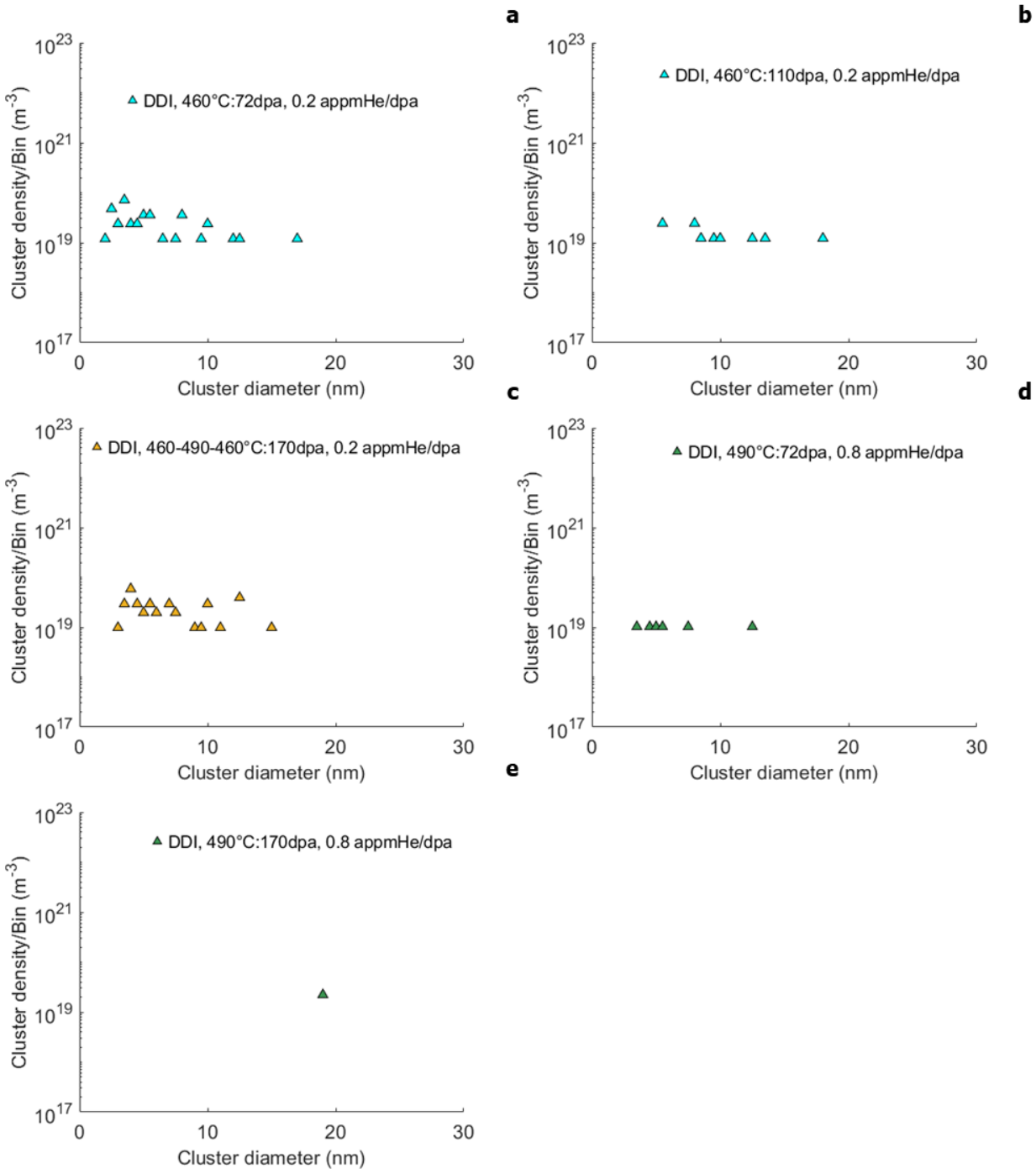


Figure 5.70: Cluster size distributions of dual-ion-irradiated T91 30176 at 460°C:0.2appmHe/dpa to (a) 72 dpa, (b) 110 dpa, at 460-490-460°C:0.2appmHe/dpa (c) to 170 dpa, at 490°C:0.8appmHe/dpa to (d) 72 dpa and (e) 170 dpa.

Table 5.20: Ni/Si-cluster microstructures of dual-ion-irradiated T91 30176.

Irradiation mode	Sample	Condition	Cluster density ($\times 10^{20}$ m^{-3})	Average cluster diameter (nm)	Volume fraction (%)	Number of clusters counted (-)
DDI	062424	460C-0.2Hedpa-72dpa	4.1 ± 0.8	6.1 ± 1.6	0.011 ± 0.002	34
DDI	012025-2	460C-0.2Hedpa-110dpa	1.2 ± 0.4	10.2 ± 1.7	0.010 ± 0.002	10
DDI	050825	460-490-460C-0.2Hedpa-170dpa	3.6 ± 0.7	7.2 ± 1.6	0.012 ± 0.002	36
DDI	040225	490C-0.8Hedpa-72dpa	0.6 ± 0.3	6.7 ± 1.6	0.002 ± 0.001	6
DDI	040425	490C-0.8Hedpa-170dpa	0.2 ± 0.2	19.3 ± 2.0	0.008 ± 0.002	2

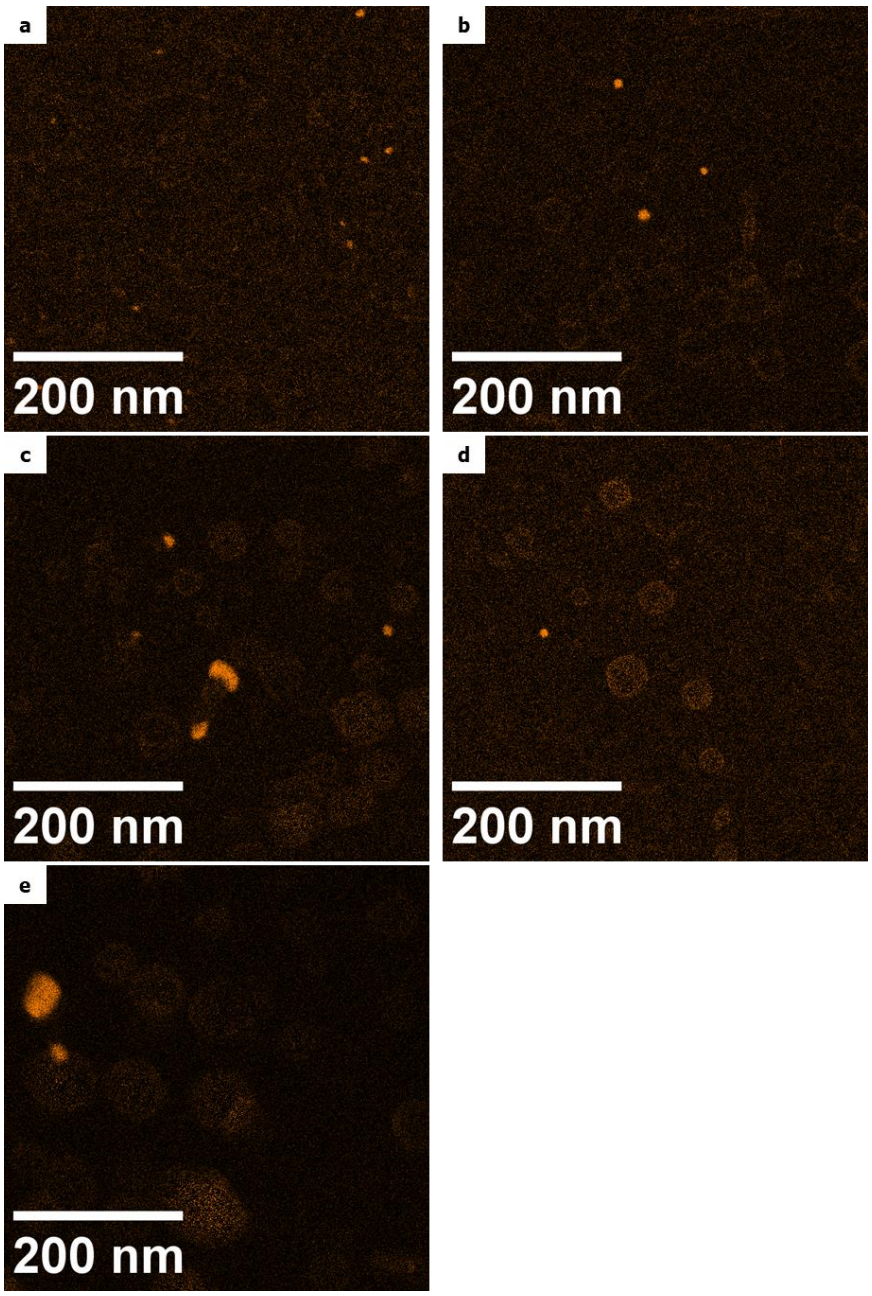


Figure 5.71: EDS Ni map (wt%) of dual-ion-irradiated T91 30176 at 460°C:0.2appmHe/dpa to (a) 72 dpa and (b) 110 dpa, at 460-490-460°C:0.2appmHe/dpa to (c) 170 dpa, at 490°C:0.8appmHe/dpa to (d) 72 dpa and (e) 170 dpa.

Chapter 6 Discussion

In this chapter, Section 6.1 compares the microstructures of BOR-60-irradiated samples and companion dual-ion-irradiated specimens to assess their match. The special case of BOR-60 samples irradiated at 402-404°C in light of temperature inaccuracies is discussed. In Section 6.2, the rate theory model is fitted using the experimental measurements of samples from BOR-60 and companion dual-ion irradiations. Multiple sets of modeling parameters are explored and compared to values from literature. In Section 6.3, the ability of the model to predict cavity microstructure evolution in different conditions is validated against measured cavity size distributions from dual-ion irradiation conducted at various temperatures and helium injection rates. Section 6.4 discusses the match between FFTF and companion dual-ion irradiations first. The importance of considering irradiation history is affirmed and sheds light on the dual-ion condition required to match FFTF cavity microstructures. The rate theory model is used to evaluate the effect of temperature excursion on the cavity microstructure evolution and determines the temperature and helium injection rate of the perturbation during MOTA-1C. Finally, Section 6.5 discusses the justification for a temperature shift and revised helium injection rate when matching neutron-irradiated cavity microstructures with dual-ion irradiation.

6.1 Comparison of BOR-60 and dual-ion-irradiated microstructures

This section discusses the characterization results from Chapter 5 by comparing the microstructure evolution of BOR-60 samples to that of companion dual-ion samples. BOR-60 specimens irradiated at 369-376°C, 450-453°C and 515-517°C are examined together in a

subsection distinct from specimens irradiated at 402-404°C due to inconsistencies in microstructure evolution in the latter.

In fast reactors, ferritic-martensitic steels are candidate materials for fuel pin cladding and wrapper material [5]. The major degradation modes in alloy T91 are dimensional instability and hardening [13]. Therefore, each subsection first discusses the match of cavity and loop microstructures since they are the largest contributors to void swelling and hardening. Radiation-induced segregation and precipitation are also discussed, although in less detail.

6.1.1 Comparison of BOR-60-irradiated microstructure at 369-376°C, 450-453°C and 515-517°C and companion dual-ion irradiations

Matching and comparison of size distributions is rarely quantitatively reported in literature, and no criteria defining what constitutes a match between the two irradiation methods are universally agreed upon. The criteria in this work are selected based on discussion with experts in the field and typical measured variability between characterization of the same condition from one sample/lift-out to another. At low damage levels, the nucleation of bubbles exhibits strong stochastic variations and difference in densities and swelling by a factor of 1-4 are not unusual between two matching microstructures. With increasing damage level, the growth of voids becomes the dominant contributor to swelling which is less susceptible to variations. In this case, for cavities, close average void diameters (typically within 2 nm) and a difference in void densities less than a factor of 2 is considered a match. Indeed, the important spatial inhomogeneity in ferritic-martensitic steels due to small grain size and grain-to-grain variations in dislocation density can significantly affect the void density from one region to another but usually does not affect the shape or average diameter of the size distributions. When these two criteria are met, the swelling difference is typically a factor of 2 or less between the irradiation methods. If multiple irradiation

conditions meet these criteria, the best match is established based on the shape of the size distributions (valley between bubbles and voids, maximum void diameter). Comparisons of the loop and cluster microstructures are based on the same parameters. For radiation-induced segregation, there can be a lot of grain-boundary-to-grain-boundary variation due to proximity to precipitates and angle of the grain boundary. A match between the two irradiation methods is considered if the data points are within error bars or, if segregation is less than 1 wt% and the values are within a factor of 3 of each other.

To match the cavity microstructures of BOR-60-irradiated T91 30176 up to 35 dpa via dual-ion irradiation, Taller et al. [16] used a temperature shift of 50-70°C and a helium injection rate of 4.3 appmHe/dpa. These values were selected from temperature and helium injection rate series of dual-ion irradiations [17] because they provided the best match with the neutron-irradiated cavity microstructures. In the present work, the same temperature shift and increased helium injection rate are used to match the BOR-60 microstructures up to 72 dpa. Additionally, two dual-ion irradiations with a reduced helium injection rate after 35 dpa were conducted to evaluate whether the lower helium content would better match BOR-60 samples by preventing the overnucleation of bubbles. Results are presented in Appendix A.

The first step in evaluating the match of cavity microstructures between BOR-60 and dual-ion irradiation is to look at swelling, void densities and average void diameters. Figure 6.1 shows the ratios of these values between the two irradiation methods when voids are present. When voids are not present (BOR-60 at 450-517°C), the swelling values can be quite different between the two irradiation methods but remain very low as indicated in Table 6.1 and are not shown in Figure 6.1. When swelling is dominated by bubbles (BOR-60 at 369°C:16dpa and dual-ion at 445°C:16.6dpa), any difference in bubble density has a large impact on swelling, even if values stay low. For BOR-

60 at 369-376°C and companion dual-ion irradiation, ratios are close to 1 across damage levels indicating the match in cavity microstructure between the two irradiation methods.

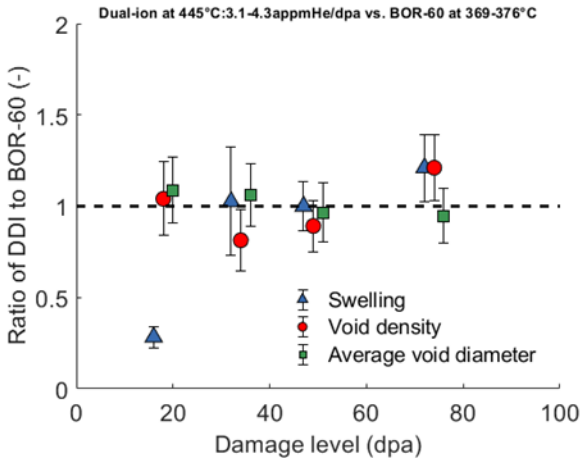


Figure 6.1: Ratios of swelling, void density and average void diameter between dual-ion irradiation at 445°C:3.1-4.3appmHe/dpa and BOR-60 at 369-376°C.

Looking at cavity size distributions, Figure 6.2, Figure 6.3 and Figure 6.4 confirm that the cavity microstructure of BOR-60 samples irradiated at 369-376°C, 450-453°C and 515-517°C match those of dual-ion irradiations conducted at 445°C:3.1-4.3appmHe/dpa, 520°C:3.2-4.3appmHe/dpa and 570°C:4.3appmHe/dpa, respectively.

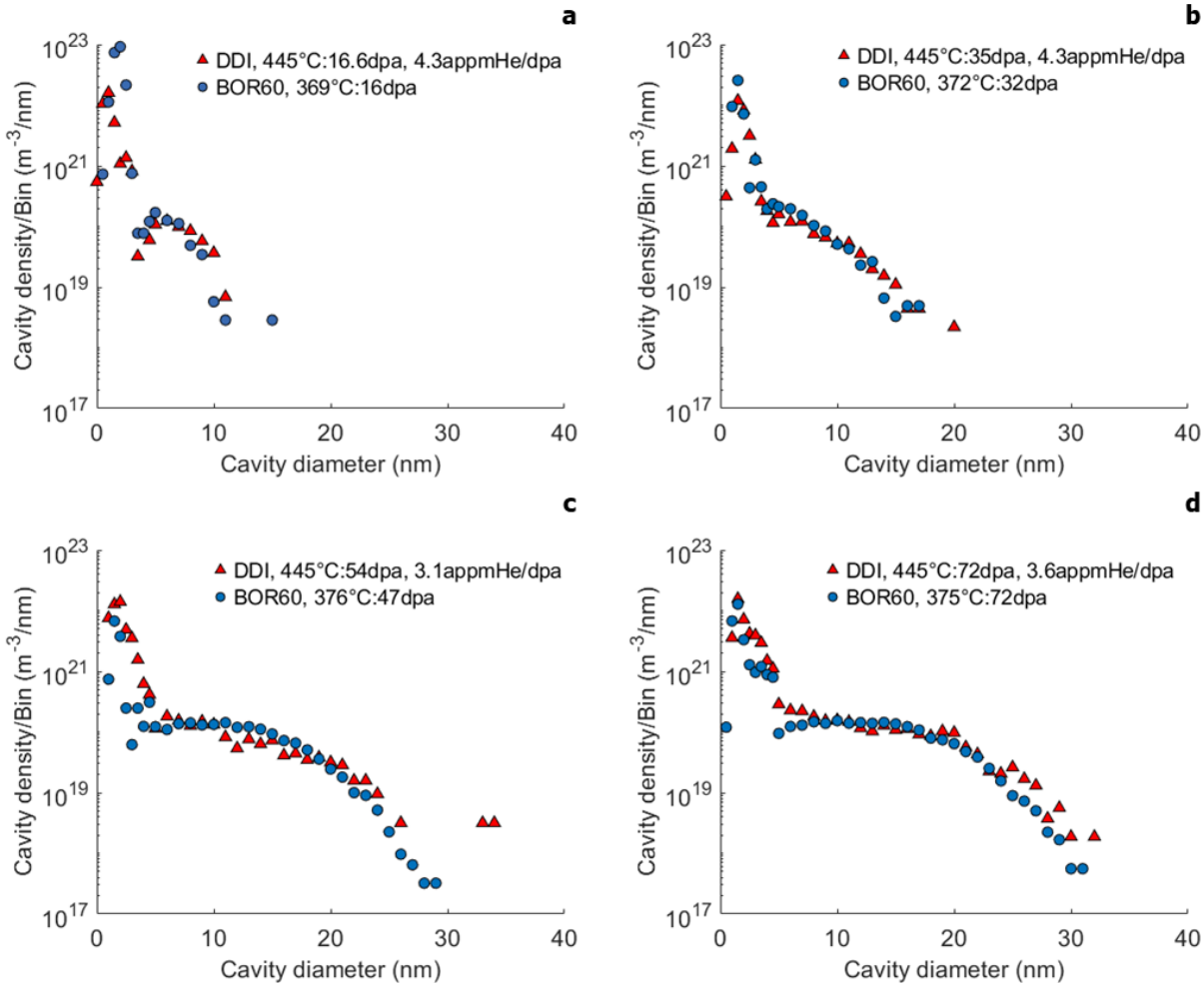


Figure 6.2: Cavity size distributions of irradiated T91 30176 for BOR-60 at 369-375°C and dual-ion conditions at 445°C to (a) 16 dpa, (b) 32-35 dpa, (c) 47-54 dpa and (d) 72 dpa.

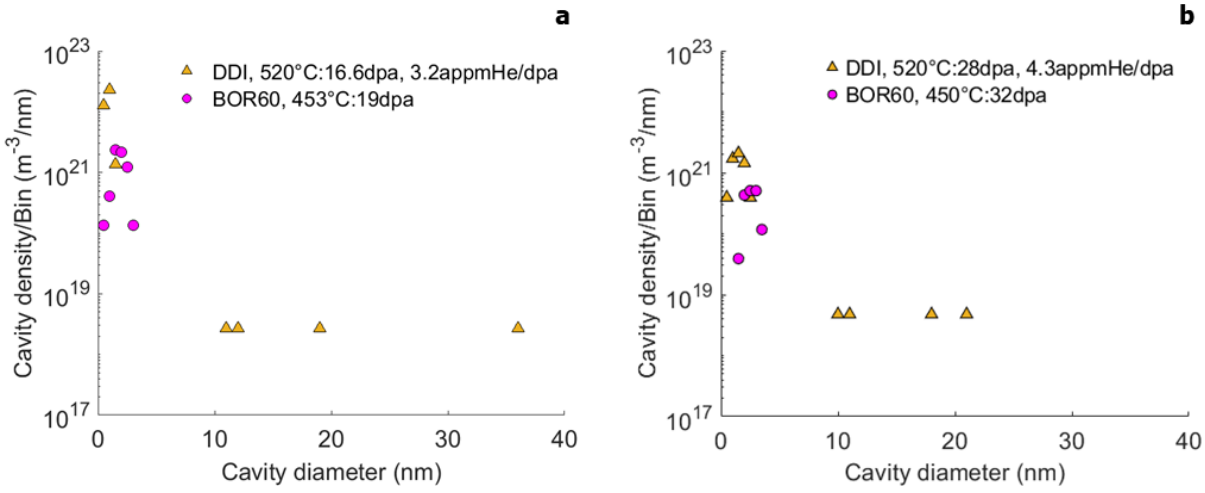


Figure 6.3: Cavity size distributions of irradiated T91 30176 for BOR-60 at 450-453°C and dual-ion conditions at 520°C to (a) 16.6-19 dpa and (b) 28-32 dpa.

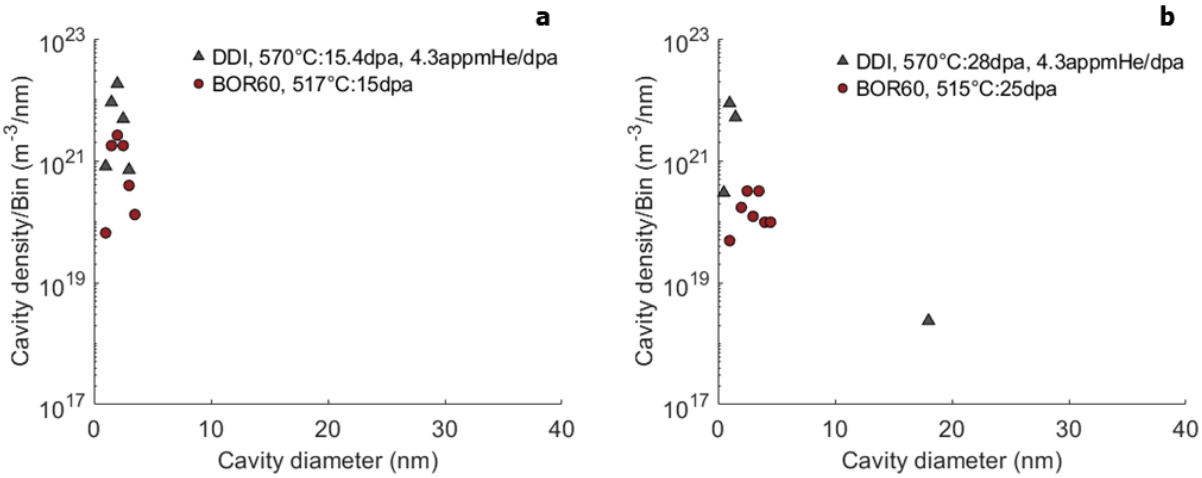


Figure 6.4: Cavity size distributions of irradiated T91 30176 for BOR-60 at 515-517°C and dual-ion conditions at 570°C to (a) 15 dpa and (b) 25-28 dpa.

In cases where a void microstructure develops (BOR-60 at 369-376°C and dual-ion at 445°C), the evolution of the cavity size distributions (Figure 6.2) reveals that the increase in swelling results from a combination of continuous void nucleation and growth, which is characteristic of the mixed/transition regime between incubation regime and bias-driven growth regime. In these same cases, the bimodality of cavity size distributions comes from the presence of helium atoms which stabilize small cavity nuclei [67].

As reported in Table 6.1, some differences in bubble densities are noted between the two irradiation methods (largely attributable to the difficulty of imaging bubbles smaller than 1.5 nm in diameter). The average bubble diameters of high-temperature conditions are slightly larger than at lower temperatures, but densities are lower (6-32 × 10^{20} m^{-3}), which is consistent with the critical bubble model [17].

Table 6.1: Cavity microstructures of irradiated T91 30176 for BOR-60 conditions and companion dual-ion irradiations.

Irradiation mode	Sample	Condition	Swelling (%)	Bubble density ($\times 10^{20}$ m^{-3})	Average bubble diameter (nm)	Void density ($\times 10^{20}$ m^{-3})	Average void diameter (nm)
BOR60	P027-T03	369C-0.77Hedpa-16dpa	0.06 ± 0.01	1000 ± 119	2.07 ± 0.29	5.0 ± 0.7	6.9 ± 0.8
DDI	092717	445C-4.3Hedpa-16.6dpa	0.017 ± 0.002	178 ± 21	1.31 ± 0.26	5.2 ± 0.7	7.5 ± 0.9
BOR60	P028-T05	372C-0.77Hedpa-32dpa	0.04 ± 0.01	219 ± 26	1.78 ± 0.28	9.1 ± 1.3	8.0 ± 0.9
DDI	053018-1	445C-4.3Hedpa-35dpa	0.041 ± 0.006	140 ± 17	2.09 ± 0.29	7.4 ± 1.1	8.5 ± 1.0
BOR60	P031-T98	376C-0.77Hedpa-47dpa	0.21 ± 0.02	61 ± 8	2.04 ± 0.29	16.6 ± 1.8	11.8 ± 1.1
DDI	070120-1	445C-3.1Hedpa-54dpa	0.21 ± 0.02	227 ± 26	2.19 ± 0.29	14.8 ± 1.7	11.4 ± 1.6
BOR60	P029-T11	375C-0.77Hedpa-72dpa	0.38 ± 0.04	141 ± 16	2.03 ± 0.29	20.9 ± 2.2	13.2 ± 1.2
DDI	102120-1	445C-3.6Hedpa-72dpa	0.46 ± 0.05	200 ± 22	2.37 ± 0.35	25.3 ± 2.7	12.5 ± 1.6
BOR60	P037-T55	453C-0.77Hedpa-19dpa	0.002 ± 0.000	32 ± 4	2.09 ± 0.29	N/O	N/O
DDI	020320	520C-3.2Hedpa-16.6dpa	0.010 ± 0.002	188 ± 28	1.09 ± 0.25	0.11 ± 0.02	19.8 ± 1.9
BOR60	P038-T61	450C-0.77Hedpa-32dpa	0.001 ± 0.000	8 ± 1	2.82 ± 0.40	N/O	N/O
DDI	091719	520C-4.3Hedpa-28dpa	0.006 ± 0.001	30 ± 4	1.73 ± 0.27	0.19 ± 0.03	15.5 ± 1.8
BOR60	P042-T67	517C-0.77Hedpa-15dpa	0.003 ± 0.000	34 ± 4	2.33 ± 0.35	N/O	N/O
DDI	110117	570C-4.3Hedpa-15.4dpa	0.010 ± 0.001	168 ± 20	2.18 ± 0.29	N/O	N/O
BOR60	P043-T108	515C-0.77Hedpa-25dpa	0.001 ± 0.000	6 ± 1	3.23 ± 0.45	N/O	N/O
DDI	111219	570C-4.3Hedpa-28dpa	0.002 ± 0.000	71 ± 8	1.42 ± 0.26	Negl.	Negl.

N/O = Not observed

In all BOR-60 and companion dual-ion conditions, dislocation loops are mostly of a⟨100⟩ type with a/2⟨111⟩-type loops representing less than 10% of the total density. The ratios of loop density, average loop diameter and loop sink strength presented in Figure 6.5 indicate the match in loop microstructure across damage levels between BOR-60 samples irradiated at 369-376°C and dual-ion samples irradiated at 445°C:3.1-4.3appmHe/dpa. This match is confirmed by the comparison of the loop size distributions presented in Figure 6.6 and tabulated values in Table 6.2. Neither the BOR-60 samples, nor the dual-ion-irradiated samples at higher temperatures exhibit any dislocation loops. Thus, the loop microstructure evolution of dual-ion-irradiated samples at 445°C:3.1-4.3appmHe/dpa, 520°C:3.2-4.3appmHe/dpa and 570°C:4.3appmHe/dpa match those of BOR-60 samples irradiated at 369-376°C, 450-453°C and 515-517°C, respectively. Of note, a single temperature shift and helium injection rate increase is sufficient to replicate both the cavity and loop microstructure of BOR-60 samples via dual-ion irradiation at damage levels ranging from 16 to 72 dpa.

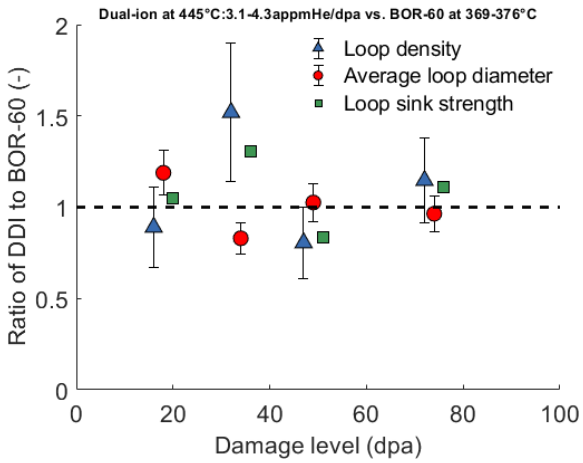


Figure 6.5: Ratios of loop density, average loop diameter and loop sink strength between dual-ion irradiation at 445°C:3.1-4.3appmHe/dpa and BOR-60 at 369-376°C.

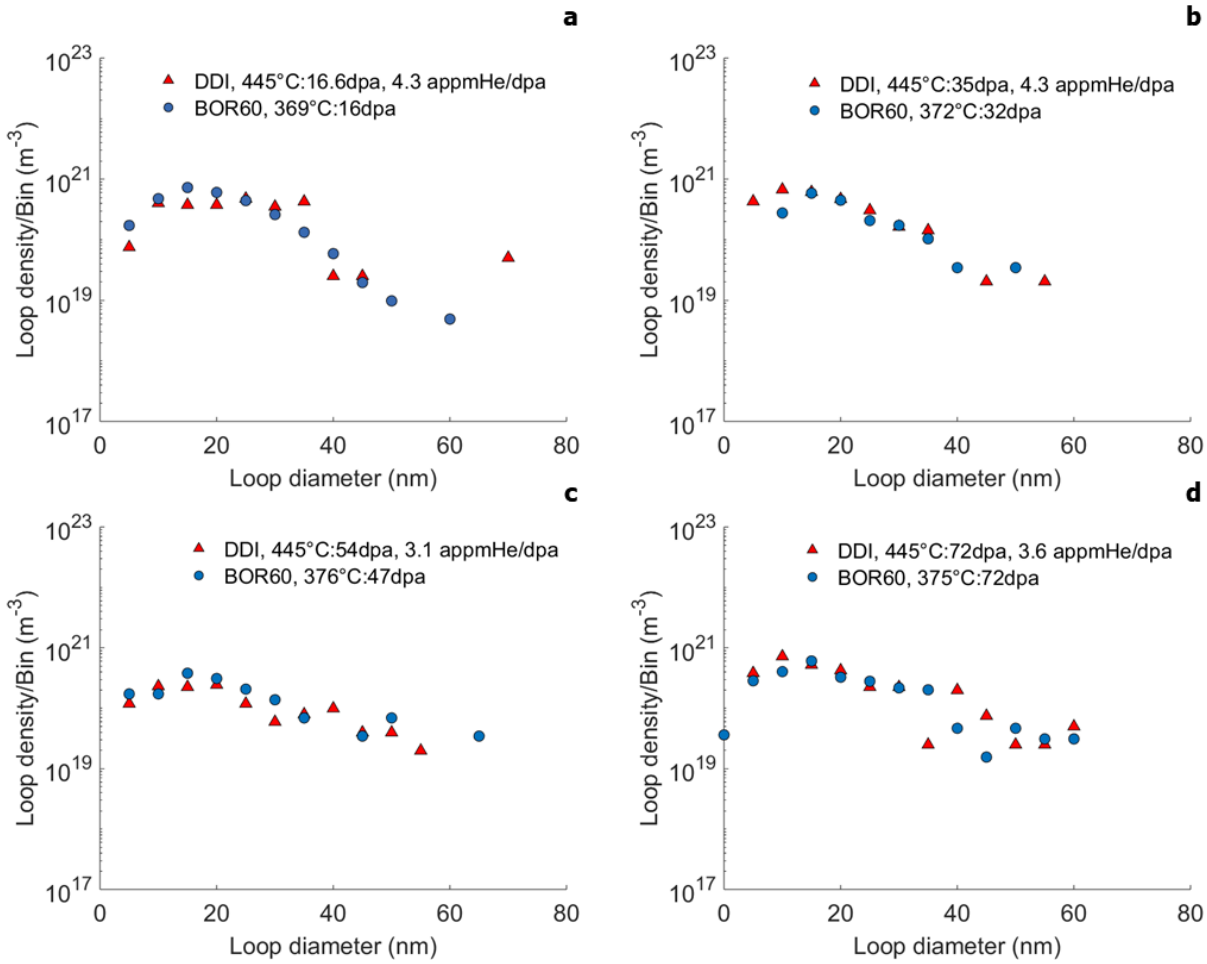


Figure 6.6: Dislocation loop size distributions of irradiated T91 30176 for BOR-60 at 369-376°C and dual-ion at 445°C to (a) 16 dpa, (b) 32-35 dpa, (c) 47-54 dpa and (d) 72 dpa.

Table 6.2: Dislocation loop microstructures for BOR-60 samples and companion dual-ion irradiations.

Irradiation mode	Sample	Condition	Loop density ($\times 10^{20}$ m^{-3})	Average loop diameter (nm)	Loop sink strength ($\times 10^{14}$ m^{-2})
BOR60	P027-T03	369C-0.77Hedpa-16dpa	29.1 ± 5.1	21.8 ± 1.6	2.0
DDI	092717	445C-4.3Hedpa-16.6dpa	25.9 ± 4.6	25.9 ± 1.9	2.1
BOR60	P028-T05	372C-0.77Hedpa-32dpa	18.7 ± 3.3	22.9 ± 1.7	1.3
DDI	053018-1	445C-4.3Hedpa-35dpa	28.4 ± 5.0	19.0 ± 1.4	1.7
BOR60	P031-T98	376C-0.77Hedpa-47dpa	15.9 ± 2.9	23.4 ± 1.7	1.2
DDI	070120-1	445C-3.1Hedpa-54dpa	12.8 ± 2.1	24.0 ± 1.7	1.0
BOR60	P029-T11	375C-0.77Hedpa-72dpa	25.3 ± 3.3	22.3 ± 1.6	1.8
DDI	102120-1	445C-3.6Hedpa-72dpa	29.0 ± 4.5	21.5 ± 1.5	2.0
BOR60	P037-T55	453C-0.77Hedpa-19dpa	Negl.	Negl.	Negl.
DDI	020320	520C-3.2Hedpa-16.6dpa	N/O	N/O	-
BOR60	P038-T61	450C-0.77Hedpa-32dpa	N/O	N/O	-
DDI	091719	520C-4.3Hedpa-28dpa	N/O	N/O	-
BOR60	P042-T67	517C-0.77Hedpa-15dpa	N/O	N/O	-
DDI	110117	570C-4.3Hedpa-15.4dpa	N/O	N/O	-
BOR60	P043-T108	515C-0.77Hedpa-25dpa	N/O	N/O	-
DDI	111219	570C-4.3Hedpa-28dpa	N/O	N/O	-

*N/O = Not observed

The comparison of the radiation-induced segregation behavior at grain boundaries indicates that dual-ion and BOR-60 irradiations partially match. Although both irradiation methods lead to a depletion of Fe at the grain boundary at low temperature, the depletion is more significant in BOR-60 samples as shown by the ratios in Figure 6.7. This observation is consistent with the simultaneous enrichment of Cr at the grain boundary, which is greater in BOR-60 samples compared to dual-ion samples. In fact, one dual-ion sample (445°C:70dpa) exhibits Cr depletion at the grain boundary. Potential differences in the nature (prior austenite or lath) and angle (low or high) of the measured grain boundaries contribute to the observed variability in Cr segregation in dual-ion-irradiated samples. At high temperature, BOR-60 samples exhibit clear depletion of Fe and enrichment of Cr at grain boundaries while dual-ion samples show no segregation behavior for these elements. Except at low temperature at 35 dpa, the segregation behavior of Ni matches between the two irradiation methods across temperatures as shown in Figure 6.7, with a decrease

in enrichment with increasing temperature. At low temperatures, both irradiation methods lead to an enrichment in Si at the grain boundary that increases with increasing damage level. At high temperature, Si segregation decreases but the match between BOR-60 samples (450-453°C and 515-517°C) and dual-ion samples (520°C and 570°C) is still present. All results are tabulated in Table 6.3.

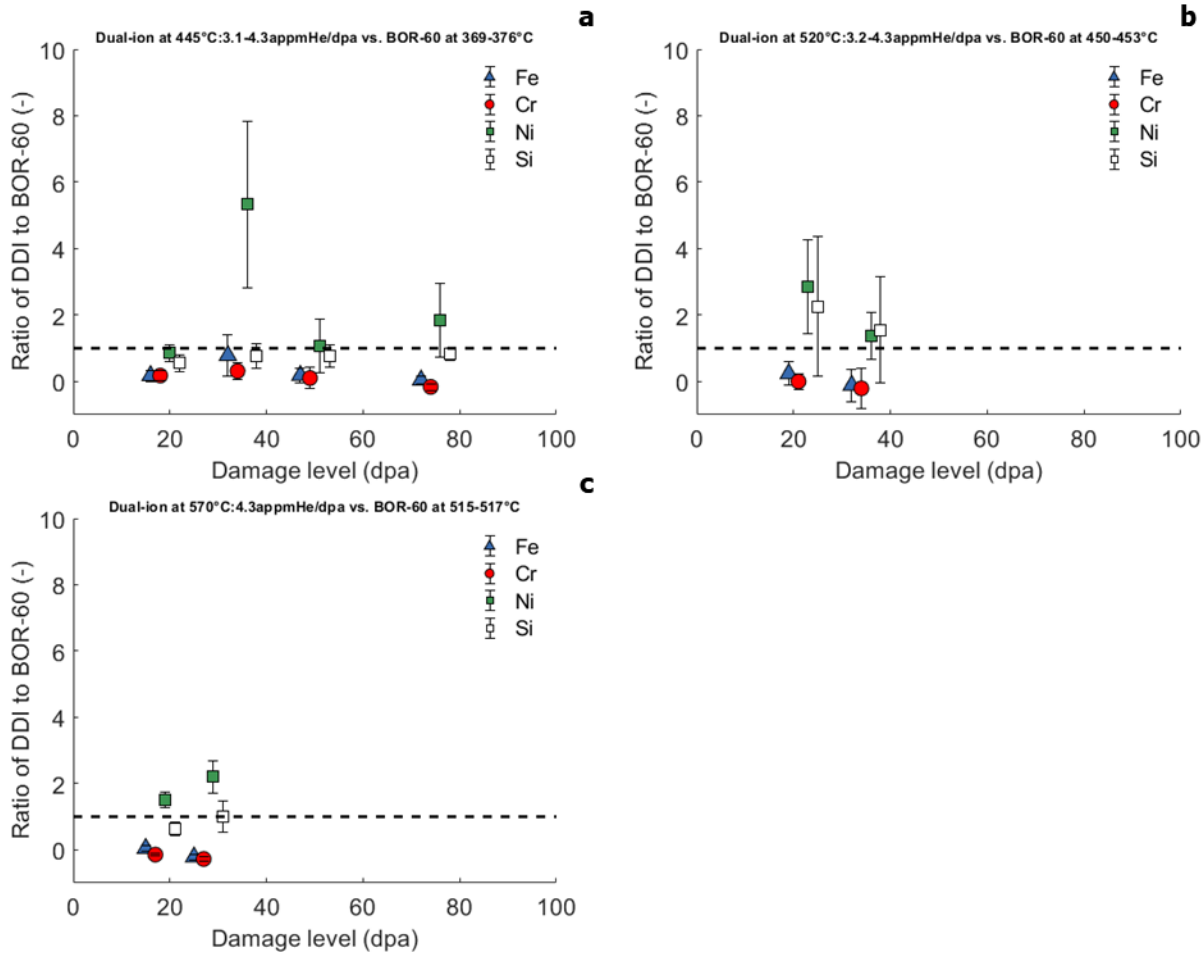


Figure 6.7: Ratios of segregation at grain boundaries of Fe, Cr, Ni and Si (a) between dual-ion irradiation at 445°C:3.1-4.3appmHe/dpa and BOR-60 at 369-376°C, (b) between dual-ion irradiation at 520°C:3.2-4.3appmHe/dpa and BOR-60 at 450-453°C, and (c) between dual-ion irradiation at 570°C:4.3appmHe/dpa and BOR-60 at 515-517°C.

Table 6.3: Radiation-induced segregation of irradiated T91 30176 for BOR-60 conditions and companion dual-ion irradiations.

Irradiation mode	Sample	Condition	Fe (wt%)		Cr (wt%)		Ni (wt%)		Si (wt%)	
			Peak	ΔFe	Peak	ΔCr	Peak	ΔNi	Peak	ΔSi
BOR60	P027-T03	369C-0.77Hedpa-16dpa	85.9±1.7	-4.0±1.7	10.9±1.5	3.4±1.5	0.32±0.06	0.22±0.06	0.60±0.07	0.31±0.07
DDI	092717	445C-4.3Hedpa-16.6dpa	89.5±0.7	-0.7±0.6	8.2±0.6	0.6±0.5	0.31±0.02	0.19±0.02	0.39±0.02	0.17±0.07
BOR60	P028-T05	372C-0.77Hedpa-32dpa	88.3±1.2	-2.3±1.2	9.5±0.8	1.6±0.8	0.31±0.07	0.18±0.08	0.72±0.19	0.38±0.16
DDI	053018-1	445C-4.3Hedpa-35dpa	87.7±1.1	-1.8±1.1	6.9±0.2	0.5±0.3	1.42±0.15	0.96±0.15	0.75±0.06	0.29±0.06
BOR60	P031-T98	376C-0.77Hedpa-47dpa	86.5±2.2	-3.8±2.2	10.5±2.0	2.9±2.2	0.43±0.17	0.30±0.21	0.70±0.21	0.45±0.15
DDI	070120-1	445C-3.1Hedpa-54dpa	89.1±1.2	-0.7±0.7	8.2±1.1	0.3±0.9	0.45±0.08	0.32±0.09	0.71±0.01	0.34±0.10
BOR60	P029-T11	375C-0.77Hedpa-72dpa	86.0±2.0	-4.8±2.3	11.0±2.2	3.7±2.2	0.45±0.02	0.31±0.04	0.75±0.02	0.50±0.03
DDI	020720	445C-3.2Hedpa-70dpa	89.4±0.3	-0.2±0.5	7.5±0.2	-0.6±0.1	0.72±0.35	0.57±0.34	0.67±0.08	0.41±0.09
BOR60	P037-T55	453C-0.77Hedpa-19dpa	86.3±2.6	-3.4±2.8	9.7±2.1	2.5±2.2	0.31±0.09	0.21±0.10	0.39±0.09	0.12±0.09
DDI	020320	520C-3.2Hedpa-16.6dpa	89.5±1.2	-0.8±1.0	7.6±0.7	0.0±0.6	0.74±0.08	0.60±0.08	0.49±0.16	0.27±0.15
BOR60	P038-T61	450C-0.77Hedpa-32dpa	86.6±1.6	-3.2±2.3	10.3±1.3	2.4±1.8	0.30±0.04	0.22±0.05	0.33±0.03	0.11±0.03
DDI	091719	520C-4.3Hedpa-28dpa	90.7±2.2	0.4±1.7	7.0±1.8	-0.5±1.4	0.41±0.14	0.30±0.14	0.44±0.17	0.17±0.17
BOR60	P042-T67	517C-0.77Hedpa-15dpa	84.8±0.5	-4.7±0.2	10.7±0.1	3.4±0.2	0.19±0.01	0.08±0.01	0.40±0.01	0.08±0.02
DDI	110117	570C-4.3Hedpa-15.4dpa	88.4±0.4	-0.2±0.4	7.1±0.1	-0.5±0.1	0.23±0.01	0.12±0.01	0.30±0.01	0.05±0.01
BOR60	P043-T108	515C-0.77Hedpa-25dpa	87.7±0.2	-2.3±0.2	9.8±0.2	1.8±0.1	0.14±0.02	0.05±0.01	0.25±0.06	0.03±0.01
DDI	111219	570C-4.3Hedpa-28dpa	90.7±0.1	0.5±0.2	7.5±0.1	-0.5±0.1	0.22±0.00	0.11±0.01	0.23±0.00	0.03±0.01

*Values estimated from [16]

The Ni-Si cluster microstructure evolution of dual-ion samples irradiated at 445°C:3.1-4.3appmHe/dpa exhibits a stark difference with that of BOR-60 samples irradiated at 369-376°C. Although both irradiation methods induced the precipitation of clusters with an average diameter around 6 nm at all damage levels, BOR-60 cluster densities are more than an order of magnitude higher than dual-ion as shown in Figure 6.8. At high temperatures, no Ni/Si clusters are observed in either irradiation method. Figure 6.9 shows the size distributions and indicates that Ni-Si-Mn clusters are denser for all diameters and can be much larger in the BOR-60 conditions. Results are tabulated in Table 6.4. As described in Section 4.4.2.3, these results are not validated against APT, and the magnitude of the measured densities and diameters might be inaccurate since they do not consider clusters smaller than 2 nm in diameter, but comparisons between conditions are still expected to provide reliable conclusions regarding the capability of dual-ion irradiation to match precipitation in neutron-irradiated specimens.

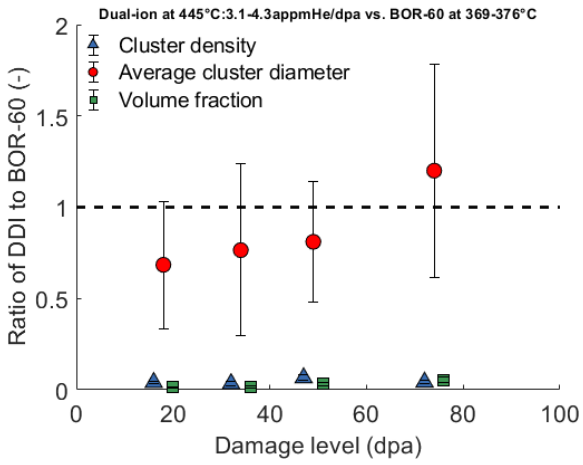


Figure 6.8: Ratios of cluster density, average cluster diameter and volume fraction between dual-ion irradiation at 445°C:3.1-4.3appmHe/dpa and BOR-60 at 369-376°C.

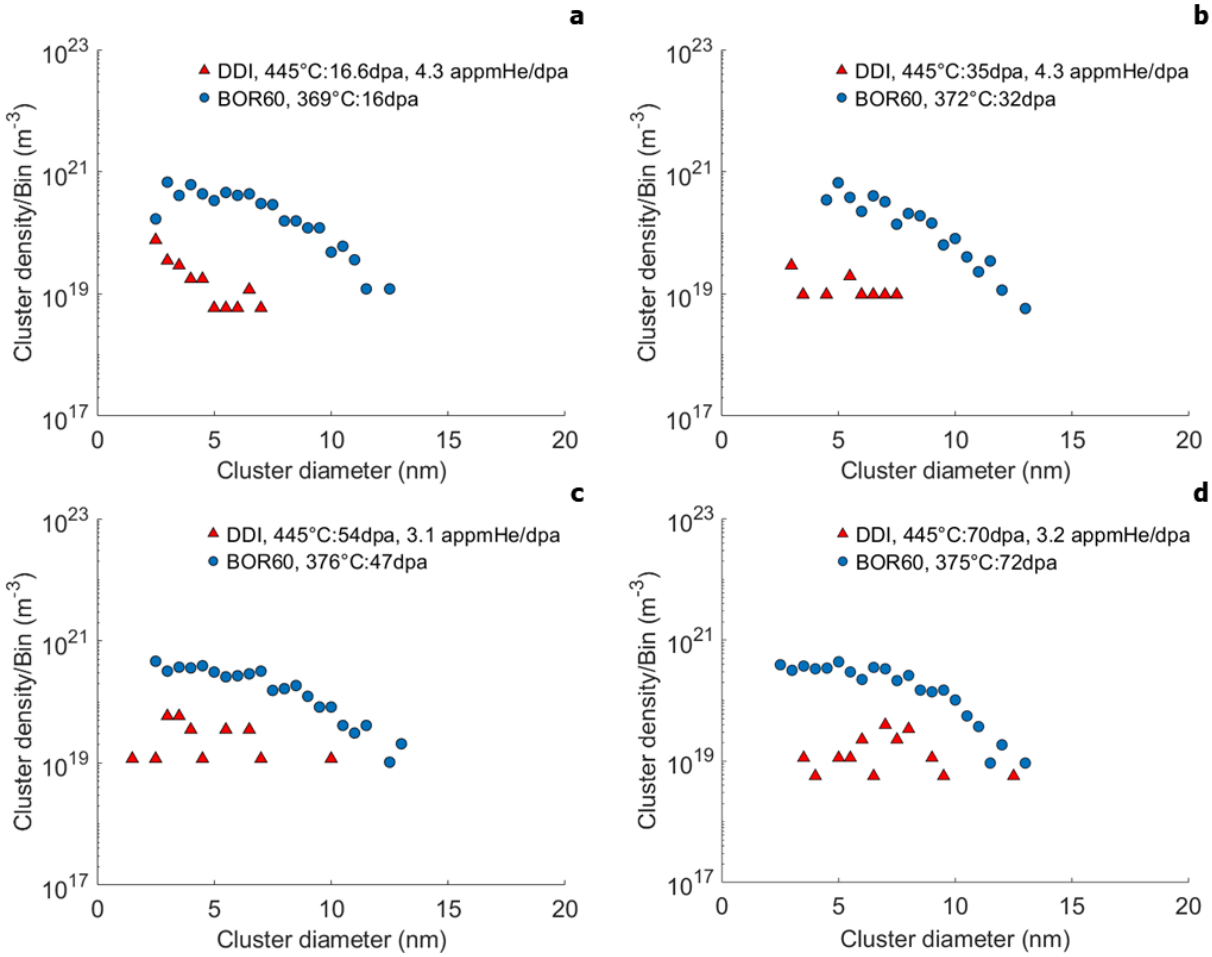


Figure 6.9: Cluster size distributions of irradiated T91 30176 for BOR-60 at 369-376°C and dual-ion irradiations at 445°C to (a) 16 dpa, (b) 32-35 dpa, (c) 47-57 dpa and (d) 70-72 dpa.

Table 6.4: Ni/Si-cluster microstructures of irradiated T91 30176 for BOR-60 conditions and companion dual-ion irradiations.

Irradiation mode	Sample	Condition	Cluster density ($\times 10^{20}$ m^{-3})	Average cluster diameter (nm)	Volume fraction (%)
BOR60	P027-T03	369C-0.77Hedpa-16dpa	52.6 ± 5.8	5.7 ± 1.9	0.07 ± 0.01
DDI	092717	445C-4.3Hedpa-16.6dpa	2.1 ± 0.4	3.9 ± 1.5	0.0009 ± 0.0002
BOR60	P028-T05	372C-0.77Hedpa-32dpa	32.8 ± 3.6	6.8 ± 3.7	0.07 ± 0.01
DDI	053018-1	445C-4.3Hedpa-35dpa	1.1 ± 0.3	5.2 ± 1.5	0.001 ± 0.0003
BOR60	P031-T98	376C-0.77Hedpa-47dpa	42.8 ± 4.8	5.8 ± 1.5	0.07 ± 0.01
DDI	070120-1	445C-3.1Hedpa-54dpa	2.8 ± 0.6	4.7 ± 1.5	0.0023 ± 0.0005
BOR60	P029-T11	375C-0.77Hedpa-72dpa	45.5 ± 5.0	6.0 ± 1.5	0.08 ± 0.01
DDI	020720	445C-3.2Hedpa-70dpa	1.9 ± 0.4	7.2 ± 3.0	0.0044 ± 0.0011
BOR60	P037-T55	453C-0.77Hedpa-19dpa	N/O	N/O	-
DDI	020320	520C-3.2Hedpa-16.6dpa	N/O	N/O	-
BOR60	P038-T61	450C-0.77Hedpa-32dpa	N/O	N/O	-
DDI	091719	520C-4.3Hedpa-28dpa	N/O	N/O	-
BOR60	P042-T67	517C-0.77Hedpa-15dpa	N/O	N/O	-
DDI	110117	570C-4.3Hedpa-15.4dpa	N/O	N/O	-
BOR60	P043-T108	515C-0.77Hedpa-25dpa	N/O	N/O	-
DDI	111219	570C-4.3Hedpa-28dpa	N/O	N/O	-

*N/O = Not observed

These differences in RIS and RIP behaviors can be explained by different phenomena. Wharry et al. [41,95] showed that the Inverse Kirkendall (IK) effect describes the segregation of Cr as a function of temperature. Cr diffuses faster than Fe via both vacancies and interstitials in FM steels: both point defects contribute to Cr segregation. As temperature increases, vacancies become more mobile and contribute more to Cr diffusion which leads to a decrease of the Cr enrichment and Fe depletion at grain boundaries. Additionally, lower damage rates typically lead to higher Cr segregation in FM steels [275]. BOR-60 irradiations being at a lower temperature and lower damage rate than dual-ion irradiations while exhibiting more Cr enrichment is consistent with this analysis. For solute atoms, the solute drag effect must be considered on top of the Inverse Kirkendall effect. If the solute-point-defect interaction is strongly attractive, the solute and the point defect will migrate as a complex specie, in which the solute is dragged in the direction of

point defect flux. The solute-vacancy interaction is strong in a wide temperature regime (<600°C) and predicts enrichment of Ni and Si at grain boundaries consistent with results presented above for both irradiation methods [276]. In both irradiation methods, ballistic mixing occurs. Under dual-ion irradiation, higher damage rate can increase the ballistic mixing higher than the back diffusion of solutes to clusters which can reduce their size and density, since the distance a solute atom travels due to ballistic mixing is estimated to be around 1 nm, larger than the interaction distance of nucleating sinks [102]. Additionally, the lack of time for solutes to migrate under high-damage-rate dual-ion irradiation reduces their diffusion distance [102] and contributes to the reduced cluster density in dual-ion irradiation.

In conclusion, the cavity and loop microstructures of dual-ion-irradiated samples with a temperature shift of 50-70°C and an increase in helium injection rate of 4-6 times match those of BOR-60 samples irradiated at 369-376°C and 450-517°C up to 72 dpa. For radiation-induced segregation, both Cr and Fe segregate less under ion irradiation compared to that in BOR-60 because of higher irradiation temperature, as explained by the Inverse Kirkendall effect, and higher damage rate. Ni and Si segregation under ion irradiation matches that of BOR-60 since the vacancy-drag effect that dominates their diffusion persists at higher temperature. Ni/Si clustering is reduced under dual-ion irradiation due to increased ballistic mixing and shorter solute diffusion distance resulting from the lack of time for migration.

6.1.2 The special case of BOR-60-irradiated microstructure at 402-404°C and companion dual-ion irradiation

The microstructure evolution of BOR-60 samples irradiated at 402-404°C is discussed separately due to inconsistencies.

The cavity microstructures of these BOR-60 samples exhibit a sharp decrease in void density from 17 dpa (2.8×10^{20} m^{-3}) to 29 dpa (0.03×10^{20} m^{-3}) and 86 dpa (0.46×10^{20} m^{-3}). As explained in Section 2.2.1.1, the void density is expected to increase with increasing damage level like what has been observed for T91 irradiated in other BOR-60 and FFTF conditions presented in Chapter 5. To explain the evolution of the cavity microstructure in BOR-60 at 402-404°C, swelling and void density data from ferritic-martensitic steels is compiled from literature [49–54,277–281] alongside the dual-ion irradiation results presented in this work (each plotted at the BOR-60 temperature that dual-ion irradiation is matching) in Figure 6.10 and Figure 6.11. Yan et al. [282] reported that dislocation loops with density ~ 9×10^{21} m^{-3} and Ni/Si clusters with density ~ 8×10^{22} m^{-3} formed after 0.5 dpa at 601°C in ATR-irradiated T91 but disappeared by 3 dpa. Thus, only data from samples irradiated to 16 dpa and above is considered since loop, cavity and cluster microstructures from the early stages of irradiation (~ few dpa) have been shown to not be representative of the microstructures at higher damage levels especially at high temperatures (> 500°C). The data points for BOR-60 402°C:29dpa and 402°C:86dpa are circled in red. For samples irradiated around 400°C, these two data points exhibit the lowest swelling and void density of any condition and any material (except HT-9 which has a better swelling resistance than T91), and are actually closer to samples irradiated at 450+°C. Looking at the dual-ion data points, the evolution of their swelling and void density as a function of temperature is consistent with the reactor database.

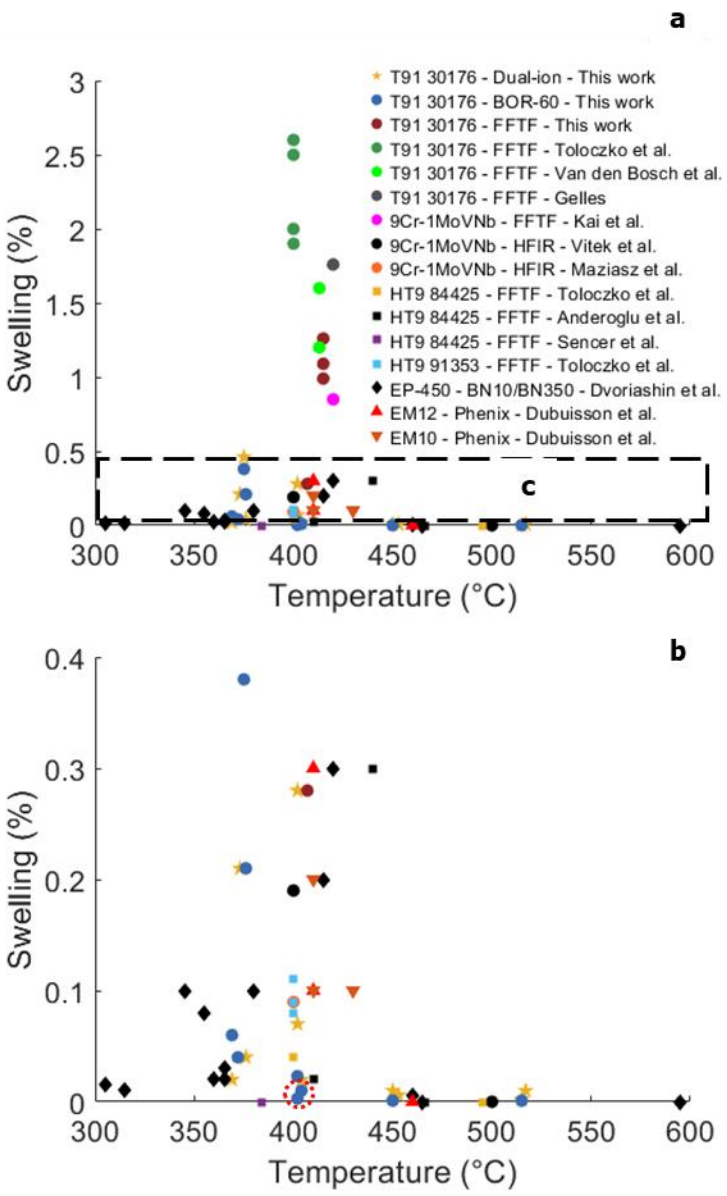


Figure 6.10: Swelling (inset in (b)) as a function of temperature in ferritic-martensitic steels irradiated in various reactors and equivalent dual-ion irradiation to 16-208 dpa. The legend is the same for both plots.

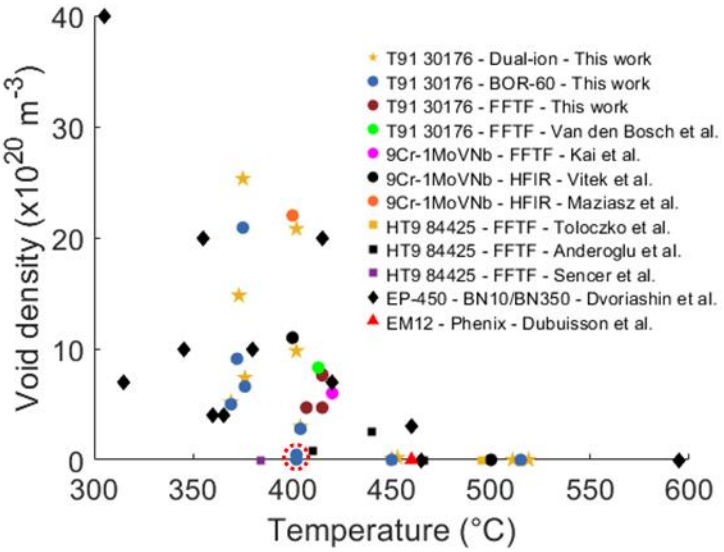


Figure 6.11: Void density as a function of temperature in ferritic-martensitic steels irradiated in various reactors and equivalent dual-ion irradiation to 16-184 dpa.

At the same time, dislocation loops observed at 404°C:17dpa are not present in samples irradiated to 402°C:29dpa and 402°C:86dpa contrary to the expected saturation in loop microstructure past ~5 dpa that has been observed for T91 irradiated in other BOR-60 and FFTF conditions in this work. Compared with literature results, Figure 6.12 indicates that the 402°C:29dpa and 402°C:86dpa cases (circled in red) are the only data points to exhibit no dislocation loops around 400°C. The temperature evolution of the loop density of dual-ion datapoints is consistent with the reactor database. Only samples irradiated at 450+°C typically do not exhibit loops.

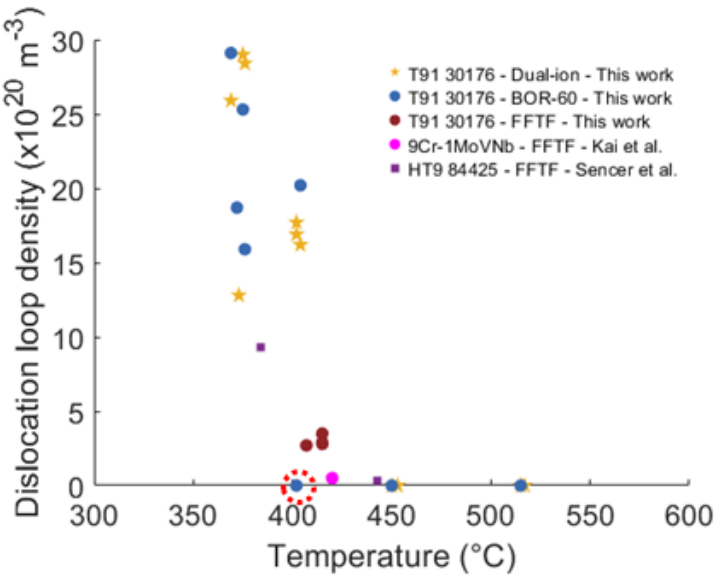


Figure 6.12: Dislocation loop density as a function of temperature in ferritic-martensitic steels irradiated in various reactors and equivalent dual-ion irradiation to 16-184 dpa.

The radiation-induced segregation behavior in BOR-60 at 404°C:17dpa is similar to that of lower temperature samples: enrichment of Cr, Ni and Si and depletion of Fe. However, samples irradiated to 29 dpa and 86 dpa do not exhibit the Si enrichment that is present at 16 dpa. In fact, the Si enrichment at 29 and 86 dpa is closer to the enrichment measured at 450-453°C and 515-517°C in BOR-60.

Finally, Ni/Si clusters observed at 404°C:17dpa are not present in samples irradiated to 402°C:29dpa and 402°C:86dpa. These clusters are expected to coarsen (slow increase in diameter and decrease in density) over the course of hundreds of dpa as indicated in Section 2.2.3.2 and as observed for T91 irradiated in other BOR-60 and FFTF conditions in this work. Compared with literature results, Figure 6.13 indicates that the 402°C:29dpa and 402°C:86dpa cases (circled in red) are the only data points to exhibit no Ni/Si clusters in FM steels around 400°C. Only samples irradiated at 450+°C typically do not exhibit any clustering of Ni and Si.

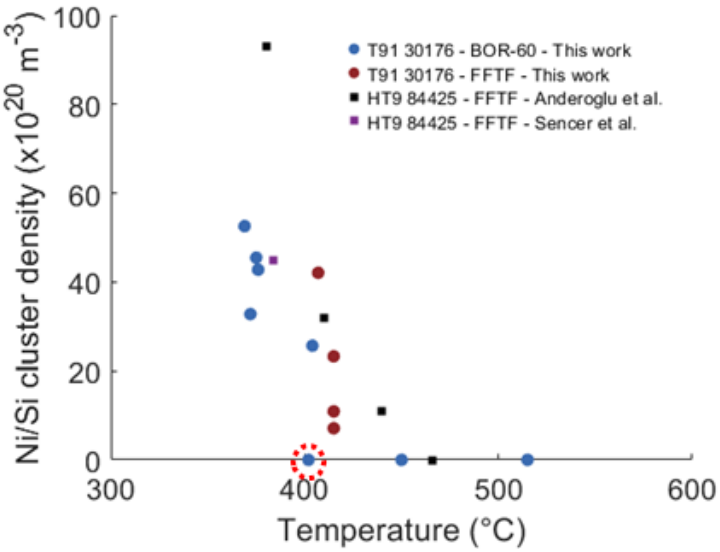


Figure 6.13: Ni/Si cluster density as a function of temperature in ferritic-martensitic steels irradiated in various reactors and equivalent dual-ion irradiation to 16-184 dpa.

Overall, the microstructures of samples irradiated at 402°C:29dpa and 402°C:86dpa in BOR-60 are close to that of samples irradiated in reactor at 450+°C (no loops, no clusters, reduced Si segregation and very low void density). Additionally, dual-ion-irradiated samples exhibit cavity and loop microstructures evolution as a function of temperature consistent with the reactor database. From Section 6.1.1, it is established that, with a single temperature shift and helium injection rate, dual-ion irradiation can match the evolution of BOR-60 cavity and loop microstructures across damage levels at temperatures below (369-376°C) and above (450-517°C) that of samples under scrutiny (402-404°C). Thus, the mismatch between BOR-60 at 402°C:29-86dpa and dual-ion at 460°C:33-72dpa (temperature shift and helium injection rate consistent with other matches) indicate that the reported temperature for BOR-60 is erroneous. Results for cavity microstructures are tabulated in Table 6.5 and results for loop microstructures are tabulated in Table 6.6.

Table 6.5: Cavity microstructures of irradiated T91 30176 for BOR-60 conditions and dual-ion irradiations.

Irradiation mode	Sample	Condition	Swelling (%)	Bubble density ($\times 10^{20}$ m^{-3})	Average bubble diameter (nm)	Void density ($\times 10^{20}$ m^{-3})	Average void diameter (nm)
BOR-60	P033-T24	404C-0.77Hedpa-17dpa	0.01 ± 0.00	160 ± 19	1.79 ± 0.28	2.8 ± 0.4	6.8 ± 0.8
DDI	092917	460C-4.3Hedpa-16.6dpa	0.015 ± 0.002	123 ± 15	1.64 ± 0.27	3.0 ± 0.4	8.1 ± 0.9
BOR-60	P036-T100	402C-0.77Hedpa-29dpa	0.003 ± 0.001	123 ± 14	1.59 ± 0.27	0.03 ± 0.01	9.6 ± 1.0
DDI	071320-1	460C-3.1Hedpa-33dpa	0.07 ± 0.01	96 ± 12	1.80 ± 0.28	9.8 ± 1.1	9.9 ± 1.5
BOR-60	P034-T32	402C-0.77Hedpa-86dpa	0.023 ± 0.003	393 ± 42	1.63 ± 0.28	0.46 ± 0.05	16.2 ± 1.4
DDI	091420-1	460C-3.2-3.7Hedpa-72dpa	0.28 ± 0.03	756 ± 82	1.55 ± 0.27	20.8 ± 2.4	11.7 ± 1.6

Table 6.6: Dislocation loop microstructures for BOR-60 samples and companion dual-ion irradiations.

Irradiation mode	Sample	Condition	Loop density ($\times 10^{20}$ m^{-3})	Average loop diameter (nm)	Loop sink strength ($\times 10^{14}$ m^{-2})
BOR-60	P033-T24	404C-0.77Hedpa-17dpa	20.2 ± 3.6	25.8 ± 1.9	1.7
DDI	092917	460C-4.3Hedpa-16.6dpa	16.2 ± 2.9	29.5 ± 2.1	1.5
BOR-60	P036-T100	402C-0.77Hedpa-29dpa	N/O	N/O	-
DDI	071320-1	460C-3.1Hedpa-33dpa	17.7 ± 3.8	27.3 ± 2.0	1.5
BOR-60	P034-T32	402C-0.77Hedpa-86dpa	N/O	N/O	-
DDI	091420-1	460C-3.2-3.7Hedpa-72dpa	16.9 ± 3.6	27.0 ± 2.0	1.5

The temperature estimates were computed from gamma heating values that are subject to large uncertainties from changes in fuel loading, burnup and control rod movements. Additionally, material experiments often operate in parasitic mode since reactors are rarely designed for materials testing. Reactor operators are often required to run reactivity feedback tests at a fraction of full power or to reduce the power level when off-normal conditions are detected [283]. The effect of inaccuracies in temperature and helium production rate is also discussed in the context of model predictions in Appendix B.

Comparison with the database of reactor irradiations of Fe-Cr alloys indicates that the reported temperature for the BOR-60 samples irradiated at 402°C:29dpa and 402°C:86dpa is erroneous and likely to be closer to 450°C. This comparison demonstrates the importance of accurate reporting of irradiation conditions for dual-ion irradiation to match neutron-irradiated microstructures.

6.2 Rate theory model fitting

In this section, the rate theory model is fitted on the dual-ion irradiation conducted at 445°C first. The second subsection discusses a different set of parameters to fit the model on BOR-60

irradiations. The last subsection presents a set of parameters that correctly predict both datasets at once. Values of the modeling parameters are compared with literature.

6.2.1 Initial fit using dual ion irradiation at 445°C

The rate theory model developed in this work requires fitting to unlock predictive capabilities for cavity microstructures created in reactor environments. Several model parameters (cascade efficiency, dislocation bias, vacancy capture efficiency at dislocations and helium binding energy to cavities) are adjusted within bounds of reasonable values found in literature, so that the predicted cavity size distribution and swelling match with experimental results as closely as possible. These parameters are selected for fitting because they have the largest effect on the evolution of the cavity microstructure and exhibit relatively large ranges of values reported in literature.

The first step is to select the microstructures that will be used for fitting. Since the objective of the model is to simulate and predict the evolution of the cavity microstructure with increasing damage level, only BOR-60 and companion dual-ion conditions in which a void microstructure developed will be used for fitting (BOR-60 at 369-376°C and dual-ion at 445°C:3.1-4.3appmHe/dpa). Chapter 5 compiles characterization results that can be used for this purpose, but it is important to realize that these measured microstructures are not perfectly representative since the sampling volumes of the techniques used are very small. Even minute variations in starting or target microstructures can affect the quality of the fit. Thus, a regularization process is applied to the bubble and void densities of the cavity microstructures to smooth the cavity microstructure evolution across damage levels and to provide values for bubble and void nucleation rates. For BOR-60 and dual-ion series to intermediate damage levels (<= 100dpa), samples are assumed to be in the incubation regime, and the void densities can be interpolated using a linear regression

with an intercept of 0 void/m^{-3} at 0 dpa. On the other hand, bubble densities exhibit much more variability and no trend with increasing damage level. To obtain a sensible estimate, bubble densities from BOR-60 and dual-ion irradiations at 445°C:3.1-4.3appmHe/dpa and 460°C:3.1-4.3appmHe/dpa (because it is at the same helium injection rate as 445°C) are used to obtain a linear regression of bubble density as a function of damage level as shown in Figure 6.14(d). Note that values more than double the computed average are removed from the analysis (crossed out in Table 6.7). The bubble and void densities to be used in the model for fitting and validation are the interpolated values. Although bubble microstructures of 460°C:3.1-4.3appmHe/dpa are used for the regularization process, this condition is not used for fitting since it does not match with any BOR-60 condition. The complete regularization of dual-ion samples irradiated at 460°C:3.1-4.3appmHe/dpa is still presented in this subsection and later used in Section 6.3. Results of all regressions are shown in Figure 6.14 and Table 6.7.

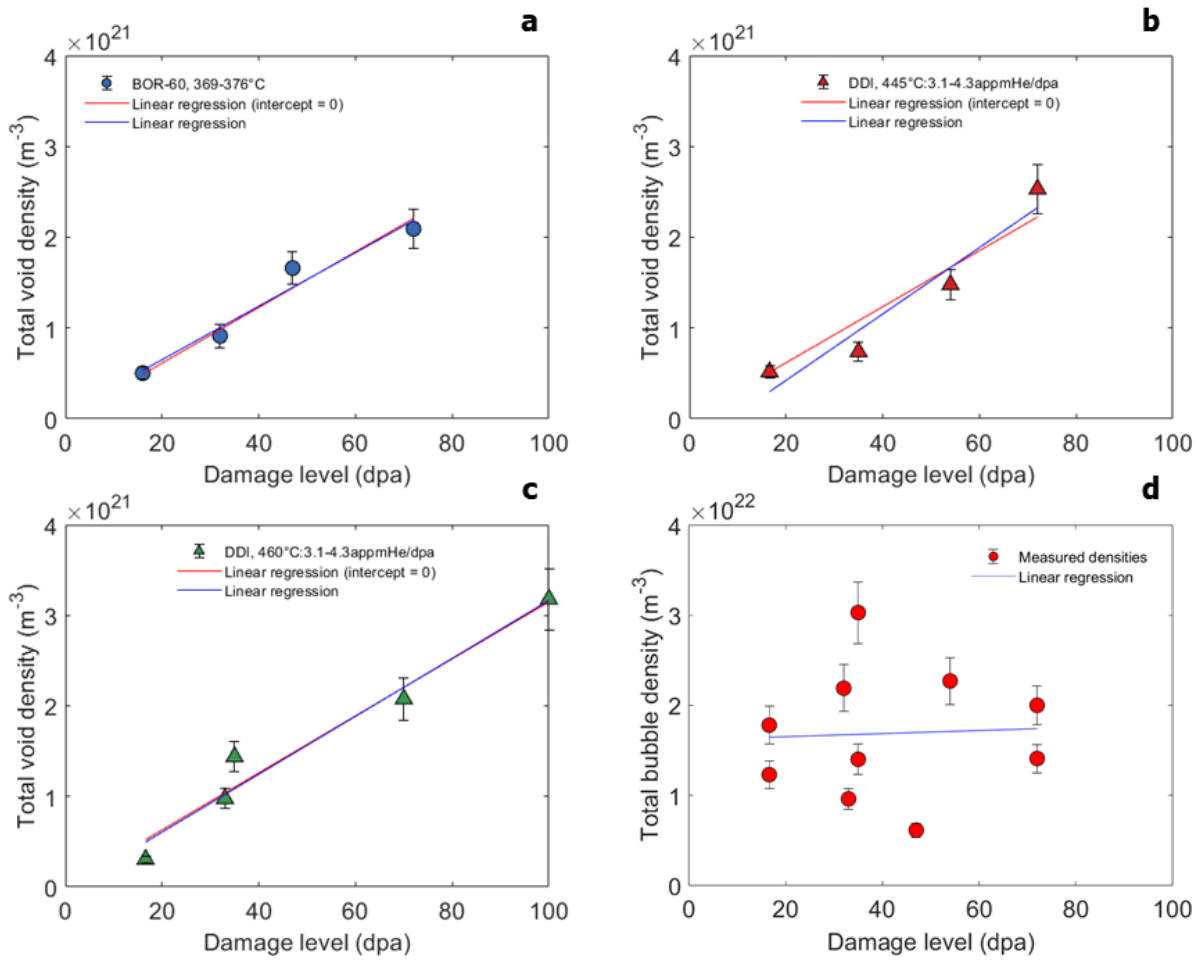


Figure 6.14: Linear regressions of (a) BOR-60 void densities (369-376°C), (b) dual-ion void densities at 445°C:3.1-4.3appmHe/dpa, (c) dual-ion void densities at 460°C:3.1-4.3appmHe/dpa, and (d) bubble densities (BOR-60 at 369-376°C, dual-ion at 445°C and 460°C).

Table 6.7: Cavity densities, swelling and nucleation rates of regularized BOR-60 and dual-ion conditions.

Irradiation mode	Sample	Condition	Measured densities ($\times 10^{20}$ m^{-3}) and swelling (%)			Regularized densities ($\times 10^{20}$ m^{-3}) and swelling (%)			Bubble nucleation rate ($\times 10^{20}$ m^{-3})	Void nucleation rate ($\times 10^{20}$ m^{-3})
			Bubble density	Void density	Swelling	Bubble density	Void density	Swelling		
BOR-60	P027-T03	369C-0.77Hedpa-16dpa	~~1000~~	5.0	0.06	164	4.9	0.02	0.175	0.307
BOR-60	P028-T05	372C-0.77Hedpa-32dpa	219	9.1	0.04	167	9.8	0.04		
BOR-60	P031-T98	376C-0.77Hedpa-47dpa	61	16.6	0.21	170	14.4	0.19		
BOR-60	P029-T11	375C-0.77Hedpa-72dpa	141	20.9	0.38	174	22.1	0.40		
DDI	092717	445C-4.3Hedpa-16.6dpa	178	5.2	0.02	164	5.1	0.02		0.309
DDI	053018-1	445C-4.3Hedpa-35dpa	140	7.4	0.04	169	10.8	0.06		
DDI	070120-1	445C-3.1Hedpa-54dpa	227	14.8	0.21	171	16.7	0.23		
DDI	102120-1	445C-3.6Hedpa-72dpa	200	25.3	0.46	174	22.2	0.40		
DDI	092917	460C-4.3Hedpa-16.6dpa	123	3.0	0.01	164	5.2	0.02		0.312
DDI	071320-1	460C-3.1Hedpa-33dpa	96	9.8	0.07	167	10.3	0.08		
DDI	021121	460C-4.3Hedpa-35dpa	303	14.4	0.12	168	10.9	0.09		
DDI	091420-1	460C-3.2-3.7Hedpa-72dpa	~~756~~	20.8	0.28	174	22.5	0.28		
DDI	030621-1	460C-4.3Hedpa-100dpa	~~610~~	31.8	0.65	179	31.2	0.62		

Following the regularization step, the fitting of the model is first applied on the dual-ion irradiations that match the BOR-60 cavity microstructures (445°C:3.1-4.3appmHe/dpa, 16.6-72 dpa). Parameters for the model described in Section 4.5.2 are adjusted until the predicted cavity microstructure at 35, 54 and 72 dpa from the starting microstructure at 16.6 dpa match the regularized microstructures. The nucleation rates of bubbles and voids used during this fitting are extracted from the regularized size distributions (Table 6.7). The parameters used for this fit are those presented in Section 4.5.2 with slight differences in dislocation bias (9.5%), cascade efficiency (3%) and helium binding energy to cavities $\left(3.3 - \left(\frac{He}{vac}\right)^2 - 1.06 \times \frac{He}{vac}\right)$. The results of this fit are shown in Figure 6.15 and Table 6.8 and exhibit excellent agreement with the regularized dual-ion cavity microstructures. For clarity, the modeling parameters used in all simulations is specified at the top of each figure.

Note that measured cavities can have low counting statistics due to the small sampling volume of characterization techniques. This limits the minimum measurable density of voids in a bin of a size distribution. This shortcoming essentially creates a threshold density below which cavities cannot be correctly represented in measured size distributions. Simulated size distributions from the rate theory model do not have such limitations. To ensure fair comparisons, predictions falling in the 'undetectable' regions for measured samples are excluded from the swelling and diameter values presented in tables.

The same model parameters are then used to simulate the cavity microstructure evolution of BOR-60 samples irradiated at 369-376°C to 32, 47 and 72 dpa from the starting microstructure at 16 dpa. Results are shown in Figure 6.15 and Table 6.8. The model simulation overestimates void growth and leads to predicted swelling, average diameter and root-mean-cube diameter higher than the measured values.

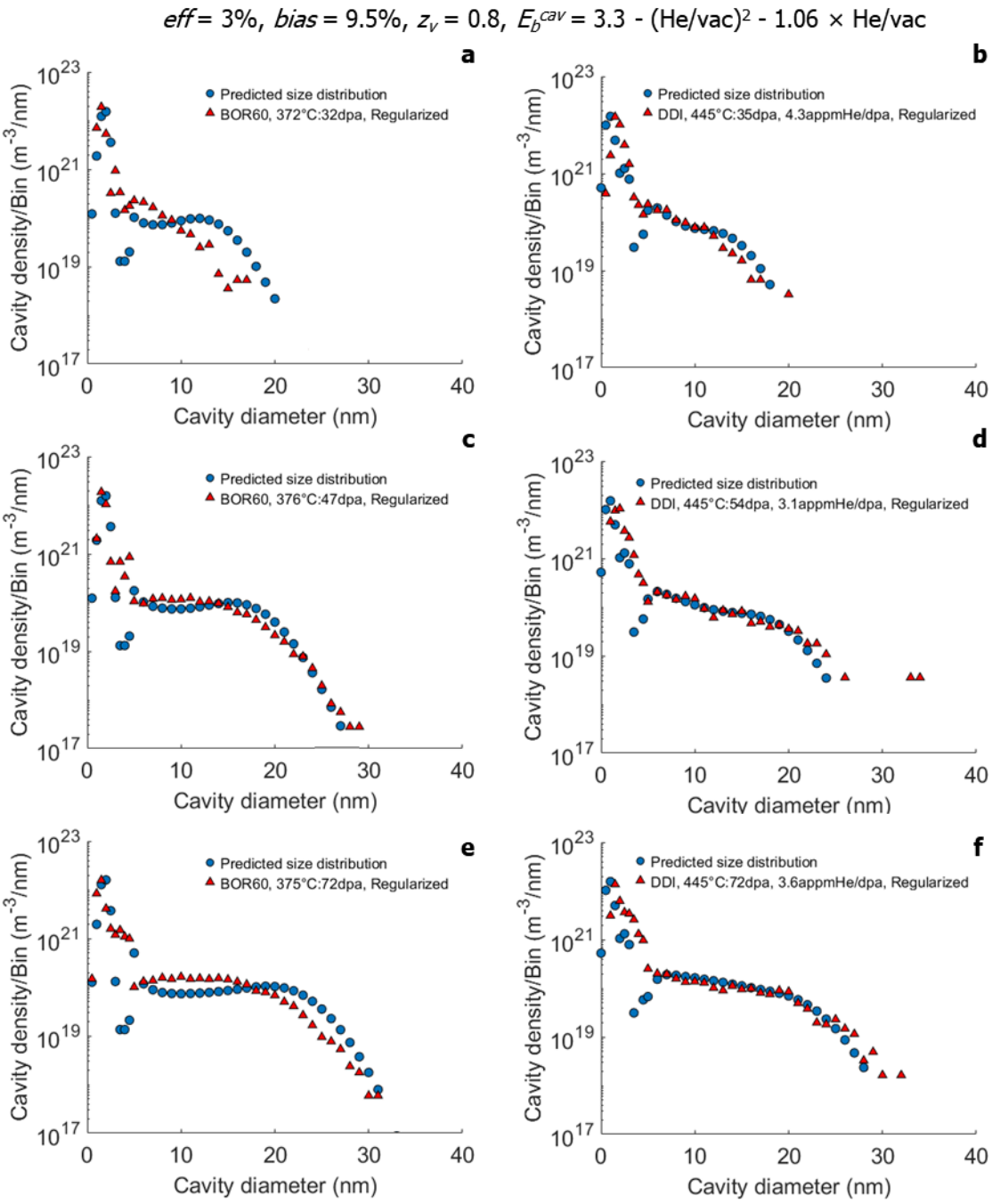


Figure 6.15: Prediction of the BOR-60-irradiated cavity microstructures at (a) 32 dpa, (c) 47 dpa and (e) 72 dpa, and of the dual-ion-irradiated cavity microstructures at (b) 35dpa:4.3appmHe/dpa, (d) 54dpa:3.1appmHe/dpa and (f) 72dpa:3.6appmHe/dpa.

Table 6.8: Comparison of predicted vs. measured (regularized) dual-ion- and BOR-60-irradiated cavity microstructures.

Irradiation mode	Sample	Condition	Regularized swelling (%), average diameter (nm), root-mean-cube diameter (nm) and densities (10^{20} m^{-3})					Predicted swelling (%), average diameter (nm), root-mean-cube diameter (nm) and densities (10^{20} m^{-3})				
			Swelling	Average diameter	RMC diameter	Bubble density	Void density	Swelling	Average diameter	RMC diameter	Bubble density	Void density
BOR60	P028-T05	372C-0.77Hedpa-32dpa	0.04	7.8	8.7	167	9.8	0.09	10.8	11.9	167	9.8
DDI	053018-1	445C-4.3Hedpa-35dpa	0.06	8.5	9.5	169	10.8	0.07	9.2	10.4	169	10.8
BOR60	P031-T98	376C-0.77Hedpa-47dpa	0.19	11.8	13.3	170	14.4	0.23	12.6	14.3	170	14.4
DDI	070120-1	445C-3.1Hedpa-54dpa	0.23	11.5	13.6	171	16.7	0.20	11.2	13.0	171	16.7
BOR60	P029-T11	375C-0.77Hedpa-72dpa	0.40	13.2	15.0	174	22.1	0.52	13.6	16.4	174	22.1
DDI	102120-1	445C-3.6Hedpa-72dpa	0.40	12.5	14.8	174	22.2	0.39	13.0	14.9	174	22.2

6.2.2 Fit using BOR-60 irradiation at 369-376°C

The objective of this work is to correctly predict the evolution of neutron-irradiated cavity microstructures. While the model parameters were selected to match dual-ion irradiation, they also need to match those from BOR-60. The parameters used for this new fit are those presented in Section 4.5.2 with a couple of exceptions: dislocation bias is 8.5% instead of 10%, cascade efficiency is 3% instead of 2.5%, helium binding energy to cavities is $\left(3.2 - \left(\frac{He}{vac}\right)^2 - 1.06 \times \frac{He}{vac}\right)$ instead of $\left(3.5 - 2 \times \frac{He}{vac}\right)$ and vacancy capture efficiency at dislocation is 1.5 instead of 0.8. Nucleation rates used are presented in Table 6.7.

Results for this new fit are shown in Figure 6.16 and Table 6.9, and exhibit a match of the BOR-60 size distribution and a mismatch of the dual-ion size distributions.

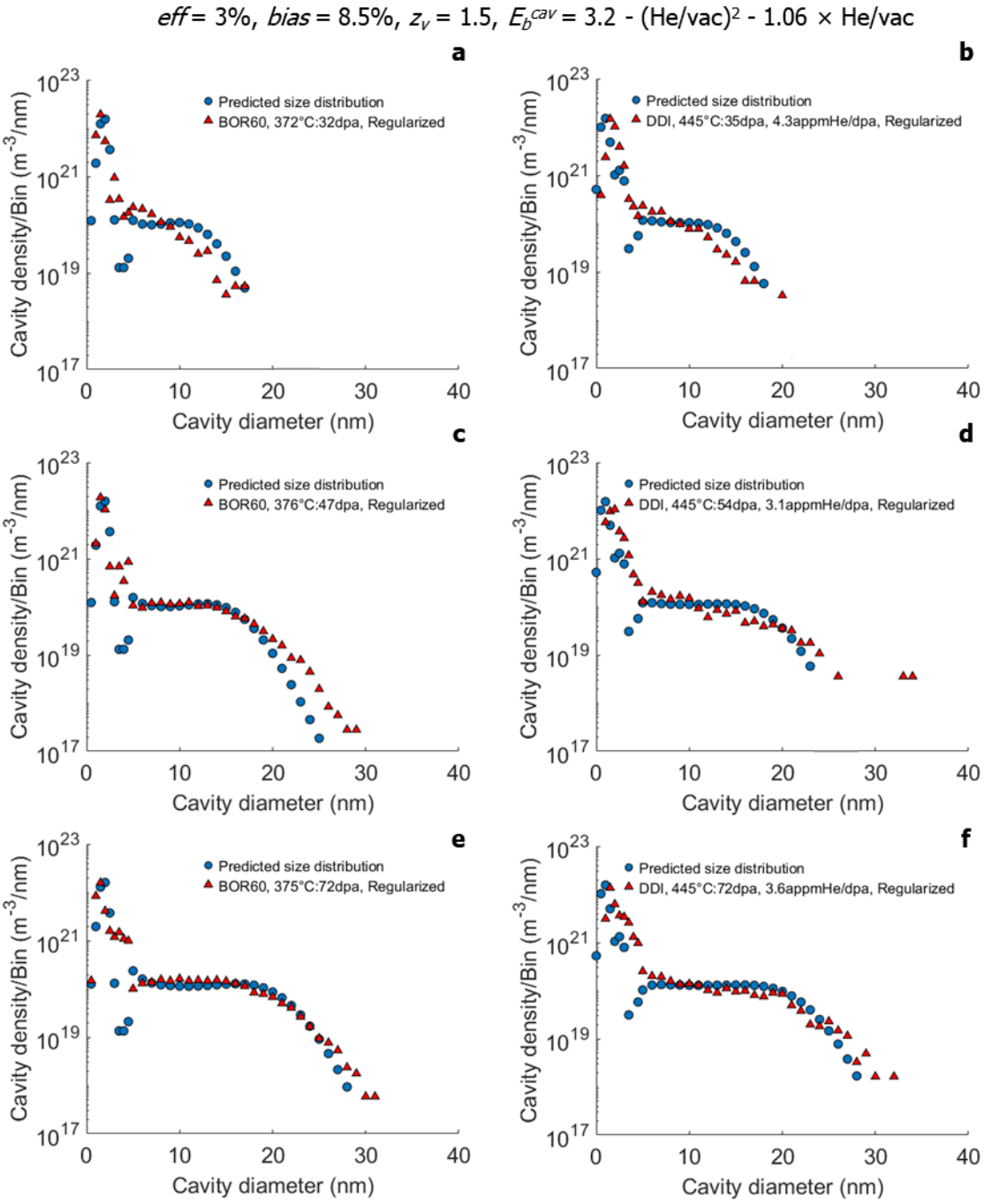


Figure 6.16: Adjusted prediction of the BOR-60-irradiated cavity microstructures at (a) 32 dpa, (c) 47 dpa and (e) 72 dpa, and of the dual-ion-irradiated cavity microstructures at (b) 35dpa:4.3appmHe/dpa, (d) 54dpa:3.1appmHe/dpa and (f) 72dpa:3.6appmHe/dpa.

Table 6.9: Comparison of predicted vs. measured (regularized) dual-ion- and BOR-60-irradiated cavity microstructures.

Irradiation mode	Sample	Condition	Regularized swelling (%), average diameter (nm), root-mean-cube diameter (nm) and densities ($10^{20}m^{-3}$)					Predicted swelling (%), average diameter (nm), root-mean-cube diameter (nm) and densities ($10^{20}m^{-3}$)				
			Swelling	Average diameter	RMC diameter	Bubble density	Void density	Swelling	Average diameter	RMC diameter	Bubble density	Void density
BOR60	P028-T05	372C-0.77Hedpa-32dpa	0.04	7.8	8.7	167	9.8	0.07	9.7	10.6	167	9.8
DDI	053018-1	445C-4.3Hedpa-35dpa	0.06	8.5	9.5	169	10.8	0.08	10.2	11.2	169	10.8
BOR60	P031-T98	376C-0.77Hedpa-47dpa	0.19	11.8	13.3	170	14.4	0.16	11.4	12.7	170	14.4
DDI	070120-1	445C-3.1Hedpa-54dpa	0.23	11.5	13.6	171	16.7	0.24	12.4	13.9	171	16.7
BOR60	P029-T11	375C-0.77Hedpa-72dpa	0.40	12.5	14.8	174	22.2	0.46	13.9	15.7	174	22.2
DDI	102120-1	445C-3.6Hedpa-72dpa	0.40	13.2	15.0	174	22.1	0.41	13.1	15.1	174	22.1

6.2.3 Optimizing the fit for BOR-60 and dual-ion collectively

A final, adjusted fitting is conducted to optimize the match with regularized cavity microstructures of BOR-60 and dual-ion-irradiated samples collectively. Nucleation rates used are presented in Table 6.7. The parameters used for this adjusted fit are those presented in Section 4.5.2 and only required minor adjustments from the two initial attempts: dislocation bias changed from 9.5% (resp. 8.5% for BOR-60-only fit) to 10%, cascade efficiency from 3% to 2.5%, helium binding energy to cavities from $\left(3.3 - \left(\frac{He}{vac}\right)^2 - 1.06 \times \frac{He}{vac}\right)$ (resp. $\left(3.2 - \left(\frac{He}{vac}\right)^2 - 1.06 \times \frac{He}{vac}\right)$) to $\left(3.5 - 2 \times \frac{He}{vac}\right)$ and vacancy capture efficiency at dislocation from 1.5 in the BOR-60-only case to 0.8. Results for this adjusted fit are shown in Table 6.10, and Figure 6.17, and exhibit a successful match between the predicted and regularized size distributions for both irradiation modes. The parameters considered are all physically reasonable and consistent with values found in literature as indicated throughout Section 4.5.2. The two exceptions are the vacancy capture efficiency at dislocations (0.8 used, 1-3 in literature) and the cascade efficiency (2.5% used, 5-10% in literature). A vacancy capture efficiency of 1 is used regularly in rate theory models and the slight difference used in this fit could come from the dislocation network density (5×10^{14} m^{-2}) measured in an unirradiated specimen being higher than under irradiation or changing with temperature. For cascade efficiency, 5-10% values given in literature [265] correspond to crc-dpa estimates in pure Fe above 500K and do not take into account cascade overlap effect with high densities of pre-existing sinks (grain boundaries, network dislocations and precipitates) that are present in ferritic-martensitic steels or debris from previous cascades. Cascade overlap can constitute up to 40% reduction in damage efficiency [284,285] and an efficiency value of 2.5% is consistent with values used in cluster dynamics models.

In conclusion, with careful fitting from experimental results, a rate theory model correctly predicts the cavity microstructure evolution of T91 30176 irradiated with dual-ion and in BOR-60 up to 72 dpa using the same irradiation and materials parameters that all fall within the range of reasonability based on measurements or calculation.

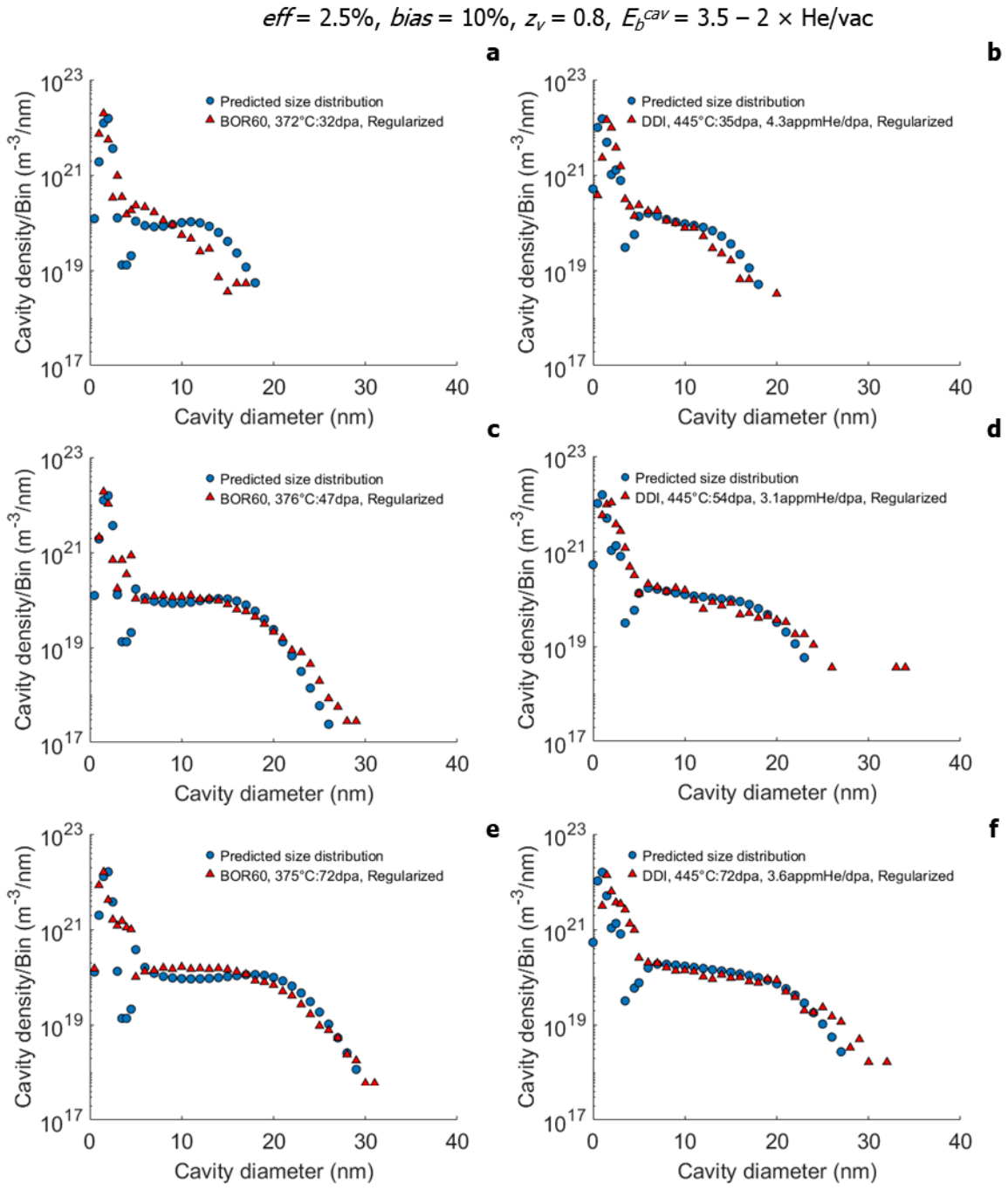


Figure 6.17: Adjusted prediction of the BOR-60-irradiated cavity microstructures at (a) 32 dpa, (c) 47 dpa and (e) 72 dpa, and of the dual-ion-irradiated cavity microstructures at (b) 35dpa:4.3appmHe/dpa, (d) 54dpa:3.1appmHe/dpa and (f) 72dpa:3.6appmHe/dpa.

Table 6.10: Comparison of predicted vs. measured (regularized) dual-ion- and BOR-60-irradiated cavity microstructures.

Irradiation mode	Sample	Condition	Regularized swelling (%), average diameter (nm), root-mean-cube diameter (nm) and densities ($10^{20}m^{-3}$)					Predicted swelling (%), average diameter (nm), root-mean-cube diameter (nm) and densities ($10^{20}m^{-3}$)				
			Swelling	Average diameter	RMC diameter	Bubble density	Void density	Swelling	Average diameter	RMC diameter	Bubble density	Void density
BOR60	P028-T05	372C-0.77Hedpa-32dpa	0.04	7.8	8.7	167	9.8	0.08	10.4	11.3	167	9.8
DDI	053018-1	445C-4.3Hedpa-35dpa	0.06	8.5	9.5	169	10.8	0.07	9.7	10.7	169	10.8
BOR60	P031-T98	376C-0.77Hedpa-47dpa	0.19	11.8	13.3	170	14.4	0.20	12.0	13.6	170	14.4
DDI	070120-1	445C-3.1Hedpa-54dpa	0.23	11.5	13.6	171	16.7	0.21	11.8	13.4	171	16.7
BOR60	P029-T11	375C-0.77Hedpa-72dpa	0.40	13.2	15.0	174	22.1	0.45	13.2	15.6	174	22.1
DDI	102120-1	445C-3.6Hedpa-72dpa	0.40	12.5	14.8	174	22.2	0.38	13.1	14.8	174	22.2

6.3 Validation of the model on additional dual-ion irradiations

After their final fit, model parameters listed in Sections 4.5.2 and 6.2.3 are kept constant. The capability of the model to predict the cavity microstructure in conditions with different temperatures, helium injection rates, starting microstructures and cavity nucleation rates can then be validated. Attempts at mimicking FFTF cavity microstructures provide additional dual-ion irradiations (460°C:0.2appmHe/dpa, 475°C:0.2appmHe/dpa, 475°C:0.8appmHe/dpa and 490°C:0.8appmHe/dpa) which can be regularized as shown in Figure 6.18, Figure 6.19 and Table 6.11 for this purpose. Since these conditions extend to damage levels past the incubation/nucleation regime, both the bubble and void densities are interpolated using a linear regression with a free intercept at 0 dpa which translates to, effectively, no regularization when the irradiation series only contains two damage levels.

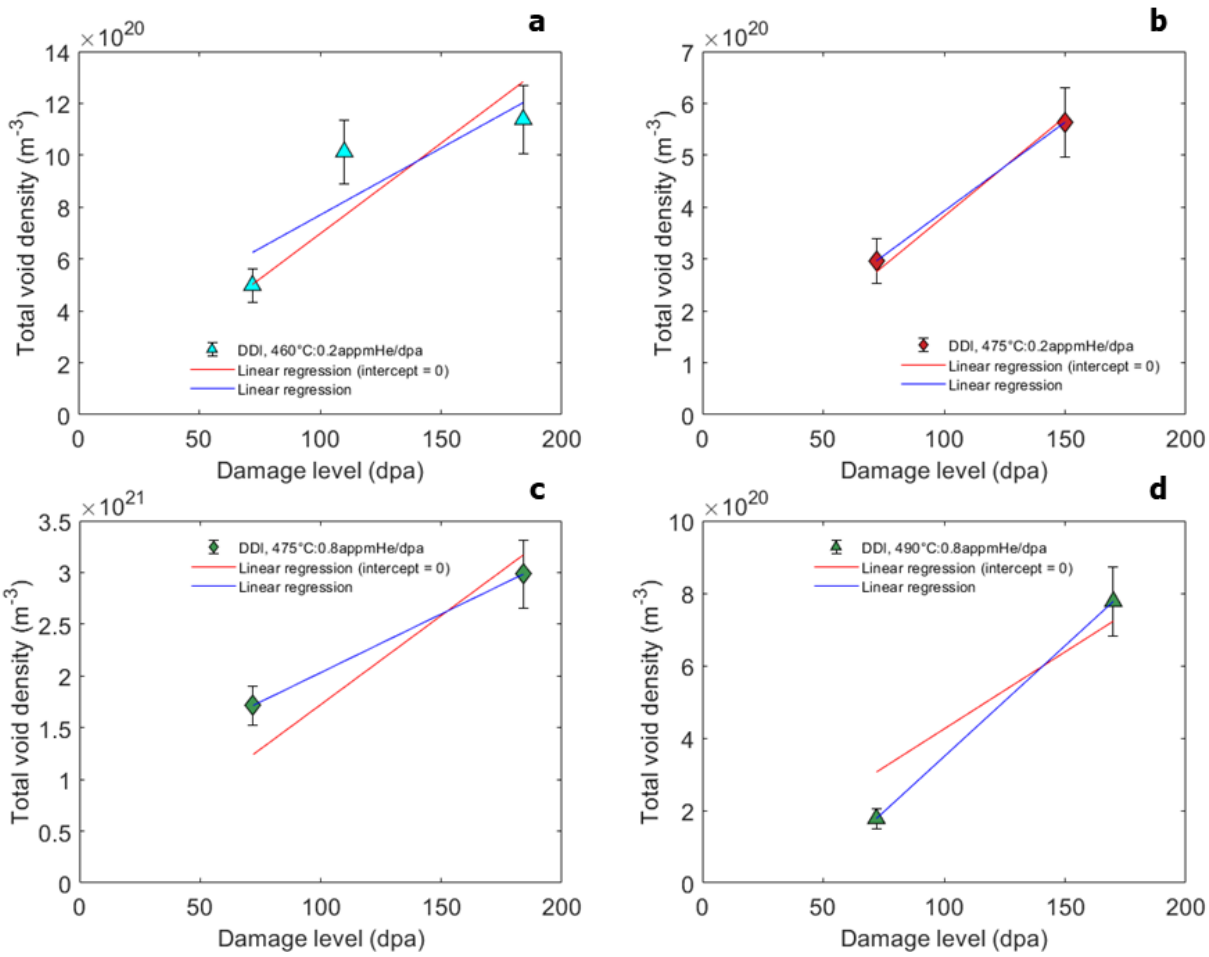


Figure 6.18: Linear regressions of (a) dual-ion void densities at 460°C:0.2appmHe/dpa (b) dual-ion void densities at 475°C:0.2appmHe/dpa, (c) dual-ion void densities at 475°C:0.8appmHe/dpa, and (d) dual-ion void densities at 490°C:0.8appmHe/dpa.

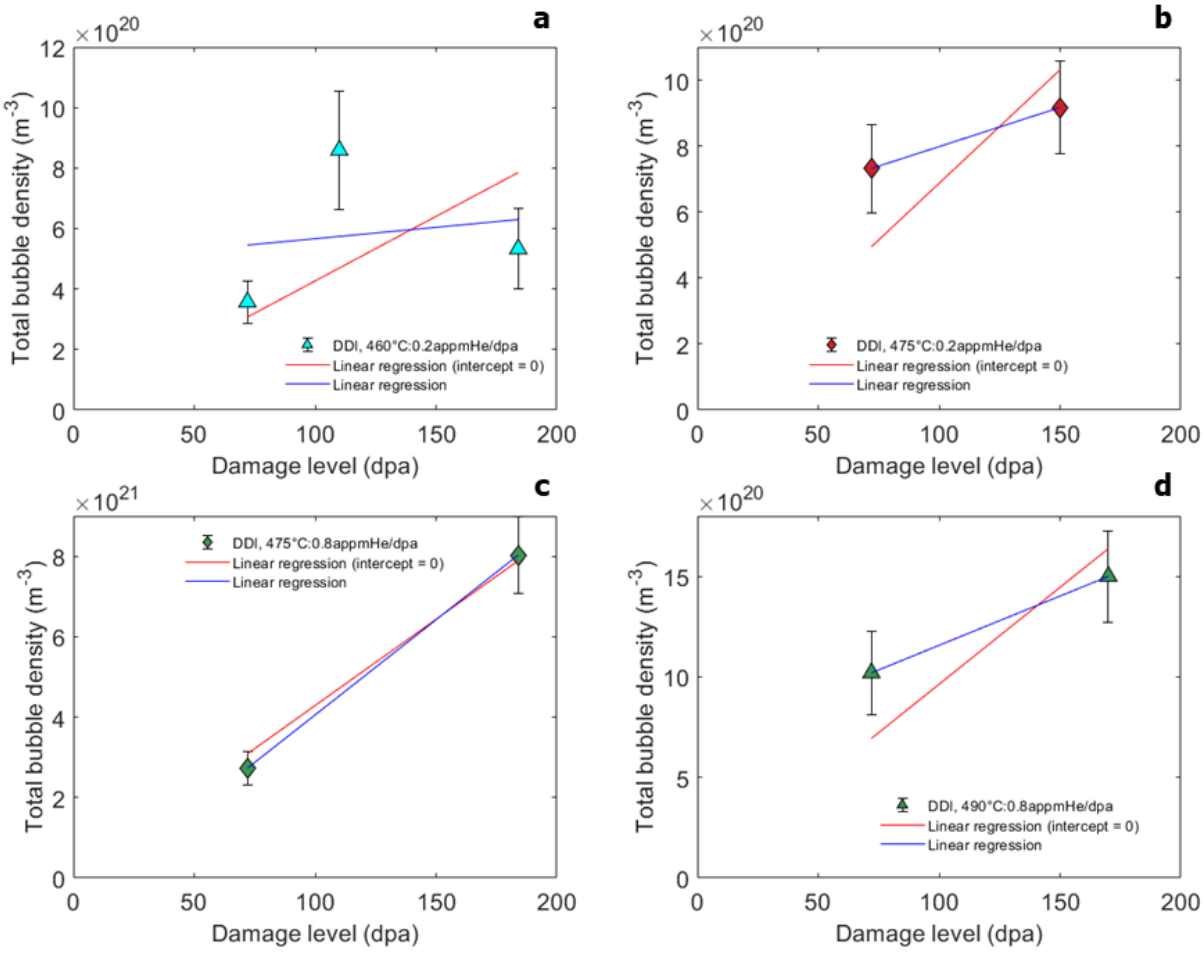


Figure 6.19: Linear regressions of (a) dual-ion bubble densities at 460°C:0.2appmHe/dpa (b) dual-ion bubble densities at 475°C:0.2appmHe/dpa, (c) dual-ion bubble densities at 475°C:0.8appmHe/dpa, and (d) dual-ion bubble densities at 490°C:0.8appmHe/dpa.

Table 6.11: Cavity densities, swelling and nucleation rates of regularized dual-ion conditions.

Irradiation mode	Sample	Condition	Measured densities ($\times 10^{20}$ m^{-3}) and swelling (%)			Regularized densities ($\times 10^{20}$ m^{-3}) and swelling (%)			Bubble nucleation rate ($\times 10^{20}$ m^{-3})	Void nucleation rate ($\times 10^{20}$ m^{-3})
			Bubble density	Void density	Swelling	Bubble density	Void density	Swelling		
DDI	062424	460C-0.2Hedpa-72dpa	3.6	5.0	0.31	5.4	6.3	0.39	0.0076	0.0516
DDI	012025-2	460C-0.2Hedpa-110dpa	8.6	10.2	1.64	5.7	8.2	1.30		
DDI	101424	460C-0.2Hedpa-184dpa	5.3	11.4	5.78	6.3	12.0	5.75		
DDI	020325-2	475C-0.2Hedpa-72dpa	7.3	3.0	0.41	7.3	3.0	0.41	0.0237	0.0344
DDI	020325-2	475C-0.2Hedpa-150dpa	9.2	5.6	2.56	9.2	5.6	2.56		
DDI	050224	475C-0.8Hedpa-72dpa	27.3	17.1	0.82	27.3	17.1	0.82	0.4732	0.1134
DDI	012524-4	475C-0.8Hedpa-184dpa	80.3	30.0	2.99	80.3	30.0	2.99		
DDI	040225	490C-0.8Hedpa-72dpa	10.2	1.8	0.12	10.2	1.8	0.12	0.0490	0.0611
DDI	040425	490C-0.8Hedpa-170dpa	15.0	7.8	2.04	15.0	7.8	2.04		

Following the regularization of these conditions, the prediction of the cavity microstructures using existing starting microstructures and calculated nucleation rates (Table 6.11) is conducted and reported for 460°C:3.1-4.3appmHe/dpa (Figure 6.20), 460°C:0.2appmHe/dpa (Figure 6.21), 475°C:0.2appmHe/dpa (Figure 6.22), 475°C:0.8appmHe/dpa (Figure 6.23) and 490°C:0.8appmHe/dpa (Figure 6.24). All results are tabulated in Table 6.12.

At 460°C:3.1-4.3appmHe/dpa, the predictions match the measured size distributions up to 35 dpa. At 72 and 100 dpa, the model over predicts the growth of voids which leads to higher swelling and average diameter values. A similar behavior is observed at 475°C:0.8appmHe/dpa going from 72 to 170 dpa. At 460°C:0.2appmHe/dpa, the predictive capability from 72 to 110 dpa is excellent, but the model underestimates the growth of cavities up to 184 dpa. Predictions at 475°C:0.2appmHe/dpa to 150 dpa and 490°C:0.8appmHe/dpa to 170 dpa are comparable to measured size distributions.

Despite this validation, note that the model still requires nucleation rates of bubbles and voids as an input. In this work, these are computed from the neutron or dual-ion specimens' characterization which constitutes one of the strongest limitations of the model. The predictive capability of the model would be greatly improved if nucleation rates could be computed through materials and irradiation parameters. Cluster dynamics models are a promising avenue for this purpose as shown in [19,21,249,286].

In conclusion, the predictive capability of the model is validated on a majority of other dual-ion irradiations. The fact that the model does not systematically overestimate or underestimate the cavity microstructure evolution at different temperatures and helium injection rates could indicate that any discrepancies between predictions and measurements can be

attributed to external factors such as inaccuracies in starting microstructures or nucleation rates of bubbles and voids.

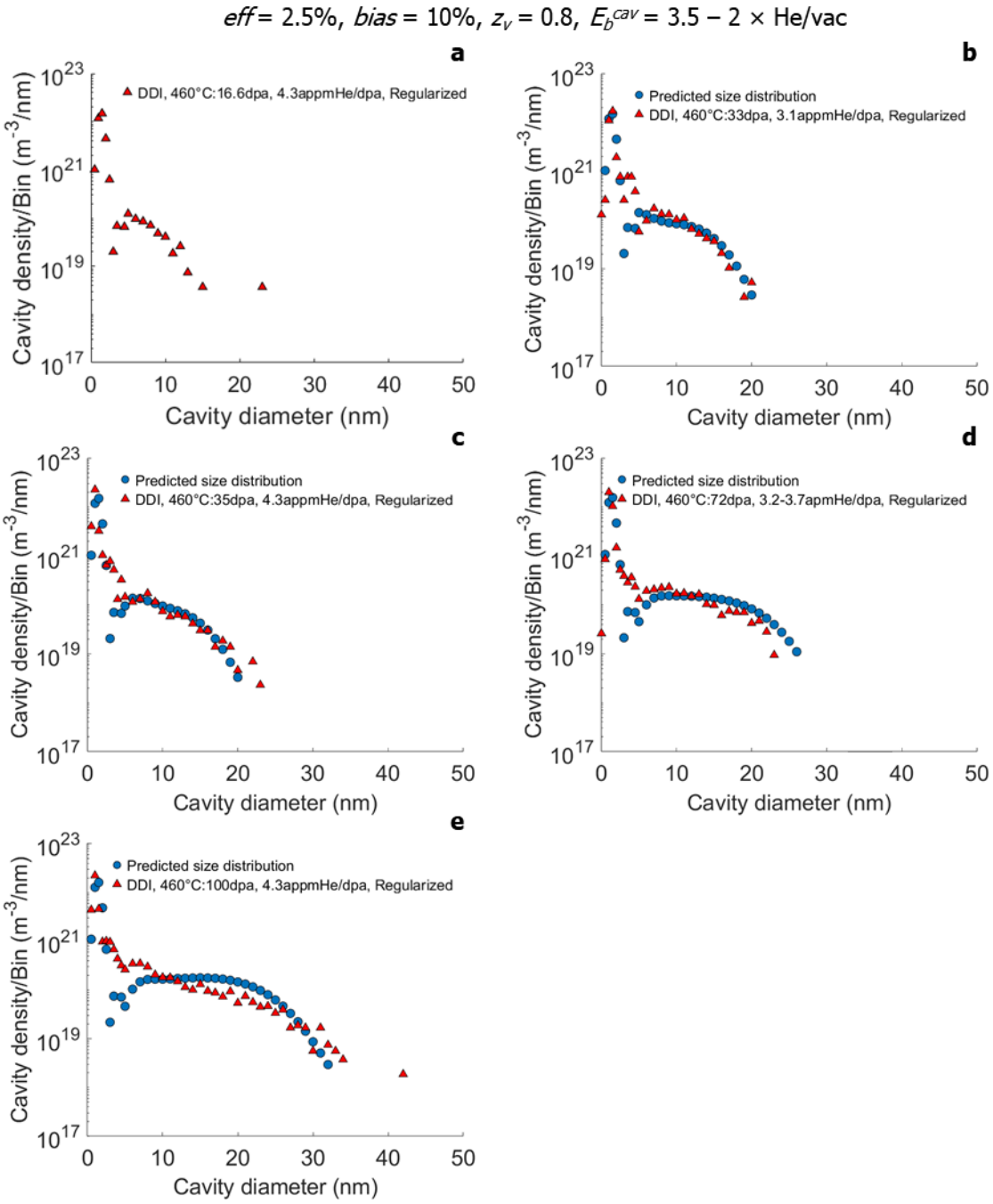


Figure 6.20: (a) Starting cavity microstructure from dual-ion irradiation at 460°C:4.3appmHe/dpa at 16.6 dpa used to predict the dual-ion-irradiated cavity microstructures at (b) 33dpa:3.1appmHe/dpa, (c) 35dpa:4.3appmHe/dpa, (d) 72dpa:3.7appmHe/dpa and (e) 100dpa:4.3appmHe/dpa.

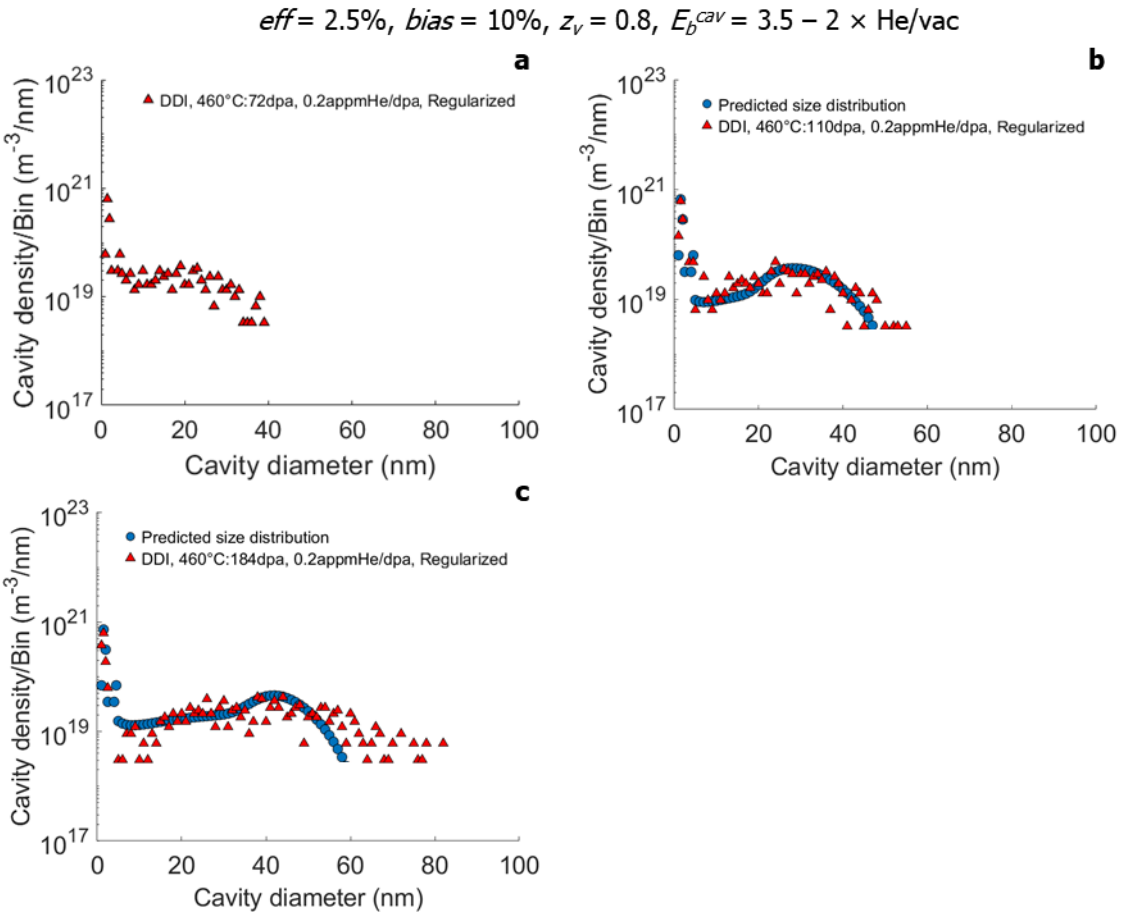


Figure 6.21: (a) Starting cavity microstructure from dual-ion irradiation at 460°C:0.2appmHe/dpa at 72 dpa used to predict the dual-ion-irradiated cavity microstructures to (b) 110 dpa and (c) 184 dpa.

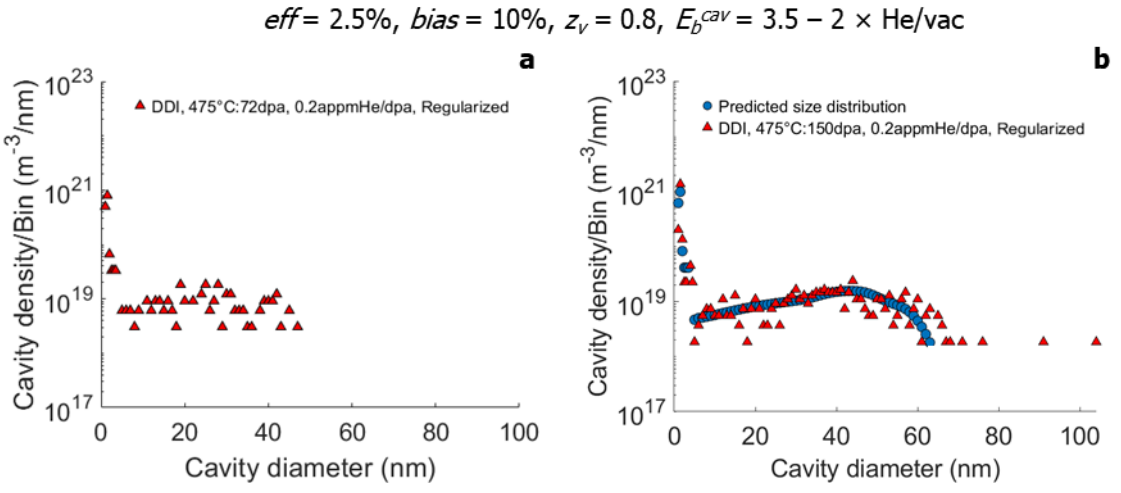


Figure 6.22: (a) Starting cavity microstructure from dual-ion irradiation at 475°C:0.2appmHe/dpa at 72 dpa used to predict the dual-ion-irradiated cavity microstructures to (b) 150 dpa.

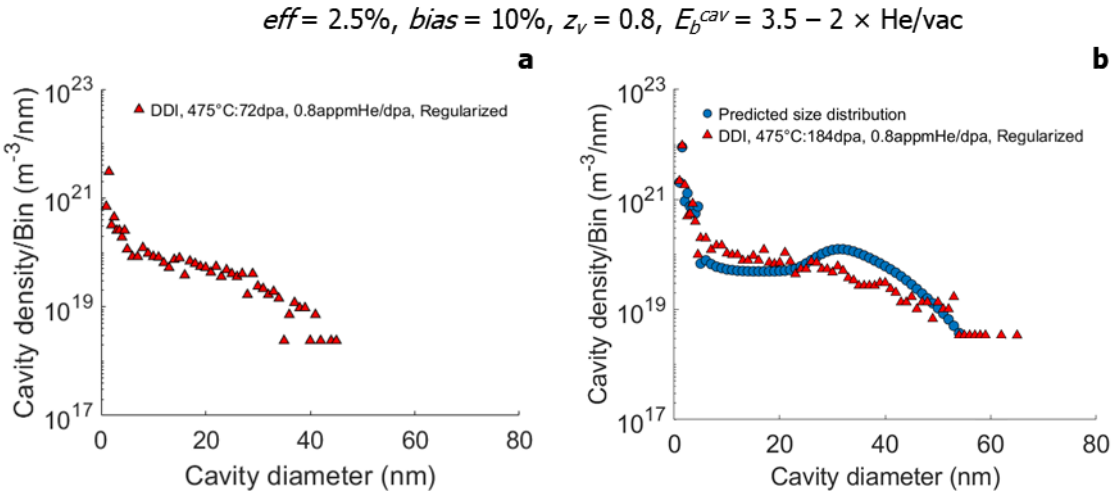


Figure 6.23: (a) Starting cavity microstructure from dual-ion irradiation at 475°C:0.8appmHe/dpa at 72 dpa used to predict the dual-ion-irradiated cavity microstructures to (b) 184 dpa.

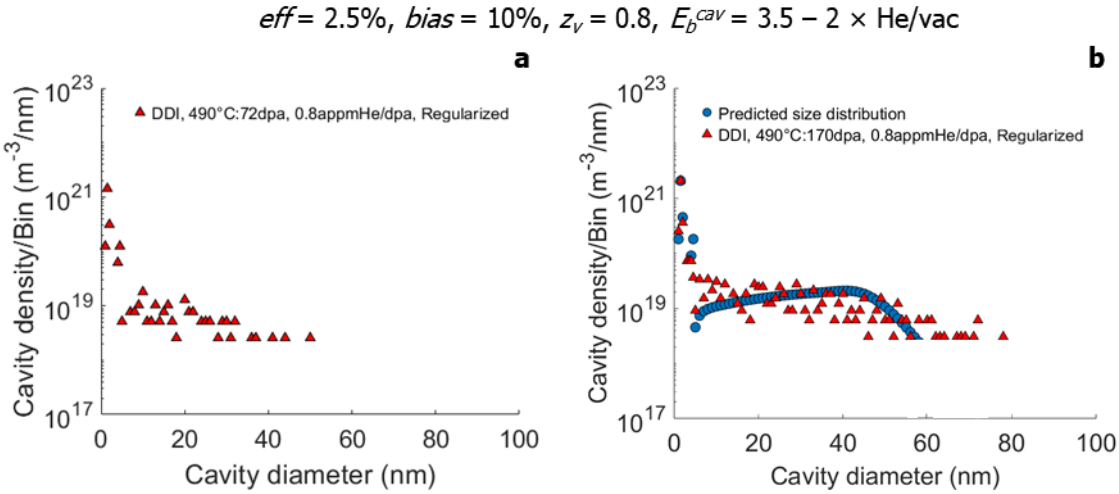


Figure 6.24: (a) Starting cavity microstructure from dual-ion irradiation at 490°C:0.8appmHe/dpa at 72 dpa used to predict the dual-ion-irradiated cavity microstructures to (b) 170 dpa.

Table 6.12: Comparison of predicted vs. measured (regularized) dual-ion- and BOR-60-irradiated cavity microstructures.

Irradiation mode	Sample	Condition	Regularized swelling (%), average diameter (nm), root-mean-cube diameter (nm) and densities ($10^{20}m^{-3}$)					Predicted swelling (%), average diameter (nm), root-mean-cube diameter (nm) and densities ($10^{20}m^{-3}$)				
			Swelling	Average diameter	RMC diameter	Bubble density	Void density	Swelling	Average diameter	RMC diameter	Bubble density	Void density
DDI	071320-1	460C-3.1Hedpa-33dpa	0.08	10.0	10.8	167	10.3	0.08	10.0	11.2	167	10.2
DDI	021121	460C-4.3Hedpa-35dpa	0.09	9.9	11.3	168	10.9	0.09	10.1	11.3	168	10.9
DDI	091420-1	460C-3.2-3.7Hedpa-72dpa	0.28	11.7	13.3	174	22.5	0.46	14.0	15.7	174	22.4
DDI	030621-1	460C-4.3Hedpa-100dpa	0.62	12.5	15.5	179	31.2	0.90	15.7	17.7	179	31.1
DDI	012025-2	460C-0.2Hedpa-110dpa	1.30	27.3	31.1	5.7	8.2	1.21	27.7	30.5	5.7	8.2
DDI	101424	460C-0.2Hedpa-184dpa	5.75	39.3	45.1	6.3	12.0	3.64	34.4	38.7	6.3	12.0
DDI	020325-2	475C-0.2Hedpa-150dpa	2.56	37.7	43.9	9.2	5.6	2.01	36.1	40.9	9.2	5.6
DDI	012524-4	475C-0.8Hedpa-184dpa	2.99	20.0	26.6	80.3	30.0	4.86	27.3	31.4	80.3	29.8
DDI	040425	490C-0.8Hedpa-170dpa	2.04	28.6	36.9	15.0	7.8	1.94	31.8	36.4	15.0	7.7

6.4 Dual-ion and FFTF irradiations

In this section, the match between FFTF and companion dual-ion-irradiated microstructures is discussed first with an emphasis on cavities and dislocation loops. An explanation for the discrepancy in damage levels between matching FFTF and dual-ion irradiations is provided in the first subsection and validated using the rate theory model in the second subsection.

6.4.1 Comparison of FFTF and dual-ion-irradiated microstructures

In this subsection, multiple dual-ion irradiation conditions are compared to the FFTF microstructures. Cavities and dislocation loops are discussed first. Radiation-induced segregation and precipitation are discussed second in less detail. The comparison with 460°C:0.2appmHe/dpa demonstrates the match of the cavity microstructures while the comparison with 490°C:0.8appmHe/dpa demonstrates the match of the loop microstructures. One sample is irradiated with a 30°C temperature excursion for 38 dpa after an initial 72 dpa (460-490-460°C:0.2appmHe/dpa) to mimic the temperature excursion that occurred in FFTF as explained below.

Original attempts at matching the FFTF-irradiated cavity microstructures were based on the temperature shift and increased helium injection rate used to match BOR-60 samples. Early dual-ion irradiations did not provide good matches (as shown in Appendix A) and irradiation temperature and helium injection rate were adjusted until the cavity microstructures matched those of FFTF.

The FFTF cavity size distributions and swelling values are presented in Figure 6.25 and Figure 6.26. In all conditions, a valley is present between the bubble and void distributions around

5 nm in diameter. The densities of cavities between 5 and 20 nm in diameter remain constant with increasing damage level (except at 184 dpa) while the overall size distribution extends to larger void diameters. The measured swelling values as presented in Figure 6.26 are consistent with literature data in which authors used SANS [50], TEM [50] or density measurements [62,287].

From Table 6.14, swelling and void density increases with increasing damage level in FFTF samples (except at 184 dpa). Since the cavity microstructures of FFTF samples are very close between 151 and 170 dpa, and the sample at 184 dpa exhibit unexpected void microstructure evolution, dual-ion-irradiated samples at high damage level (150-184 dpa) are only compared to the FFTF sample irradiated to 170 dpa since it is considered the most representative microstructure at high damage level.

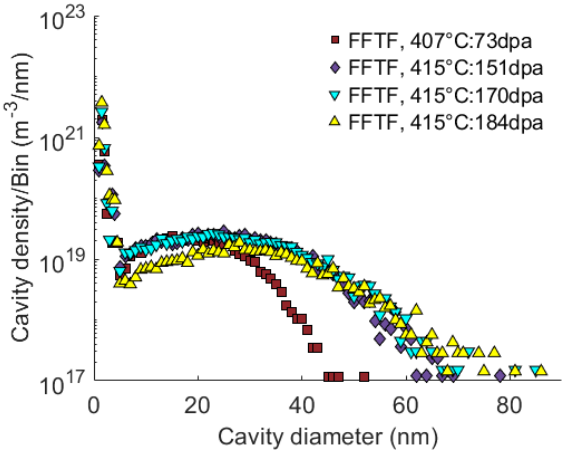


Figure 6.25: Cavity size distributions of irradiated T91 30176 for all FFTF conditions.

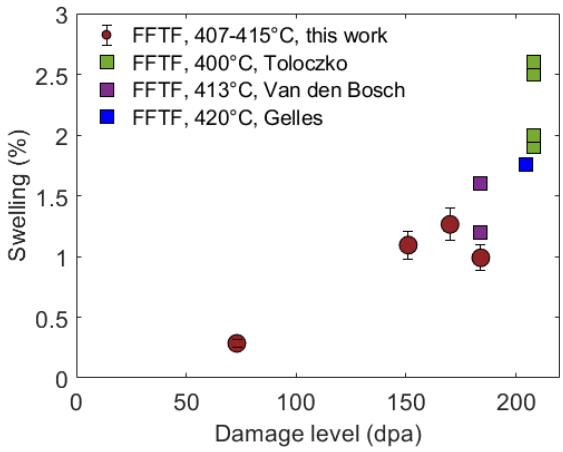


Figure 6.26: Swelling values of T91 samples irradiated in FFTF at 400-420°C [50,62,287].

Cavity size distributions for dual-ion-irradiated samples exhibit more noise and variation from one bin to another due to the much lower counting statistics compared to neutron-irradiated samples. In addition, the smaller sampling volume of dual-ion-irradiated specimens compared to FFTF samples when characterizing cavities limits the minimum measurable density of voids in a bin of a size distribution to ~3×10^{18} m^{-3}. This shortcoming virtually creates a threshold density below which cavities cannot be correctly represented in dual-ion size distributions. These 'undetectable' regions are shown in the comparison of the size distributions in Figure 6.27.

At 72 dpa, the dual-ion irradiation at 460°C:0.2appmHe/dpa matches with the FFTF cavity size distribution as shown in Figure 6.27 (a). When the damage increases to 184 dpa, the dual-ion-irradiated cavity microstructure does not match the FFTF cavity size distribution at 170 dpa because its maximum cavity diameter extends past that of FFTF as shown in Figure 6.27 (b). Since the dual-ion irradiation to 184 dpa exceeds the swelling, void density and void diameter targets, the possibility of an intermediate damage level matching the high-damage FFTF microstructure is considered. In walking up the damage ladder, the 460°C:0.2appmHe/dpa, 110 dpa dual-ion irradiation is selected as a match with the high-damage FFTF condition as shown in Figure 6.27 (c).

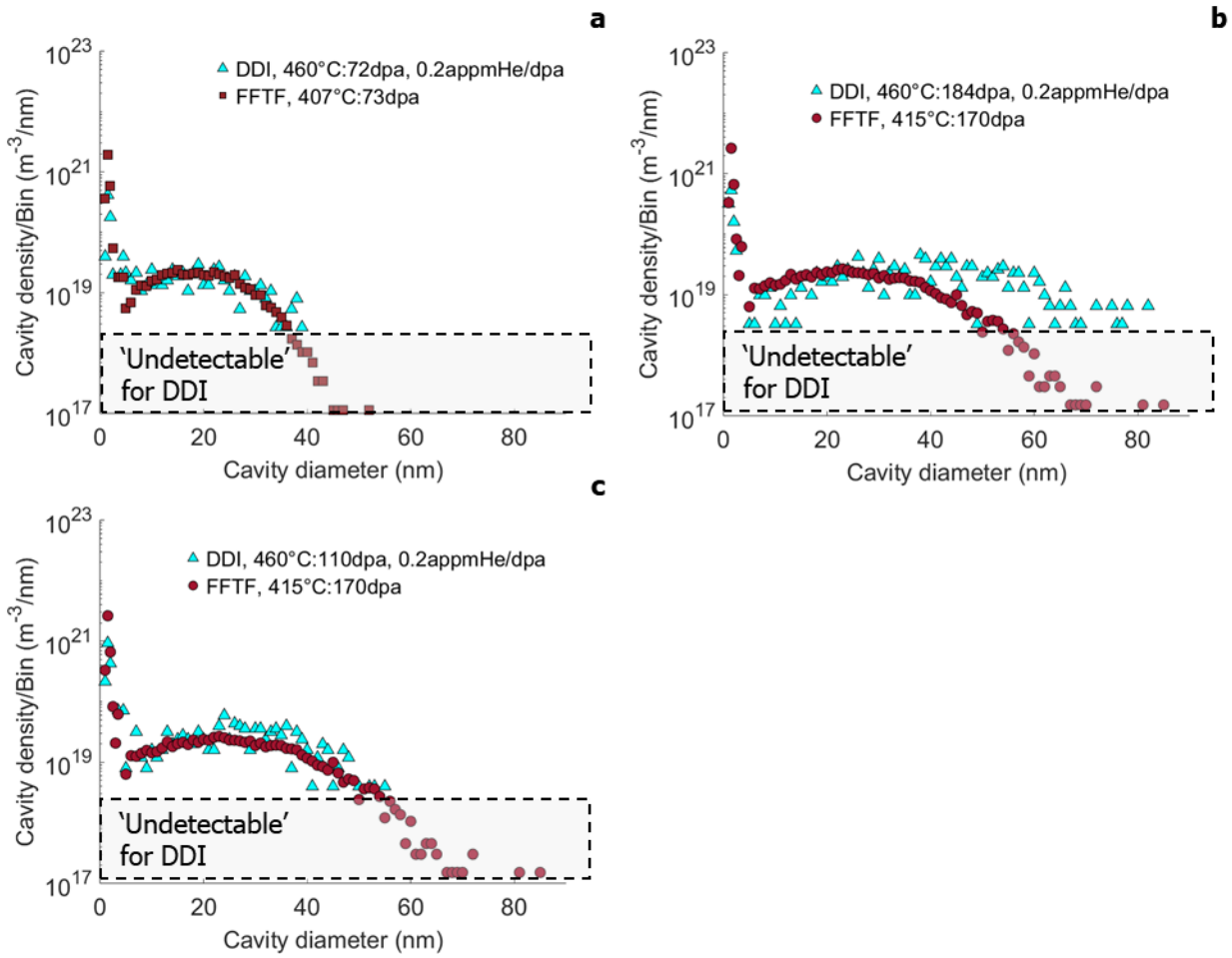


Figure 6.27: Cavity size distributions of irradiated T91 30176 for (a) FFTF:73dpa and 460°C:72dpa, 0.2appmHe/dpa, (b) FFTF:170dpa and 460°C:184dpa, 0.2appmHe/dpa, and (c) FFTF:170dpa and 460°C:110dpa, 0.2appmHe/dpa.

The discrepancy in damage level to match the cavity microstructure of the FFTF sample irradiated to 170 dpa can be explained by the irradiation history of FFTF. Samples irradiated at 151, 170 and 184 dpa were all subject to experiment MOTA-1C which exhibited an average temperature of 439°C for 38-40 dpa, or about 30°C higher than the average temperature of the other experiments (404-410°C). In addition, note that the increase in swelling and average void diameter is modest between 73 dpa and 151-184 dpa in FFTF compared to what is expected for damage levels high enough to be in the bias-driven growth regime. These observations indicate that this temperature excursion had a significant impact on the cavity microstructure. Assuming

the temperature was high enough to anneal most of the cavity microstructure, the effective damage level can be estimated from the experiments after MOTA-1C by revising damage levels from 151, 170 and 184 dpa to 104, 104 and 110 dpa, respectively as shown in Table 6.13.

Table 6.13: Irradiation history for FFTF reactor specimens considering annealing during MOTA-1C (crossed out values are not considered in the effective temperature, damage level and damage rate).

Sample	MOTA	1A	1B	1C	1D	1E	1F	Total
VH03	Temperature (°C)					410	404	407 ± 3
	Damage level (dpa)					35.7	37.4	73
	Damage rate (× 10^{-6} dpa/s)					1.21	1.30	1.25
VH20	Temperature (°C)		~~409~~	~~439~~	408	410	404	407 ± 3
	Damage level (dpa)		~~9.2~~	~~38~~	27.5	38.6	37.4	104
	Damage rate (× 10^{-6} dpa/s)		~~0.97~~	~~1.71~~	1.71	1.31	1.30	1.41
NP04	Temperature (°C)	~~410~~	~~409~~	~~439~~	408	410	404	407 ± 3
	Damage level (dpa)	~~18.2~~	~~9.9~~	~~38~~	27.5	38.6	38	104
	Damage rate (× 10^{-6} dpa/s)	~~1.05~~	~~1.05~~	~~1.71~~	1.71	1.31	1.31	1.42
FA33	Temperature (°C)	~~410~~	~~409~~	~~439~~	408	410	404	407 ± 3
	Damage level (dpa)	~~22~~	~~11.9~~	~~40.4~~	29.2	41.4	39	110
	Damage rate (× 10^{-6} dpa/s)	~~1.26~~	~~1.26~~	~~1.82~~	1.82	1.40	1.35	1.49

The effective average temperature of FFTF specimens is now the same (407°C) from 73 to 110 dpa. Samples VH20, NP04 and FA33 exhibit very similar effective irradiation conditions which explains why their cavity microstructures are alike as shown in Figure 6.25. Additionally, the effective damage increase between VH03 and VH20/NP04/FA33 is only 31-37 dpa instead of 78-111 dpa previously, which is consistent with the void density and average void diameter only increasing moderately between VH03 and the other samples. The reduction in effective damage level from 170 to 104 dpa for NP04 can also explain why dual-ion irradiation conducted at 460°C:0.2appmHe/dpa to 110 dpa provides the best match of the FFTF cavity microstructure.

The irradiation history of sample NP04 can be split into three steps: initial irradiation at 410°C:28.1dpa followed by the MOTA-1C temperature excursion at 439°C:38dpa and final irradiation at 407°C:104dpa. To replicate the suspected annealing of the FFTF cavity

microstructure, a sample can be dual-ion-irradiated with a temperature excursion similar to MOTA-1C (+30°C for 38 dpa). Ideally, this temperature excursion would occur after the first 28.1 dpa to mimic the irradiation history of NP04. However, this would require conducting an additional irradiation to 28.1 dpa. Due to time and scheduling constraints, the sample irradiated at 460°C:0.2appmHe/dpa to 72 dpa is used as the starting point of the temperature excursion instead, which gives the following irradiation history: 460°C:0.2appmHe/dpa to 72 dpa, followed by 490°C:0.2appmHe/dpa for 38 dpa and back to 460°C:0.2appmHe/dpa for 60 dpa (170 dpa total). This temperature excursion experiment creates a cavity size distribution that does not match FFTF sample NP04 as well because of the higher density of 5-20 nm and 50-70 nm voids it creates compared to FFTF as shown in Figure 6.28 and Table 6.14.

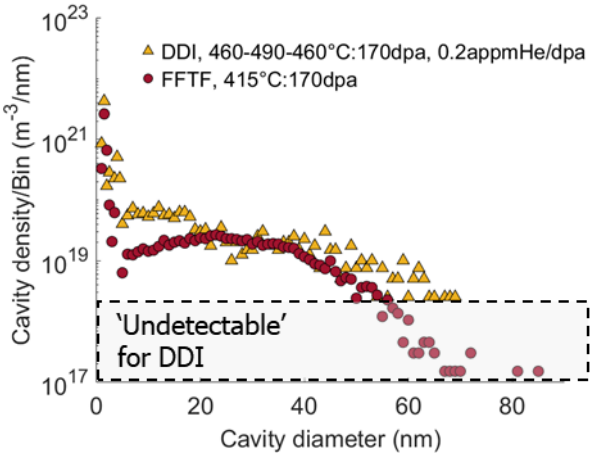


Figure 6.28: Cavity size distributions of irradiated T91 30176 to FFTF:170dpa and 460-490-460°C:170dpa, 0.2appmHe/dpa.

Multiple reasons could explain this discrepancy:

- The temperature excursion in dual-ion irradiation occurred much later (72 dpa) than in FFTF (28.1 dpa) which means the cavity microstructure is more established and resilient to annealing: more cavities might have survived the temperature change which eventually leads to higher swelling and void density.

- The temperature reported for experiment MOTA-1C is an average over the course of the irradiation cycles. The microstructure could have been exposed to an even higher (30+°C) peak temperature excursion than the average reported. Cavities are relatively stable defects (especially with high helium content) and often require annealing above 460°C to start shrinking as shown for a 6 nm cavity in Eurofer97 irradiated to 15 dpa at 330°C in BOR-60 [288].
- Although the damage level of the temperature excursion in FFTF and under dual-ion irradiation are the same, the time held at higher temperature is about 500 times longer in FFTF. Thus, even if short variations (<3% of the total dose corresponding to 1 day at lower temperature in a 11.5-day cycle) in reactor conditions have been shown to have large effects on microstructures [132,289], processus like thermal vacancy emission and helium detrapping are function of the time held at temperature and would be different between reactor and dual-ion.
- A 30°C temperature excursion in reactor might not correspond to a 30°C excursion in dual-ion irradiation.

The size distribution can also be compared to that irradiated at 460°C:0.2appmHe/dpa to 184 dpa (closest damage to 170 dpa available for this condition). The temperature excursion reduces the swelling (2.57%) below that of the specimen irradiated at a constant temperature (5.78%) which indicates the potential for a temperature excursion like that of MOTA-1C to significantly alter the cavity size distribution.

Unlike cavities, the loop microstructures of dual-ion samples irradiated at 460°C:0.2appmHe/dpa to 72 and 110 dpa do not match those of FFTF samples, because of their higher density and lower average diameter as shown in Figure 6.29 (a). The dual-ion sample

irradiated with the temperature excursion exhibits a loop microstructure comparable to constant 460°C to 110 dpa which indicates that loops are unaffected by the increase in temperature or, more likely, that they reform after the temperature is brought back to 460°C. Increasing the irradiation temperature of dual-ion samples to 490°C lowers the density and increases the average diameter which matches the FFTF loop microstructures as shown in Figure 6.29 (c). In all FFTF and companion dual-ion conditions, dislocation loops are mostly of a⟨100⟩ type with a/2⟨111⟩-type loops representing less than 10% of the total density.

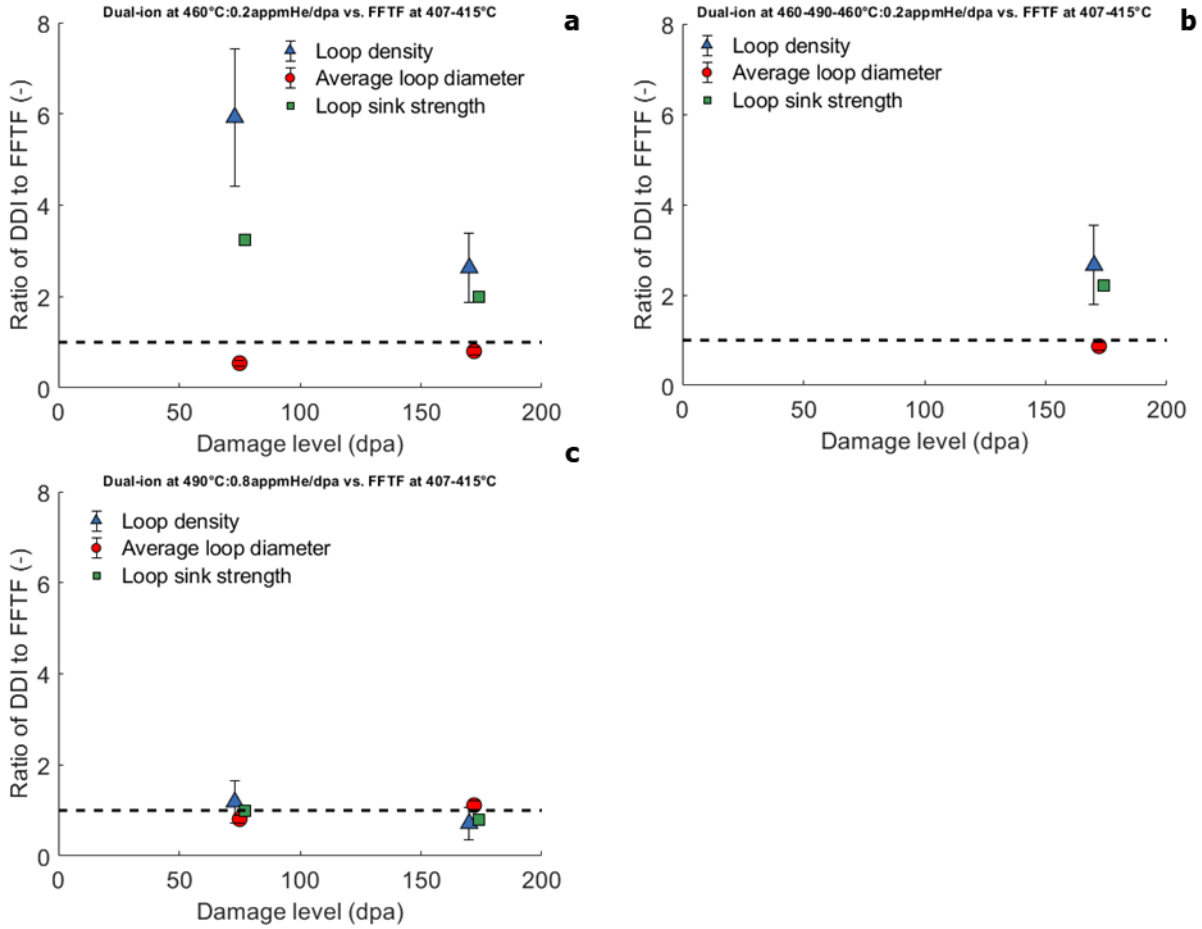


Figure 6.29: Ratios of loop density, average loop diameter and loop sink strength (a) between dual-ion irradiation at 460°C:0.2appmHe/dpa and FFTF, (b) between dual-ion irradiation at 460-490-460°C:0.2appmHe/dpa and FFTF, and (c) between dual-ion irradiation at 490°C:0.8appmHe/dpa and FFTF.

Several helium injection rates (0.2, 0.4 (shown in Appendix A) and 0.8 appmHe/dpa) were tested at 490°C:170dpa to find a set of irradiation parameters which could replicate the cavity and loop microstructures at once. Although the best attempt of 490°C:0.8appmHe/dpa exhibit swelling comparable to FFTF at 170 dpa, the shape of the size distribution does not match at 72 nor 170 dpa as shown in Figure 6.30. Therefore, it is unlikely that even a sample irradiated to 104 dpa to match the effective damage level of NP04 as explained above would create a cavity microstructure comparable to FFTF.

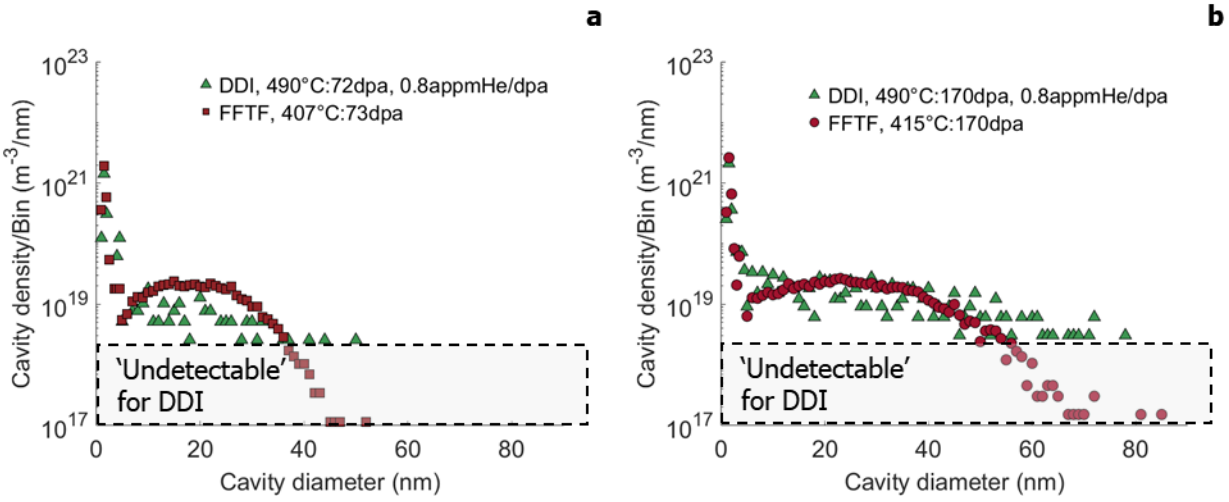


Figure 6.30: Cavity size distributions of irradiated T91 30176 for (a) FFTF:73dpa and 460°C:72dpa, 0.2appmHe/dpa, (b) FFTF:170dpa and 460°C:184dpa, 0.2appmHe/dpa, and (c) FFTF:170dpa and 460°C:110dpa, 0.2appmHe/dpa.

Figure 6.31 shows the ratios of swelling, void density and average void diameter between FFTF and the dual-ion irradiation conditions. For the comparison with 460°C:0.2appmHe/dpa, the ratios at 170 dpa are calculated using 460°C:110dpa, 0.2appmHe/dpa since it offers the best match with the cavity size distribution of FFTF. Ratios are closest to 1 for the 460°C:0.2appmHe/dpa condition which confirms it matches FFTF cavity microstructures at both damage levels best compared to the other two dual-ion irradiation conditions.

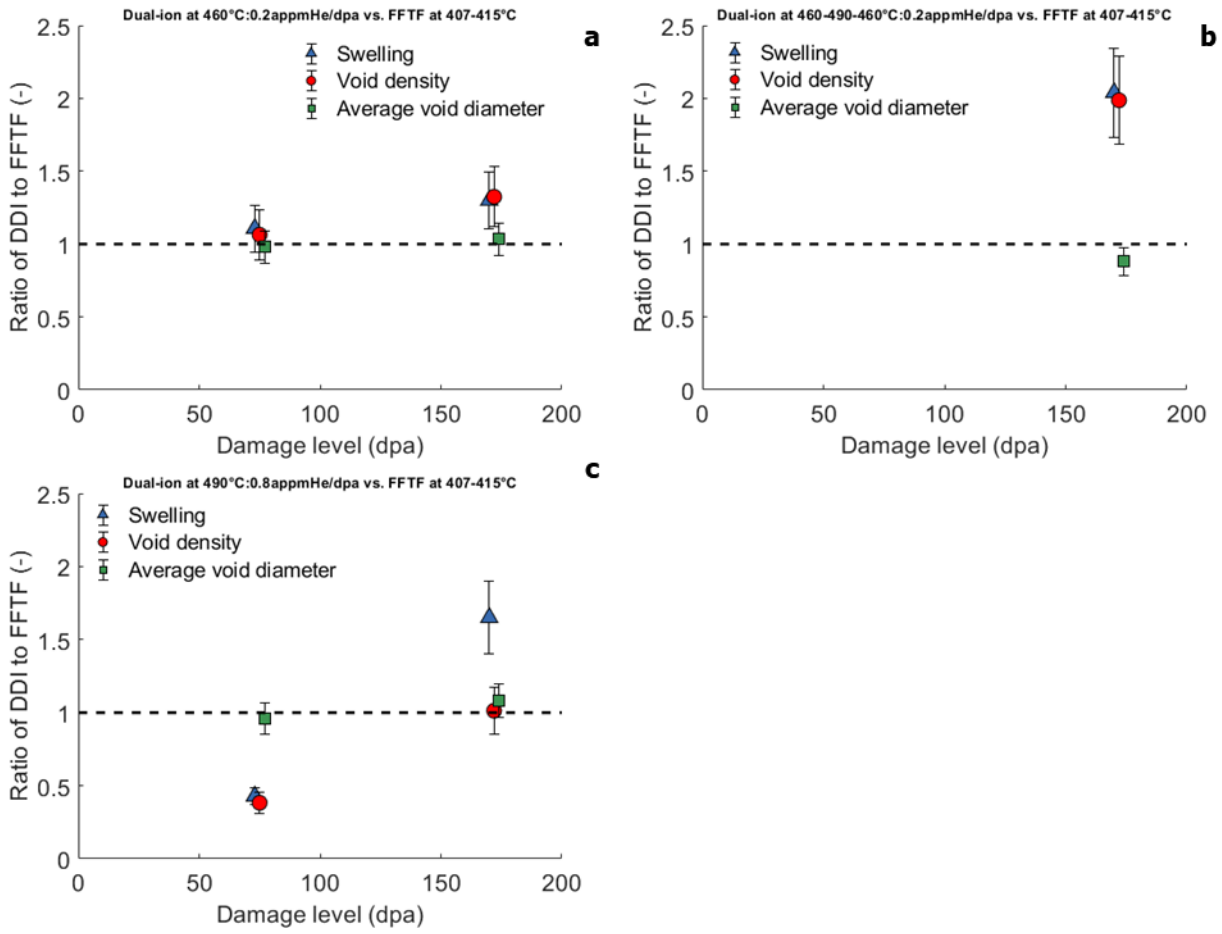


Figure 6.31: Ratios of swelling, void density and average void diameter (a) between dual-ion irradiation at 460°C:0.2appmHe/dpa and FFTF, (b) between dual-ion irradiation at 460-490-460°C:0.2appmHe/dpa and FFTF, and (c) between dual-ion irradiation at 490°C:0.8appmHe/dpa and FFTF.

Bubble density is comparable between FFTF conditions and dual-ion samples irradiated at 490°C:0.8appmHe/dpa or 460-490-460°C:0.2appmHe/dpa, while it is slightly lower for samples irradiated at 460°C:0.2appmHe/dpa as shown in Figure 6.32 (a). Average bubble diameter is comparable across all conditions as shown in Figure 6.32 (b).

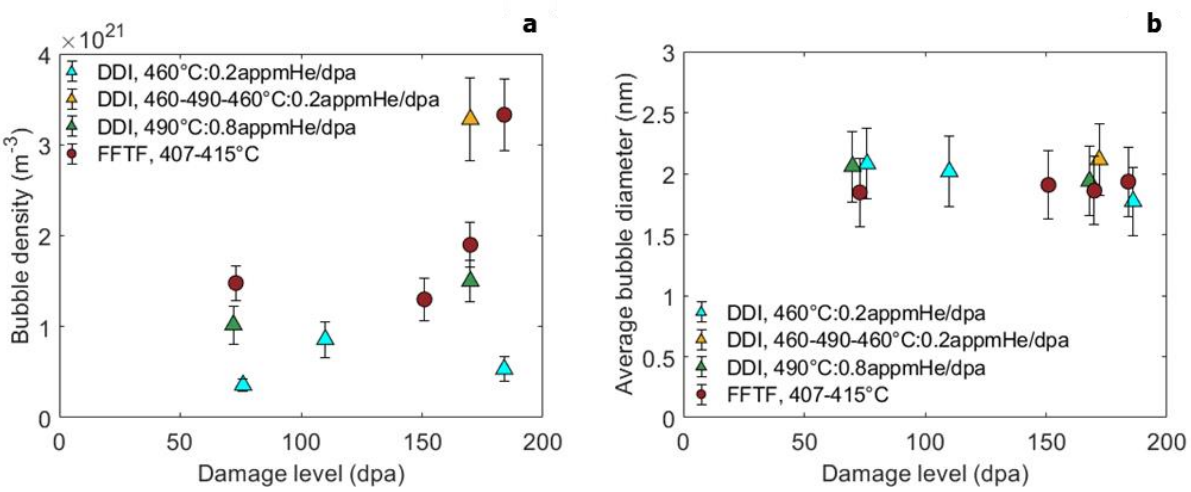


Figure 6.32: (a) Bubble density and (b) average bubble diameter for samples irradiated in FFTF and companion dual-ion irradiations.

These results indicate that the cavity and loop microstructures of T91 30176 irradiated in FFTF can be replicated via dual-ion irradiation, but unlike BOR-60, the matching dual-ion irradiation conditions are different for cavities and loops.

Multiple studies show an increase in loop nucleation with higher helium content in-reactor. Examples include low-boron and high-boron 316SS annealed after irradiation in JRR-2 at low temperatures (67°C and 250°C) [290], F82H doped with ^{10}B irradiated in HFIR at 250°C:2.8dpa [291], 9Cr-2WVTa doped with ^{58}Ni or ^{60}Ni after irradiation at 300, 400 and 500°C to 24 dpa in HFIR [292], and nickel-doped 9Cr–1MoVNb and 9Cr–2WVTa irradiated in HFIR at 400°C to 12 dpa [293]. Several phenomena are thought to contribute to this observation like the reduced recombination of point defects due to the reduced mobility and increased stability of vacancies when tied with a helium atom [294,295], or the increase in point defect cluster density that are nucleation sites for interstitial loops [296,297], or the decreased mobility of loops when helium segregates around them [88–90,292] which limits their annihilation and coalescence.

The dislocation sink strength of T91 irradiated in BOR-60 at 404°C:17dpa is 1.7×10^{14} m^{-2} compared to an average of 4.5×10^{13} m^{-2} in FFTF at 407-417°C:73-184dpa. Assuming the

reported temperatures are correct, this difference of a factor 3.78 is very close to the ratio in helium production rate (0.77/0.21 = 3.67) and shows that helium has an impact on dislocation loop microstructure in reactor irradiations conducted at the same temperature and comparable damage rates.

For dual-ion irradiation, the loop microstructures at 460°C:0.2appmHe/dpa (9.2-16 × 10^{20} m^{-3} and 26-36 nm average diameter) are close to those at 460°C:3.1-4.3appmHe/dpa (16.2-17.7 × 10^{20} m^{-3} and 27.0-29.5 nm average diameter) which confirms the absence of helium effect in that injection range (0-4 appmHe/dpa) on loop microstructure in dual-ion-irradiated FM steels to high damage levels reported in literature [17,67,68,273]. Since damage rate is the same for all dual-ion irradiations, temperature is then the only parameter to adjust the dual-ion loop microstructure if damage rate is constant.

Taller et al. [21] concluded that the temperature shift necessary to match the cavity microstructure at higher damage rates depends on in-reactor helium trapping at fixed-density nucleation sites and helium partitioning in the microstructure, both of which are influenced by reactor temperature and helium production rate.

In summary, the dual-ion temperature necessary to match the cavity microstructure and that necessary to match the loop microstructure both depends on reactor temperature and helium production rates but in different ways. For loops, density of nucleation sites and loop mobility are affected by reactor parameters and dictate the temperature shift to match loops, while helium trapping at fixed-density nucleation sites and helium partitioning in the microstructure influence the temperature shift for cavities. Thus, a neutron-irradiated material may require two different temperature shifts for cavities and loops.

In the case of BOR-60, the temperature to match cavities and the temperature to match loops are the same, whereas they are different in FFTF for this reason. Dual-ion irradiations at 490°C:0.2appmHe/dpa would likely match the loop microstructures of FFTF samples since irradiations at 0.8appmHe/dpa do and there is no effect of helium on loops in dual-ion irradiations. Thus, a single helium injection rate would match cavities and loops, similar to what is observed in BOR-60.

Table 6.14: Cavity microstructures of irradiated T91 30176 for FFTF conditions and companion dual-ion irradiations.

Irradiation mode	Sample	Condition	Swelling (%)	Bubble density ($\times 10^{20}$ m^{-3})	Average bubble diameter (nm)	Void density ($\times 10^{20}$ m^{-3})	Average void diameter (nm)
FFTF	VH03	407C-0.21Hedpa-73dpa	0.28 ± 0.03	14.8 ± 1.9	1.85 ± 0.28	4.7 ± 0.5	19.8 ± 1.6
DDI	062424	460C-0.2Hedpa-72dpa	0.31 ± 0.03	3.6 ± 0.7	2.08 ± 0.29	5.0 ± 0.6	19.4 ± 1.5
DDI	040225	490C-0.8Hedpa-72dpa	0.12 ± 0.01	10.2 ± 2.1	2.06 ± 0.29	1.8 ± 0.3	19.0 ± 1.5
FFTF	VH20	415C-0.21Hedpa-151dpa	1.09 ± 0.12	13.0 ± 2.3	1.91 ± 0.28	7.6 ± 0.8	25.6 ± 1.9
FFTF	NP04	415C-0.21Hedpa-170dpa	1.26 ± 0.13	19.0 ± 2.4	1.86 ± 0.28	7.7 ± 0.8	26.4 ± 2.0
DDI	012025-2	460C-0.2Hedpa-110dpa	1.64 ± 0.18	8.6 ± 2.0	2.02 ± 0.29	10.2 ± 1.2	27.3 ± 2.1
DDI	101424	460C-0.2Hedpa-184dpa	5.78 ± 0.64	5.3 ± 1.3	1.77 ± 0.28	11.4 ± 1.3	39.3 ± 2.9
DDI	050825	460-490-460C-0.2Hedpa-170dpa	2.57 ± 0.28	32.8 ± 4.6	2.11 ± 0.29	15.3 ± 1.7	23.3 ± 1.8
DDI	040425	490C-0.8Hedpa-170dpa	2.08 ± 0.23	15.0 ± 2.3	1.94 ± 0.28	7.8 ± 0.9	28.5 ± 2.1
FFTF	FA33	415C-0.21Hedpa-184dpa	0.99 ± 0.10	33.3 ± 3.9	1.93 ± 0.28	4.7 ± 0.5	29.3 ± 2.2

Table 6.15: Dislocation loop microstructures of irradiated T91 30176 for FFTF samples and companion dual-ion irradiations.

Irradiation mode	Sample	Condition	Loop density ($\times 10^{20}$ m^{-3})	Average loop diameter (nm)	Loop sink strength ($\times 10^{14}$ m^{-2})
FFTF	VH03	407C-0.21Hedpa-73dpa	2.7 ± 0.5	48.1 ± 3.4	0.4
DDI	062424	460C-0.2Hedpa-72dpa	16.0 ± 2.8	26.0 ± 1.8	1.3
DDI	040225	490C-0.8Hedpa-72dpa	3.2 ± 1.1	38.9 ± 2.7	0.4
FFTF	VH20	415C-0.21Hedpa-151dpa	2.9 ± 0.8	58.1 ± 4.0	0.5
FFTF	NP04	415C-0.21Hedpa-170dpa	3.5 ± 0.8	41.5 ± 2.9	0.5
DDI	012025-2	460C-0.2Hedpa-110dpa	9.2 ± 1.6	33.3 ± 2.3	1.0
DDI	050825	460-490-460C-0.2Hedpa-170dpa	9.3 ± 2.2	36.0 ± 2.5	1.1
DDI	040425	490C-0.8Hedpa-170dpa	2.5 ± 1.1	46.2 ± 3.2	0.4
FFTF	FA33	415C-0.21Hedpa-184dpa	2.8 ± 0.8	51.4 ± 3.6	0.4

In terms of radiation-induced segregation, clear enrichment in Cr, Ni and Si and depletion in Fe is observed in FFTF without any clear trend with increasing damage level as shown in Figure 6.33 and Table 6.16. Saturation of the segregation behavior above 72 dpa is observed. The depletion of Fe and enrichment of Cr is significantly lower than FFTF for all dual-ion conditions as shown in Figure 6.34. Except for 460°C:0.2appmHe/dpa at 72 dpa, the Ni and Si enrichments in dual-ion samples match with those of FFTF since they are within a factor of 3. This comparison indicates that, similarly to BOR-60, the RIS behavior is not completely matched via dual-ion irradiation and might require a different set of irradiation parameters. The explanation for this discrepancy in RIS behavior is the same as what is presented in Section 6.1.1.

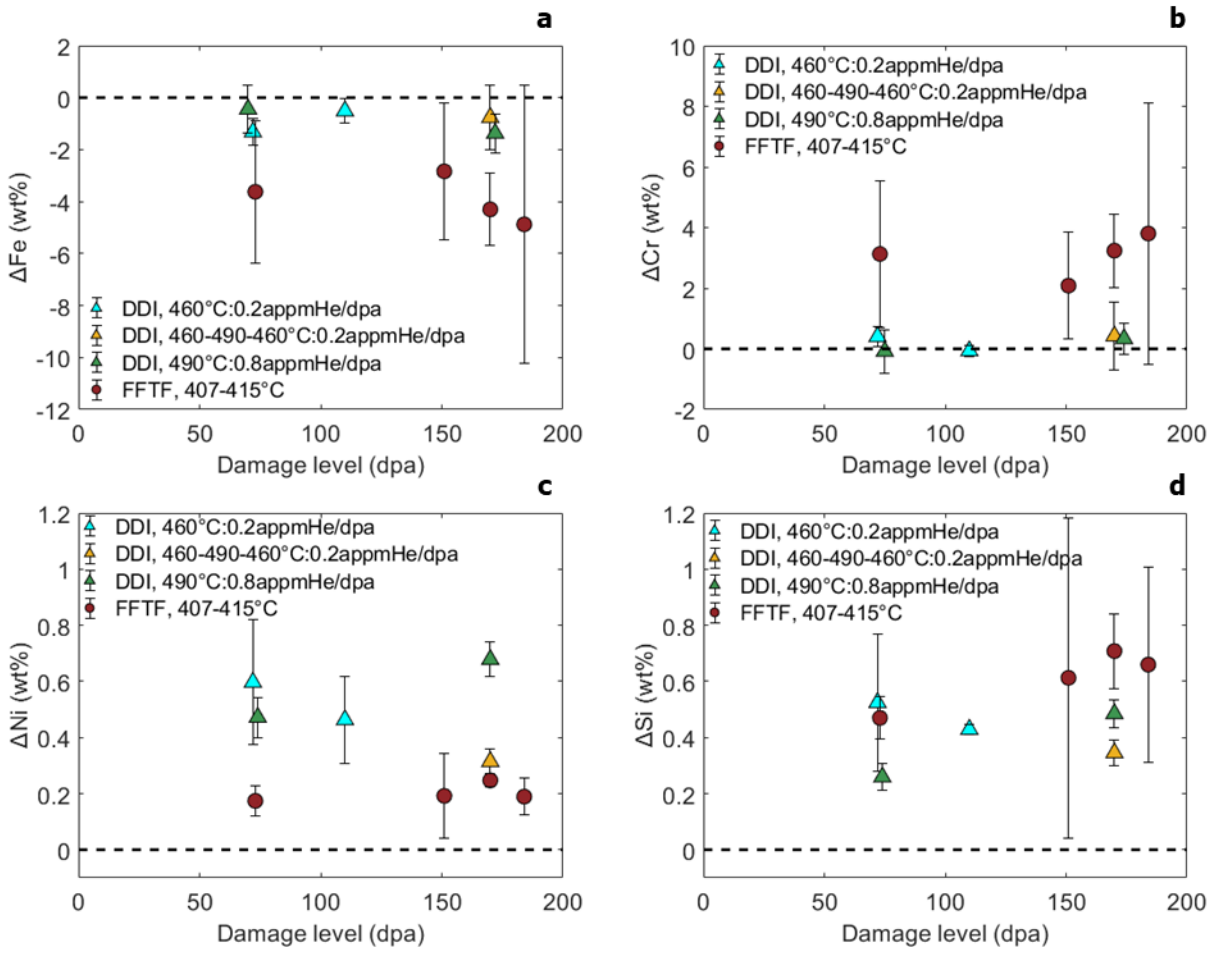


Figure 6.33: (a) Fe, (b) Cr, (c) Ni and (d) Si enrichments at grain boundaries of irradiated T91 30176 for FFTF conditions and companion dual-ion irradiations.

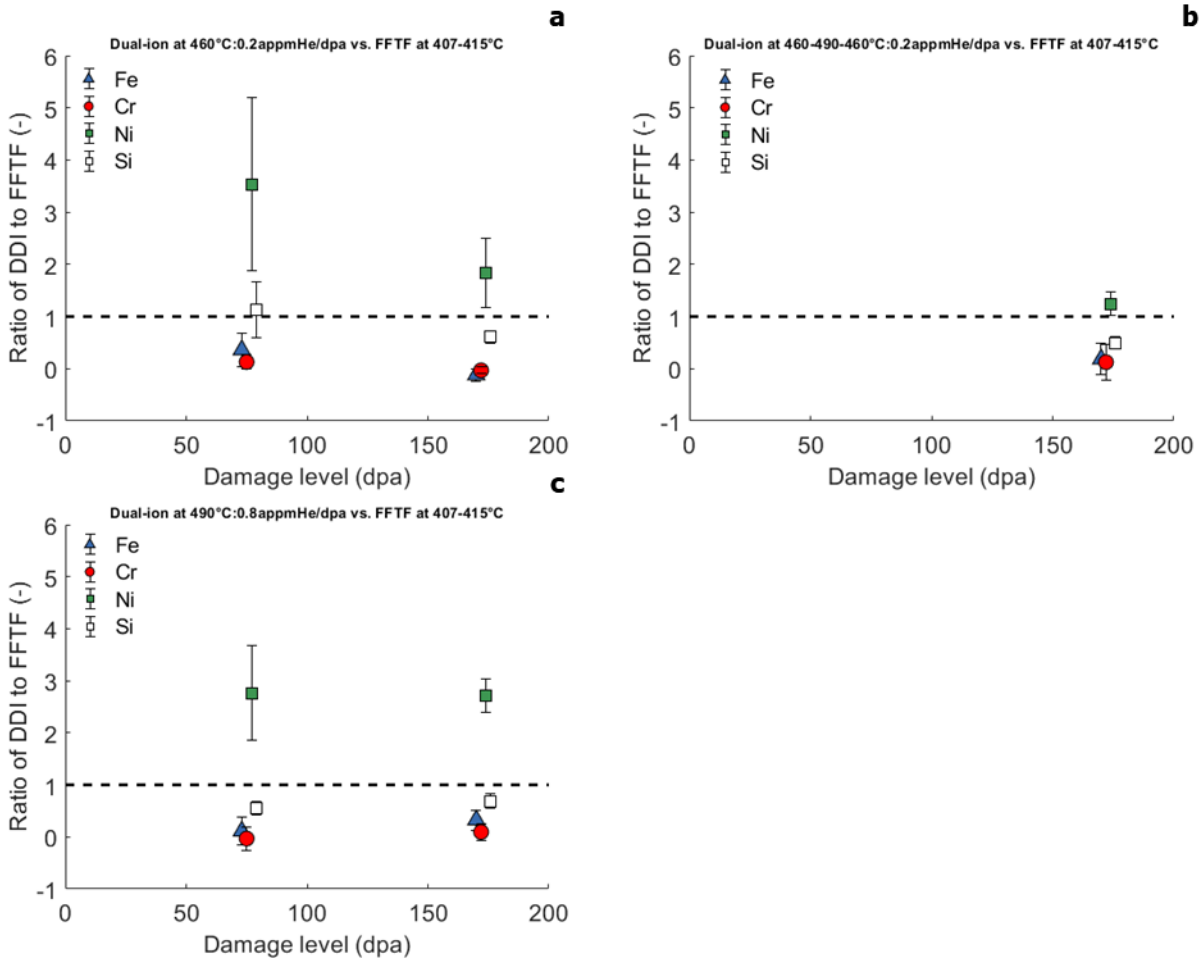


Figure 6.34: Ratios of segregation of Fe, Cr, Ni and Si (a) between dual-ion irradiation at 460°C:0.2appmHe/dpa and FFTF, (b) between dual-ion irradiation at 460-490-460°C:0.2appmHe/dpa and FFTF, and (c) between dual-ion irradiation at 490°C:0.8appmHe/dpa and FFTF.

Table 6.16: Radiation-induced segregation of irradiated T91 30176 for all FFTF conditions and companion dual-ion irradiations.

Irradiation mode	Sample	Condition	Fe (wt%)		Cr (wt%)		Ni (wt%)		Si (wt%)	
			Peak	ΔFe	Peak	ΔCr	Peak	ΔNi	Peak	ΔSi
FFTF	VH03	407C-0.21Hedpa-73dpa	87.1±2.5	-3.6±2.8	10.3±2.3	3.1±2.4	0.25±0.04	0.17±0.05	0.67±0.05	0.47±0.07
DDI	062424	460C-0.2Hedpa-72dpa	88.3±0.6	-1.3±0.5	8.6±0.1	0.4±0.3	0.70±0.23	0.60±0.22	0.76±0.29	0.53±0.24
DDI	040225	490C-0.8Hedpa-72dpa	89.6±0.9	-0.4±0.9	8.1±0.6	-0.1±0.7	0.57±0.06	0.47±0.07	0.46±0.07	0.26±0.05
FFTF	VH20	415C-0.21Hedpa-151dpa	87.5±2.4	-2.8±2.7	9.7±1.4	2.1±1.8	0.27±0.15	0.19±0.15	0.84±0.61	0.61±0.57
FFTF	NP04	415C-0.21Hedpa-170dpa	85.4±2.3	-4.3±1.4	11.3±1.7	3.2±1.2	0.34±0.04	0.25±0.02	0.97±0.18	0.71±0.13
DDI	012025-2	460C-0.2Hedpa-110dpa	89.9±0.1	-0.5±0.5	7.6±0.2	-0.1±0.2	0.57±0.17	0.46±0.16	0.64±0.04	0.43±0.02
DDI	050825	460-490-460C-0.2Hedpa-170dpa	88.7±0.5	-0.8±1.3	8.8±0.4	0.4±1.1	0.41±0.05	0.31±0.05	0.56±0.03	0.35±0.05
DDI	040425	490C-0.8Hedpa-170dpa	88.5±0.8	-1.4±0.7	8.3±0.5	0.3±0.5	0.79±0.07	0.68±0.06	0.74±0.07	0.49±0.05
FFTF	FA33	415C-0.21Hedpa-184dpa	85.4±4.7	-4.9±5.4	11.4±3.8	3.8±4.3	0.29±0.07	0.19±0.06	0.94±0.31	0.66±0.35

In terms of Ni/Si clusters, FFTF exhibits an increase in average cluster diameter, decrease in cluster density and saturation of the volume fraction, as shown in Figure 6.35, which is consistent with Ostwald ripening observed in FM steels [99,298]. Similar behavior is observed in dual-ion irradiations. Figure 6.36 and Table 6.17 shows that average cluster diameter is comparable between FFTF and dual-ion irradiation but the cluster densities and volume fractions are an order of magnitude lower in dual-ion-irradiated samples, echoing the observations made when comparing BOR-60 cluster microstructures to those of dual-ion irradiations in Section 6.1.1.

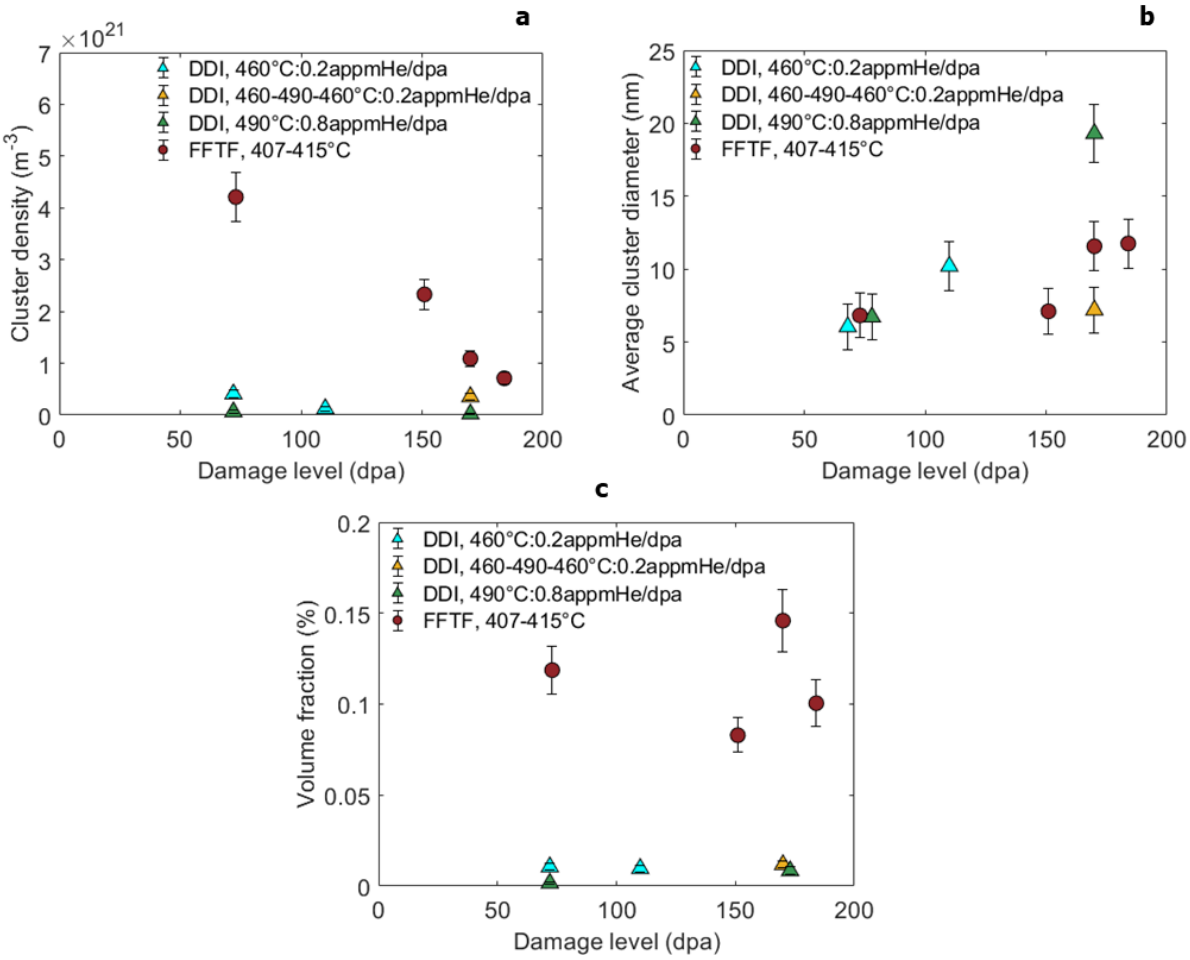


Figure 6.35: (a) Cluster density, (b) average cluster diameter and (c) volume fraction of irradiated T91 30176 for all FFTF conditions and companion dual-ion irradiations.

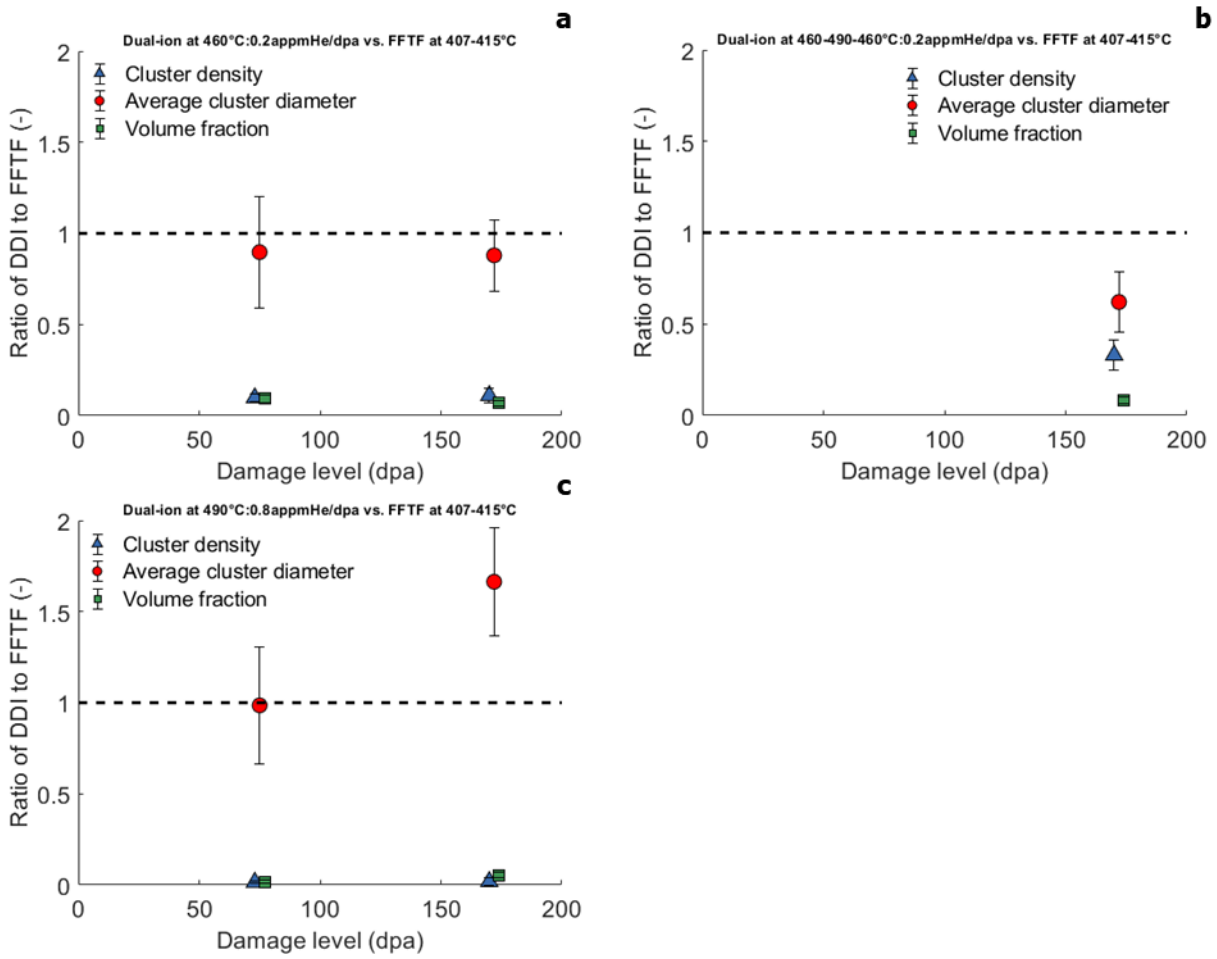


Figure 6.36: Ratios of cluster density, average cluster diameter and volume fraction (a) between dual-ion irradiation at 460°C:0.2appmHe/dpa and FFTF, (b) between dual-ion irradiation at 460-490-460°C:0.2appmHe/dpa and FFTF, and (c) between dual-ion irradiation at 490°C:0.8appmHe/dpa and FFTF.

Table 6.17: Ni/Si-cluster microstructures of irradiated T91 30176 for all FFTF conditions and companion dual-ion irradiations.

Irradiation mode	Sample	Condition	Cluster density ($\times 10^{20}$ m^{-3})	Average cluster diameter (nm)	Volume fraction (%)
FFTF	VH03	407C-0.21Hedpa-73dpa	42.1 ± 4.7	6.8 ± 1.5	0.119 ± 0.013
DDI	062424	460C-0.2Hedpa-72dpa	4.1 ± 0.8	6.1 ± 1.6	0.011 ± 0.002
DDI	040225	490C-0.8Hedpa-72dpa	0.6 ± 0.3	6.7 ± 1.6	0.002 ± 0.001
FFTF	VH20	415C-0.21Hedpa-151dpa	23.3 ± 2.9	7.1 ± 1.6	0.083 ± 0.010
FFTF	NP04	415C-0.21Hedpa-170dpa	10.9 ± 1.6	11.6 ± 1.7	0.146 ± 0.017
DDI	012025-2	460C-0.2Hedpa-110dpa	1.2 ± 0.4	10.2 ± 1.7	0.010 ± 0.002
DDI	050825	460-490-460C-0.2Hedpa-170dpa	3.6 ± 0.7	7.2 ± 1.6	0.012 ± 0.002
DDI	040425	490C-0.8Hedpa-170dpa	0.2 ± 0.2	19.3 ± 2.0	0.008 ± 0.002
FFTF	FA33	415C-0.21Hedpa-184dpa	7.1 ± 1.2	11.8 ± 1.7	0.101 ± 0.013

In conclusion, the cavity and loop microstructures of samples irradiated between 407°C and 415°C up to 170 dpa in FFTF are matched via dual-ion irradiation with two different temperature shifts (~50°C for cavities and ~80°C for loops) and comparable helium injection rate. Density of loop nucleation sites and loop mobility are affected by reactor parameters and dictate the temperature shift to match loop microstructure. Helium trapping at fixed-density nucleation sites and helium partitioning in the microstructure influence the temperature shift to match cavity microstructure. This explains the two different temperature shifts used to mimic the FFTF cavity and loop microstructures. Both FFTF and companion dual-ion cluster microstructures exhibit an evolution consistent with Ostwald ripening. The discrepancy in radiation-induced segregation and

precipitation behaviors between FFTF and dual-ion samples is comparable to that between BOR-60 and companion dual-ion specimens, and the reasons for it are similar.

6.4.2 Modeling of temperature excursion effect on size distribution

The FFTF measured cavity microstructures are regularized in a similar fashion as in Section 6.3. Regularization using reported damage levels is first conducted as shown in Figure 6.37 (a-b) and Table 6.18. Another regularization is conducted using effective damage level as described in Section 6.4.1 and shown in Figure 6.37 (c-d) and Table 6.18.

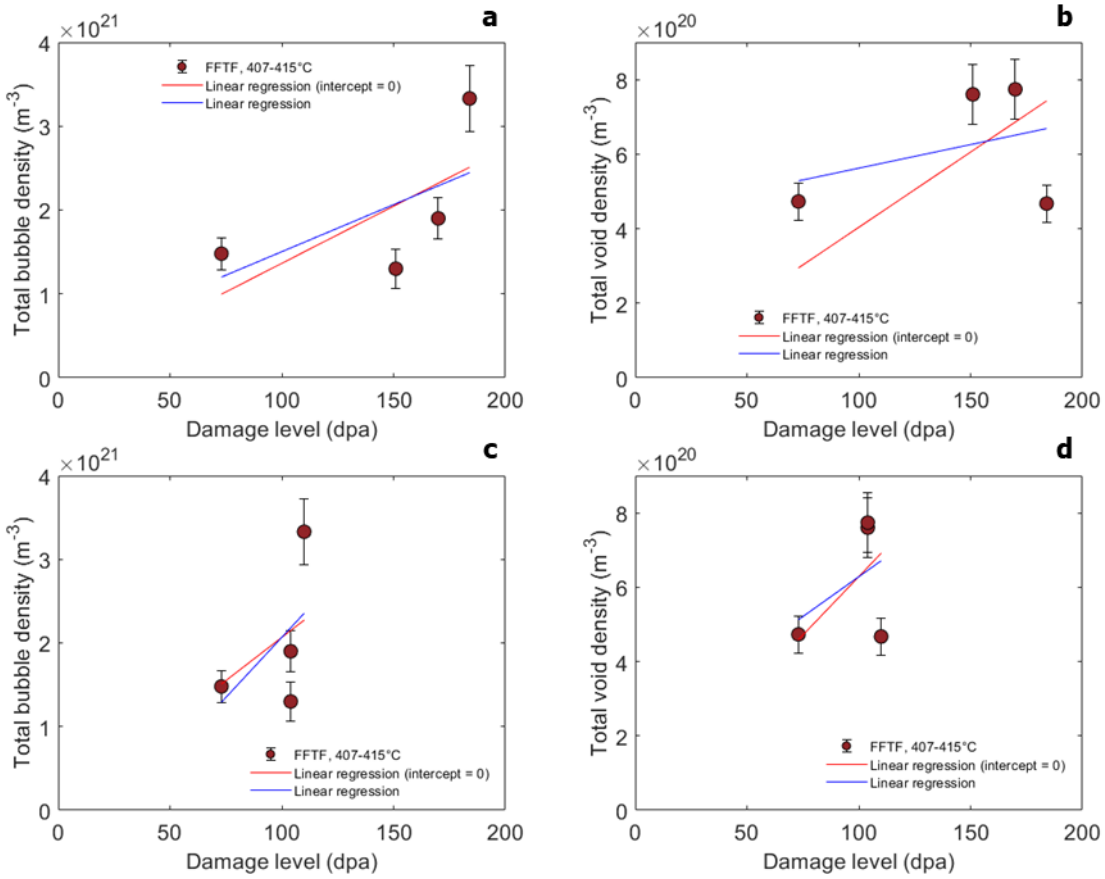


Figure 6.37: Linear regressions of (a) FFTF bubble densities (407-417°C), (b) FFTF void densities, (c) FFTF bubble densities with adjusted damage levels, and (d) FFTF void densities with adjusted damage levels.

Table 6.18: Cavity densities, swelling and nucleation rates of regularized FFTF conditions.

Irradiation mode	Sample	Condition	Measured densities ($\times 10^{20}$ m^{-3}) and swelling (%)			Regularized densities ($\times 10^{20}$ m^{-3}) and swelling (%)			Bubble nucleation rate ($\times 10^{20}$ m^{-3})	Void nucleation rate ($\times 10^{20}$ m^{-3})
			Bubble density	Void density	Swelling	Bubble density	Void density	Swelling		
FFTF	VH03	407C-0.21Hedpa-73dpa	15	4.7	0.28	12	5.3	0.32	0.1123	0.0126
FFTF	VH20	415C-0.21Hedpa-151dpa	13	7.6	1.09	21	6.3	0.90		
FFTF	NP04	415C-0.21Hedpa-170dpa	19	7.7	1.26	23	6.5	1.06		
FFTF	FA33	415C-0.21Hedpa-184dpa	33	4.7	0.99	24	6.7	1.40		
FFTF	VH03	407C-0.21Hedpa-73dpa	15	4.7	0.28	13	5.1	0.31	0.2876	0.0429
FFTF	VH20	407C-0.21Hedpa-104dpa	13	7.6	1.09	22	6.5	0.93		
FFTF	NP04	407C-0.21Hedpa-104dpa	19	7.7	1.26	22	6.5	1.04		
FFTF	FA33	407C-0.21Hedpa-110dpa	33	4.7	0.99	24	6.7	1.40		

The model predicts a cavity microstructure for 460°C:72dpa + 490°C:38dpa + 460°C:60dpa, 0.2appmHe/dpa comparable to the measured size distribution as shown in Figure 6.38 and Table 6.19. The nucleation rates of bubbles (2.98×10^{18} m^{-3}/s) and voids (2.62×10^{18} m^{-3}/s) from a dual-ion irradiation conducted to 490°C:170dpa, 0.2appmHe/dpa are used to mimic the temperature excursion nucleation rates. The match between predicted and measured size distributions indicates the capacity of the model to predict the cavity microstructure evolution during temperature excursions. An approximate curve of the swelling evolution with increasing damage levels is drawn to guide the eye.

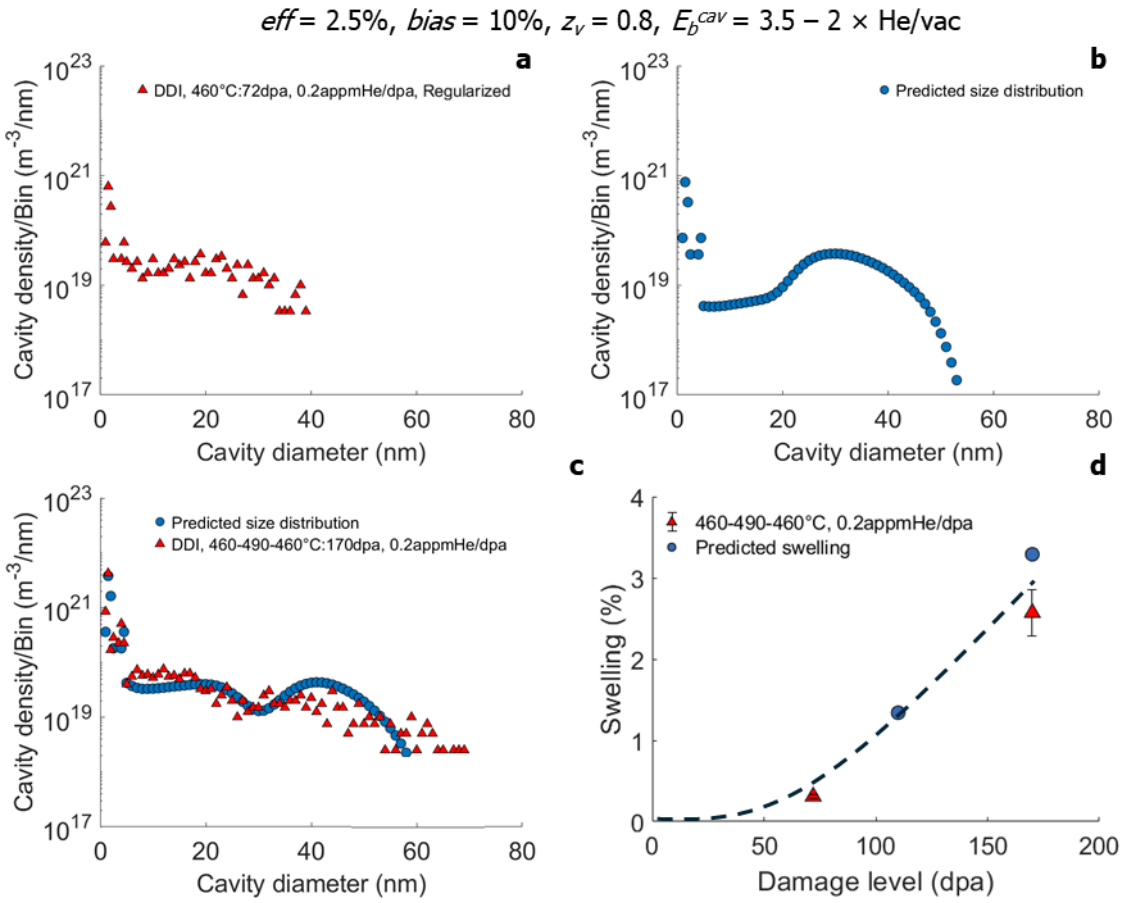


Figure 6.38: (a) Starting cavity microstructure from dual-ion irradiation at 460°C:0.2appmHe/dpa at 72 dpa used to predict the dual-ion-irradiated cavity microstructures (b) after temperature excursion of 490°C for 38 dpa and, (c) with an added 60 dpa at 460°C after temperature excursion. (d) Swelling of measured and predicted size distributions with temperature excursion.

Since the model is validated for the companion dual-ion irradiations of FFTF (460°C:0.2appmHe/dpa to 72 and 110 dpa), it is expected to correctly predict the cavity microstructure evolution of FFTF. Predicted cavity microstructures of sample NP04 from the 73 dpa starting microstructure and using nucleation rates from Table 6.18 are shown in Figure 6.39 and Table 6.19. The prediction to 170 dpa assumes that the temperature excursion during MOTA-1C did not significantly alter the cavity microstructure and uses an average temperature of 415°C for the whole simulation. In this case, the predicted swelling and average void diameter are much larger than the measured values: this mismatch points toward the irradiation parameters being inaccurate. The prediction to 104 dpa assumes that the temperature excursion during MOTA-1C completely annealed the cavity microstructure and that the microstructure at 73 dpa, following this annealing, matches that of sample VH03 (407°C:73dpa free of any temperature excursion). The predicted swelling and size distribution aligns much better with measured values and reinforces the suspected effect of the MOTA-1C temperature excursion.

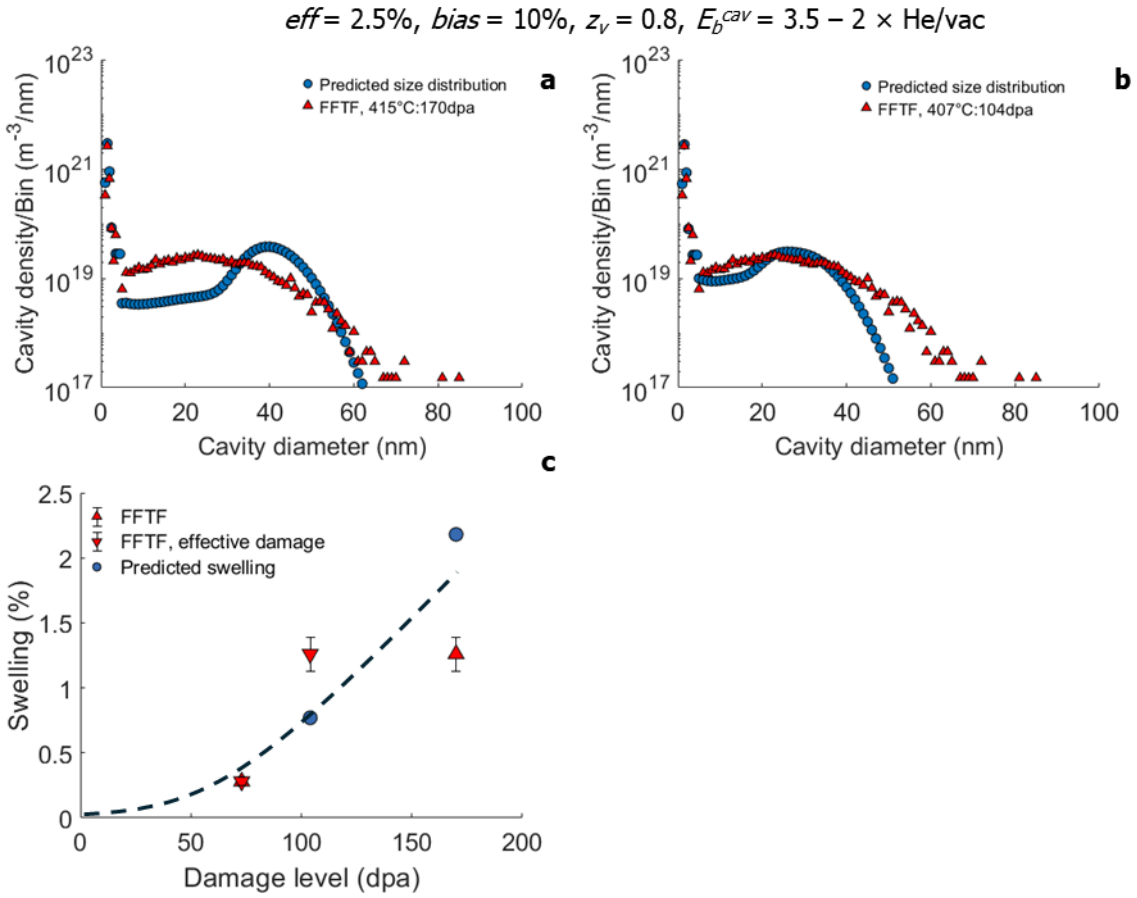


Figure 6.39: Predicted FFTF-irradiated cavity microstructures (a) to 170 dpa and (b) to 104 dpa. (c) Swelling of the measured and predicted FFTF size distributions.

To simulate the impact of the temperature excursion on the cavity microstructure, an estimate of the size distribution of sample NP04 before MOTA-1C (equivalent to 407°C:28dpa) is required. Figure 6.40 and Table 6.19 shows the predicted cavity microstructure in FFTF from 0 to 28 dpa and from 0 to 73 dpa using linear non-regularized nucleation rates from 0 to 73 dpa (6.44 × 10^{18} m^{-3}/s for voids and 2.06 × 10^{19} m^{-3}/s). The prediction to 73 dpa matches with the FFTF measured size distribution which shows the capability for the model to predict microstructure evolution from 0 dpa.

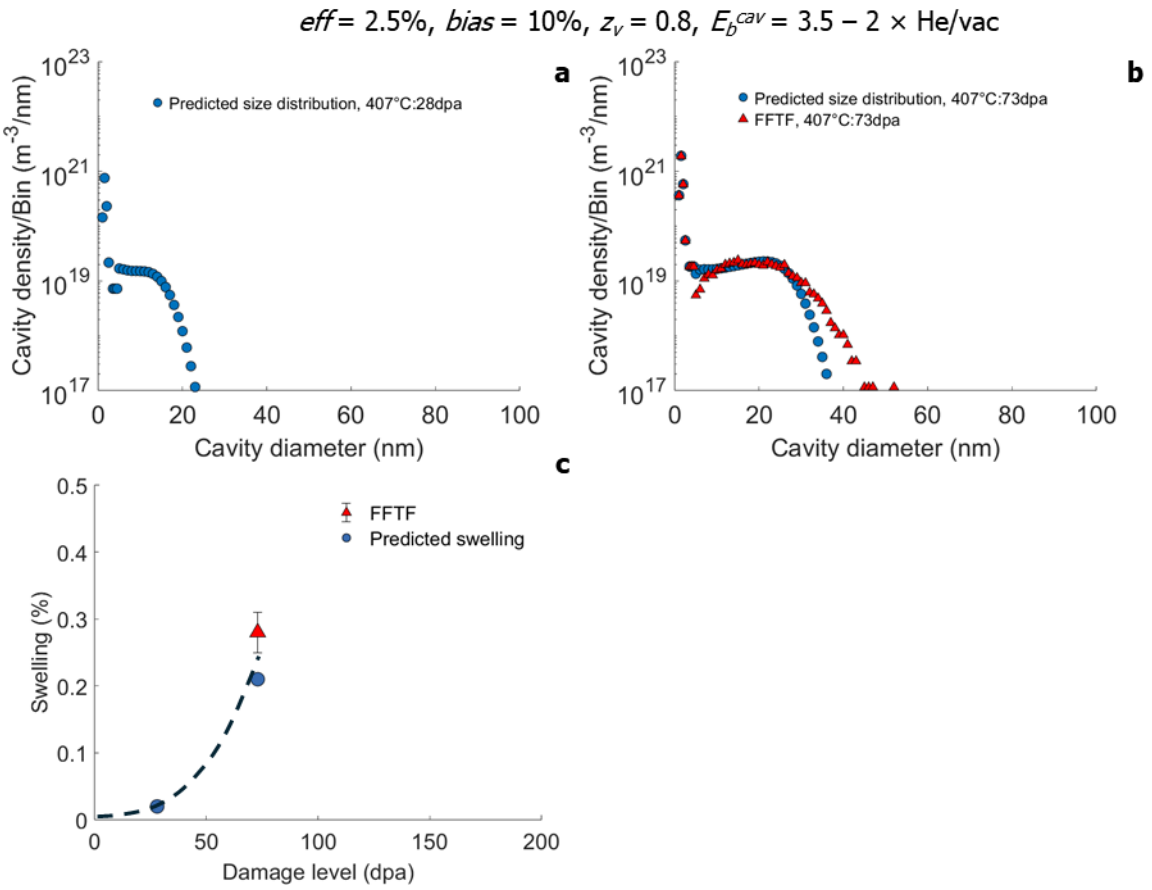


Figure 6.40: Predicted FFTF-irradiated cavity microstructures at 407°C (a) to 28 dpa and (b) to 73 dpa. (c) Swelling of the measured and predicted FFTF size distributions to 73 dpa.

Figure 6.41 (b) and Table 6.19 show the predicted effect of a 439°C temperature excursion for 38 dpa in FFTF on the 407°C:28dpa cavity microstructure predicted above. During the temperature excursion, it is assumed that no cavities are being nucleated, dislocation loops are annealed, and Ni/Si cluster microstructure is that of NP04. The model predicts that voids keep growing during the temperature excursion: the void density is maintained while the average void diameter and swelling increase. Following the temperature excursion, the cavity microstructure for the remaining 407°C:104dpa is predicted as shown in Figure 6.41 (c). The shape and values of the simulated size distribution do not match that of NP04 which indicates that the temperature excursion is not simulated correctly.

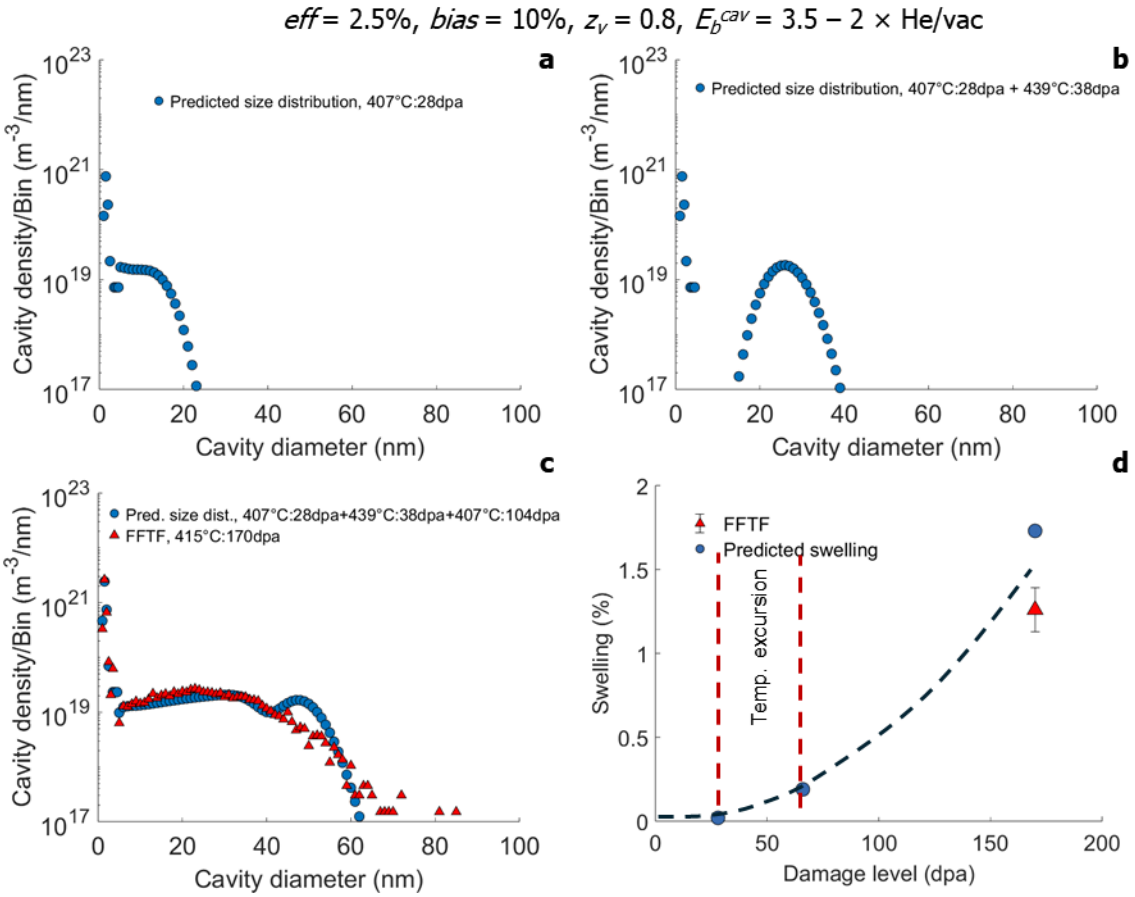


Figure 6.41: Predicted FFTF-irradiated cavity microstructures of (a) 407°C:28dpa, (b) 407°C:28dpa + 439°C:38dpa and (c) 407°C:28dpa + 439°C:38dpa + 407°C:104dpa. (d) Swelling of the measured and predicted size distributions.

Only the average temperature of MOTA-1C is accessible from reports and no information about the maximum temperature, frequency or chronology of the excursion is available. The model can determine the specifics of the temperature excursion that would lead to the measured size distribution of NP04. Figure 6.42 (a) and Table 6.19 show the predicted cavity microstructure of T91 irradiated to 407°C:52.2dpa (24.2 dpa into MOTA-1C for NP04). The model predicts that if the rest of MOTA-1C is at 495°C for 13.8dpa (equals an average of 439°C over 38 dpa, as reported) the cavity microstructure shrinks and a high density of voids (~3 × 10^{20} m^{-3}) transitions back to bubbles as shown in Figure 6.42 (b). Since the bubble microstructure in simulations is fixed, these transitioned bubbles are all 4.75 nm in diameter which creates a bubble microstructure not

representative of the measured ones: the bubble size distribution is adjusted to have the same density but the shape of the distribution at 407°C:52.2dpa. Adding the remaining 104 dpa at 407°C after temperature excursion, the model predicts a cavity microstructure matching that of NP04 as shown in Figure 6.42 (c).

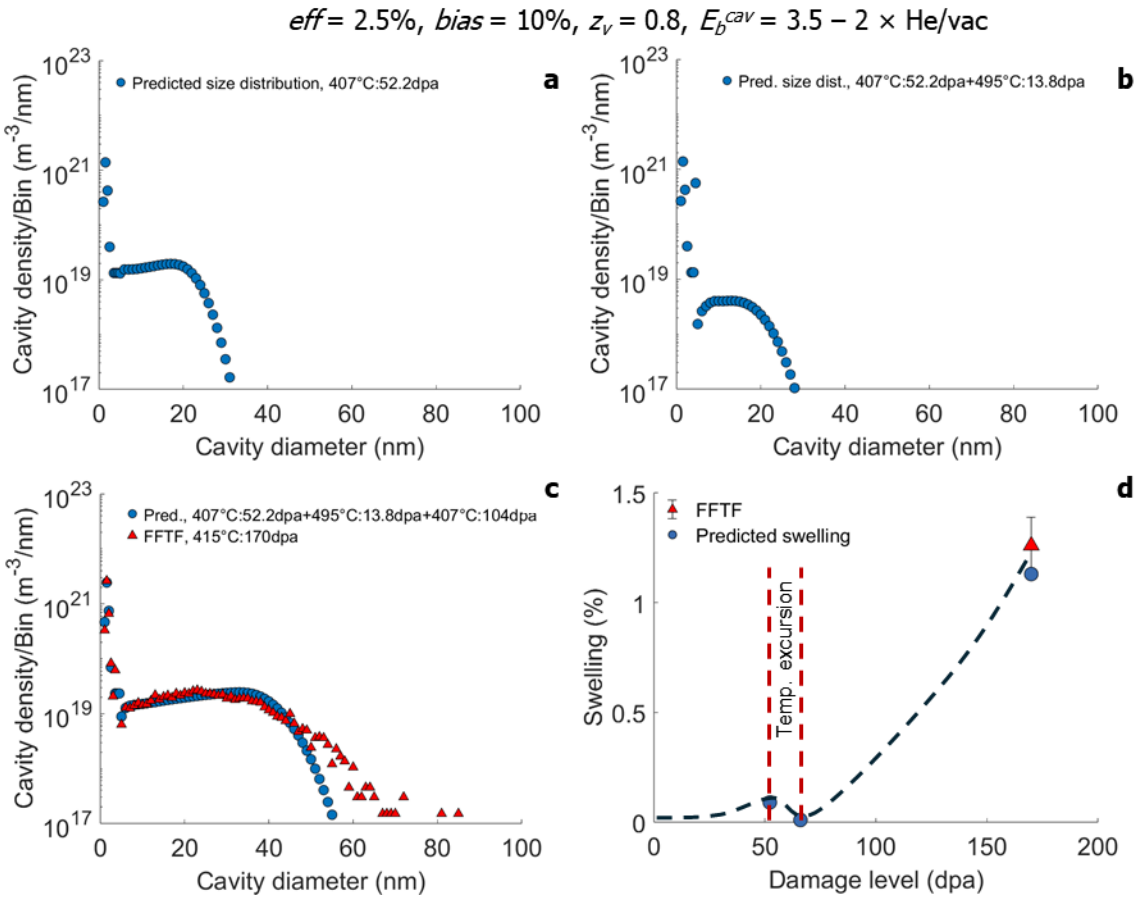


Figure 6.42: Predicted FFTF-irradiated cavity microstructures (a) at 407°C:52.2dpa, (b) at 407°C:52.2dpa + 495°C:13.8dpa, and (c) at 407°C:52.2dpa + 495°C:13.8dpa + 407°C:104dpa. (d) Swelling of measured and predicted size distributions.

In conclusion, the rate theory model can simulate the effect of temperature excursions on the cavity microstructure evolution in dual-ion and reactor irradiations. Simulations and experiments both indicate that FFTF samples underwent a concentrated temperature excursion on the order of 495°C for ~13.8dpa occurring at the end of MOTA-1C, higher than the reported

439°C for 38 dpa. When irradiation history is taken into account, the rate theory model correctly predicts the cavity microstructure evolution of T91 30176 in FFTF up to 170 dpa.

Table 6.19: Comparison of predicted vs. measured FFTF-irradiated cavity microstructures.

Irradiation mode	Sample	Condition	Measured swelling (%), average diameter (nm), root-mean-cube diameter (nm) and densities ($10^{20}m^{-3}$)					Model parameters	Predicted swelling (%), average diameter (nm), root-mean-cube diameter (nm) and densities ($10^{20}m^{-3}$)				
			Swelling	Aver. diam.	RMC diam.	Bub. dens.	Void dens.		Swelling	Aver. diam.	RMC diam.	Bub. dens.	Void dens.
FFTF	VH03	407C-0.21Hedpa-73dpa	0.28	19.8	22.5	15	4.7	407°C:73dpa	0.21	18.0	20.4	15	4.6
FFTF	NP04	415C-0.21Hedpa-170dpa	1.26	26.4	31.4	19	7.7	415°C:170dpa	2.18	37.6	39.9	23	6.6
								407°C:104dpa	0.77	25.6	28.4	22	6.5
								407°C:28dpa + 439°C:38dpa + 407°C:104dpa	1.73	29.7	35.0	19	7.7
								407°C:52.2dpa + 495°C:13.8dpa + 407°C:104dpa	1.13	26.5	30.4	19	7.7
DDI	050825	460-490-460C-0.2Hedpa-170dpa	2.57	23.3	31.5	33	15.3	460°C:72dpa + 490°C:38dpa + 460°C:60dpa	3.29	28.4	34.9	33	15.3

6.5 Justification for temperature shift and increase in helium production rate

This section evaluates the impact of increasing the damage rate, temperature and helium injection rate on the simulated cavity microstructure evolution. This discussion provides insights into the partitioning of helium in the microstructure and the reason for the temperature shift and occasional increase in helium production rate going from reactor to dual-ion irradiation.

Replicating the cavity microstructure of neutron-irradiated samples via dual-ion irradiation is directly linked to matching the net flux of vacancies going to voids. From literature, the need for a temperature shift and an increase in helium injection rate in dual-ion irradiation stems from balancing the increase in damage rate which causes higher point defect supersaturations and reduced time for helium atoms to migrate to cavities [21,107].

Figure 6.43 (a), Figure 6.44 (a) and Figure 6.45 (a) show the predicted net flux of vacancies, helium content in sinks and cavity microstructure for BOR-60 going from 16.6 dpa to 72 dpa at 369°C:0.77appmHe/dpa and 8×10^{-7} dpa/s. Helium is predominantly contained in cavities and the net flux of vacancies is comparable between bubbles and voids.

To determine the effect of damage rate on the simulated cavity microstructure, the damage rate is changed from 8×10^{-7} dpa/s to 7.5×10^{-4} dpa/s. Since increasing the damage rate decreases the Ni/Si cluster density in T91 [102], the cluster density of dual-ion irradiation is used while keeping the cavity, loop microstructures and nucleation rates the same. Figure 6.44 (b) shows that increasing the damage rate causes a lot of the helium to be retained in sinks other than voids and bubbles which increases the bubble interstitial bias (Figure 6.46, except for the smallest bubbles < 1 nm in radius) and causes them to absorb fewer vacancies. Additionally, the point defect concentration in the matrix also increases significantly with increasing damage rate. These result

in a much larger net flux of vacancies to voids compared to a low damage rate (Figure 6.43 (b)), and more than double the swelling (Figure 6.45 (b) and Table 6.20).

To determine the temperature shift and helium injection rate required to create the same cavity microstructure at a higher damage rate, the temperature is first increased to ion irradiation level to balance the production and loss of point defects [21,107]. Additionally, increased temperature increases the helium content in bubbles by enabling more detrapping from weaker helium sinks (dislocations, precipitates, grain boundaries). This decreases the cavity interstitial bias and promotes vacancy absorption at bubbles to decrease the net flux of vacancies to voids. Increasing the irradiation temperature to 445°C drastically reduces the helium content in other sinks to the benefit of bubbles and voids (Figure 6.44 (c)). Yet, Figure 6.43 (c) indicates that it only slightly decreases the net flux of vacancies to voids and does not significantly affect swelling (Table 6.20). Thus, increasing the temperature alone is not sufficient to balance the increase in damage rate.

By increasing the helium injection rate, the helium content in bubbles can be high enough to decrease the bubble interstitial bias significantly. Figure 6.43 (d) shows that by increasing the helium injection rate from 0.77 (BOR-60 value) to 3 appmHe/dpa (×3.9 increase), bubbles can absorb more vacancies which in return reduces the net flux of vacancies to voids and reduces the swelling to the same level as low damage rate. The predicted value of 3 appmHe/dpa is close to the actual value of 3.1-4.3 appmHe/dpa used experimentally during dual-ion irradiation, which is consistent with the fitting conducted in Section 6.2.

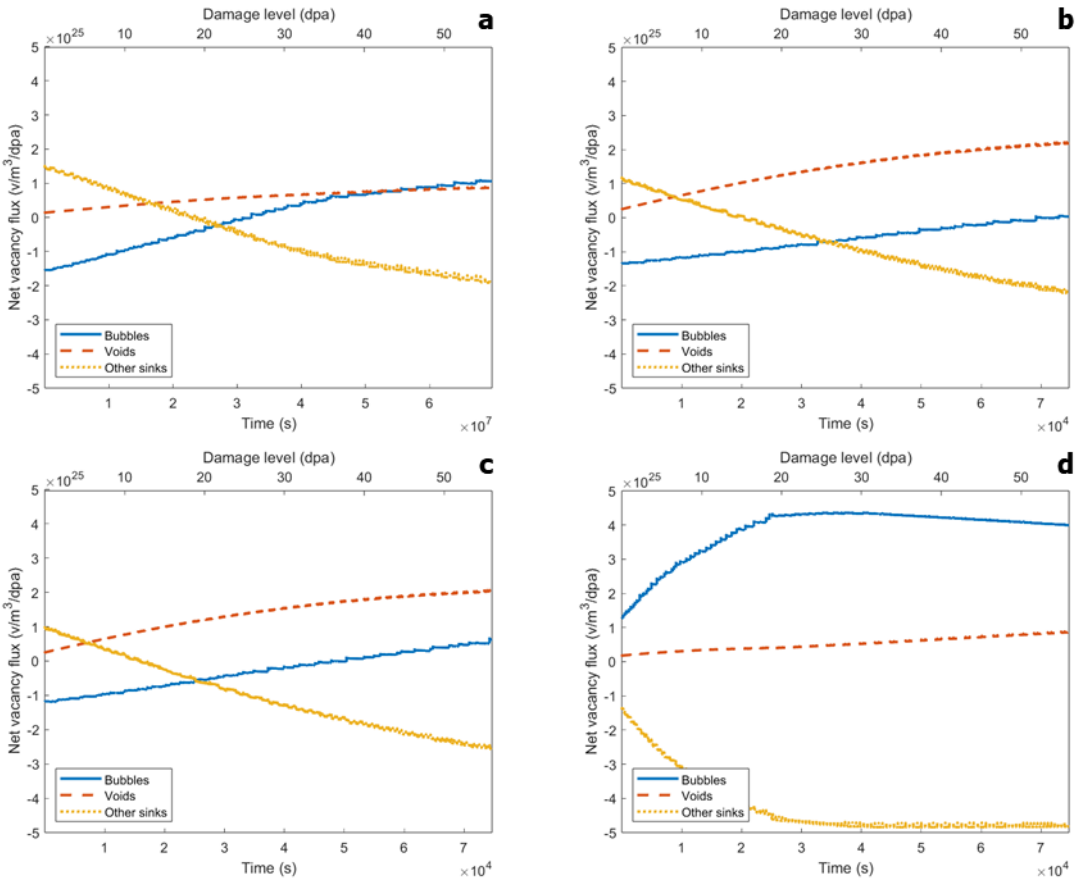


Figure 6.43: Predicted net vacancy fluxes in the BOR-60 microstructure irradiated at (a) 369°C:0.77appmHe/dpa, 8×10^{-7} dpa/s, (b) 369°C:0.77appmHe/dpa, 7.5×10^{-4} dpa/s, (c) 445°C:0.77appmHe/dpa, 7.5×10^{-4} dpa/s and (d) 445°C:3appmHe/dpa, 7.5×10^{-4} dpa/s.

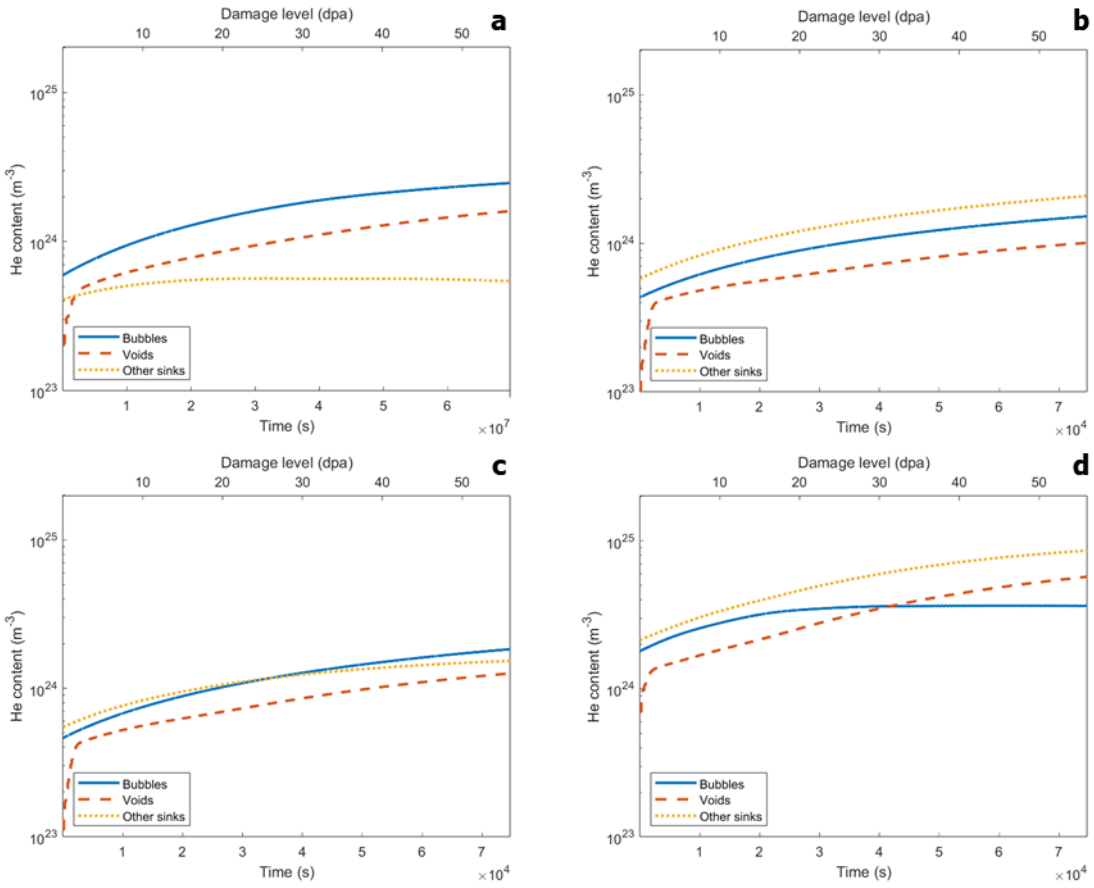


Figure 6.44: Predicted helium content in the BOR-60 microstructure irradiated at (a) 369°C:0.77appmHe/dpa, 8×10^{-7} dpa/s, (b) 369°C:0.77appmHe/dpa, 7.5×10^{-4} dpa/s, (c) 445°C:0.77appmHe/dpa, 7.5×10^{-4} dpa/s and (d) 445°C:3appmHe/dpa, 7.5×10^{-4} dpa/s.

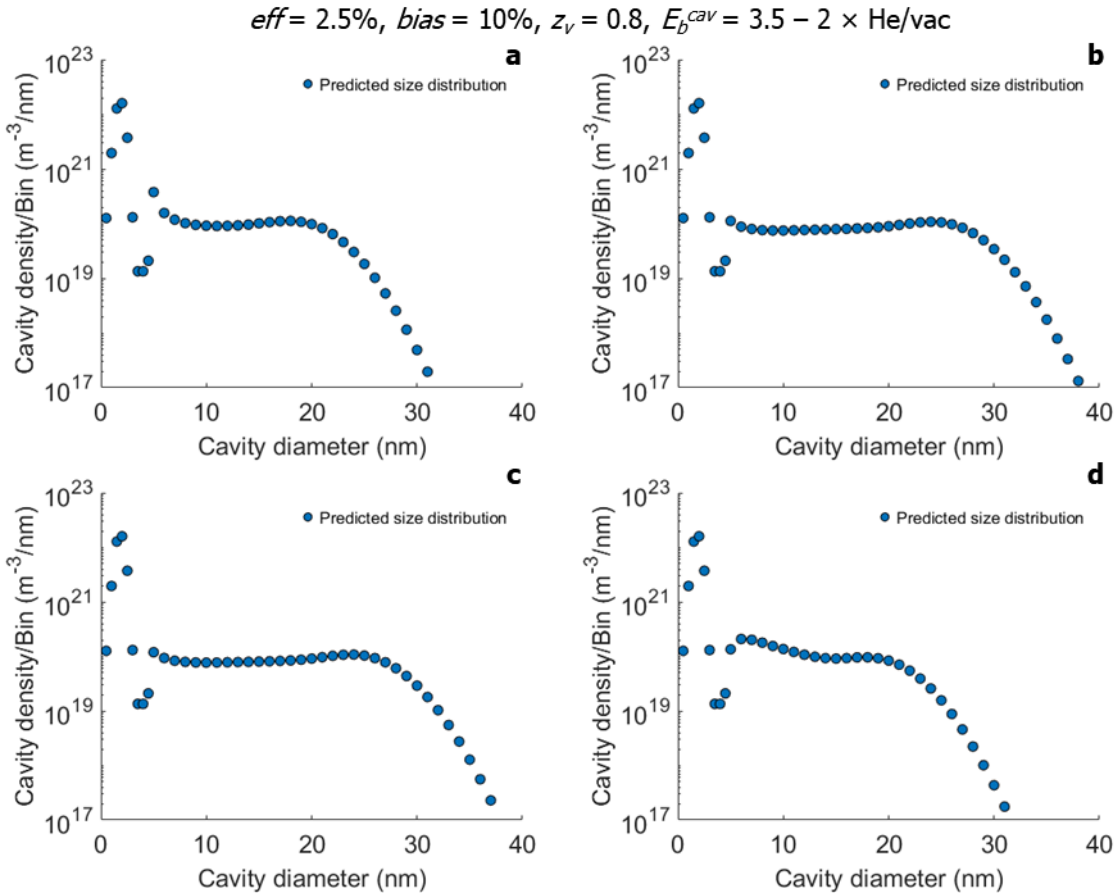


Figure 6.45: Predicted cavity microstructure in BOR-60 irradiated at (a) 369°C:0.77appmHe/dpa, 8×10^{-7} dpa/s, (b) 369°C:0.77appmHe/dpa, 7.5×10^{-4} dpa/s, (c) 445°C:0.77appmHe/dpa, 7.5×10^{-4} dpa/s and (d) 445°C:3appmHe/dpa, 7.5×10^{-4} dpa/s.

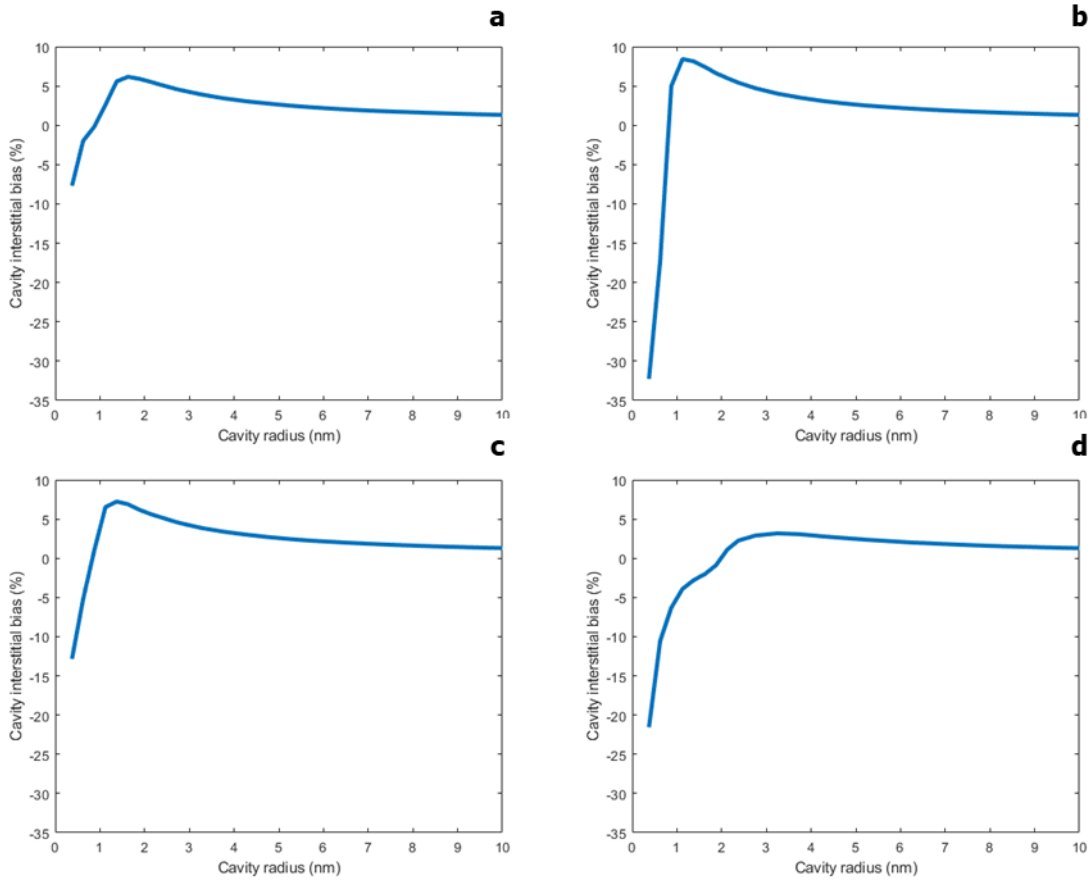


Figure 6.46: Predicted cavity interstitial bias at 72 dpa in the BOR-60 microstructure irradiated at (a) 369°C:0.77appmHe/dpa, 8×10^{-7} dpa/s, (b) 369°C:0.77appmHe/dpa, 7.5×10^{-4} dpa/s, (c) 445°C:0.77appmHe/dpa, 7.5×10^{-4} dpa/s and (d) 445°C:3appmHe/dpa, 7.5×10^{-4} dpa/s.

Table 6.20: Simulated BOR-60-equivalent cavity microstructures in various irradiation conditions.

Model parameters	Predicted swelling (%), average diameter (nm), root-mean-cube diameter (nm) and densities ($10^{20}m^{-3}$)				
	Swelling	Average diameter	RMC diameter	Bubble density	Void density
369°C, 0.77appmHe/dpa, 8×10^{-7} dpa/s, 72 dpa	0.45	13.2	15.6	174	22.1
369°C, 0.77appmHe/dpa, 7.5×10^{-4} dpa/s, 72 dpa	1.05	18.1	20.8	174	22.1
445°C, 0.77appmHe/dpa, 7.5×10^{-4} dpa/s, 72 dpa	1.00	17.8	20.5	174	22.1
445°C, 3appmHe/dpa, 7.5×10^{-4} dpa/s, 72 dpa	0.41	12.9	15.1	174	22.1

A similar analysis is conducted for FFTF-equivalent irradiation parameters. Figure 6.47 (a), Figure 6.48 (a) and Figure 6.49 (a) show the predicted net flux of vacancies, helium content in sinks and simulated cavity microstructure for the FFTF microstructure going from 73 dpa to 104 dpa at 407°C:0.21appmHe/dpa and 1.25×10^{-6} dpa/s. Unlike the BOR-60 case, most of the helium is contained in the voids while bubbles represent about 20% of the total content. Bubbles in FFTF exhibit lower density (~15×10^{20} m^{-3} in FFTF and ~150×10^{20} m^{-3} in BOR-60) and higher interstitial bias (up to -8% in FFTF and up to -30% in BOR-60) which limit their role in taking vacancies away from voids at low damage rate. Thus, the net flux of vacancies is higher for voids compared to bubbles (close to 0).

The damage rate is increased to 7.5×10^{-4} dpa/s and the clusters changed to the dual-ion case at 460°C:0.2appmHe/dpa that matches FFTF. The helium content in cavities (Figure 6.48 (b)) and vacancy flux to bubbles (Figure 6.47 (b)) decrease but not enough to drastically increase the vacancy flux to voids. As a result, the swelling only increases slightly (Table 6.21) and it does not seem that a temperature shift or increase in helium injection rate is necessary to compensate for the higher damage rate in terms of vacancy flux.

Increasing the temperature to 460°C allows helium to detrap from other sinks and to migrate to bubbles and voids as shown in Figure 6.48 (c). However, similar to the BOR-60 case, this change in helium partitioning only has a minor impact on the net flux of vacancies to sinks.

If the helium injection rate increase from the BOR-60 case is replicated (×3.9 increase) bringing the rate to 0.82 appmHe/dpa, the helium content in bubbles increases (Figure 6.48 (d)) but not to the same extent as seen in the BOR-60 analysis. Thus, it does not affect the net flux of vacancies to voids significantly (Figure 6.47 (d)).

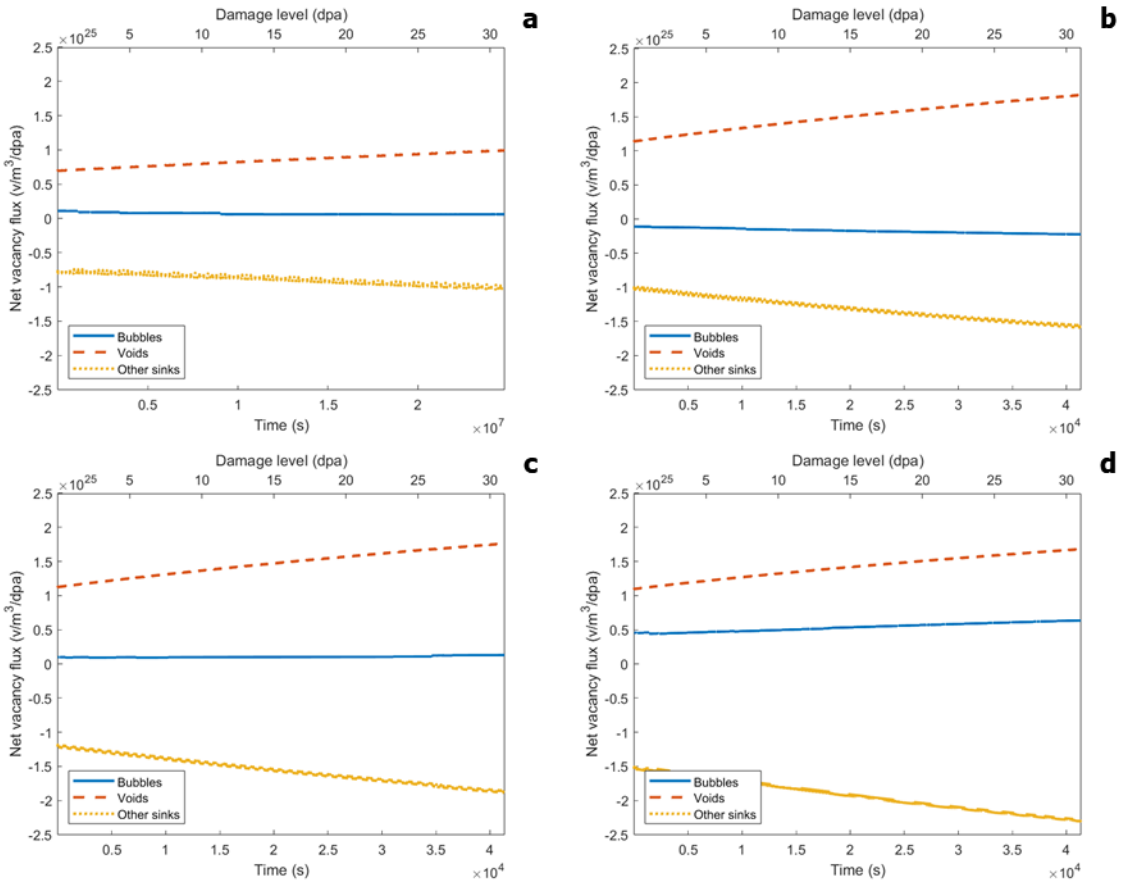


Figure 6.47: Predicted net vacancy fluxes in the FFTF microstructure irradiated at (a) 407°C:0.21appmHe/dpa, 1.25×10^{-6} dpa/s, (b) 407°C:0.21appmHe/dpa, 7.5×10^{-4} dpa/s, (c) 460°C:0.21appmHe/dpa, 7.5×10^{-4} dpa/s and (d) 460°C:0.82appmHe/dpa, 7.5×10^{-4} dpa/s.

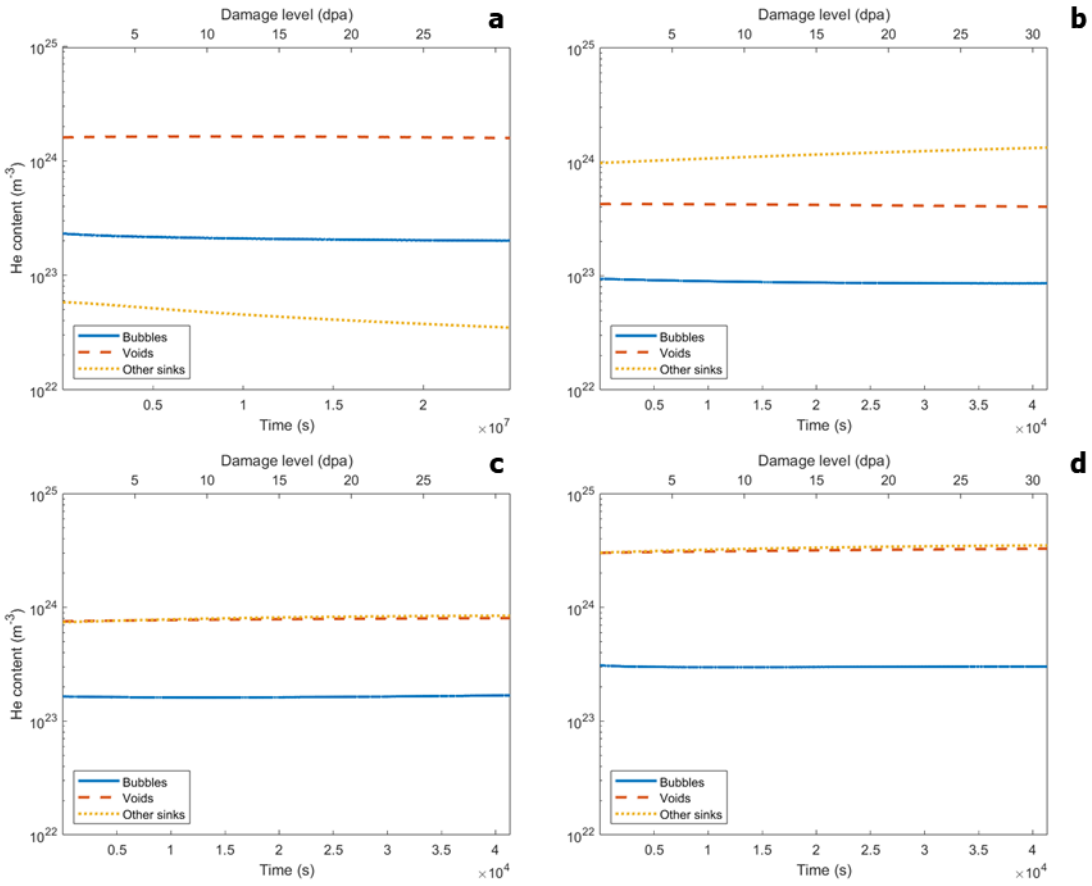


Figure 6.48: Predicted helium content in the FFTF microstructure irradiated at (a) 407°C:0.21appmHe/dpa, 1.25×10^{-6} dpa/s, (b) 407°C:0.21appmHe/dpa, 7.5×10^{-4} dpa/s, (c) 460°C:0.21appmHe/dpa, 7.5×10^{-4} dpa/s and (d) 460°C:0.82appmHe/dpa, 7.5×10^{-4} dpa/s.

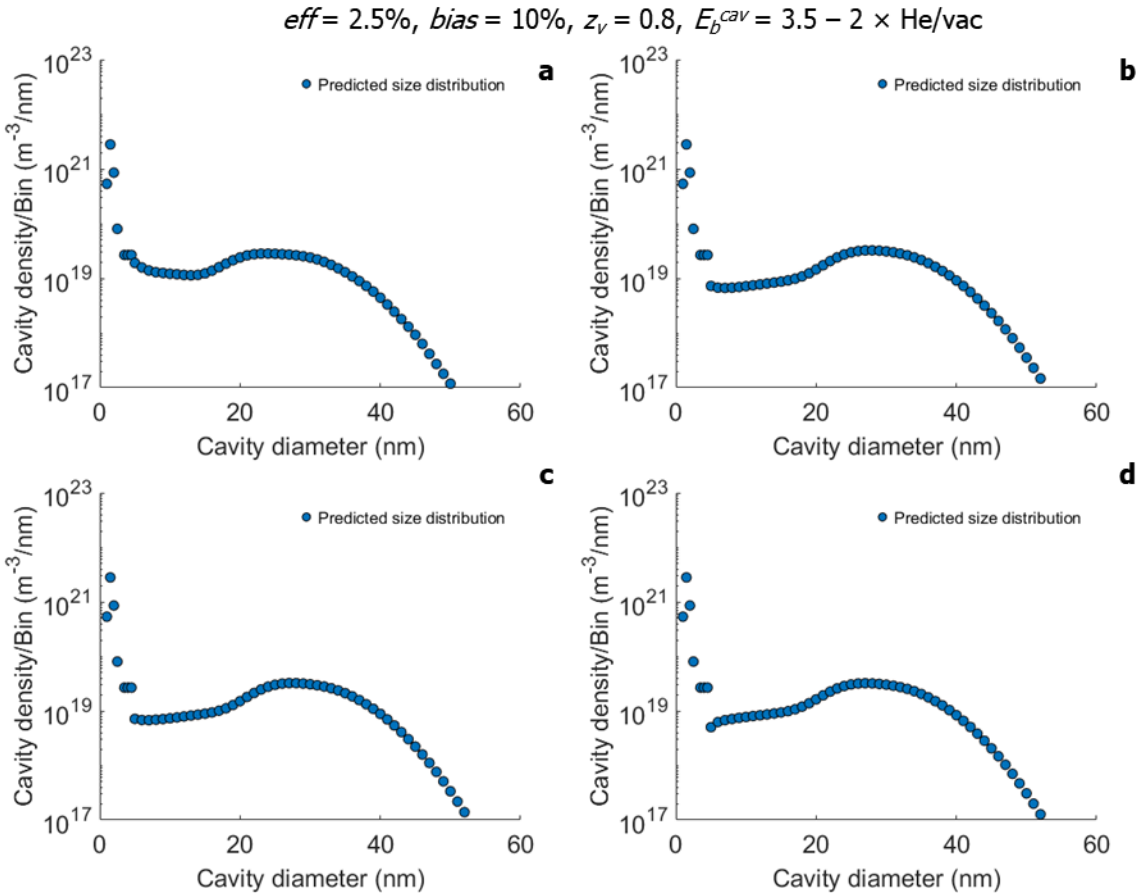


Figure 6.49: Predicted cavity microstructure in FFTF irradiated at (a) 407°C:0.21appmHe/dpa, 1.25×10^{-6} dpa/s, (b) 407°C:0.21appmHe/dpa, 7.5×10^{-4} dpa/s, (c) 460°C:0.21appmHe/dpa, 7.5×10^{-4} dpa/s and (d) 460°C:0.82appmHe/dpa, 7.5×10^{-4} dpa/s.

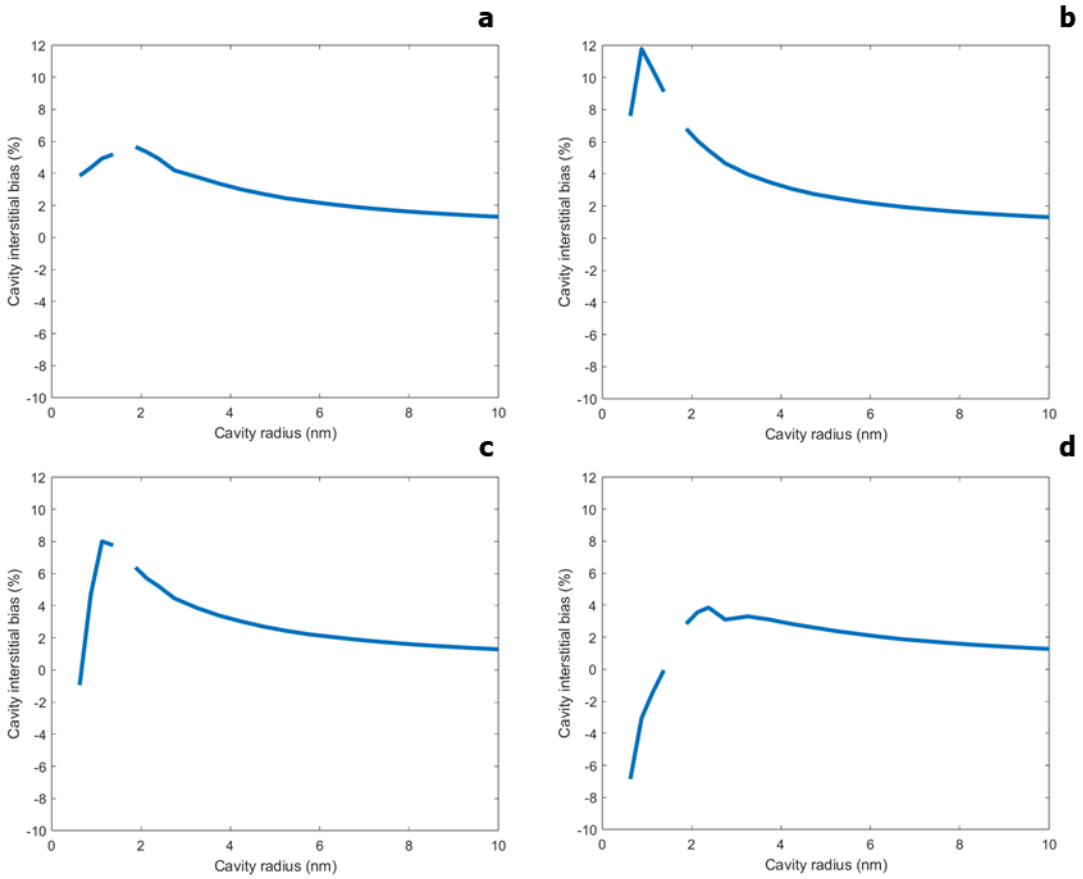


Figure 6.50: Predicted cavity interstitial bias in the FFTF microstructure irradiated at (a) 407°C:0.21appmHe/dpa, 1.25×10^{-6} dpa/s, (b) 407°C:0.21appmHe/dpa, 7.5×10^{-4} dpa/s, (c) 460°C:0.21appmHe/dpa, 7.5×10^{-4} dpa/s and (d) 460°C:0.82appmHe/dpa, 7.5×10^{-4} dpa/s.

In conclusion, the rate theory model reveals two cases when matching the cavity microstructure evolution at higher damage rate: intermediate/high helium production rate, and low helium production rate. At intermediate/high reactor helium production rate (equivalent to BOR-60), combined temperature shift and increased helium injection rate maintain the helium content in bubbles to a high level at higher damage rates. This results in a net flux of vacancies to voids comparable to reactor level due to a high consumption rate by bubbles. In the case of low reactor helium production rate (equivalent to FFTF), the bubble density is lower, and their interstitial bias is higher. In this scenario, there is no need for an increased helium injection rate

under dual-ion irradiation since the vacancy absorption rate by bubbles is low in reactor, and the vacancy flux to voids remains high to maintain their growth.

Table 6.21: Simulated FFTF-equivalent cavity microstructures in various irradiation conditions.

Model parameters	Predicted swelling (%), average diameter (nm), root-mean-cube diameter (nm) and densities ($10^{20}m^{-3}$)				
	Swelling	Average diameter	RMC diameter	Bubble density	Void density
407°C, 0.21appmHe/dpa, 1.25×10^{-6} dpa/s, 104 dpa	0.63	23.3	26.5	22	6.5
407°C, 0.21appmHe/dpa, 7.5×10^{-4} dpa/s, 104 dpa	0.89	27.2	29.7	22	6.5
460°C, 0.21appmHe/dpa, 7.5×10^{-4} dpa/s, 104 dpa	0.88	0.27	29.6	22	6.5
460°C, 0.82appmHe/dpa, 7.5×10^{-4} dpa/s, 104 dpa	0.85	26.8	29.3	22	6.5

Chapter 7 Conclusions

This chapter presents the conclusions drawn from the discussion in Chapter 6 to address the objective of **determining how temperature shift and helium injection rate interact in ion irradiation so as to replicate the neutron-irradiated cavity microstructure in ferritic-martensitic alloy T91.**

- For the first time, the cavity and loop microstructures of a ferritic-martensitic steel irradiated to high damage level (up to 170 dpa) over a range of temperatures (369-517°C) in two different reactors are matched via dual-ion irradiation using a temperature shift and similar or increased helium injection rate.
- For BOR-60, a single temperature shift (50-70°C) and increase in helium injection rate (×4-6) match the cavity and loop microstructures together up to 72 dpa.
- For FFTF, a temperature shift of ~50°C matches the cavity microstructure and a temperature shift of ~80°C matches the loop microstructure.
- Precise control and reporting of irradiation conditions are two reasons why dual-ion irradiation is an excellent tool for investigating radiation effects but also for investigating reported neutron irradiation parameters. For BOR-60, companion dual-ion irradiations contributed to identifying the erroneous reported temperature of some samples in-reactor. For FFTF, companion dual-ion irradiations clearly revealed the temperature excursion affecting high damage level samples.

- Density of loop nucleation sites and loop mobility are affected by reactor temperature and helium production rate and dictate the temperature shift to match loop microstructure. Helium trapping at fixed-density nucleation sites and helium partitioning in the microstructure influence the temperature shift to match cavity microstructure. This difference in phenomena influencing temperature shift explains the two different temperature shifts used to mimic the FFTF cavity and loop microstructures.
- The radiation-induced segregation behavior of Cr in neutron samples is not replicated with dual-ion irradiation because of the higher temperature increasing the diffusion of Cr away from grain boundaries and higher damage rate that reduces the time for diffusion.
- Ni and Si enrichment in dual-ion irradiations match that in reactor irradiations because of the vacancy-drag effect persisting at higher temperature.
- Clustering of Ni and Si still occurs during dual-ion irradiation. However, it is reduced due to higher ballistic mixing and the lack of time for migration which results in shorter diffusion distances under high-damage-rate dual-ion irradiation.
- Following fitting on BOR-60 and companion dual-ion irradiations, a rate theory model predicts the cavity microstructure evolution of other neutron and dual-ion conditions using the same irradiation and materials parameters that all fall within the range of reasonability based on measurements or calculation.
- The temperature excursion in MOTA-1C modeled to be 495°C for ~13.8 dpa resulted in reasonable agreement in the cavity size distribution and swelling between the FFTF

results and that using dual ion irradiation, indicating that the temperature increase may have been large but lasted for a short period of time.

- The rate theory model reveals two cases when matching the cavity microstructure evolution at higher damage rate based on helium production. At intermediate/high reactor helium production rate, combined temperature shift and increased helium injection rate maintain the helium content in bubbles to a high level at higher damage rates. This results in a net flux of vacancies to voids comparable to reactor level due to a high consumption rate by bubbles. In the case of low reactor helium production rate, the bubble density is lower, and their interstitial bias is higher. In this scenario, there is no need for an increased helium injection rate under dual-ion irradiation since the vacancy absorption rate by bubbles is low in reactor, and the vacancy flux to voids remains high to maintain their growth.
- Reactor designers, manufacturers, and utilities will benefit from this work as it provides a computational tool, backed by dual-ion irradiation data and validated against reactor data, that tracks the cavity microstructure evolution under irradiation. It offers a new approach to qualifying nuclear materials that bypasses the lengthy and expensive reactor irradiation campaigns, while providing licensees with a justification of the efficacy of their core material performance when establishing their safety case for the regulator.

Chapter 8 Future Work

By combining dual-ion irradiation and rate theory modeling, this dissertation provided insights into the relationship between temperature shift and helium injection rate in dual-ion irradiation to match neutron-irradiated cavity microstructures. Yet, some areas require further study to obtain a better predictive tool for microstructure evolution in reactor.

The prediction of point defect cluster nucleation rates. In this work, the nucleation rates of bubbles and voids in reactor and during dual-ion irradiation were estimated from experiments and assumed constant over time in the rate theory model. To develop a model that can predict the cavity microstructure evolution of any material in any reactor environment, it would be interesting to calculate nucleation rates of cavities, loops and clusters from an unirradiated microstructure based on reactor parameters. Although such a tool would still require fitting via dual-ion irradiation and reactor surveillance programs, it would enable the testing of many materials without the need for lengthy and expensive irradiations. Tools such as cluster dynamics models are promising approaches for this purpose.

Better reporting of reactor irradiation history. This work illustrated the importance of accurately reporting irradiation histories. In BOR-60, one set of samples had a reported irradiation temperature of 402°C, but characterization results revealed that the temperature was likely 450+°C. In FFTF, dual-ion experimental results combined with rate theory simulations indicated that samples had undergone a significant temperature excursion that annealed part of the cavity microstructure. The fitting of predictive models and tools to evaluate neutron-irradiated

microstructure evolution relies on accurate reporting of reactor irradiation history. Use of thermocouples and passive temperature sensors (such as SiC) to measure sample temperature over time or maximum temperature during irradiation are better approaches than calculated temperature from gamma heating. Use of active temperature control capsules in reactor would circumvent the risk of temperature transient caused by reactivity feedback tests or reduced the power level when off-normal conditions are detected [283]. Measurement of helium content in samples via thermal desorption or other analysis techniques would help with fitting of neutron damage codes that calculate helium production rates.

Better helium equation of state and binding energy. The mean-field rate theory model developed in this work relies on a modified hard-sphere equation of state to estimate the helium pressure in cavities. Multiple equations of state can be found in the literature, and their results can vary drastically, especially for small cavities [213,216–220]. The difference in computed helium pressures can have an impact on the calculated thermal emission of vacancy which can be significant in reactor environments [21]. Similarly, the helium binding energy to cavities used in this work is derived from capillarity laws [213,219,237] that are fitted from Molecular Dynamics or thermal desorption results. Accurate helium binding energies to sinks are necessary to determine their helium content during irradiation. Improved and validated helium equation of state and binding energies would greatly enhance the predictive capability of rate theory and cluster dynamics models.

Descriptive formula for cavity interstitial bias. The model in this work extrapolates results from Kinetic Monte Carlo and Molecular Dynamics simulations conducted in pure Fe up to 0.75-nm radius [215] to calculate the cavity interstitial bias of helium-filled cavities. The cavity interstitial bias dictates the evolution of the bubble microstructure under irradiation and also affects

the fluxes of vacancies to the different sinks in the microstructure. A parametric description of the cavity interstitial bias to high radius (>10 nm) in relevant ferritic-martensitic steels would greatly improve the fidelity of predictive models like the one presented in this work.

Matching of Ni/Si microstructure and radiation-induced segregation. The dual-ion irradiation results presented in this work only partially matched the neutron-irradiation segregation and precipitation behavior. In materials where embrittlement and cracking are life-limiting factors, it is important to correctly match the microchemical aspects of the microstructure if dual-ion irradiation is to be used as a tool for accelerated qualification. Reducing the damage rate would allow more solute diffusion and mitigate the effect of ballistic dissolution as indicated in previous work [176]. Additionally, temperature has a significant impact on radiation-induced segregation via the Inverse Kirkendall effect and on the thermodynamics of cluster precipitation. Adjustments to both irradiation parameters would provide a better match with the neutron-irradiated microchemistry.

Application to other materials. The experimental results and simulations from this work were conducted for ferritic-martensitic steel T91 only. Most of the findings would likely still be applicable to other FM steels in fast reactor environments even if adjustments to the starting microstructures, especially other precipitates such as α‘, and nucleation rates would be necessary. To apply this approach to materials from a different class such as austenitic steels, ODS steels or castable nanostructured alloys, the effect of helium should be carefully revisited since new microstructural features will exhibit new binding energies. Experimental results conducted in alloy 800H, for the overarching project this work is part of, indicate that the helium injection rate has to be decreased compared to reactor to match the cavity microstructure of BOR-60-irradiated samples via dual-ion irradiation. Additionally, hydrogen production and its impact on surface energy and

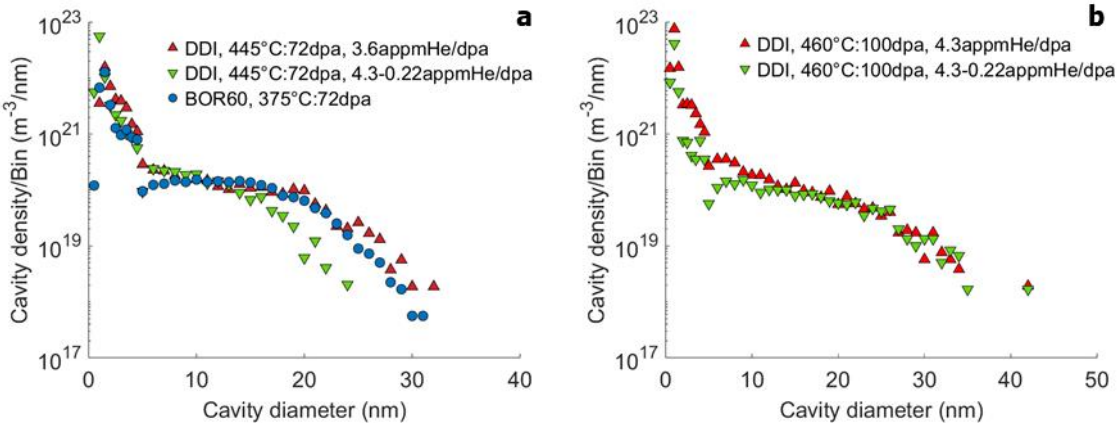
cavity growth in samples irradiated in fusion reactors would also need to be considered in these environments.

Appendices

Appendix A Neutron and Dual-Ion Irradiations

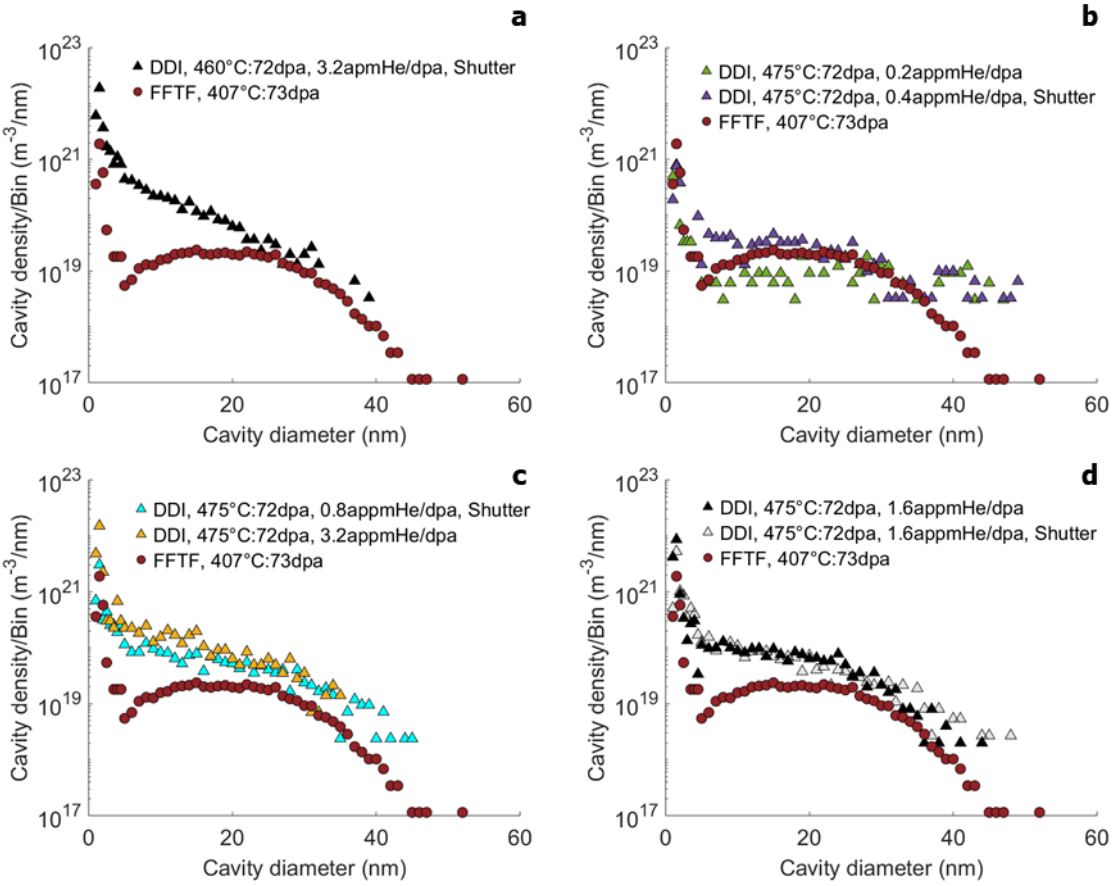
Many attempts at matching the BOR-60 and FFTF cavity microstructures were conducted and some of them were unfruitful. The characterization of all neutron-irradiated and dual-ion-irradiated cavity microstructures are tabulated in Appendix Table 1.

Two dual-ion irradiations (445°C:72dpa and 460°C:100dpa) with an initial 3.6 or 4.3 appmHe/dpa followed by a reduced helium injection rate (0.22 appmHe/dpa which corresponded to the initial estimate of the BOR-60 helium production rate) after 35 dpa were conducted to evaluate whether the lower helium content would better match BOR-60 samples by preventing the overnucleation of bubbles. Appendix Figure 1 shows the size distributions compared to the constant helium dual-ion irradiations and BOR-60 when applicable. At both temperatures, the void density and swelling were lower in the reduced helium case, but the average void diameter did not change consistently making it difficult to draw any clear conclusions.

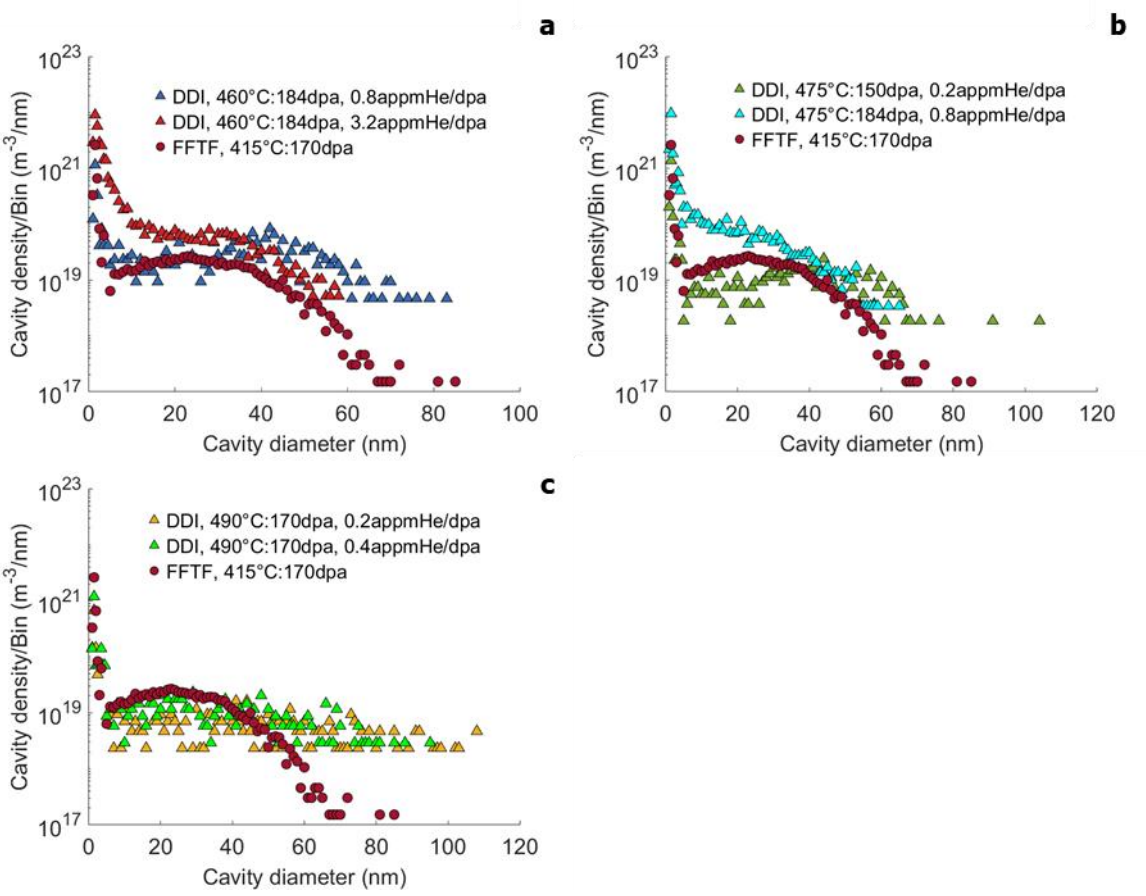


Appendix Figure 1: Size distributions of dual-ion-irradiated T91 with and without helium reduction at (a) 445°C with comparison with BOR-60, and at (b) 460°C.

Appendix Figure 2 and Appendix Figure 3 show the size distributions of the dual-ion irradiation attempted to match the FFTF cavity microstructures. Dual-ion irradiations conducted at 0.2 appmHe/dpa are the only ones consistently creating a valley between bubbles and voids at all temperatures and damage levels studied which justifies why this helium injection rate was selected to match FFTF.



Appendix Figure 2: Size distributions of T91 irradiated in FFTF to 73 dpa and after dual-ion irradiation to 72 dpa at (a) 460°C:3.2appmHe/dpa, (b) 475°C:0.2appmHe/dpa and 475°C:0.4appmHe/dpa, (c) 475°C:0.8appmHe/dpa and 475°C:3.2appmHe/dpa, and (d) 475°C:1.6appmHe/dpa with and without using shutters.



Appendix Figure 3: Size distributions of T91 irradiated in FFTF to 170 dpa and after dual-ion irradiation to 150-184 dpa at (a) 460°C:0.8appmHe/dpa and 460°C:3.2appmHe/dpa, (b) 475°C:0.2appmHe/dpa and 475°C:0.8appmHe/dpa, and (c) 490°C:0.2appmHe/dpa and 490°C:0.4appmHe/dpa.

Appendix Table 1: Complete list of cavity microstructures of irradiated T91 30176.

Irradiation mode	Sample	Condition	Swelling (%)	Bubble density ($\times 10^{20}$ m^{-3})	Average bubble diameter (nm)	Void density ($\times 10^{20}$ m^{-3})	Average void diameter (nm)	Number of bubbles/ voids counted (-)
BOR-60	P027-T03	369C-0.77Hedpa-16dpa	0.06 ± 0.01	1000 ± 119	2.07 ± 0.29	5.0 ± 0.7	6.9 ± 0.8	254/549
BOR-60	P028-T05	372C-0.77Hedpa-32dpa	0.04 ± 0.01	219 ± 26	1.78 ± 0.28	9.1 ± 1.3	8.0 ± 0.9	218/240
BOR-60	P031-T98	376C-0.77Hedpa-47dpa	0.21 ± 0.02	61 ± 8	2.04 ± 0.29	16.6 ± 1.8	11.8 ± 1.1	198/5145
BOR-60	P029-T11	375C-0.77Hedpa-72dpa	0.38 ± 0.04	141 ± 16	2.03 ± 0.29	20.9 ± 2.2	13.2 ± 1.2	703/3744
BOR-60	P033-T24	404C-0.77Hedpa-17dpa	0.01 ± 0.00	160 ± 19	1.79 ± 0.28	2.8 ± 0.4	6.8 ± 0.8	218/549
BOR-60	P036-T100	402C-0.77Hedpa-29dpa	0.003 ± 0.001	123 ± 14	1.59 ± 0.27	0.03 ± 0.01	9.6 ± 1.0	508/12
BOR-60	P034-T32	402C-0.77Hedpa-86dpa	0.023 ± 0.003	393 ± 42	1.63 ± 0.28	0.46 ± 0.05	16.2 ± 1.4	1824/325
BOR-60	P037-T55	453C-0.77Hedpa-19dpa	0.002 ± 0.000	32 ± 4	2.09 ± 0.29	N/O	N/O	47/0
BOR-60	P038-T61	450C-0.77Hedpa-32dpa	0.001 ± 0.000	8 ± 1	2.82 ± 0.40	N/O	N/O	N/R /0
BOR-60	P042-T67	517C-0.77Hedpa-15dpa	0.003 ± 0.000	34 ± 4	2.33 ± 0.35	N/O	N/O	103/0
BOR-60	P043-T108	515C-0.77Hedpa-25dpa	0.001 ± 0.000	6 ± 1	3.23 ± 0.45	N/O	N/O	N/R /0
FFTF	VH03	407C-0.21Hedpa-73dpa	0.28 ± 0.03	14.8 ± 1.9	1.85 ± 0.28	4.7 ± 0.5	19.8 ± 1.6	163/4135
FFTF	VH20	415C-0.21Hedpa-151dpa	1.09 ± 0.12	13.0 ± 2.3	1.91 ± 0.28	7.6 ± 0.8	25.6 ± 1.9	46/6266
FFTF	NP04	415C-0.21Hedpa-170dpa	1.26 ± 0.13	19.0 ± 2.4	1.86 ± 0.28	7.7 ± 0.8	26.4 ± 2.0	183/5125
FFTF	FA33	415C-0.21Hedpa-184dpa	0.99 ± 0.10	33.3 ± 3.9	1.93 ± 0.28	4.7 ± 0.5	29.3 ± 2.2	356/3287
DDI	092717	445C-4.3Hedpa-16.6dpa	0.017 ± 0.002	178 ± 21	1.31 ± 0.26	5.2 ± 0.7	7.5 ± 0.9	131/423
DDI	053018-1	445C-4.3Hedpa-35dpa	0.041 ± 0.006	140 ± 17	2.09 ± 0.29	7.4 ± 1.1	8.5 ± 1.0	573/426
DDI	070120-1	445C-3.1Hedpa-54dpa	0.21 ± 0.02	227 ± 26	2.19 ± 0.29	14.8 ± 1.7	11.4 ± 1.6	437/466
DDI	102120-1	445C-3.6Hedpa-72dpa	0.46 ± 0.05	200 ± 22	2.37 ± 0.35	25.3 ± 2.7	12.5 ± 1.6	1043/1352
DDI	111620	445C-4.3/0.2Hedpa-72dpa	0.18 ± 0.02	409 ± 44	1.47 ± 0.27	19.0 ± 2.1	10.6 ± 1.5	1596/935
DDI	092917	460C-4.3Hedpa-16.6dpa	0.015 ± 0.002	123 ± 15	1.64 ± 0.27	3.0 ± 0.4	8.1 ± 0.9	657/161
DDI	071320-1	460C-3.1Hedpa-33dpa	0.07 ± 0.01	96 ± 12	1.80 ± 0.28	9.8 ± 1.1	9.9 ± 1.5	261/397
DDI	021121	460C-4.3Hedpa-35dpa	0.12 ± 0.01	303 ± 34	1.40 ± 0.27	14.4 ± 1.6	9.9 ± 1.6	515/474
DDI	062424	460C-0.2Hedpa-72dpa	0.31 ± 0.03	3.6 ± 0.7	2.08 ± 0.29	5.0 ± 0.6	19.4 ± 1.5	36/187
DDI	062424	460C-3.2Hedpa-72dpa-shutter	0.64 ± 0.07	173 ± 19	2.02 ± 0.29	34.9 ± 3.8	12.0 ± 1.1	842/1056
DDI	091420-1	460C-3.2-3.7Hedpa-72dpa	0.28 ± 0.03	756 ± 82	1.55 ± 0.27	20.8 ± 2.4	11.7 ± 1.6	1338/478
DDI	030621-1	460C-4.3Hedpa-100dpa	0.65 ± 0.07	610 ± 65	1.48 ± 0.27	31.8 ± 3.4	12.5 ± 1.6	2365/1665
DDI	032321	460C-4.3/0.2Hedpa-100dpa	0.56 ± 0.06	295 ± 32	1.34 ± 0.27	19.3 ± 2.1	14.8 ± 1.7	1000/1155
DDI	012025-2	460C-0.2Hedpa-110dpa	1.64 ± 0.18	8.6 ± 2.0	2.02 ± 0.29	10.2 ± 1.2	27.3 ± 2.1	24/255

DDI	101424	460C-0.2Hedpa-184dpa	5.78 ± 0.64	5.3 ± 1.3	1.77 ± 0.28	11.4 ± 1.3	39.3 ± 2.9	20/394
DDI	101424	460C-0.8Hedpa-184dpa-shutter	7.57 ± 0.86	9 ± 2	1.98 ± 0.29	17.4 ± 2.0	36.5 ± 2.7	44/375
DDI	101424	460C-3.2Hedpa-184dpa-shutter	3.41 ± 0.37	134 ± 15	2.38 ± 0.30	37.4 ± 4.0	18.0 ± 1.5	439/1460
DDI	050825	460-490-460C-0.2Hedpa-170dpa	2.57 ± 0.28	32.8 ± 4.6	2.11 ± 0.29	15.3 ± 1.7	23.3 ± 1.8	115/605
DDI	020325-2	475C-0.2Hedpa-72dpa	0.41 ± 0.05	7 ± 1	1.70 ± 0.28	3.0 ± 0.4	25.7 ± 2.0	44/97
DDI	050224	475C-0.4Hedpa-72dpa-shutter	0.53 ± 0.06	7 ± 2	2.00 ± 0.29	7.8 ± 1.0	18.7 ± 1.5	15/241
DDI	050224	475C-0.8Hedpa-72dpa-shutter	0.82 ± 0.09	27 ± 4	2.15 ± 0.29	17.1 ± 1.9	16.7 ± 1.4	86/720
DDI	072723-2/4	475C-1.6Hedpa-72dpa	0.76 ± 0.08	74 ± 9	1.77 ± 0.28	19.5 ± 2.1	16.1 ± 1.4	438/980
DDI	050224	475C-1.6Hedpa-72dpa-shutter	0.77 ± 0.08	46 ± 6	2.20 ± 0.29	18.7 ± 2.1	15.6 ± 1.3	160/703
DDI	091323-1/2	475C-3.2Hedpa-72dpa	0.78 ± 0.08	120 ± 15	1.85 ± 0.28	26.5 ± 3.1	14.4 ± 1.3	218/428
DDI	020325-2	475C-0.2Hedpa-150dpa	2.56 ± 0.28	9 ± 1	1.86 ± 0.28	5.6 ± 0.7	37.7 ± 2.8	81/305
DDI	012524-4	475C-0.8Hedpa-184dpa	2.99 ± 0.32	80 ± 10	2.01 ± 0.29	30.0 ± 3.3	19.8 ± 1.6	322/846
DDI	040225	490C-0.8Hedpa-72dpa	0.12 ± 0.01	10.2 ± 2.1	2.06 ± 0.29	1.8 ± 0.3	19.0 ± 1.5	33/69
DDI	040425	490C-0.2Hedpa-170dpa-shutter	4.39 ± 0.49	5 ± 1	1.74 ± 0.28	4.5 ± 0.6	45.1 ± 3.3	21/191
DDI	040425	490C-0.4Hedpa-170dpa-shutter	3.24 ± 0.36	9 ± 2	2.18 ± 0.29	6.6 ± 0.8	35.3 ± 2.6	26/228
DDI	040425	490C-0.8Hedpa-170dpa	2.08 ± 0.23	15.0 ± 2.3	1.94 ± 0.28	7.8 ± 0.9	28.5 ± 2.1	82/254
DDI	020320	520C-3.2Hedpa-16.6dpa	0.010 ± 0.002	188 ± 28	1.09 ± 0.25	0.11 ± 0.02	19.8 ± 1.9	440/4
DDI	091719	520C-4.3Hedpa-28dpa	0.006 ± 0.001	30 ± 4	1.73 ± 0.27	0.19 ± 0.03	15.5 ± 1.8	N/R
DDI	110117	570C-4.3Hedpa-15.4dpa	0.010 ± 0.001	168 ± 20	2.18 ± 0.29	N/O	N/O	334/0
DDI	111219	570C-4.3Hedpa-28dpa	0.002 ± 0.000	71 ± 8	1.42 ± 0.26	Negl.	Negl.	N/R

Appendix B Effect of Temperature and Helium on Predicted Cavity Microstructures

The goal of the rate theory model is to predict the cavity microstructure evolution in reactors. Estimates of the reactor temperature and helium production rate are required for these predictions. However, the BOR-60 microstructure evolution at 402-404°C presented in Chapter 5 and discussed in Section 6.1.2 demonstrates that reported temperatures (especially when they are calculated and not measured) are not always consistent with characterization results, with suspected inaccuracies as high as 50°C. Additionally, materials experiments in reactor can be subject to temperature excursion, sometimes planned (reactivity feedback tests, shut-downs and start-ups) but also resulting from operator errors (as high as 280°C in some FFTF experiments [157]). The effect of these temperature excursions on microstructure can be significant [113,299,300]. Similarly, inaccuracies in reported helium production rates would have an impact on the accuracy of the predicted microstructure evolution. Although helium content in samples can be measured via analysis techniques (Nuclear Reaction Analysis, Rutherford Backscattering [152], Time-of-Flight Elastic Recoil Detection [301], Thermal Desorption [201,241,302], etc.), the helium production rate is often computed from neutron spectrum data that may include inaccuracies. Additionally, these computations are done via neutron damage codes such as SPECTER [154] or FISPACT [155] and using cross section libraries like ENDF/B-VII.0 [156] and TENDL [303] which can lead to additional uncertainties. Over the course of this work, BOR-60 temperatures and helium production rates have been reevaluated multiple times with

differentials between estimates as high as 58°C and spanning between 0.20 and 0.77 appmHe/dpa for the same sample.

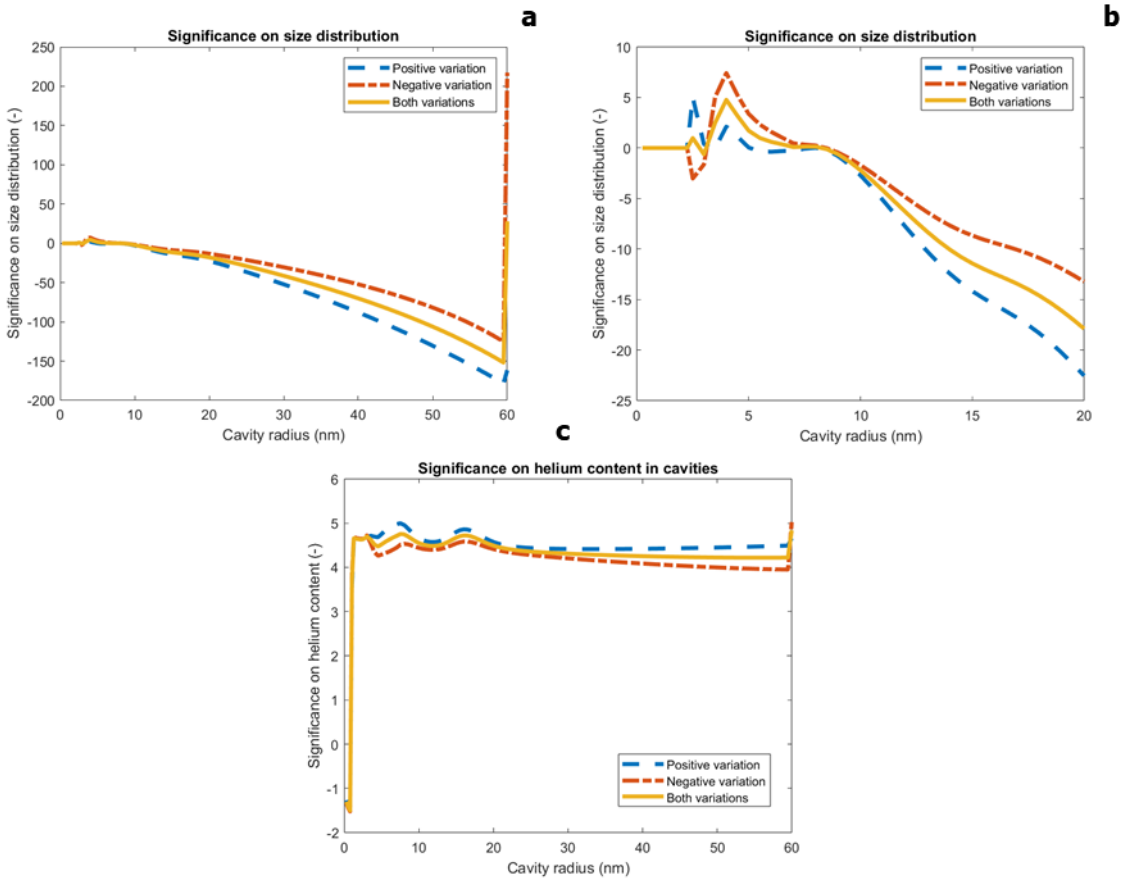
In this subsection, the effect of temperature and helium production rate on the predicted BOR-60 cavity microstructure is discussed. Appendix Figure 4 shows the significance of temperature on the predicted cavity microstructure and helium content in cavities of BOR-60 irradiated to 72 dpa. Increasing the temperature decreases the helium content in bubbles smaller than 1 nm in radius but drastically increases the helium content in cavities 1 nm and larger in radius. Overall, this change decreases the cavity interstitial bias and limits the net flux of vacancies to larger voids which in turn reduces swelling, average void diameter and root-mean-cube diameter. Appendix Table 2 shows the significance of temperature on swelling, average void diameter, void density and root-mean-cube diameter across damage levels. The significances are slightly more pronounced at 47 and 72 dpa than at 32 dpa which is consistent with temperature influencing void growth which is a bigger contributor to swelling than void nucleation as damage increases. Also, since the same nucleation rates are kept the same for these significance simulations, the significance on void density cannot be evaluated properly, hence its value being equal to 0 (within machine error).

Appendix Figure 5 shows the significance of helium production rate on the predicted cavity microstructure and helium content in cavities of BOR-60 samples irradiated to 72 dpa. Increasing the helium production rate significantly increases the helium content in all cavities. This change decreases the cavity interstitial bias and limits the net flux of vacancies to larger voids which in turn reduces swelling, average void diameter and root-mean-cube diameter.

Appendix Table 3 shows the significance of helium production rate on swelling, average void diameter, void density and root-mean-cube diameter across damage levels. Similar to

temperature, the significances are more pronounced at 47 and 72 dpa than at 32 dpa. This is consistent with the model only capturing the effect of helium on growth and not on nucleation which is a bigger contributor to swelling than void growth at low damage level.

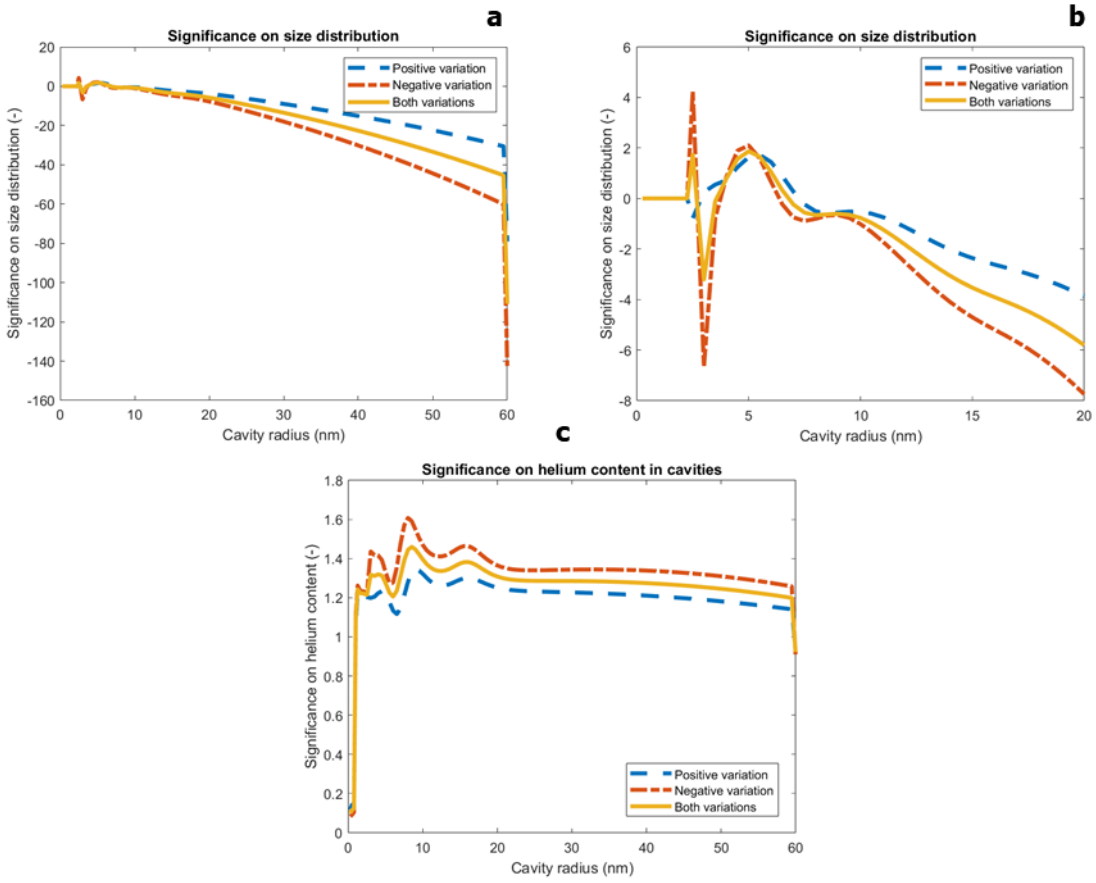
It is difficult to compare these model significances to experimental variations since the effect on starting microstructure and nucleation rates are not considered in the model (as shown by a negligible significance of both parameters on void density). However, the large sensitivities of swelling to temperature (~ -2.4) and helium production rate (~ -1) at intermediate damage level underscores the need for accurate reporting of reactor values for precise prediction of the cavity size distributions.



Appendix Figure 4: Significance of temperature (+/- 1°C) on the predicted BOR-60-irradiated (a-b) cavity size distribution and (c) helium content in cavities at 369°C:72dpa, 0.77appmHe/dpa.

Appendix Table 2: Significance of temperature (+/- 1°C) in the prediction of the BOR-60-irradiated cavity microstructure at 369°C:32-72dpa, 0.77appmHe/dpa.

Condition	Swelling significance (%/%)	Average diameter significance (%/%)	Void density significance (%/%)	Root-mean-cube diameter (%/%)
BOR-60, 369°C:32dpa	-1.5275	-0.61218	-2.4631×10^{-14}	-0.56635
BOR-60, 369°C:47dpa	-2.5361	-1.0322	-6.7068×10^{-14}	-0.88449
BOR-60, 369°C:72dpa	-2.3144	-0.83632	-6.5661×10^{-14}	-0.78818

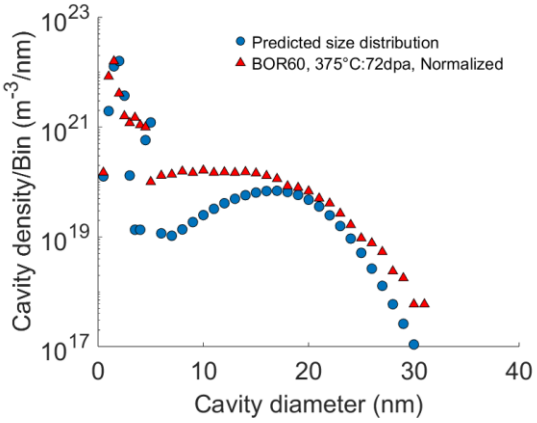


Appendix Figure 5: Significance of helium production rate (+/- 10^{-4}) on the predicted BOR-60-irradiated (a-b) cavity size distribution and (c) helium content in cavities at 369°C:72dpa, 0.77appmHe/dpa.

Appendix Table 3: Significance of helium rate (+/- 10^{-4}) in the prediction of the BOR-60-irradaited cavity microstructure at 369°C:32-72dpa, 0.77appmHe/dpa.

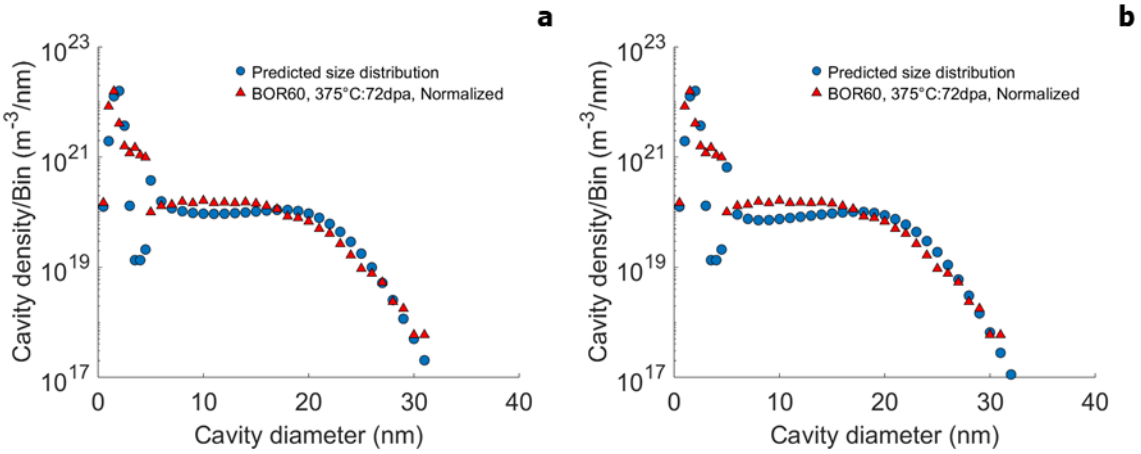
Condition	Swelling significance (%/%)	Average diameter significance (%/%)	Void density significance (%/%)	Root-mean-cube diameter (%/%)
BOR-60, 369°C:32dpa	0.061085	0.023764	-2.0025×10^{-12}	0.022645
BOR-60, 369°C:47dpa	-1.1855	-0.57794	9.0878×10^{-13}	-0.41339
BOR-60, 369°C:72dpa	-0.81426	-0.32062	4.152×10^{-12}	-0.27693

Based on the suspected error in the reported temperature for BOR-60 samples at 402-404°C presented in Section 6.1.2, the possibility for other temperature-helium production rate combinations to predict the BOR-60 cavity microstructures are considered. First, a predicted cavity size distribution at 420°C:0.77appmHe/dpa is compared to BOR-60 at 72 dpa to evaluate the influence that a ~50°C error (consistent with the estimate from Section 6.1.2) would have on the prediction (Appendix Figure 6). The increased temperature limits the growth of cavities in the starting microstructure (16.6dpa) and the nucleation of voids by increasing the thermal emission of vacancies and decreasing the bubble interstitial bias by way of increasing bubble helium content.



Appendix Figure 6: Predictions of BOR-60-irradiated cavity microstructures to 72 dpa at 420°C:0.77appmHe/dpa.

Although the prediction at 420°C shows that changing the irradiation temperature without conducting a new fitting cannot correctly predict the BOR-60 cavity microstructure at 72 dpa, there exist temperature-helium combination with the same fit that offer decent predictions. As discussed above, temperature error up to 50°C and helium production rate as low as 0.22 appmHe/dpa are considered since it represents the lowest value calculated for BOR-60 over the multiple revisions throughout the duration of this work. For instance, 405°C:0.55appmHe/dpa and 420°C:0.3appmHe/dpa can lead to acceptable predictions without a new fit as shown in Appendix Figure 7. Although the shapes of these predictions do not match that of the regularized size distribution as close as the prediction at 369°C:0.77appmHe/dpa, the descriptive values are very comparable as shown in Appendix Table 4.



Appendix Figure 7: Predictions of BOR-60-irradiated cavity microstructures to 72 dpa at (a) 405°C:0.55appmHe/dpa and (b) 420°C:0.3appmHe/dpa.

Appendix Table 4: Comparison of predicted vs. measured (regularized) BOR-60-irradiated cavity microstructures to 72 dpa at multiple temperature-helium-rate combinations.

Condition	Regularized swelling (%), average diameter (nm), root-mean-cube diameter (nm) and densities ($10^{20}m^{-3}$)					Predicted swelling (%), average diameter (nm), root-mean-cube diameter (nm) and densities ($10^{20}m^{-3}$)				
	Swelling	Average diameter	RMC diameter	Bubble density	Void density	Swelling	Average diameter	RMC diameter	Bubble density	Void density
369°C:0.77appmHe/dpa	0.40	13.2	15.0	174	22.1	0.45	13.2	15.6	174	22.1
405°C:0.55appmHe/dpa						0.44	13.1	15.5	174	22.1
420°C:0.3appmHe/dpa						0.42	12.4	15.2	174	22.1

Appendix C Significance Analysis of Rate Theory Model

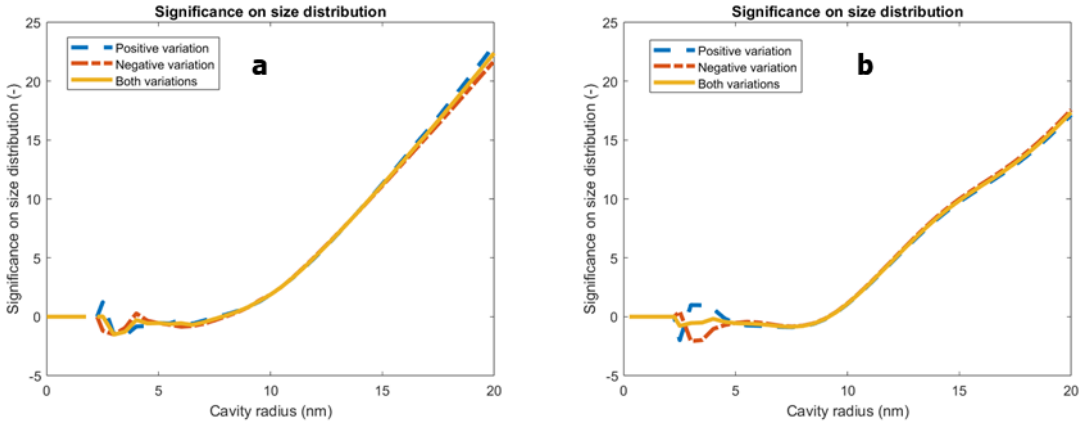
The significance of parameters used in the fitting process described in Section 6.2 are shown in Appendix Table 5. *eff* is the cascade efficiency (default 2.5%), *bias* is the dislocation bias (default 10%), z_v is the vacancy capture efficiency at dislocations (default 0.8) and $E_b^{He,cav1}$ is the first term in the equation describing the helium binding energy (default 3.5 eV), chosen because it is the most impactful term. For all four parameters, the significance was evaluated with a variation corresponding to 0.001 (or 0.1%) of the default value.

For all parameters, the significance of void density is negligible since the nucleation rate is kept constant throughout the simulations and is the only factor affecting density at these conditions. The significances of cascade efficiency are comparable between the two irradiation methods because this parameter mostly influences the amount of point defects available for cavity growth in the microstructure and both conditions have similar cavity size distribution evolution (also shown in Appendix Figure 8). As described in Section 6.5, helium plays a crucial role in the growth of cavities in the dual-ion case which explains why the significance of $E_b^{He,cav1}$ is much more important than in BOR-60 as shown in Appendix Figure 11. Plus, a substantial amount of helium is retained at dislocations at high damage rates, thus the significances of both dislocation bias and vacancy capture efficiency at dislocations is higher in dual-ion because it also affects the amount of helium absorbed at dislocations. In fact, Appendix Figure 10 shows that for the dual-ion case, increasing the vacancy capture efficiency of dislocations tends to decrease the density of smaller voids (<7.5 nm in radius) because more helium is retained at dislocations and less in bubbles,

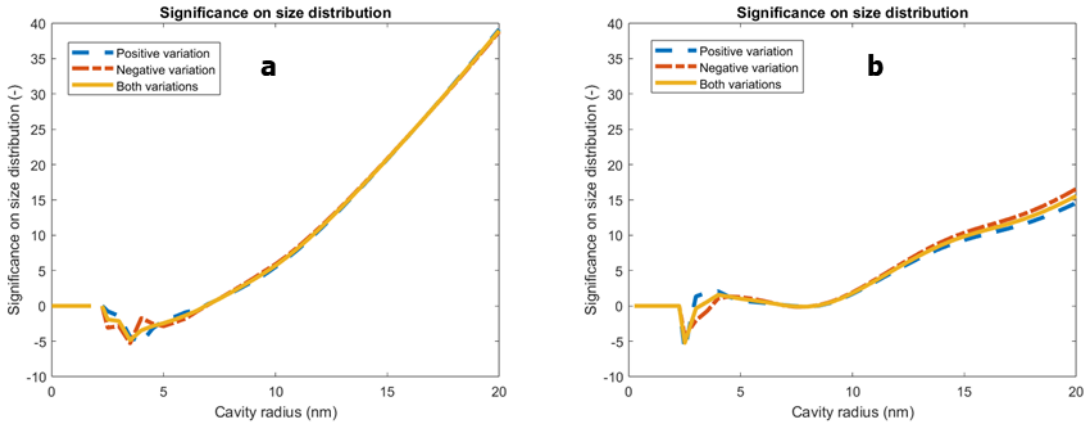
which allows for more void growth. In the case of BOR-60, increasing the vacancy capture efficiency only contributes to taking vacancies away from cavities and limits their growth which causes an increase in the density of smaller voids (<7.5 nm).

Appendix Table 5: Significance of key parameters in the prediction of the irradiated cavity microstructure.

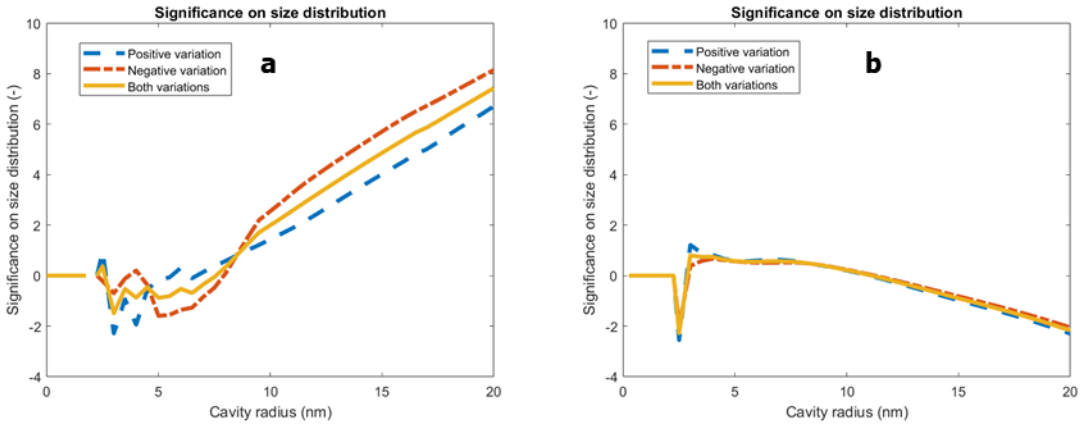
Condition	Parameter	Swelling significance (%/%)	Average diameter significance (%/%)	Void density significance (%/%)	Root-mean-cube diameter (%/%)
DDI, 445C-3.6Hedpa-72dpa	*eff*	1.4083	0.4369	-2.357×10^{-13}	0.47381
	bias	3.9472	1.3554	-1.1785×10^{-13}	1.3281
	z_v	1.1577	0.38025	5.8926×10^{-14}	0.38954
	$E_b^{He,cav1}$	-20.3401	-7.172	5.8926×10^{-13}	-6.7876
BOR-60, 369C-0.77Hedpa-72dpa	*eff*	1.4195	0.46674	1.1863×10^{-13}	0.48279
	bias	2.1036	0.94026	-1.7794×10^{-13}	0.71551
	z_v	0.19582	0.1865	-2.3726×10^{-13}	0.066601
	$E_b^{He,cav1}$	-2.6901	-1.5237	-1.1863×10^{-13}	-0.91632



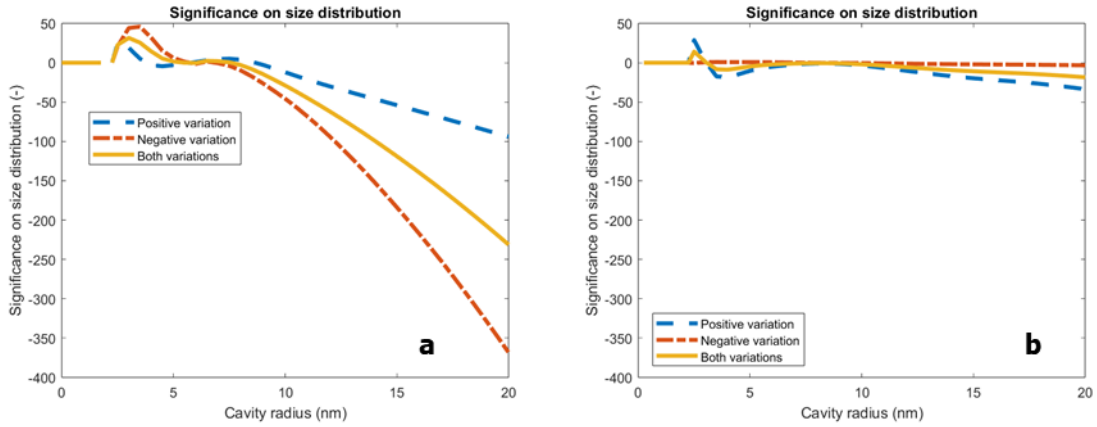
Appendix Figure 8: Significance of *eff* on size distribution for (a) DDI, 445C-3.6Hedpa-72dpa and (b) BOR-60, 369C-0.77Hedpa-72dpa.



Appendix Figure 9: Significance of *bias* on size distribution for (a) DDI, 445C-3.6Hedpa-72dpa and (b) BOR-60, 369C-0.77Hedpa-72dpa.



Appendix Figure 10: Significance of z_v on size distribution for (a) DDI, 445C-3.6Hedpa-72dpa and (b) BOR-60, 369C-0.77Hedpa-72dpa.



Appendix Figure 11: Significance of $E_b^{He,cav1}$ on size distribution for (a) DDI, 445C-3.6Hedpa-72dpa and (b) BOR-60, 369C-0.77Hedpa-72dpa.

Bibliography

[1] International Energy Agency, Nuclear Power in a Clean Energy System, 2019.

[2] World Nuclear Association, Generation IV Nuclear Reactors, Https://World-Nuclear.Org/Information-Library/Nuclear-Fuel-Cycle/Nuclear-Power-Reactors/Generation-Iv-Nuclear-Reactors (n.d.).

[3] G.S. Was, Challenges to the use of ion irradiation for emulating reactor irradiation, J Mater Res 30 (2015) 1158–1182. https://doi.org/10.1557/jmr.2015.73.

[4] G.S. Was, D. Petti, S. Ukai, S. Zinkle, Materials for future nuclear energy systems, Journal of Nuclear Materials 527 (2019) 151837. https://doi.org/10.1016/j.jnucmat.2019.151837.

[5] R.L. Klueh, D.R. Harries, ASTM International., High-chromium ferritic and martensitic steels for nuclear applications, ASTM, 2001.

[6] G.S. Was, Fundamentals of Radiation Materials Science, Second Edi, 2017. https://doi.org/10.1007/978-1-4939-3438-6_1.

[7] H. Finkler, M. Schirra, Transformation behaviour of the high temperature martensitic steels with 8 - 14% chromium, Steel Research 67 (1996) 328–342. https://doi.org/10.1002/srin.199605498.

[8] S. Agarwal, M. Butterling, M.O. Liedke, K.H. Yano, D.K. Schreiber, A.C.L. Jones, B.P. Uberuaga, Y.Q. Wang, M. Chancey, H. Kim, B.K. Derby, N. Li, D.J. Edwards, P. Hosemann, D. Kaoumi, E. Hirschmann, A. Wagner, F.A. Selim, The mechanism behind the high radiation tolerance of Fe–Cr alloys, J Appl Phys 131 (2022) 125903. https://doi.org/10.1063/5.0085086.

[9] F. Abe, T. Noda, H. Araki, M. Okada, Development of reduced-activation martensitic 9Cr steels for fusion reactor, J Nucl Sci Technol 31 (1994) 279–292. https://doi.org/10.1080/18811248.1994.9735152.

[10] G.R. Odette, On mechanisms controlling swelling in ferritic and martensitic alloys, Journal of Nuclear Materials 155–157 (1988) 921–927. https://doi.org/10.1016/0022-3115(88)90442-4.

[11] R.L. Klueh, K. Ehrlich, F. Abe, Ferritic/martensitic steels: promises and problems, Journal of Nuclear Materials 191–194 (1992) 116–124. https://doi.org/10.1016/S0022-3115(09)80018-4.

[12] Y. Dai, G.R. Odette, T. Yamamoto, The Effects of Helium in Irradiated Structural Alloys, Elsevier Ltd., 2020. https://doi.org/10.1016/b978-0-12-803581-8.12046-6.

[13] Z. Jiao, S. Taller, K. Field, G. Yeli, M.P. Moody, G.S. Was, Microstructure evolution of T91 irradiated in the BOR60 fast reactor, Journal of Nuclear Materials 504 (2018) 122–134. https://doi.org/10.1016/j.jnucmat.2018.03.024.

[14] G.S. Was, Z. Jiao, E. Getto, K. Sun, A.M. Monterrosa, S.A. Maloy, O. Anderoglu, B.H. Sencer, M. Hackett, Emulation of reactor irradiation damage using ion beams, Scr Mater 88 (2014) 33–36. https://doi.org/10.1016/j.scriptamat.2014.06.003.

[15] G.S. Was, S.J. Zinkle, Toward the Use of Ion Irradiation to Predict Reactor Irradiation Effects, Elsevier Ltd., 2020. https://doi.org/10.1016/b978-0-12-803581-8.12053-3.

[16] S. Taller, Z. Jiao, K. Field, G.S. Was, Emulation of fast reactor irradiated T91 using dual ion beam irradiation, Journal of Nuclear Materials 527 (2019). https://doi.org/10.1016/j.jnucmat.2019.151831.

[17] S. Taller, The Role of Damage Rate on Cavity Nucleation with Co-Injected Helium in Dual Ion Irradiated T91 Steel, University of Michigan, 2020.

[18] D. Woodley, The Role of Helium on Cavity Growth and Swelling at High Damage Levels in Ferritic-Martensitic Steels, University of Michigan, 2020.

[19] A.A. Kohnert, B.D. Wirth, L. Capolungo, Modeling microstructural evolution in irradiated materials with cluster dynamics methods: A review, Comput Mater Sci 149 (2018) 442–459. https://doi.org/10.1016/j.commatsci.2018.02.049.

[20] B.D. Wirth, X. Hu, A. Kohnert, D. Xu, Modeling defect cluster evolution in irradiated structural materials: Focus on comparing to high-resolution experimental characterization studies, J Mater Res 30 (2015) 1440–1455. https://doi.org/10.1557/jmr.2015.25.

[21] S. Taller, G. VanCoevering, B.D. Wirth, G.S. Was, Predicting structural material degradation in advanced nuclear reactors with ion irradiation, Sci Rep 11 (2021) 1–14. https://doi.org/10.1038/s41598-021-82512-w.

[22] G. Pastore, N. Militello, S. Blondel, B.D. Wirth, Single-size and cluster dynamics modeling of intra-granular fission gas bubbles in UO2, Journal of Nuclear Materials 583 (2023) 154453. https://doi.org/10.1016/j.jnucmat.2023.154453.

[23] A. V Barashev, S.I. Golubov, R.E. Stoller, A Model of Radiation-induced Microstructural Evolution, ORNL/LTR-2014/487, Oak Ridge, 2014.

[24] R.L. Klueh, D.J. Alexander, Embrittlement of 9Cr-1MoVNb and 12Cr-1MoVW steels irradiated in HFIR, Journal of Nuclear Materials 187 (1992) 60–69. https://doi.org/10.1016/0022-3115(92)90319-G.

[25] R.L. Klueh, Elevated temperature ferritic and martensitic steels and their application to future nuclear reactors, (2013). https://doi.org/10.1179/174328005X41140.

[26] H. Bhadeshia, R. Honeycombe, Strengthening of Iron and Its Alloys, in: Steels: Microstructure and Properties, Elsevier, 2017: pp. 23–57. https://doi.org/10.1016/b978-0-08-100270-4.00002-0.

[27] J.M. Vitek, R.L. Klueh, Precipitation Reactions during the Heat Treatment of Ferritic Steels, Metallurgical Transactions A 14 (1983) 1047–1055. https://doi.org/10.1007/BF02659853.

[28] R.W. Conn, E.E. Bloom, J.W. Davis, R.E. Gold, R. Little, K.R. Schultz, D.L. Smith, F.W. Wiffen, Panel Report on Low Activation Materials for Fusion Applications, UCLA Report PPG-728 (1983).

[29] J. Orr, F.R. Beckitt, G.D. Fawkes, The Physical Metallurgy of Chromium-Molybedenum Steels for Fast Reactor Boilers, BNES 1 (1978) 91–109.

[30] P. Hosemann, S. Kabra, E. Stergar, M.J. Cappillo, S.A. Maloy, Micro-structural characterization of laboratory heats of the Ferric/Martensitic steels HT-9 and T91, Journal of Nuclear Materials 403 (2010) 7–14. https://doi.org/10.1016/j.jnucmat.2010.05.005.

[31] V.G. Rivlin, G. V. Raynor, 1: Critical evaluation of constitution of chromium-iron-nickel system, International Metals Reviews 25 (1980) 21–37. https://doi.org/10.1179/imtr.1980.25.1.21.

[32] W. Tofaute, A. Sponheuer, H. Bennek, Umwandlungs-, Härtungs- und Anlaßvorgänge in Stählen mit Gehalten bis 1% C und bis 12% Cr, Archiv Für Das Eisenhüttenwesen 8 (1935) 499–506. https://doi.org/10.1002/srin.193500173.

[33] M. Wall, TEMPER EMBRITTLEMENT IN 9 % CHROMIUM STEELS, 1985.

[34] C.A. Hippsley, N.P. Haworth, Hydrogen and temper embrittlement in 9Cr-1 Mo steel, Materials Science and Technology (United Kingdom) 4 (1988) 791–802. https://doi.org/10.1179/mst.1988.4.9.791.

[35] R.G. Faulkner, Combined grain boundary equilibrium and non-equilibrium segregation in ferritic/martensitic steels, Acta Metallurgica 35 (1987) 2905–2914. https://doi.org/10.1016/0001-6160(87)90289-6.

[36] R.G. Faulkner, L. Schafer, G.J. Adetunji, E.A. Little, Embrittlement Processes in 1.4914 Ferritic-Martensitic Steel, Journal of Nuclear Materials 155–157 (1988) 612–615.

[37] K. Suzuki, S. Kumai, Y. Toda, H. Kushima, K. Kimura, Two-phase separation of primary MX carbonitride during tempering in creep resistant 9Cr1MoVNb steel, ISIJ International 43 (2003) 1089–1094. https://doi.org/10.2355/isijinternational.43.1089.

[38] A. Zeman, L. Debarberis, J. Kočík, V. Slugeň, E. Keilová, Microstructural analysis of candidate steels pre-selected for new advanced reactor systems, Journal of Nuclear Materials 362 (2007) 259–267. https://doi.org/10.1016/j.jnucmat.2007.01.068.

[39] Y. Hosoi, N. Wade, S. Kunimitsu, T. Urita, Precipitation behavior of laves phase and its effect on toughness of 9Cr-2Mo Ferritic-martensitic steel, Journal of Nuclear Materials 141–143 (1986) 461–467. https://doi.org/10.1016/S0022-3115(86)80083-6.

[40] J. Orr, L. Woollard, The development of 9% CrMo steels from steel 91 to E911, in: Microstructural Development and Stability in High Chromium Ferritic Power Plant Steels, 1997.

[41] J.P. Wharry, The Mechanism of Radiation-Induced Segregation in Ferritic-Martensitic Steels, University of Michigan, 2012.

[42] K. Anderko, L. Schäfer, E. Materna-Morris, Effect of the δ-ferrite phase on the impact properties of martensitic chromium steels, Journal of Nuclear Materials 179–181 (1991) 492–495. https://doi.org/10.1016/0022-3115(91)90132-Q.

[43] K. Tokuno, K. Hamada, R. Uemori, T. Takeda, K. Itoh, Role of a complex carbonitride of niobium and vanadium in creep strength of 9% Cr ferritic steels, Scripta Metallurgica et Materiala 25 (1991) 1763–1768. https://doi.org/10.1016/0956-716X(91)90301-G.

[44] B. Singh, A. Foreman, An assessment of void nucleation by gas atoms during irradiation, Journal of Nuclear Materials 103 (1981) 1469–1474.

[45] B.N. Singh, A.J.E. Foreman, Summary of a theory for void nucleation during irradiation in terms of brownian motion of vacancy-gas atoms, Scripta Metallurgica 9 (1975) 1135–1139. https://doi.org/10.1016/0036-9748(75)90393-2.

[46] K. Farrell, P.J. Maziasz, E.H. Lee, L.K. Mansur, Modification of Radiation Damage Microstructure By Helium., Radiat Eff 78 (1982) 277–295. https://doi.org/10.1080/00337578308207378.

[47] A.J.E. Foreman, B.N. Singh, Bubble nucleation in grain interior and its influence on helium accumulation at grain boundaries, Journal of Nuclear Materials 133–134 (1985) 451–454. https://doi.org/10.1016/0022-3115(85)90187-4.

[48] L.K. Mansur, Theory and experimental background on dimensional changes in irradiated alloys, Journal of Nuclear Materials 216 (1994) 97–123. https://doi.org/10.1016/0022-3115(94)90009-4.

[49] F.A. Garner, M.B. Toloczko, B.H. Sencer, Comparison of swelling and irradiation creep behavior of fcc-austenitic and bcc-ferritic/martensitic alloys at high neutron exposure, Journal of Nuclear Materials 276 (2000) 123–142. https://doi.org/10.1016/S0022-3115(99)00225-1.

[50] J. Van Den Bosch, O. Anderoglu, R. Dickerson, M. Hartl, P. Dickerson, J.A. Aguiar, P. Hosemann, M.B. Toloczko, S.A. Maloy, SANS and TEM of ferritic-martensitic steel T91

irradiated in FFTF up to 184 dpa at 413 °C, Journal of Nuclear Materials 440 (2013) 91–97. https://doi.org/10.1016/j.jnucmat.2013.04.025.

[51] J.J. Kai, R.L. Klueh, Microstructural analysis of neutron-irradiated martensitic steels, Journal of Nuclear Materials 230 (1996) 116–123. https://doi.org/10.1016/0022-3115(96)00165-1.

[52] P.J. Maziasz, R.L. Klueh, J.M. Vitek, Helium effects on void formation in 9Cr-1MoVNb and 12Cr-1MoVW irradiated in HFIR, Journal of Nuclear Materials 141–143 (1986) 929–937. https://doi.org/10.1016/0022-3115(86)90120-0.

[53] J.M. Vitek, R.L. Klueh, Microstructure of 9 Cr-1 MoVNb steel irradiated to 36 dpa at elevated temperatures in HFIR, Journal of Nuclear Materials 122 (1984) 254–259. https://doi.org/10.1016/0022-3115(84)90606-8.

[54] B.H. Sencer, J.R. Kennedy, J.I. Cole, S.A. Maloy, F.A. Garner, Microstructural analysis of an HT9 fuel assembly duct irradiated in FFTF to 155 dpa at 443 °C, Journal of Nuclear Materials 393 (2009) 235–241. https://doi.org/10.1016/j.jnucmat.2009.06.010.

[55] D.S. Gelles, Microstructural examination of commercial ferritic alloys at 200 dpa, Journal of Nuclear Materials 233–237 (1996) 293–298. https://doi.org/10.1016/S0022-3115(96)00222-X.

[56] J.G. Gigax, T. Chen, H. Kim, J. Wang, L.M. Price, E. Aydogan, S.A. Maloy, D.K. Schreiber, M.B. Toloczko, F.A. Garner, L. Shao, Radiation response of alloy T91 at damage levels up to 1000 peak dpa, Journal of Nuclear Materials 482 (2016) 257–265. https://doi.org/10.1016/j.jnucmat.2016.10.003.

[57] E. Getto, Z. Jiao, A.M. Monterrosa, K. Sun, G.S. Was, Effect of pre-implanted helium on void swelling evolution in self-ion irradiated HT9, Journal of Nuclear Materials 462 (2015) 458–469. https://doi.org/10.1016/j.jnucmat.2015.01.045.

[58] K. Asano, Y. Kohno, A. Kohyama, G. Ayrault, Microstructural evolution of HT9 under dual-beam charged particle irradiation, Journal of Nuclear Materials 155–157 (1988) 912–915. https://doi.org/10.1016/0022-3115(88)90440-0.

[59] G. Ayrault, Cavity formation during single- and dual-ion irradiation in a 9Cr-1Mo ferritic alloy, Journal of Nuclear Materials 114 (1983) 34–40. https://doi.org/10.1016/0022-3115(83)90070-3.

[60] E. Getto, K. Sun, A.M. Monterrosa, Z. Jiao, M.J. Hackett, G.S. Was, Void swelling and microstructure evolution at very high damage level in self-ion irradiated ferritic-martensitic steels, Journal of Nuclear Materials 480 (2016) 159–176. https://doi.org/10.1016/j.jnucmat.2016.08.015.

[61] E. Getto, K. Sun, S. Taller, A.M. Monterrosa, Z. Jiao, G.S. Was, Methodology for determining void swelling at very high damage under ion irradiation, Journal of Nuclear Materials 477 (2016) 273–279. https://doi.org/10.1016/j.jnucmat.2016.05.026.

[62] D.S. Gelles, Microstructural development in reduced activation ferritic alloys irradiated to 200 dpa at 420°C, Journal of Nuclear Materials 212–215 (1994) 714–719. https://doi.org/10.1016/0022-3115(94)90150-3.

[63] Y.R. Lin, A. Bhattacharya, D. Chen, J.J. Kai, J. Henry, S.J. Zinkle, Temperature-dependent cavity swelling in dual-ion irradiated Fe and Fe-Cr ferritic alloys, Acta Mater 207 (2021) 116660. https://doi.org/10.1016/j.actamat.2021.116660.

[64] B.N. Singh, H. Trinkaus, An analysis of the bubble formation behaviour under different experimental conditions, Journal of Nuclear Materials 186 (1992) 153–165. https://doi.org/10.1016/0022-3115(92)90330-N.

[65] R.E. Stoller, The influence of helium on microstructural evolution: Implications for DT fusion reactors, 1990.

[66] X. Wang, A.M. Monterrosa, F. Zhang, H. Huang, Q. Yan, Z. Jiao, G.S. Was, L. Wang, Void swelling in high dose ion-irradiated reduced activation ferritic-martensitic steels, Journal of Nuclear Materials 462 (2015) 119–125. https://doi.org/10.1016/j.jnucmat.2015.03.050.

[67] D. Woodley, S. Taller, Z. Jiao, K. Sun, G.S. Was, The Role of Co-injected Helium on Swelling and Cavity Evolution at High Damage Levels in Ferritic-Martensitic Steels, Journal of Nuclear Materials 550 (2021). https://doi.org/10.1016/j.jnucmat.2021.152912.

[68] A.M. Monterrosa, Z. Jiao, G.S. Was, The influence of helium on cavity evolution in ion-irradiated T91, Journal of Nuclear Materials 509 (2018) 707–721. https://doi.org/10.1016/j.jnucmat.2018.06.033.

[69] Y.-R. Lin, A. Bhattacharya, S.J. Zinkle, The effect of helium on cavity swelling in dual-ion irradiated Fe and Fe-10Cr ferritic alloys, Journal of Nuclear Materials 569 (2022) 153907. https://doi.org/10.1016/j.jnucmat.2022.153907.

[70] B. Li, Z. Yang, S. Xu, K. Wei, Z. Wang, T. Shen, T. Zhang, Q. Liao, Comparison of helium bubble formation in F82H, ODS, SIMP and T91 steels irradiated by Fe and He ions simultaneously, Chinese Physics B 30 (2021). https://doi.org/10.1088/1674-1056/abc2b4.

[71] E.A. Little, D.A. Stow, Void-swelling in irons and ferritic steels. II. An experimental survey of materials irradiated in a fast reactor, Journal of Nuclear Materials 87 (1979) 25–39. https://doi.org/10.1016/0022-3115(79)90123-5.

[72] S. Taller, G.S. Was, Understanding bubble and void nucleation in dual ion irradiated T91 steel using single parameter experiments, Acta Mater 198 (2020) 47–60. https://doi.org/10.1016/j.actamat.2020.07.060.

[73] E.A. Little, Microstructural evolution in irradiated ferritic-martensitic steels: transitions to high dose behaviour, Journal of Nuclear Materials 206 (1993) 324–334. https://doi.org/10.1016/0022-3115(93)90131-H.

[74] S.S. Huang, T. Yoshiie, Q. Xu, K. Sato, T.D. Troev, Positron annihilation studies of electron-irradiated F82H model alloys, Journal of Nuclear Materials 440 (2013) 617–621. https://doi.org/10.1016/j.jnucmat.2013.05.015.

[75] I.S. Kim, J.D. Hunn, N. Hashimoto, D.L. Larson, P.J. Maziasz, K. Miyahara, E.H. Lee, Defect and void evolution in oxide dispersion strengthened ferritic steels under 3.2 MeV Fe+ ion irradiation with simultaneous helium injection, Journal of Nuclear Materials 280 (2000) 264–274. https://doi.org/10.1016/S0022-3115(00)00066-0.

[76] H. Kim, J.G. Gigax, C.J. Rietema, O. El Atwani, M.R. Chancey, J.K. Baldwin, Y. Wang, S.A. Maloy, Void swelling of conventional and composition engineered HT9 alloys after high-dose self-ion irradiation, Journal of Nuclear Materials 560 (2022). https://doi.org/10.1016/j.jnucmat.2021.153492.

[77] F.A. Garner, J.S. Perrin, Horton, L. L. and Mansur, L. K., “Experimental Determination of the Critical Cavity Radius in Fe-10Cr for Ion Irradiation,” in: Effects of Radiation on Materials: Twelfth International Symposium, ASTM STP 870, 1984: pp. 344–362. https://doi.org/10.4271/580009.

[78] E. Wakai, K. Kikuchi, S. Yamamoto, T. Aruga, M. Ando, H. Tanigawa, T. Taguchi, T. Sawai, K. Oka, S. Ohnuki, Swelling behavior of F82H steel irradiated by triple/dual ion

beams, Journal of Nuclear Materials 318 (2003) 267–273. https://doi.org/10.1016/S0022-3115(03)00122-3.

[79] W. Van Renterghem, D. Terentyev, M.J. Konstantinović, Transmission electron analysis of dislocation loops in T91 steels from MEGAPIE and MIRE irradiation experiments, Journal of Nuclear Materials 506 (2018) 43–52. https://doi.org/10.1016/j.jnucmat.2017.10.045.

[80] G. Gupta, Z. Jiao, A.N. Ham, J.T. Busby, G.S. Was, Microstructural evolution of proton irradiated T91, Journal of Nuclear Materials 351 (2006) 162–173. https://doi.org/10.1016/j.jnucmat.2006.02.028.

[81] Z. Jiao, N. Ham, G.S. Was, Microstructure of helium-implanted and proton-irradiated T91 ferritic/martensitic steel, Journal of Nuclear Materials 367-370 A (2007) 440–445. https://doi.org/10.1016/j.jnucmat.2007.03.118.

[82] J.P. Wharry, Z. Jiao, V. Shankar, J.T. Busby, G.S. Was, Radiation-induced segregation and phase stability in ferritic-martensitic alloy T 91, Journal of Nuclear Materials 417 (2011) 140–144. https://doi.org/10.1016/j.jnucmat.2010.12.052.

[83] X. Liu, Y. Miao, M. Li, M.K. Kirk, S.A. Maloy, J.F. Stubbins, Ion-irradiation-induced microstructural modifications in ferritic/martensitic steel T91, Journal of Nuclear Materials 490 (2017) 305–316. https://doi.org/10.1016/j.jnucmat.2017.04.047.

[84] C. Zheng, E.R. Reese, K.G. Field, E. Marquis, S.A. Maloy, D. Kaoumi, Microstructure response of ferritic/martensitic steel HT9 after neutron irradiation: effect of dose, Journal of Nuclear Materials 523 (2019) 421–433. https://doi.org/10.1016/j.jnucmat.2019.06.019.

[85] P. Xiu, Effects of Sink Strength and Irradiation Parameters on Defect Evolution in Additively Manufactured HT9, University of Michigan, 2022.

[86] T. Ezawa, T. Akashi, R. Oshima, Damage structures and precipitation in electron-irradiated iron-chromium alloys, Journal of Nuclear Materials 212–215 (1994) 252–257. https://doi.org/10.1016/0022-3115(94)90066-3.

[87] L. Tan, B.K. Kim, Y. Yang, K.G. Field, S. Gray, M. Li, Microstructural evolution of neutron-irradiated T91 and NF616 to ~4.3 dpa at 469 °C, Journal of Nuclear Materials 493 (2017) 12–20. https://doi.org/10.1016/j.jnucmat.2017.05.041.

[88] A. Prokhodtseva, B. Décamps, R. Schäublin, Comparison between bulk and thin foil ion irradiation of ultra high purity Fe, Journal of Nuclear Materials 442 (2013). https://doi.org/10.1016/j.jnucmat.2013.04.032.

[89] R. Schäublin, B. Décamps, A. Prokhodtseva, J.F. Löffler, On the origin of the primary ½ a0 <111> and a0 <100> loops in irradiated Fe(Cr) alloys, Acta Mater 133 (2017) 427–439. https://doi.org/10.1016/j.actamat.2017.02.041.

[90] D. Brimbal, B. Décamps, J. Henry, E. Meslin, A. Barbu, Single- and dual-beam in situ irradiations of high-purity iron in a transmission electron microscope: Effects of heavy ion irradiation and helium injection, Acta Mater 64 (2014) 391–401. https://doi.org/10.1016/j.actamat.2013.10.052.

[91] A. Bhattacharya, J. Henry, B. Décamps, S.J. Zinkle, E. Meslin, Helium causing disappearance of a/2<111> dislocation loops in binary Fe-Cr ferritic alloys, Journal of Nuclear Materials 556 (2021). https://doi.org/10.1016/j.jnucmat.2021.153213.

[92] S.B. Adisa, R. Blair, M.J. Swenson, Comparison of microstructure evolution in Fe2+ or neutron-irradiated T91 at 500°C, Materialia (Oxf) 12 (2020) 100770. https://doi.org/10.1016/j.mtla.2020.100770.

[93] M.J. Swenson, J.P. Wharry, TEM characterization of irradiated microstructure of Fe-9%Cr ODS and ferritic-martensitic alloys, Journal of Nuclear Materials 502 (2018) 30–41. https://doi.org/10.1016/j.jnucmat.2018.01.062.

[94] Z. Jiao, V. Shankar, G.S. Was, Phase stability in proton and heavy ion irradiated ferritic-martensitic alloys, Journal of Nuclear Materials 419 (2011) 52–62. https://doi.org/10.1016/j.jnucmat.2011.08.020.

[95] J.P. Wharry, Z. Jiao, G.S. Was, Application of the inverse Kirkendall model of radiation-induced segregation to ferritic-martensitic alloys, Journal of Nuclear Materials 425 (2012) 117–124. https://doi.org/10.1016/j.jnucmat.2011.10.035.

[96] J.P. Wharry, G.S. Was, A systematic study of radiation-induced segregation in ferritic-martensitic alloys, Journal of Nuclear Materials 442 (2013) 7–16. https://doi.org/10.1016/j.jnucmat.2013.07.071.

[97] Z. Jiao, G.S. Was, Precipitate evolution in ion-irradiated HCM12A, Journal of Nuclear Materials 425 (2012) 105–111. https://doi.org/10.1016/j.jnucmat.2011.12.017.

[98] C. Zheng, M.A. Auger, M.P. Moody, D. Kaoumi, Radiation induced segregation and precipitation behavior in self-ion irradiated Ferritic/Martensitic HT9 steel, Journal of Nuclear Materials 491 (2017) 162–176. https://doi.org/10.1016/j.jnucmat.2017.04.040.

[99] M.J. Swenson, J.P. Wharry, Nanocluster irradiation evolution in Fe-9%Cr ODS and ferritic-martensitic alloys, Journal of Nuclear Materials 496 (2017) 24–40. https://doi.org/10.1016/j.jnucmat.2017.08.045.

[100] G.S. Was, T. Allen, Intercomparison of microchemical evolution under various types of particle irradiation, Journal of Nuclear Materials 205 (1993) 332–338. https://doi.org/10.1016/0022-3115(93)90097-I.

[101] R.G. Faulkner, S. Song, P.E.J. Flewitt, Irradiation-induced silicon segregation in ferritic steels, Journal of Nuclear Materials 212–215 (1994) 608–611. https://doi.org/10.1016/0022-3115(94)90132-5.

[102] S. Taller, V. Pauly, Z. Jiao, R. Hanbury, G.S. Was, Solute segregation and precipitation across damage rates in dual-ion–irradiated T91 steel, Journal of Nuclear Materials 563 (2022) 153626. https://doi.org/10.1016/j.jnucmat.2022.153626.

[103] S.J. Zinkle, L.L. Snead, Opportunities and limitations for ion beams in radiation effects studies: Bridging critical gaps between charged particle and neutron irradiations, Scr Mater 143 (2018) 154–160. https://doi.org/10.1016/j.scriptamat.2017.06.041.

[104] J.G. Gigax, E. Aydogan, T. Chen, D. Chen, L. Shao, Y. Wu, W.Y. Lo, Y. Yang, F.A. Garner, The influence of ion beam rastering on the swelling of self-ion irradiated pure iron at 450 °C, Journal of Nuclear Materials 465 (2015) 343–348. https://doi.org/10.1016/j.jnucmat.2015.05.025.

[105] G.S. Was, T. Allen, Radiation-induced segregation in multicomponent alloys: Effect of particle type, Mater Charact 32 (1994) 239–255. https://doi.org/10.1016/1044-5803(94)90101-5.

[106] F.A. Garner, Impact of the injected interstitial on the correlation of charged particle and neutron-induced radiation damage, Journal of Nuclear Materials 117 (1983) 177–197. https://doi.org/10.1016/0022-3115(83)90023-5.

[107] L.K. Mansur, Correlation of neutron and heavy-ion damage. II. The predicted temperature shift if swelling with changes in radiation dose rate, Journal of Nuclear Materials 78 (1978) 156–160. https://doi.org/10.1016/0022-3115(78)90514-7.

[108] L.K. Mansur, Void swelling in metals and alloys under irradiation: An assessment of the theory, Nucl Technol 40 (1978) 5–34. https://doi.org/10.13182/NT78-2.

[109] L.K. Mansur, Theory of transitions in dose dependence of radiation effects in structural alloys, Journal of Nuclear Materials 206 (1993) 306–323. https://doi.org/10.1016/0022-3115(93)90130-Q.

[110] L.K. Mansur, K. Farrell, On mechanisms by which a soft neutron spectrum may induce accelerated embrittlement, Journal of Nuclear Materials 170 (1990) 236–245. https://doi.org/10.1016/0022-3115(90)90294-W.

[111] L.E. Rehn, Production of freely-migrating defects, Journal of Nuclear Materials 174 (1990) 144–150. https://doi.org/10.1016/0022-3115(90)90228-F.

[112] R.S. Averback, Atomic displacement processes in irradiated metals, Journal of Nuclear Materials 216 (1994) 49–62. https://doi.org/10.1016/0022-3115(94)90006-X.

[113] M. Kiritani, The need for improved temperature control during reactor irradiation, Journal of Nuclear Materials 160 (1988) 135–141. https://doi.org/10.1016/0022-3115(88)90040-2.

[114] F.A. Garner, N. Sekimura, M.L. Grossbeck, A.M. Ermi, J.W. Newkirk, H. Watanabe, M. Kiritani, Influence of details of reactor history on microstructural development during neutron irradiation, Journal of Nuclear Materials 205 (1993) 206–218. https://doi.org/10.1016/0022-3115(93)90083-B.

[115] R.W. Clark, A.S. Kumar, F.A. Garner, Dimensional Change Correlations for 20% Cold-Worked AISI 316 Stainless Steel for Fusion Applications, Journal of Nuclear Materials 155–157 (1988) 845–849.

[116] S. Kasahara, Y. Kitsunai, Y. Chimi, K. Chatani, M. Koshiishi, Y. Nishiyama, Influence of temperature histories during reactor startup periods on microstructural evolution and

mechanical properties of austenitic stainless steel irradiated with neutrons, Journal of Nuclear Materials 480 (2016) 386–392. https://doi.org/10.1016/j.jnucmat.2016.06.017.

[117] N. Okubo, E. Wakai, T. Tomita, S. Jitsukawa, Mechanical properties and microstructures in F82H steel irradiated under alternating temperature, Journal of Nuclear Materials 367-370 A (2007) 112–116. https://doi.org/10.1016/j.jnucmat.2007.03.158.

[118] T. Muroga, Dislocation evolution in a model and a candidate ferritic alloy during steady and varying temperature electron irradiations, Journal of Nuclear Materials 233–237 (1996) 1035–1039. https://doi.org/10.1016/S0022-3115(96)00105-5.

[119] Q. Xu, Microstructural evolution in Fe-Cr-Ni alloy irradiated with Ni ion under varying temperature, Journal of Nuclear Materials 233–237 (1996) 1057–1061. https://doi.org/10.1016/S0022-3115(96)00118-3.

[120] Q. Xu, H. Watanabe, T. Muroga, N. Yoshida, Effects of temperature variation on damage microstructures in Fe-Cr-Ni alloy induced by heavy ion irradiation, Journal of Nuclear Materials 212–215 (1994) 258–262. https://doi.org/10.1016/0022-3115(94)90067-1.

[121] H. Watanabe, T. Arinaga, K. Ochiai, T. Muroga, N. Yoshida, Microstructure of vanadium alloys during ion irradiation with stepwise change of temperature, Journal of Nuclear Materials 283–287 (2000) 286–290. https://doi.org/10.1016/S0022-3115(00)00307-X.

[122] K. Ochiai, H. Watanabe, T. Muroga, N. Yoshida, H. Matsui, Microstructural evolution in vanadium irradiated during ion irradiation at constant and varying temperature, Journal of Nuclear Materials 271–272 (1999) 376–380. https://doi.org/10.1016/S0022-3115(98)00751-X.

[123] Q. Xu, T. Yoshiie, Influence of temperature change on microstructure evolution in Ni alloys irradiated with neutrons, Journal of Nuclear Materials 307–311 (2002) 380–384. https://doi.org/10.1016/S0022-3115(02)01004-8.

[124] Y. Satoh, S. Abe, H. Matsui, I. Yamagata, Void swelling behavior in electron irradiated Fe-Cr-Ni model alloys under temperature variation, Journal of Nuclear Materials 367-370 B (2007) 972–976. https://doi.org/10.1016/j.jnucmat.2007.03.057.

[125] D. Hamaguchi, H. Watanabe, T. Muroga, N. Yoshida, Influence of variable temperatures irradiation on microstructural evolution in phosphorus doped Fe-Cr-Ni alloys, Journal of Nuclear Materials 283–287 (2000) 319–323. https://doi.org/10.1016/S0022-3115(00)00133-1.

[126] M. Kiritani, T. Yoshiie, M. Iseki, S. Kojima, K. Hamada, M. Horiki, Y. Kizuka, H. Inoue, T. Tada, Y. Ogasawara, Microstructure evolution by neutron irradiation during cyclic temperature variation, Journal of Nuclear Materials 212–215 (1994) 241–245. https://doi.org/10.1016/0022-3115(94)90064-7.

[127] S.J. Zinkle, N. Hashimoto, D.T. Hoelzer, A.L. Qualls, T. Muroga, B.N. Singh, Effect of periodic temperature variations on the microstructure of neutron-irradiated metals, Journal of Nuclear Materials 307–311 (2002) 192–196. https://doi.org/10.1016/S0022-3115(02)01137-6.

[128] M. Matsuda, N. Yoshida, T. Muroga, M. Kiritani, Modification of microstructures induced by temperature variation during irradiation with 14 MeV neutrons, Journal of Nuclear Materials 179–181 (1991) 962–965. https://doi.org/10.1016/0022-3115(91)90250-B.

[129] M. Matsuda, N. Yoshida, T. Muroga, M. Kiritani, Modification of microstructures induced by temperature variation during irradiation with 14 MeV neutrons, Journal of Nuclear Materials 179–181 (1991) 962–965. https://doi.org/10.1016/0022-3115(91)90250-B.

[130] H. Watanabe, T. Muroga, N. Yoshida, The study of temperature variation during HFIR irradiation on vanadium, Journal of Nuclear Materials 329–333 (2004) 425–428. https://doi.org/10.1016/j.jnucmat.2004.04.075.

[131] N. Yoshida, Q. Xu, H. Watanabe, Y. Miyamoto, T. Muroga, Effect of cyclic temperature change on microstructural evolution in austenitic stainless steels under fission neutron irradiation, Journal of Nuclear Materials 212–215 (1994) 471–475. https://doi.org/10.1016/0022-3115(94)90106-6.

[132] M. Kiritani, T. Yoshiie, S. Kojima, Y. Satoh, K. Hamada, Fission-fusion correlation by fission reactor irradiation with improved control, Journal of Nuclear Materials 174 (1990) 327–351. https://doi.org/10.1016/0022-3115(90)90245-I.

[133] N. Yoshida, Q. Xu, H. Watanabe, T. Muroga, M. Kiritani, Low dose fission neutron irradiation on P- and Ti-modified austenitic alloys with improved temperature control, Journal of Nuclear Materials 191–194 (1992) 1114–1118. https://doi.org/10.1016/0022-3115(92)90648-5.

[134] M. Horiki, M. Kiritani, Microstructural evolution in low-dose neutron-irradiated Fe-16Ni-15Cr alloy, Journal of Nuclear Materials 212–215 (1994) 246–251. https://doi.org/10.1016/0022-3115(94)90065-5.

[135] E. Getto, Z. Jiao, A.M. Monterrosa, K. Sun, G.S. Was, Effect of irradiation mode on the microstructure of self-ion irradiated ferritic-martensitic alloys, Journal of Nuclear Materials 465 (2015) 116–126. https://doi.org/10.1016/j.jnucmat.2015.05.016.

[136] E.P. Simonen, N.M. Ghoniem, N.H. Packan, Pulsed flux effects on radiation damage, Journal of Nuclear Materials 122 (1984) 391–401. https://doi.org/10.1016/0022-3115(84)90628-7.

[137] N.M. Ghoniem, G.L. Kulcinski, The Effect of Pulsed Irradiation on the Swelling of 316 Stainless Steel in Fusion Reactors, Nuclear Engineering and Design (1979) 111–125.

[138] N.M. Ghoniem, G.L. Kulcinski, The use of the fully dynamic rate theory to predict void growth in metals, Radiat Eff 41 (1979) 81–89. https://doi.org/10.1080/00337577908236951.

[139] N.M. Ghoniem, G.L. Kulcinski, A Critical Assessment of the Effects of Pulsed Irradiation on the Microstructure, Swelling, and Creep of Materials, Nuclear Technology - Fusion 2 (1982) 165–198. https://doi.org/10.13182/FST82-A20749.

[140] Y. Li, A. French, Z. Hu, A. Gabriel, L.R. Hawkins, F.A. Garner, L. Shao, A quantitative method to determine the region not influenced by injected interstitial and surface effects during void swelling in ion-irradiated metals, Journal of Nuclear Materials 573 (2023) 154140. https://doi.org/10.1016/j.jnucmat.2022.154140.

[141] J.B. Whitley, G.L. Kulcinski, P. Wilkes, H. V. Smith, The depth dependent damage profile in nickel irradiated with nickel or copper ions, Journal of Nuclear Materials 79 (1979) 159–169. https://doi.org/10.1016/0022-3115(79)90443-4.

[142] L.K. Mansur, M.H. Yoo, Advances in the theory of swelling in irradiated metals and alloys, Journal of Nuclear Materials 85–86 (1979) 522–532.

[143] J. Wang, M.B. Toloczko, K. Kruska, D.K. Schreiber, D.J. Edwards, Z. Zhu, J. Zhang, Carbon Contamination during Ion Irradiation-Accurate Detection and Characterization of

its Effect on Microstructure of Ferritic/Martensitic Steels, Sci Rep 7 (2017) 1–12. https://doi.org/10.1038/s41598-017-15669-y.

[144] G.S. Was, S. Taller, Z. Jiao, A.M. Monterrosa, D. Woodley, D. Jennings, T. Kubley, F. Naab, O. Toader, E. Uberseder, Resolution of the carbon contamination problem in ion irradiation experiments, Nucl Instrum Methods Phys Res B 412 (2017) 58–65. https://doi.org/10.1016/j.nimb.2017.08.039.

[145] A.M. Monterrosa, D. Woodley, Z. Jiao, G.S. Was, The influence of carbon on cavity evolution in ion-irradiated ferritic-martensitic steels, Journal of Nuclear Materials 509 (2018) 722–735. https://doi.org/10.1016/j.jnucmat.2018.05.012.

[146] ASTM International, ASTM E1019-24 Standard Test Methods for Determination of Carbon, Sulfur, Nitrogen, and Oxygen in Steel, Iron, Nickel, and Cobalt Alloys by Various Combustion and Inert Gas Fusion Techniques, ASTM International, West Conshohocken, PA, 2024. https://doi.org/10.1520/E1019-24.

[147] ASTM International, ASTM E1097-12 Standard Guide for Determination of Various Elements by Direct Current Plasma Atomic Emission Spectrometry, ASTM International, West Conshohocken, PA, 2017. https://doi.org/10.1520/E1097-12R17.

[148] A. Monterrosa, The Role of Pre-Implanted Helium and Carbon on Cavity Evolution in Ion-Irradiated T91, University of Michigan, 2018. https://deepblue.lib.umich.edu/handle/2027.42/143960.

[149] S. Taller, D. Woodley, E. Getto, A.M. Monterrosa, Z. Jiao, O. Toader, F. Naab, T. Kubley, S. Dwaraknath, G.S. Was, Multiple ion beam irradiation for the study of radiation damage in materials, Nucl Instrum Methods Phys Res B 412 (2017) 1–10. https://doi.org/10.1016/j.nimb.2017.08.035.

[150] J.F. Ziegler, M.D. Ziegler, J.P. Biersack, SRIM - The stopping and range of ions in matter (2010), Nucl Instrum Methods Phys Res B 268 (2010) 1818–1823. https://doi.org/10.1016/j.nimb.2010.02.091.

[151] ASTM International, Standard Practice for Neutron Radiation Damage Simulation by Charged-Particle Irradiation, 2009. https://doi.org/10.1520/E0521-96R09E01.

[152] S. Taller, F. Naab, G.S. Was, A methodology for customizing implantation profiles of light ions using a single thin foil energy degrader, Nucl Instrum Methods Phys Res B 478 (2020) 274–283. https://doi.org/10.1016/j.nimb.2020.07.017.

[153] O. Toader, F. Naab, E. Uberseder, T. Kubley, S. Taller, G.S. Was, Technical Aspects of Delivering Simultaneous Dual and Triple Ion Beams to a Target at the Michigan Ion Beam Laboratory, Phys Procedia 90 (2017) 385–390. https://doi.org/10.1016/j.phpro.2017.09.039.

[154] L.R. Greenwood, R.K. Smither, SPECTER: Neutron Damage Calculations for Materials Irradiations, ANL/FPP/TM-197, Argonne, 1985. https://doi.org/https://doi.org/10.2172/6022143.

[155] J.C. Sublet, J.W. Eastwood, J.G. Morgan, M.R. Gilbert, M. Fleming, W. Arter, FISPACT-II: An Advanced Simulation System for Activation, Transmutation and Material Modelling, Nuclear Data Sheets 139 (2017) 77–137. https://doi.org/10.1016/j.nds.2017.01.002.

[156] M.B. Chadwick, P. Obložinský, M. Herman, N.M. Greene, R.D. McKnight, D.L. Smith, P.G. Young, R.E. MacFarlane, G.M. Hale, S.C. Frankle, A.C. Kahler, T. Kawano, R.C. Little, D.G. Madland, P. Moller, R.D. Mosteller, P.R. Page, P. Talou, H. Trellue, M.C. White, W.B. Wilson, R. Arcilla, C.L. Dunford, S.F. Mughabghab, B. Pritychenko, D. Rochman, A.A. Sonzogni, C.R. Lubitz, T.H. Trumbull, J.P. Weinman, D.A. Brown, D.E.

Cullen, D.P. Heinrichs, D.P. McNabb, H. Derrien, M.E. Dunn, N.M. Larson, L.C. Leal, A.D. Carlson, R.C. Block, J.B. Briggs, E.T. Cheng, H.C. Huria, M.L. Zerkle, K.S. Kozier, A. Courcelle, V. Pronyaev, S.C. van der Marck, ENDF/B-VII.0: Next Generation Evaluated Nuclear Data Library for Nuclear Science and Technology, Nuclear Data Sheets 107 (2006) 2931–3060. https://doi.org/10.1016/j.nds.2006.11.001.

[157] A.M. Ermi, L.R. Greenwood, H.L. Heinisch, Irradiation Parameters for the FFTF Materials Open Test Assemblies from 1983 Through 1992, Oak Ridge, TN, 1995.

[158] Oak Ridge National Laboratory, Fusion Reactor Materials Semiannual Progress Report for Period Ending September 30, 1993, DOE/ER-0313/15, Oak Ridge, Tennessee, 1994.

[159] Oak Ridge National Laboratory, Fusion Reactor Materials Semiannual Progress Report for Period Ending March 31, 1993, DOE/ER-0313/14, Oak Ridge, Tennessee, 1993.

[160] Oak Ridge National Laboratory, Fusion Materials Semiannual Progress Report for Period Ending March 31, 1994, DOE/ER-0313/16, Oak Rigde, Tennessee, 1994.

[161] Oak Ridge National Laboratory, Fusion Materials Semiannual Progress Report for Period Ending September 30, 1990, DOE/ER-0313/9, Oak Ridge, Tennessee, 1991.

[162] Oak Ridge National Laboratory, Fusion Materials Semiannual Progress Report for Period Ending March 31, 1992, DOE/ER-0313/12, Oak Ridge, Tennessee, 1992.

[163] S. Pearlstein, R. Kinsey, C. Dunford, Characteristics of ENDF/B-V, BNL-NCS-24133, Upton, NY 11973, n.d.

[164] F.A. Garner, N. Sekimura, W.G. Wolfer, Synergistic influence of displacement rate and helium/dpa ratio on swelling of Fe-(9, 12)Cr binary alloys in FFTF at ~ 400 °C, Journal of Nuclear Materials 329–333 (2004) 1008–1012. https://doi.org/10.1016/j.jnucmat.2004.04.346.

[165] C.M. Parish, N.A.P. Kiran Kumar, L.L. Snead, P.D. Edmondson, K.G. Field, C. Silva, A. Marie Williams, K. Linton, K.J. Leonard, LAMDA: Irradiated-Materials Microscopy at Oak Ridge National Laboratory, Microscopy and Microanalysis 21 (2015) 1003–1004. https://doi.org/10.1017/s1431927615005814.

[166] Michigan Center for Materials Characterization, Thermo Fisher Talos F200X G2 S/TEM, Https://Mc2.Engin.Umich.Edu/Techniques/Thermo-Fisher-Talos-F200x-G2-s-Tem/ (2024).

[167] Michigan Center for Materials Characterization, Thermo Fisher Tecnai G2 F30 TWIN TEM, Https://Mc2.Engin.Umich.Edu/Techniques/Fei-Tecnai-G2-F30-Tem/ (2024).

[168] T. Malis, S.C. Cheng, R.F. Egerton, EELS log-ratio technique for specimen-thickness measurement in the TEM, J Electron Microsc Tech 8 (1988) 193–200. https://doi.org/10.1002/jemt.1060080206.

[169] B. Yao, D.J. Edwards, R.J. Kurtz, G.R. Odette, T. Yamamoto, Multislice simulation of transmission electron microscopy imaging of helium bubbles in Fe, J Electron Microsc (Tokyo) 61 (2012) 393–400. https://doi.org/10.1093/jmicro/dfs065.

[170] J. Schindelin, I. Arganda-Carreras, E. Frise, V. Kaynig, M. Longair, T. Pietzsch, S. Preibisch, C. Rueden, S. Saalfeld, B. Schmid, J.Y. Tinevez, D.J. White, V. Hartenstein, K. Eliceiri, P. Tomancak, A. Cardona, Fiji: An open-source platform for biological-image analysis, Nat Methods 9 (2012) 676–682. https://doi.org/10.1038/nmeth.2019.

[171] E.M. Getto, The Co-Evolution of Microstructure Features in Self-Ion Irradiated HT9 at Very High Damage Levels, University of Michigan, 2016. https://doi.org/2027.42/135912.

[172] B. Yao, D.J. Edwards, R.J. Kurtz, TEM characterization of dislocation loops in irradiated bcc Fe-based steels, Journal of Nuclear Materials 434 (2013) 402–410. https://doi.org/10.1016/j.jnucmat.2012.12.002.

[173] C.M. Parish, K.G. Field, A.G. Certain, J.P. Wharry, Application of STEM characterization for investigating radiation effects in BCC Fe-based alloys, J Mater Res 30 (2015) 1275–1289. https://doi.org/10.1557/jmr.2015.32.

[174] T.G. Lach, M.J. Olszta, S.D. Taylor, K.H. Yano, D.J. Edwards, T.S. Byun, P.H. Chou, D.K. Schreiber, Correlative STEM-APT characterization of radiation-induced segregation and precipitation of in-service BWR 304 stainless steel, Journal of Nuclear Materials 549 (2021). https://doi.org/10.1016/j.jnucmat.2021.152894.

[175] Z. Yu, M. Bachhav, F. Teng, L. He, M. Dubey, A. Couet, STEM/EDS and APT study on the microstructure and microchemistry of neutron irradiated ZIRLOTM, Journal of Nuclear Materials 573 (2023). https://doi.org/10.1016/j.jnucmat.2022.154139.

[176] K.N. Thomas, Effect of Cascade Size and Damage Rate on α' Precipitate Stability on Fe-15Cr, University of Michigan, 2022.

[177] G. Cliff, G.W. Lorimer, The quantitative analysis of thin specimens, J Microsc 103 (1975) 203–207. https://doi.org/10.1111/j.1365-2818.1975.tb03895.x.

[178] J.B. Whitley, G.L. Kulcinski, P. Wilkes, H. V. Smith, The depth dependent damage profile in nickel irradiated with nickel or copper ions, Journal of Nuclear Materials 79 (1979) 159–169. https://doi.org/10.1016/0022-3115(79)90443-4.

[179] J.G. Gigax, E. Aydogan, T. Chen, D. Chen, L. Shao, Y. Wu, W.Y. Lo, Y. Yang, F.A. Garner, The influence of ion beam rastering on the swelling of self-ion irradiated pure iron at 450

°C, Journal of Nuclear Materials 465 (2015) 343–348. https://doi.org/10.1016/j.jnucmat.2015.05.025.

[180] D.L. Plumton, W.G. Wolfer, Suppression of Void Nucleation by Injected Interstitials during Heavy Ion Bombardment, Journal of Nuclear Materials 120 (1984) 245–253.

[181] C. Yang, Z. Wang, M. Yu, W. Ma, H. Wang, Z. Wei, N. Gao, Z. Yao, Prediction of the swelling rate of irradiated type 316 stainless steels via machine learning methods, Journal of Nuclear Materials 600 (2024). https://doi.org/10.1016/j.jnucmat.2024.155288.

[182] P. Korotaev, A. Yanilkin, Neural networks for prediction of swelling in austenitic steels irradiated by fast neutrons, Comput Mater Sci 246 (2025). https://doi.org/10.1016/j.commatsci.2024.113408.

[183] S.I. Golubov, A.V. Barashev, R.E. Stoller, Reaction Rate Theory, 2020. https://doi.org/10.1016/b978-0-12-803581-8.00663-9.

[184] P.C. Millett, S. Rokkam, A. El-Azab, M. Tonks, D. Wolf, Void nucleation and growth in irradiated polycrystalline metals: A phase-field model, Model Simul Mat Sci Eng 17 (2009). https://doi.org/10.1088/0965-0393/17/6/064003.

[185] I. Steinbach, Phase-field models in materials science, Model Simul Mat Sci Eng 17 (2009). https://doi.org/10.1088/0965-0393/17/7/073001.

[186] N. Moelans, B. Blanpain, P. Wollants, An introduction to phase-field modeling of microstructure evolution, CALPHAD 32 (2008) 268–294. https://doi.org/10.1016/j.calphad.2007.11.003.

[187] P. Bellon, L. Thuinet, Phase Field Methods, 2020. https://doi.org/10.1016/b978-0-12-803581-8.00665-2.

[188] X. Zhu, X. Li, M. Zheng, Predicting the Irradiation Swelling of Austenitic and Ferritic/Martensitic Steels, Based on the Coupled Model of Machine Learning and Rate Theory, Metals (Basel) 12 (2022). https://doi.org/10.3390/met12040651.

[189] J.P. Wharry, G.S. Was, The mechanism of radiation-induced segregation in ferritic-martensitic alloys, Acta Mater 65 (2014) 42–55. https://doi.org/10.1016/j.actamat.2013.09.049.

[190] L. Malerba, Molecular dynamics simulation of displacement cascades in α-Fe: A critical review, Journal of Nuclear Materials 351 (2006) 28–38. https://doi.org/10.1016/j.jnucmat.2006.02.023.

[191] N. Juslin, K. Nordlund, Molecular dynamics simulations of collision cascades in FeCrHe, Nucl Instrum Methods Phys Res B 267 (2009) 3420–3423. https://doi.org/10.1016/j.nimb.2009.07.012.

[192] Y.N. Osetsky, A. Serra, Vacancy and interstitial diffusion in bcc-Fe, Defect and Diffusion Forum 143–147 (1997) 155–160. https://doi.org/10.4028/www.scientific.net/ddf.143-147.155.

[193] H. Matter, J. Winter, W. Triftshiiuser, Phase Transformations and Vacancy Formation Energies of Transition Metals by Positron Annihilation, Applied Physics 20 (1979) 135–140. https://doi.org/10.1007/BF00885934.

[194] J.L. Campbell, C.W. Schulte, Positron Trapping and Self-Diffusion Activation Energies in Chromium, Applied Physics 19 (1979) 149–152. https://doi.org/10.1007/BF00932389.

[195] S. Choudhury, L. Barnard, J.D. Tucker, T.R. Allen, B.D. Wirth, M. Asta, D. Morgan, Ab-initio based modeling of diffusion in dilute bcc Fe-Ni and Fe-Cr alloys and implications for

radiation induced segregation, Journal of Nuclear Materials 411 (2011) 1–14. https://doi.org/10.1016/j.jnucmat.2010.12.231.

[196] S.L. Dudarev, Density functional theory models for radiation damage, Annu Rev Mater Res 43 (2013) 35–61. https://doi.org/10.1146/annurev-matsci-071312-121626.

[197] H.L. Heinisch, F. Gao, R.J. Kurtz, Atomic-scale modeling of interactions of helium, vacancies and helium-vacancy clusters with screw dislocations in alpha-iron, Philosophical Magazine 90 (2010) 885–895. https://doi.org/10.1080/14786430903294932.

[198] K. Morishita, R. Sugano, B.D. Wirth, MD and KMC modeling of the growth and shrinkage mechanisms of helium-vacancy clusters in Fe, Journal of Nuclear Materials 323 (2003) 243–250. https://doi.org/10.1016/j.jnucmat.2003.08.019.

[199] K. Morishita, R. Sugano, B.D. Wirth, T. Diaz de la Rubia, Thermal stability of helium-vacancy clusters in iron, Nucl Instrum Methods Phys Res B 202 (2003) 76–81. https://doi.org/10.1016/S0168-583X(02)01832-3.

[200] D. Terentyev, N. Juslin, K. Nordlund, N. Sandberg, Fast three dimensional migration of He clusters in bcc Fe and Fe-Cr alloys, J Appl Phys 105 (2009). https://doi.org/10.1063/1.3126709.

[201] D. Xu, B.D. Wirth, Modeling spatially dependent kinetics of helium desorption in BCC iron following He ion implantation, Journal of Nuclear Materials 403 (2010) 184–190. https://doi.org/10.1016/j.jnucmat.2010.06.025.

[202] C.J. Ortiz, M.J. Caturla, C.C. Fu, F. Willaime, Impurity effects on He diffusion in α-Fe, Journal of Nuclear Materials 386–388 (2009) 33–35. https://doi.org/10.1016/j.jnucmat.2008.12.101.

[203] C.J. Ortiz, M.J. Caturla, C.C. Fu, F. Willaime, He diffusion in irradiated α-Fe: An ab-initio-based rate theory model, Phys Rev B Condens Matter Mater Phys 75 (2007). https://doi.org/10.1103/PhysRevB.75.100102.

[204] C.C. Fu, F. Willaime, First principles calculations in iron: structure and mobility of defect clusters and defect complexes for kinetic modelling, C R Phys 9 (2008) 335–342. https://doi.org/10.1016/j.crhy.2007.09.018.

[205] K. Nakashima, R.E. Stoller, H. Xu, Recombination radius of a Frenkel pair and capture radius of a self-interstitial atom by vacancy clusters in bcc Fe, Journal of Physics Condensed Matter 27 (2015). https://doi.org/10.1088/0953-8984/27/33/335401.

[206] D. Terentyev, N. Castin, C.J. Ortiz, Correlated recombination and annealing of point defects in dilute and concentrated Fe-Cr alloys, Journal of Physics Condensed Matter 24 (2012). https://doi.org/10.1088/0953-8984/24/47/475404.

[207] D.A. Terentyev, L. Malerba, M. Hou, Dimensionality of interstitial cluster motion in bcc-Fe, Phys Rev B Condens Matter Mater Phys 75 (2007). https://doi.org/10.1103/PhysRevB.75.104108.

[208] S. Bukkuru, U. Bhardwaj, K.S. Rao, A.D.P. Rao, M. Warrier, M.C. Valsakumar, Kinetics of self-interstitial migration in bcc and fcc transition metals, Mater Res Express 5 (2018). https://doi.org/10.1088/2053-1591/aab418.

[209] C.C. Fu, F. Willaime, Ab initio study of helium in α-Fe: Dissolution, migration, and clustering with vacancies, Phys Rev B Condens Matter Mater Phys 72 (2005) 1–6. https://doi.org/10.1103/PhysRevB.72.064117.

[210] Y.N. Osetsky, D.J. Bacon, A. Serra, B.N. Singh, S.I. Golubov, One-dimensional atomic transport by clusters of self-interstitial atoms in iron and copper, Philosophical Magazine 83 (2003) 61–91. https://doi.org/10.1080/0141861021000016793.

[211] L. Pizzagalli, M.-L. David, Surface stress calculations for nanoparticles and cavities in aluminum, silicon, and iron: influence of pressure and validity of the Young-Laplace equation, Materials Theory 5 (2021). https://doi.org/10.1186/s41313-021-00028-2.

[212] A. Jelea, On the Laplace-Young equation applied to spherical fluid inclusions in solid matrices, Journal of Nuclear Materials 505 (2018) 127–133. https://doi.org/10.1016/j.jnucmat.2018.03.051.

[213] A. Caro, D. Schwen, J. Hetherly, E. Martinez, The capillarity equation at the nanoscale: Gas bubbles in metals, Acta Mater 89 (2015) 14–21. https://doi.org/10.1016/j.actamat.2015.01.048.

[214] H. Trinkaus, W.G. Wolfer, Conditions for Dislocation Loop Punching by Helium Bubbles, Journal of Nuclear Materials (1984) 552–557.

[215] Y. Wang, Multi-scale Simulations on Preferential Absorption Behaviors of Cavities in BCC Fe, University of Michigan, 2025. https://doi.org/https://dx.doi.org/10.7302/25696.

[216] R.E. Stoller, G.R. Odette, Analytical solutions for helium bubble and critical radius parameters using a hard sphere equation of state, Journal of Nuclear Materials 131 (1985) 118–125. https://doi.org/10.1016/0022-3115(85)90450-7.

[217] H. Trinkaus, Energetics and formation kinetics of helium bubbles in metals, Radiat Eff 78 (1983) 189–211. https://doi.org/10.1080/00337578308207371.

[218] I.R. Brearley, D.A. MacInnes, An improved equation of state for inert gases at high pressures, Journal of Nuclear Materials 95 (1980) 239–252. https://doi.org/10.1016/0022-3115(80)90365-7.

[219] R.E. Stoller, Y.N. Osetsky, An atomistic assessment of helium behavior in iron, Journal of Nuclear Materials 455 (2014) 258–262. https://doi.org/10.1016/j.jnucmat.2014.06.020.

[220] A. Jelea, Molecular dynamics modeling of helium bubbles in austenitic steels, Nucl Instrum Methods Phys Res B 425 (2018) 50–54. https://doi.org/10.1016/j.nimb.2018.04.008.

[221] S. Schönecker, X. Li, B. Johansson, S.K. Kwon, L. Vitos, Thermal surface free energy and stress of iron, Sci Rep 5 (2015). https://doi.org/10.1038/srep14860.

[222] M.J.S. Spencer, A. Hung, I.K. Snook, I. Yarovsky, Density functional theory study of the relaxation and energy of iron surfaces, Surf Sci (2002). https://doi.org/10.1016/S0039-6028(02)01809-5.

[223] P. Błoński, A. Kiejna, Structural, electronic, and magnetic properties of bcc iron surfaces, Surf Sci 601 (2007) 123–133. https://doi.org/10.1016/j.susc.2006.09.013.

[224] W.R. Tyson, W.A. Miller, Surface Free Energies of Solid Metals: Estimation from Liquid Surface Tension Measurements, Surf Sci (1977) 267–276. https://doi.org/10.1016/0039-6028(77)90442-3.

[225] S. Schönecker, S.K. Kwon, B. Johansson, L. Vitos, Surface parameters of ferritic iron-rich Fe-Cr alloy, Journal of Physics Condensed Matter 25 (2013). https://doi.org/10.1088/0953-8984/25/30/305002.

[226] H.L. Heinisch, F. Gao, R.J. Kurtz, Atomistic modeling of helium interacting with screw dislocations in α-Fe, Journal of Nuclear Materials 367-370 A (2007) 311–315. https://doi.org/10.1016/j.jnucmat.2007.03.035.

[227] H.L. Heinisch, F. Gao, R.J. Kurtz, E.A. Le, Interaction of helium atoms with edge dislocations in α-Fe, Journal of Nuclear Materials 351 (2006) 141–148. https://doi.org/10.1016/j.jnucmat.2006.02.027.

[228] J.J. Burton, Vacancy-Formation Entropy in Cubic Metals, Phys Rev B 5 (1972) 2948–2957.

[229] M.N. Magomedov, Parameters of the vacancy formation and self-diffusion in the iron, Journal of Physics and Chemistry of Solids 172 (2023). https://doi.org/10.1016/j.jpcs.2022.111084.

[230] D.R. Olander, A.T. Motta, Light Water Reactor Materials, 2017.

[231] T.M.K. Green, T. Gräning, W. Zhong, Y. Yang, K.G. Field, MX precipitate behavior in an irradiated advanced Fe-9Cr steel: Self-ion irradiation effects on phase stability, Acta Mater 296 (2025). https://doi.org/10.1016/j.actamat.2025.121203.

[232] Metals Piping, T91 / P91 Steel, (2025). http://www.metalspiping.com/t91-p91-steel.html (accessed April 23, 2025).

[233] ThyssenKrupp Materials International, Material Data Sheet for P/T91, 2025. https://4.imimg.com/data4/FT/YG/MY-4947466/p92-alloy-steel.pdf (accessed April 23, 2025).

[234] Y. Wang, B. Yu, S. Gao, Q. Liu, J. Xu, Performance Analysis of Cooling Wall of Supercritical CO2 Coal-Fired Plants, Journal of Thermal Science 31 (2022) 1881–1890. https://doi.org/10.1007/s11630-022-1526-8.

[235] MakeItFrom.Com, ASTM A387 Grade 91 Class 2 (K90901) 9Cr-1Mo Steel, (2025). https://www.makeitfrom.com/material-properties/ASTM-A387-Grade-91-Class-2-K90901-9Cr-1Mo-Steel (accessed April 23, 2025).

[236] Alloy Digest, T91/P91, ASM International, 1993. https://doi.org/10.31399/asm.ad.sa0465.

[237] A.A. Kohnert, M.A. Cusentino, B.D. Wirth, Molecular statics calculations of the biases and point defect capture volumes of small cavities, Journal of Nuclear Materials 499 (2018) 480–489. https://doi.org/10.1016/j.jnucmat.2017.12.005.

[238] Y. Wang, F. Gao, B.D. Wirth, Atomic modeling assessment of the interaction distance and effective bias for small defect clusters absorption at a void in BCC Fe, Journal of Nuclear Materials 568 (2022). https://doi.org/10.1016/j.jnucmat.2022.153882.

[239] R.L. Mills, D.H. Liebenberg, J.C. Bronson, Equation of state and melting properties of He from measurements to 20 kbar, Phys Rev B 21 (1980) 5137–5148.

[240] A. Caro, J. Hetherly, A. Stukowski, M. Caro, E. Martinez, S. Srivilliputhur, L. Zepeda-Ruiz, M. Nastasi, Properties of Helium bubbles in Fe and FeCr alloys, Journal of Nuclear Materials 418 (2011) 261–268. https://doi.org/10.1016/j.jnucmat.2011.07.010.

[241] X.Z. Cao, Q. Xu, K. Sato, T. Yoshiie, Effects of dislocations on thermal helium desorption from nickel and iron, Journal of Nuclear Materials 417 (2011) 1034–1037. https://doi.org/10.1016/j.jnucmat.2010.12.212.

[242] P. Trocellier, S. Agarwal, S. Miro, A review on helium mobility in inorganic materials, Journal of Nuclear Materials 445 (2014) 128–142. https://doi.org/10.1016/j.jnucmat.2013.10.061.

[243] M.A. Tschopp, F. Gao, L. Yang, K.N. Solanki, Binding energetics of substitutional and interstitial helium and di-helium defects with grain boundary structure in α-Fe, J Appl Phys 115 (2014). https://doi.org/10.1063/1.4861719.

[244] M.A. Tschopp, F. Gao, K.N. Solanki, Binding of HenV clusters to α-Fe grain boundaries, J Appl Phys 115 (2014). https://doi.org/10.1063/1.4883357.

[245] L. Ventelon, B. Wirth, C. Domain, Helium-self-interstitial atom interaction in α-iron, Journal of Nuclear Materials 351 (2006) 119–132. https://doi.org/10.1016/j.jnucmat.2006.02.029.

[246] D. Stewart, Y. Osetskiy, R. Stoller, Atomistic studies of formation and diffusion of helium clusters and bubbles in BCC iron, Journal of Nuclear Materials 417 (2011) 1110–1114. https://doi.org/10.1016/j.jnucmat.2010.12.217.

[247] Z. Chang, D. Terentyev, N. Sandberg, K. Samuelsson, P. Olsson, Anomalous bias factors of dislocations in bcc iron, Journal of Nuclear Materials 461 (2015) 221–229. https://doi.org/10.1016/j.jnucmat.2015.03.025.

[248] W.G. Wolfer, The dislocation bias, Journal of Computer-Aided Materials Design 14 (2007) 403–417. https://doi.org/10.1007/s10820-007-9051-3.

[249] T. Jourdan, Influence of dislocation and dislocation loop biases on microstructures simulated by rate equation cluster dynamics, Journal of Nuclear Materials 467 (2015) 286–301. https://doi.org/10.1016/j.jnucmat.2015.09.046.

[250] D. Carpentier, T. Jourdan, Y. Le Bouar, M.C. Marinica, Effect of saddle point anisotropy of point defects on their absorption by dislocations and cavities, Acta Mater 136 (2017) 323–334. https://doi.org/10.1016/j.actamat.2017.07.013.

[251] E. Kuramoto, T. Tsutsumi, Computer simulation of the bias factor in void swelling in metals, Journal of Nuclear Materials 212–215 (1994) 175–178. https://doi.org/10.1016/0022-3115(94)90051-5.

[252] Y. Watanabe, K. Morishita, T. Nakasuji, M. Ando, H. Tanigawa, Helium effects on microstructural change in RAFM steel under irradiation: Reaction rate theory modeling,

Nucl Instrum Methods Phys Res B 352 (2015) 115–120. https://doi.org/10.1016/j.nimb.2014.12.031.

[253] V.I. Dubinko, A.S. Abyzov, A.A. Turkin, Numerical evaluation of the dislocation loop bias, Journal of Nuclear Materials 336 (2005) 11–21. https://doi.org/10.1016/j.jnucmat.2004.07.034.

[254] L. Huang, M. Nastar, L. Messina, T. Schuler, Elastodiffusion calculation of asymptotic absorption efficiencies and bias factors of dislocations in Al, Ni and Fe, Journal of Nuclear Materials 570 (2022). https://doi.org/10.1016/j.jnucmat.2022.153959.

[255] A. Bakaev, D. Terentyev, Z. Chang, M. Posselt, P. Olsson, E.E. Zhurkin, Effect of isotropic stress on dislocation bias factor in bcc iron: an atomistic study, Philosophical Magazine 98 (2018) 54–74. https://doi.org/10.1080/14786435.2017.1390325.

[256] Z. Yu, H. Xu, Dislocation loop bias and void swelling in irradiated α-iron from mesoscale and atomistic simulations, Commun Mater 4 (2023). https://doi.org/10.1038/s43246-023-00356-5.

[257] A.A. Kohnert, L. Capolungo, Sink strength and dislocation bias of three-dimensional microstructures, Phys Rev Mater 3 (2019). https://doi.org/10.1103/PhysRevMaterials.3.053608.

[258] R. Schäublin, P. Spätig, M. Victoria, Microstructure assessment of the low activation ferritic/ martensitic steel F82H, Journal of Nuclear Materials 258–263 (1998) 1178–1182. https://doi.org/10.1016/S0022-3115(98)00182-2.

[259] F. HajyAkbary, J. Sietsma, A.J. Böttger, M.J. Santofimia, An improved X-ray diffraction analysis method to characterize dislocation density in lath martensitic structures, Materials

Science and Engineering: A 639 (2015) 208–218. https://doi.org/10.1016/j.msea.2015.05.003.

[260] E. Aydogan, O. Anderoglu, S.A. Maloy, V. Livescu, G.T. Gray, S. Perez-Bergquist, D.J. Williams, Effect of shock loading on the microstructure, mechanical properties and grain boundary characteristics of HT-9 ferritic/martensitic steels, Materials Science and Engineering: A 651 (2016) 75–82. https://doi.org/10.1016/j.msea.2015.10.102.

[261] H. Sun, L.K. Béland, Statistical distribution of spontaneous recombination radii of Frenkel pairs in FCC and BCC metals, Acta Mater 229 (2022). https://doi.org/10.1016/j.actamat.2022.117814.

[262] T. Diaz De La Rubia, N. Soneda, M.J. Caturla, E.A. Alonso, Defect production and annealing kinetics in elemental metals and semiconductors, Journal of Nuclear Materials 25 (1997) 13–33. https://doi.org/10.1016/S0022-3115(97)00265-1.

[263] C.H.M. Broeders, A.Y. Konobeyev, Defect production efficiency in metals under neutron irradiation, Journal of Nuclear Materials 328 (2004) 197–214. https://doi.org/10.1016/j.jnucmat.2004.05.002.

[264] Nuclear Energy Agency, Primary Radiation Damage in Materials, 2015. www.oecd-nea.org.

[265] S.J. Zinkle, R.E. Stoller, Quantifying defect production in solids at finite temperatures: Thermally-activated correlated defect recombination corrections to DPA (CRC-DPA), Journal of Nuclear Materials 577 (2023). https://doi.org/10.1016/j.jnucmat.2023.154292.

[266] R.J. Kurtz, H.L. Heinisch, F. Gao, Modeling of He-defect interactions in ferritic alloys for fusion, Journal of Nuclear Materials 382 (2008) 134–142. https://doi.org/10.1016/j.jnucmat.2008.08.020.

[267] Y. Zhao, G. Lu, QM/MM study of dislocation - Hydrogen/helium interactions in α-Fe, Model Simul Mat Sci Eng 19 (2011). https://doi.org/10.1088/0965-0393/19/6/065004.

[268] E. Martínez, D. Schwen, A. Caro, Helium segregation to screw and edge dislocations in α-iron and their yield strength, Acta Mater 84 (2015) 208–214. https://doi.org/10.1016/j.actamat.2014.10.066.

[269] B. Zhu, M. Huang, Z. Li, Influence of helium-decoration on the interaction between 1/2<111> dislocation loop and edge dislocation in BCC iron, Journal of Nuclear Materials 528 (2020). https://doi.org/10.1016/j.jnucmat.2019.151866.

[270] M.A. Tschopp, F. Gao, K.N. Solanki, He–V cluster nucleation and growth in α-Fe grain boundaries, Acta Mater 124 (2017) 544–555. https://doi.org/10.1016/j.actamat.2016.11.027.

[271] J.L. Cao, W. Xiao, Q. Cao, B.L. He, First-Principles Study of Helium Trapping in Carbide Precipitates (Cr23C6) in Ferritic-Martensitic Steels, Fusion Science and Technology 74 (2018) 177–185. https://doi.org/10.1080/15361055.2017.1416245.

[272] Y. Jing, J. Ding, X. Wang, P. Zhang, S. Huang, J. Zhao, Helium behaviors at Mn6Ni16Si7 precipitate in α-Fe: Insights from ab initio modeling, Comput Mater Sci 181 (2020). https://doi.org/10.1016/j.commatsci.2020.109735.

[273] L.N. Clowers, The Role of Hydrogen Co-Injection on the Cavity Microstructure of Triple Ion Irradiated F82H-IEA, University of Michigan, 2025.

[274] C. Xu, G.S. Was, Anisotropic dislocation loop distribution in alloy T91 during irradiation creep, Journal of Nuclear Materials 454 (2014) 255–264. https://doi.org/10.1016/j.jnucmat.2014.07.062.

[275] K.G. Field, B.D. Miller, H.J.M. Chichester, K. Sridharan, T.R. Allen, Relationship between lath boundary structure and radiation induced segregation in a neutron irradiated 9 wt.% Cr model ferritic/martensitic steel, Journal of Nuclear Materials 445 (2014) 143–148. https://doi.org/10.1016/j.jnucmat.2013.10.056.

[276] L. Messina, M. Nastar, T. Garnier, C. Domain, P. Olsson, Exact ab initio transport coefficients in bcc Fe-X (X=Cr, Cu, Mn, Ni, P, Si) dilute alloys, Phys Rev B Condens Matter Mater Phys 90 (2014). https://doi.org/10.1103/PhysRevB.90.104203.

[277] M.B. Toloczko, F.A. Garner, Irradiation creep and void swelling of two LMR heats of HT9 at ~ 400°C and 165 dpa, Journal of Nuclear Materials 233–237 (1996) 289–292. https://doi.org/10.1016/S0022-3115(96)00413-8.

[278] O. Anderoglu, J. Van Den Bosch, P. Hosemann, E. Stergar, B.H. Sencer, D. Bhattacharyya, R. Dickerson, P. Dickerson, M. Hartl, S.A. Maloy, Phase stability of an HT-9 duct irradiated in FFTF, Journal of Nuclear Materials 430 (2012) 194–204. https://doi.org/10.1016/j.jnucmat.2012.06.038.

[279] A.M. Dvoriashin, S.I. Porollo, Y. V. Konobeev, F.A. Garner, Influence of high dose neutron irradiation on microstructure of EP-450 ferritic-martensitic steel irradiated in three Russian fast reactors, in: Journal of Nuclear Materials, 2004: pp. 319–323. https://doi.org/10.1016/j.jnucmat.2004.04.309.

[280] P. Dubuisson, D. Gilbon, J.L. Séran, Microstructural Evolution of Ferritic-Martensitic Steels Irradiated in the Fast Breeder Reactor Phenix, Journal of Nuclear Materials 205 (1993) 178.

[281] B.H. Sencer, J.R. Kennedy, J.I. Cole, S.A. Maloy, F.A. Garner, Microstructural stability of an HT-9 fuel assembly duct irradiated in FFTF, Journal of Nuclear Materials 414 (2011) 237–242. https://doi.org/10.1016/j.jnucmat.2011.03.050.

[282] H. Yan, X. Liu, L. He, J. Stubbins, Early-stage microstructural evolution and phase stability in neutron-irradiated ferritic-martensitic steel T91, Journal of Nuclear Materials 557 (2021). https://doi.org/10.1016/j.jnucmat.2021.153207.

[283] F.A. Garner, N. Sekimura, M.L. Grossbeck, A.M. Ermi, J.W. Newkirk, H. Watanabe, M. Kiritani, Influence of details of reactor history on microstructural development during neutron irradiation, Journal of Nuclear Materials 205 (1993) 206–218. https://doi.org/10.1016/0022-3115(93)90083-B.

[284] J. Byggmästar, F. Granberg, A.E. Sand, A. Pirttikoski, R. Alexander, M.C. Marinica, K. Nordlund, Collision cascades overlapping with selfinterstitial defect clusters in Fe and W, Journal of Physics Condensed Matter 21 (2019). https://doi.org/10.1088/1361-648X/ab0682.

[285] A.E. Sand, J. Byggmästar, A. Zitting, K. Nordlund, Defect structures and statistics in overlapping cascade damage in fusion-relevant bcc metals, Journal of Nuclear Materials 511 (2018) 64–74. https://doi.org/10.1016/j.jnucmat.2018.08.049.

[286] G. VanCoevering, Prediction of Bubble and Cavity Nucleation in High Damage Rate Irradiation of Simulated Fe-Cr Alloys Using a Hybrid Cluster Dynamics Model, University of Michigan, 2020. http://jurnal.globalhealthsciencegroup.com/index.php/JPPP/article/download/83/65%0Ahttp://www.embase.com/search/results?subaction=viewrecord&from=export&id=L6035468

64%5Cnhttp://dx.doi.org/10.1155/2015/420723%0Ahttp://link.springer.com/10.1007/978-3-319-76.

[287] M.B. Toloczko, F.A. Garner, C.R. Eiholzer, Irradiation creep and swelling of the US fusion heats of HT9 and 9Cr-1Mo to 208 dpa at ~ 400°C, Journal of Nuclear Materials 212–215 (1994) 604–607. https://doi.org/10.1016/0022-3115(94)90131-7.

[288] J. Gao, Q. Yuan, E. Gaganidze, J. Aktaa, On the shrinkage of neutron irradiation-induced cavities in Eurofer97 steel upon heating, Philosophical Magazine 103 (2023) 240–265. https://doi.org/10.1080/14786435.2022.2143593.

[289] M. Kiritani, The need for improved temperature control during reactor irradiation, Journal of Nuclear Materials 160 (1988) 135–141. https://doi.org/10.1016/0022-3115(88)90040-2.

[290] K. Shiraishi, K. Fukaya, K. Fukai, EFFECT OF HELIUM ON MICROSTRUCTURE IN TYPE 316 STAINLESS STEEL, Journal of Nuclear Materials 119 (1983) 268–277.

[291] E. Wakai, Y. Miwa, N. Hashimoto, J.P. Robertson, R.L. Klueh, K. Shiba, K. Abiko, S. Furuno, S. Jitsukawa, Microstructural study of irradiated isotopically tailored F82H steel, Journal of Nuclear Materials (2002) 203–211. www.elsevier.com/locate/jnucmat.

[292] B.K. Kim, L. Tan, H. Sakasegawa, C.M. Parish, W. Zhong, H. Tanigawa, Y. Katoh, Effects of helium on irradiation response of reduced-activation ferritic-martensitic steels: Using nickel isotopes to simulate fusion neutron response, Journal of Nuclear Materials 545 (2021). https://doi.org/10.1016/j.jnucmat.2020.152634.

[293] N. Hashimoto, R.L. Klueh, Microstructural evolution of nickel-doped 9Cr steels irradiated in HFIR, Journal of Nuclear Materials (2002) 153–158. https://doi.org/https://doi.org/10.1016/S0022-3115(02)01026-7.

[294] W. Zhang, Y. Chen, W. Cheng, L. Guo, S. Jin, Study on the mechanism of He effect on dislocation loop formation in three types of dual ion beam irradiations, Journal of Nuclear Materials 588 (2024). https://doi.org/10.1016/j.jnucmat.2023.154782.

[295] Q. Zheng, M. Chen, B. Chen, S. Wen, C. Zheng, S. Liu, G. Bai, J. Li, Evolution of dislocation loops in chromium under single hydrogen and helium ion irradiation, Nucl Instrum Methods Phys Res B 559 (2025). https://doi.org/10.1016/j.nimb.2024.165602.

[296] K. Arakawa, H. Mori, K. Ono, Formation process of dislocation loops in iron under irradiations with low-energy helium, hydrogen ions or high-energy electrons, Journal of Nuclear Materials (2002) 272–277. www.elsevier.com/locate/jnucmat.

[297] M. Wu, J. Huang, Z. Cao, Y. Ding, Q. Zhong, Y. Zhao, G. Ran, Effect of hydrogen, helium and dose rate on the evolution of dislocation loop in pure iron during in-situ ion irradiation, Journal of Nuclear Materials 598 (2024). https://doi.org/10.1016/j.jnucmat.2024.155161.

[298] M.L. Lescoat, J. Ribis, Y. Chen, E.A. Marquis, E. Bordas, P. Trocellier, Y. Serruys, A. Gentils, O. Kaïtasov, Y. De Carlan, A. Legris, Radiation-induced Ostwald ripening in oxide dispersion strengthened ferritic steels irradiated at high ion dose, Acta Mater 78 (2014) 328–340. https://doi.org/10.1016/j.actamat.2014.06.060.

[299] F.A. Garner, A.M. Ermi, N. Sekimura, J.W. Newkirk, Effect of MOTA Shutdown Procedure on Radiation-Induced Microstructural Evolution in: Fusion Reactor Materials Semiannual Progress Report for Period Ending September 30, 1991, 1991.

[300] M. Horiki, T. Yoshiie, Q. Xu, M. Iseki, M. Kiritani, Defect structures introduced in iron under varying temperature neutron irradiation, Journal of Nuclear Materials 283–287 (2000) 282–285. https://doi.org/10.1016/S0022-3115(00)00105-7.

[301] R. Mateus, N. Catarino, M. Dias, L.C. Alves, O. Romanenko, Z. Siketić, I.B. Radović, A. Hakola, E. Grigore, E. Alves, Deuterium and helium retention in W and W-Ta coatings irradiated with energetic ion beams, Nucl Instrum Methods Phys Res B 538 (2023) 41–46. https://doi.org/10.1016/j.nimb.2023.02.028.

[302] X. Hu, K.G. Field, S. Taller, Y. Katoh, B.D. Wirth, Impact of neutron irradiation on thermal helium desorption from iron, Journal of Nuclear Materials 489 (2017) 109–117. https://doi.org/10.1016/j.jnucmat.2017.03.034.

[303] A.J. Koning, D. Rochman, J.C. Sublet, N. Dzysiuk, M. Fleming, S. van der Marck, TENDL: Complete Nuclear Data Library for Innovative Nuclear Science and Technology, Nuclear Data Sheets 155 (2019) 1–55. https://doi.org/10.1016/j.nds.2019.01.002.